Muon $(g-2)$ Conceptual Design Report

E989 Collaboration

Wednesday 8th May, 2013

DISCLAIMER

Executive Summary

This Conceptual Design Report details a new experiment for Fermilab to measure the muon anomalous magnetic dipole moment, or anomaly, at least a factor of four more precisely than the E821 collaboration did at the Brookhaven AGS. The muon anomaly a_μ is a low-energy observable, which can be both measured and computed to high precision, with both theory and experiment having reached the sub-part-per-million (ppm) level of precision. For many years, a_μ has played an important role in constraining models of "New Physics" beyond the standard model, and will continue to do so in the LHC era. The Standard-Model value has contributions from quantum electrodynamics (QED), the weak interaction, and from strongly interacting particles in vacuum polarization and "light-by-light" scattering diagrams.

The present experimental value appears to be larger than the expected Standard-Model value by greater than three standard deviations, which could be a harbinger of New Physics, and strongly motivates the new experiment. In addition to the expected experimental improvement of a factor of four, the uncertainly on the Standard-Model value will also be improved. One very important recent theoretical development is that lattice calculations are becoming relevant in the determination of the strong-interaction contributions.

BNL E821 has been a very high-impact experiment, with over 2000 citations to their four major papers, and over 2200 citations to all of those reporting physics results.

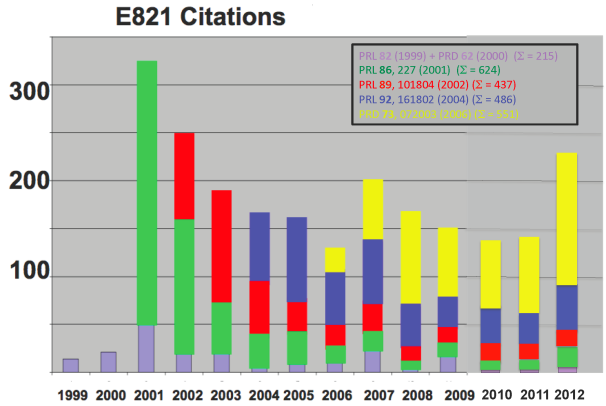

The experiment will also be optimised to improve significantly on the CP-forbidden electric dipole moment (EDM) of the muon. This presents a unique opportunity to search for an EDM of a second-generation particle. With proper design, the EDM sensitivity could reach two orders of magnitude beyond the present limit of $d_\mu < 1.8 \times 10^{-18}\, e$cm obtained by BNL E821.

A number of major components from E821 will be relocated to Fermilab and reused. The precision 700 T superconducting storage ring magnet built at Brookhaven will be relocated to Fermilab and installed in a new building on the Muon Campus. An 8 GeV proton beam from the Booster Accelerator will be injected into the recycler ring, rebunched, and one bunch at at time will be extracted to a a new pion production target at the location of the former antiproton production target. The resulting pion beam will be transported to the repurposed antiproton debuncher ring, now called the Delivery Ring, which will be used as

a 1,900 m decay line. The resulting muon beam will be extracted from the Delivery Ring and brought to the new MC1 building and injected into the muon storage ring. The MC1 building will be a general purpose building, suitable for the $(g-2)$ experiment, as well as for future experiments on the muon campus.

While the storage ring magnet, power supply, and vacuum chambers are being reused, the fast muon kicker, the electrostatic quadrupole system, the field monitoring and control system, the detectors, electronics, data acquisition system will all be upgraded.

...

(includes intro, precision goal, scope, capabilities, cost and schedule)

Contents

Chapter 1

Project Overview

1.1 Mission and Scope

1.1.1 Muon Beam

1.1.2 Storage Ring

1.1.3 Precision Magnetic Field

1.1.4 Detectors

1.2 $(g-2)$ and the Muon Campus

1.3 Conventional Facilities

1.4 Organization

1.4.1 Management

1.4.2 WBS

1.4.3 Controls

1.4.4 Quality Assurance

1.4.5 ES&H

1.4.6 Configuration Management

1.4.7 Risk Management

1.4.8 Cost and Schedule

1.5 References

Chapter 2

Introduction and Physics Motivation

2.1 Introduction

This chapter gives the physics context of magnetic moment measurements, the Standard Model expectations, along with the reach of such experiments to identify and constrain physics beyond the Standard Model. Except for a broad-brush mention of the experimental technique, the details are left for later chapters. Chapter 3 gives an overview of the experimental method, and the subsequent chapters give the details. We attempt to follow the WBS structure in those later chapters.

2.2 Magnetic and Electric Dipole Moments

The study of magnetic moments of subatomic particles grew up with the development of quantum mechanics. For fermions the magnetic dipole moment (MDM) is related to the spin by

$$\vec{\mu} = g\frac{Qe}{2m}\vec{s}. \tag{2.1}$$

where $Q = \pm 1$ and $e > 0$. Our modern interpretation of the Stern-Gerlach experiments [1] is that their observation that: "to within 10% the magnetic moment of the silver atom is one Bohr magneton" was telling us that the g-factor of the un-paired electron is equal to 2. However, reaching this conclusion required the discovery of spin [3], quantum mechanics [4] along with with Thomas' relativistic correction [5]. Phipps and Taylor [6] repeated the Stern-Gerlach experiment in hydrogen, and mentioned the electron spin explicitly. One of the great successes of Dirac's relativistic theory [7] was the prediction that $g \equiv 2$.

For some years, the experimental situation remained the same. The electron had $g = 2$, and the Dirac equation seemed to describe nature. Then a surprising and completely unexpected result was obtained. In 1933, against the advice of Pauli who believed that the proton was a pure Dirac particle [8], Stern and his collaborators [9] showed that the g-factor of the proton was ~ 5.5, not the expected value of 2. Even more surprising was the discovery in 1940 by Alvarez and Bloch [10] that the neutron had a large magnetic moment.

In 1947, motivated by measurements of the hyperfine structure in hydrogen that obtained splittings larger than expected from the Dirac theory [11, 12, 13], Schwinger [14] showed that

from a theoretical viewpoint these "discrepancies can be accounted for by a small additional electron spin magnetic moment" that arises from the lowest-order radiative correction to the Dirac moment[1],

$$\frac{\delta\mu}{\mu} = \frac{1}{2\pi}\frac{e^2}{\hbar c} = 0.001162. \tag{2.2}$$

It is useful to break the magnetic moment into two terms:

$$\mu = (1+a)\,\frac{e\hbar}{2m}, \quad \text{where} \quad a = \frac{(g-2)}{2}. \tag{2.3}$$

The first term is the Dirac moment, 1 in units of the appropriate magneton $e\hbar/2m$. The second term is the anomalous (Pauli) moment [15], where the dimensionless quantity a (Schwinger's $\delta\mu/\mu$) is sometimes referred to as the *anomaly*.

2.2.1 The Muon

The muon was first observed in a Wilson cloud chamber by Kunze[16] in 1933, where it was reported to be "a particle of uncertain nature." In 1936 Anderson and Neddermeyer[17] reported the presence of "particles less massive than protons but more penetrating than electrons" in cosmic rays, which was confirmed in 1937 by Street and Stevenson[18], Nishina, Tekeuchi and Ichimiya[19], and by Crussard and Leprince-Ringuet[20]. The Yukawa theory of the nuclear force had predicted such a particle, but this "mesotron" as it was called, interacted too weakly with matter to be the carrier of the strong force. Today we understand that the muon is a second generation lepton, with a mass about 207 times the electron's. Like the electron, the muon obeys quantum electrodynamics, and can interact with other particles through the electromagnetic and weak forces. Unlike the electron which appears to be stable, the muon decays through the weak force predominantly by $\mu^- \to e^-\nu_\mu\bar{\nu}_e$. The muon's long lifetime of $\simeq 2.2$ μs permits precision measurements of its mass, lifetime, and magnetic moment.

2.2.2 The Muon Magnetic Moment

The magnetic moment of the muon played an important role in the discovery of the generation structure of the Standard Model (SM). The pioneering muon spin rotation experiment at the Nevis cyclotron observed parity violation in muon decay [21], and also showed that g_μ was consistent with 2. Subsequent experiments at Nevis [24] and CERN [25] showed that $a_\mu \simeq \alpha/(2\pi)$, implying that in a magnetic field, the muon behaves like a heavy electron. Two additional experiments at CERN required that contributions from higher-order QED [26], and then from virtual hadrons [27] be included into the theory in order to reach agreement with experiment.

2.2.3 The Muon Electric Dipole Moment

Dirac [7] discovered an electric dipole moment (EDM) term in his relativistic electron theory. Like the magnetic dipole moment, the electric dipole moment must be along the spin. We

[1] A misprint in the original paper has been corrected here.

can write an EDM expression similar to Eq. (2.1),

$$\vec{d} = \eta \left(\frac{Qe}{2mc} \right) \vec{s}, \tag{2.4}$$

where η is a dimensionless constant that is analogous to g in Eq. (2.1). While magnetic dipole moments (MDMs) are a natural property of charged particles with spin, electric dipole moments (EDMs) are forbidden both by parity and by time reversal symmetry.

The search for an EDM dates back to the suggestion of Purcell and Ramsey [28] in 1950, well in advance of the paper by Lee and Yang [29], that a measurement of the neutron EDM would be a good way to search for parity violation in the nuclear force. An experiment was mounted at Oak Ridge [30] soon thereafter that placed a limit on the neutron EDM of $d_n < 5 \times 10^{-20}$ e-cm, although the result was not published until after the discovery of parity violation.

Once parity violation was established, Landau [31] and Ramsey [32] pointed out that an EDM would violate both P and T symmetries. This can be seen by examining the Hamiltonian for a spin one-half particle in the presence of both an electric and magnetic field,

$$\mathcal{H} = -\vec{\mu} \cdot \vec{B} - \vec{d} \cdot \vec{E}. \tag{2.5}$$

The transformation properties of $\vec{E}$, $\vec{B}$, $\vec{\mu}$ and $\vec{d}$ are given in Table 2.2.3, and we see that while $\vec{\mu} \cdot \vec{B}$ is even under all three symmetries, $\vec{d} \cdot \vec{E}$ is odd under both P and T. Thus the existence of an EDM implies that both P and T are not good symmetries of the interaction Hamiltonian, Eq. (2.5). The EDM is a CP-odd quantity, and if observed, would be the manifestation of a new source of CP violation. The search for a muon EDM provides a unique opportunity to search for an EDM of a second-generation particle.

Table 2.1: Transformation properties of the magnetic and electric fields and dipole moments.

	$\vec{E}$	$\vec{B}$	$\vec{\mu}$ or $\vec{d}$
P	-	+	+
C	-	-	-
T	+	-	-

Concerning these symmetries, Ramsey states [32]:

> "However, it should be emphasized that while such arguments are appealing from the point of view of symmetry, they are not necessarily valid. Ultimately the validity of all such symmetry arguments must rest on experiment."

Fortunately this advice has been followed by many experimental investigators during the intervening 50 years. Since the Standard Model CP violation observed in the neutral kaon and B-meson systems is inadequate to explain the predominance of matter over antimatter in the universe, the search for new sources of CP violation beyond that embodied in the CKM formalism takes on a certain urgency. Searches for a permanent electric dipole moment of

the electron, neutron, and of an atomic nucleus have become an important part of the search for physics beyond the Standard Model. The present limits on subatomic EDMs is given in Table 2.2.3.

Table 2.2: EDM Limits for various systems

Particle	EDM Limit (e-cm)	SM value (e-cm)
p [33]	7.9×10^{-25}	
n [34]	2.9×10^{-26}	$\simeq 10^{-32}$
^{199}Hg [33]	3.1×10^{-29}	$\simeq 10^{-32}$
e^- [35]	1.05×10^{-27}	$< 10^{-41}$
μ [36]	1.8×10^{-19}	$< 10^{-38}$

2.3 Quick Summary of the Experimental Teachnique

Polarized muons are produced (see Chapter 7) and injected into the storage ring (see Chapter 12). The magnetic field is a dipole field, shimmed to ppm level uniformity. Vertical focusing is provided by electrostatic quadrupoles (see Chapter 13).

Two frequencies are measured experimentally: The rate at which the muon polarization turns relative to the momentum, called ω_a, and the value of the magnetic field, normalized in terms normalized to the Larmor frequency of a free proton, ω_p.

The rate at which the spin[2] turns relative to the momentum, $\vec{\omega}_a = \vec{\omega}_S - \vec{\omega}_C$, where S and C stand for spin and cyclotron. These two frequencies are given by

$$\omega_S = -g\frac{Qe}{2m}B - (1-\gamma)\frac{Qe}{\gamma m}B; \tag{2.6}$$

$$\omega_C = -\frac{Qe}{m\gamma}B; \tag{2.7}$$

$$\omega_a = \omega_S - \omega_C = -\left(\frac{g-2}{2}\right)\frac{Qe}{m}B = -a\frac{Qe}{m}B \tag{2.8}$$

(where $e > 0$ and $Q = \pm 1$). There are two important features of ω_a: (i) It only depends on the anomaly rather than on the full magnetic moment; (ii) It depends linearly on the applied magnetic field. In the presence of an electric field ω_a is modified

$$\vec{\omega}_a = -\frac{Qe}{m}\left[a_\mu \vec{B} + \left(a_\mu - \left(\frac{m}{p}\right)^2\right)\frac{\vec{\beta}\times\vec{E}}{c}\right] - \eta\frac{Qe}{2m} \tag{2.9}$$

If operated at the "magic" momentum $p_{magic} = m/\sqrt{a_\mu} \simeq 3.09$ GeV/c the electric field contribution cancels in first order, and requires a small correction in second order.

[2]The term 'spin' is often used in place of the more accurate term 'polarization'

The magnetic field is weighted by the muon distribution, and also averaged over the running time weighed by the number of stored muons to determine the value of ω_p which is combined with the average ω_a to determine a_μ. The reason for the use of these two frequencies, rather than B measured in tesla can be understood from Eq. 2.9. To obtain a_μ from this relationship requires precise knowledge of the muon charge to mass ratio.

To determine a_μ from the two frequencies ω_a and ω_p, we use the relationship

$$a_\mu = \frac{\omega_a/\omega_p}{\lambda_+ - \omega_a/\omega_p} = \frac{\mathcal{R}}{\lambda_+ - \mathcal{R}}\,, \tag{2.10}$$

where the ratio $\lambda_+ = \mu_{\mu^+}/\mu_p = 3.183\,345\,137\,(85)$ is the muon-to-proton magnetic moment ratio [41] measured from muonium (the μ^+e^- atom) hyperfine structure[43]. Of course, to use λ_+ to determine a_{μ^-} requires the assumption of *CPT* invariance, *viz.* ($a_{\mu^+} = a_{\mu^-}$; $\lambda_+ = \lambda_-$). The comparison of $\mathcal{R}_{\mu^+}$ with $\mathcal{R}_{\mu^-}$ provides a *CPT* test. In E821

$$\Delta\mathcal{R} = \mathcal{R}_{\mu^-} - \mathcal{R}_{\mu^+} = (3.6 \pm 3.7) \times 10^{-9} \tag{2.11}$$

2.4 Results from E821

2.4.1 Measurement of a_μ

The E821 Collaboration working at the Brookhaven Laboratory AGS used an electric quadrupole field to provide vertical focusing in the storage ring, and shimmed the magnetic field to ± 1 ppm uniformity on average. The storage ring was operated at the "magic" momentum, $p_{magic} = 3.094$ GeV/c, ($\gamma_{magic} = 29.3$), such that $a_\mu = (m/p)^2$ and the electric field did not contribute to ω_a.[3] The result is [38, 39]

$$a_\mu^{\rm E821} = 116\,592\,089(54)_{stat}(33)_{syst}(63)_{tot} \times 10^{-11} \quad (\pm 0.54\,\text{ppm}). \tag{2.12}$$

The results from E821 are shown in Fig. 2.1 along with the Standard-Model value which is discussed below in Section 2.5

2.4.2 Measurement of the Muon EDM: d_μ

If the muon has an electric dipole moment (EDM) then the dominant effect in the spin motion is the motional electric field proportional to $\vec{\beta} \times \vec{B}$. This motional electric field produces a torque on the EDM $\vec{d} \times \vec{\beta} \times \vec{B}$ that is perpindicular to $\vec{B}$ and $\vec{\beta}$. The result is is an up-down oscillation of the spin out of phase with ω_a, as discussed below in Section 3.7. No evidence for an up-down oscillation was seen, and the result is[36]

$$d_\mu = (0.1 \pm 0.9) \times 10^{-19} e{-}\text{cm};\ |d_\mu| < 1.9 \times 10^{-19} e{-}\text{cm}\ (95\%\ \text{C.L.})\,, \tag{2.13}$$

a factor of five smaller than the previous limit.

[3] The magic momentum was first employed by the third CERN collaboration [27].

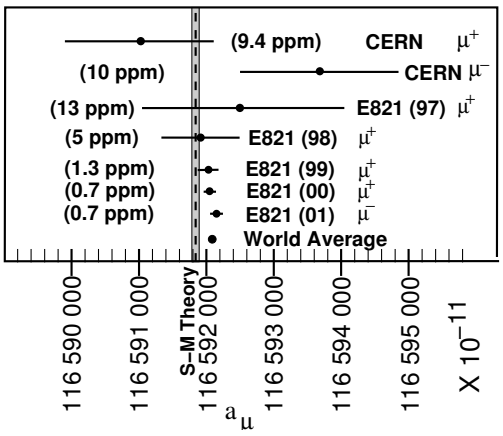

Figure 2.1: Measurements of a_μ from CERN and BNL E821. The vertical band is the SM value using the hadronic contribution from Ref. [47] (see Table 2.3).

2.5 The Standard-Model Value of a_μ

In this section we present the standard model (SM) theory of the muon anomalous magnetic moment (anomaly). In the following section we discuss physics beyond the standard model (BSM) that could contribute to the anomaly at a measurable level. The conclusion is that muon $(g-2)$ will play a powerful role in the interpretation of new phenomena that might be discovered at the LHC. If new phenomena are not discovered there, then muon $(g-2)$ becomes even more important, since it would provide one of the few remaining ways to search for new physics at the TeV scale.

2.5.1 Introduction

The magnetic moment of the muon (or electron), which is aligned with its spin, is given by

$$\vec{\mu} = g\frac{Qe}{2m_{\mu,e}}\vec{s}, \qquad \underbrace{g=2}_{\text{Dirac}}(1+a_\mu)\,; \tag{2.14}$$

where the quantity g is exactly 2 in the Dirac theory, $Q = \pm 1$ with e a positive number. The small number a, the anomaly, arises from quantum fluctuations, with the largest contribution coming from the single loop diagram in Fig. 2.2(a). This contribution was first calculated by Schwinger [14], who obtained $a = (\alpha/2\pi) = 0.00116\cdots$. These calculations have been extended to higher powers in α/π, with the fourth- $(\alpha/\pi)^2$ and sixth-order $(\alpha/\pi)^3$ contributions having been carried out analytically.

The electron anomaly is relatively insensitive to heavier physics, so in principle the 0.03 ppb measurement of the electron anomaly [67] should provide a test of QED, but the few ppb precision of the *independent* measurements of α prevents this comparison. Alternately, one can accept that QED is valid and use the electron anomaly to determine the most precise measurement of α [68].

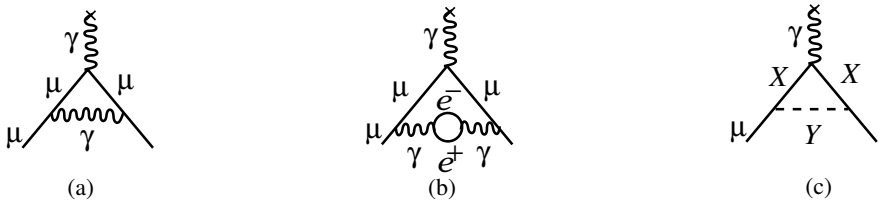

Figure 2.2: The Feynman graphs for: (a) The lowest-order (Schwinger) contribution to the lepton anomaly ; (b) The vacuum polarization contribution, which is one of five fourth-order, $(\alpha/\pi)^2$, terms; (c) The schematic contribution of new particles X and Y that couple to the muon. **The $\times$ indicates the virtual photon from the magnetic field.**

The muon anomaly is an entirely different case. The relative contribution to the muon anomaly of heavier virtual particles goes as $(m_\mu/m_e)^2 \simeq 43000$, so with much less precision when compared with the electron, the muon anomaly is sensitive to mass scales in the several hundred GeV region. This not only includes the expected contribution of the W and Z bosons, but perhaps contributions from new, as yet undiscovered, particles such as the supersymmetric partners of the electro-weak gauge bosons (see Fig. 2.2(c)).

The standard-model value of a_μ has three contributions from radiative processes: QED loops containing leptons (e, μ, τ) and photons; loops containing hadrons in vacuum polarization loops where the e^+e^- pair in Fig 2.2(b) is replaced by hadrons; and weak loops involving the weak gauge bosons W, Z, and Higgs such as is shown in Fig. 2.2(c) where $X = W$ and $Y = \nu$, or $X = \mu$ and $Y = Z$. Thus

$$a_\mu^{\rm SM} = a_\mu^{\rm QED} + a_\mu^{\rm hadronic} + a_\mu^{\rm weak}. \tag{2.15}$$

The QED and weak contributions to the muon anomaly are now well understood at the level needed for the comparison of Standard-Model theory with experiment.

The hadronic contribution must be determined from a dispersion relation using experimental data, namely the cross sections for electron-positron annihilation to hadrons. The determination of this contribution represents a worldwide effort which was driven primarily by the existence of BNL experiment E821. The possibility of a new Fermilab experiment has already stimulated further work that will certainly continue unabated if P989 turns into an approved and funded experiment.

2.5.2 QED Contribution

The QED and electroweak contributions to a_μ are well understood. Recently the four-loop contribution has been updated and the full five-loop contribution has been calculated [66].

We take the numerical values from the review by Miller, et al, [75] with the QED contribution updated to the Höcker and Marciano [70]. The QED contribution to a_μ has been calculated through tenth order (five loops) [66]. The present value is

$$a_\mu^{\rm QED} = 116\ 584\ 718.951\ (0.009)(0.019)(0.007)(.077) \times 10^{-11} \tag{2.16}$$

where the uncertainties are from the lepton mass ratios, the eight-order term, the tenth-order term, and the value of α taken from the ^{87}Rb atom $\alpha^{-1}(Rb) = 137.035\,999\,049(90)$ [0.66 ppb]. [69].

2.5.3 Weak contributions

The electroweak contribution (shown in Fig. 2.3) is now calculated through two loops [50, 51, 52, 53, 56]. The single loop result

$$\begin{aligned} a_\mu^{\mathrm{EW}(1)} &= \frac{G_F}{\sqrt{2}}\frac{m_\mu^2}{8\pi^2}\left\{ \underbrace{\frac{10}{3}}_{W} + \underbrace{\frac{1}{3}(1-4\sin^2\theta_W)^2 - \frac{5}{3}}_{Z} \right. \\ &+ \left. \mathcal{O}\left(\frac{m_\mu^2}{M_Z^2}\log\frac{M_Z^2}{m_\mu^2}\right) + \frac{m_\mu^2}{M_H^2}\int_0^1 dx \frac{2x^2(2-x)}{1-x+\frac{m_\mu^2}{M_H^2}x^2} \right\} \\ &= 194.8\times 10^{-11}\,, \end{aligned} \tag{2.17}$$

was calculated by five separate groups shortly after the Glashow-Salam-Weinberg theory was shown by 't Hooft to be renormalizable. With the present limit on the Higgs boson mass, only the W and Z contribute to the lowest-order electroweak at a measurable level.

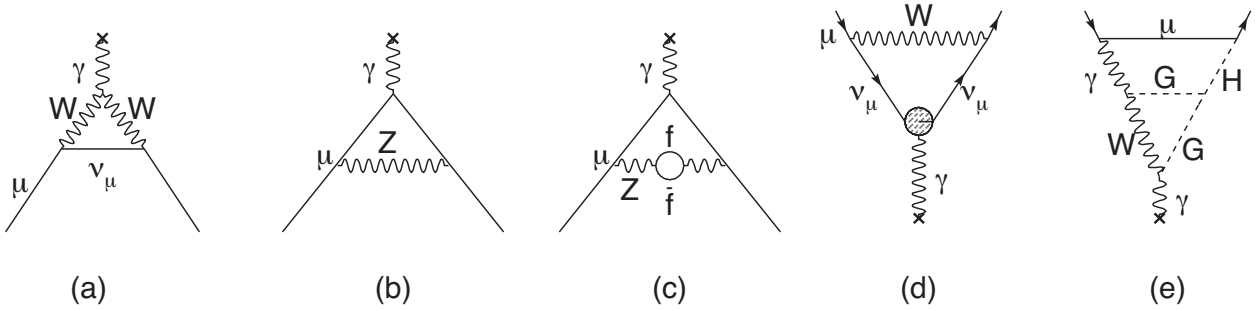

Figure 2.3: Weak contributions to the muon anomalous magnetic moment. Single-loop contributions from (a) virtual W and (b) virtual Z gauge bosons. These two contributions enter with opposite sign, and there is a partial cancellation. The two-loop contributions fall into three categories: (c) fermionic loops which involve the coupling of the gauge bosons to quarks, (d) bosonic loops which appear as corrections to the one-loop diagrams, and (e) a new class of diagrams involving the Higgs where G is the longitudinal component of the gauge bosons. See Ref. [54] for details. The $\times$ indicates the virtual photon from the magnetic field.

The two-loop weak contribution, (see Figs. 2.3(c-e) for examples) is negative, and the total electroweak contribution is [75]

$$a_\mu^{\mathrm{EW}} = 154(1)\times 10^{-11} \tag{2.18}$$

where the error comes from hadronic effects in the second-order electroweak diagrams with quark triangle loops. and the latter comes from the uncertainty on the Higgs mass [52, 51,

50, 17, 55]. The leading logs for the next-order term have been shown to be small [56]. The weak contribution is about 1.3 ppm of the anomaly, so the experimental uncertainty on a_μ of ± 0.54 ppm now probes the weak scale of the standard model.

Hadronic contribution

The hadronic contribution to a_μ is about 60 ppm of the total value. The lowest-order diagram shown in Fig. 2.4(a) dominates this contribution and its error, but the hadronic light-by-light contribution Fig. 2.4(e) is also important. We discuss both of these contributions below.

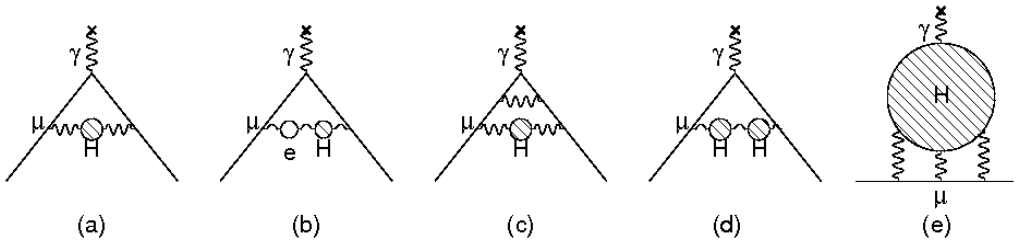

Figure 2.4: The hadronic contribution to the muon anomaly, where the dominant contribution comes from the lowest-order diagram (a). The hadronic light-by-light contribution is shown in (e).

The energy scale for the virtual hadrons is of order $m_\mu c^2$, well below the perturbative region of QCD. Thus it must be calculated from the dispersion relation shown pictorially in Fig. 2.5,

$$a_\mu^{\mathrm{had;LO}} = \left(\frac{\alpha m_\mu}{3\pi}\right)^2 \int_{4m_\pi^2}^{\infty} \frac{ds}{s^2} K(s) R(s), \quad \text{where} \quad R \equiv \frac{\sigma_{\mathrm{tot}}(e^+e^- \to \text{hadrons})}{\sigma(e^+e^- \to \mu^+\mu^-)}\,, \tag{2.19}$$

using the measured cross sections for $e^+e^- \to$ hadrons as input, where $K(s)$ is a kinematic factor ranging from **0.63** at $s = 4m_\pi^2$ to 1 at $s = \infty$. This dispersion relation relates the bare cross section for e^+e^- annihilation into hadrons to the hadronic vacuum polarization contribution to a_μ. Because the integrand contains a factor of s^{-2}, the values of $R(s)$ at low energies (the ρ resonance) dominate the determination of $a_\mu^{\mathrm{had;LO}}$, however at the level of precision needed, the data up to 2 GeV are very important. This is shown in Fig. 2.6, where the left-hand chart gives the relative contribution to the integral for the different energy regions, and the right-hand gives the contribution to the error squared on the integral. The contribution is dominated by the two-pion final state, but other low-energy multi-hadron cross sections are also important.

These data for e^+e^- annihilation to hadrons are also important as input into the determination of $\alpha_s(M_Z)$ and other electroweak precision measurements, including the limit on the Higgs mass [71].

In the 1980s when E821 was being proposed at Brookhaven, the hadronic contribution was know to about 10 ppm. It now is known to about 0.4 ppm. This improvement has come from the hard work of many experimental and theoretical physicists. The low energy e^+e^- data of the 80s have been replaced by very precise data from the CMD2 and SND collaborations

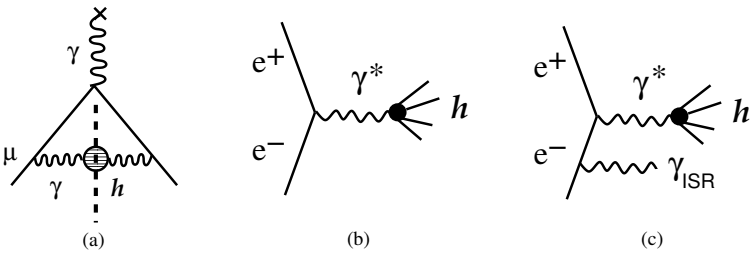

Figure 2.5: (a) The "cut" hadronic vacuum polarization diagram; (b) The e^+e^- annihilation into hadrons; (c) Initial state radiation accompanied by the production of hadrons.

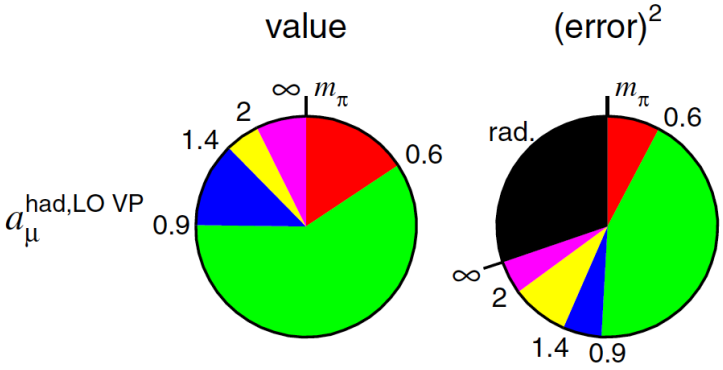

Figure 2.6: Contributions to the dispersion integral, and to the error on the dispersion integral. Taken from Hagirawa, et al., [48]

in Novosibirsk, the KLOE collaboration at Frascati, and the BaBar collaboration at SLAC. The new VEPP-2000 collider in Novosibirsk has been operational for several years, with two upgraded detectors, CMD-3 and SND-2000. This new facility will permit both energy scans, and the use of initial-state radiation to measure cross sections up to 2.0 GeV. Additional data on multi-hadron final states are expected from the Belle detector at KEK **and BES-III at BEPC**.

In addition to the collider experiments, significant theoretical work has been carried out in generating the radiator functions used in the initial-state radiation (ISR) experiments, as KLOE and BaBar [81, 82], as well as on the hadronic light-by-light contribution shown in Fig. 2.4(e).

The worldwide effort to improve our knowledge of the hadronic contribution continues to this day [90, 91]. The most recent $\pi\pi$-final state measurements were reported by the BaBar [83] and KLOE [86, 87] collaborations. An independent analysis of KLOE data using the direct measurement of $\sigma(e^+e^- \to \pi^+\pi^-)/\sigma(e^+e^- \to \mu^+\mu^-)$, which agreed well with their previous analysis using the luminosity measurement and QED calculations, **has been recently published** [92].

Muon $(g-2)$, and the determination of the hadronic contribution continues to feature prominently in the international workshops Tau [84] and PHIPSI [85], where sessions were devoted to all issues around muon $(g-2)$. We emphasize that while this is a difficult subject,

progress will continue to be made, provided that a new experiment does indeed go forward at Fermilab.

Lowest- and next-lowest-order hadronic contribution

The cross sections at low energies dominate the dispersion relation, and until recently the low-energy electron-positron storage rings in Novosibirsk and Frascati provided the bulk of the new measurements. The Novosibirsk experiments CMD2 (cryogenic magnetic detector) and SND (spherical neutral detector) collected data **up to 1.4 GeV** using the traditional e^+e^- energy scan. The KLOE experiment ran at a fixed energy around 1 GeV, either on the ϕ-resonance or just below it, using initial-state radiation to lower the collision energy and provide the full energy range in a single measurement (see Fig. 2.5(c)). The BaBar experiment also used the ISR technique, but operated at a much higher energy at or near the $\Upsilon(4s)$, which easily permitted observation of the ISR photon. At Tau2012 the Belle experiment reported new results on the $\pi^+\pi^-\pi^0$ final state [89] using ISR data. The ISR (sometimes called "radiative return") technique is possible because of the development of the necessary theory [81, 82], which provides the effective virtual photon spectrum, called the "radiator function."

While the KLOE experiment was limited to the $\pi\pi\gamma$ channel, the higher energy of the PEP-2 collider permitted BaBar to detect the ISR photon and to measure many multiple hadron final states along with the $\pi\pi\gamma$ final state, thus providing important data from channels which were either very imprecise, or simply not available before. The first $\pi^+\pi^-$ data from BaBar were released in August 2009 [83], and covered the energy range from threshold to 3 GeV. Unlike the other experiments that used a calculated $\mu\mu$ cross section for the denominator in Eq. (2.19), the BaBar experiment measured the $\mu\mu$ production directly and took the ratio of experimental numbers to determine $R(s)$ directly. This had the benefit of canceling a number of systematic errors, and significantly lowered the uncertainty on the cross section. **I suggest to drop - If BaBar had used the calculated $\mu\mu$ cross section, the cross section errors would have been at the $\sim 5\%$ level, much too large to be useful in the determination of $a_\mu^{\rm had}$.**

Published cross sections from the BaBar, KLOE, CMD2 and SND experiments are shown in Fig. 2.7. The KLOE re-analysis of their small-angle data using the ratio of the $\pi\pi$ $\mu\mu$ cross sections, compared large-angle data[87], and are displayed in Fig. 2.8 as the pion form factor $|F_\pi|^2$, which is related to the cross section by

$$\sigma_{e^+e^-\to\pi^+\pi^-} = \frac{\pi\alpha^2}{3s}\beta_\pi^3|F_\pi|^2. \tag{2.20}$$

They were analyzed by a different group of collaborators who worked independently from those involved in the the KLOE08 [86] analysis.

Two recent analyses [47, 48] of the e^+e^- hadroproduction data obtained:

$$a_\mu^{\rm had;LO} = 6\ 923 \pm 42 \times 10^{-11}\,. \tag{2.21}$$

$$a_\mu^{\rm had;LO} = 6\ 949 \pm 43 \times 10^{-11}\,. \tag{2.22}$$

Important earlier global analyses include those of HMNT [72], Davier, et al., [73], Jegerlehner [74].

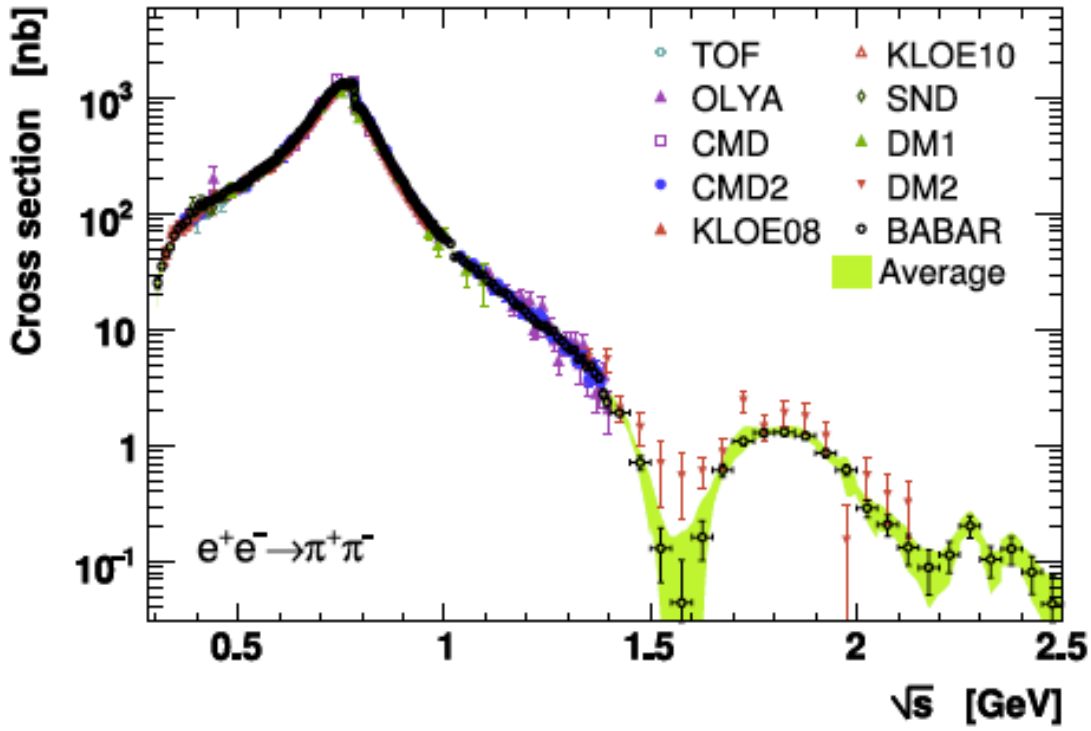

(a)

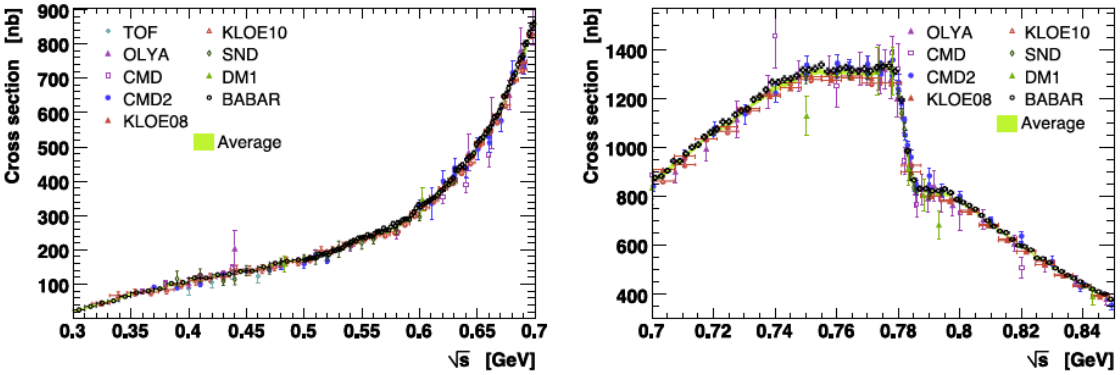

(b)

Figure 2.7: The $\pi\pi$ cross section from BaBar, CMD2, KLOE and SND. The lower left-hand figure shows the threshold region, the right-hand figure shows a blowup of the ρ resonance region. The sharp cusp comes from $\rho - \omega$ interference.

The most recent evaluation of the next-order hadronic contribution shown in Fig. 2.4(b-d) can also be determined from a dispersion relation, and the result is [48]

$$a_\mu^{\text{had:NLO}} = (-98.4 \pm 0.6_{\text{exp}} \pm 0.4_{\text{rad}}\ ) \times 10^{-11}\,. \tag{2.23}$$

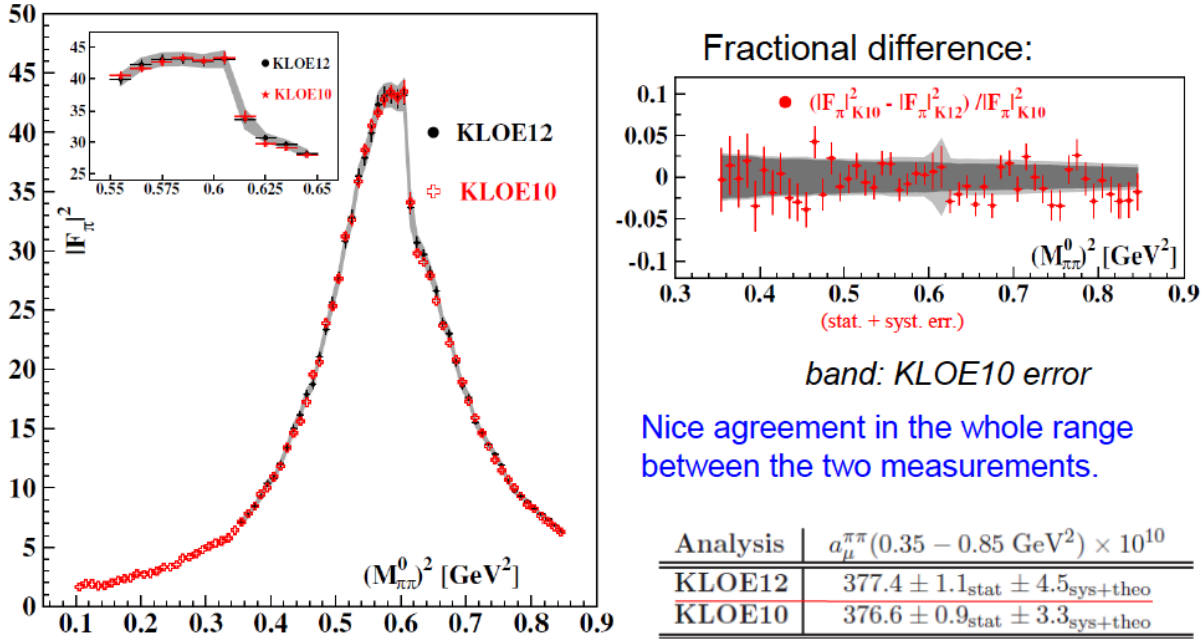

Analysis	$a_\mu^{\pi\pi}(0.35-0.85\ \mathrm{GeV}^2)\times 10^{10}$
KLOE12	$377.4 \pm 1.1_{\mathrm{stat}} \pm 4.5_{\mathrm{sys+theo}}$
KLOE10	$376.6 \pm 0.9_{\mathrm{stat}} \pm 3.3_{\mathrm{sys+theo}}$

Figure 2.8: The pion form factor $|F_\pi|^2$ from KLOE2010 [87] and the re-analysis of the 2008 data [86] using the cross-section ratio described above [88]. The right-hand side shows the fractional difference between the two analyses.

$a_\mu^{\mathrm{had;LO}}$ from hadronic τ decay

The value of $a_\mu^{\mathrm{had;LO}}$ from threshold up to m_τ could in principle be obtained from hadronic τ^- decays (See Fig. 2.4)**?????**, provided that the necessary isospin corrections are known. This was first demonstrated by Almany, Davier and Höcker [76]. In the absence of second-class currents, hadronic τ decays to an *even* number of pions such as $\tau^- \to \pi^-\pi^0\nu_\tau$ goes through the vector part of the weak current, and can be related to e^+e^- annihilation into $\pi^+\pi^-$ through the CVC hypothesis and isospin conservation (see Fig. 2.5.3**???**) [76, 80]. The τ-data only contain an isovector piece, and the isoscalar piece present in e^+e^- annihilation has to be put in "by hand" to evaluate $a_\mu^{\mathrm{had;LO}}$. Until recently there were 3.5 to 4.5 standard deviation differences when e^+e^- data and the CVC hypothesis were used to determine the $\tau^- \to \nu_\tau\pi^-\pi^0$ or $\tau^- \to \nu_\tau 2\pi^-\pi^+\pi^0$ branching fractions, when compared with the experimental values. Thus until recently most authors [48, 75, 74] concluded that there are unresolved issues, most likely incorrect isospin breaking corrections, that make it difficult to use the τ data on an equal

footing with the e^+e^- data. New isospin corrections reduced the disagreement between the two methods [47]. However, none of the analyses using tau data have tried to combine the CVC determined part with that obtained from e^+e^- data. Were this to be done, the addition of the e^+e^- data would decrease the overall tau-based evaluation of to a_μ^{had}. Even so, the tau-based evaluation has to use e^+e^- data to determine the isoscalar part, so that the tau-based evaluation by Davier, et al., [47] can never be completely independent of the e^+e^- data.

More recently, Jegerlehner and Szafron [77] appear to have resolved this problem by calculating the correction from $\rho - \gamma$ mixing, which had not been included correctly in the previous evaluations. A subsequent hidden local symmetry calculation [78, 79] further refines these ideas and includes the τ-data in a combined analysis. They conclude that their analysis yields a 4.7 to 4.9 σ difference with the Standard Model.

We should note that the theoretical uncertainties on the dispersion relation in Eq. (2.19), which assumes analyticity and the optical theorem, are negligible. The cross section that enters in Eq. (2.19) is the bare cross section, and some of the early experiments were not so careful in their reporting the data and being clear on what, if any radiative corrections were applied. All of the modern experiments are well aware of these issues, and their reported errors include any uncertainties introduced in determining the bare cross section.

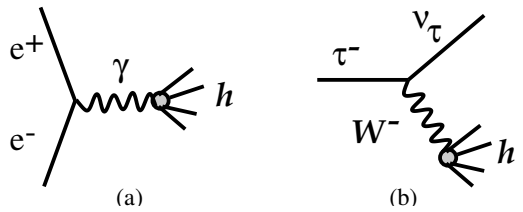

Figure 2.9: e^+e^- annihilation into hadrons (a), and hadronic τ decay (b).

Hadronic light-by-light contribution

The hadronic light-by-light contribution, (Fig. 2.4(e)) cannot at present be determined from data, but rather must be calculated using hadronic models that correctly reproduce the properties of QCD. A number of authors have calculated portions of this contribution, and recently a synthesis of all contributions has become available from Prades, de Rafael and Vainshtein [58][4], which has been agreed to by authors from each of the leading groups working in this field. They obtain

$$a_\mu^{\rm HLbL} = (105 \pm 26) \times 10^{-11}\,. \tag{2.24}$$

Additional work on this contribution is underway on a number of fronts, including on the lattice. A workshop was held in March 2011 at the Institute for Nuclear Theory in Seattle [59] which brought together almost all of the interested experts.

One important point should be made here. The main physics of the hadronic light-by-light scattering contribution is well understood. In fact, but for the sign error unraveled

[4]This compilation is generally referred to as the "Glasgow Consensus" since it grew out of a workshop in Glasgow in 2007.

in 2002, the theoretical predictions for $a_\mu^{\rm HLbL}$ have been relatively stable for more than ten years. We summarize with a quote from Eduardo de Rafael [61]:

> "For the time being, concerning the issue of errors, and after the work in PdeRV, I personally think that a 25% error on the HLbL is quite a generous one. One of my reasons is the fact that in the comparable HVP contribution—assuming that we did not have data from ee-annihilations nor tau-decays—I claim that from the underlying physics which we know, and using the same techniques as in the HLbL calculation, we are presently able to make there an estimate which, when compared to the one with data, turns out to be quite good: at the 10% to 15% level."

There is one calculation which used a Dyson-Schwinger approach, that appeared to strongly disagree with all of the other model calculations of the hadronic-light-by-light contribution [63]. However, recently these authors found several sign mistakes that change their result, moving it closer to other calculations [64].

At Tau2012, Blum reported that the lattice calculation of the hadronic-light-by-light contribution had started to see a signal [65]. "Signal may be emerging in the model ballpark". Blum also had encouraging words about the precision that the lattice might reach on the lowest-order hadronic contribution.

In addition to the theoretical work on the HLbL, a new facility is being commissioned at DAϕNE which will provide tagged virtual photons for $\gamma^*\gamma^*$ physics. Both high- and low-energy taggers are being constructed on both sides of the interaction region to detect and measure the scattered electron and positron. Thus a coincidence between the scattered electrons and a π^0 would provide information on $\gamma^*\gamma^* \to \pi^0$, etc. [62], and will provide experimental constraints on the models used to calculate the hadronic light-by-light contribution[93].

2.5.4 Summary of the Standard-Model Value and Comparison with Experiment

We determine the SM value using the new QED calculation from Aoyama [66]; the electroweak from Ref. [75], the hadronic light-by-light contribution from the "Glasgow Consensus" [58]; and lowest-order hadronic contribution from Davier, et al., [47], or Hagawara et al., [48], and the higher-order hadronic from Ref. [48] A summary of these values is given in Table 2.3.

This SM value is to be compared with the combined a_μ^+ and a_μ^- values from E821 [6] corrected for the revised value of λ as mentioned above:

$$a_\mu^{\rm E821} = (116\,592\,089 \pm 63) \times 10^{-11} \quad (0.54\,{\rm ppm}), \tag{2.25}$$

which give a difference of

$$\begin{aligned} \Delta a_\mu({\rm E821 - SM}) &= (286 \pm 80) \times 10^{-11}\ [47] && (2.26)\\ &= (260 \pm 80) \times 10^{-11}\ [48] && (2.27) \end{aligned}$$

Table 2.3: Summary of the Standard-Model contributions to the muon anomaly. Two values are quoted because of the two recent evaluations of the lowest-order hadronic vacuum polarization.

	VALUE ($\times 10^{-11}$) UNITS
QED ($\gamma + \ell$)	$116\,584\,718.951 \pm 0.009 \pm 0.019 \pm 0.007 \pm 0.077_{\alpha}$
HVP(lo) [47]	$6\,923 \pm 42$
HVP(lo) [48]	$6\,949 \pm 43$
HVP(ho) [48]	-98.4 ± 0.7
HLbL	105 ± 26
EW	$153 \pm 1 \pm 1$
Total SM [47]	$116\,591\,802 \pm 42_{\text{H-LO}} \pm 26_{\text{H-HO}} \pm 2_{\text{other}}\,(\pm 49_{\text{tot}})$
Total SM [48]	$116\,591\,828 \pm 43_{\text{H-LO}} \pm 26_{\text{H-HO}} \pm 2_{\text{other}}\,(\pm 50_{\text{tot}})$

depending on which evaluation of the lowest-order hadronic contribution that is used [47, 48]. This comparison between the experimental values and the present Standard-Model value is shown graphically in Fig. 2.1.

This difference of **3.3** to 3.6 standard deviations is tantalizing, but we emphasize that whatever the final agreement between the measured and SM value turns out to be, it will have significant implications on the interpretation of new phenomena that might be found at the LHC and elsewhere. This point is discussed in detail below.

The present theoretical error is dominated by the uncertainty on the lowest-order hadronic contribution and uncertainty on the hadronic light-by-light contribution (see Table 2.3). The lowest-order hadronic contribution could be reduced to 25×10^{-11} based on the analysis of existing data and on the data sets expected from future efforts, e.g. VEPP-2000 in Novosibirsk, BES-III **and a possible upgrade in energy of DAΦNE [91]**. When combined with future theoretical progress on the hadronic light-by-light contribution, the total SM error could reach 30×10^{-11}.

With the proposed experimental error of $\pm 16 \times 10^{-11}$, the combined uncertainty for the difference between theory and experiment could be as small as $\pm 34 \times 10^{-11}$, which is to be compared with the $\pm 81 \times 10^{-11}$ in Eq. (2.27).

2.5.5 Expected Improvements in the Standard-Model Value

Much experimental and theoretical work is going on worldwide to refine the hadronic contribution. The theory of $(g-2)$, relevant experiments to determine the hadronic contribution, including work on the lattice, have featured prominently in the series of tau-lepton workshops and PHIPSI workshops which are held in alternate years.

Over the development period of our new experiment, we expect further improvements in the SM-theory evaluation. This projection is based on the following developments and facts:

- **Novosibirsk:** The VEPP2M machine has been upgraded to VEPP-2000. The maximum energy has been increased from $\sqrt{s} = 1.4$ GeV to 2.0 GeV. Additionally, the

SND detector has been upgraded and the CMD2 detector was replaced by the much-improved CMD3 detector. The cross section will be measured from threshold to 2.0 GeV using an energy scan, filling in the energy region between 1.4 GeV, where the previous scan ended, up to 2.0 GeV, the lowest energy point reached by the BES collaboration in their measurements. See Fig. 2.6 for the present contribution to the overall error from this region. Engineering runs began in 2009, and data collection started in 2011. So far two independent energy scans between 1.0 and 2.0 GeV were performed in 2011 and 2012. The peak luminosity of $3 \times 10^{31} cm^{-2} s^{-1}$ was achieved, which is limited by the positron production rate. The new injection facility, scheduled to be commissioned during the 2013-2014 upgrade, should permit the luminosity to reach $10^{32} cm^{-2} s^{-1}$. Data collection **had resumed** by the end of 2012 with new energy scan at energies below 1.0 GeV. The goal of experiments at VEPP-2000 is to achieve a systematic error 0.3-0.5% in $\pi^+\pi^-$ channel with negligble statistical error in the integral. The high statistics, expected at VEPP-2000, should allow a detailed comparison of the measured cross-sections with ISR results at BaBar and DAϕNE. After the upgrade, experiments at VEPP-2000 plan to take a large amount of data at 1.8-2 GeV, around $N\bar{N}$ threshold. This will permit ISR data with the beam energy of 2 GeV, which is between the PEP2 energy at the $\Upsilon(4s)$ and the 1 GeV ϕ energy at the DAϕNE facility in Frascati. The dual ISR and scan approach will provide an important cross check on the two central methods to determine HVP.

- **KLOE:** The KLOE collaboration has just reported the analysis of their 2008 data set using the experimental ratio $\pi\pi/\mu\mu$ final states, rather than the luminosity to get the cross sections [92]. In the future, they will begin the program of two-photon physics will be ramping up, which will provide experimental input to the hadronic light-by-light theory.

- **BaBar:**A significant amount of new data exists from BaBar, which can be used to provide another ISR measurement from threshold to 3 GeV. It is not at all clear that the Collaboration will be able to take on the analysis challenge.

- **Belle:** Some work on ISR measurements of $R(s)$ is going on in multi-hadron channels. These studies will complement those completed at BaBar and provide an important check.

- **BES-III: BES-III can perform a direct measurement of R above 2 GeV with an energy scan. It can use ISR to access the region below it.**

- **Calculations on the Lattice for Lowest-Order HVP:** With the increased computer power available for lattice calculations, it may be possible for lattice calculations to contribute to our knowledge of the lowest-order hadronic contribution. Blum and his collaborators are continuing to work on the lowest-order contribution, Several groups, UKQCD (Edinburg), DESY-Zeuthen (Renner and Jansen), and the LSD (lattice strong dynamics) group in the US are all working on the lowest-order contribution.

- **Calculations on the Lattice of Hadronic Light-by-Light:** The hadronic light-

by-light contribution has a magnitude of $(105 \pm 26) \times 10^{-11}$, ~ 1 ppm of a_μ. A modest calculation on the lattice would have a large impact. Blum and his collaborators at BNL, RIKEN and Nagoya are working on HLbL, and are beginning to see a signal.

2.6 Physics Beyond the Standard Model

For many years, the muon anomaly has played an important role in constraining physics beyond the SM [45, 46, 98, 99, 100]. The more than 2000 citations to the major E821 papers [6, 5, 22, 21], demonstrates that this role continues. The citations are shown as a function of year in Fig. 2.10. It is apparent that with the LHC results available in 2012, interest in the BNL results has risen significantly. As discussed in the previous section, the present SM value is smaller than the experimental value by $\Delta a_\mu(\text{E821} - \text{SM})$. The discrepancy depends on the SM evaluation, but it is generally in the $> 3\sigma$ region; a representative value is $(286 \pm 80) \times 10^{-11}$, see Eq. (2.27).

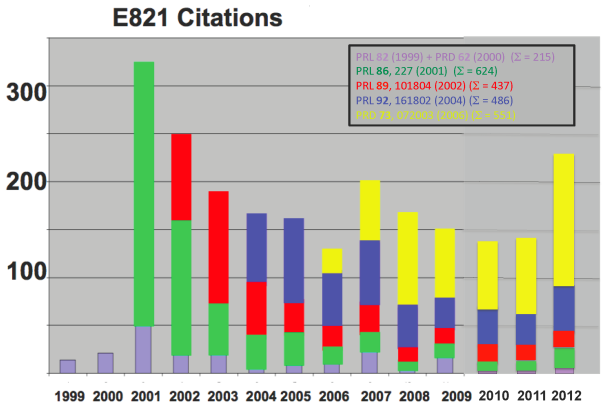

Figure 2.10: Citations by year to the E821 papers reporting physics results as of July 2012: light blue [19] plus [20]; green [21]; red [22]; blue [5]; and yellow the Physical Review article [6].

In this section, we discuss how the muon anomaly provides a unique window to search for physics beyond the standard model. If such new physics is discovered elsewhere, e.g. at the LHC, then a_μ will play an important role in sorting out the interpretation of those discoveries. We discuss examples of constraints placed on various models that have been proposed as extensions of the standard model. Perhaps the ultimate value of an improved limit on a_μ will come from its ability to constrain the models that have not yet been invented.

Varieties of physics beyond the Standard Model

The LHC era has had its first spectacular success in summer 2012 with the discovery of a new particle compatible with the standard model Higgs boson. With more data, the LHC experiments will continue to shed more light on the nature of electroweak symmetry breaking (EWSB). It is very likely that EWSB is related to new particles, new interactions, or maybe

to new concepts such as supersymmetry, extra dimensions, or compositeness. Further open questions in particle physics, related e.g. to the nature of dark matter, the origin of flavor or grand unification, indicate that at or even below the TeV scale there could be rich physics beyond the standard model.

Unravelling the existence and the properties of such new physics requires experimental information complementary to the LHC. The muon $(g-2)$, together with searches for charged lepton flavor violation, electric dipole moments, and rare decays, belongs to a class of complementary low-energy experiments.

In fact, the muon magnetic moment has a special role because it is sensitive to a large class of models related and unrelated to EWSB and because it combines several properties in a unique way: it is a flavour- and CP-conserving, chirality-flipping and loop-induced quantity. In contrast, many high-energy collider observables at the LHC and a future linear collider are chirality-conserving, and many other low-energy precision observables are CP- or flavour-violating. These unique properties might be the reason why the muon $(g-2)$ is the only among the mentioned observables which shows a significant deviation between the experimental value and the SM prediction, see Eq. (2.27). Furthermore, while $g-2$ is sensitive to leptonic couplings, b- or K-physics more naturally probe the hadronic couplings of new physics. If charged lepton-flavor violation exists, observables such as $\mu \to e$ conversion can only determine a combination of the strength of lepton-flavor violation and the mass scale of new physics. In that case, $g-2$ can help to disentangle the nature of the new physics.

The role of $g-2$ as a discriminator between very different standard model extensions is well illustrated by a relation stressed by Czarnecki and Marciano [46]. It holds in a wide range of models as a result of the chirality-flipping nature of both $g-2$ and the muon mass: If a new physics model with a mass scale Λ contributes to the muon mass $\delta m_\mu(\text{N.P.})$, it also contributes to a_μ, and the two contributions are related as

$$a_\mu(\text{N.P.}) = \mathcal{O}(1) \times \left(\frac{m_\mu}{\Lambda}\right)^2 \times \left(\frac{\delta m_\mu(\text{N.P.})}{m_\mu}\right). \tag{2.28}$$

The ratio $C(\text{N.P.}) \equiv \delta m_\mu(\text{N.P.})/m_\mu$ cannot be larger than unity unless there is fine-tuning in the muon mass. Hence a first consequence of this relation is that new physics can explain the currently observed deviation (2.27) only if Λ is at the few-TeV scale or smaller.

In many models, the ratio C arises from one- or even two-loop diagrams, and is then suppressed by factors like $\alpha/4\pi$ or $(\alpha/4\pi)^2$. Hence, even for a given Λ, the contributions to a_μ are highly model dependent.

It is instructive to classify new physics models as follows:

- Models with $C(\text{N.P.}) \simeq 1$: Such models are of interest since the muon mass is essentially generated by radiative effects at some scale Λ. A variety of such models have been discussed in [46], including extended technicolor or generic models with naturally vanishing bare muon mass. For examples of radiative muon mass generation within supersymmetry, see e.g. [101, 102]. In these models the new physics contribution to a_μ can be very large,

$$a_\mu(\Lambda) \simeq \frac{m_\mu^2}{\Lambda^2} \simeq 1100 \times 10^{-11} \left(\frac{1\ \text{TeV}}{\Lambda}\right)^2. \tag{2.29}$$

and the difference Eq. (2.27) can be used to place a lower limit on the new physics mass scale, which is in the few TeV range [103, 102].

- Models with $C(\text{N.P.}) = \mathcal{O}(\alpha/4\pi)$: Such a loop suppression happens in many models with new weakly interacting particles like Z' or W', little Higgs or certain extra dimension models. As examples, the contributions to a_μ in a model with $\delta = 1$ (or 2) universal extra dimensions (UED) [104] and the Littlest Higgs model with T-parity (LHT) [105] are given by

$$a_\mu(\text{UED}) \simeq -5.8 \times 10^{-11}(1 + 1.2\delta)S_{\text{KK}}, \tag{2.30}$$
$$a_\mu(\text{LHT}) < 12 \times 10^{-11} \tag{2.31}$$

with $|S_{\text{KK}}| \lesssim 1$ [104]. A difference as large as Eq. (2.27) is very hard to accommodate unless the mass scale is very small, of the order of M_Z, which however is often excluded e.g. by LEP measurements. So typically these models predict very small contributions to a_μ and will be disfavored if the current deviation will be confirmed by the new a_μ measurement.

Exceptions are provided by models where new particles interact with muons but are otherwise hidden from searches. An example is the model with a new gauge boson associated to a gauged lepton number $L_\mu - L_\tau$ [106], where a gauge boson mass of $\mathcal{O}(100\text{ GeV})$ and large a_μ are viable.

- Models with intermediate values for $C(\text{N.P.})$ and mass scales around the weak scale: In such models, contributions to a_μ could be as large as Eq. (2.27) or even larger, or smaller, depending on the details of the model. This implies that a more precise a_μ-measurement will have significant impact on such models and can even be used to measure model parameters. Supersymmetric (SUSY) models are the best known examples, so muon $g-2$ would have substantial sensitivity to SUSY particles. Compared to generic perturbative models, supersymmetry provides an enhancement to $C(\text{SUSY}) = \mathcal{O}(\tan\beta \times \alpha/4\pi)$ and to $a_\mu(\text{SUSY})$ by a factor $\tan\beta$ (the ratio of the vacuum expectation values of the two Higgs fields). Typical SUSY diagrams for the magnetic dipole moment, the electric dipole moment, and the lepton-number violating conversion process $\mu \to e$ in the field of a nucleus are shown pictorially in Fig. 2.11. The shown diagrams contain the SUSY partners of the muon, electron and the SM $\text{U}(1)_Y$ gauge boson, $\tilde{\mu}$, $\tilde{e}$, $\tilde{B}$. The full SUSY contributions involve also the SUSY partners to the neutrinos and all SM gauge and Higgs bosons. In a model with SUSY masses equal to Λ the SUSY contribution to a_μ is given by [46]

$$a_\mu(\text{SUSY}) \simeq \text{sgn}(\mu)\ 130 \times 10^{-11}\ \tan\beta\ \left(\frac{100\text{ GeV}}{\Lambda}\right)^2 \tag{2.32}$$

which indicates the dependence on $\tan\beta$, and the SUSY mass scale, as well as the sign of the SUSY μ-parameter. The formula still approximately applies even if only the smuon and chargino masses are of the order Λ but e.g. squarks and gluinos are much heavier. However the SUSY contributions to a_μ depend strongly on the details of mass splittings between the weakly interacting SUSY particles. Thus muon $g-2$ is sensitive

to SUSY models with SUSY masses in the few hundred GeV range, and it will help to measure SUSY parameters.

There are also non-supersymmetric models with similar enhancements. For instance, lepton flavor mixing can help. An example is provided in Ref. [107] by a model with two Higgs doublets and four generations, which can accommodate large Δa_μ without violating constraints on lepton flavor violation. In variants of Randall-Sundrum models [108, 109, 110] and large extra dimension models [111], large contributions to a_μ might be possible from exchange of Kaluza-Klein gravitons, but the theoretical evaluation is difficult because of cutoff dependences. A recent evaluation of the non-graviton contributions in Randall-Sundrum models, however, obtained a very small result [112].

Further examples include scenarios of unparticle physics [113, 114] (here a more precise a_μ-measurement would constrain the unparticle scale dimension and effective couplings), generic models with a hidden sector at the weak scale [115] or a model with the discrete flavor symmetry group T' and Higgs triplets [116] (here a more precise a_μ-measurement would constrain hidden sector/Higgs triplet masses and couplings), or the model proposed in Ref. [117], which implements the idea that neutrino masses, leptogenesis and the deviation in a_μ all originate from dark matter particles. In the latter model, new leptons and scalar particles are predicted, and a_μ provides significant constraints on the masses and Yukawa couplings of the new particles.

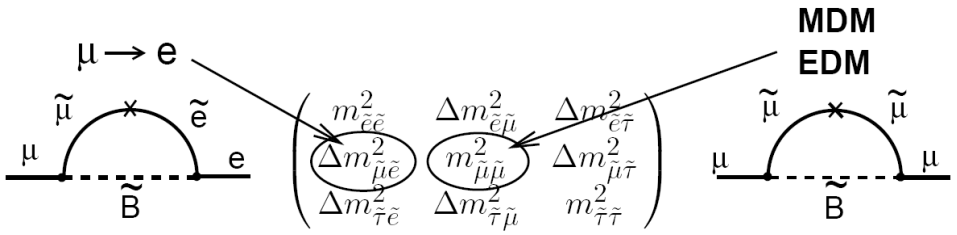

Figure 2.11: The SUSY contributions to the anomaly, and to $\mu \to e$ conversion, showing the relevant slepton mixing matrix elements. The MDM and EDM give the real and imaginary parts of the matrix element, respectively. The $\times$ indicates a chirality flip.

The following types of new physics scenarios are quite different from the ones above:

- Models with extended Higgs sector but without the $\tan\beta$-enhancement of SUSY models. Among these models are the usual two-Higgs-doublet models. The one-loop contribution of the extra Higgs states to a_μ is suppressed by two additional powers of the muon Yukawa coupling, corresponding to $a_\mu(\text{N.P.}) \propto m_\mu^4/\Lambda^4$ at the one-loop level. Two-loop effects from Barr-Zee diagrams can be larger [118], but typically the contributions to a_μ are negligible in these models.

- Models with additional light particles with masses below the GeV-scale, generically called dark sector models: Examples are provided by the models of Refs. [119, 120], where additional light neutral gauge bosons can affect electromagnetic interactions. Such models are intriguing since they completely decouple $g-2$ from the physics of

EWSB, and since they are hidden from collider searches at LEP or LHC (see however Refs. [121, 122] for studies of possible effects at dedicated low-energy colliders and in Higgs decays at the LHC). They can lead to contributions to a_μ which are of the same order as the deviation in Eq. (2.27). Hence the new $g-2$ measurement will provide an important test of such models.

To summarize: many well-motivated models can accommodate larger contributions to a_μ — if any of these are realized $g-2$ can be used to constrain model parameters; many well-motivated new physics models give tiny contributions to a_μ and would be disfavored if the more precise $g-2$ measurement confirms the deviation in Eq. (2.27). There are also examples of models which lead to similar LHC signatures but which can be distinguished using $g-2$.

In the following it is discussed in more detail how a_μ will be useful in understanding TeV-scale physics in the event that the LHC established the existence of physics beyond the standard model [99].

a_μ and supersymmetry

We first focus on the case of supersymmetry, which provides a particularly well-defined and calculable framework. We illustrate the sensitivity of $g-2$ to the SUSY parameters and the complementarity to LHC measurements.

As discussed above, supersymmetry with $\tan\beta$ up to 50 and masses in the 100–700 GeV range can easily explain the currently observed deviation (2.27). Now the SUSY contributions are discussed in more detail. At the one-loop level, the diagrams of the minimal supersymmetric standard model (MSSM) involve the SUSY partners the gauge and Higgs bosons and the muon-neutrino and the muon, the so-called charginos, neutralinos and sneutrinos and smuons. The relevant parameters are thus the SUSY breaking mass parameters for the 2nd generation sleptons, the bino and wino masses M_2, M_1, and the Higgsino mass parameter μ. Strongly interacting particles, squarks and gluinos, and their masses are irrelevant on this level.

If all the relevant mass parameters are equal, the approximation (2.32) is valid, and the dominant contribution is from the chargino–sneutrino diagrams. If μ is very large, the bino-like neutralino contribution of Fig. 2.11 is approximately linear in μ and can dominate. If there is a large mass splitting between the left- and right-handed smuon, even the sign can be opposite to Eq. (2.32), see the discussions in [123, 124].

As a result, a_μ(SUSY) depends not only on the overall SUSY masses but on the individual values of the parameters M_1, M_2, and μ. Exchanging these parameters can leave the spectrum of SUSY particle masses unchanged but will have an effect on $a_\mu^{\rm SUSY}$. It is shown later that this will help to disentangle different possible interpretations of LHC data.

On the two-loop level, further contributions exist which are typically subleading but can become important in regions of parameter space. For instance, there are diagrams without smuons or sneutrinos but with e.g. a pure chargino or stop loop [125]. Such diagrams can even be dominant if first and second generation sfermions are very heavy, a scenario called effective SUSY [126].

To date, the LHC experiments have not found indications for SUSY particles but only for a Higgs-like particle with mass around 126 GeV. This leads to the following conclusions:

- If supersymmetry is the origin of the deviation in a_μ, at least some SUSY particles cannot be much heavier than around 700 GeV (for $\tan\beta = 50$), most favorably the smuons and charginos/neutralinos.

- The negative results of the LHC searches for SUSY particles imply lower limits of around 1 TeV, in particular on squark and gluino masses. The bounds are not model-independent but valid in scenarios with particular squark and gluino decay patterns.

- The constraint that a SM-like Higgs boson mass is around 126 GeV requires either very large loop corrections from large logarithms or non-minimal tree-level contributions from additional non-minimal particle content.

- The requirement of small fine-tuning between supersymmetry-breaking parameters and the Z-boson mass prefers certain particles, in particular stops, gluinos and Higgsinos to be rather light.

A tension between these constraints seems to be building up, but the constraints act on different aspects of SUSY models. Hence it is in principle no problem to accommodate all the experimental data in the general minimal supersymmetric standard model, for most recent analyses see Refs. [127, 128].

However, strongly restricted models, such as the Constrained MSSM (CMSSM) cannot anymore simultaneously explain all data. For a long time, many analyses have used a_μ as a central observable to constrain the CMSSM parameters, see e.g. [129]. The most recent analyses show that the LHC determination of the Higgs boson mass turns out to be incompatible with an explanation of the current Δa_μ within the CMSSM [130, 131, 132]. Hence, the CMSSM is already disfavored now, and it will be excluded if the future a_μ measurement confirms the current Δa_μ.

The issue of fine-tuning has led to many proposals for SUSY models in which some or all of the experimental constraints are satisfied in a technically natural way. For instance, the model of Ref. [133] is based on gauge-mediated SUSY breaking and extra vector-like matter, and it is naturally in agreement with FCNC constraints and the Higgs boson mass value. But if the SUSY particles are light enough to explain $g-2$, it is on the verge of being excluded by LHC data. Conversely, the so-called natural SUSY scenarios (see e.g. [134, 135]), where the spectrum is such that fine-tuning is minimized while squarks and gluinos evade LHC bounds, can explain the Higgs boson mass but completely fail to explain $g-2$. Similarly so-called compressed supersymmetry [136] can be a natural explanation of the Higgs mass and the negative LHC SUSY searches but, at least in the version of Ref. [137] fails to accommodate a large Δa_μ.

These considerations show that a definitive knowledge of $a_\mu^{\rm SUSY}$ will be very beneficial for the interpretation of LHC data in terms of SUSY.

In the general model classification of the previous subsection the possibility of radiative muon mass generation was mentioned. This idea can be realized within supersymmetry, and it leads to SUSY scenarios quite different from the ones discussed so far. Since the muon mass at tree level is given by the product of a Yukawa coupling and the vacuum expectation value of the Higgs doublet H_d, there are two kinds of such scenarios. First, one can postulate that

the muon Yukawa coupling is zero but chiral invariance is broken by soft supersymmetry-breaking A-terms. Then, the muon mass, and $a_\mu^{\rm SUSY}$, arise at the one-loop level and there is no relative loop suppression of $a_\mu^{\rm SUSY}$ [101, 102]. Second, one can postulate that the vacuum expectation value $\langle H_d \rangle$ is very small or zero [138, 139]. Then, the muon mass and $a_\mu^{\rm SUSY}$ arise at the one-loop level from loop-induced couplings to the other Higgs doublet. Both scenarios could accommodate large $a_\mu^{\rm SUSY}$ and TeV-scale SUSY particle masses.

a_μ and model selection and parameter measurement

The LHC is sensitive to virtually all proposed weak-scale extensions of the standard model, ranging from supersymmetry, extra dimensions and technicolor to little Higgs models, unparticle physics, hidden sector models and others. However, even if the existence of physics beyond the standard model is established, it will be far from easy for the LHC alone to identify which of these — or not yet thought of — alternatives is realized. Typically LHC data will be consistent with several alternative models.

For example, a situation is possible where the LHC finds many new heavy particles which are compatible with supersymmetry. Since spin measurements are difficult, these new states might allow alternative interpretations in terms of other models. In particular universal-extra-dimension models (UED) [140], or the Littlest Higgs model with T-parity (LHT) [141, 142] have been called "bosonic SUSY" since they can mimick SUSY but the partner particles have the opposite spin as the SUSY particles, see e.g. [143]. The muon $g-2$ would especially aid in the selection since UED or Littlest Higgs models predict a tiny effect to a_μ [104, 105], while SUSY effects are usually much larger.

On the other hand, a situation where the LHC finds no physics beyond the standard model but the a_μ measurement establishes a deviation, might be a signal for dark sector models such as the secluded U(1) model [119], with new very weakly interacting light particles which are hard to identify at the LHC [121, 120, 122].

Next, if new physics is realized in the form of a non-renormalizable theory, a_μ might not be fully computable but depend on the ultraviolet cutoff. Randall-Sundrum or universal extra dimension models are examples of this situation. In such a case, the a_μ measurement will not only help to constrain model parameters but it will also help to get information on the ultraviolet completion of the theory.

Within the framework of SUSY there are many different well-motivated scenarios that are not always easy to distinguish at the LHC. Fig. 2.12 illustrates this.

The left plot in Fig. 2.12 shows the values for the so-called SPS benchmark points [147]. These span a wide range and can be positive or negative, due to the factor sign(μ) in Eq. (2.32). The discriminating power of the current (yellow band) and an improved (blue band) measurement is evident from Fig. 2.12(a).

One might think that if SUSY exists, the LHC-experiments will find it and measure its parameters. Above it has been mentioned that SUSY can be mimicked by "bosonic SUSY" models. The green points illustrate that even within SUSY, certain SUSY parameter points can be mimicked by others. The green points correspond to "degenerate solutions" of Ref. [144] — different SUSY parameter points which cannot be distinguished at the LHC alone (see also Ref. [145] for the LHC inverse problem). They have very different a_μ predictions, and hence a_μ can resolve such LHC degeneracies.

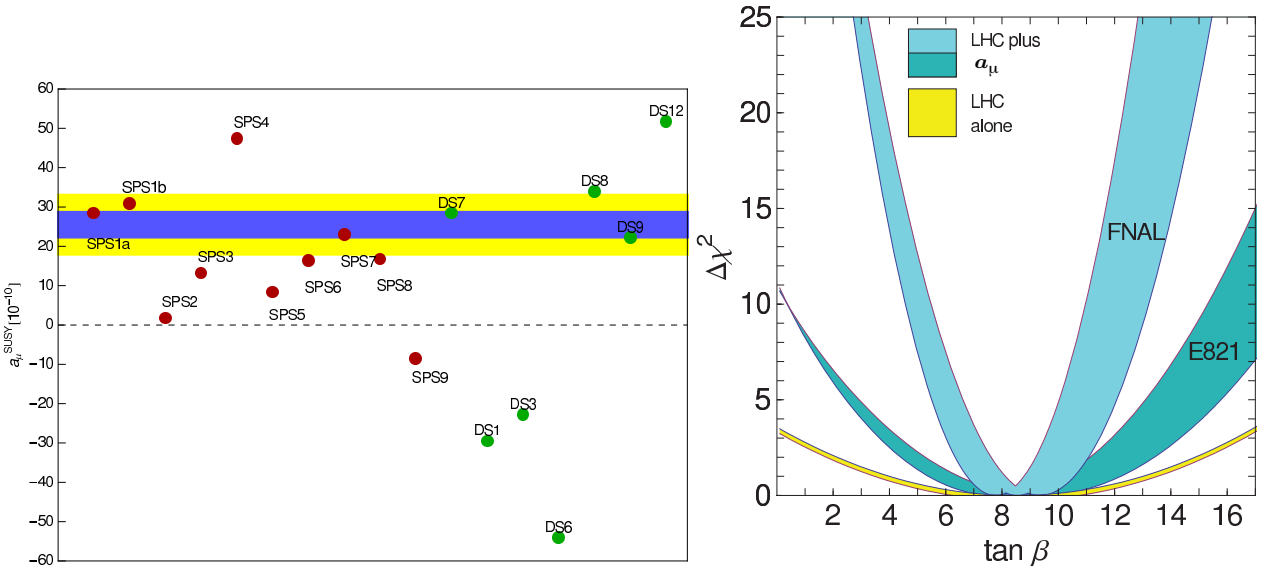

(a) (b)

Figure 2.12: (a) SUSY contributions to a_μ for the SPS benchmark points (red), and for the "degenerate solutions" from Ref. [144]. The yellow band is the ± 1 σ error from E821, the blue is the projected sensitivity of E989. (b) Possible future $\tan\beta$ determination assuming that a slightly modified MSSM point SPS1a (see text) is realized. The bands show the $\Delta\chi^2$ parabolas from LHC-data alone (yellow) [146], including the a_μ with current precision (dark blue) and with prospective precision (light blue). The width of the blue curves results from the expected LHC-uncertainty of the parameters (mainly smuon and chargino masses) [146].

In a similar spirit, Ref. [148] discussed "supersymmetry without prejudice." First a large set of supersymmetry parameter points ("models") in a 19-dimensional parameter space was identified, which was in agreement with many important existing experimental and theoretical constraints. Then the implications for observables such as $g-2$ were studied. The result for $g-2$ was rather similar to Fig. 2.12(a), although the context was far more general: the entire range $a_\mu^{\rm SUSY} \sim (-100 \ldots + 300) \times 10^{-11}$ was populated by a reasonable number of "models." Therefore, a precise measurement of $g-2$ to $\pm 16 \times 10^{-11}$ will be a crucial way to rule out a large fraction of models and thus determine SUSY parameters.

The right plot of Fig. 2.12 illustrates that the SUSY parameter $\tan\beta$ can be measured more precisely by combining LHC-data with a_μ. It is based on the assumption that SUSY is realized, found at the LHC and the origin of the observed a_μ deviation (2.27). To fix an example, we use a slightly modified SPS1a benchmark point with $\tan\beta$ scaled down to $\tan\beta = 8.5$ such that $a_\mu^{\rm SUSY}$ is equal to an assumed deviation $\Delta a_\mu = 255 \times 10^{-11}$.[5] Ref. [146] has shown that then mass measurements at the LHC alone are sufficient to determine $\tan\beta$ to a precision of ± 4.5 only. The corresponding $\Delta\chi^2$ parabola is shown in yellow in the plot. In such a situation one can study the SUSY prediction for a_μ as a function of $\tan\beta$ (all other parameters are known from the global fit to LHC data) and compare it to the measured value, in particular after an improved measurement. The plot compares the LHC $\Delta\chi^2$ parabola with the ones obtained from including a_μ, $\Delta\chi^2 = [(a_\mu^{\rm SUSY}(\tan\beta) - \Delta a_\mu)/\delta a_\mu]^2$ with the errors $\delta a_\mu = 80 \times 10^{-11}$ (dark blue) and 34×10^{-11} (light blue). As can be seen from the Figure, using today's precision for a_μ would already improve the determination of $\tan\beta$, but the improvement will be even more impressive after the future a_μ measurement.

One should note that even if better ways to determine $\tan\beta$ at the LHC alone might be found, an independent determination using a_μ will still be highly valuable, as $\tan\beta$ is one of the central MSSM parameters; it appears in all sectors and in almost all observables. In non-minimal SUSY models the relation between $\tan\beta$ and different observables can be modified. Therefore, measuring $\tan\beta$ in different ways, e.g. using certain Higgs- or b-decays at the LHC or at b-factories and using a_μ, would constitute a non-trivial and indispensable test of the universality of $\tan\beta$ and thus of the structure of the MSSM.

The anomalous magnetic moment of the muon is sensitive to contributions from a wide range of physics beyond the standard model. It will continue to place stringent restrictions on all of the models, both present and yet to be written down. If physics beyond the standard model is discovered at the LHC or other experiments, a_μ will constitute an indispensable tool to discriminate between very different types of new physics, especially since it is highly sensitive to parameters which are difficult to measure at the LHC. If no new phenomena are found elsewhere, then it represents one of the few ways to probe physics beyond the standard model. In either case, it will play an essential and complementary role in the quest to understand physics beyond the standard model at the TeV scale.

[5] The actual SPS1a point is ruled out by LHC, however for our purposes only the weakly interacting particles are relevant, and these are not excluded. The following conclusions are neither very sensitive to the actual $\tan\beta$ value nor to the actual value of the deviation Δa_μ.

References

[1] O. Stern, Z. Phys. **7**, 249 (1921);

[2] W. Gerlach and O. Stern, , Z. Phys. **8**, 110 (1922); Z. Phys. **9** and 349(1922), Z. Phys. **9**, 353 (1924); W. Gerlach and O. Stern, Ann. Phys. **74**, 673 (1924).

[3] G.E. Uhlenbeck and S. Goudsmit, Naturwissenschaften **47**, 953 (1925); G.E. Uhlenbeck and S. Goudsmit, Nature **117** (1926) 264.

[4] E. Schrödinger, Ann. Phys. **79** (1926) 361.

[5] L.H. Thomas, Nature **117**, (1926) 514 and Phil. Mag. **3** (1927) 1.

[6] T.E. Phipps and J.B. Taylor, Phys. Rev. **29**, 309 (1927).

[7] P.A.M. Dirac, Proc. R. Soc. (London) **A117**, 610 (1928), and **A118**, 351 (1928). See also, P.A.M. Dirac, *The Principles of Quantum Mechanics*, 4th edition, Oxford University Press, London, 1958.

[8] Sin-itiro Tomonaga, *The Story of Spin*, translated by Takeshi Oka, U. Chicago Press, 1997.

[9] R. Frisch and O. Stern, Z. Phys. **85**, 4 (1933), and I. Estermann and O. Stern, Z. Phys. **85**, 17 (1933).

[10] Luis W. Alvarez and F. Bloch, Phys. Rev. **57**, 111 (1940).

[11] J.E. Nafe, E.B. Nelson and I.I. Rabi Phys. Rev. **71**, 914(1947).

[12] D.E. Nagel, R.S. Julian and J.R. Zacharias, Phys. Rev. **72**, 971 (1947).

[13] P. Kusch and H.M Foley, Phys. Rev **72**, 1256 (1947).

[14] J. Schwinger, Phys. Rev. **73**, 416L (1948), and Phys. Rev. **76** 790 (1949). The former paper contains a misprint in the expression for a_e that is corrected in the longer paper.

[15] Hans A. Bethe and Edwin E. Salpeter, *Quantum Mechanics of One- and Two-Electron Atoms*, Springer-Verlag, (1957), p. 51.

[16] See Figure 5 in Paul Kunze, Z. Phys. **83**, 1 (1933).

[17] Carl D. Anderson and Seth H. Neddermeyer, Phys. Rev. **50** (1936) 263, and Seth H. Neddermeyer and Carl D. Anderson, Phys. Rev. **51** (1937) 844.

[18] J.C. Street, E.C. Stevenson, Phys. Rev. **52** (1937) 1003.

[19] Y. Nishina, M. Tekeuchi and T. Ichimiya, Phys. Rev. **52** (1937) 1198.

[20] M.M. Jean Crussard and L. Leprince-Ringuet, Compt. Rend. **204** (1937) 240.

[21] Garwin RL, Lederman LM, Weinrich M, Phys. Rev. 105:1415 (1957)

[22] J.I. Friedman and V.L. Telegdi, Phys. Rev. **105**, 1681 (1957).

[23] E.J. Konopinski, Ann. Rev. Nucl. Sci. **9** 99, (1959).

[24] Garwin RL, Hutchinson DP, Penman S, Shapiro G, Phys. Rev. 118:271 (1960)

[25] Charpak G, et al. Phys. Rev. Lett. 6:28 (1961), Nuovo Cimento. 22:1043 (1961), Phys. Lett. 1:16 (1962), Nuovo Cimento. 37:1241 (1965) and Charpak G. et al. Phys. Lett. 1:16 (1962)

[26] Bailey J, et al. Phys. Lett. 28B:287 (1968). Additional details can be found in Bailey J, et al. Nuovo Cimento. A9:369 (1972) and references therein.

[27] Bailey J, et al. Nucl. Phys. B150:1 (1979)

[28] E.M. Purcell and N.F. Ramsey, Phys. Rev. **78**, 807 (1950).

[29] T.D. Lee and C.N. Yang, Phys. Rev. **104** (1956) 254.

[30] J.H. Smith, E.M. Purcell and N.F. Ramsey, Phys. Rev. **108**, 120 (1957).

[31] L. Landau, Nucl. Phys. **3**, 127 (1957).

[32] N.F. Ramsey Phys. Rev. **109**, 225 (1958).

[33] W.C. Griffith, et al., Phys. Rev. Lett. **102**, 101601 (2009).

[34] C.A. Baker, et al., Phys. Rev. Lett. **97**, 131801 (2006).

[35] J.J. Hudson, et al., Nature **473**, 493 (2011).

[36] G.W. Bennett, et al., Phys. Rev. **D 80**, 052008 (2009).

[37] Bargmann V, Michel L, Telegdi VL, Phys. Rev. Lett. 2:435 (1959)

[38] Bennett GW, et al. (The $g-2$ Collab.) Phys. Rev. Lett. 92:161802 (2004)

[39] Bennett GW, et al.(The $g-2$ Collab.) Phys. Rev. D, 73:072003 (2006)

[40] C.S. Wu, E. Ambler, R.W. Hayward, D.D. Hoppes, R.P. Hudson, Phys. Rev. **105**, 1413 (1957).

[41] Mohr PJ, Taylor BN, Newell DB, (CODATA recommended values). *Rev. Mod. Phys.* 80:633 (2008)

[42] R. Prigl, *et al.*, Nucl. Inst. Methods Phys. Res. **A374** 118 (1996).

[43] W. Liu et al., Phys. Rev. Lett. **82**, 711 (1999).

[44] Topical Workshop on The Muon Magnetic Dipole Moment; Oct. 2007 School of Physics and Astronomy, The University of Glasgow. See: www.ippp.dur.ac.uk/old/MuonMDM/.

[45] T. Kinoshita and W.J. Marciano in *Quantum Electrodynamics* (Directions in High Energy Physics, Vol. 7), ed. T. Kinoshita, (World Scientific, Singapore, 1990), p. 419.

[46] Andrzej Czarnecki and William J. Marciano, Phys. Rev. **D64** 013014 (2001).

[47] Davier M, et al.M. Davier1, A. Hoecker2,a, B. Malaescu1,b, Z. Zhang1 Eur. Phys. J. C 71:1515 (2011), erratum Eur. Phys. J. C 72:1874 (2012).

[48] Koru Hagiwara, Ruofan Liao, Alan D. Martin, Daisuke Nomura and Thomas Teubner, J. Phys. G**38**, 085003 (2011).

[49] Xu Feng, Karl Jansen, Marcus Perschlies and Dru B. Renner, Phys. Rev. Lett. 107 081802 (2011).

[50] A. Czarnecki, B. Krause and W.J. Marciano, Phys. Rev. Lett. **76** (1996) 3267.

[51] S. Peris, M. Perrottet and E. de Rafael, Phys. Lett. **B355** (1995) 523.

[52] A. Czarnecki, B. Krause and W. Marciano, Phys. Rev. **D52** (1995) R2619.

[53] A. Czarnecki, W.J. Marciano and A. Vainshtein, Phys. Rev. **D67** (2003) 073006. A. Czarnecki, W.J. Marciano and A. Vainshtein, Phys. Rev. **D67** (2003) 073006.

[54] James P. Miller, Eduardo de Rafael and B. Lee Roberts, Rept. Prog. Phys. **70**, 795-881, 2007.

[55] W.J. Marciano pointed out at the Intensity Frontier Workshop, Argonne, Nat. Lab. April 2013, that the Higgs' mass measurement from CERN increased the weak contribution by 1×10^{-11}. https://indico.fnal.gov/conferenceDisplay.py?confId=6248

[56] Andzrej Czarnecki and William J. Marciano in *Lepton Dipole Moments*, ed. B. Lee Roberts and William J. Marciano, Advanced Series on Directions in High Energy Physics, Vol. 20, World Scientific, 2010 p. 11 and references therin.

[57] Miller JP, Roberts BL, Jungmann K. *Lepton Dipole Moments*, ed Roberts BL, Marciano WJ, p.333. World Scientific (2010)

[58] Prades J, Rafael E. de, Vainshtein A. *Lepton Dipole Moments*, ed Roberts BL, Marciano WJ, World Scientific (2010), p.303; and arXiv:0901.0306v1 [hep-ph].

[59] http://www.int.washington.edu/PROGRAMS/11-47w/

[60] Stöckinger D. *Lepton Dipole Moments*, ed Roberts BL, Marciano WJ, p.393. World Scientific (2010)

J. Phys.G G 34:R45 (2007)

[61] Eduardo de Rafael, private communication.

[62] G. Amelino-Camelia, et al., (KLOE-2 Collaboration) arXiv:1003.3868v1 [hep-ex] March 2010.

[63] Tobias Goecke, Christian S. Fischer, Richard Williams Phys. Rev. **D83**, 094006 (2011).

[64] C. Fischer, private communication, October 2012.

[65] . Tom Blum, The 12th International Workshop on Tau Lepton Physics, 17-21 September 2012,Nagoya University.

[66] Tatsumi Aoyama, Masashi Hayakawa, Toichiro Kinoshita, Makiko Nio. May 2012. May 2012, arXiv:1205.5370 [hep-ph], Phys. Rev. Lett. **109**, 111808 (2012).

[67] D. Hanneke, S. Fogwell and G. Gabrielse, Phys. Rev. Lett. 100, 120801 (2008).

[68] rTatsumi Aoyama, Masashi Hayakawa, Toichiro Kinoshita, Makiko Nio. May 2012, e-Print: arXiv:1205.5368 [hep-ph], Phys. Rev. Lett. **109**, 111807 (2012).

[69] R. Bouchendira, P. Clade, S. Guellati-Khelifa, F. Nez, and F. Biraben, Phys. Rev. Lett. 106, 080801 (2011).

[70] A. Höcker and W.J. Marciano, Particle Data Group, Review *THE MUON ANOMALOUS MAGNETIC MOMENT* Updated July 2009, http://pdg.lbl.gov/

[71] M. Passera, W.J. Marciano and A. Sirlin, Phys. Rev. **D 78**, 013009 (2008).

[72] K. Hagiwara, A.D. Martin, D. Nomura and T. Teubner, Phys. Lett. **B649** 173 (2007).

[73] M. Davier, hep-ph/0701163v2, Jan. 2007.

[74] Fred Jegerlehner and Andreas Nyffeler, Phys.Rept. **477** 1 ((2009)

[75] James P. Miller, Eduardo de Rafael, B. Lee Roberts and Dominik Stöckinger, Ann. Rev. Nucl. Part. Sci. 62, 237 (2012).

[76] R. Alemany, M. Davier and A. Höcker, Eur.Phys.J. **C2** 123 (1998).

[77] Fred Jegerlehner, Robert Szafron, Eur.Phys.J. C71 (2011) 1632.

[78] M. Benayoun, P. David, L. DelBuono, F. Jegerlehner, Eur. Phys. J. **C72** (2012) 1848.

[79] M. Benayoun, P. David, L. DelBuono, F. Jegerlehner, arXiv:1210.7184v2 [hep-ph] 9 Nov 2012.

[80] M. Davier and A. Höcker, Phys. Lett.**B435**, 427 (1998).

[81] S. Binner, J.H. Kühn and K. Melnikov, Phys. Lett. **B 459**, 279 (1999).

[82] S. Actis, et al., (Working Group on Radiative Corrections and Monte Carlo Generators for Low Energies), arXiv0912.0749, Dec. 2009, submitted to Eur. Phys. J. **C**.

[83] BABAR Collaboration, B. Aubert et al., Phys. Rev. Lett. 103:231801 (2009).

[84] http://tau08.inp.nsk.su/ ; http://www.hep.manchester.ac.uk/TAU2010 ; http://tau2012.hepl.phys.nagoya-u.ac.jp/

[85] http://phipsi11.inp.nsk.su/

[86] F. Ambrosino et al., (KLOE Collaboration), Phys. Lett. **B 670**, 285 (2009).

[87] F. Ambrosino et al., (KLOE Collaboration), Phys. Lett. **B 700**, 102 (2011).

[88] Giuseppe Mandaglio, The 12th International Workshop on Tau Lepton Physics, 17-21 September 2012,Nagoya University.

[89] Jason Crnkovic, The 12th International Workshop on Tau Lepton Physics, 17-21 September 2012,Nagoya University.

[90] G. Venanzoni, Frascati Phys. Ser. **54** (2012) 52 [arXiv:1203.1501 [hep-ex]].

[91] D. Babusci, C. Bini, F. Bossi, G. Isidori, D. Moricciani, F. Nguyen, P. Raimondi and G. Venanzoni *et al.*, collider upgraded in energy," arXiv:1007.5219 [hep-ex].

[92] D. Babusci *et al.* [KLOE Collaboration], Phys. Lett. B **720** (2013) 336.

[93] D. Babusci, H. Czyz, F. Gonnella, S. Ivashyn, M. Mascolo, R. Messi, D. Moricciani and A. Nyffeler *et al.*, width and the $\gamma^*\gamma to \pi^0$ transition form factor with the KLOE-2 experiment," Eur. Phys. J. C **72** (2012) 1917.

[94] T. Blum, Phys. Rev. Lett. **91**, 052001-1 (2003).

[95] T. Blum, Nucl. Phys. Proc. Suppl. **129**, 904-906,2004, and arXiv hep-lat/0310064,

[96] T. Blum, private communication, February 2012.

[97] M. Davier and W.J. Marciano, Ann. Rev. Nucl. Part. Phys. **54**, 115 (2004).

[98] J. P. Miller, E. de Rafael, B. L. Roberts, and D. Stöckinger, Ann. Rev. Nucl. Part. Science **62** (2012) 237-264.

[99] D. W. Hertzog, J. P. Miller, E. de Rafael, B. Lee Roberts and D. Stöckinger, arXiv:0705.4617 [hep-ph].

[100] The articles listed in the SPIRES citations to Ref. [21] contain many different models beyond the standard model.

[101] F. Borzumati, G. R. Farrar, N. Polonsky and S. D. Thomas, Nucl. Phys. B **555** (1999) 53 [hep-ph/9902443].

[102] A. Crivellin, J. Girrbach and U. Nierste, Phys. Rev. D **83** (2011) 055009 [arXiv:1010.4485 [hep-ph]].

[103] E. Eichten, et al., Phys. Rev. Lett. **45**, 225 (1980); K. Lane, arXiv [hep-ph/0102131].

[104] T. Appelquist and B. A. Dobrescu, Phys. Lett. B **516** (2001) 85 [arXiv:hep-ph/0106140].

[105] M. Blanke, A. J. Buras, B. Duling, A. Poschenrieder and C. Tarantino, JHEP **0705** (2007) 013 [arXiv:hep-ph/0702136].

[106] S. Baek, N. G. Deshpande, X. G. He and P. Ko, Phys. Rev. D **64**, 055006 (2001) [hep-ph/0104141]; E. Ma, D. P. Roy and S. Roy, Phys. Lett. B **525** (2002) 101 [hep-ph/0110146]; J. Heeck and W. Rodejohann, Phys. Rev. D **84** (2011) 075007 [arXiv:1107.5238 [hep-ph]].

[107] S. Bar-Shalom, S. Nandi and A. Soni, Phys. Lett. B **709**, 207 (2012) [arXiv:1112.3661 [hep-ph]].

[108] H. Davoudiasl, J. L. Hewett and T. G. Rizzo, Phys. Lett. B **493** (2000) 135 [arXiv:hep-ph/0006097].

[109] S. C. Park and H. S. Song, Phys. Lett. B **506** (2001) 99 [arXiv:hep-ph/0103072].

[110] C. S. Kim, J. D. Kim and J. H. Song, Phys. Lett. B **511** (2001) 251 [arXiv:hep-ph/0103127].

[111] M. L. Graesser, Phys. Rev. D **61** (2000) 074019 [arXiv:hep-ph/9902310].

[112] M. Beneke, P. Dey and J. Rohrwild, arXiv:1209.5897 [hep-ph].

[113] K. Cheung, W. Y. Keung and T. C. Yuan, Phys. Rev. Lett. **99** (2007) 051803 [arXiv:0704.2588 [hep-ph]].

[114] J. A. Conley and J. S. Gainer, arXiv:0811.4168 [hep-ph].

[115] D. McKeen, arXiv:0912.1076 [hep-ph].

[116] C. M. Ho and T. W. Kephart, Phys. Lett. B **687**, 201 (2010) [arXiv:1001.3696 [hep-ph]].

[117] T. Hambye, K. Kannike, E. Ma and M. Raidal, Phys. Rev. D **75** (2007) 095003 [arXiv:hep-ph/0609228].

[118] M. Krawczyk, Acta Phys. Polon. B **33**, 2621 (2002) [hep-ph/0208076].

[119] M. Pospelov, Phys. Rev. D **80** (2009) 095002 [arXiv:0811.1030 [hep-ph]].

[120] H. Davoudiasl, H. -S. Lee and W. J. Marciano, Phys. Rev. Lett. **109**, 031802 (2012) [arXiv:1205.2709 [hep-ph]].

[121] R. Essig, P. Schuster and N. Toro, Phys. Rev. D **80** (2009) 015003 [arXiv:0903.3941 [hep-ph]].

[122] H. Davoudiasl, H. -S. Lee and W. J. Marciano, Phys. Rev. D **86**, 095009 (2012) [arXiv:1208.2973 [hep-ph]].

[123] T. Moroi, Phys. Rev. D **53** (1996) 6565 [Erratum-ibid. **56** (1997) 4424].

[124] D. Stöckinger, J. Phys. G **34** (2007) R45 [arXiv:hep-ph/0609168].

[125] S. Heinemeyer, D. Stöckinger and G. Weiglein, Nucl. Phys. B **690** (2004) 62 [arXiv:hep-ph/0312264]; S. Heinemeyer, D. Stöckinger and G. Weiglein, Nucl. Phys. B **699** (2004) 103 [arXiv:hep-ph/0405255].

[126] A. Arhrib and S. Baek, Phys. Rev. D **65**, 075002 (2002) [hep-ph/0104225].

[127] R. Benbrik, M. Gomez Bock, S. Heinemeyer, O. Stal, G. Weiglein and L. Zeune, Eur. Phys. J. C **72**, 2171 (2012) [arXiv:1207.1096 [hep-ph]].

[128] A. Arbey, M. Battaglia, A. Djouadi and F. Mahmoudi, JHEP **1209**, 107 (2012) [arXiv:1207.1348 [hep-ph]].

[129] R. Ruiz de Austri, R. Trotta and L. Roszkowski, JHEP **0605** (2006) 002 [arXiv:hep-ph/0602028]; JHEP **0704** (2007) 084 [arXiv:hep-ph/0611173]; JHEP **0707** (2007) 075 [arXiv:0705.2012]; B. C. Allanach, C. G. Lester and A. M. Weber, JHEP **0612** (2006) 065; B. C. Allanach, K. Cranmer, C. G. Lester and A. M. Weber, JHEP **0708**, 023 (2007); J. R. Ellis, S. Heinemeyer, K. A. Olive, A. M. Weber and G. Weiglein, JHEP **0708** (2007) 083; S. Heinemeyer, X. Miao, S. Su and G. Weiglein, JHEP **0808**, 087 (2008).

[130] P. Bechtle, T. Bringmann, K. Desch, H. Dreiner, M. Hamer, C. Hensel, M. Kramer and N. Nguyen *et al.*, JHEP **1206**, 098 (2012) [arXiv:1204.4199 [hep-ph]].

[131] C. Balazs, A. Buckley, D. Carter, B. Farmer and M. White, arXiv:1205.1568 [hep-ph].

[132] O. Buchmueller, R. Cavanaugh, M. Citron, A. De Roeck, M. J. Dolan, J. R. Ellis, H. Flacher and S. Heinemeyer *et al.*, Eur. Phys. J. C **72**, 2243 (2012) [arXiv:1207.7315 [hep-ph]].

[133] M. Endo, K. Hamaguchi, S. Iwamoto, K. Nakayama and N. Yokozaki, Phys. Rev. D **85** (2012) 095006 [arXiv:1112.6412 [hep-ph]].

[134] H. Baer, V. Barger, P. Huang and X. Tata, JHEP **1205** (2012) 109 [arXiv:1203.5539 [hep-ph]].

[135] M. Papucci, J. T. Ruderman and A. Weiler, JHEP **1209**, 035 (2012) [arXiv:1110.6926 [hep-ph]].

[136] T. J. LeCompte and S. P. Martin, Phys. Rev. D **85**, 035023 (2012) [arXiv:1111.6897 [hep-ph]].

[137] H. Murayama, Y. Nomura, S. Shirai and K. Tobioka, Phys. Rev. D **86**, 115014 (2012) [arXiv:1206.4993 [hep-ph]].

[138] B. A. Dobrescu and P. J. Fox, Eur. Phys. J. C **70** (2010) 263 [arXiv:1001.3147 [hep-ph]].

[139] W. Altmannshofer and D. M. Straub, JHEP **1009** (2010) 078 [arXiv:1004.1993 [hep-ph]].

[140] T. Appelquist, H. -C. Cheng and B. A. Dobrescu, Phys. Rev. D **64**, 035002 (2001) [hep-ph/0012100].

[141] I. Low, JHEP **0410**, 067 (2004) [hep-ph/0409025].

[142] J. Hubisz and P. Meade, Phys. Rev. D **71**, 035016 (2005) [hep-ph/0411264].

[143] J. M. Smillie and B. R. Webber, JHEP **0510** (2005) 069 [arXiv:hep-ph/0507170].

[144] Adam C, Kneur J -L, Lafaye R, Plehn T, Rauch M, Zerwas D. *Eur. Phys. J. C* 71:1520 (2011) [arXiv:1007.2190 [hep-ph]]

[145] N. Arkani-Hamed, G. L. Kane, J. Thaler and L. T. Wang, JHEP **0608**, 070 (2006) [arXiv:hep-ph/0512190].

[146] M. Alexander, S. Kreiss, R. Lafaye, T. Plehn, M. Rauch, and D. Zerwas, Chapter 9 in M. M. Nojiri *et al.*, *Physics Beyond the Standard Model: Supersymmetry,* arXiv:0802.3672 [hep-ph].

[147] B. C. Allanach *et al.*, *Proc. of the APS/DPF/DPB Summer Study on the Future of Particle Physics (Snowmass 2001)* ed. N. Graf, Eur. Phys. J. C **25** (2002) 113 [eConf **C010630** (2001) P125].

[148] C. F. Berger, J. S. Gainer, J. L. Hewett and T. G. Rizzo, JHEP **0902**, 023 (2009) [arXiv:0812.0980 [hep-ph]].

Chapter 3

Overview of the Experimental Technique

In this chapter we give an overview of how the experiment is done. This is followed by a number of chapters that give the details of the specific hardware being developed for E989. The order of those chapters follows the WBS as closely as possible.

The experiment consists of the following steps:

1. Production of an appropriate pulsed proton beam by an accelerator complex.
2. Production of pions using the proton beam that has been prepared.
3. Collection of polarized muons from pion decay $\pi^+ \to \mu^+ \nu_\mu$
4. Transporting the muon beam to the $(g-2)$ storage ring.
5. Injection of the muon beam into the storage ring.
6. Kicking the muon beam onto stored orbits.
7. Measuring the arrival time and energy of positrons from the decay $\mu^+ \to e^+ \bar{\nu}_\mu \nu_e$

Central to the determination of a_μ is the spin equation[1]

$$\vec{\omega}_a = -\frac{Qe}{m}\left[a_\mu \vec{B} + \left(a_\mu - \left(\frac{m}{p}\right)^2\right)\frac{\vec{\beta}\times\vec{E}}{c}\right], \tag{3.1}$$

that gives the rate at which the spin turns relative the the momentum vector, which turns with the cyclotron frequency. The electric field term is there since we use electrostatic vertical focusing in the ring. At the magic momentum, $p_{\rm m} = 3.09$ GeV/c, the effect of the motional magnetic field (the $\vec{\beta}\times\vec{E}$ term) vanishes.

Measurement of a_μ requires the determination of the muon spin frequency ω_a and the magnetic field averaged over the muon distribution.

[1] See Section 3.3 for the details.

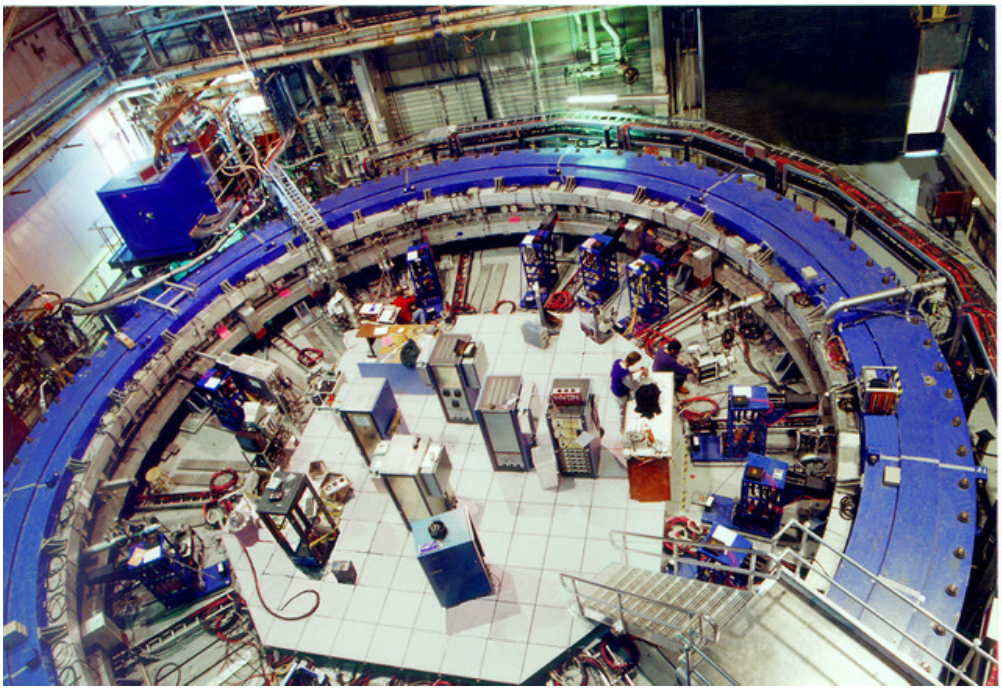

Figure 3.1: The E821 storage-ring magnet at Brookhaven Lab.

3.1 Production and Preparation of the Muon Beam

E989 will bring a bunched beam from the 8 GeV Booster to a pion production target located where the antiproton production target was in the Tevatron collider program (see Chapter 7). Pions of 3.11 GeV/c ±5% will be collected and sent into a large-acceptance beamline. Muons are produced in the weak pion decay

$$\pi^{\mp} \rightarrow \mu^{\mp} + \bar{\nu}_{\mu}(\nu_{\mu}). \tag{3.2}$$

Since the antineutrino (neutrino) is right-handed (left-handed) the μ^- (μ^+) is left-handed (right-handed). A beam of polarized muons can be obtained from a beam of pions by selecting the highest-energy muons (a "forward beam") or by selecting the lowest-energy muons (a "backward beam"), where forward or backward refers to whether the decay is forward of backward in the center-of-mass frame relative to the pion momentum. Polarizations significantly greater than 90% are easily obtained in such beams. The pions and daughter muons will be injected into the Delivery Ring (the re-purposed $\bar{p}$ debuncher ring), where after several turns the remaining pions decay. The surviving muon beam will be extracted and brought to the muon storage ring built for E821 at Brookhaven.

3.2 Injection into the Storage Ring

A photograph of the E821 magnet is shown in Figure 3.1. It is clear from the photo that this "storage ring" is very different from the usual one that consists of lumped elements. The

storage ring magnet is energized by three superconducting coils shown in Fig 3.2(b). The continuous "C" magnet yoke is built from twelve 30° segments of iron that was designed to eliminate the end effects present in lumped magnets. This construction eliminates the large gradients that would make the determination of average magnetic field, $\langle B \rangle$, very difficult. Furthermore, a small perturbation in the yoke can effect the field halfway around the ring at the ppm level. Thus every effort is made to minimize holes in the yoke, and other perturbations. The only penetrations through the yoke are to permit the muon beam to enter the magnet as shown in Fig 3.2(a), and to connect cryogenic services and power to the inflector magnet and to the outer radius coil (see Fig. 3.2(b)). Where a hole in the yoke is necessary, extra steel was placed around the hole on the outside of the yoke to compensate for the missing material.

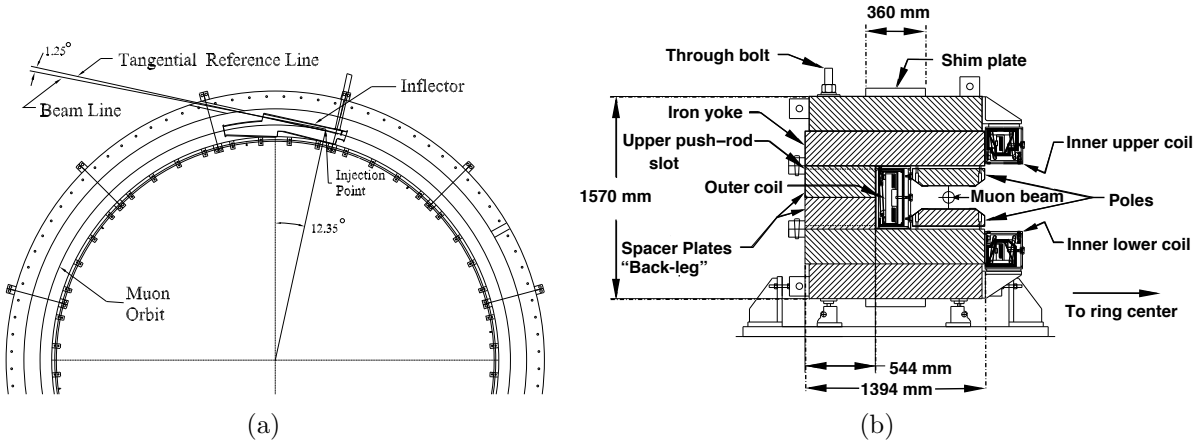

Figure 3.2: (a) Plan view of the beam entering the storage ring. (b) Elevation view of the storage-ring magnet cross section.

The beam enters through a hole in the "back-leg" of the magnet and then crosses into the inflector magnet, which provides an almost field free region, delivering the beam to the edge of the storage region. The geometry is rather constrained, as can be seen in Fig. 3.3(a). The injection geometry is sketched in Fig. 3.3(b). The kick required to put magic momentum muons onto a stable orbit centered at magic radius is on the order of 10 mrad.

The requirements on the muon kicker are rather severe:

1. Since the magnet is continuous, any kicker device has to be inside of the precision magnetic field region.

2. The kicker hardware cannot contain magnetic elements such as ferrites, because they will spoil the uniform magnetic field.

3. Any eddy currents produced in the vacuum chamber, or in the kicker electrodes by the kicker pulse must be negligible by 10 to 20 μs after injection, or must be well known and corrected for in the measurement.

4. Any kicker hardware must fit within the real estate occupied by the E821 kicker, which employed three 1.7 m long devices.

5. The kicker pulse should be shorter than the cyclotron period of 149 ns.

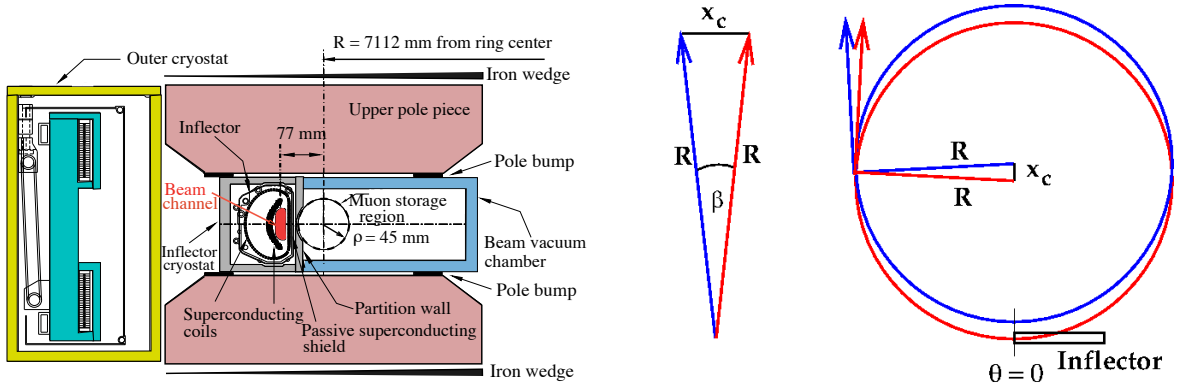

Figure 3.3: (a) The inflector exit showing the incident beam center 77 mm from the center of the storage region. The incident muon beam channel is highlighted in red. (b) The geometry of the necessary kick. The incident beam is the red circle, and the kick effectively moves the red circle over to the blue one.

I would remove this since we cover the Quads in much more detail later

The layout of the ring is shown in Fig. 3.4. The Quadrupoles cover 43% of the circumference, leaving space for the kicker and other devices. Each of the three kicker modules are 1.7 m long.

3.3 The Spin Equations

Measurements of magnetic and electric dipole moments make use of the torque on a dipole in an external field:

$$\vec{\tau} = \vec{\mu} \times \vec{B} + \vec{d} \times \vec{E}, \tag{3.3}$$

where we include the possibility of an electric dipole moment ($\vec{d}$). Except for the original Nevis spin rotation experiment, the muon magnetic dipole moment experiments inject a beam of polarized muons into a magnetic field and measure the rate at which the spin turns relative to the momentum, $\vec{\omega}_a = \vec{\omega}_S - \vec{\omega}_C$, where S and C stand for spin and cyclotron, respectively. These two frequencies, in the absence of any other external fields, are given by

$$\omega_S = -g\frac{Qe}{2m}B - (1-\gamma)\frac{Qe}{\gamma m}B; \tag{3.4}$$

$$\omega_C = -\frac{Qe}{m\gamma}B; \tag{3.5}$$

$$\omega_a = \omega_S - \omega_C = -\left(\frac{g-2}{2}\right)\frac{Qe}{m}B = -a_\mu\frac{Qe}{m}B \tag{3.6}$$

(where $e > 0$ and $Q = \pm 1$). There are two important features of ω_a: (i) It only depends on the anomaly rather than on the full magnetic moment; (ii) It depends linearly on the applied magnetic field.

To measure the anomaly, it is necessary to measure ω_a, and to determine the magnetic field B. The relevant quantity is $\langle B \rangle$, which is the magnetic field convolved with the muon beam distribution, M defined as

$$\langle B \rangle = \int M(r,\theta) B(r,\theta) r dr d\theta, \tag{3.7}$$

where the magnetic field $B(r,\theta)$ is expressed as the multipole expansion

$$B(r,\theta) = \sum_{n=0}^{\infty} r^n \left[c_n \cos n\theta + s_n \sin n\theta \right], \tag{3.8}$$

and the muon distribution is expressed in terms of moments

$$M(r,\theta) = \sum_{m=0}^{\infty} [\xi_m(r) \cos m\theta + \sigma_m(r) \sin m\theta]. \tag{3.9}$$

Because the harmonics $\sin n\theta \sin m\theta$, etc., orthogonal when integrated over one period, non-vanishing integrals come from products of the same moment/multipole, in the expression for $\langle B \rangle$. To determine $\langle B \rangle$ to sub-part-per-million (ppm) precision, one either needs excellent knowledge of the multipole and moment distributions for B and M; or care must be taken to minimize the number of terms, with only the leading term being large, so that only the first few multipoles are important. This was achieved in the most recent experiment [6] by using a circular beam aperture, and making a very uniform dipole magnetic field.

However there is one important issue to be solved: How can the muon beam be confined to a storage ring if significant magnetic gradients cannot be used to provide vertical focusing? The answer to this question was discovered by the third CERN collaboration [1], which used an electric quadrupole field to provide vertical focusing. Of course, a relativistic particle feels a motional magnetic field proportional to $\vec{\beta} \times \vec{E}$, but the full relativistic spin equation contains a cancellation as can be seen below. Assuming that the velocity is transverse to the magnetic field ($\vec{\beta} \cdot \vec{B} = 0$), one obtains [2, 3]

$$\vec{\omega}_{a\eta} = \vec{\omega}_a + \vec{\omega}_\eta = -\frac{Qe}{m} \left[a_\mu \vec{B} + \left(a_\mu - \left(\frac{m}{p} \right)^2 \right) \frac{\vec{\beta} \times \vec{E}}{c} \right] - \eta \frac{Qe}{2m} \left[\frac{\vec{E}}{c} + \vec{\beta} \times \vec{B} \right]. \tag{3.10}$$

There are both motional magnetic and electric fields in this equation – the terms which are proportional to $\vec{\beta} \times \vec{E}$ and $\vec{\beta} \times \vec{B}$, respectively.

The expression for ω_a is

$$\vec{\omega}_a = -\frac{Qe}{m} \left[a_\mu \vec{B} + \left(a_\mu - \left(\frac{m}{p} \right)^2 \right) \frac{\vec{\beta} \times \vec{E}}{c} \right]. \tag{3.11}$$

For the "magic" momentum $p_{\rm magic} = m/\sqrt{a} \simeq 3.09$ GeV/c ($\gamma_{\rm magic} = 29.3$), the second term vanishes, and the electric field does not contribute to the spin motion relative to the

momentum.[2] Note that if $g = 2$, then $a = 0$ and the spin would follow the momentum, turning at the cyclotron frequency.

3.4 Vertical Focusing with Electrostatic Quadrupoles

The storage ring acts as a weak-focusing betatron, with the vertical focusing provided by electrostatic quadrupoles. The ring is operated at the magic momentum, so that the electric field does not contribute to the spin precession. However there is a second-order correction to the spin frequency from the radial electric field, which is discussed below. There is also a correction from the vertical betatron motion, since the spin equations in the previous section were derived with the assumption that $\vec{\beta} \cdot \vec{B} = 0$.

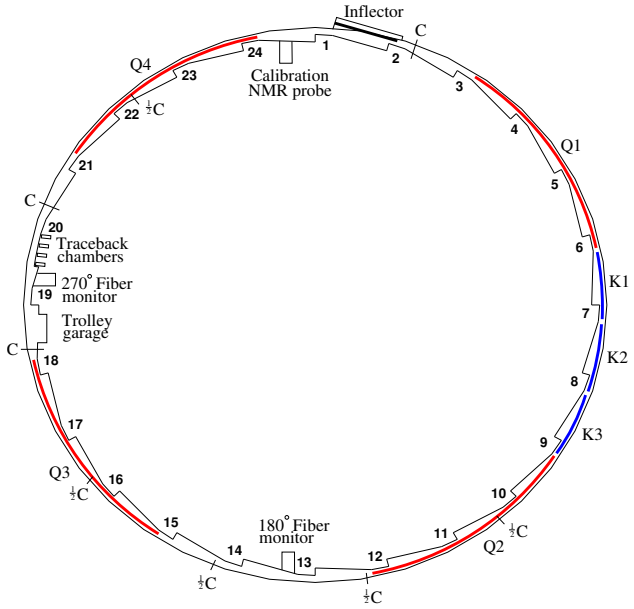

Figure 3.4: The layout of the storage ring, as seen from above, showing the location of the inflector, the kicker sections (labeled K1-K3), and the quadrupoles (labeled Q1-Q4). The beam circulates in a clockwise direction. Also shown are the collimators, which are labeled "C", or "$\frac{1}{2}$C" indicating whether the Cu collimator covers the full aperture, or half the aperture. The collimators are rings with inner radius: 45 mm, outer radius: 55 mm, thickness: 3 mm. The scalloped vacuum chamber consists of 12 sections joined by bellows. The chambers containing the inflector, the NMR trolley garage, and the trolley drive mechanism are special chambers. The other chambers are standard, with either quadrupole or kicker assemblies installed inside. An electron calorimeter is placed behind each of the radial windows, at the position indicated by the calorimeter number.

[2]Small corrections to the measured frequency must be applied since $\vec{\beta} \cdot \vec{B} \simeq 0$ and not all muons are at the magic momentum. These are discussed in Chapter 4.

3.5 Muon Decay

The dominant muon decay is

$$\mu^{\mp} \to e^{\mp} + \nu_{\mu}(\bar{\nu}_{\mu}) + \bar{\nu}_{e}(\nu_{e}) \tag{3.12}$$

which also violates parity.

Since the kinematics of muon decay are central to the measurements of a_{μ}, we discuss the general features in this section. Additional details are given in Ref. [17]. From a beam of pions traversing a straight beam-channel consisting of focusing and defocusing elements (FODO), a beam of polarized, high energy muons can be produced by selecting the "forward" or "backward" decays. The forward muons are those produced, in the pion rest frame, nearly parallel to the pion laboratory momentum and are the decay muons with the highest laboratory momenta. The backward muons are those produced nearly anti-parallel to the pion momentum and have the lowest laboratory momenta. The forward μ^{-} (μ^{+}) are polarized along (opposite) their lab momenta respectively; the polarization reverses for backward muons. The E821 experiment used forward muons, as will E989, the difference being the length of the pion decay line, which in E989 will be 1,900 m.

The pure $(V-A)$ three-body weak decay of the muon, $\mu^{-} \to e^{-} + \nu_{\mu} + \bar{\nu}_{e}$ or $\mu^{+} \to e^{+} + \bar{\nu}_{\mu} + \nu_{e}$, is "self-analyzing", that is, the parity-violating correlation between the directions in the muon rest frame (MRF) of the decay electron and the muon spin can provide information on the muon spin orientation at the time of the decay. When the decay electron has the maximum allowed energy in the MRF, $E'_{\rm max} \approx (m_{\mu}c^2)/2 = 53$ MeV. The neutrino and anti-neutrino are directed parallel to each other and at 180° relative to the electron direction. The $\nu\bar{\nu}$ pair carry zero total angular momentum; the electron carries the muon's angular momentum of 1/2. The electron, being a lepton, is preferentially emitted left-handed in a weak decay, and thus has a larger probability to be emitted with its momentum *anti-parallel* rather than parallel to the μ^{-} spin. Similarly, in μ^{+} decay, the highest-energy positrons are emitted *parallel* to the muon spin in the MRF.

In the other extreme, when the electron kinetic energy is zero in the MRF, the neutrino and anti-neutrino are emitted back-to-back and carry a total angular momentum of one. In this case, the electron spin is directed opposite to the muon spin in order to conserve angular momentum. Again, the electron is preferentially emitted with helicity -1, however in this case its momentum will be preferentially directed *parallel* to the μ^{-} spin. The positron, in μ^{+} decay, is preferentially emitted with helicity +1, and therefore its momentum will be preferentially directed *anti-parallel* to the μ^{+} spin.

With the approximation that the energy of the decay electron $E' >> m_e c^2$, the differential decay distribution in the muon rest frame is given by[23],

$$dP(y', \theta') \propto n'(y') \left[1 \pm \mathcal{A}(y') \cos\theta'\right] dy' d\Omega' \tag{3.13}$$

where y' is the momentum fraction of the electron, $y' = p'_e/p'_{e\ \rm max}$, $d\Omega'$ is the solid angle, $\theta' = \cos^{-1}(\hat{p}'_e \cdot \hat{s})$ is the angle between the muon spin and $\vec{p}\,'_e$, $p'_{e\ \rm max}c \approx E'_{max}$, and the $(-)$ sign is for negative muon decay. The number distribution $n(y')$ and the decay asymmetry $\mathcal{A}(y')$ are given by

$$n(y') = 2y'^2(3-2y') \quad \text{and} \quad \mathcal{A}(y') = \frac{2y'-1}{3-2y'}. \tag{3.14}$$

Note that both the number and asymmetry reach their maxima at $y' = 1$, and the asymmetry changes sign at $y' = \frac{1}{2}$, as shown in Figure 3.5(a).

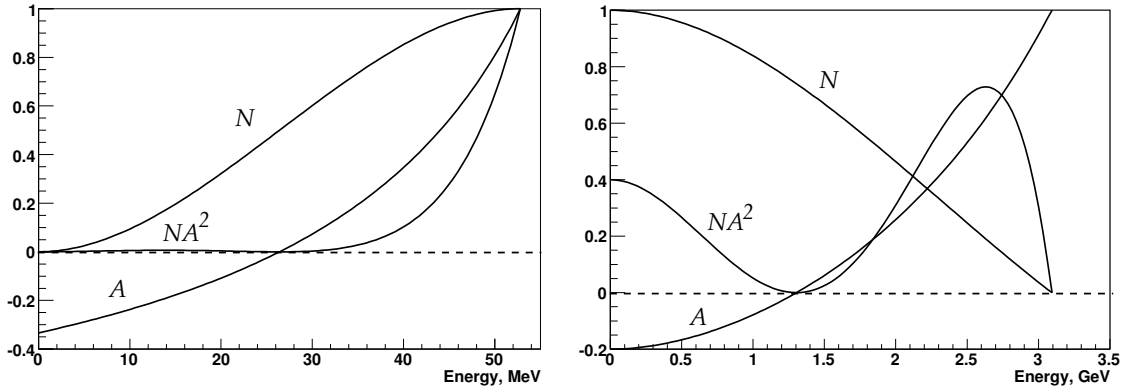

(a) Muon Rest Frame (b) Laboratory Frame

Figure 3.5: Number of decay electrons per unit energy, N (arbitrary units), value of the asymmetry A, and relative figure of merit NA^2 (arbitrary units) as a function of electron energy. Detector acceptance has not been incorporated, and the polarization is unity. For the third CERN experiment and E821, $E_{max} \approx 3.1$ GeV ($p_\mu = 3.094$ GeV/c) in the laboratory frame.

The CERN and Brookhaven based muon $(g-2)$ experiments stored relativistic muons of the magic momentum in a uniform magnetic field, which resulted in the muon spin precessing with constant frequency $\vec{\omega}_a$, while the muons traveled in circular orbits. If *all* decay electrons were counted, the number detected as a function of time would be a pure exponential; therefore we seek cuts on the laboratory observable to select subsets of decay electrons whose numbers oscillate at the precession frequency. The number of decay electrons in the MRF varies with the angle between the electron and spin directions, the electrons in the subset should have a preferred direction in the MRF when weighted according to their asymmetry as given in Equation 3.13. At $p_\mu \approx 3.094$ GeV/c the directions of the electrons resulting from muon decay in the laboratory frame are very nearly parallel to the muon momentum regardless of their energy or direction in the MRF. The only practical remaining cut is on the electron's laboratory energy. An energy subset will have the desired property: there will be a net component of electron MRF momentum either parallel or antiparallel to the laboratory muon direction. For example, suppose that we only count electrons with the highest laboratory energy, around 3.1 GeV. Let $\hat{z}$ indicate the direction of the muon laboratory momentum. The highest-energy electrons in the laboratory are those near the maximum MRF energy of 53 MeV, and with MRF directions nearly parallel to $\hat{z}$. There are more of these high-energy electrons when the μ^- spins are in the direction opposite to $\hat{z}$ than when the spins are parallel to $\hat{z}$. Thus the number of decay electrons reaches a maximum when the muon spin direction is opposite to $\hat{z}$, and a minimum when they are parallel. As the spin precesses the number of high-energy electrons will oscillate with frequency ω_a. More generally, at laboratory energies above ~ 1.2 GeV, the electrons have a preferred average MRF direction parallel to $\hat{z}$ (see Figure 3.5). In this discussion, it is assumed that the

spin precession vector, $\vec{\omega}_a$, is independent of time, and therefore the angle between the spin component in the orbit plane and the muon momentum direction is given by $\omega_a t + \phi$, where ϕ is a constant.

Equations 3.13 and 3.14 can be transformed to the laboratory frame to give the electron number oscillation with time as a function of electron energy,

$$N_d(t, E) = N_{d0}(E)e^{-t/\gamma\tau}[1 + A_d(E)\cos(\omega_a t + \phi_d(E))], \tag{3.15}$$

or, taking all electrons above threshold energy E_{th},

$$N(t, E_{th}) = N_0(E_{th})e^{-t/\gamma\tau}[1 + A(E_{th})\cos(\omega_a t + \phi(E_{th}))]. \tag{3.16}$$

In Equation 3.15 the differential quantities are,

$$A_d(E) = \mathcal{P}\frac{-8y^2 + y + 1}{4y^2 - 5y - 5}, \quad N_{d0}(E) \propto (y - 1)(4y^2 - 5y - 5), \tag{3.17}$$

and in Equation 3.16,

$$N(E_{th}) \propto (y_{th} - 1)^2(-y_{th}^2 + y_{th} + 3), \qquad A(E_{th}) = \mathcal{P}\frac{y_{th}(2y_{th} + 1)}{-y_{th}^2 + y_{th} + 3}. \tag{3.18}$$

In the above equations, $y = E/E_{max}$, $y_{th} = E_{th}/E_{max}$, $\mathcal{P}$ is the polarization of the muon beam, and E, E_{th}, and $E_{max} = 3.1$ GeV are the electron laboratory energy, threshold energy, and maximum energy, respectively.

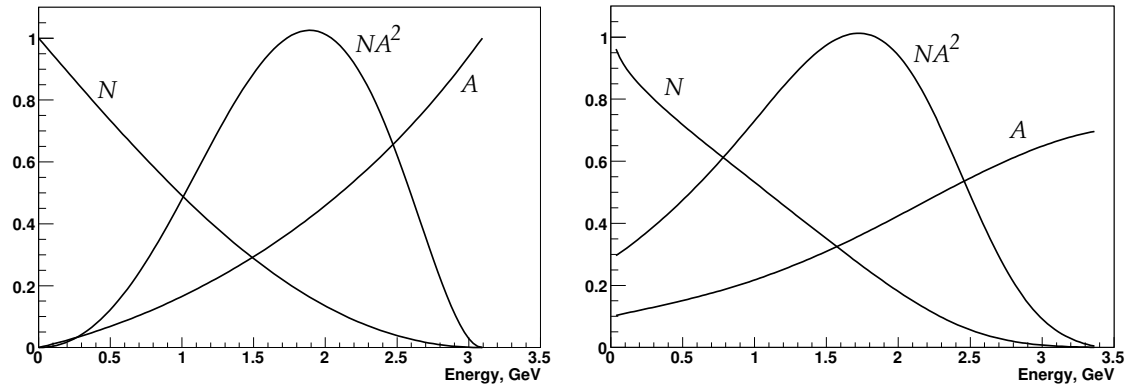

(a) No detector acceptance or energy resolution included

(b) Detector acceptance and energy resolution included

Figure 3.6: The integral N, A, and NA^2 (arbitrary units) for a single energy-threshold as a function of the threshold energy; (a) in the laboratory frame, not including and (b) including the effects of detector acceptance and energy resolution for the E821 calorimeters discussed below. For the third CERN experiment and E821, $E_{max} \approx 3.1$ GeV ($p_\mu = 3.094$ GeV/c) in the laboratory frame.

The fractional statistical error on the precession frequency, when fitting data collected over many muon lifetimes to the five-parameter function (Equation 3.16), is given by

$$\delta\epsilon = \frac{\delta\omega_a}{\omega_a} = \frac{\sqrt{2}}{2\pi f_a \tau_\mu N^{\frac{1}{2}} A}. \tag{3.19}$$

where N is the total number of electrons, and A is the asymmetry, in the given data sample. For a fixed magnetic field and muon momentum, the statistical figure of merit is NA^2, the quantity to be maximized in order to minimize the statistical uncertainty.

The energy dependencies of the numbers and asymmetries used in Equations 3.15 and 3.16, along with the figures of merit NA^2, are plotted in Figures 3.5 and 3.6 for the case of E821. The statistical power is greatest for electrons at 2.6 GeV (Figure 3.5). When a fit is made to all electrons above some energy threshold, the optimal threshold energy is about 1.7-1.8 GeV (Figure 3.6).

The resulting arrival-time spectrum of electrons with energy greater than 1.8 GeV from the final E821 data run is shown in Fig. 3.7. While this plot clearly exhibits the expected features of the five-parameter function, a least-square fit to these 3.6 billion events gives an unacceptably large chi-square. A number of small effects must be taken into account to obtain a reasonable fit, which will be discussed in detail in the section on systematic errors.

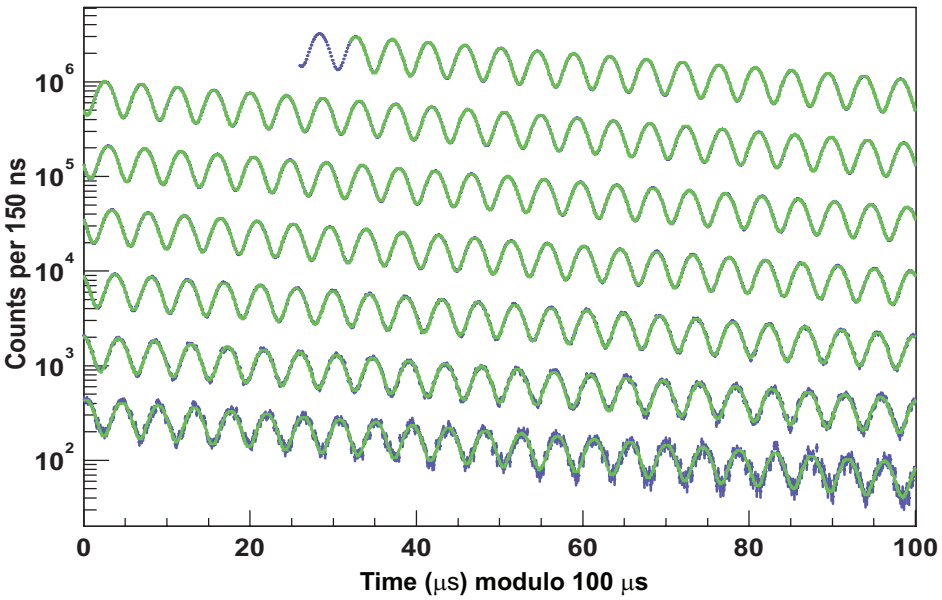

Figure 3.7: Histogram, modulo 100 μ s, of the number of detected electrons above 1.8 GeV for the 2001 data set as a function of time, summed over detectors, with a least-squares fit to the spectrum superimposed. Total number of electrons is 3.6×10^9. The data are in blue, the fit in green.

3.6 The Magnetic Field

The rate at which the muon spin turns relative to its momentum (Eq. 3.11) depends on the anomaly a_μ and on the average magnetic field given by Eq. 3.7. Thus the determination of a_μ to sub-tenths of a ppm requires that both ω_a and $\langle B \rangle$ be determined to this level. The muon beam is confined to a cylindrical region of 9 cm diameter, which is 44.7 m in length. The volume of this region is $\simeq 1.14$ m^3 or $\simeq 40$ ft^3, which sets the scale for the magnetic field measurement and control. The E989 goal is to know the magnetic field averaged over the muon distribution to an uncertainty of ± 70 parts per billion (ppb).

The problem breaks into several pieces:

1. Producing as uniform magnetic field as possible by shimming the magnet.

2. Stabilizing B in time at the sub-ppm level by feedback, with mechanical and thermal stability.

3. Monitoring B to the 20 ppb level around the storage ring during data collection.

4. Periodically mapping the field throughout the storage region and correlating the field map to the monitoring information without turning off the magnet between data collection and field mapping. It is essential that the magnet not be powered off unless absolutely necessary.

5. Obtaining an absolute calibration of the B-field relative to the Larmor frequency of the free proton.

The only magnetic field measurement technique with the sensitivity needed to measure and control the B-field to the tens of ppb is nuclear magnetic resonance (NMR). Pulsed NMR was used, where a $\pi/2$ RF pulse rotated the spins and the resulting free-induction decay (FID) was detected by a pickup coil around the sample. The E821 baseline design used the NMR of protons in a water sample with a $CuSO_4$ additive that shortened the relaxation time, with the probes tuned to operate in a 1.45 T field. When the water evaporated from a few of the probes, the water was replaced with petrolium jelly, which the added features of a smaller sensitivity to temperature changes and no evaporation.

Special nuclear magnetic resonance (NMR) probes [42, 6] were used in E821 to measure and monitor the magnetic field during the experimental data collection.[3] Three types of probes were used: a spherical water probe that provided the absolute calibration to the free proton; cylindrical probes that were used monitor the field during data collection and in an NMR trolley to map the field; and a smaller spherical probe which could be plunged into the muon storage region by means of a bellows system to transfer the absolute calibration to the trolley probes. A collection of 378 cylindrical probes placed in symmetrically machined grooves on the top and bottom of the muon beam vacuum chamber gave a point to point measure of the magnetic field while beam was in the storage ring. Probes at the same azimuthal location but different radii gave information on changes to the quadrupole component of the field at that location.

[3] The probes are described in Chapter 15

The field mapping trolley contained 17 cylindrical probes arranged in concentric circles as shown in Figure 3.8. At several-day intervals during the running periods, the beam was turned off, and the field mapping trolley was driven around inside of the evacuated beam chamber measuring the magnetic field with each of the 17 trolley probes at 6,000 locations around the ring. One of the resulting field maps, averaged over azimuth, is shown in Figure 3.8(b).

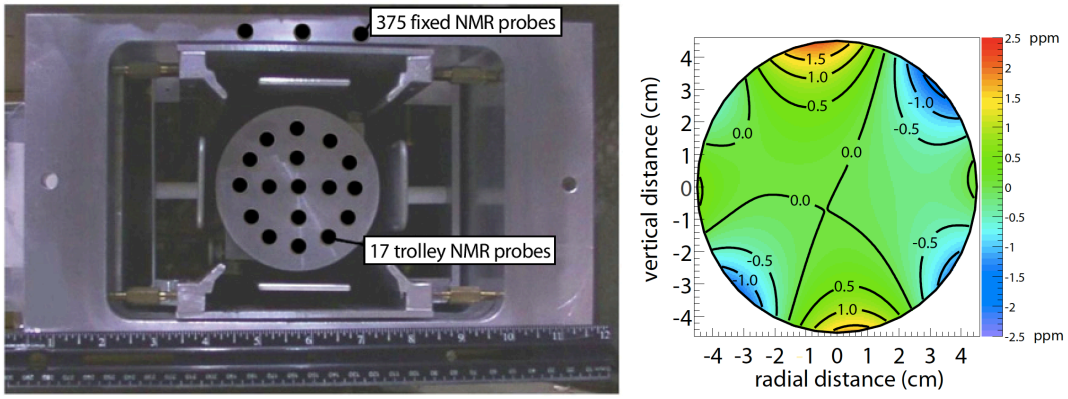

(a) (b)

Figure 3.8: (a)The electrostatic quadrupole assembly inside a vacuum chamber showing the NMR trolley sitting on the rails of the cage assembly. Seventeen NMR probes are located just behind the front face in the places indicated by the black circles. The inner (outer) circle of probes has a diameter of 3.5 cm (7 cm) at the probe centers. The storage region has a diameter of 9 cm. The vertical location of three of the 180 upper fixed probes is also shown. An additional 180 probes are located symmetrically below the vacuum chamber. (Reprinted with permission from [6]. Copyright 2006 by the American Physical Society.) (b) A contour plot of the magnetic field averaged over azimuth, 0.5 ppm intervals.

The absolute calibration utilizes a probe with a spherical water sample [7]. The Larmor frequency of a proton in a spherical water sample is related to that of the free proton through $f_{\rm L}({\rm sph}-{\rm H_2O},T) = [1-\sigma({\rm H_2O},T)]\, f_{\rm L}({\rm free})$, [8, 9] where $\sigma({\rm H_2O},T) = 25.790(14)\times 10^{-6}$ is from the diamagnetic shielding of the proton in the water molecule, determined from [10]

$$\sigma({\rm H_2O}, 34.7^{\circ}C) = 1 - \frac{g_p({\rm H_2O}, 34.7^{\circ}C)}{g_J(H)}\,\frac{g_J(H)}{g_p(H)}\,\frac{g_p(H)}{g_p({\rm free})}\,. \tag{3.20}$$

The terms are: the ratio of the g-factors of the proton in a spherical water sample to that of the electron in the hydrogen ground state ($g_J(H)$) [10]; the ratio of electron to proton g-factors in hydrogen [11]; the bound-state correction relating the g-factor of the proton bound in hydrogen to the free proton [12, 13]. The temperature dependence is from Reference [14]. An alternate absolute calibration would be to use an optically pumped ^{3}He NMR probe [15]. This has several advantages: the sensitivity to the probe shape is negligible, and the temperature dependence is also negligible. This option is being explored for E989.

The calibration procedure used above permits the magnetic field to be expressed in terms of the Larmor frequency of a free proton, ω_p. The magnetic field is weighted by the muon

distribution, and also averaged over the running time weighed by the number of stored muons to determine the value of ω_p which is combined with the average ω_a to determine a_μ. The reason for the use of these two frequencies, rather than B measured in tesla can be understood from Eq. 3.11. To obtain a_μ from this relationship requires precise knowledge of the muon charge to mass ratio.

To determine a_μ from the two frequencies ω_a and ω_p, we use the relationship

$$a_\mu = \frac{\omega_a/\omega_p}{\lambda_+ - \omega_a/\omega_p} = \frac{\mathcal{R}}{\lambda_+ - \mathcal{R}}\,, \tag{3.21}$$

where the ratio

$$\lambda_+ = \mu_{\mu^+}/\mu_p = 3.183\,345\,137\,(85) \tag{3.22}$$

is the muon-to-proton magnetic moment ratio [16] measured from muonium (the μ^+e^- atom) hyperfine structure[18]. Of course, to use λ_+ to determine a_{μ^-} requires the assumption of *CPT* invariance, *viz.* ($a_{\mu^+} = a_{\mu^-}$; $\lambda_+ = \lambda_-$). The comparison of $\mathcal{R}_{\mu^+}$ with $\mathcal{R}_{\mu^-}$ provides a *CPT* test. In E821

$$\Delta\mathcal{R} = \mathcal{R}_{\mu^-} - \mathcal{R}_{\mu^+} = (3.6 \pm 3.7) \times 10^{-9} \tag{3.23}$$

3.7 Measuring the Muon EDM: d_μ

If an EDM is present, the measured frequency is the vector sum of two terms: the spin motion from the torques $\vec{\mu} \times \vec{B}$ and from $\vec{d} \times \vec{E}$, as shown in Eq. 3.10; $\vec{\omega}_{a\eta} = \vec{\omega}_a + \vec{\omega}_\eta$. The first term comes from the anomalous magnetic moment, a, and the second from the electric dipole moment. The motional electric field is much larger than any electric field in the lab, so the observed frequency $\vec{\omega}$ is (essentially) the vector sum of two orthogonal angular frequencies, $\vec{\omega}_a$ and $\vec{\omega}_\eta$. These two frequencies are shown in Fig. 3.9, where the EDM related frequency ω_η is greatly exaggerated.

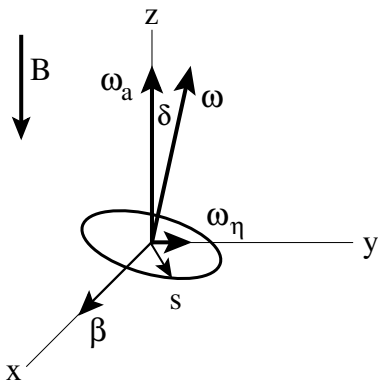

Figure 3.9: The two frequencies present if the muon has both a magnetic and electric dipole moment (not to scale). Note that the EDM ω_η is much smaller than ω_a. The muon spin precession plane is tilted by an angle proportional to the particle's EDM value.

Thus there are *two* effects due to an electric dipole moment:

1. The observed frequency is the vector sum of ω_a and ω_η so the magnitude of the observed frequency is increased from ω_a to

$$\omega_{a\eta} \simeq \sqrt{\omega_a^2 + \omega_\eta^2} = \omega_a \sqrt{1 + \left(\frac{\eta\beta}{2a}\right)^2} \tag{3.24}$$

2. The spin precession plane is tilted (everywhere around the ring) by a (very small) angle

$$\delta = \tan^{-1}\frac{\omega_\eta}{\omega_a} = \tan^{-1}\left(\frac{\eta\beta}{2a}\right) \tag{3.25}$$

as shown in Fig. 3.9

The tilting of the spin precession plane everywhere around the ring, is very much like there is a net radial magnetic field which when integrated around the ring is not zero. In a ring with a purely magnetic field, the average radial B-field for a stored particle is zero, since the particle adjusts its vertical position in the focusing system to ensure this. However, in the presence of other forces, like vertical E-fields, gravity, etc., this is not strictly true and must be taken into account for systematic error estimation. A major tool against these types of systematic errors, which is only possible in a dedicated EDM storage ring experiment, would be the ability to inject into the storage ring both in a clockwise (CW) and counter-clockwise (CCW) sense, where the non-magnetic forces are kept the same while the EDM signal changes sign.

The tipping of the plane of precession around the ring has an important implication for the resulting decay positrons. As the muon spin turns with the frequency ω_a, following the circle shown in Fig. 3.9, the EDM causes an up-down oscillation of the muon spin which is out of phase by $\pi/2$ with the $(g-2)$ precession. Thus the trajectories of the decay positrons (electrons) will oscillate between upward-going to downward-going with the frequency ω_a out of phase with ω_a. It was this effect which was searched for in the third $(g-2)$ experiment at CERN, and in E821 at Brookhaven. At CERN one detector station was outfitted with two scintillators, one just above the mid-plane, one just below.

Assuming the gain and acceptance of the upper and lower detectors are equal and the storage ring and vertical detector mid-plane are identical, the number of electrons above (+) or below (-) the mid-plane is given by[4]

$$N^{\pm}(t) \propto [1 \mp A_\eta \sin(\omega t + \phi) + A_\mu \cos(\omega t + \phi)] \tag{3.26}$$

where A_η is proportional to d_μ. A major source of systematic error arises if there is an offset between the average vertical position of the beam and the position of the boundary between the upper and lower detectors.

3.7.1 Search for d_μ in E821

In E821, three separate methods were used to search for the up-down oscillations[4]. Five-element hodoscopes were placed in front of about half of the 24 electron calorimeters, and the vertical centroid of the decay electron distribution was fit as a function of time. Five

calorimeter stations had finer-grained hodoscopes which also provided the vertical electron distribution of decay electrons as a function of time. One of the stations was equipped with a straw tube array that gave both x and y information, so that the electron tracks could be fit to search for the oscillation in upward- and downward-going tracks. These "traceback" chambers were primarily designed to provide information on the muon distribution in the storage ring[4], but turned out to be a powerful tool to search for the EDM signal. No evidence for an up-down oscillation was seen, and the result is[4]

$$d_\mu = (0.1 \pm 0.9) \times 10^{-19} e\text{−cm};\ |d_\mu| < 1.9 \times 10^{-19} e\text{−cm}\ (95\%\ \text{C.L.})\,, \tag{3.27}$$

a factor of five smaller than the previous limit.

3.7.2 Search for d_μ at Fermilab

Only the tracking detector in E821 had manageable systematic errors that could be reduced significantly in a new experiment.

References

[1] J. Bailey, et al., Nucl. Phys. **B150**, 1 (1979).

[2] L.H. Thomas, Nature **117**, (1926) 514 and Phil. Mag. **3** (1927) 1.

[3] Bargmann V, Michel L, Telegdi VL, Phys. Rev. Lett. 2:435 (1959)

[4] G.W. Bennett, et al., Phys. Rev. **D 80**, 052008 (2009).

[5] Bennett GW, et al. (The $g-2$ Collab.) Phys. Rev. Lett. 92:161802 (2004)

[6] Bennett GW, et al.(The $g-2$ Collab.) Phys. Rev. D, 73:072003 (2006)

[7] Fei X, Hughes V, Prigl R, *Nucl. Inst. Methods Phys. Res.* A394:349 (1997)

[8] Abragam A. In *Principles of Nuclear Magnetism'*, p. 173-178. Oxford U. Press, (1961)

[9] Mohr PJ, Taylor BH, *Rev. Mod. Phys.* 77:1 (2005)

[10] Phillips WD, et al. *Metrologia* 13:179 (1979)

[11] Winkler PF, Kleppner D, Myint T, Walther FG, *Phys. Rev.* A5:83 (1972)

[12] Lamb Jr. WE. *Phys. Rev.* 60:817 (1941)

[13] Grotch H, Hegstrom RA. *Phys. Rev.* A4:59 (1971)

[14] B.W. Petley et al. *Metrologia.***20**, 81 (1984)

[15] J.L. Flowers, B.W. Petley and M.G. Richards, Metrologia **30**, 75 (1993).

[16] Mohr PJ, Taylor BN, Newell DB, (CODATA recommended values). *Rev. Mod. Phys.* 80:633 (2008)

[17] James P. Miller, Eduardo de Rafael and B. Lee Roberts, Rept. Prog. Phys. **70**, 795-881, 2007.

[18] W. Liu et al., Phys. Rev. Lett. **82**, 711 (1999).

[19] The $g-2$ Collaboration: R.M. Carey et al., Phys. Rev. Lett. **82**, 1632 (1999).

[20] The $g-2$ Collaboration: H.N. Brown et al., Phys. Rev. D **62**, 091101 (2000).

[21] The $g-2$ Collaboration: H.N. Brown et al., Phys. Rev. Lett. **86**, 2227 (2001).

[22] The $g-2$ Collaboration: G.W. Bennett et al., Phys. Rev. Lett. **89**, 101804 (2002); Erratum-ibid. **89**, 129903 (2002).

Chapter 4

The Physics of Muon Storage

In this chapter we discuss the behavior of a beam in a weak-focusing betatron, and the features of the injection of a bunched beam that are important in the determination of ω_a. We also discuss the corrections to the measured frequency ω_a that come from the the vertical betatron motion, and the fact that not all muons are at the magic momentum (central radius) in the storage ring. The final section of this chapter discusses the systematic errors that come from the pion and muon beamlines.

The behavior of the beam in the $(g-2)$ storage ring directly affects the measurement of a_μ. Since the detector acceptance for decay electrons depends on the radial coordinate of the muon at the point where it decays, coherent radial motion of the stored beam can produce an amplitude modulation in the observed electron time spectrum. Resonances in the storage ring can cause particle losses, thus distorting the observed time spectrum, and must be avoided when choosing the operating parameters of the ring. Care is taken in setting the frequency of coherent radial beam motion, the "coherent betatron oscillation" (CBO) frequency, which lies close to the second harmonic of $f_a = \omega_a/(2\pi)$. If $f_{\rm CBO}$ is too close to $2f_a$, the beat frequency, $f_- = f_{CBO} - f_a$, complicates the extraction of f_a from the data, and can introduce a significant systematic error.

A pure quadrupole electric field provides a linear restoring force in the vertical direction, and the combination of the (defocusing) electric field and the central magnetic field provides a linear restoring force in the radial direction. The $(g-2)$ ring is a weak focusing ring[1, 2, 3] with the field index

$$n = \frac{\kappa R_0}{\beta B_0}, \tag{4.1}$$

where κ is the electric quadrupole gradient, B_0 is the magnetic field strength, R_0 is the magic radius $\equiv 7112$ mm, and β is the relativistic velocity of the muon beam. For a ring with a uniform vertical dipole magnetic field and a uniform quadrupole field that provides vertical focusing covering the full azimuth, the stored particles undergo simple harmonic motion called betatron oscillations, in both the radial and vertical dimensions.

The horizontal and vertical motion are given by

$$x = x_e + A_x \cos(\nu_x \frac{s}{R_0} + \delta_x) \quad \text{and} \quad y = A_y \cos(\nu_y \frac{s}{R_0} + \delta_y), \tag{4.2}$$

where s is the arc length along the trajectory. The horizontal and vertical tunes are given by $\nu_x = \sqrt{1-n}$ and $\nu_y = \sqrt{n}$. Several n - values were used in E821 for data acquisition:

$n = 0.137,\ 0.142$ and 0.122. The horizontal and vertical betatron frequencies are given by

$$f_x = f_C\sqrt{1-n} \simeq 0.929 f_C \quad \text{and} \quad f_y = f_C\sqrt{n} \simeq 0.37 f_C, \tag{4.3}$$

where f_C is the cyclotron frequency and the numerical values assume that $n = 0.137$. The corresponding betatron wavelengths are $\lambda_{\beta_x} = 1.08(2\pi R_0)$ and $\lambda_{\beta_y} = 2.7(2\pi R_0)$. It is important that the betatron wavelengths are not simple multiples of the circumference, as this minimizes the ability of ring imperfections and higher multipoles to drive resonances that would result in particle losses from the ring.

The field index also determines the angular acceptance of the ring. The maximum horizontal and vertical angles of the muon momentum are given by

$$\theta^x_{\max} = \frac{x_{\max}\sqrt{1-n}}{R_0}, \quad \text{and} \quad \theta^y_{\max} = \frac{y_{\max}\sqrt{n}}{R_0}, \tag{4.4}$$

where $x_{\max}, y_{\max} = 45$ mm is the radius of the storage aperture. For a betatron amplitude A_x or A_y less than 45 mm, the maximum angle is reduced, as can be seen from the above equations.

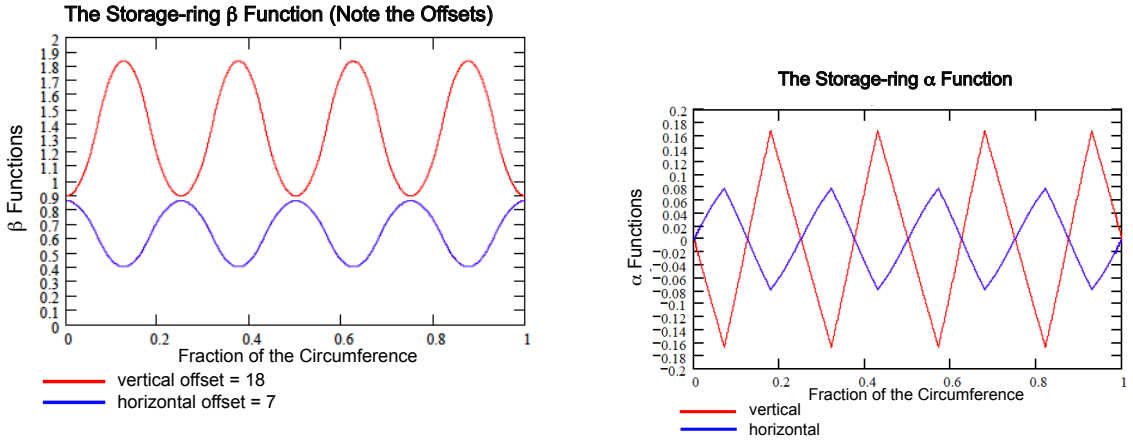

(a) (b)

Figure 4.1: (a) The horizontal (radial) and vertical beta functions for the E821 lattice. Note the scale offset. (b) The horizontal (radial) and vertical alpha functions for the E821 lattice. The n-value is 0.134 for both. (From Ref. [9]

For a ring with discrete quadrupoles, the focusing strength changes as a function of azimuth, and the equation of motion looks like an oscillator whose spring constant changes as a function of azimuth s. The motion is described by

$$x(s) = x_e + A\sqrt{\beta(s)}\cos(\psi(s) + \delta), \tag{4.5}$$

where $\beta(s)$ is one of the three Courant-Snyder parameters.[2]

The layout of the storage ring is shown in Figure 3.4. The four-fold symmetry of the quadrupoles was chosen because it provided quadrupole-free regions for the kicker, traceback

chambers, fiber monitors, and trolley garage; but the most important benefit of four-fold symmetry is to reduce the peak-to-peak betatron oscillation amplitudes, with $\sqrt{\beta_{\max}/\beta_{\min}} = 1.03$. The beta and alpha functions for the $(g-2)$ storage ring [9] are shown in Fig. 4.1.

fix this part

average magnetic field weighted by the muon distribution that appears in the ω_a equation

$$\vec{\omega}_a = -\frac{Qe}{m}\left[a_\mu \vec{B} + \left(a_\mu - \left(\frac{m}{p}\right)^2\right)\frac{\vec{\beta}\times\vec{E}}{c}\right]. \tag{4.6}$$

Resonances in the storage ring will occur if $L\nu_x + M\nu_y = N$, where L, M and N are integers, which must be avoided in choosing the operating value of the field index. These resonances form straight lines on the tune plane shown in Figure 4.2, which shows resonance lines up to fifth order. The operating point lies on the circle $\nu_x^2 + \nu_y^2 = 1$.

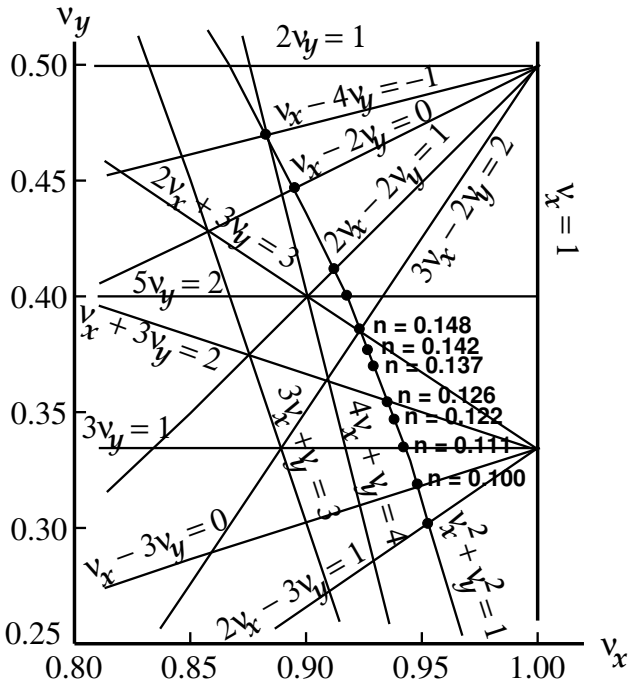

Figure 4.2: The tune plane, showing the three operating points used during our three years of running.

The detector acceptance depends on the radial position of the muon when it decays, so that any *coherent* radial beam motion will amplitude modulate the decay $e^{\pm}$ distribution. This can be understood by examining Fig. 4.3. A narrow bunch of muons starts its radial betatron oscillation at the point $s = 0$. The circumference of the ring is $2\pi\rho$ so the x-axis shows successive revolutions around the ring. The radial betatron wavelength is longer than the circumference $2\pi\rho$. The rate at which the muon bunch moves toward and then away from the detector is given by $f_{CBO} = f_C - f_x$. The CBO wavelength is slightly over 14 revolutions of the ring.

I would probably remove this paragraph since it only provides historical context to the CBO and the previous section already describes its effects.

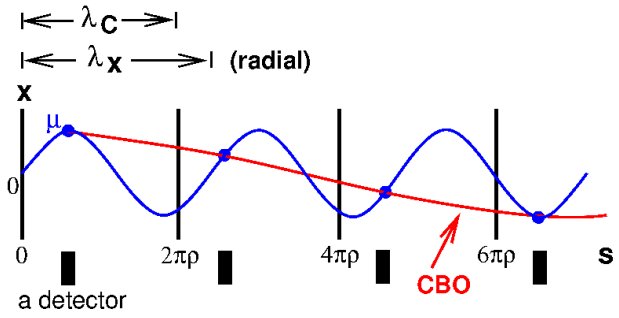

Figure 4.3: A cartoon of the coherent betatron motion (CBO). The radial CBO oscillation is shown in blue for 3 successive betatron wavelengths, the cyclotron wavelength (the circumference) is marked by the black vertical lines. One detector location is shown. Since the radial betatron wavelength is larger than the circumference, the detector sees the bunched beam slowly move closer and then further away. The frequency that the beam appears to move in and out is f_{CBO} .

The presence of the CBO was first discovered in E821 from a plot that showed an azimuthal variation in the value of a_μ shown in Fig. 4.4(a). When the CBO is included, this azimuthal dependence disappears. Because the CBO wavelenth is only slightly greater than the circumference, its effect washes out when all detectors are added together. Adding all detectors together was one of the techniques used in E821 to eliminate CBO effect. Since some detectors saw more injection flash than others, this meant that data at times earlier than around 40 μs was discarded in those analyses. Other analyzers included the CBO and were able to use data from the "quiet" detectors at earlier times.

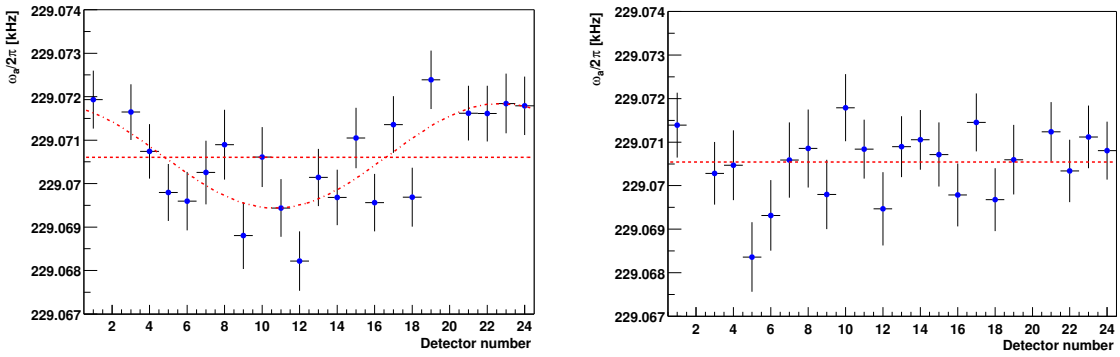

(a) No CBO in Fit

(b) CBO in Fit

Figure 4.4: The dependence of the extracted value of a_μ vs. detector number. (a)With no CBO in the fit function. (b) With CBO included in the fit function.

The principal frequency will be the "Coherent Betatron Frequency,"

$$f_{\rm CBO} = f_C - f_x = (1 - \sqrt{1-n}) f_C \simeq 470 \text{ kHZ}, \tag{4.7}$$

which is the frequency at which a single fixed detector sees the beam coherently moving

back and forth radially. This CBO frequency is close to the second harmonic of the $(g-2)$ frequency, $f_a = \omega_a/2\pi \simeq 228$ Hz.

An alternative way of thinking about the CBO motion is to view the ring as a spectrometer where the inflector exit is imaged at each successive betatron wavelength, λ_{β_x}. In principle, an inverted image appears at half a betatron wavelength; but the radial image is spoiled by the $\pm 0.3\%$ momentum dispersion of the ring. A given detector will see the beam move radially with the CBO frequency, which is also the frequency at which the horizontal waist precesses around the ring. Since there is no dispersion in the vertical dimension, the vertical waist (VW) is reformed every half wavelength $\lambda_{\beta_y}/2$. A number of frequencies in the ring are tabulated in Table 4.1

Table 4.1: Frequencies in the $(g-2)$ storage ring, assuming that the quadrupole field is uniform in azimuth and that $n = 0.137$.

Quantity	Expression	Frequency [MHz]	Period [μs]
f_a	$\frac{e}{2\pi mc} a_\mu B$	0.228	4.37
f_C	$\frac{v}{2\pi R_0}$	6.7	0.149
f_x	$\sqrt{1-n} f_c$	6.23	0.160
f_y	$\sqrt{n} f_c$	2.48	0.402
$f_{\rm CBO}$	$f_c - f_x$	0.477	2.10
$f_{\rm VW}$	$f_c - 2f_y$	1.74	0.574

The CBO frequency and its sidebands are clearly visible in the Fourier transform to the residuals from a fit to the five-parameter fitting function Equation 3.16, and are shown in Figure 4.5. The vertical waist frequency is barely visible. In 2000, the quadrupole voltage was set such that the CBO frequency was uncomfortably close to the second harmonic of f_a, thus placing the difference frequency $f_- = f_{CBO} - f_a$ next to f_a. This nearby sideband forced us to work very hard to understand the CBO and how its related phenomena affect the value of ω_a obtained from fits to the data. In 2001, we carefully set f_{CBO} at two different values, one well above, the other well below $2f_a$, which greatly reduced this problem.

4.0.3 Monitoring the Beam Profile

Two tools are available to us to monitor the muon distribution. Study of the beam debunching after injection yields information on the distribution of equilibrium radii in the storage ring. The traceback chambers will provide information on the vertical centroid along with the vertical distribution of the beam.

The beam bunch that enters the storage ring is expected to have a time spread with of around $\simeq 100$ ns, while the cyclotron period is 149 ns. The momentum distribution of stored muons produces a corresponding distribution in radii of curvature. The distributions depend on the phase-space acceptance of the ring, the phase space of the beam at the injection point, and the kick given to the beam at injection.

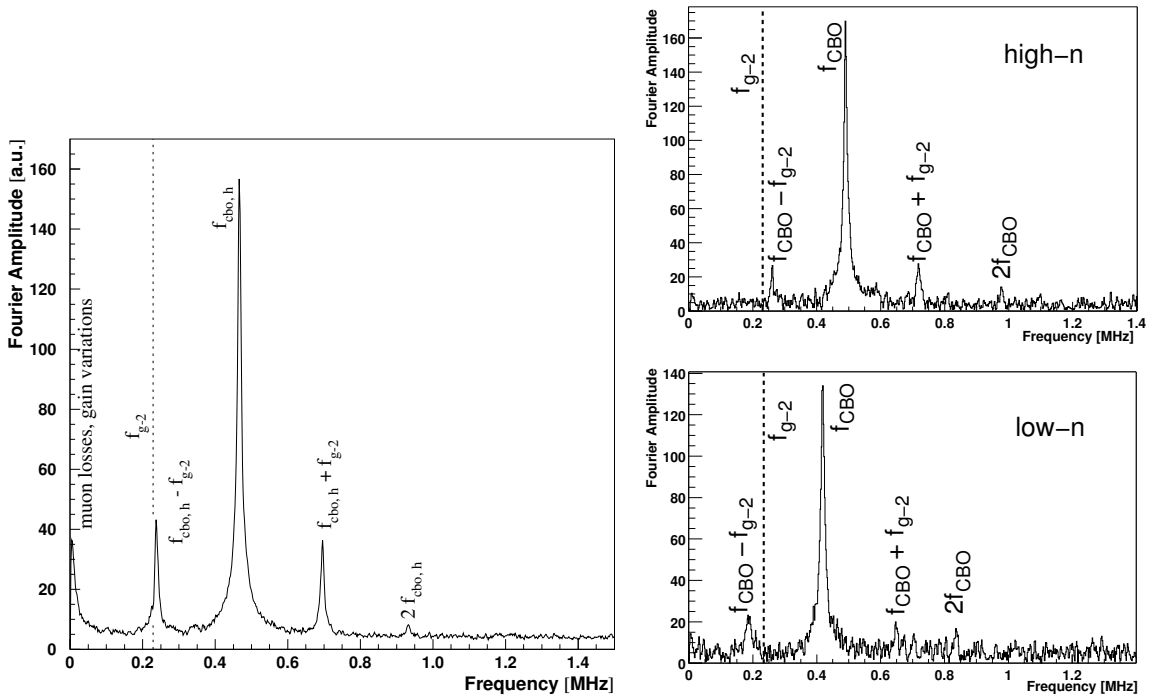

(a) (b)

Figure 4.5: The Fourier transform to the residuals from a fit to the five-parameter function, showing clearly the coherent beam frequencies. (a) is from 2000, when the CBO frequency was close to $2\omega_a$, and (b) shows the Fourier transform for the two n-values used in the 2001 run period.

There are too many time constants in this paragraph, 23 ns, 60 μs , 36 μs , 149 ns. I would probably unify the 36 and 60 μs numbers somehow to avoid confusion.

With the E821 inflector magnet, the narrow horizontal dimension of the beam at the injection point, about 18 mm, restricts the stored momentum distribution to about $\pm 0.3\%$. As the muons circle the ring, the muons at smaller radius (lower momentum) eventually pass those at larger radius repeatedly after multiple transits around the ring, and the bunch structure largely disappears after 60 μs . This de-bunching can be seen in the E821 data ($\sigma \simeq 23$ ns) in Figure 4.6 where the signal from a single detector is shown at two different times following injection. The bunched beam is seen very clearly in the left figure, with the 149 ns cyclotron period being obvious. The slow amplitude modulation comes from the $(g-2)$ precession. By 36 μs the beam has largely de-bunched.

Only muons with orbits centered at the central radius have the "magic" momentum, so knowledge of the momentum distribution, or equivalently the distribution of equilibrium radii, is important in determining the correction to ω_a caused by the radial electric field used for vertical focusing. Two methods of obtaining the distribution of equilibrium radii from the beam debunching are employed in E821. One method uses a model of the time evolution

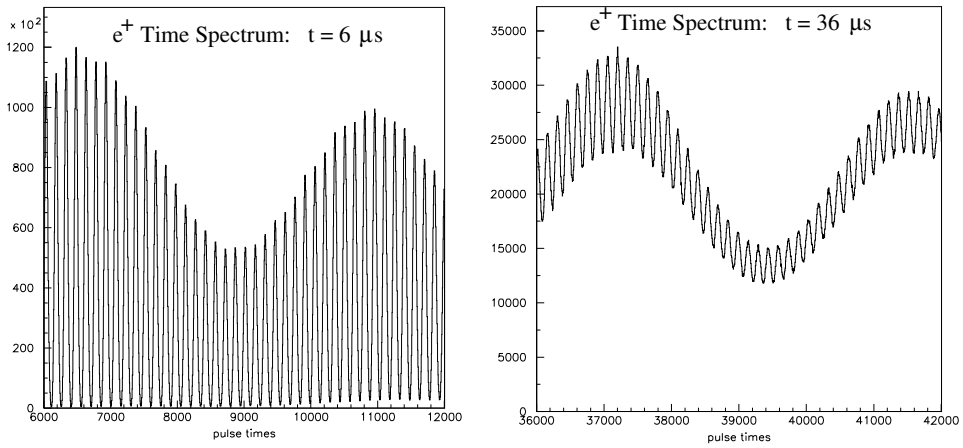

Figure 4.6: The time spectrum of a single calorimeter soon after injection. The spikes are separated by the cyclotron period of 149 ns.

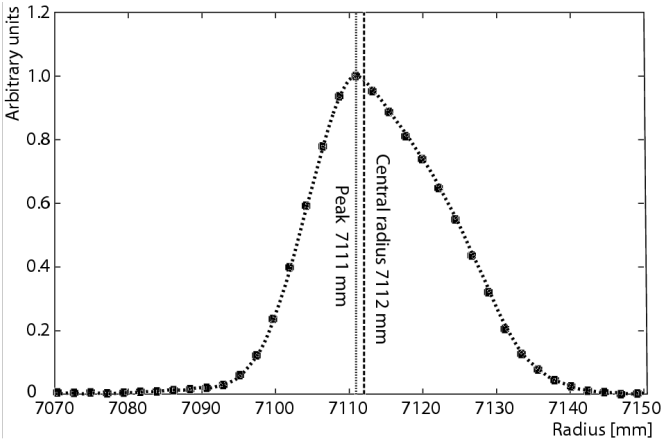

Figure 4.7: The distribution of equilibrium radii obtained from the beam de-bunching. The solid circles are from a de-bunching model fit to the data, and the dotted curve is obtained from a modified Fourier analysis.

of the bunch structure. A second, alternative procedure uses modified Fourier techniques[8]. The results from these analyses are shown in Figure 4.7. The discrete points were obtained using the model, and the dotted curve was obtained with the modified Fourier analysis. The two analyses agree. The measured distribution is used both in determining the average magnetic field seen by the muons and the radial electric field correction discussed below.

The scintillating-fiber monitors show clearly the vertical and horizontal tunes as expected. In Figure 4.8, the horizontal beam centroid motion is shown, with the quadrupoles powered asymmetrically during scraping, and then symmetrically after scraping. A Fourier transform of the latter signal shows the expected frequencies, including the cyclotron frequency of protons stored in the ring. The traceback system also sees the CBO motion.

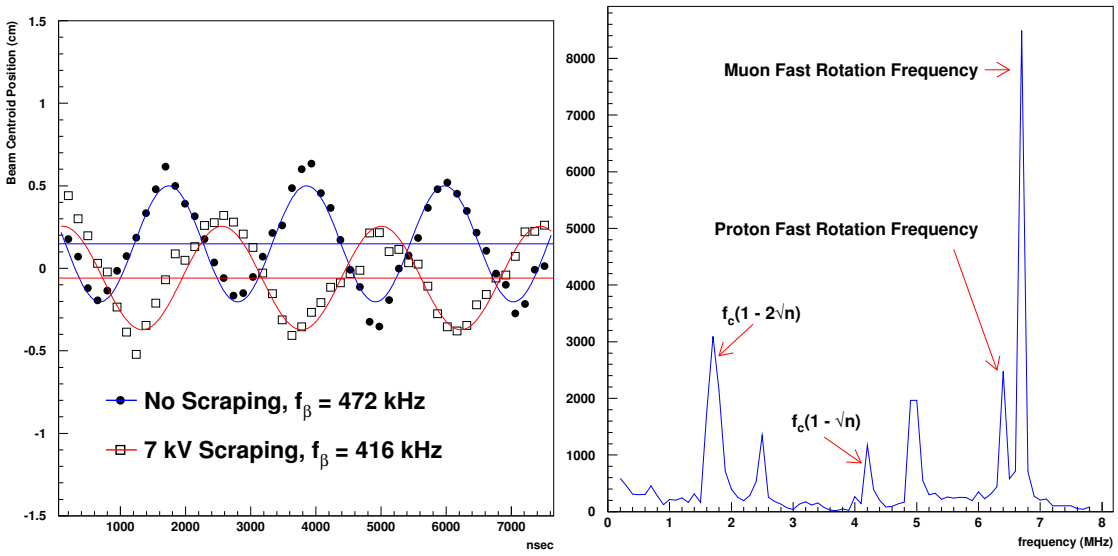

(a) (b)

Figure 4.8: (a) The horizontal beam centroid motion with beam scraping and without, using data from the scintillating fiber hodoscopes; note the tune change between the two. (b) A Fourier transform of the pulse from a single horizontal fiber, which shows clearly the vertical waist motion, as well as the vertical tune. The presence of stored protons is clearly seen in this frequency spectrum.

4.0.4 Corrections to ω_a: Pitch and Radial Electric Field

In the simplest case, the rate at which the spin turns relative to the momentum is given by

$$\omega_a = \omega_S - \omega_C = -\left(\frac{g-2}{2}\right)\frac{Qe}{m}B = -a\frac{Qe}{m}B \tag{4.8}$$

The spin equation modified by the presence of an electric field was introduced earlier, with the assumption that the velocity is transverse to the magnetic field, and that all muons are at $\gamma_{\rm magic}$. Neither of these assumptions are valid, since the vertical betatron motion must be included, and the momentum acceptance of $\pm 0.5\%$ means the muon ensemble has a range of momenta. Corrections for these two effects were the only corrections made to the data In E821. In the 2001 data set, the electric field correction for the low n-value data set was $+0.47 \pm 0.05$. The pitch correction was $+0.27 \pm 0.04$. These are the only corrections made to the ω_a data.

We sketch the derivation for E821 and E989 below[4]. For a general derivation the reader is referred to References [6, 7].

Without the assumption that $\vec{\beta} \cdot \vec{B} = 0$ the cyclotron and spin rotation frequencies become:

$$\vec{\omega}_C = -\frac{q}{m}\left[\frac{\vec{B}}{\gamma} - \frac{\gamma}{\gamma^2-1}\left(\frac{\vec{\beta}\times\vec{E}}{c}\right)\right], \tag{4.9}$$

and the spin precession frequency becomes[5]

$$\vec{\omega}_S = -\frac{q}{m}\left[\left(\frac{g}{2}-1+\frac{1}{\gamma}\right)\vec{B} - \left(\frac{g}{2}-1\right)\frac{\gamma}{\gamma+1}(\vec{\beta}\cdot\vec{B})\vec{\beta} - \left(\frac{g}{2}-\frac{\gamma}{\gamma+1}\right)\left(\frac{\vec{\beta}\times\vec{E}}{c}\right)\right]. \tag{4.10}$$

Substituting for $a_\mu = (g_\mu - 2)/2$, we find that the spin difference frequency is

$$\vec{\omega}_a = -\frac{q}{m}\left[a_\mu\vec{B} - a_\mu\left(\frac{\gamma}{\gamma+1}\right)(\vec{\beta}\cdot\vec{B})\vec{\beta} - \left(a_\mu - \frac{1}{\gamma^2-1}\right)\frac{\vec{\beta}\times\vec{E}}{c}\right]. \tag{4.11}$$

If $\vec{\beta}\cdot\vec{B} = 0$, this reduces to

$$\vec{\omega}_a = -\frac{q}{m}\left[a_\mu\vec{B} - \left(a_\mu - \frac{1}{\gamma^2-1}\right)\frac{\vec{\beta}\times\vec{E}}{c}\right]. \tag{4.12}$$

For $\gamma_{\text{magic}} = 29.3$ ($p_\mu = 3.09$ GeV/c), the second term vanishes; and the electric field does not contribute to the spin precession relative to the momentum. The spin precession is independent of muon momentum; *all* muons precess at the same rate. Because of the high uniformity of the B-field, a precision knowledge of the stored beam trajectories in the storage region is not required.

First we calculate the effect of the electric field, for the moment neglecting the $\vec{\beta}\cdot\vec{B}$ term. If the muon momentum is different from the magic momentum, the precession frequency is given by

$$\omega_a' = \omega_a\left[1 - \beta\frac{E_r}{B_y}\left(1 - \frac{1}{a_\mu\beta^2\gamma^2}\right)\right]. \tag{4.13}$$

Using $p = \beta\gamma m = (p_m + \Delta p)$, after some algebra one finds

$$\frac{\omega_a' - \omega_a}{\omega_a} = \frac{\Delta\omega_a}{\omega_a} = -2\frac{\beta E_r}{B_y}\left(\frac{\Delta p}{p_m}\right). \tag{4.14}$$

Thus the effect of the radial electric field reduces the observed frequency from the simple frequency ω_a given in Equation 4.11 Now

$$\frac{\Delta p}{p_m} = (1-n)\frac{\Delta R}{R_0} = (1-n)\frac{x_e}{R_0}, \tag{4.15}$$

where x_e is the muon's equilibrium radius of curvature relative to the central orbit. The electric quadrupole field is

$$E = \kappa x = \frac{n\beta B_y}{R_0}x. \tag{4.16}$$

We obtain

$$\frac{\Delta\omega}{\omega} = -2n(1-n)\beta^2\frac{xx_e}{R_0^2 B_y}, \tag{4.17}$$

so clearly the effect of muons not at the magic momentum is to lower the observed frequency. For a quadrupole focusing field plus a uniform magnetic field, the time average of x is just x_e, so the electric field correction is given by

$$C_E = \frac{\Delta\omega}{\omega} = -2n(1-n)\beta^2\frac{\langle x_e^2\rangle}{R_0^2 B_y}, \tag{4.18}$$

where $\langle x_e^2 \rangle$ is determined from the fast-rotation analysis (see Figure 4.6). The uncertainty on $\langle x_e^2 \rangle$ is added in quadrature with the uncertainty in the placement of the quadrupoles of $\delta R = \pm 0.5$ mm (± 0.01 ppm), and with the uncertainty in the mean vertical position of the beam, ± 1 mm (± 0.02 ppm). For the low-n 2001 sub-period, $C_E = 0.47 \pm 0.054$ ppm.

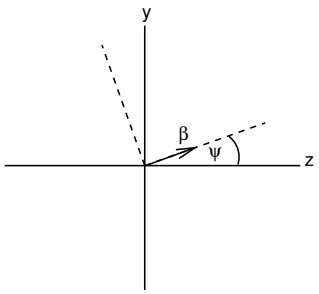

Figure 4.9: The coordinate system of the pitching muon. The angle ψ varies harmonically. The vertical direction is $\hat{y}$ and $\hat{z}$ is the azimuthal (beam) direction.

The vertical betatron oscillations of the stored muons lead to $\vec{\beta} \cdot \vec{B} \neq 0$. Since the $\vec{\beta} \cdot \vec{B}$ term in Equation 4.10 is quadratic in the components of $\vec{\beta}$, its contribution to ω_a will not generally average to zero. Thus the spin precession frequency has a small dependence on the betatron motion of the beam. It turns out that the only significant correction comes from the vertical betatron oscillation; therefore it is called the pitch correction (see Equation 4.11). As the muons undergo vertical betatron oscillations, the "pitch" angle between the momentum and the horizontal (see Figure 4.9) varies harmonically as $\psi = \psi_0 \cos \omega_y t$, where ω_y is the vertical betatron frequency $\omega_y = 2\pi f_y$, given in Equation 4.3. In the approximation that all muons are at the magic γ, we set $a_\mu - 1/(\gamma^2 - 1) = 0$ in Equation 4.11 and obtain

$$\vec{\omega}_a' = -\frac{q}{m}\left[a_\mu \vec{B} - a_\mu \left(\frac{\gamma}{\gamma+1}\right)(\vec{\beta} \cdot \vec{B})\vec{\beta}\right], \tag{4.19}$$

where the prime indicates the modified frequency as it did in the discussion of the radial electric field given above, and $\vec{\omega}_a = -(q/m)a_\mu \vec{B}$. We adopt the (rotating) coordinate system shown in Figure 4.9, where $\vec{\beta}$ lies in the zy-plane, z being the direction of propagation, and y being vertical in the storage ring. Assuming $\vec{B} = \hat{y}B_y$, $\vec{\beta} = \hat{z}\beta_z + \hat{y}\beta_y = \hat{z}\beta\cos\psi + \hat{y}\beta\sin\psi$, we find

$$\vec{\omega}_a' = -\frac{q}{m}[a_\mu \hat{y} B_y - a_\mu \left(\frac{\gamma}{\gamma+1}\right)\beta_y B_y(\hat{z}\beta_z + \hat{y}\beta_y)]. \tag{4.20}$$

The small-angle approximation $\cos\psi \simeq 1$ and $\sin\psi \simeq \psi$ gives the component equations

$$\omega_{ay}' = \omega_a \left[1 - \left(\frac{\gamma-1}{\gamma}\right)\psi^2\right] \tag{4.21}$$

and

$$\omega_{az}' = -\omega_a \left(\frac{\gamma-1}{\gamma}\right)\psi. \tag{4.22}$$

Rather than use the components given above, we can resolve ω_a' into components along the coordinate system defined by $\vec{\beta}$ (see Figure 4.9) using the standard rotation formula. The transverse component of ω' is given by

$$\omega_\perp = \omega'_{ay}\cos\psi - \omega'_{az}\sin\psi. \tag{4.23}$$

Using the small-angle expansion for $\cos\psi \simeq 1 - \psi^2/2$, we find

$$\omega_\perp \simeq \omega_a\left[1 - \frac{\psi^2}{2}\right]. \tag{4.24}$$

As can be seen from Table 4.1, the pitching frequency ω_y is an order of magnitude larger than the frequency ω_a, so that in one $g-2$ period $\omega_\parallel$ oscillates more than ten times, thus averaging out its effect on ω_a' so $\omega_a' \simeq \omega_\perp$. Thus

$$\omega_a \simeq -\frac{q}{m}a_\mu B_y\left(1 - \frac{\psi^2}{2}\right) = -\frac{q}{m}a_\mu B_y\left(1 - \frac{\psi_0^2 cos^2\omega_y t}{2}\right). \tag{4.25}$$

Taking the time average yields a pitch correction

$$C_p = -\frac{\langle\psi^2\rangle}{2} = -\frac{\langle\psi_0^2\rangle}{4} = -\frac{n}{4}\frac{\langle y^2\rangle}{R_0^2}, \tag{4.26}$$

where we have used Equation 4.4 $\langle\psi_0^2\rangle = n\langle y^2\rangle/R_0^2$. The quantity $\langle y_0^2\rangle$ was both determined experimentally and from simulations. For the 2001 period, $C_p = 0.27 \pm 0.036$ ppm, the amount the precession frequency is lowered from that given in Equation 4.6 because $\vec{\beta}\cdot\vec{B} \neq 0$.

We see that both the radial electric field and the vertical pitching motion *lower* the observed frequency from the simple difference frequency $\omega_a = (e/m)a_\mu B$, which enters into our determination of a_μ using Equation 3.21. Therefore our observed frequency must be *increased* by these corrections to obtain the measured value of the anomaly. Note that if $\omega_y \simeq \omega_a$ the situation is more complicated, with a resonance behavior that is discussed in References [6, 7].

References

[1] H. Wiedemann, *Particle Accelerator Physics* Vol. 1, Springer-Verlag, (1993) p. 54.

[2] D.A. Edwards and M.J. Syphers, *An Introduction to the Physics of High Energy Accelerators*, John Wiley & Sons, (1993) p. 75.

[3] F. Combley and E. Picasso, Phys. Rept. **14**, 1 (1974).

[4] We follow the approach given by J.M. Paley, Ph.D. Dissertation, Boston University, 2004.

[5] L.H. Thomas, Nature **117**, (1926) 514 and Phil. Mag. **3** (1927) 1, Bargmann V, Michel L, Telegdi VL, Phys. Rev. Lett. 2:435 (1959)

[6] F.J.M. Farley and E. Picasso, in Quantum Electrodynamics, Adv. Series on Dir. in H.E.P., V7, T. Kinoshita, ed., World Scientific, 479, (1990).

[7] F.J.M. Farley, Phys.Lett. **B 42**, 66 (1972), and J.H. Field, and G. Fiorentini, Nuovo Cimento, **21 A**, 297 (1974).

[8] Y. Orlov, et al., Nucl. Instrum. Meth. **A482**, 767 (2002).

[9] P. Debevec, Ringbeta, DocDB document #762.

Chapter 5

Statistical and Systematic Errors for E989

E989 must obtain twenty-one times the amount of data collected for E821. Using the T method to evaluate the uncertainty, 1.8×10^{11} events are required in the final fitted histogram to realize a 0.10 ppm statistical uncertainty. The systematic errors on the anomalous precession frequency ω_a, and on the magnetic field normalized to the proton Larmor frequency ω_p, must be reduced by a factor of three, down to the ±0.07 ppm level. E989 will have three main categories of uncertainties:

- **Statistical.** The least-squares or maximum likelihood fits to the histograms describing decay electron events vs. time in the fill will determine ω_a, the anomalous precession frequency. The uncertainty $\delta\omega_a$ from the fits will be purely statistical (assuming a good fit). A discussion of the fitting sensitivity using various weighting schemes is given in Chapter 16, Section 16.2. The final uncertainty depends on the size of the data set used in the fit, which in turn depends on the data accumulation *rate* and the *running time*. These topics are discussed here.

- ω_a **Systematics.** Additional systematic uncertainties that will affect $\delta\omega_a$ might be anything that can will cause the extracted value of ω_a from the fit to differ from the true value, beyond statistical fluctuations. Categories of concern include the detection system (e.g., gain stability and pileup immunity), the incoming beamline (lost muons, spin tracking), and the stored beam (coherent betatron oscillations, differential decay, E and pitch correction uncertainties). These topics are discussed in Chapter 4.

- ω_p **Systematics.** The magnetic field is determined from proton NMR in a procedure described in Chapter 15. The uncertainties are related to how well known are the individual steps from absolute calibration to the many stages of relative calibration and time-dependent monitoring. The"statistical" component to these measurements is negligible.

The purpose of this chapter is twofold. First, we summarize the event-rate calculation from initial proton flux to fitted events in the final histograms in order to determine the running time required to meet the statistical goals of the experiment. We also gather the

results of many systematic uncertainty discussions that are are described in various chapters throughout this document and roll up the expected systematic uncertainty tables for E989.

5.1 Event Rate Calculation Methodologies

The E989 Proposal [1] event rate estimate was made by making a **relative comparison approach** using like terms with respect to the known situation for rates in the E821 BNL experiment. Many factors allow for trivial adjustments (proton fills per second, kinematics of the decay line length, kinematics of the decay line capture), while others rely on expected improvements in specific hardware components (optimized storage ring kicker pulse shape and magnitude, open-ended inflector, thinner Q1 outer plate and standoffs). In E821, the transmission through the inflector, passage through the Q1 outer plates and the kick onto the orbit all multiply to give the storage ring efficiency, but individually the contribution from each is not known as well as the product. However, we can deduce the realized stored muon fraction compared to the incoming muon beam intensity. For the new experiment, each of these beam-storage elements is being optimized and we can make good estimates of the expected improvement.

We are also developing a stand-alone **bottom up** approach in which each factor is individually studied or measured to obtain the final event rate. While not complete at this time, this approach is converging with several factor represented by a range, owing to ongoing design development. We present our progress on this approach in the section that follow the Relative Comparison discussion.

5.1.1 Event Rate by a Relative Comparison to E821

Table 5.1 contains a sequential list of factors that affect the event rate from proton on target to events in the final histogram. It is modified, where appropriate, compared to the 2010 Proposal based on new information and studies to date.

A pion production calculation using MARS was made to estimate the number of 3.1 GeV/c pions emitted into the accepted phase space of the AP2 line. From this point, a conservative approach was to compare known factors between the muon capture and transmission at Fermilab to those same factors at BNL. Many of the factors are relatively trivial to compute, while others rely on our detailed Decay Turtle simulations of the BNL lattice and modifications of this lattice for Fermilab. We are in the process of a complete end-to-end calculation of the beamline, but this work will take additional time. In the comparison to BNL approach, we find the important increase of stored muons per incident proton of 11.5, assuming an improved kicker and an open-ended inflector. We require a factor of at least 6 for an experiment that can be done in less than 2 years. We use the factor of 6 in our beam estimates, thus introducing a "beam-time contingency" factor of nearly 100% from the beginning. Experience from E821 suggests that 1 month of setup time with beam will be required before "good" data are obtained and an integrated second month devoted to systematic studies will be distributed throughout the data collection period. We assume a possibly aggressive 75% factor the the efficiency of data taking during normal running. The down time includes the accelerator complex inefficiency (unknown to us for this new

operation) and the time to be spent mapping the magnet with the trolley (mapping will take place whenever the accelerator is down or will interrupt data taking periodically if the uninterrupted machine uptime exceeds, for example, 2 days. Mapping will take approximately 3 hours. The origin of each factor in Table 5.1, is explained in a series of notes following the Table.

Table 5.1: Event rate calculation using known factors and a comparison to the realized stored muon fraction at BNL. This table has been updated compared to the 2010 E989 Proposal.

Item	**Value**	**Rates**	**Note**
Booster cycle (BC) - 15 Hz operation	1.33 s/BC	0.75 BC/s	1
Proton Batches to $g-2$	4/BC	3 batch/s	2
Proton Bunches $\rightarrow$ fill	4/batch	12 fill/s	3
Protons on target	10^{12} p/bunch	1.2 $\times 10^{13}$ p/s	4
BNL realized stored μ/p efficiency	1 $\times 10^{-9}$ μ/p		5
FNAL estimated μ/p improvement factor	6	6000 μ/fill	6
Positrons accepted with $E > 1.8$ GeV	0.15	720 e^+/fill	7
Positrons with $t > 30$ μs	0.63	567 e^+/fill	8
Number of fills for 1.8 $\times 10^{11}$ events	3.17×10^8 fills	–	9
DAQ and experiment production uptime	0.75	–	10
Time to collect statistics	14 months	–	11
Beam-on commissioning	2 months	–	12
Dedicated systematic studies periods	2 months	–	13
Net running time required	18 months	–	14

Notes explaining entries in Table 5.1 and comparison remarks to what was assumed in the E989 Proposal.

1. 15 Hz Booster operation remains a valid assumption.

2. Neutrino program uses 12 out of 20 batches; 8 out of 20 are in principle available, but preparation of the 4 separated bunches of proton in the Recycler requires two Booster cycles. Therefore, only 4 of the 8 can be used. This is a change compared to the Proposal, which assumed 6/8 were useable.

3. Subdivision in Recycler of each batch into 4 "bunches" with roughly equal intensity of $\approx 1 \times 10^{12}$ p/bunch. Each is extracted separately with ~ 12 ms spacing and each initiates a storage ring "fill."

4. Expected proton intensity per Bunch, or per fill, striking target.

5. Measured stored muon fraction per 24-GeV proton on target at BNL per 10^{12} p (Tp). This number rolls up individual factors including the FODO line length, the non-forward muon acceptance used to minimize the hadronic flash, the transmission through the closed-ended inflector, the losses in the outer Q1 quadrupole plate and standoffs, and the sub-optimal storage ring kicker efficiency

6. The improvement factor was estimated by comparing to the known situation at BNL. We arrive at the following factors: $\times 0.4$ for the reduced pion yield; $\times 1.8$ for the AP2 line with smaller beta function; $\times 2$ for the longer decay channel; $\times 3$ for the forward decay optimal muon tune; $\times 1.33$ for opening up the pion momentum acceptance; $\times 2$ for the open inflector and improved kicker = 11.5. We use a factor of 6 to be very conservative. The factors here are most important at this Conceptual Design phase.

7. Monte Carlo acceptance of 15% for events with energy above 1.8 GeV and striking the front face of one of the 24 calorimeter stations.

8. Assume fit can be started at 30 μs, the factor of 0.63 represents those muons that have not yet decayed, given a 64.6 μs muon lifetime in the ring.

9. The required number of fills to obtain the full statistical precision.

10. Estimate of the uptime for the experiment and accelerator complex during steady-state data production running. Downtime will occur from accelerator issues related to the new operational modes and to routine maintenance and servicing; time required by the experiment to run trolley field mapping program (typically 3 h / 2 days), and ordinary DAQ and experimental issues requiring intervention. This is a slightly aggressive number.

11. Estimate of 2 months to commission the new experiment and machine operation sequence. This is based, in part, on past experience at BNL, and allowing for the new configuration at FNAL.

12. Estimate of periodic dedicated systematic study weeks during data taking periods. These are crucial to establish uncertainties, but this data typically will not be included in the final statistics.

13. Net data taking in months.

5.1.2 Bottom-Up Event Rate Calculation

Table 5.2 contains a sequential list of factors that affect the event rate based on a bottom-up approach. The beamline momentum bite is set at $dp/p = \pm 2\%$ all the way to the inflector. This is wider than the E821 line and much wider than the acceptance of the storage ring ($\sim \pm 0.15\%$). However, the calculation to date on the muon capture fraction used 0.5% from a wide pion momentum bite. Thus, we include that here. As in the previous section, the last column points to a list of Notes that explain the individual entries. Notes explaining

Table 5.2: Event rate calculation using a bottom-up approach.

Item	Estimate	CDR Reference	**Note**
Protons per fill on target	10^{12} p	7.3	1
Positive-charged secondaries with $dp/p = \pm 2\%$	4.8×10^7	7.4.1	2
π^+ fraction of secondaries	0.48	7.4.1	2
π^+ flux entering FODO decay line	$> 2 \times 10^7$	7.4.1	2
Pion decay to muons in 220 m of M2/M3 line	0.72	–	3
Muon capture fraction with $dp/p < \pm 0.5\%$	0.0036	DocDB 895	4
Muon survive decay 1800 m to storage ring	0.90	–	5
Muons flux at inflector entrance (per fill)	4.7×10^4	–	5
Transmission and storage using $(dp/p)_\mu = \pm 0.5\%$	0.10 ± 0.04	10.5.1	6
Stored muons per fill	$(4.7 \pm 1.9) \times 10^3$	–	6
Positrons accepted per fill (factors 0.15 x 0.63)	444 ± 180	–	7
Number of fills for 1.8 $\times 10^{11}$ events	$(1.4 \pm 0.4) \times 10^8$ fills	–	8
Time to collect statistics	(13 ± 5) months	–	8
Beam-on commissioning	2 months	–	9
Dedicated systematic studies periods	2 months	–	10
Net running time required	17 ± 5 months	–	11

entries in Table 5.2.

1. Same starting point as in Table 5.1.

2. MARS calculation, backed up with 2012 measurement. Assumes improved proton spot size on target to 0.15 mm, which increases the yield by $40 - 60\%$ compared to the measured rates at 0.5 mm spot size. Assumes 40-mm-mr emittance. Measurement verifies yield of positive particles. Simulation shows that 45% of them are pions. The target yield could increase by $14 - 22\%$ if the target geometry were further optimized; see Fig. 7.10 and the text in that section.

3. Pion decay length = 173 m. M2 line = 115.6 m; M3 = 96.7 m; use 220 m total.

4. Preliminary fraction based on a phase Space simulations assuming pion emittance = beam admittance = 40 mm mrad both in x and y; pions fill the phase space uniformly; muon momentum: $p_{magic} \pm 0.5\%$; These studies are being repeated using full Monte Carlo with G4Beamline. See Tishchenko and Morse, DocDB 895.

5. Transmission to storage ring; survive 1800 m; $(c\beta\gamma\tau)_\mu = 19280m$.

6. Average results form studies of transmission through the inflector, through the outer Q1 quadrupole and standoffs, and then kicked onto orbit and stored. The kicker is assumed to be perfect and that its kick width covers the entire incoming pulse train (to be determined). The inflector is modeled as having either closed ends, as in the present E821 inflector that will be used initially, or as open-ended, meaning a material free version of the same device. Additional studies look at not only an open inflector, but also a large one. We do not include that here. The Q1 and standoff intercept the incoming beam. If they were massless, a greater fraction of muons is stored. Plans are in place to reduce mass and move the standoffs. The transmission fraction for a 0.5% dp/p muon beam ranges from 6.5% to 14.5% depending on mass options used for inflector and Q1. We take a central value of 10% here and propagate the range of uncertainty, which depends on what will be built. The simulation is described in 10.5.1.

7. Monte Carlo acceptance of 15% for events with energy above 1.8 GeV and striking the front face of one of the 24 calorimeter stations and assume fit can be started at 30 μs; factor 0.63.

8. This row gives the required number of fills to obtain the full statistical precision.

9. Estimate of the uptime for the experiment and accelerator complex during steady-state data production running. Downtime will occur from accelerator issues related to the new operational modes and to routine maintenance and servicing; time required by the experiment to run trolley field mapping program (typically 3 h / 2 days), and ordinary DAQ and experimental issues requiring intervention. This is a slight aggressive number.

10. Estimate of 2 months to commission the new experiment and machine operation sequence. This is based, in part, on past experience at BNL, and allowing for the new configuration at FNAL.

11. Estimate of periodic dedicated systematic study weeks during data taking periods. These are crucial to establish uncertainties, but this data typically will not be included in the final statistics.

12. Net data taking in months.

Table 5.3: The largest systematic uncertainties for the final E821 ω_a analysis and proposed upgrade actions and projected future uncertainties for data analyzed using the T method. The relevant Chapters and Sections are given where specific topics are discussed in detail.

E821 Error	Size [ppm]	Plans for E989 Improvements	Goal [ppm]	Chapter & Section
Gain changes	0.12	Better laser calibration		
		low-energy threshold	0.02	16.3.1
Pileup	0.08	Low-energy samples recorded		
		calorimeter segmentation	0.04	16.3.2
Lost muons	0.09	Better collimation in ring	0.02	13.4
CBO	0.07	Higher n value (frequency)		
		Better match of beamline to ring	< 0.03	13.3.1
E and pitch	0.05	Improved traceback		
		Precise storage ring simulations	0.03	13.3.2
Total	0.18	Quadrature sum	0.07	

5.2 ω_a systematic uncertainty summary

Our plan of data taking and hardware changes address the largest systematic uncertainties and aims to keep the total combined uncertainty below 0.07 ppm. Experience shows that many of the "known" systematic uncertainties can be addressed in advance and minimized, while other more subtle uncertainties appear only when the data is being analyzed. Because we have devised a method to take more complete and complementary data sets, we anticipate the availability of more tools to diagnose such mysteries should they arise. Table 5.3 summarizes this section.

Table 5.4: Systematic uncertainties estimates for the magnetic field, ω_p, measurement. The final E821 values are given for reference and the proposed upgrade actions are projected. Note, several items involve ongoing R&D, while others have dependencies on the uniformity of the final shimmed field, which cannot be known accurately at this time. The relevant Chapters and Sections are given where specific topics are discussed in detail.

E821 Error	Size [ppm]	Plans for E989 Improvements	Goal [ppm]	Chapter & Section
Some Item	0.0X	Improved blah blah blah	0.02*	15
Some Item	0.0X	Depends on field uniformity	0.03**	15
Total	0.18	Quadrature sum (see notes below)	0.085	

*We have an R&D plan here to try to lower this systematic uncertainty

**We can better assess this systematic error only after the Field has been mapped

5.3 ω_p systematic uncertainty summary

The magnetic field is mapped by use of NMR probes. A detailed discussion is found in Chapter 15. Here we produce a summary Table of the expected systematic uncertainties.

References

[1] R. M. Carey, K. R. Lynch, J. P. Miller, B. L. Roberts, W. M. Morse, Y. K. Semertzides, V. P. Druzhinin and B. I. Khazin *et al.*,"The New (g-2) Experiment: A proposal to measure the muon anomalous magnetic moment to +-0.14 ppm precision," FERMILAB-PROPOSAL-0989.

[2] Bennett GW, et al.(The $g-2$ Collab.) Phys. Rev. D, 73:072003 (2006)

[3] B. Morse, Phase Space Calculations of Muon Injection, Brookhaven National Laboratory, 1998, (g-2) note #303, 1998.

[4] V. Tishchenko and W.M. Morse, Phase-Space Calculations of the Muon Acceptance by the Straight Section of the Fermilab Beamline, Brookhaven National Laboratory, docdb #487, 2012.

Chapter 6

Civil Construction Off-Project

The experimental hall is funded as a General Plant Project (GPP), as part of the Muon Campus Program. The beamline and tunnel from the delivery ring to the hall are separate GPP and Accelerator Improvement Projects (AIP). The locations of the buildings on the muon campus is shown in Fig. 6.1.

6.1 The MC1 Building

The muon storage ring will be located in the MC-1 Building on the Muon Campus, which is shown in Fig. 6.2. While it is a general purpose building, the design and features are extremely important to the success of E989. The principal design considerations are a very stable floor, and good temperature stability in the experimental hall. Both of these features were absent at Brookhaven, and presented difficulties to the measurement of the precision field. This design will serve E989, and subsequent experiments well. One portion of the MC1 building will house beamline power supplies and cryo facilities for the two initial experiments on the muon campus: $(g-2)$ and Mu2e.

The floor in the experimental area will be reinforced concrete $2'\ 9''$ (84 cm) thick. The floor is $12'$ below grade. Core samples show that the soil at the location is very compacted, the floor settling is expected to be about $0.25''$ fully loaded.

This floor will be significantly better than the floor in Building 919 at Brookhaven, where the ring was housed for E821. That floor consisted of three separate pieces: a concrete spine down the middle of the room, with a concrete pad on each side of the spine. Thus the foundation of the ring will be much more mechanically stable than it was at BNL.

Even more important is the temperature stability available in MC-1. The HVAC system will hold the temperature steady to $\pm 2^{\circ}$ F during magnet operation and data collection. This stability, combined with thermal insulation around the magnet will minimize the changes in the field due to temperature changes in the experimental hall.

A floor plan of MC-1 is shown in Fig. 6.3. The experimental hall is $80' \times 80'$ with a 30 ton overhead crane. The loading dock in the lower left-hand corner is accessed through the roll-up door labeled in Fig. 6.2 . Unlike in BNL 919, the crane coverage is significantly larger than the storage-ring diameter, simplifying many tasks in assembling the ring.

A detailed MC-1 document is available from FESS, titled "MC-1 Building", dated March

Figure 6.1: The layout of the Muon Campus, which lies between the former Antiproton Rings and the Booster Accelerator. The locations of the $(g-2)$ and Mu2e experiments are labeled.

2012.

Figure 6.2: A rendering of the MC1 building.

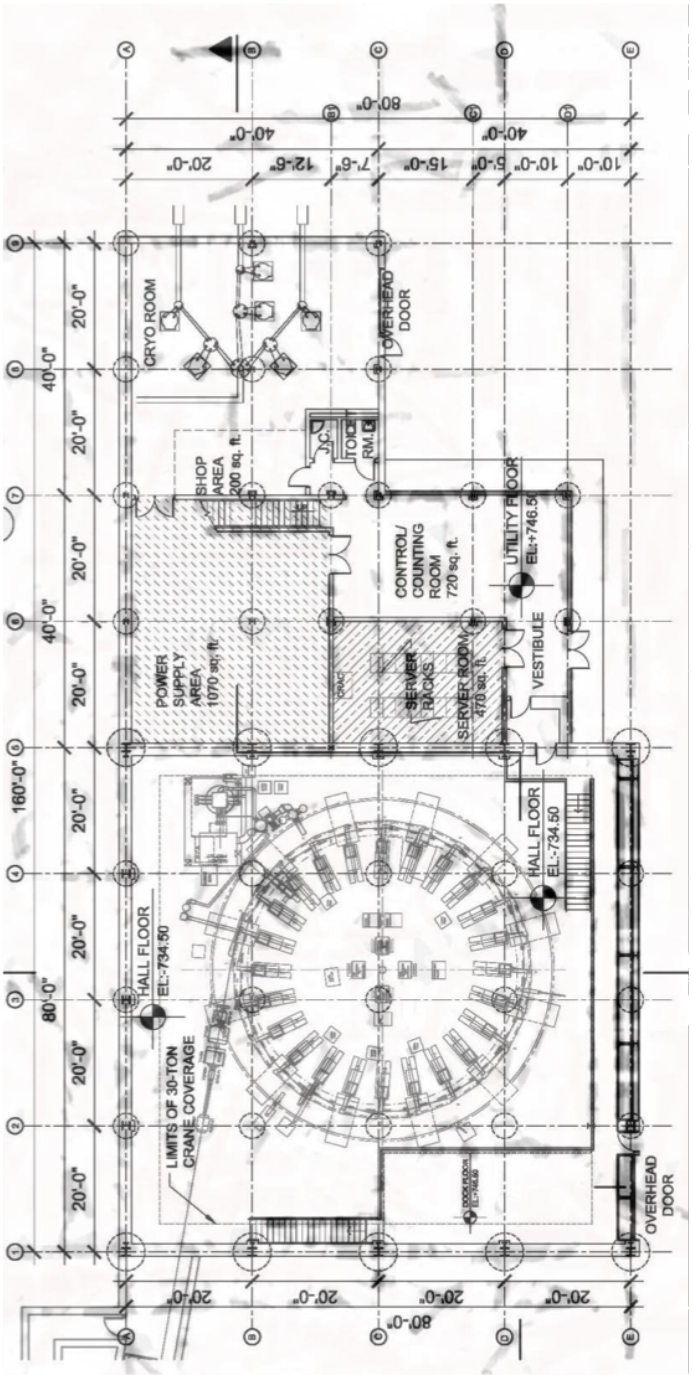

Figure 6.3: The first-floor layout of the MC1 building.

Chapter 7

Accelerator and Muon Delivery

In order to achieve a statistical uncertainty of 0.1 ppm, the total $(g-2)$ data set must contain at least 1.8×10^{11} detected positrons with energy greater than 1.8 GeV, and arrival time greater than 30 μs after injection into the storage ring. This is expected to require 4×10^{20} protons on target including commissioning time and systematic studies. For optimal detector performance, the number of protons in a single pulse to the target should be no more than 10^{12} and the number of secondary protons transported into the muon storage ring should be as small as possible. Data acquisition limits the time between pulses to be at least 10 ms. The revolution time of muons around the storage ring is 149 ns, and therefore the experiment requires the bunch length to be no more than ∼100 ns. Systematic effects on muon polarization limit the momentum spread dp/p of the secondary beam. Requirements and general accelerator parameters are given in Table 7.1.

Parameter	Design Value	Requirement	Unit
Total protons on target	2.3×10^{20}/year	4×10^{20}	protons
Interval between beam pulses	10	≥ 10	ms
Max bunch length (full width)	120 (95%)	< 149	ns
Intensity of single pulse on target	10^{12}	10^{12}	protons
Max Pulse to Pulse intensity variation	± 10	± 50	%
$\lvert dp/p \rvert$ of pions accepted in decay line	2-5	2	%
Momentum of muon beam	3.094	3.094	GeV/c
Muons to ring per 10^{12} protons on target	$(0.5 - 1.0) \times 10^5$	≥ 6000 stored	muons

Table 7.1: General beam requirements and design parameters.

7.1 Overall Strategy

The $(g-2)$ experiment at Fermilab is designed to take advantage of the infrastructure of the former Antiproton Source, as well as improvements to the Proton Source and the conversion of the Recycler to a proton-delivery machine. It is also designed to share as much infrastructure as possible with the Mu2e experiment in order to keep overall costs low.

The Antiproton Accumulator will no longer be in use, and many of its components will be reused for the new and redesigned Muon beamlines. Stochastic cooling components and other infrastructure no longer needed in the Debuncher ring will be removed in order to improve the aperture, proton abort functionality will be added, and the ring will be renamed the Delivery Ring (DR). The former AP1, AP2, and AP3 beamlines will be modified and renamed M1, M2, and M3. The DR Accelerator Improvement Project (AIP) will provide upgrades to the Delivery Ring. The Beam Transport AIP will provide aperture improvements to the P1, P2, and M1 lines needed for future muon experiments using 8 GeV protons, including $(g-2)$. The layout of the beamlines is shown in Fig. 7.1.

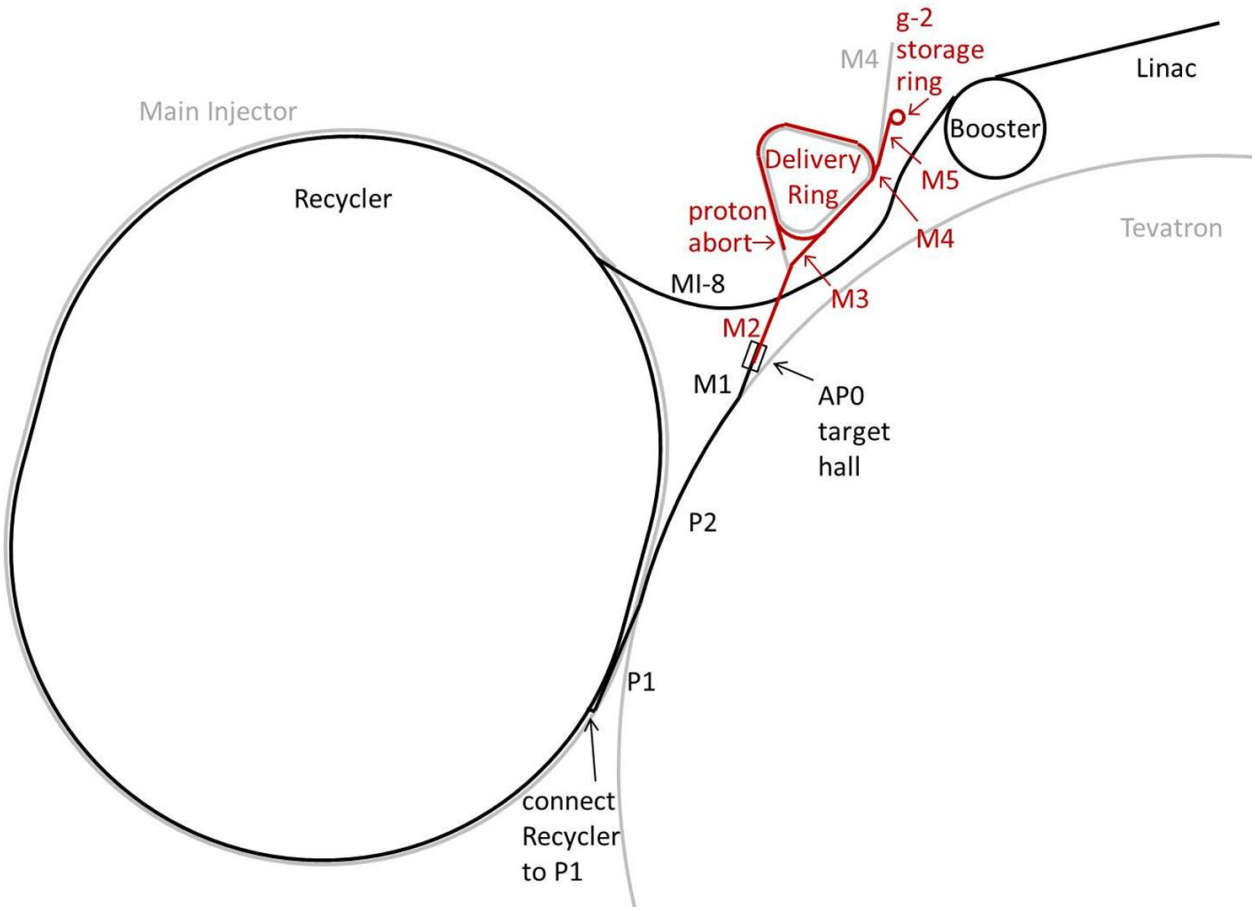

Figure 7.1: Path of the beam to $(g-2)$. Protons (black) are accelerated in the Linac and Booster, are re-bunched in the Recycler, and then travel through the P1, P2, and M1 lines to the AP0 target hall. Secondary beam (red) then travels through the M2 and M3 lines, around the Delivery Ring, and then through the M4 and M5 lines to the muon storage ring.

The Proton Improvement Plan [1], currently underway, will allow the Booster to run at 15 Hz, at intensities of 4×10^{12} protons per Booster batch. Following the completion of the Accelerator and NuMI Upgrades (ANU) subproject at Fermilab to prepare for the NOνA experiment [2], the Main Injector (MI) will run with a 1.333 s cycle time for its neutrino program, with twelve batches of beam from the Booster being accumulated in the Recycler

and single-turn injected into the MI at the beginning of the cycle. While the NOνA beam is being accelerated in the MI, eight Booster batches will be available for experimental programs such as $(g-2)$ which use 8 GeV protons. The ANU subproject will also enable injection from the Booster into the Recycler. Extraction from the Recycler to the P1 beamline, required for $(g-2)$, will be implemented in the Beam Transport AIP.

Protons from the Booster with 8 GeV kinetic energy will be re-bunched into four smaller bunches in the Recycler and transported through the P1, P2, and M1 beamlines to a target at AP0. Secondary beam from the target will be collected using a focusing device, and positively-charged particles with a momentum of 3.11 GeV/c ($\pm \sim 5\%$) will be selected using a bending magnet. Secondary beam leaving the target station will travel through the M2 and M3 lines which are designed to capture as many muons with momentum 3.094 GeV/c from pion decay as possible. The beam will then be injected into the Delivery Ring. After several revolutions around the DR, essentially all of the pions will have decayed into muons, and the muons will have separated in time from the heavier protons. A kicker will then be used to abort the protons, and the muon beam will be extracted into the new M4 line, and finally into the new M5 beamline which leads to the $(g-2)$ storage ring. Note that the M3 line, Delivery Ring, and M4 line are also designed to be used for 8 GeV proton transport by the Mu2e experiment.

The expected number of muons transported to the storage ring, based on target-yield simulations using the antiproton-production target and simple acceptance assumptions, is $(0.5-1.0)\times 10^5$. Beam tests were conducted using the existing Antiproton-Source configuration with total charged-particle intensities measured at various points in the beamline leading to the Debuncher, which confirmed the predicted yields to within a factor of two [3]. More details are given in Sec. 7.4.1.

7.2 Protons from Booster

During the period when $(g-2)$ will take data, the Booster is expected to run with present intensities of 4×10^{12} protons per batch, and with a repetition rate of 15 Hz. In a 1.333 s Main-Injector super cycle, twelve Booster batches are slip-stacked in the Recycler and then accelerated in the MI and sent to NOνA. While the Main Injector is ramping, a time corresponding to eight Booster cycles, the Recycler is free to send 8 GeV (kinetic energy) protons to $(g-2)$. The RF manipulations of beam for $(g-2)$ in the Recycler (Sec. 7.3.1) allow $(g-2)$ to take four of the eight available Booster batches. Figure 7.2 shows a possible time structure of beam pulses to $(g-2)$.

The following section describes improvements needed to run the proton source reliably at 15 Hz.

7.2.1 Proton Improvement Plan

The Fermilab Accelerator Division has undertaken a Proton Improvement Plan (PIP) [1] with the goals of maintaining viable and reliable operation of the Linac and Booster through 2025, increasing the Booster RF pulse repetition rate, and doubling the proton flux without increasing residual activation levels.

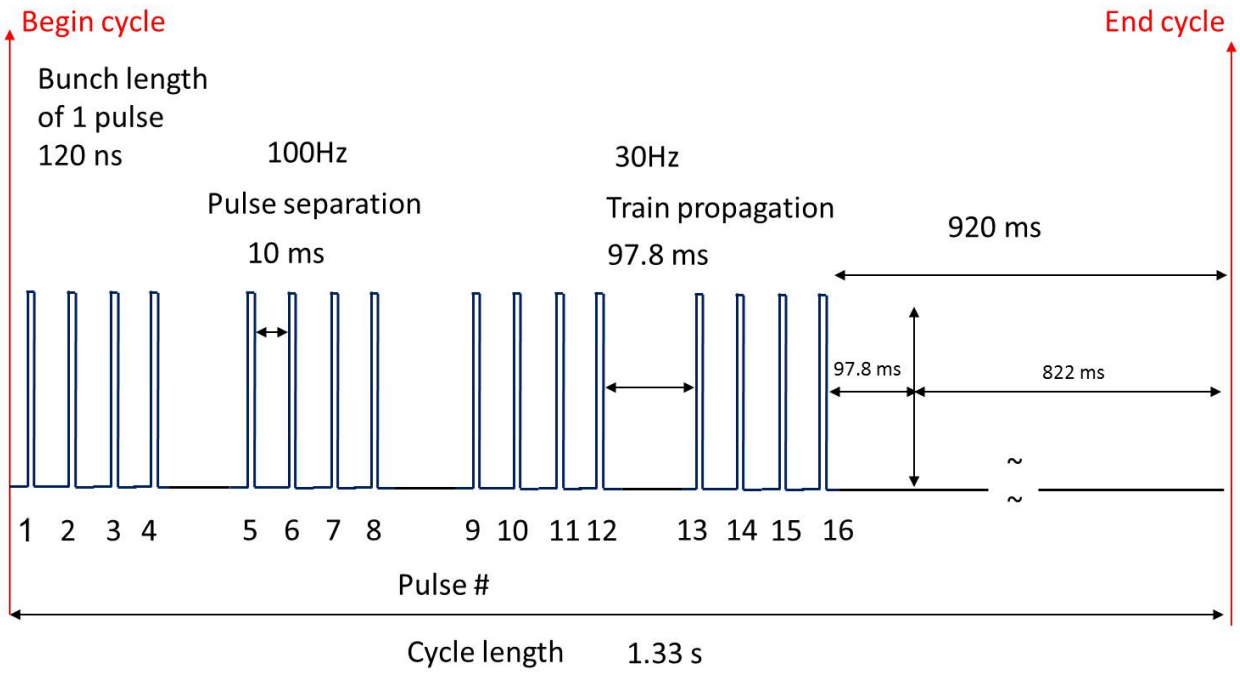

Figure 7.2: Time structure of beam pulses to $(g-2)$.

The replacement of the Cockroft-Walton pre-accelerator with a radio-frequency quadrupole (RFQ) during the 2012 shutdown is expected to increase reliability of the pre-accelerator and to improve beam quality.

The Booster RF solid-state upgrade is necessary for reliable 15 Hz RF operations. This involves the replacement of 40-year-old electronics that are either obsolete, difficult to find, or unable to run at the required higher cycle-rate of 15 Hz, and will allow for easier maintenance, shorter repair times, and less radiation exposure to personnel. The solid-state upgrade will be completed in 2013.

Refurbishment of the Booster RF cavities and tuners, in particular, cooling, is also necessary in order to operate at a repetition rate of 15 Hz.

Other upgrades, replacements, and infrastructure improvements are needed for viable and reliable operation. Efforts to reduce beam loss and thereby lower radiation activation include improved methods for existing processes, and beam studies, e.g., aimed at finding and correcting aperture restrictions due to misalignment of components.

The proton flux through the Booster over the past two decades and projected into 2016 based on expected PIP improvements is shown in Fig. 7.3.

The new PIP flux goal will double recent achievements and needs to be completed within five years. Figure 7.4 shows both the increase in flux as well as planned users. The goal of doubling the proton flux will be achieved by increasing the number of cycles with beam. The intensity per cycle is not planned to increase.

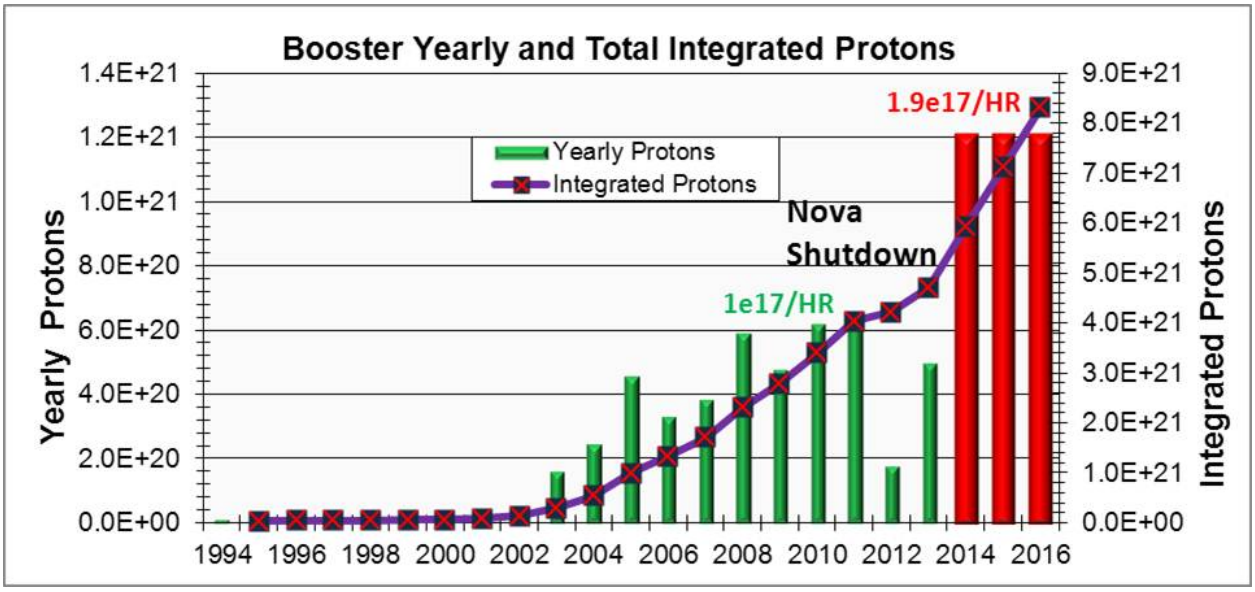

Figure 7.3: Yearly and integrated proton flux (including PIP planned flux increase).

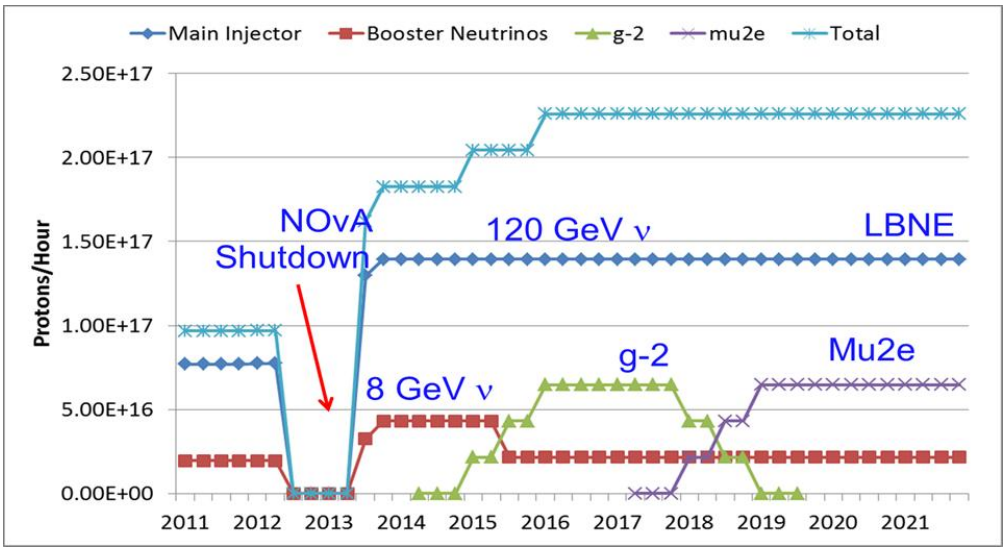

Figure 7.4: Expectations for increases in the proton flux from the Proton Source needed for future experiments.

7.3 Recycler

The $(g-2)$ experiment requires a low number of decay positrons in a given segment of the detector, and therefore requires that the full-intensity (4×10^{12} protons) bunches be redistributed into four bunches of 1×10^{12} protons. These bunches should be spaced no closer than 10 ms to allow for muon decay and data acquisition in the detector. Because the revolution time of muons in the $(g-2)$ ring is 149 ns, the longitudinal extent of the bunches should be no more than 120 ns. The Recycler modifications needed to achieve these requirements will be made under the Recycler AIP, and are described below.

7.3.1 Recycler RF

The proposed scheme for $(g-2)$ bunch formation [4] uses one RF system, 80 kV of 2.5 MHz RF. The design of the RF cavities will be based on that of existing 2.5 MHz cavities which were used in collider running, but utilizing active ferrite cooling. The ferrites of the old cavities and the old power amplifiers will be reused in the new system.

In order to avoid bunch rotations in a mismatched bucket, the 2.5 MHz is ramped "adiabatically" from 3 to 80 kV in 90 ms. Initially the bunches are injected from the Booster into matched 53 MHz buckets (80 kV of 53 MHz RF), then the 53 MHz voltage is turned off and the 2.5 MHz is turned on at 3 kV and then ramped to 80 kV. The first 2.5 MHz bunch is then extracted and the remaining three bunches are extracted sequentially in 10 ms intervals. The formation and extraction of all four bunches takes two Booster ticks or 133 ms. This limits the $(g-2)$ experiment to using four of the available eight Booster ticks in every Main-Injector super cycle.

Simulated 2.5 MHz bunch profiles are shown in Fig. 7.5. The 53 MHz voltage was ramped down from 80 to 0 kV in 10 ms and then turned off. The 2.5 MHz voltage was snapped to 3 kV and then adiabatically raised to 80 kV in 90 ms. The maximum momentum spread is $dp/p = \pm 0.28\%$. The overall efficiency is 95%, and 95% of the beam captured is contained within 120 ns. Roughly 75% of the beam is contained in the central 90 ns and 60% in 50 ns.

Although the Recycler is not yet configured to do such RF manipulations, by using the 2.5 MHz coalescing cavities in the Main Injector, the proposed bunch-formation scheme was tested with beam. In general, the agreement between simulations and data is very good. For illustration, the comparison between the beam measurements and the simulations for the case in which the 2.5 MHz voltage is ramped adiabatically from 3 to 70 kV in 90 ms is shown in Fig. 7.6.

Extraction from the Recycler and primary proton beam transport will be described in the beamline section, Sec. 7.5.

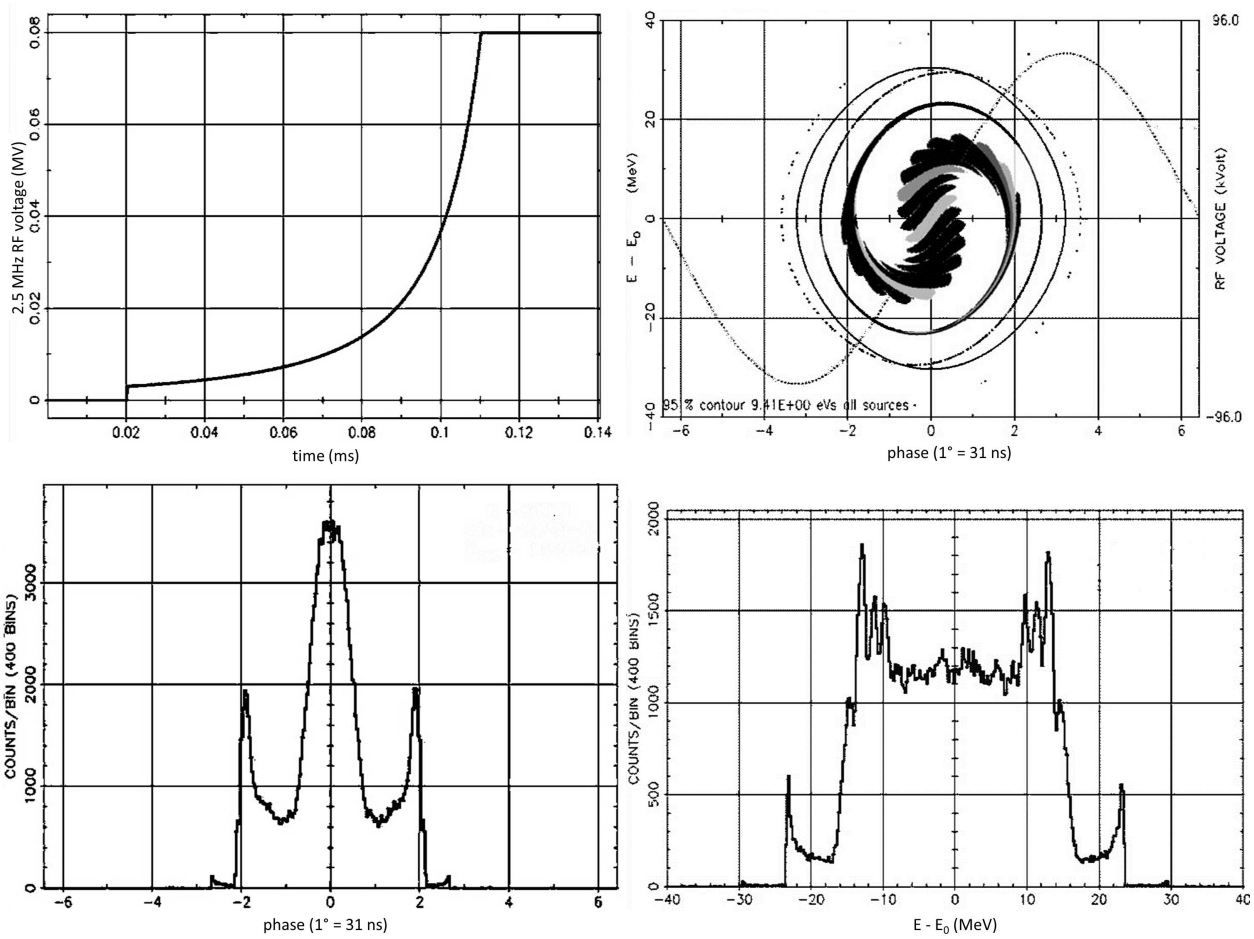

Figure 7.5: Results of RF simulations: 2.5 MHz voltage curve (upper left), phase space distribution (upper right), phase projection (lower left) and momentum projection (lower right).

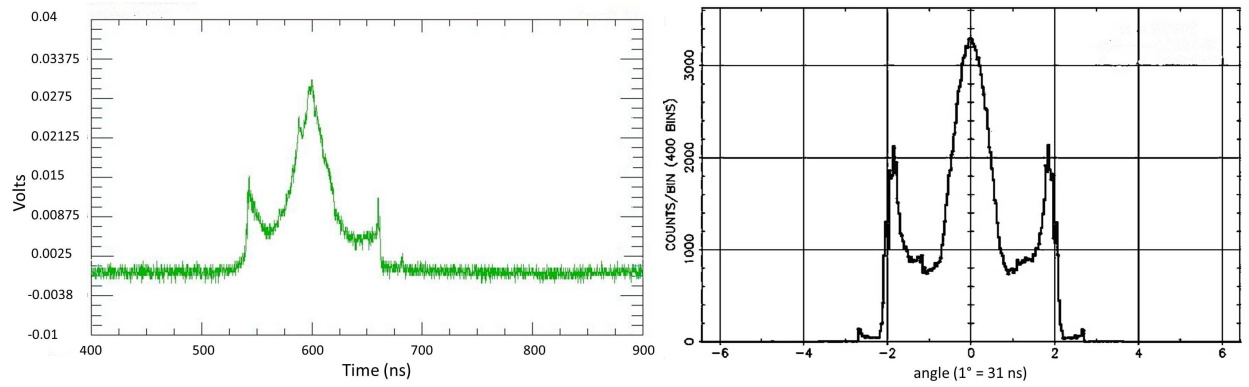

Figure 7.6: Comparison of beam profile (left) with simulation (right) for the case in which the 2.5 MHz voltage is ramped "adiabatically" from 3-70 kV in 90 ms. In both profiles, 95% of the particles captured are contained within 120 ns.

7.4 Target station

The $(g-2)$ production target station will reuse the existing target station that has been in operation for antiproton production for the Tevatron Collider for 23 years, while incorporating certain modifications. The $(g-2)$ target station will be optimized for maximum π^+ production per proton on target (POT) since the experiment will utilize muons from pion decay. Repurposing the antiproton target station to a pion production target station takes full advantage of a preexisting tunnel enclosure and service building with no need for civil construction. Also included are target vault water cooling and air ventilation systems, target systems controls, remote handling features with sound working procedures and a module test area. Figure 7.7 shows the current target-station (vault) layout. The overall layout of the target-vault modules will be unchanged from that used for antiproton production. The major differences in design will include different primary and secondary beam energies, polarity of the selected particles and pulse rate. Upgrades to pulsed power supplies, target design, pulsed-magnet design and the target dump are all considered.

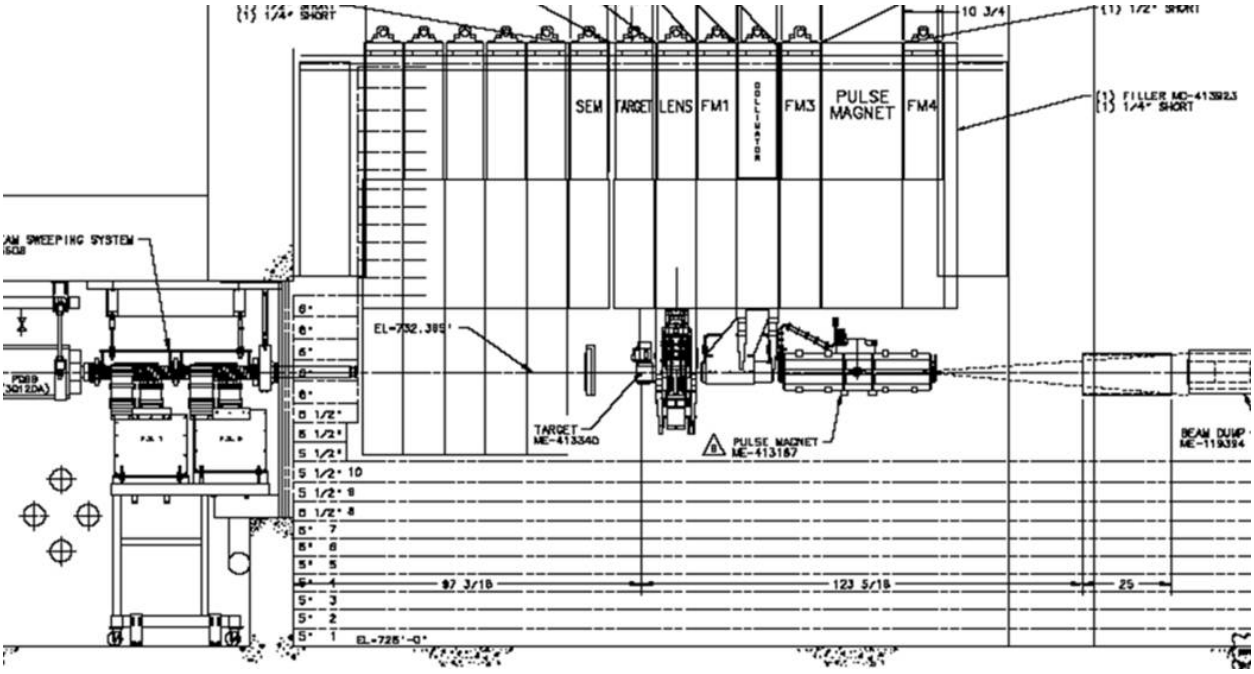

Figure 7.7: Layout of the $(g-2)$ target station.

The production target station consists of five main devices: the pion production target, the lithium lens, a collimator, a pulsed magnet, and a beam dump. Once the primary beam impinges on the target, secondaries from the proton-target interaction are focused by the lithium lens and then momentum-selected, centered around a momentum of 3.11 GeV/c, by a pulsed dipole magnet (PMAG). This momentum is slightly above the magic momentum needed to measure the muon anomalous magnetic moment in the downstream muon ring. The momentum-selected particles are bent 3° into a channel that begins the M2 beamline. Particles that are not momentum-selected will continue forward and are absorbed into the target-vault dump. An overview of some of the required beam design parameters for the

$(g-2)$ target system can be found in Table 7.2.

Parameter	FNAL $(g-2)$ 12 Hz
Intensity per pulse	10^{12} p
Total POT per cycle	16×10^{12} p
Number of pulses per cycle	16
Cycle length	1.33 s
Primary energy	8.89 GeV
Secondary energy	3.1 GeV
Beam power at target	17.2 kW
Beam size σ at target	0.15-0.30 mm
Selected particle	π^+
$\lvert dp/p \rvert$ (PMAG selection)	5%

Table 7.2: Beam parameters for the target station.

One significant difference the $(g-2)$ production target station will have from the antiproton production target station is the pulse rate at which beam will be delivered to the target station. The $(g-2)$ production rate will need to accommodate 16 pulses in 1.33 s with a beam pulse-width of 120 ns. This is an average pulse rate of 12 Hz. The antiproton production pulse rate routinely operated at 1 pulse in 2.2 s or 0.45 Hz. This will be a challenging factor that can drive the cost of the design since the lithium lens and pulsed magnet will need to pulse at a significantly higher rate. Figure 7.2 shows a possible $(g-2)$ pulse scenario for pulsed devices and timing for proton beam impinging on the target.

7.4.1 The $(g-2)$ production target and optimization of production

The current default target to be used for the $(g-2)$ experiment is the antiproton production target used at the end of the Tevatron Collider Run II. This target should be able to produce a suitable yield of approximately 10^{-5} π^+/POT within $|dp/p| < 2\%$. This target design has a long history of improvements for optimization and performance during the collider run. The target is constructed of a solid Inconel 600 core and has a radius of 5.715 cm with a typical chord length of 8.37 cm. The center of the target is bored out to allow for pressurized air to pass from top to bottom of the target to provide internal cooling to the Inconel core. It also has a cylindrical beryllium outer cover to keep Inconel from being sputtered onto the lithium lens from the impinging protons. The target has a motion control system that provides three-dimensional positioning with rotational motion capable of 1 turn in 45 s. This target and the target motion system need no modifications or enhancements to run for the $(g-2)$ experiment. Figure 7.8 shows a drawing and a photo of the current target.

Beam tests were performed to measure the yield from this target in 2012 [3]. The instrumentation measured total number of charged particles and did not differentiate between particle species. Plans are in place to repeat the test in 2013 using a Cherenkov counter to measure the particle composition of the beam. The yield of positive 3.1-GeV secondaries

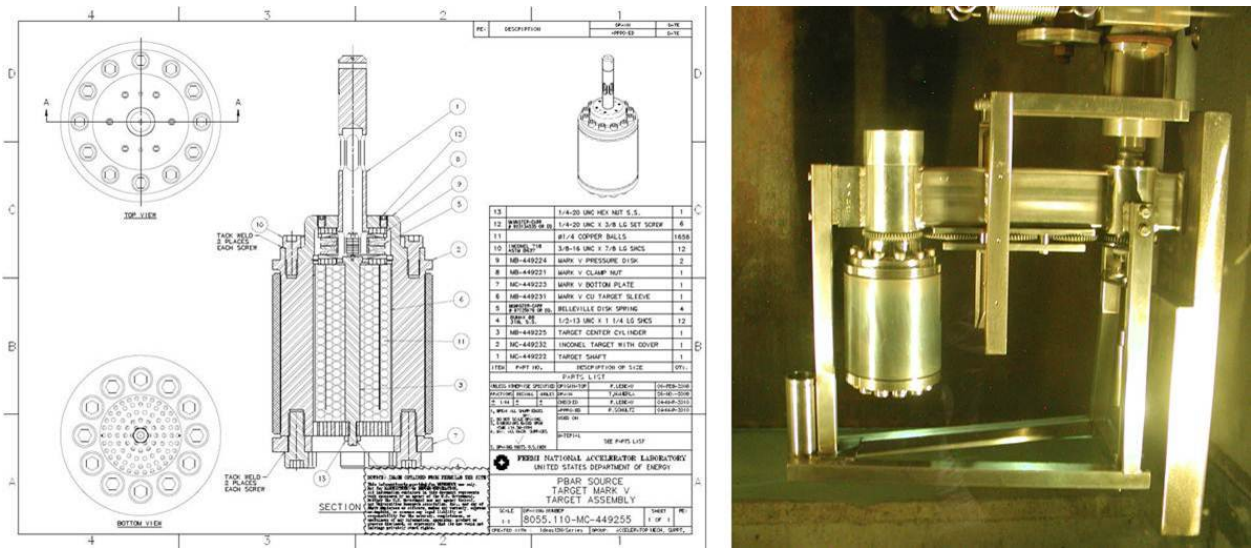

Figure 7.8: Current default target to be used for the $(g-2)$ target station.

from 10^{12} 8-GeV protons on target measured in the beam test was almost a factor of four higher than the 2.2×10^{8} particles with $|dp/p| < 10\%$ and 40π mm mr emittance predicted by MARS [6] simulations at the beginning of the AP2 line, and was about 60-80% of the number predicted at the end of the AP2 line with $|dp/p| < 2\%$ and 35π mm mr. Extrapolated back to the start of the AP2 line, that prediction is 4.8×10^{7} positive secondaries. The spot size of the beam on target was $\sigma_x = \sigma_y = 0.5$ mm. As discussed later in this section and in the beamlines section, we plan to reduce the spot size to 0.15 mm, which is expected to increase the yield of particles with $|dp/p| < 2\%$ by 40-60%. The expected yield of positive 3.1-GeV secondaries with $|dp/p| < 2\%$ exiting the target station will then be at least 4×10^{8}, with the simulation predicting 48% or 2×10^{7} of these to be π^{+}'s.

Even though this target is thus expected to produce a reasonable yield of more than 10^{-5} π^{+}/POT for the $(g-2)$ experiment, considerable effort has been put into investigating a cost-effective, practical target design optimized for 3.11 GeV pion production. Simulations have been conducted using MARS to determine the optimal parameters, including impinging proton spot size at the target, target material, target length and thickness, and target orientation [7]. A graphical representation of the target system as implemented in the MARS15 code is shown in Fig. 7.9.

The spot size of the beam on the target is an important parameter in determining the pion yield. Initial values for the spot size were simply scaled from the $\sigma_x = \sigma_y = 0.15$ mm size of the beam for 120 GeV antiproton production to $\sigma_x = \sigma_y = 0.55$ mm for 8.9 GeV. Optimized results from the MARS simulations for the impinging-proton spot size can be seen in Fig. 7.10. This plot shows the dependence of pion yield per POT on the beta function β at half distance into the target for the current default target. A reasonable range of expected β's which can be achieved is from 2.5 to 3.5 cm. The simulation result demonstrates that if the spot size is reduced from the original 0.55 mm to 0.15 mm, a 40-60% increase in pion production can be achieved [8] depending on β. These modifications are not directly made to the target station or target components but to the beamline just upstream of the target.

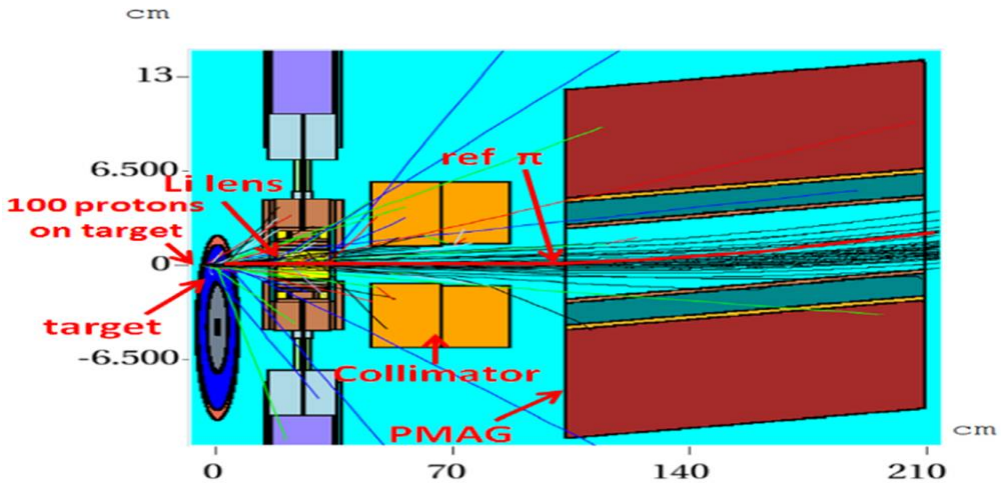

Figure 7.9: Graphical representation of target system used in MARS for simulated yield results.

Details of the beamline optics incorporating this optimization for pion yield can be found in Sec 7.5.4.

Also, optimizations concerning parameters for the target material, target length, and target width were also considered. First considered were optimizations to the target material. Three materials were simulated: Inconel, tantalum and carbon. Figure 7.11 illustrates the dependence of yield vs. β at the target for different materials with optimized lengths. Inconel and carbon are shown to have higher yields than tantalum. These results, combined with Fermilab's long history of building antiproton targets with Inconel, make Inconel the favored target material.

Next considering the dimensions of the target, Fig. 7.12a illustrates that a longer target will produce higher yields, while Fig. 7.12b demonstrates a weak dependence on the target thickness or radius. Therefore, the optimal pion production target may be a cylindrical rod with a length of 89 mm and a radius of 0.6 mm. However, to favor a more practical target design that will be able to be incorporated into the existing target mechanical and cooling systems, horizontal slabs made of Inconel of various heights were simulated. The output of the MARS simulation was then placed into G4beamline [9] in order to propagate particles through the first four quadrupoles in the M2 beamline. Particles yields were tallied at the end of these quadrupoles with appropriate acceptance cuts for the elements. Figure 7.13 shows the pion yield for two optimized horizontal slab targets one of height 0.60 mm and the second of 0.75 mm. They are both approximately 107 mm long. Simulations for these slab targets predict that a 22% and 14% gain in pion yield from optimized horizontal slabs could be obtained, respectively.

The actual details for the design of the alternate target are currently being worked out. However, it is preferred that the simulated horizontal slabs transition into target discs that could be mounted on a stacked-disc style target incorporating the simulated dimensions. In order to provide cooling to the target material, the target discs would be separated by discs of low Z material like beryllium or aluminum. Figure 7.14 is a picture of a proposed design of a target incorporating stacked target and cooling discs. The blue material represents discs

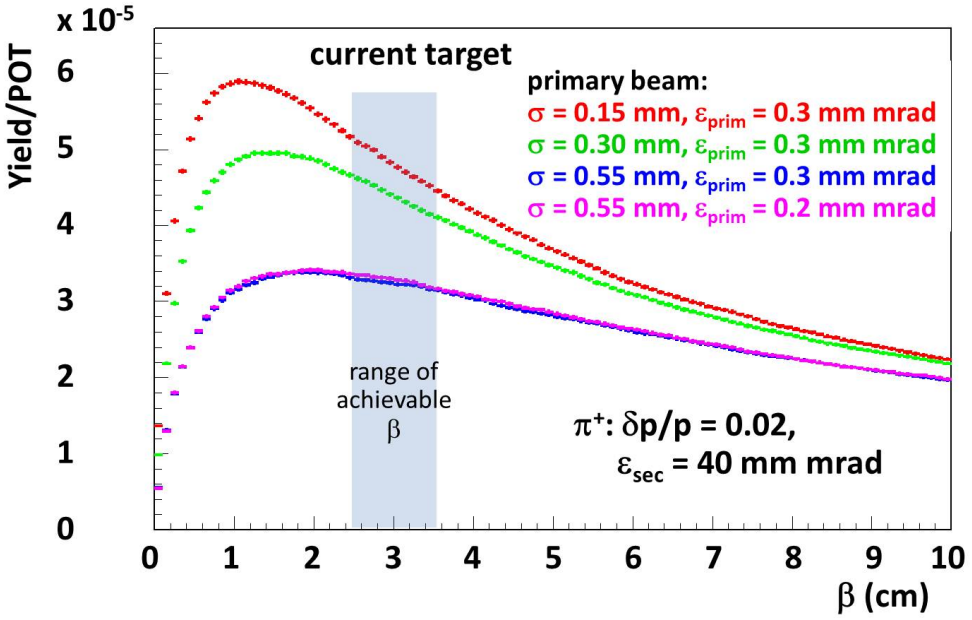

Figure 7.10: MARS simulation result for dependence of pion yield on β for different target spot sizes for a proton beam of emittance ε_{prim} and secondary beam momentum spread $|dp/p| = 0.02$ and emittance $\varepsilon_{sec} = 40$ mm mr.

of Inconel separated by the grey shaded areas which would be beryllium. One consideration for operating with the stacked discs that are very thin, approximately 0.6 mm, is the need for beam stability on the target. This may require improvements in upstream trim power supplies to achieve appropriate stability. A prototype stacked-disc target could be constructed and tested with beam to narrow and confirm the design of the alternate target if the default target is determined to be inadequate.

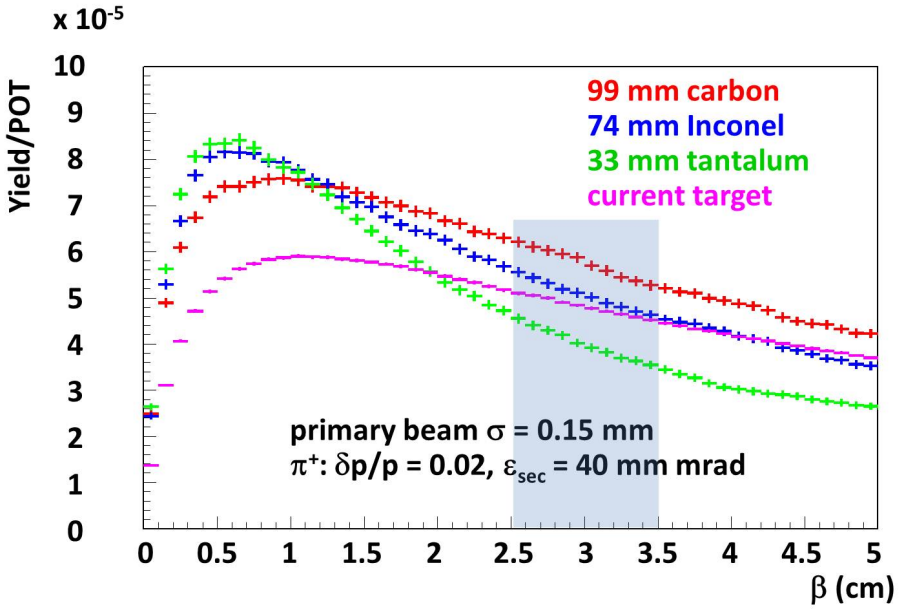

Figure 7.11: MARS simulation result for dependence of pion yield on β for different target materials. The length of the target is proportional to the interaction length of the material.

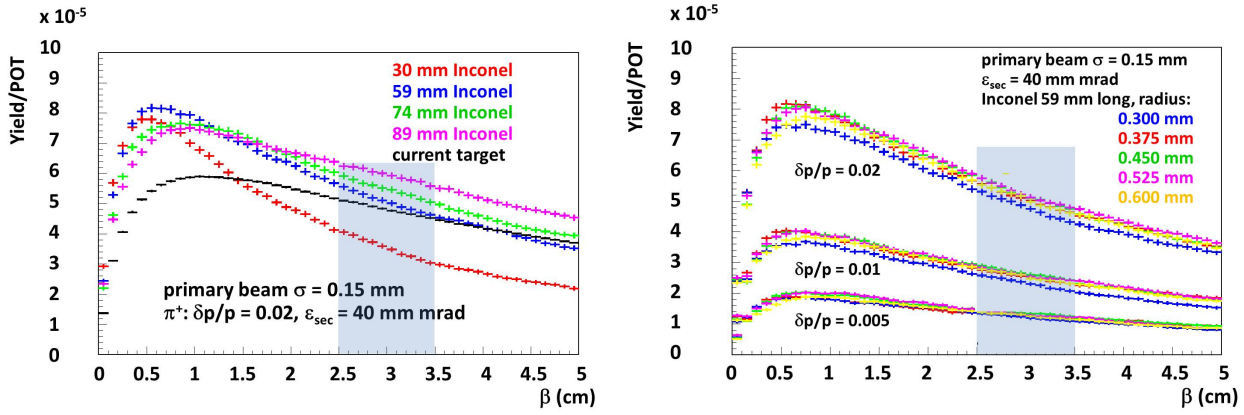

Figure 7.12: MARS simulation result for dependence of pion yield on β for different target lengths (a) and thicknesses (b).

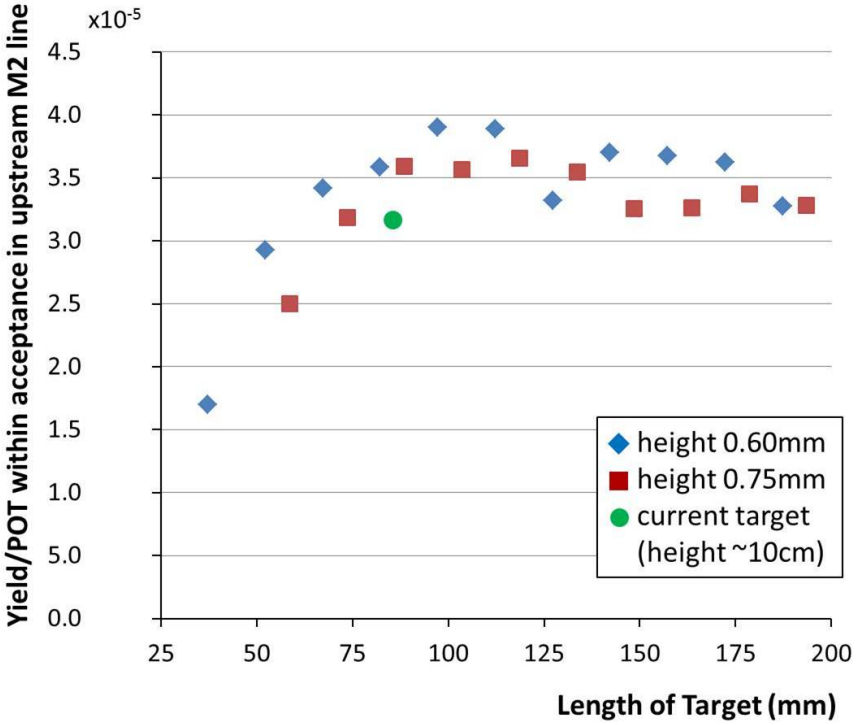

Figure 7.13: MARS/G4beamline predictions for number of pion secondaries from an Inconel target making it to the upstream M2 line as a function of target slab length for a slab of height 0.60 mm (with the upstream end of the target 56 mm from the lens focal point), a slab of height 0.75 mm (with the upstream end of the target 67 mm from the lens focal point), and the current target (assuming a chord length of 75 mm). The location of the target for a given height slab was optimized to give maximum yield. The spot size of beam on the target is taken to be 15 mm and the acceptance 40 mm mr. A thin target of length 107 mm is predicted to give an increase in yield of 14-22% over the existing target.

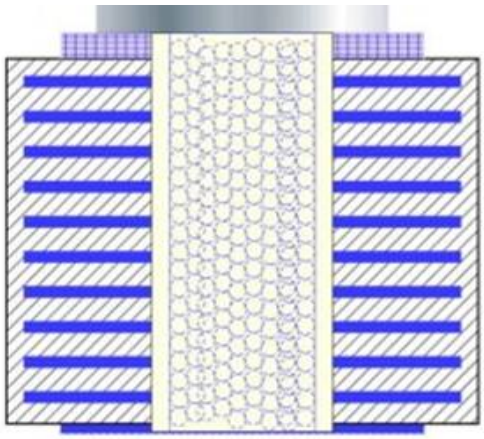

Figure 7.14: Proposal for new $(g-2)$ target design utilizing stacked thin slabs of Inconel (blue) separated by Beryllium (hashed grey). Target material air cooling channels are in the middle of the target.

7.4.2 Focusing of secondaries from the target

The lithium collection lens is a 1 cm radius cylinder of lithium that is 15 cm long and carries a large current pulse that provides a strong isotropically focusing effect to divergent incoming secondaries after the initial interaction of impinging particles with the target [10]. The lithium lens cylinder is contained within a toroidal transformer, and both lens and transformer are water cooled. Figure 7.15 is a drawing of the lithium lens depicting (a) the transformer and lens body, and (b) details of the lithium cylinder.

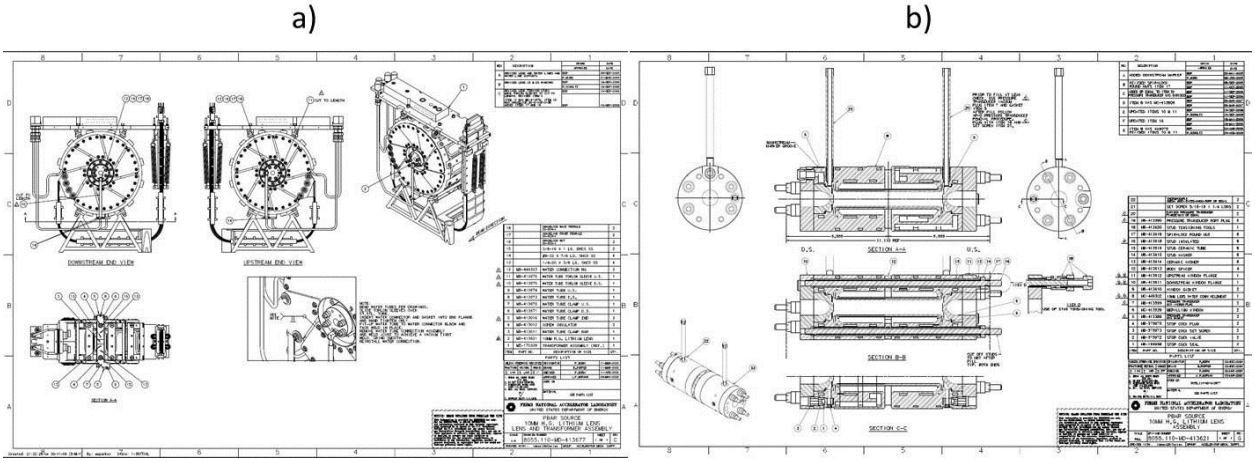

Figure 7.15: Drawing of the lithium lens and transformer (a) and the lithium cylinder body (b).

During antiproton production for the Collider Run II, the lens pulsed at a peak current of 62 kA, which is equivalent to a gradient of 670 T/m at 8.9 GeV/c with a base pulse width of 400 μs. Scaling the lens gradient for use at 3.11 GeV/c for $(g-2)$ and in order to accommodate a similar range of focal lengths from the target to the lens of roughly 28 cm, the gradient required will be 230 T/m at a pulsed peak current of 22 kA with the same 400 μs pulse width. Table 7.3 provides an overview of required operating parameters. Accommodating the $(g-2)$ 12 Hz average pulse rate for the lithium lens is one of the biggest challenges and concerns for repurposing the antiproton target station for $(g-2)$. Even though peak current and gradient will be reduced by a factor of about 3, the pulse rate will increase by a factor of 24 compared to the operation for antiproton production. Resistive and beam heating loads, cooling capacity, and mechanical fatigue are all concerns that are warranted for running the lithium lens at the $(g-2)$ repetition rate.

Lens operation	Pulse width (μs)	Peak current (kA)	Gradient (T/m)	Pulses per day
Antiproton production	400	62.0	670	38,880
$(g-2)$ pion production	400	22.6	230	1,036,800

Table 7.3: Lithium lens operation parameters.

Therefore, in order to gain confidence that the lens will be able to run under these conditions, a preliminary ANSYS [11] analysis has been conducted. This analysis simulated

thermal and mechanical fatigue for the lens based on the pulse timing scenario in Fig 7.2 and at a gradient of 230 T/m. These results were compared to results from a similar analysis for the lens operating under the antiproton-production mode of a gradient of 670 T/m at a pulse rate of 0.5 Hz [12]. Figure 7.16 (left) shows the ANSYS output thermal profile of a cutaway of the lens operating at 12 Hz. The lithium body corner is a temperature-sensitive location and should avoid lithium melting temperatures of 453.75 K. The corner temperature reaches a maximum temperature of 376 K. The plot on the right of Fig. 7.16 is the increase in maximum temperature of the lithium over the 16 pulses, depicting a change in temperature of 22 K when the operating temperature has come to equilibrium. We conclude from this analysis that the lithium lens is adequately cooled to operate at the nominal $(g-2)$ pulse rate.

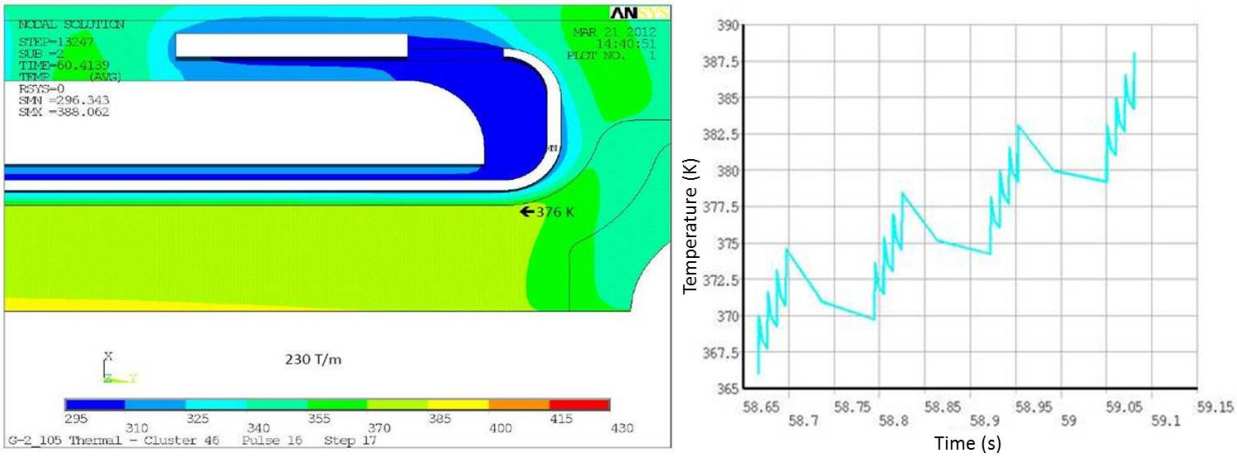

Figure 7.16: Simulated thermal profile from ANSYS for the lens operating at an average pulse rate of 12 Hz (left) depicting little beam heating and a corner temperature of 376 K. (Right) Plots showing lens temperature increase over the 16 pulses.

Mechanical fatigue was also assessed for the lithium lens. Figure 7.17 depicts a constant life fatigue plot developed for the lens from the ANSYS analysis. The two red lines represent upper and lower estimates of fatigue limits for the lens material. The red data points represent fatigues for gradients of 1000 T/m, 670 T/m, and two points at 230 T/m for a preload pressure of 3800 and 2200 psi, respectively. For the lens operating in the antiproton production conditions of 670 T/m, the mechanical fatigue was a large concern in the lens design. It appears that for the $(g-2)$ case, the mechanical fatigue will be a comparatively small concern.

This initial assessment of the lithium lens suggests that is should be able to operate at the $(g-2)$ repetition rate. However, since the operation of the lithium lens at the average 12 Hz rate is crucial, testing of the lens at 12 Hz is needed. The lens has been pulsed in a test station at a 12 Hz rate in order to confirm that 1M pulses per day can be achieved and sustained over many months. The lens has been pulsed 70 million times without problems, and data from these tests were used to confirm predictions of the ANSYS model.

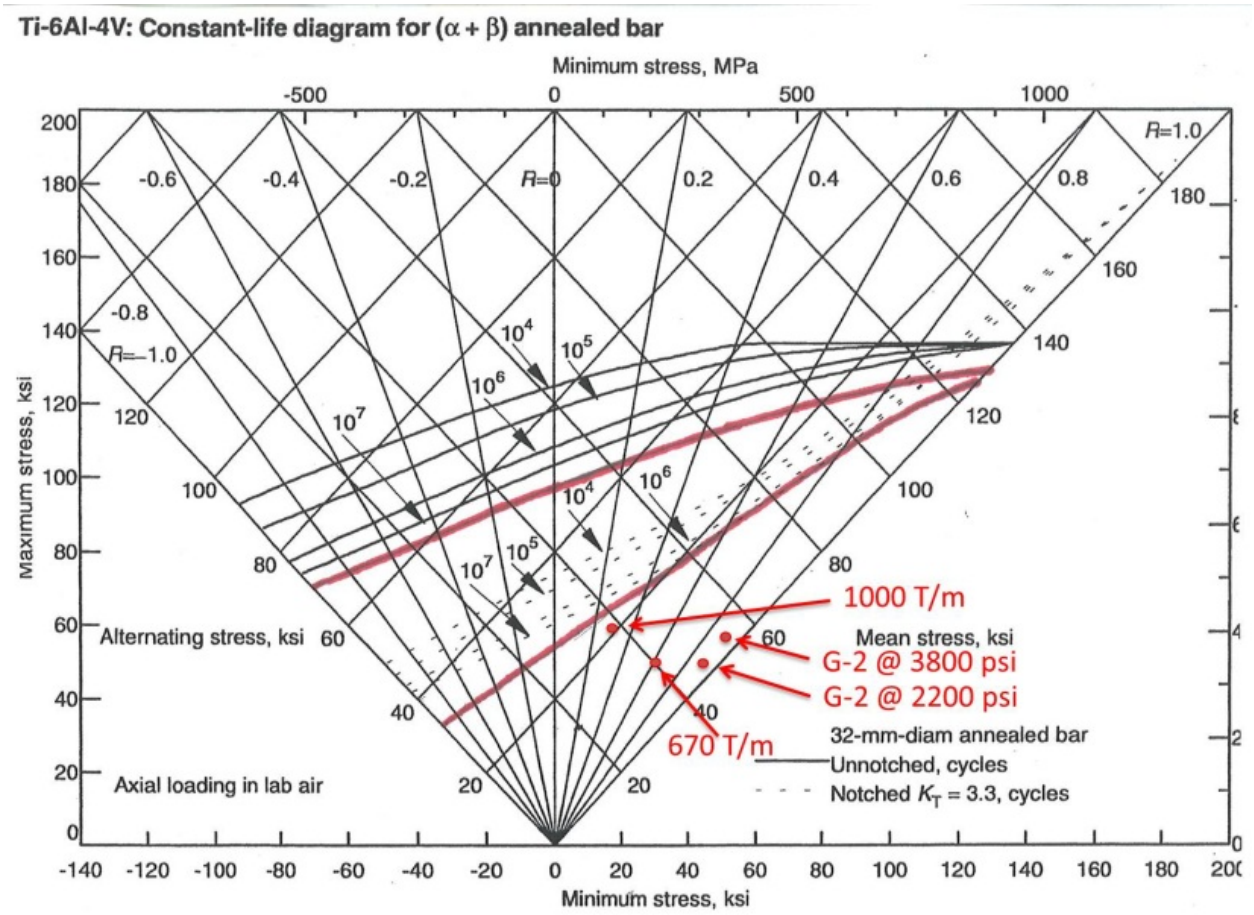

Figure 7.17: Constant-life fatigue plot of the lithium lens for antiproton and $(g-2)$ modes showing that mechanical fatigue for the $(g-2)$ pulse rate is a small concern.

7.4.3 Pulsed magnet (PMAG) and collimator

The pulsed magnet, shown in Fig. 7.18, selects 3.115 Gev/c positive particles and bends them 3° into the channel that begins the M2 beamline. The magnet will operate with a field of 0.53 T and is a 1.07 m long magnet with an aperture of 5.1 cm horizontally and 3.5 cm vertically. It is a single-turn magnet that has incorporated radiation-hard hardware such as ceramic insulation between the magnet steel and the single conductor bars, as well as Torlon-insulated bolts [10]. The pulsed magnet has a typical pulse width of 350 μs and similarly to the lithium lens, will need to accommodate the $(g-2)$ pulse rate shown in Fig. 7.2. The pulsed magnet is water cooled. In addition to the magnet currently in the target vault, there are three spares.

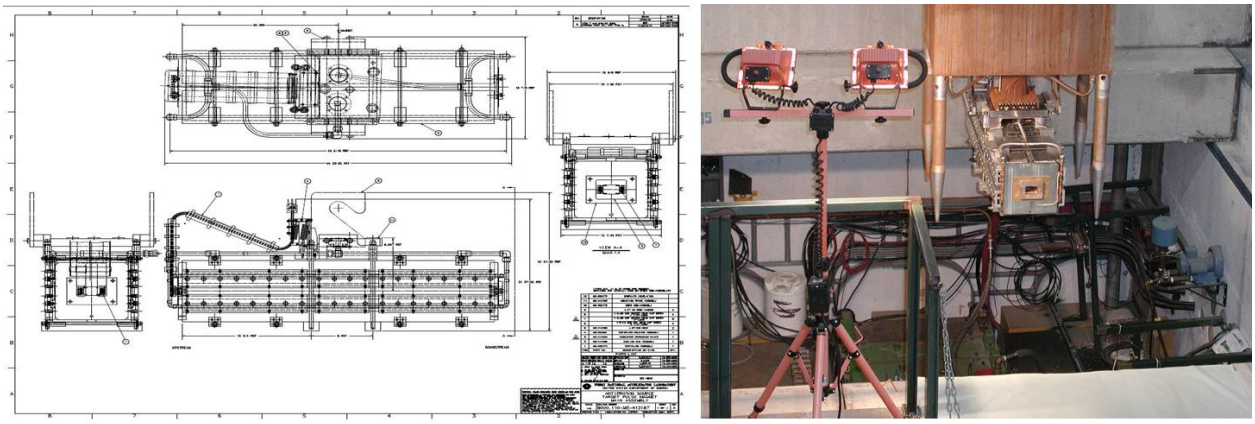

Figure 7.18: Pulsed magnet (PMAG) used for momentum-selection of pions.

One initial concern regarding the pulsed magnet was that while operating in the polarity needed to collect positive secondaries, the magnet would have an increase in energy deposited in the downstream end of the magnet compared to antiproton production where negative secondaries were collected. An increase in energy deposition could potentially lead to magnet failures, and therefore running with positive polarity might require a redesign of the magnet. A MARS simulation was conducted to look at the energy deposition across the entire pulsed magnet compared to the antiproton production case. The simulated magnet was segmented in order to highlight sensitive areas. The simulation concluded that although the map of energy deposition for the positive particle polarity with 8-GeV protons on target was different than for the antiproton production case (120-GeV protons on target), there were no locations where the deposited energy was higher, and the total was an order of magnitude lower [13]. The negative particle polarity case was more than two times lower for 8-GeV primary beam than for 120-GeV. Therefore a new pulsed magnet design will not needed and the default plan is to use the device currently installed.

In order to accommodate the $(g-2)$ pulse rate, the pulsed magnet power supply will also need to be modified or replaced with one similar to the new supply for the lithium lens with improved charging capability.

The collimator is located directly upstream of the pulsed magnet. The purpose of the collimator is to provide radiation shielding to the pulsed magnet to improve its longevity. It is a water-cooled copper cylinder 12.7 cm in diameter and 50.8 cm long. The hole through

the center of the cylinder is 2.54 cm diameter at the upstream end, widening to a diameter of 2.86 cm at the downstream end. The existing collimator is currently planned to be used without modification.

7.4.4 Target station beam dump

The target-station beam dump absorbs particles which are not momentum-selected by the pulsed dipole magnet and continue straight ahead. The location of the beam dump can be seen in Fig. 7.19. The current beam dump has a graphite and aluminum core which is water cooled, surrounded by an outer steel box. The graphite core is 16 cm in diameter and 2 m in length, and is designed to handle a beam power of 80 kW [14]. The existing dump has a known water leak that developed at the end of the collider run. Therefore, consideration for replacing the beam dump will need to be made. The current plan is to replace the beam dump with an updated copy of the 80 kW beam dump. The maximum beam energy load for $(g-2)$ would occur if $(g-2)$ takes advantage of extra cycles, for example if the NOνA experiment were not able to run. At a rate of 18 Hz, the beam energy load would be 25 kW, which is easily accommodated with the current dump design.

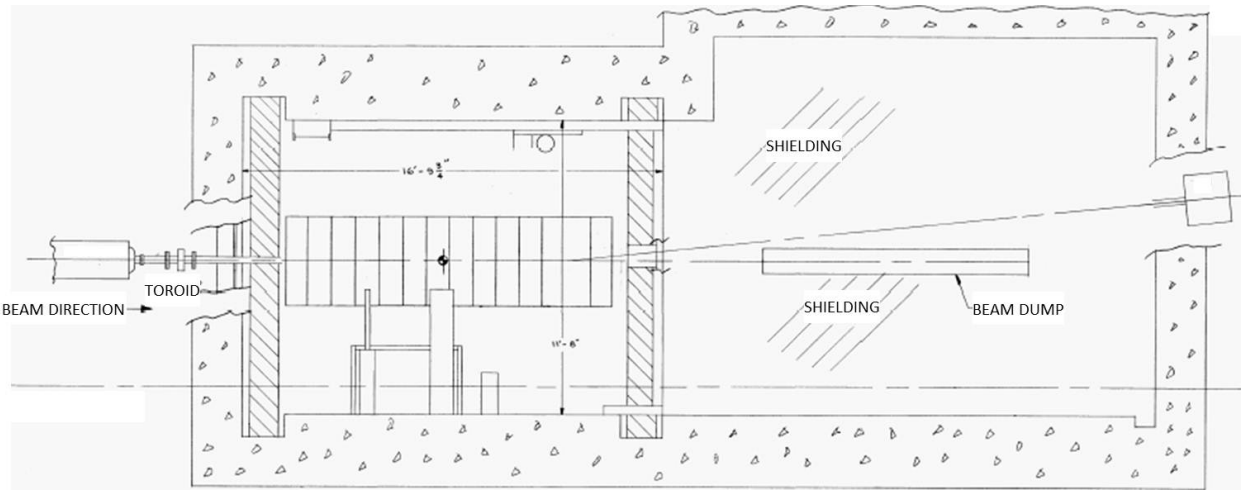

Figure 7.19: Layout of the target-station beam dump.

An alternative, shorter dump was also considered and designed at an operating capacity of 25 kW. This design resulted in a copper cylinder 2 ft long and 6 in in diameter, with copper cooling tubes vacuum-brazed around the outside of the cylinder. The cost was found to be similar to that of replacing the dump with a copy of the current 80-kW one.

7.5 Beam Transport Lines

7.5.1 Overview of $(g-2)$ beamlines

The existing tunnel enclosures and beamlines connecting the Recycler Ring to the Delivery Ring will be largely reused for $(g-2)$ operation. However, there are fundamental differences between the way the Rings and beamlines were operated for Collider Operation and how they will be used to support the Muon Campus. A high-intensity, 8 GeV kinetic energy proton beam will be transported to the AP0 Target Station in $(g-2)$ operation and to the Delivery Ring for the Mu2e experiment. The increase in intensity from Collider Operation in conjunction with the beam size of the 8 GeV beam will present challenges for efficient beam transfer. The beamlines downstream of the AP0 Target Station will need to be reconfigured to connect to the D30 straight section of the Delivery Ring. New extraction lines will be constructed to transport beam from the D30 straight section to the $(g-2)$ and Mu2e experiments. Careful planning is required for the D30 straight section of the Delivery Ring due to the presence of both the injection and extraction points. The extraction line will also need to support both single-turn extraction for $(g-2)$ and resonant extraction for Mu2e.

7.5.2 Beamline Changes from Collider Operation

During Pbar operation in Collider Run II, the P1 line connected to the Main Injector at the MI 52 location. The P1 line supported operation with three different beam energies, 150 GeV for protons to the Tevatron, 120 GeV for Pbar production and SY120 operation, and 8 GeV for protons and antiprotons to and from the Antiproton Source. (SY120 refers to the "Switchyard" of beamlines used for the 120-GeV fixed-target program.) The junction between the P1 and P2 lines occurs at F0 in the Tevatron enclosure. The P2 line ran at two different beam energies, 120 GeV for antiproton production and SY120 operation and 8 GeV for protons and antiprotons to and from the Antiproton Source. The P2, P3 (for SY120 operation), and AP1 lines join at the F17 location in the Tevatron enclosure. The AP1 line also operated at 120 GeV and 8 GeV, but is not used for SY120 operation. The AP3 line only runs at a kinetic energy of 8 GeV. The AP3 line connects with the AP1 line in the Pre-Vault beam enclosure near the Target Vault and terminates at the Accumulator.

After the conversion from collider to NOνA and $(g-2)$ operation, the Recycler will become part of the proton transport chain and will connect directly with the Booster. There will be a new beamline connection between the Recycler Ring and the P1 line. The P1 line will become a dual energy line, with no further need to deliver 150 GeV protons with the decommissioning of the Tevatron. The P2 line will continue to operate at both 8 GeV for the Muon experiments and 120 GeV for SY120 operation. The AP2 and AP3 lines will need to be almost completely dismantled and reconfigured to support both the transport of muon secondaries via the Target Station for $(g-2)$ and protons via the target bypass for Mu2e. The $(g-2)$ 3.1 GeV secondary beamline emanating from the Target Station and the Mu2e 8 GeV primary beamline bypassing the Target Station will merge and follow a single line to the Delivery Ring. The new injection line will connect to the Delivery Ring in the D30 straight section. The extraction line also originates in the D30 straight section and has to be capable of supporting both resonant and single-turn extraction.

The beamlines that made up the Antiproton Source, those that have an "AP" prefix, will be modified, reconfigured and renamed prior to $(g-2)$ operation. The AP1 line will only operate at an energy of 8 GeV and will be renamed M1. The AP1 line will be largely unchanged, with the exception of the replacement of some magnets to improve aperture. The AP2 line will become two separate beamlines and no longer be continuous. The upstream end of the line is needed as a pion decay channel for the $(g-2)$ experiment and will be renamed M2. It will provide a connection from the Pbar AP0 Target Station to the M3 line. The downstream section of AP2 will become the abort and proton removal line from the Delivery Ring. The old AP3 line will be required to transport both 8 GeV beam for the Mu2e experiment and also a 3.1 GeV secondary beam for the $(g-2)$ experiment and will be renamed M3. The 18.5° right bend will be changed from a two to a three dipole configuration in order to avoid higher beta functions in this region. The M3 line will will also be modified to connect to the Delivery Ring (formerly Debuncher) instead of the Accumulator. The extraction line connecting the Delivery Ring to the experiments will be called M4. The M5 line will branch from the M4 line to the $(g-2)$ storage ring in the MC-1 Building in the "Left Bend" area. Figure 7.20 compares the Pbar beamline configuration with that proposed for $(g-2)$ and Mu2e operation. In general, the AP1, AP2 and AP3 lines will refer to the old Pbar beamline configuration and M1, M2, M3, M4 and M5 will refer to the beamline configuration for $(g-2)$ operation.

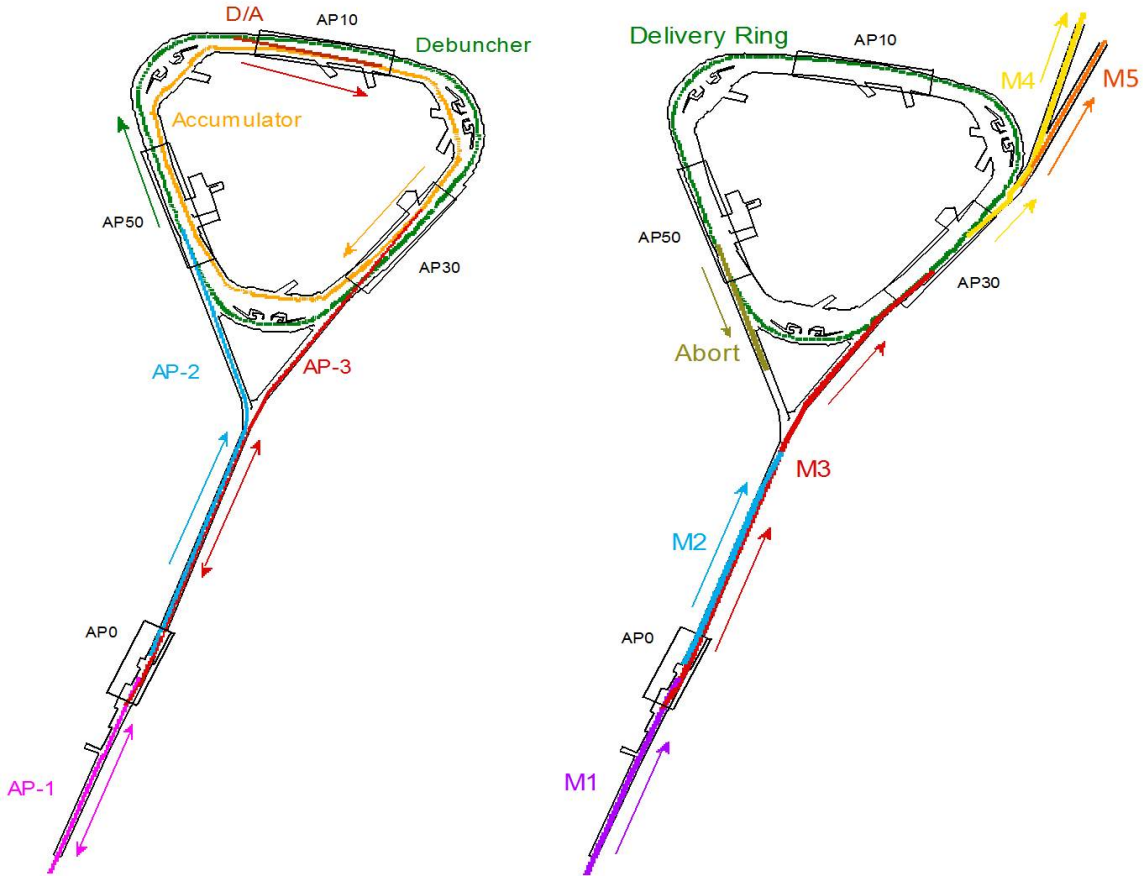

Figure 7.20: Layout of the Antiproton Source beamlines (left) and the reconfigured beamlines for $(g-2)$ operation (right).

Figure 7.21 shows another view of the Muon Campus beamlines and experimental halls.

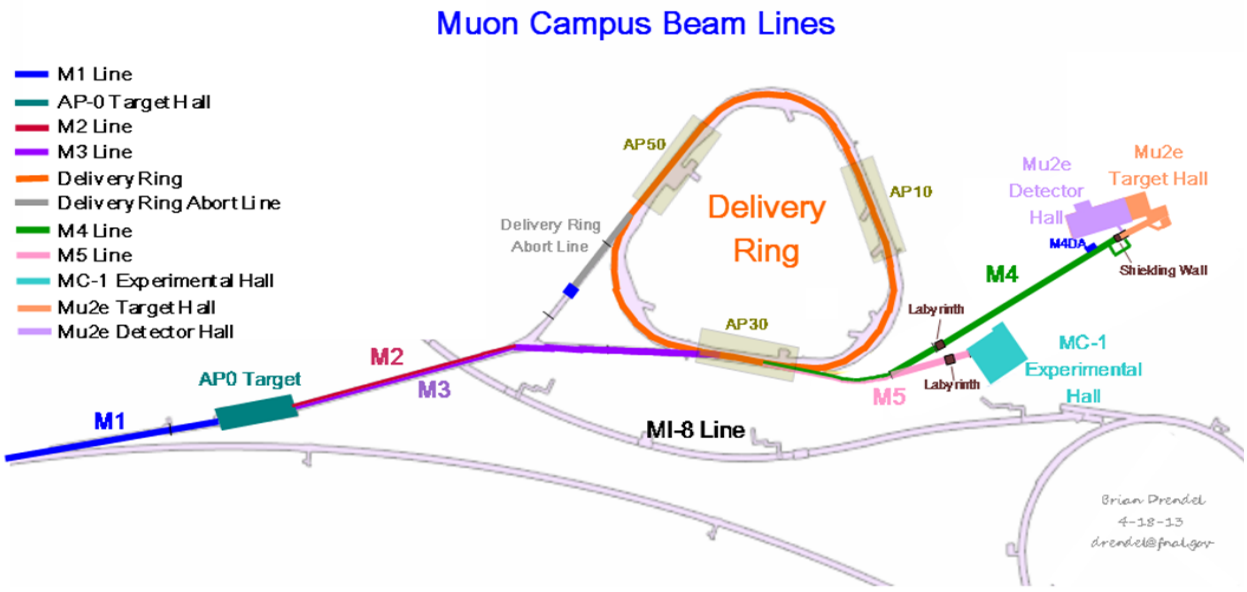

Figure 7.21: The Muon Campus beamlines and experimental halls.

Most of the common improvements to the beamlines and Delivery Ring that benefit Mu2e, $(g-2)$, and future experiments will be incorporated into several Accelerator Improvement Projects (AIPs). They are the Recycler RF AIP, Cryo AIP, Beam Transport AIP, and Delivery Ring AIP. The Cryo AIP provides cryogenics for the $(g-2)$ storage ring and to the Mu2e solenoids. Table 7.4 summarizes which improvements are contained in the various AIPs, as well as those that will be managed as part of the Mu2e and $(g-2)$ projects. Project Managers for the various projects will work closely together to ensure they interface properly. Virtually all of the work that is incorporated into the AIPs must be completed prior to beam operation to $(g-2)$.

Description	Project	Comment
Cryogenics	CR AIP	
Recycler RF upgrade	RR AIP	
Recycler extraction/P1 stub line	BT AIP	
P1,P2 and M1 aperture upgrade	BT AIP	**M1 final focus quadrupoles on $(g-2)$**
Reconfigure AP2 and AP3	**$(g-2)$**	**New lines are called M2 and M3**
Final focus to AP0 Target Station	**$(g-2)$**	
AP0 Target Station upgrades	**$(g-2)$**	
Beam transport instrumentation	BT AIP	
Beam transport infrastructure	BT AIP	
Delivery Ring injection	DR AIP	
D30 straight section preparation	**$(g-2)$**	
Delivery Ring modification	DR AIP	
DR abort/proton removal	DR AIP	
Delivery Ring RF system	*Mu2e*	
Delivery Ring controls	DR AIP	
Delivery Ring instrumentation	DR AIP	*DCCT and Tune measure are Mu2e*
Resonant extraction from DR	*Mu2e*	
Fast extraction from DR	**$(g-2)$**	
Delivery Ring infrastructure	DR AIP	
Extraction line to split	**$(g-2)$**	**Upstream M4 line**
Extraction line from split to Mu2e	*Mu2e*	*Downstream M4, including extinction*
Extraction line from split to $(g-2)$	**$(g-2)$**	**Beamline to MC-1 building**

Table 7.4: Beamline, Delivery-Ring, and other upgrades and associated project: $(g-2)$ project, Mu2e project, Delivery Ring Accelerator Improvement Project (DR AIP), Beam Transport (BT) AIP, Recycler RF (RR) AIP, and Cryo (CR) AIP.

7.5.3 Proton Beam Transport to the Target Station

Beam transport of the 8 GeV primary beam from the Recycler Ring (RR) to the Target Station closely resembles the scheme used to transport 120 GeV protons for antiproton production in Collider operation. The most notable differences are the change in beam energy and the switch from the Main Injector to the RR as the point of origin for the P1 line. The beamlines will be modified to 1) provide a connection between the RR and P1 line, 2) improve aperture to accommodate the larger beam size and intensity, and 3) reconfigure the final focus region in order to reach the desired spot size on the production target. Table 7.5 lists the beamlines connecting the RR with the Target Station and their respective lengths.

Beam Line	Length (m)
RR to P1	43
P1	182
P2	212
AP1 (M1)	144
RR to Target Total	581

Table 7.5: Recycler Ring to Target beamline lengths.

Recycler Ring to P1 line stub

Operation of $(g-2)$ and Mu2e requires the transport of protons from the RR rather than the Main Injector. A new transfer line from the RR to the P1 beamline will be constructed to facilitate proton beam transport from the RR to the Delivery Ring. This new beamline provides a way to deliver 8 GeV kinetic energy protons to the Delivery Ring, via the RR, using existing beam transport lines and without the need for new civil construction.

Beamline Design The P1 line is lower in elevation than the RR, thus the beam will be extracted downward. This will be accomplished with a horizontal kicker that will displace beam into the field region of a Lambertson magnet that will bend beam down. The kickers are located immediately downstream of the RR 520 location and the Lambertson will be just downstream of the RR 522 location. Due to space limitations, only two vertical bend centers made up of the Lambertson and a dipole are used in the new line. An integer multiple of 360° in betatron phase advance between the two bending centers is required to cancel the vertical dispersion from the bends. The new beamline needs to intercept the existing P1 line in a location that doesn't disturb the extraction trajectory from the Main Injector, which will be retained for SY120 operation. That junction point will be located near quadrupole Q703.The angles of both the Lambertson and the vertical bending magnet (VBEND) were obtained by matching the site coordinates from the RR to P1 line using TRANSPORT [15] code. Figure 7.22 shows the layout of the new line, with the existing P1 line drawn in red.

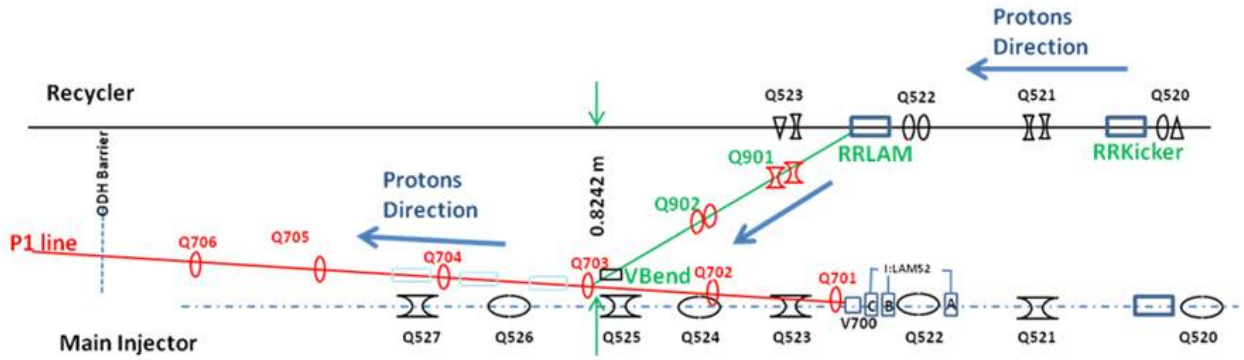

Figure 7.22: The new Recycler Ring to P1 connecting beamline.

Kickers The $(g-2)$/Mu2e extraction kicker will be of the same design as the kickers used during collider operation, but will be potted instead of using Fluorinert for electrical insulation. The physical dimensions and properties of the kickers are listed in Table 7.6. The plan is to reuse the ceramic vacuum chamber from old RR kicker magnets, which are slightly smaller than the standard RR vacuum chamber. The kicker system will be made up of two magnets producing 0.79 mr each for a total kick of 1.58 mr. The new kicker power supplies will be located in the MI-52 service building. Power supplies for the new beamline magnets will also be located at MI-52. This service building will be expanded to accommodate the new power supplies.

Recycler Extraction Kicker RKB-25	
Parameter	Value
Ferrite length	46.6 in
Case length	64.0 in
Insert length	67.78 in
Print number	ME-481284
Maximum strength (each)	0.279 kG m
Maximum kick (each)	0.94 mr @ 8 GeV/c^2
Required kick (each)	0.79 mr @ 8 GeV/c^2
Rise time, 3% - 97%	140 ns

Table 7.6: RR extraction kicker parameters.

Lambertson The Lambertson magnet will be rolled 2.7° and the vertical bend magnet -4.0° to provide a small horizontal translation in order to create the proper horizontal trajectory required to match the P1 line. The vertical dipole magnet is a 1.5 m "modified B-1" type that will provide a 21 mr bend, matching the bend of the Lambertson. There will be two quadrupoles located between the Lambertson and vertical dipole magnets that make up the dogleg between the RR and P1 line. Due to space constraints, the quadrupoles are shifted downstream from their ideal locations by 0.25 m. A more detailed technical description of

the design features of the new beam line stub can be found in Ref. [16]. Figure 7.23 shows the lattice functions for the entire RR to Target Station line.

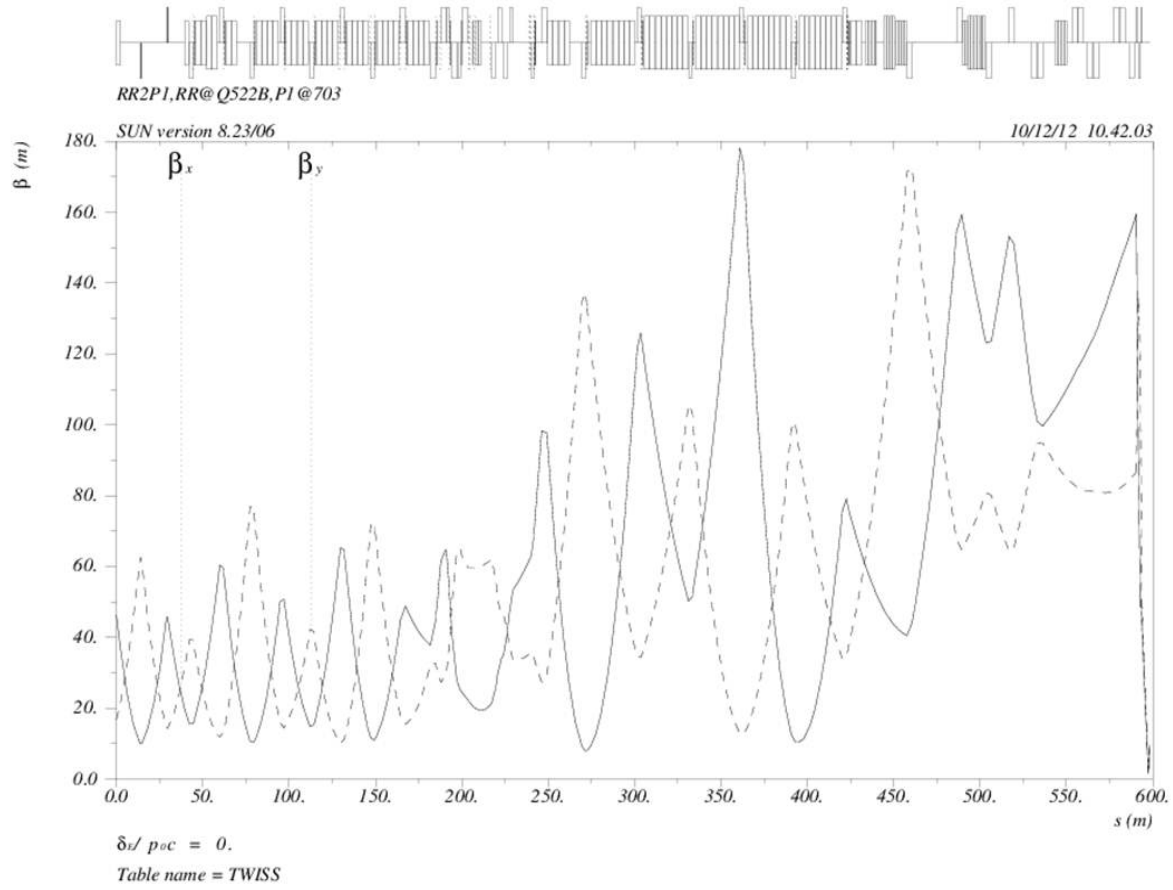

Figure 7.23: Lattice functions for primary beamlines from the Recycler to the Target Station.

Recycler orbit The RR extraction scheme incorporates a permanent horizontal 3-bump in the RR that displaces the circulating beam outward 25 mm at the upstream end of the Lambertson (RLAM). Figure 7.24 shows the trajectories of the circulating and extracted beams, including the horizontal bump at the Lambertson. The bump is created by horizontal trim dipoles at the 524, 522 and 520 locations. The extraction kickers displace the extracted beam inward 25 mm at the same location. This creates a separation of the RR circulating beam and extracted beam at the front face of the Lambertson of 50 mm.

Apertures Lambertson magnets are typically one of the limiting apertures in a beamline. The Recycler extraction Lambertson has an adequate aperture for both the circulating and extracted beams. Figure 7.25 shows the footprint of both beams at the Lambertson for both a 10σ and 6σ beam size. The vertical bend magnet has a relatively small horizontal aperture,

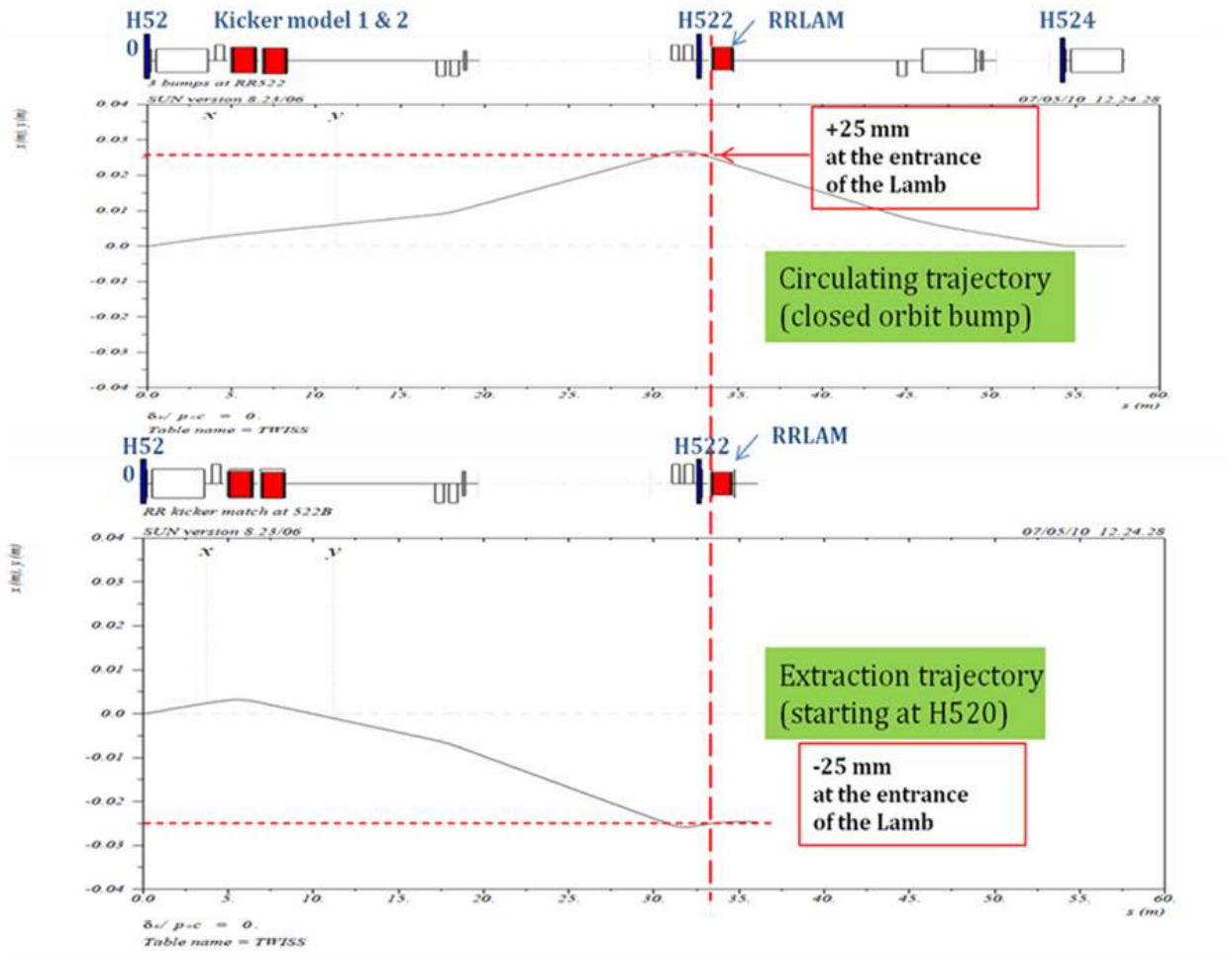

Figure 7.24: Horizontal trajectories for circulating and extracted beam from the Recycler.

but is located where the horizontal beta functions are small. The horizontal acceptance of the vertical dipole is actually larger than that of the Lambertson, despite the smaller physical aperture. The quadrupole and trim magnets are modeled after those in the Recycler and have good apertures.

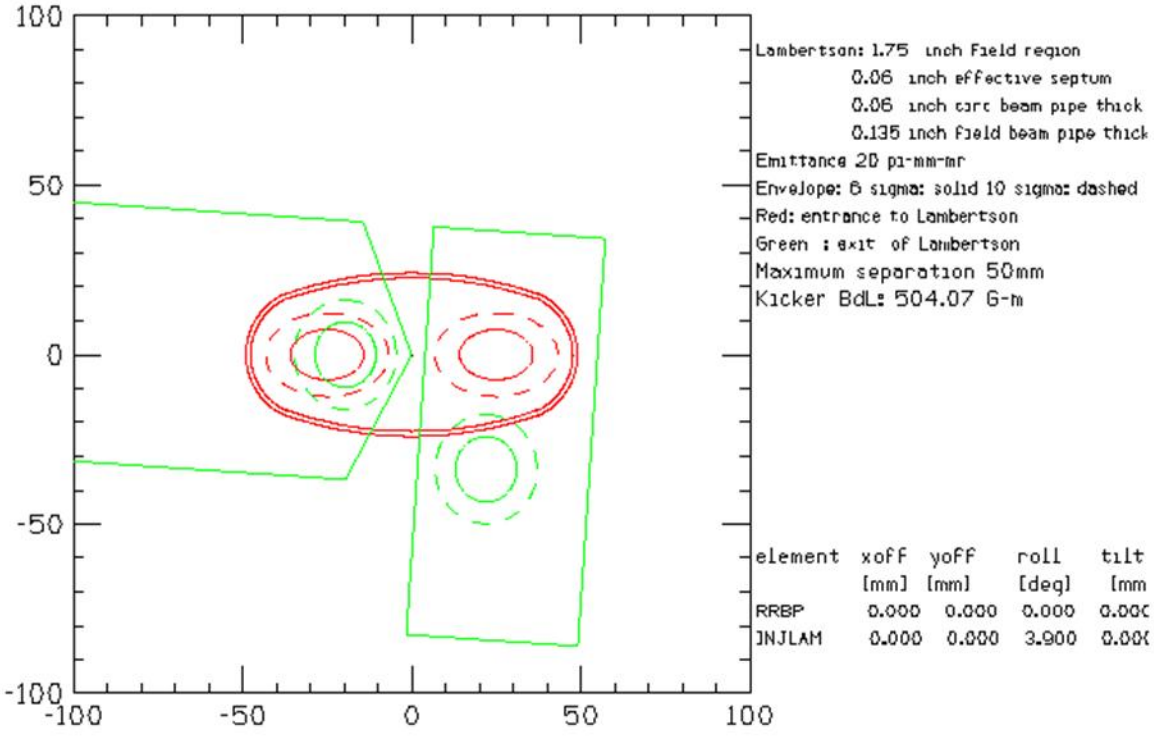

Figure 7.25: Beam sizes at the entrance (red) and exit (green) of the extraction Lambertson. The dashed outline represents 10σ and the solid outline 6σ beam for a normalized emittance of 18 π-mm-mr.

7.5.4 P1, P2 and AP1 Aperture Improvements

The increased intensity and beam size planned for muon operation will lead to unacceptably high beam loss unless apertures are improved in the P1, P2 and AP1 lines. Limiting apertures were identified during Collider Run II when evaluating possible improvements, simplifying the process of identifying locations. The elimination of AP1 120 GeV operation for antiproton stacking provides an opportunity to improve the aperture with weaker magnets that previously were not practical for use as replacements.

The introduction of the P1-line stub has eliminated several aperture restrictions that were associated with Main Injector extraction. In particular, the vertical C-magnets that follow the MI-52 Lambertson will be avoided with the new stub line. Most of the P1 line after the P1-line stub has good aperture, until the former junction area with the Tevatron. The vertical dipole at the 714 location was installed as a C-magnet because of its proximity with the Tevatron and has a small horizontal aperture. The decommissioning of the Tevatron allows the replacement of this magnet with a conventional dipole that will increase the horizontal acceptance by more than 50%. The new magnet must also be capable of producing enough field strength to operate at 120 GeV and support SY120 operation. The four Tevatron F0 Lambertsons will no longer be needed to inject protons into the Tevatron and can be removed to improve the aperture, also in the horizontal plane.

In addition to the improvements to physical aperture, a new quadrupole is proposed in the region presently occupied by the Tevatron injection Lambertsons at F0. The long drift space in the P1 and P2 lines required for Tevatron injection results in large excursions in dispersion throughout the beamlines. Unless the dispersion is reduced, the increased momentum spread created by RR bunch formation will cause high beam losses. The addition of a quadrupole (or quadrupoles) in this region will provide the means to improve the optics of the transport lines.

The P2 line will remain a dual-energy line supporting $(g-2)$ and SY120 operation, so the junction between the P2, AP1, and P3 beamlines at F17 will remain. The aperture for both $(g-2)$ and SY120 operation will substantially improve with the proposed replacement of the F17 C-magnets with a large aperture CDA magnet that both beams will pass through. The B-3 dipole at the F-17 location will remain.

AP1 will only operate at 8 GeV for $(g-2)$ operation, so the eight EPB magnets that make up the HV100 and HV102 string can be replaced with larger-aperture, weaker dipoles. The number of dipoles can be reduced from four to two in each string. The 1.5 m "modified B-1" magnets (formally known as MDC magnets) have a pole gap that is 2.25 in instead of 1.5 in and provides more than a factor of two increase in acceptance. Several trims will also be replaced or relocated to complete the aperture upgrade. The final-focus region at the end of AP1 is described separately in the next section. Table 7.7 summarizes the proposed improvements to the physical apertures in the RR to Target Station lines. Reference [16] has a more detailed explanation of the devices used to improve the aperture and how the improvements will be implemented.

Location	Existing magnet	Proposed improvement
V714	C-magnet	1 B2 magnet
F0 Lambertsons	4 Lambertsons	Remove magnets
F17 (V)	B3 and two C-magnets	1 CDA (retain B3)
HV100	4 EPB dipoles	2 MDC
HV102	4 EPB dipoles	2 MDC

Table 7.7: Proposed aperture improvements for RR to Target Station beamlines.

Final Focus Region

The desired spot size on the production target, a proton beam σ in both planes of 0.15 mm, is the same as what was used in antiproton production during collider operation. Because the beam momentum is 8.89 GeV/c for $(g-2)$ operation instead of the 120 GeV/c that was used for antiproton production, much smaller beta functions are required to achieve this spot size (0.068 m vs. 0.878 m, respectively). The existing quadrupole configuration in AP1 cannot produce the desired spot size and will need to be reconfigured. Figure 7.26 shows a modified version of the scheme proposed in Ref. [17], where a quadrupole triplet replaces the last quadrupole, PQ9B, in the AP1 line. Figure 7.26 shows the optics in the final 50 m of the AP1 line where the final focus occurs. The quadrupoles making up the triplet need to be as short as possible while concurrently producing a very strong integrated gradient. The PQ8A&B and PQ9A magnets are not powered and can be removed to improve aperture, if desired. Larger aperture NDB trim magnets from surplus Pbar inventory will replace HT107 and VT108 to provide adequate aperture.

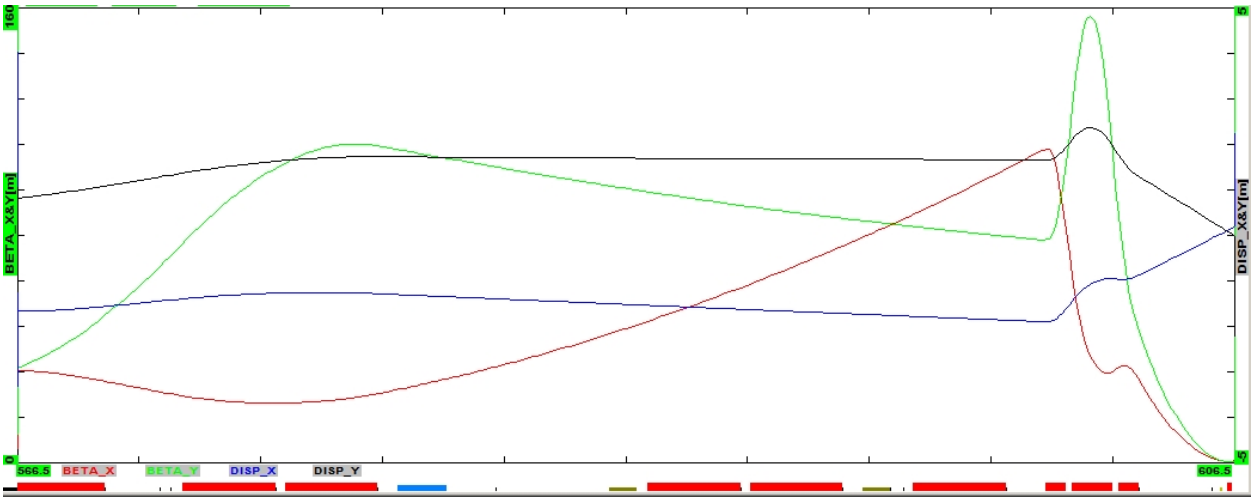

Figure 7.26: Beta functions (horizontal is red, vertical is green) and dispersion functions (horizontal is blue, vertical is black) for final focus region of AP1 line.

The best compromise between maximizing integrated field, minimizing quadrupole length and providing adequate aperture, from available magnets, is to use a triplet made of of an SQD – SQE – SQD combination. The quadrupoles are required to run between 400 and 500 Amps in order to achieve the desired 0.15 mm spot size, which equals the highest currents

these types of magnets have ever operated at. The temperature and flow of Low Conductivity Water (LCW) through these magnets will be particularly critical and may necessitate the construction of a dedicated closed-loop LCW system to prevent problems from overheating. The SQE magnet in the middle of the triplet is the strongest Pbar quadrupole available and operates at the highest current of the triplet quadrupoles (490 Amps).

7.5.5 Pion to muon decay beamlines

The M2 and M3 lines are designed to capture as many magic-momentum muons from pion decay as possible. The M2 line will be rebuilt from the former AP2 line, which transports secondary beam from the target station. The M3 line, rebuilt from the former AP3 line, begins as a target-bypass which will be used by the Mu2e experiment to transport primary 8-GeV protons. For $(g-2)$, the M2 line crosses over into the M3 line. Focusing of the secondary beam within the target station is limited by available space in the target vault. Immediately following the target station, the M2 line starts with a series of quadrupoles which then match into a regular FODO lattice.

Design layout

With the exception of a few specialized insertions, the M2 and M3 lines track the trajectories of the existing (but now defunct) AP2 and AP3 antiproton lines. The first 115.6 m of M2 downstream of the target-station lithium lens coincides with the AP2 trajectory. Pions collected from the lens are transported to and aligned parallel with the left side of the tunnel via the existing PMAG and IB1 dipoles, each of which bends the beam through 3° (52 mr). From this point, the beam travels a further 96.7 m up to, and including, the existing IQ713 AP2 quadrupole.

Through a two-step horizontal translation, the beam crosses the tunnel to merge with the incoming upstream M3 line (used by the Mu2e experiment). Each of the four horizontal bend centers in this insertion contributes 104 mr. The relatively large bends involved at each stage of this transition are driven by:

- Maintaining tight focusing quad spacing in M2 for $(g-2)$ to capture as many magic-momentum decay muons as possible;
- Minimizing the distance in which hardware would interfere with transportation / travel down the middle of the tunnel;
- Minimizing the impact of the insertion on maintaining continuous, controlled optical properties, and;
- Providing the flexibility to convert between $(g-2)$ and Mu2e operations without downtime to reconfigure hardware.

The last two magnets in the transition insertion act as a switch between $(g-2)$ and Mu2e running. A large-aperture quadrupole, Q733, followed by a modified B1 dipole are both aligned with the M3 trajectory. During $(g-2)$ operation, the beam enters the quadrupole off-axis and receives a 25 mr dipole kick. The B1 dipole provides an additional 43.6 mr to complete the merger with the M3 line. (For Mu2e operation the beam will enter the quad on-axis, and the B1 dipole is turned off).

Immediately following the transition across the aisle, a specialized insertion created by two SDB dipoles bends the trajectory through 18.5° (323 mr) to the right, aligning with the existing AP3 path in the tunnel. The beam continues for 63.0 m to the beginning of the geometric and optical matching section between the M3 line and the Delivery Ring (DR) injection point in the D30 straight section.

This final injection section satisfies multiple, interleaved design constraints:

- Providing the optical match between the lattice functions of the M3 line and those of the DR;
- A 86 mr horizontal right bend to align with the D30 straight section, and;
- An overall 4-ft elevation drop from M3 to the DR, performed in two steps.

The first step of the drop in elevation uses two SDC dipoles bending through 85 mr. The second down-bend is provided by a SDD dipole bending down at 102.7 mr.

Embedded in the level beamline section between the first and second elevation step-changes, two modified B1 dipoles bend horizontally, each through 43.1 mr to align the trajectory with the D30 straight section.

The final stages of injection occur entirely in the vertical plane, with the final up-bend produced by a combination of a C-magnet in the beamline, followed by a large-aperture focusing quadrupole Q303 and a DC septum in the DR. The C-magnet bends in the upward direction by 32.2 mr, and steers the beam 11.6-cm high off-axis through Q303, generating another 29.9 mr of vertical kick. The septum adds 45.0 mr of bend up. Three kicker modules upstream of quad Q202 close the trajectory onto the orbit of the Delivery Ring.

Total beamline length from the face of the target-station lithium lens to mid-quad Q202 in the Delivery Ring is 296 m. Parameters of the main magnets are listed in Table 7.8.

Optics

Optical properties of the $(g-2)$ beamline are defined by 65 quadrupoles of the proven Fermilab SQx and LQx types, and the 4Qx series from Brookhaven. The $(g-2)$ beamline design is comprised of distinct optical modules, as illustrated in Fig. 7.27.

- A matching section between the lithium lens and the main body of the upstream M2 lattice;
- A periodic series of thirteen FODO cells (115.6 m);
- An achromatic 18.5° right bend formed using a quadrupole triplet;
- A series of six FODO cells in the M3 line, and;
- A matching section between the M3 FODO cells and the Delivery Ring in the D30 straight section.

The extreme upstream end of the M2 line is unchanged from the existing AP2 magnet configuration. Pions from the production target are optically focused by the lithium lens and the existing Q701 - Q704 quadrupole triplet. The magnet series of PMAG, quad triplet, and IB1 form a horizontal achromat. The subsequent four quadrupoles are powered individually in order to perform the optical match to lattice functions of a long section of FODO cells.

In the M2 line, the FODO cells are characterized by their 90° of betatron phase advance and half-cell length of 4.444 m. The half-cell length is chosen to triple the existing quadrupole

Name (#)	Type	L [m]	B [T]	tilt	G [T/m]
M2 match from lithium lens to FODO section					
	PMAG	1.029	0.05283		
Q701	SQC	0.66675			-5.5725
Q701	SQC	0.66675			+4.7126
Q702	SQC	0.66675			+4.7126
Q704	SQC	0.66675			-5.6254
	MOD B1	1.5065	0.3579		
Q705	SQC	0.66675			+6.5782
Q706	SQC	0.66675			-9.6317
Q707	SQC	0.66675			+5.3884
Q708	SQC	0.4064			+3.3203
90° FODO straight section cells Q709-Q727					
QBNL (13)	4Q24	0.6096			±5.5037
QSQC (6)	SQC	0.66675			±5.1562
M2/M3 merge and 90° FODO cells Q728-Q734					
	SDE	2.500	0.4294		
Q728	4Q24	0.6096			+5.5037
	SDC	1.524	0.3812		
Q729	4Q24	0.6096			-5.5037
	SDC	1.524	0.3232		
Q730	SQC	0.66675			+5.1562
Q731	4Q24	0.6096			-5.5037
	SDE	2.500	0.4294		
Q732	4Q24	0.6096			+5.5037
	CMAG	1.524	0.2393		
Q733	LQC	0.66675			-5.1562
	MOD B1	1.5065	0.2989		
Q734	SQC	0.66675			+5.1562
Q735	SQC	0.66675			-4.4177
Q736	SQC	0.66675			+5.1562
Q737	SQC	0.66675			-3.9445
18.5° triplet achromat					
	SDB	3.048	0.548		
Q738	SQE	1.27635			+3.3814
Q739	SQE	1.27635			-3.1351
Q740	SQE	1.27635			+3.3814
	SDB	3.048	0.548		
M3 72° FODO cells					
Q741-752 (12)	SQC	0.66675			±3.3784
match to Delivery Ring Q202					
Q753	SQC	0.66675			-3.3127
	SDC	1.524	0.576	+90°	
Q754	SQC	0.66675			+3.4055
	SDC	1.524	0.576	-90°	
Q755	SQC	0.66675			-3.2048
	MOD B1	1.5065	0.2952		
Q756	SQE	1.27635			+4.3374
Q757	SQD	0.86995			-3.8292
Q758	SQD	0.86995			-3.8292
Q759	SQE	1.27635			+4.3374
	MOD B1	1.5065	0.2952		
Q760	SQC	0.66675			-3.2856
Q761	SQC	0.66675			+4.0158
	SDD	1.6605	0.638	+90°	
Q762	4Q16	0.4064			-3.3150
Q763	4Q16	0.4064			-3.3150
	CMAG	1.524	0.218	-90°	
Delivery Ring					
Q303	LQD	0.86995			+3.0580
	SEPTUM	1.8796	0.247	-90°	
Q302	SQC	0.66675			-3.9850
Q301	SQC	0.66675			+4.0224
(3)	KICKER	1.0012	0.021	-90°	
Q202	SQC	0.66675			-3.9658

Table 7.8: Main magnet parameters of the M2 and M3 beamlines for $(g-2)$ operation at 3.094 GeV/c.

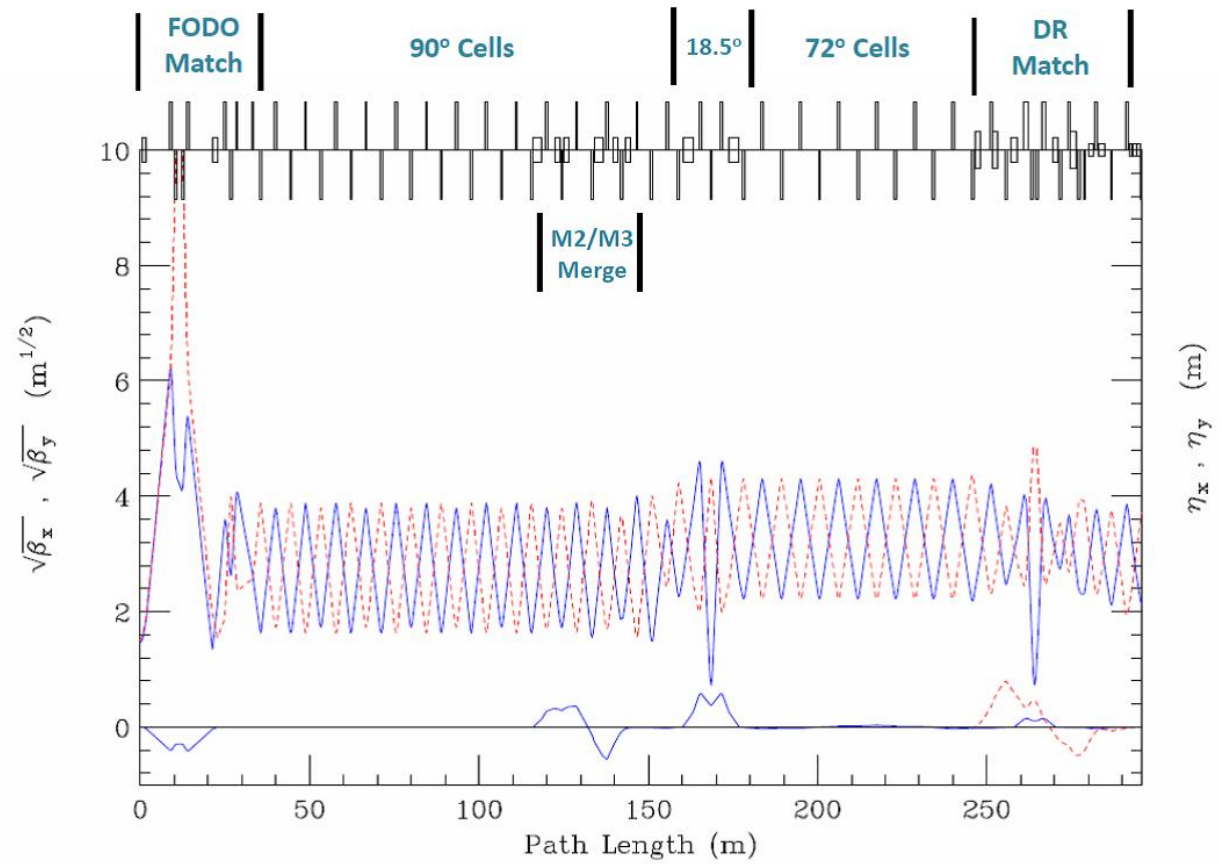

Figure 7.27: Horizontal (solid blue) and vertical (dashed red) lattice functions of the $(g-2)$ transfer line from the face of the lithium lens to mid quad Q202 in the Delivery Ring. Boxes centered along the top axis indicate dipole locations, while boxes extending up and down are focusing and defocusing quadrupoles.

density in the regularly spaced upstream portion of the M2 line. Embedded in the last four of these cells is the two-step horizontal achromat that transitions the M2 line across the tunnel to merge onto the M3 line trajectory (Fig. 7.28).

The 18.5° horizontal bend has the two bend centers separated by a quadrupole triplet of SQC.s to generate the 180° of betatron phase advance needed to kill the dispersion locally.

M3-line FODO cells are characterized by 72° of phase advance and a half-cell length of 5.613 m. These parameters are chosen to accommodate Mu2e operation at 8.889 GeV/c. The $\sim 25\%$ longer cell length and slightly weaker focusing than in the M2-line FODO section relative to M3 allow the SQC quads to operate at approximately their design gradient of 9.8 T/m.

The final nine quadrupoles in the line perform the optical match between the 72° FODO cells and the Delivery Ring. This section contains an achromatic horizontal bend embedded in an achromatic vertical descent from the M3 elevation to that of the DR. Lattice functions and bend directions are shown in Fig. 7.29.

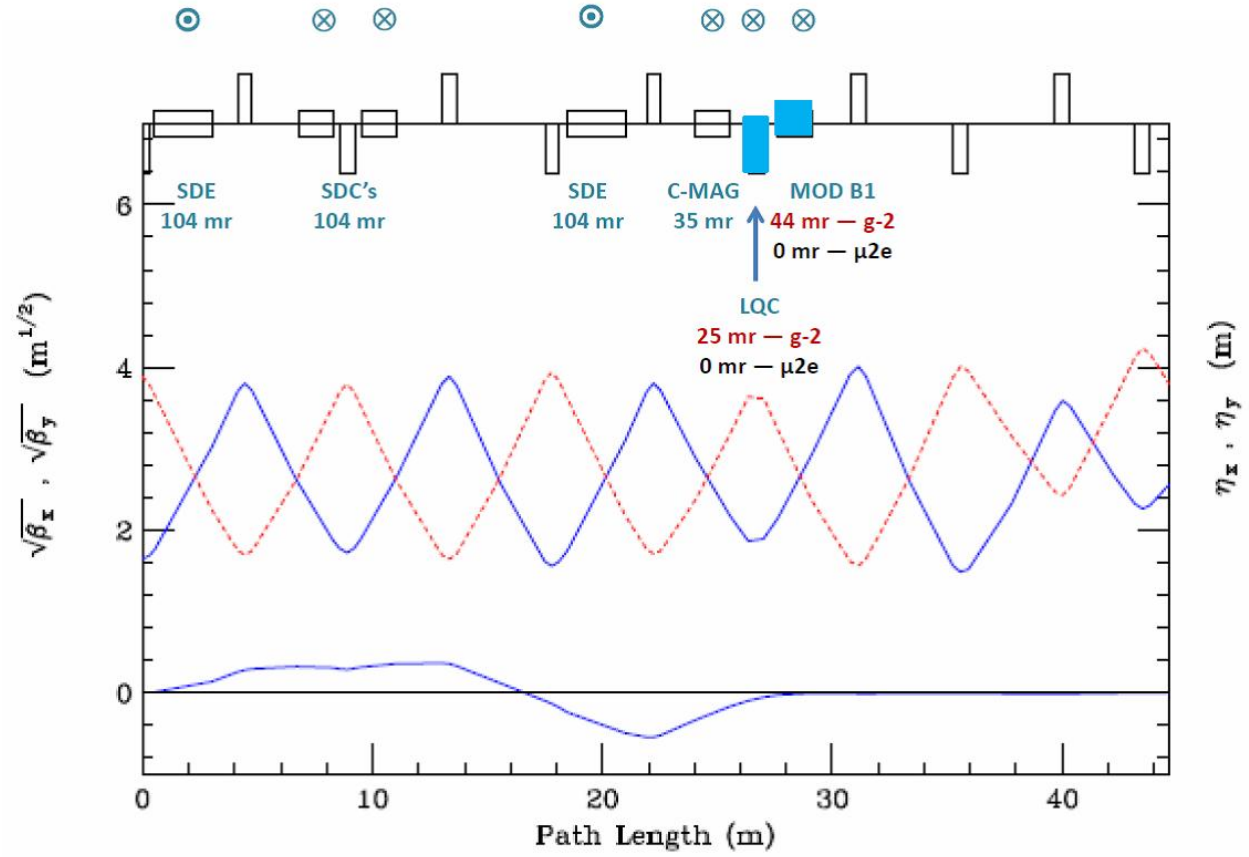

Figure 7.28: Horizontal (solid blue) and vertical (dashed red) lattice functions through the horizontal transition from the M2 line across the tunnel to merge with the M3 line. Circles shown above the upper axis indicate bend directions – those with a cross are bends left, and those with a dot are bends right. The final two (highlighted) magnets create a dipole switch between $(g-2)$ and Mu2e operations.

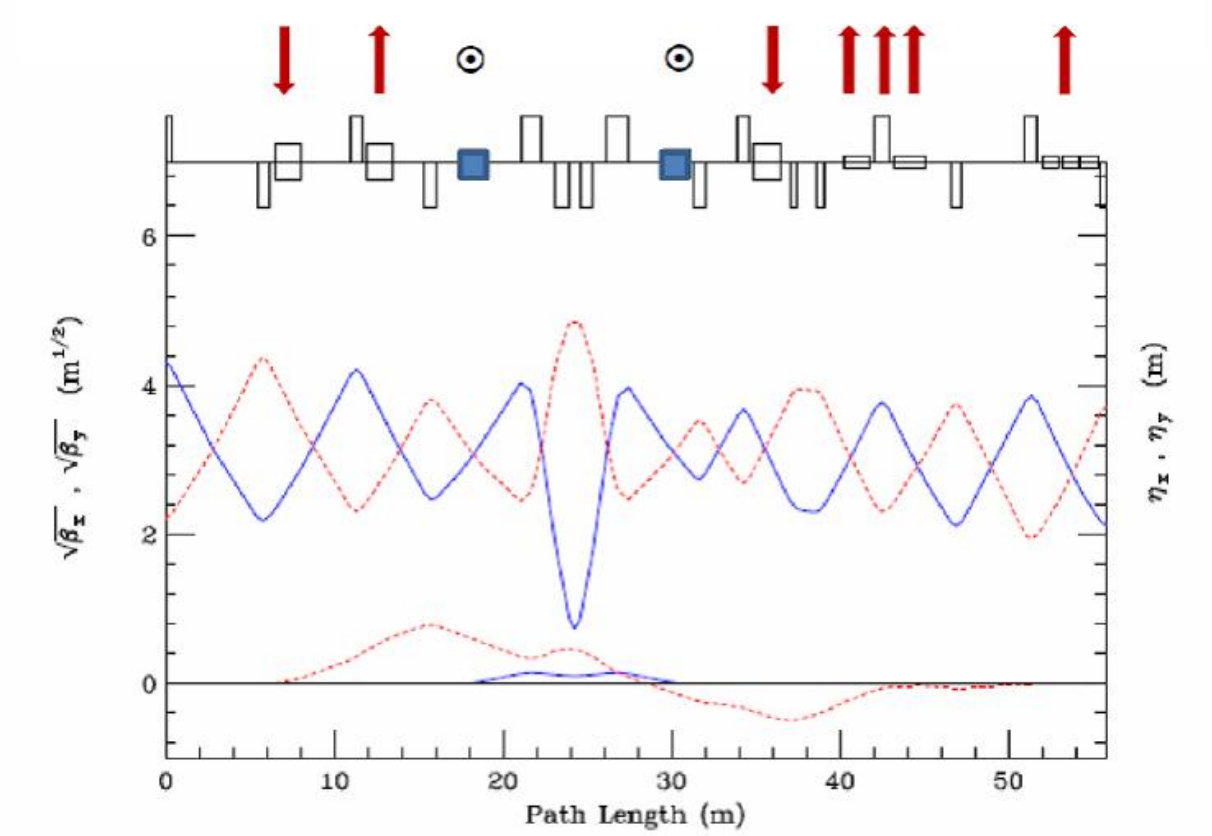

Figure 7.29: Horizontal (solid blue) and vertical (dashed red) lattice functions through the matching section from the M3 FODO cells into the DR straight. Arrows indicate the vertical bend direction in the two steps of the 4-ft drop in elevation.

7.5.6 Delivery Ring

The Pbar Debuncher ring will largely remain intact for $(g-2)$ operation and will be renamed the Delivery Ring for its new role in providing muons to the experiment. A considerable amount of equipment left over from Pbar operation will need to be removed from the Debuncher. Most of the equipment targeted for removal was used for stochastically cooling the antiproton beam during collider operation and is not needed for $(g-2)$. Some of these devices also have small apertures, so the ring acceptance will be improved with their removal. The cooling tanks in the D30 straight section also need to be removed to provide room for the new injection and extraction devices.

The Pbar Accumulator ring will not be needed for $(g-2)$ and Mu2e operation and will become a source of magnets, power supplies and other components for use in the reconfigured beamlines. In particular, the M4 (extraction) line will be largely made up of former Accumulator components. Some larger-aperture magnets will also be needed in the injection and extraction regions and will come from the Accumulator or other surplus sources.

Rings Lattice and Acceptance

The original design lattice for the Debuncher will be used for the Delivery Ring with few modifications. The lattice has a 3-fold symmetry with additional mirror symmetry in each of the three periods, with three zero-dispersion straight sections: D10, D30 and D50. The original lattice parameters were largely dictated by the requirements for Pbar stochastic cooling and the RF systems. The Debuncher was designed with a large transverse and longitudinal momentum acceptance in order to efficiently RF-debunch and stochastically cool antiprotons from the production target. This lattice design is also well suited for $(g-2)$ operation. During Collider Run II, the original lattice was distorted somewhat in order to reduce the beam size in the stochastic cooling tanks that had limiting apertures. Since these tanks will be removed, the lattice that will be used for the $(g-2)$ conceptual-design work will revert back to the original Debuncher design lattice. Figure 7.30 shows the lattice functions for one period of the Debuncher.

It should be noted that the design acceptance of the Debuncher was 20 π-mm-mr. During the 25 years of Pbar operation, numerous aperture improvements were undertaken to boost the acceptance of the Debuncher. After the final Collider Run II aperture improvements were put in place in 2007, the measured acceptance of the Debuncher was as high as 33 π-mm-mr in both transverse planes. The $(g-2)$ design goal of a 40 π-mm-mr acceptance for the Delivery Ring, while reusing as much of the original equipment as possible, presents a difficult challenge.

The transverse acceptances of the Debuncher dipole, quadrupole, sextupole, and trim magnets are quite large. The smallest magnet acceptance is in the vertical plane of the dipoles and is approximately 54 π-mm-mr on one end, growing to 79 π-mm-mr on the other end. The dipoles have a 90 π-mm-mr or larger horizontal acceptance (90 π-mm-mr for the $\pm 2\%$ momentum spread and locations with the largest dispersion) and the other magnets have a 100 π-mm-mr or larger acceptance in both planes. Since the original Debuncher lattice will not be significantly changed for $(g-2)$ operation, the main Delivery-Ring magnets will not be limiting apertures. In general, devices with a physical aperture of 50 mm or greater

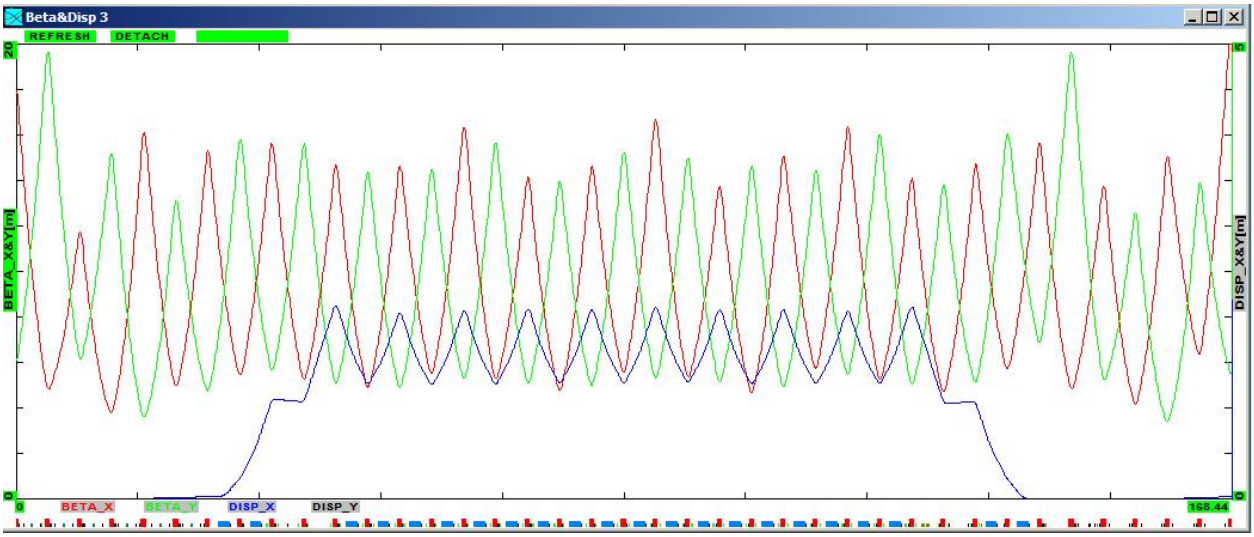

Figure 7.30: Debuncher/Delivery Ring lattice functions through 1/3 of the ring. β_x is in red, β_y in green, and horizontal dispersion in blue.

provide an acceptance of over 40 π-mm-mr in the Debuncher, and select locations can provide that acceptance for devices that have an aperture of 40 mm, as long as they are relatively short.

During Collider operation, the smallest physical apertures in the Debuncher came from stochastic cooling tanks, RF cavities, instrumentation, and devices used for injecting and extracting beam. Many of these devices will be removed as part of the repurposing of the Debuncher for the muon experiments. Some of these devices, most notably the kickers, will be retained in the interest of economy and/or complexity and lead-time of manufacture. Other devices, such as the injection septa, will be new devices with necessarily small physical apertures in order to provide enough bend strength.

During Collider Run II, the Band-4 stochastic cooling tanks were the limiting aperture in both planes of the Debuncher. The Band-4 tanks had a 38 mm physical aperture in the cooling plane, and there were both horizontal and vertical pick-up and kicker tanks in the D10 and D30 straights respectively. All of the stochastic cooling tanks will be removed prior to $(g-2)$ operation.

There is only one RF cavity planned for the Delivery Ring, which is needed to support Mu2e operation and will have an aperture similar to the Debuncher rotator cavities. Since the rotator cavities had an acceptance that was greater than 100 π-mm-mr, the new cavity will have ample aperture and need not be removed when switching from operating Mu2e to $(g-2)$. All RF cavities used for antiproton production will be removed prior to $(g-2)$ operation.

Many of the beam detectors used during Pbar operation had small physical apertures in order to improve sensitivity. Since the beam intensities when running $(g-2)$ are expected to be even smaller than those seen during Pbar operation, designers will need to be mindful of the aperture needs of the $(g-2)$ experiment. Similarly, when instrumentation is being considered for reuse in the Delivery Ring, the physical aperture and proposed tunnel location should be analyzed for adequate acceptance.

The transverse Schottky detectors used in the Debuncher had apertures that were only slightly larger than the Band-4 stochastic cooling pick-up. They were removed from the Debuncher during Run II, but have been reinstalled for use during $(g-2)$ and Mu2e studies. Although these Schottkys are slated for removal prior to $(g-2)$ operation, the Mu2e experiment may need a new device to monitor tunes during resonant extraction. If a new device is made, it will need to have adequate aperture for $(g-2)$ or will have to be removed when switching between the two experiments. The DCCT beam-intensity monitor will also be used by the Mu2e experiment. It is expected to have adequate aperture as long as it is located in the middle of a straight section half-cell, where the beam has a circular cross-section.

Both injection from the M3 line and extraction to the M4 line take place in the D30 straight section. Injection will be located in the upstream half of the straight section, and the pulsed magnetic septum and kicker magnets will have small apertures in order to provide adequate bending strength. The septum has a small aperture in both planes, while the kicker is primarily limited in the horizontal plane. The septum is a modified Booster-style (BSE) magnetic septum magnet. The septum modifications involve increasing the pole gap from 28 mm to 42 mm in order to greatly improve the horizontal acceptance, and reducing the septum thickness from 14 mm to 9 mm to increase the vertical acceptance. The injection kicker system will be made up of two surplus Pbar AP4 injection kicker magnets. The horizontal aperture is only 41 mm and will likely be one of the limiting apertures of the Delivery Ring. The extraction kicker system will be made up of two Pbar extraction kicker magnets. They have a vertical aperture of 41 mm and will also be one of the limiting apertures of the Delivery Ring.

Kickers and Septa

The kickers and septa required for $(g-2)$ operation will need to operate at a much higher frequency than that used for antiproton production, with peak rates increasing as much as a factor of 30. In an effort to make the new kicker systems more economical, existing kicker magnets will be reused. Kickers will be required for injection and extraction from the Delivery Ring as well as for proton removal. Table 7.9 compares kicker parameters for existing Pbar systems to the specifications for the $(g-2)$ injection and proton-removal kickers. The rise and fall time specifications for $(g-2)$ are generally less strict than what was needed for antiproton production, due to the short bunch length of the muons (and protons). Decreasing the rise time of the proton removal kicker, however, will reduce the number of turns required in the Delivery Ring to adequately separate the protons from the muons. Although the Pbar kicker magnets are suitable for reuse, new power supplies will be needed to operate at the increased rate. Resistive loads for the kickers will need to be cooled with Fluorinert. A single Fluorinert distribution system is planned, with piping bridging the distance between the load resistors from kickers in the D30 and D50 straight sections.

The septa and pulsed power supplies used during Pbar operation are not suitable for rapid cycling and cannot be used for $(g-2)$. The septa have no internal cooling to handle the increased heat load from the planned high duty cycle, and the power supplies are not able to charge quickly enough. The Booster-style septum magnets can be modified to have the necessary size and field strength required for use in the injection and proton removal systems, and therefore are the preferred choice. The power supplies used in the Booster to power the

Kicker (modules)	Integrated Field (kG-m)	Kick Angle (mr)	Rise Time 95%/5% (ns)	Fall Time 95%/5% (ns)	Flat Top Time (ns)
Debuncher Extraction (3)	1.34	4.6	150	150	1500
Debuncher Injection (3)	1.81	6.1	185	185	1500
Delivery-Ring Injection (2)	0.64	6.2	n/a	800	300
Delivery-Ring Extraction (2)	0.83	7.0	450	n/a	200
Delivery-Ring Proton Removal (3)	0.64	6.2	180	n/a	270

Table 7.9: Existing Pbar (top) and future $(g-2)$ (bottom) kicker strength and waveform specifications.

septum magnets also appear to be a good fit. Although they are designed to operate at a lower frequency (15 Hz) than the peak needed for $(g-2)$, the lower operating current (for 3.1 GeV/c versus 8.89 GeV/c momentum) should more than compensate for changes to the heat load and mechanical stresses due to the increased pulse rate. The Booster septum magnets are slightly shorter than their Pbar counterparts, so the new septa can comfortably fit between quadrupoles in the injection and proton removal regions.

Delivery Ring D30 straight section

The Delivery-Ring injection and extraction regions will both be located in the D30 straight section. In both cases, the tight quadrupole spacing in the Delivery Ring creates physical conflicts with existing utilities and ring devices in the areas of elevation change to and from ring level. The existing cable trays on the Debuncher side of the ring will need to be completely dismantled and relocated towards the middle of the tunnel so that the new beamlines can be hung from the ceiling. The extraction line will closely follow the trajectory of the decommissioned AP4 (Booster to Debuncher) line. The tunnel in this region has an existing stub region that the extraction line will pass through, eliminating the need for civil construction to widen and strengthen the tunnel. Figure 7.31 shows the layout of injection and extraction devices in the D30 straight section.

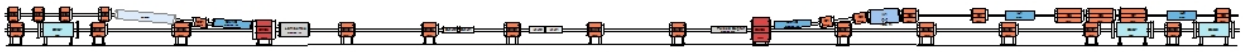

Figure 7.31: D30 straight section, injection on right, extraction on left.

Injection

The M3 line runs above the Delivery Ring in the upstream end of the D30 straight section and ends with a vertical translation into the ring. M3 injection will be achieved with a combination of a C-magnet, magnetic septum, D3Q3 quadrupole, and kicker magnets, which will all provide vertical bends. The septum and C-magnet are both based on existing designs, which reduces overall costs, but modified to improve the aperture. Both magnet designs required modifications in order to attain the $(g-2)$ acceptance goal of 40 π-mm-mr.

The magnetic septum is a modified Booster-style (BSE) magnet, with an increased pole gap and a thinner septum to improve aperture. The BSE magnet has a 1.1-in pole gap, which will be increased to 1.65 in for the new septum. Similarly, the C-magnet is a larger aperture (2.1 in instead of 1.6 in) and shorter (2.0 m instead of 3.0 m) version of the Main-Injector ICA magnet. An identical C-magnet is used in the extraction region. The descending beam in M3 will pass through the C-magnet first and will be bent upward by 38 mr. The beam will continue well above the center of the D3Q3 quadrupole and receive a 30-mr upward kick. Since the beam is up to 140 mm above the centerline of the quadrupole, a large-bore quadrupole magnet is required in order to provide adequate aperture. The large quadrupole at D3Q3 will be the LQE magnet from the D2Q5 location, which will be replaced by an 8-in quadrupole, as described below. The LQx magnets were designed to have a substantial good-field region that extends between the poles. Similar arrangements with LQ magnets can be found in Pbar at D4Q5 (former AP2 injection, planned proton removal) and D6Q6 (former Debuncher extraction). The injected beam then passes through the field region of the septum magnet and receives a 37-mr upward bend as required for the necessary trajectory entering the injection kicker magnets. The kicker magnets provide a final 6.2-mr vertical bend to place the injected beam on the closed orbit of the Delivery Ring.

The two-module kicker system is located between the D30Q and D2Q2 magnets. To minimize the horizontal β function and maximize acceptance, the kickers will be located as close to the D2Q2 quadrupole as possible. Spare Pbar injection kicker magnets will be refurbished and reused for muon injection. The magnets are already designed to be oriented vertically, so little additional effort will be required to convert them to their new application. Kicker rise and fall time specifications and power supply information was provided in Table 7.9 and the accompanying text. Figure 7.32 shows the injection devices and their location in the Delivery Ring, along with their bend angles. Due to the large vertical excursion through the top of the D3Q2 magnet, a vertical bump across the injection region will be incorporated to lower the beam and improve the aperture. The quadrupole magnets at D2Q2, D30Q and D3Q4 will be displaced to create the bump by generating steering due to the beam passing off-center through the magnets. To create a 15-mm downward displacement at D3Q2, the magnets will be lowered by 8.1, 11.0, and 4.2 mm respectively. It would be beneficial, but not necessary for 40 π-mm-mr acceptance, to install an existing "extended star chamber" quadrupole at the D3Q2 location. SQD-312, in magnet storage, was previously located at D4Q4 in the Pbar AP2 injection area and has an extended top lobe in its star chamber.

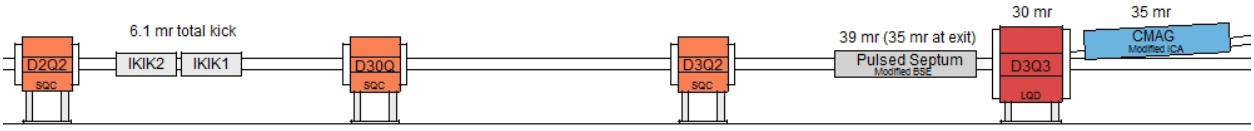

Figure 7.32: Delivery-Ring injection devices.

Extraction

Extraction from the Delivery Ring takes place in the downstream half of the D30 straight section. The extraction channel and the first 30 m of the M4 line will be used for both Mu2e resonant extraction and $(g-2)$ single-turn extraction. This arrangement avoids the complexity and additional expense of dual extraction lines in the limited available space. It also eliminates the need to remove potentially highly radioactive objects from the ring when switching between experiments. The ideal extraction configuration will provide enough aperture for both the Mu2e resonantly-extracted proton beam and the $(g-2)$ muon beam to be transported efficiently through the M4 line.

A Lambertson and C-magnet pair will be used, in conjunction with the intervening D2Q5 quadrupole, to bend the beam upward out of the Delivery Ring. In the interest of compatibility between $(g-2)$, Mu2e, and future muon experiments, a Lambertson magnet is required for extraction. The resonant-extraction process used for Mu2e is very restrictive on the size, strength, and location of the electrostatic septa that are required to split the extracted beam. The electrostatic septa must be located on either side of the D2Q3 quadrupole, and are expected to be about 1.5 m in length. In order to achieve the goal of a combined extraction channel and beamline, the $(g-2)$ extraction kickers must be located in a lattice location that is $\sim n\pi/4$ radians from the Lambertson, where n is an integer, and in an area not already occupied by injection or extraction devices.

The $(g-2)$ extraction kickers will be located between the D2Q2 and D2Q3 quadrupoles. There will be two kicker modules of approximately 0.85 m length each. During the dedicated period of $(g-2)$ operation, the kickers will be located as close to the D2Q3 quadrupole as possible in order to minimize the vertical β function and maximize acceptance. The kicker magnets will be repurposed Pbar extraction kicker magnets that have a vertical aperture of 41 mm. The kicker magnets will be powered in series from a single power supply. There is also an alternative layout planned that would allow $(g-2)$ to operate after the Mu2e electrostatic septa are installed. There is only room for a single kicker near the D2Q2 quadrupole in this arrangement, so the kicker magnet would need to be modified in order to provide enough bending strength. The relocation of the kicker would also reduce aperture unless the β functions in this region could be suppressed by about 20%. Figure 7.33 shows the layout of the extraction devices for dedicated $(g-2)$ operation and 40 π-mm-mr acceptance.

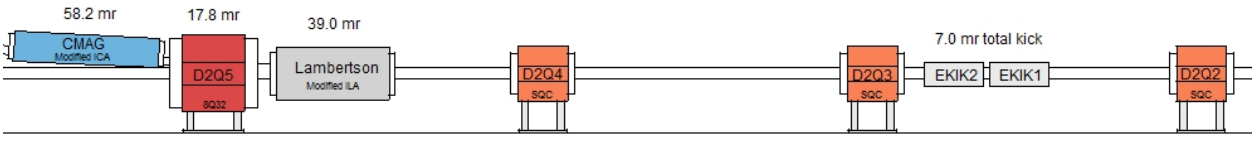

Figure 7.33: Delivery-Ring extraction devices.

Proton Removal (Abort) System

The proton removal system is an example of both repurposing an otherwise unneeded part of the Antiproton Source and implementing a dual function system that can be used by both

$(g-2)$ and Mu2e. During Mu2e operation, an abort is needed to minimize uncontrolled proton beam loss and to "clean up" beam left at the end of resonant extraction. The proton beam must be removed quickly, by means of kicker magnets, in order to minimize losses in the ring. The $(g-2)$ experiment can benefit from the removal of protons before they reach the storage ring. The abort system can serve this purpose, as long as the protons sufficiently slip in time to create a gap for the kickers to rise through.

The old Debuncher injection point from the AP2 line in the D50 straight section will be used for the abort and proton removal systems. Recall that most of the AP2 line will be removed and replaced with the new M2 line that will merge with the M3 line upstream of the right bend. The downstream end of AP2, where antiprotons were formerly injected into the Debuncher, can now be used to extract protons from the Delivery Ring. This is made possible by the change in beam direction (as viewed from above) from clockwise to counterclockwise. The existing Pbar injection kicker magnets can be reused, although a new power supply will be needed to operate at the frequency needed to support Mu2e and $(g-2)$. The septum magnet and power supply will also need to be upgraded for the same reason. The new larger-aperture septum magnet will be identical to what was previously described for injection into the Delivery Ring. The section of the AP2 beamline being repurposed will require the addition of a vertical bending magnet to steer beam into the abort dump located in the middle of the Transport tunnel. Figure 7.34 shows the layout of the abort line.

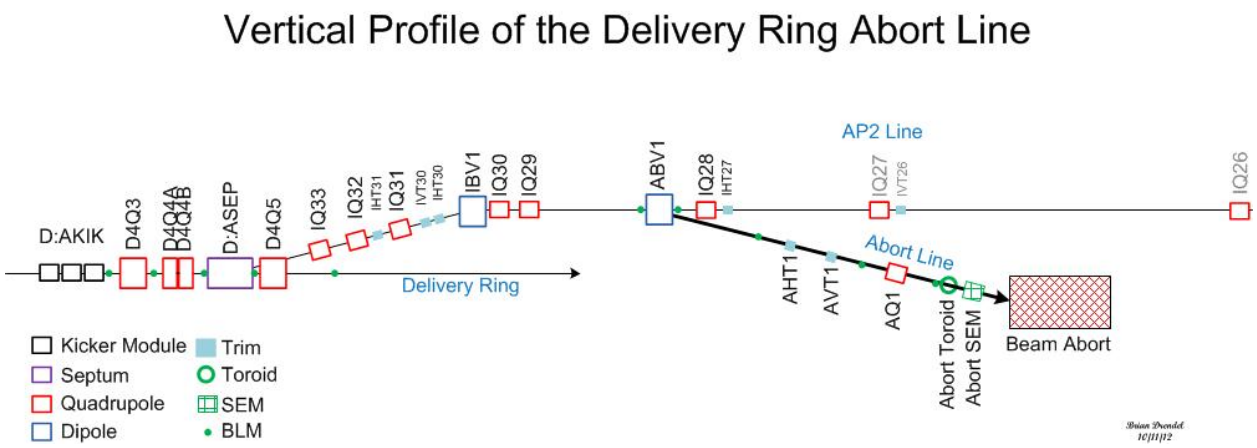

Figure 7.34: Side view of the Delivery Ring Abort/Proton Removal line.

The most economical plan is to only power the first kicker magnet, which provides the shortest rise time, a (barely) strong enough kick and requires only a single power supply. The rise time of the kickers with this configuration is about 180 ns. The kickers will be reconfigured for Mu2e operation, because all three kicker magnets are required to provide enough strength due to the higher beam momentum for Mu2e. Mu2e will also need a longer flattop to cover the entire proton revolution period of 1695 ns. For $(g-2)$ proton removal, the 180-ns rise time requires several revolutions around the Delivery Ring to provide enough gap between the muons and protons for the kicker to rise through. Table 7.10 lists the separation between the beams and the gap size for different numbers of turns. Four turns around the Delivery Ring would be required to cleanly remove all of the protons without disturbing the muons. All of the protons could be removed in three turns, but some of the

muons would also be deflected. The table is based on the assumptions already stated: that the kicker rise time is 180 ns, the proton and muon bunch lengths are 120 ns and that the kicker should not disturb any of the muons.

	Muon vs. Proton		
	Centroid time difference (ns)	Gap size (ns)	Impact of proton removal kickers
Injection	40	None	Unable to kick protons only
1^{st} turn at Abort	91	None	Unable to kick protons only
2^{nd} turn at Abort	161	41	25% of protons removed
3^{rd} turn at Abort	231	111	85% of protons removed
4^{th} turn at Abort	301	181	Protons cleanly removed
5^{th} turn at Abort	371	251	Protons cleanly removed

Table 7.10: Efficiency of proton-removal system for different number of turns in the Delivery Ring, based on a 120-ns bunch length and 180-ns kicker rise time.

As the kicker magnets "fill" during the rising current waveform, the kicker magnetic field and bending strength increase proportionally. Protons are completely removed from the Delivery Ring when the kicker strength is about 85% of what is needed to center beam in the abort channel. Between 85% and 100% of the nominal kicker strength, some of the protons will be lost on the Abort Septum instead of traveling to the abort. As the kicker strength drops below 85%, an increasing number of protons remain in the Delivery Ring. In addition to separating the beams to improve removal efficiency, the percentage of protons removed can also be increased by firing the kicker earlier and disturbing part of the muons.

A side benefit of the muons taking multiple turns around the Delivery Ring is that virtually all of the pions will have decayed before the muons reach the storage ring. The primary potential problem with this proton removal concept is due to differential decay systematic errors caused by the different muon path lengths as they travel through the Delivery Ring. Although a preliminary analysis indicates that this will not be a significant problem [18], a more thorough analysis is needed.

Vacuum Systems

The existing vacuum systems in the rings and transport lines have performed very well during Pbar operation. Typical vacuum readings in the Debuncher and transport lines were approximately 1×10^{-8} Torr. The Debuncher has good ion-pump coverage that should generally be adequate for $(g-2)$ operation. Stochastic cooling tanks, kickers and septa that will be removed during the conversion have built-in ion pumps, so some of these pumps may need to be installed in the vacated spaces. Injection and extraction devices should have ion pumps integrated into the design, or there should also be additional pumping capacity added to the surrounding area. Vacuum components from the AP2 and AP3 lines should provide most of the needs for the reconfigured M2 and M3 lines. The Accumulator has enough surplus ion pumps and vacuum pipe available to cover part of the needs for the extraction beamlines.

Infrastructure Improvements

Electrical power for the Antiproton Source is provided by Feeder 24, which operated with a power level of about 4.4 MW during Pbar operation. Although the $(g-2)$ power load is expected to be considerably less than what was used in Pbar by virtue of the reduced beam momentum, the Mu2e experiment must also be able to operate the same magnets at 8.89 GeV/c. For Mu2e, most service buildings are expected to use approximately the same amount of power as they did in Pbar operation. The exception is the AP-30 service building, where there will be an increase in power load from the injection- and extraction-line power supplies. A new transformer may be needed at AP-30 to provide the additional power. A power test was performed on the individual service building transformers to aid in predicting the power needs for Mu2e [19]. Also, since the Accumulator will no longer be used, approximately 1.4 MW will be available for new loads.

Presently, Pbar magnets and power supplies receive their cooling water from the Pbar 95° Low Conductivity Water (LCW) system. The cooling requirements for $(g-2)$ are expected to be lower than for Pbar operation. However, Mu2e will operate at 8.89 GeV/c and create a substantially larger heat load than $(g-2)$. Fortunately, the removal of the heat load from decommissioning the Accumulator and the AP2 line should be enough to offset the increase from the extraction line and other new loads. The extraction beamlines (M4 and $(g-2)$ lines) will have an LCW stub line connecting to the Debuncher header in the D30 straight section. If necessary, it is also possible to design smaller closed-loop systems that heat-exchange with the Chilled Water system. The Chilled Water system has adequate capacity and is already distributed to the Pbar service buildings.

7.5.7 Muon transport to storage ring

Considerations

The $(g-2)$ 3-GeV muon beam and the Mu2e 8-GeV proton beam must utilize common D30 extraction magnetic components to complete separation from the Delivery Ring, and extraction must occur vertically in order to accommodate the existing DR enclosure. The large differences in beam size and energy place difficult, sometimes conflicting, demands on the common extraction optics, especially the extraction Lambertson and vertical-bending dipoles. The civil constraints of the local geography further complicate execution of the two external beamlines.

The civil constraints of the local geography for what is termed the muon campus can be deduced from Fig. 7.35. The physical separation from the Delivery Ring through an achromatic vertical bend section (which separates and delivers beam into the external beamlines) must be followed by strong horizontal bends to direct beam to the two experiments. The length of the Mu2e beamline is limited by wetland avoidance and the much reduced $(g-2)$ beamline length by the storage ring enclosure location. The $(g-2)$ storage ring location is required to avoid stray magnetic fields from Mu2e components on the west and utility corridors on the east. The short distance from the common extraction Lambertson to the $(g-2)$ ring mandates efficient, space-conserving separation of the two external lines. Separation must first occur vertically component-wise and then final separation utilizing a large difference in the strengths of the left horizontal bends in the M4 and M5 lines which are now

vertically independent. With no space available for a second vertical translation (and the required achromatic conditions) the first vertical section must take the $(g-2)$ beamline to the required elevation for injection into the $(g-2)$ storage ring.

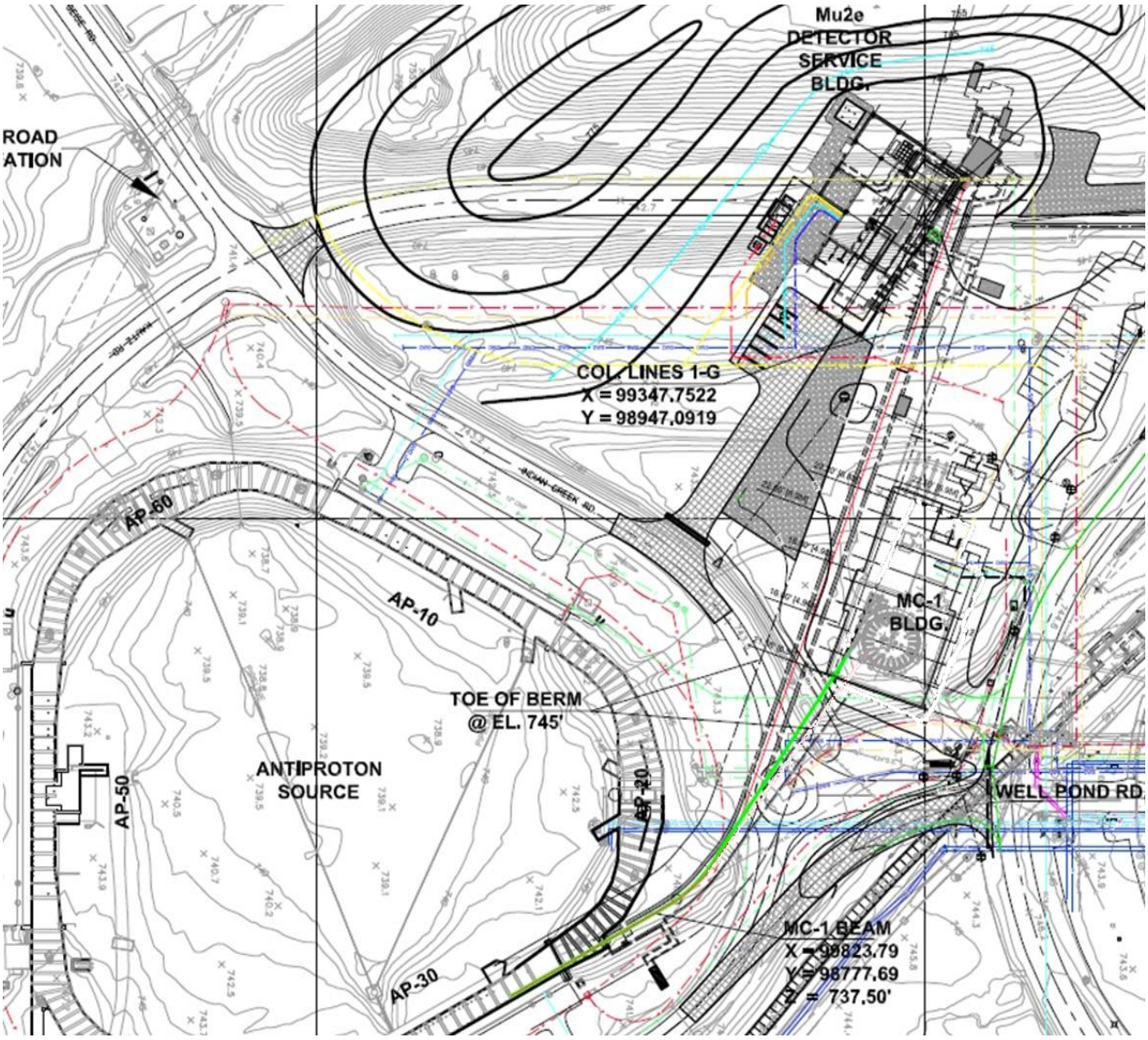

Figure 7.35: Layout of the muon campus showing the M4 and M5 external beamlines and Mu2e and $(g-2)$ experimental halls.

To appreciate the complexities of the two beamlines and $(g-2)$ beam conditions, the following criteria that must be addressed are listed under the criteria that dominate the line design.

Civil Layout

- Horizontal extraction via a kicker in the D30 straight

- Vertical separation from the Delivery Ring magnetic components (section common to Mu2e/$(g-2)$ and takes advantage of existing civil construction)
- Vertical separation from Mu2e through a reversed vertical dipole. This section cleanly derives a separate beamline for $(g-2)$ by changing the bend strength of a single dipole between $(g-2)$ and Mu2e operation. Another dipole is added to the M5 line to level the beamline off at the storage ring elevation
- The final elevation is 50" above projected civil elevation of $(g-2)$ ring enclosure floor (@734.5' above sea level) or 225.1460 m and 6.3' above the Mu2e line in this region (@223.2243 m) and 10.3' above the Delivery Ring elevation (@222.005097 m)
- A 27° horizontal bend string fixes the direction of the beamline from the D30 straight towards the geographic location chosen for the $(g-2)$ storage ring. (Mu2e has a 40.5° bend). The change in bend eventually separates the two experimental beamline enclosures.
- Tunable dispersion in the horizontal bend string (0-4 m)
- A FODO cell periodic section to propagate dispersion to the ring
- A final focus section to tune beam through the inflector to injection

Beam Properties

- Requested geometric acceptance of 40π mm-mr
- Limits the beam size or beta functions to $\sim$40 m through most of the line
- Injection matching into $(g-2)$ storage ring is strongly influenced by the inflector aperture

Beam Optics

- An achromat is required to suppress vertical dispersion from the D30 vertical extraction to the final beamline elevation. Dispersion must be suppressed upstream of the horizontal bend string to avoid coupling between the two planes. The M5 vertical achromat is a complicated 5-bend achromat (if one includes beam passing off-center through the D2Q5 quadrupole which contributes to vertical dispersion).
- An adjustable horizontal dispersion module is required for the 27° horizontal directional bend string. The dispersion can be adjusted to propagate a value between 0 and 4 m to the injection point of the $(g-2)$ storage ring.
- A periodic FODO structure is utilized to propagate either zero dispersion or a dispersion wave to the injection point at the ring. Dispersion cannot be matched at the ring as the line cannot sustain 8 m of dispersion aperture wise. If a new inflector is built, 4 m is possible. With the existing inflector, however, zero dispersion is the only solution.

- If a new inflector with a significant non-zero field is constructed then the line must move to the opposite side of the tunnel enclosure to match into the new injection trajectory. Another dipole would be required to aim correctly to injection.

- At this time, momentum collimation would be difficult to incorporate in the external beamline.

Civil and geographical constraints (avoidance of wetlands, for example) dictate a ∼27° bend after extraction from D30 to satisfy the location of experimental hall. Only ∼80 m are available for the M5 beamline after accomplishing the vertical elevation change.

7.5.8 Beam Line Sections

As stated above, the M5 beam line is best described in terms of its modular functionality. Correspondingly, the following descriptions detail the important sections, and discuss the rationale and justify the design approach for each section.

Extraction from the Delivery Ring Incorporation of $(g-2)$ and Mu2e extraction systems into the D30 straight has been carefully designed. The extraction part of the straight is considered to start at the center of D30Q (the center of the D30 straight). All quadrupoles have been carefully and relatively aligned in the optics input deck using the alignment data provided in Table 7.11. (This alignment data is considered so critical it has been included for future reference.) A number of kicker and septa locations were studied and the final location was previously described in Sec. 7.5.6.

The pulsed magnetic kicker provides a +6.1 mr easterly horizontal kick (to the right looking downstream). The downstream defocusing quadrupole – D2Q4 – enhances the effect of the kicker and maximizes the beam separation at the entrance to a Lambertson. This kicked beam is then tracked in coordinate space through the Lambertson and D2Q5 with an offset relative to the Delivery Ring central reference orbit. At the entrance to the Lambertson, the horizontal offset generated from circulating Delivery Ring beam is ∼49 mm. The Lambertson is specified to be 1.5 m in length with a 0.8 T maximum field for Mu2e beam, and is located just upstream of D2Q5 (0.4 m). It is adjusted to deliver a 40 mr upward bend for both Mu2e and $(g-2)$.

The net bend up requires additional vertical bending which comes from two more sources. The next focusing quadrupole (D2Q5) in the Delivery Ring acts like a combined-function magnet and adds to the upstream Lambertson kick. (Since D2Q5 is a horizontally focusing quadrupole, the offset of the beam vertically generates an upward kick – a kick critical to efficient separation of the extracted beam from the Delivery Ring, adding approximately 17 mr.) Just downstream of D2Q5 a 2 m-long C-magnet with a 58 mr bend angle is planned because a Lambertson-type magnet becomes difficult, but there is still insufficient separation to insert a full dipole. The combined effect of all three vertical bends (111.3 mr) allows beam to clear the next magnet – the last horizontally defocusing quadrupole in the D30 straight (D2Q6). Beampipe in the extraction line clears D2Q6 by a few inches and is 0.524 m, center to center at the upstream end. An SQA quadrupole located just downstream of D2Q6 represents the first independent quadrupole in the M4 line.

SpatialAnalyzer SA 2012.07.09 Points Relative to Coordinate Frame 'A::WORLD:FSCS_XYZ'			
location	x (m)	y (m)	z (m)
D2Q2_CT	30454.057473	30059.297097	222.005099
D2Q2_DN	30454.224153	30059.008397	222.005110
D2Q2_UP	30453.890802	30059.585847	222.005090
D2Q3_CT	30451.839361	30063.137949	222.005506
D2Q3_DN	30452.005882	30062.849149	222.005440
D2Q3_UP	30451.672881	30063.426769	222.005623
D2Q4_CT	30449.625500	30066.971251	222.004893
D2Q4_DN	30449.792071	30066.682481	222.004852
D2Q4_UP	30449.458900	30067.260031	222.004857
D2Q5_CT	30447.409089	30070.809692	222.005368
D2Q5_DN	30447.599539	30070.479722	222.005427
D2Q5_UP	30447.218599	30071.139693	222.005331
D2Q6_CT	30445.185298	30074.661744	222.006067
D2Q6_DN	30445.383758	30074.318054	222.006104
D2Q6_UP	30444.986868	30075.005454	222.006060
D3Q2_CT	30458.488435	30051.624184	222.004533
D3Q2_DN	30458.655185	30051.335484	222.004517
D3Q2_UP	30458.321735	30051.912884	222.004549
D3Q3_CT	30460.706756	30047.782592	222.004346
D3Q3_DN	30460.873366	30047.493822	222.004355
D3Q3_UP	30460.540176	30048.071372	222.004286
D3Q4_CT	30462.920737	30043.948321	222.004030
D3Q4_DN	30463.087337	30043.659580	222.003936
D3Q4_UP	30462.754087	30044.237071	222.004097
D3Q5_CT	30465.137738	30040.108389	222.004650
D3Q5_DN	30465.336018	30039.764599	222.004633
D3Q5_UP	30464.939388	30040.452149	222.004695
D3Q6_CT	30467.357589	30036.264157	222.004381
D3Q6_DN	30467.555989	30035.920447	222.004360
D30Q_CT	30456.274864	30055.456706	222.005097
D30Q_DN	30456.441694	30055.168035	222.004878
D30Q_UP	30456.108074	30055.745346	222.005317
D2Q7_CT	30442.972467	30078.493776	222.005572
D2Q7_DN	30443.139067	30078.205036	222.005532
D2Q7_UP	30442.805817	30078.782526	222.005637
D2Q8_CT	30440.580506	30082.215658	222.004713
D2Q8_DN	30440.774006	30081.944157	222.004801
D2Q8_UP	30440.387026	30082.487128	222.004573

Table 7.11: Alignment coordinates for the D30 straight provided by the Fermilab metrology group.

Device	Magnet Type (Status)	Strength	Field	Pitch
D30q	SQC (existing)	0.385 m^{-2}	3.98 T/m	0 mr
Kicker	(to be built)	4 mr	0.028 T	0 mr
d2q2	SQC (existing)	-0.388 m^{-2}	4.01 T/m	0 mr
d2q3	SQC (existing)	0.378 m^{-2}	3.91 T/m	0 mr
d2q4	SQC (existing)	-0.370 m^{-2}	3.82 T/m	0 mr
Lambertson	(to be built)	40 mr	0.28 T (0.79 T / Mu2e)	40 mr
d2q5	8Q32 (replaces SQD)	0.258 m^{-2} (13.3 mr)	2.67 T/m	53.3 mr

Table 7.12: Extraction components and parameters common to the Delivery Ring.

Once the beam clears the Delivery-Ring components, it can be steered onto a centered midplane trajectory in the combined Mu2e/$(g-2)$ section (M4) of the external beamline. Steering magnets will be strategically placed to correct for differences between the $(g-2)$/Mu2e and kicker/septa forms of extraction. The exact extraction orbit depends sensitively on the D30 quadrupole strengths and these depend on the Delivery-Ring tunes established for resonant extraction or muon beam delivery for Mu2e and $(g-2)$, respectively. It is unlikely these will be identical, however for the purposes here, a third integer resonant extraction tune was assumed for Mu2e and a lattice similar to the original Pbar design for $(g-2)$. The relevant quadrupole strength values used are given in Table 7.12 and translated into gradients for the $(g-2)$ 3.1-GeV/c beam.

The initial bend upwards is so strong in order to clear the Delivery Ring, it must be leveled before the final elevation is achieved for Mu2e or $(g-2)$; otherwise it is not possible to implement a vertical achromat, which requires significant phase advance generated by quadrupoles. Sufficient space must be allocated for a series of quadrupoles. Therefore, an EDWA dipole is installed after the first quadrupole in the subsequent D30 straight with a bend equal and opposite to the combined bends of the Lambertsons and focusing quadrupole. Leveling the line at ∼32" above the Delivery Ring centerline provides a long elevated "straight" (again extracted-beam center to DR-beam center) allowing an independent common extraction beamline to be installed without conflicts with the Delivery Ring line below. The only conflicts are with the extended saddle coils of the DR dipoles and these must be avoided. However, now an achromat can be formed using 4 quadrupoles. This straight section is followed by two MDC dipoles for Mu2e beam with reverse bends (up/down) that elevate the Mu2e extracted beam to a final elevation of 1.22 m (4') above the Delivery Ring. For $(g-2)$, three dipoles are required – the last Mu2e vertical dipole is reversed, sending the beam steeply upward to achieve rapid separation of the M5 line from the M4 line. This rapid separation proves critical in order to position the strong horizontal bend section; otherwise the ring location would move eastward into a utility corridor. The final elevation of the Mu2e line is 225.1460 m (738.6') which is 6.3' above the Mu2e beamline, 10.2' above the M4 beamline enclosure floor and 1.9' from the enclosure ceiling (@740.5' and 3.9' below the experimental hall ceiling).

Figure 7.36 displays the achromatic optics of Delivery Ring extraction from the center of the first quadrupole upstream of the Lambertsons to the end of the achromat. These optical functions are predicated on an assumed matched beam distribution extracted from the Delivery Ring. This is not likely to be the case, and extracted beam properties will

differ significantly between $(g-2)$ and Mu2e. Therefore it is important that the two vertical achromats have been separated between th M5 line and the M4 line and can be independently tuned.

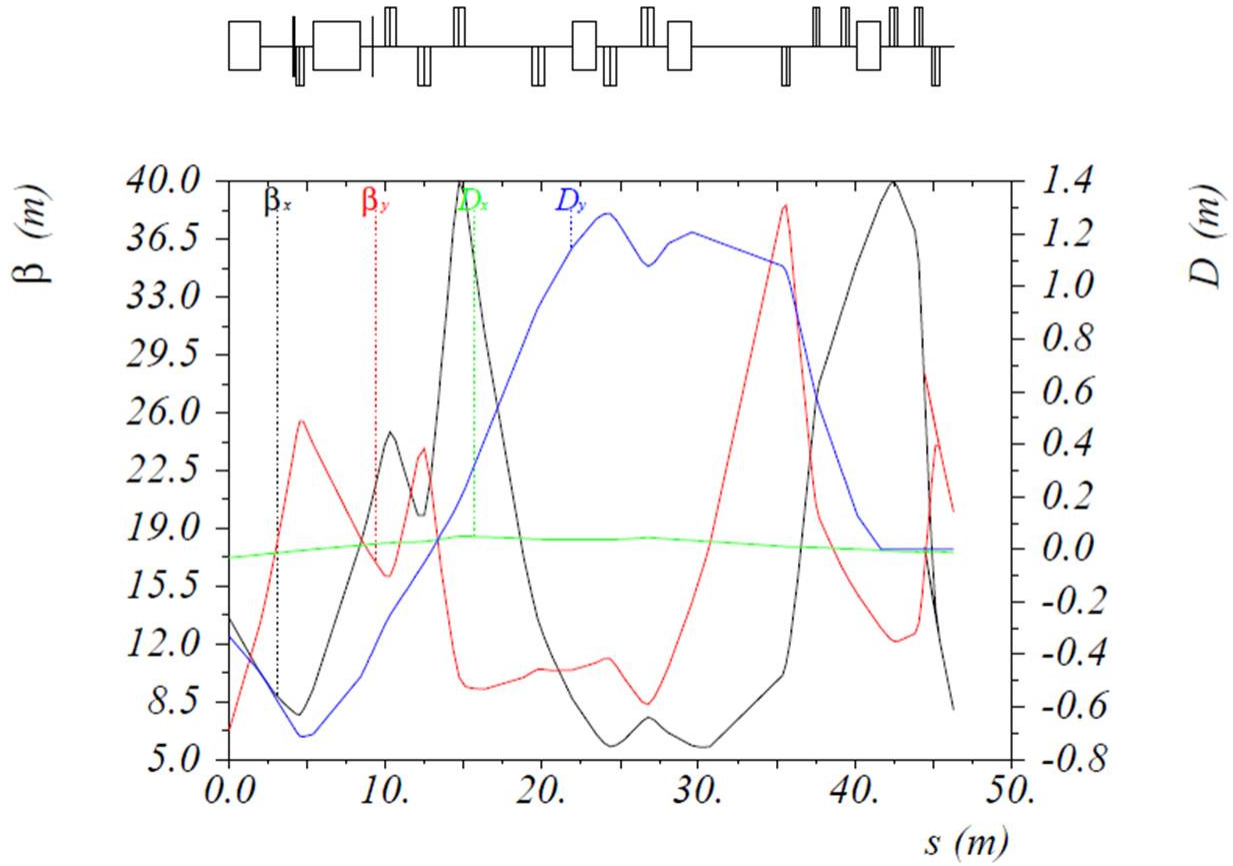

Figure 7.36: The extraction optics showing the two Lambertsons followed by an opposite-sign vertical bend, quadrupoles to form the achromat and a final bend up and then level again to the elevation of the beamline (all EDWA dipoles).

A three-dimensional drawing of Delivery-Ring injection and extraction and the M4 and M5 lines to the $(g-2)$ storage ring is shown in Fig. 7.37.

Device	Magnet Type (Status)	Strength	Field	Pitch
C-magnet	(to be built)	58 mr	0.3T (0.86 T / Mu2e)	111.3 mr
Q1	4Q24	-0.244 m^{-2}	-2.52 T/m	111.3
D1	EDWA (to be built)	-111.3 mr	0.377 T (1.08 T / Mu2e)	0 mr
Q2	SQC	0.234 m^{-2}	2.42 T/m	0 mr
Q3	SQD	-0.357 m^{-2}	-3.69 T/m	0 mr
Q4	SQD	0.311 m^{-2}	3.21 T/m	0 mr
Q5	SQD	-0.062 m^{-2}	0.64 T/m	0 mr
D2	MDC (available)	65.5 mr	0.44 T (1.27 T / Mu2e)	65.5 mr
Q6	SQD	-0.132 m^{-2}	-1.36 T/m	65.5 mr
Q7	SQD	0.205 m^{-2}	2.12 T/m	65.5 mr
D3	MDC (available)	94.7 mr	0.64T (-1.27 T / Mu2e)	160.2 mr

Table 7.13: Extraction components and parameters in the vertical translation section common to $(g-2)$ and Mu2e in the M4 line. Quadrupole strengths are given for $(g-2)$ only.

Device	Magnet Type (Status)	Strength	Field	Pitch
gQ1	4Q24	-0.339 m^{-2}	-3.51 T/m	111.3 mr
gQ2	4Q24	0.229 m^{-2}	2.37 T/m	0 mr
gQ3	4Q24	0.01 m^{-2}	0.087 T/m	0 mr
gD1	MDC	160.2 mr	1.09 T	0 mr
gQ4	4Q24	0.082 m^{-2}	0.84 T/m	0 mr
gQ5	SQA	0.073 m^{-2}	0.75 T/m	0 mr
gQ6	4Q24	0.056 m^{-2}	0.58 T/m	0 mr

Table 7.14: Components and parameters in the independent $(g-2)$ vertical translation section in the M5 line including matching quads to the horizontal bend string.

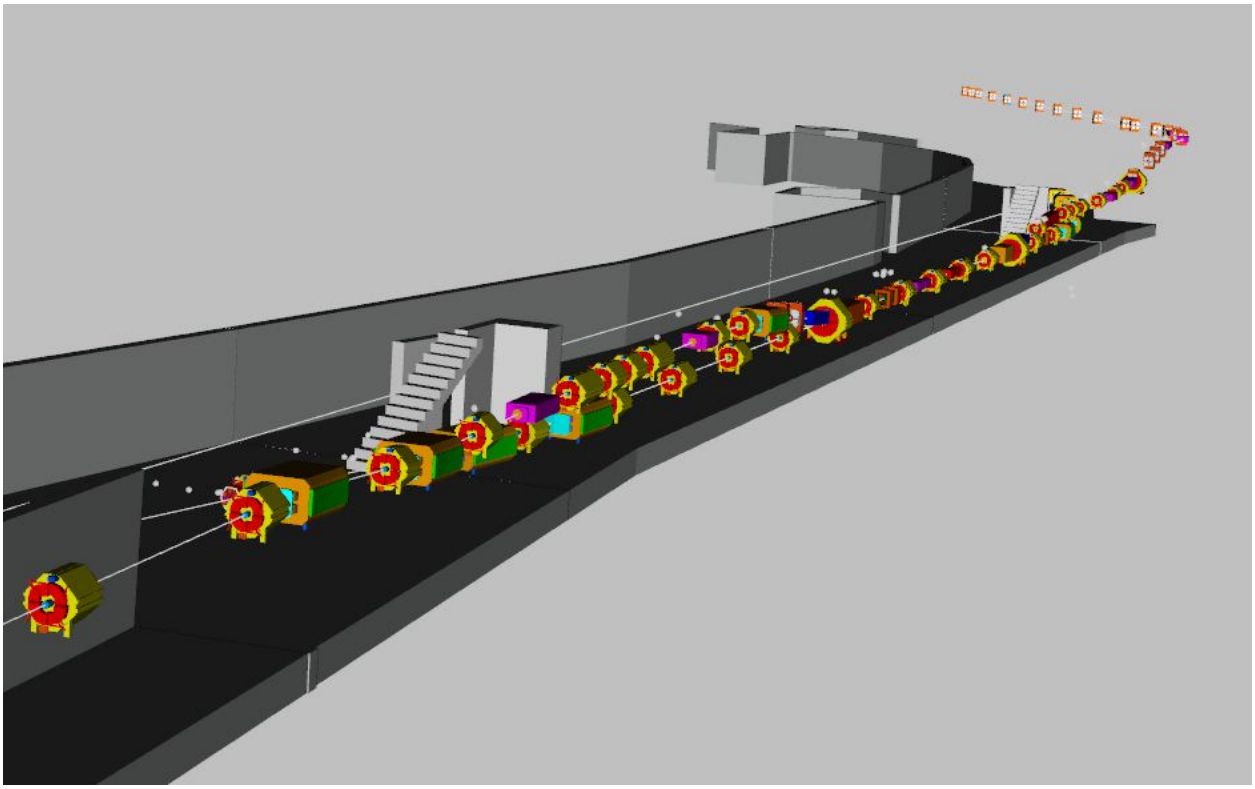

Figure 7.37: Three-dimensional view of Delivery-Ring injection and extraction and the M4 and M5 lines to the $(g-2)$ storage ring.

7.6 Controls and beam monitoring

7.6.1 Accelerator controls

A well-established controls system allows devices in the former Antiproton-Source ("Pbar"), now Muon, service buildings and tunnel enclosures to receive information such as synchronization signals and to communicate back to other accelerator systems. A map of the service buildings, labeled "AP" for former Antiproton-Source buildings, and "F" for buildings which are part of the F-sector of the Tevatron, is shown in Fig. 7.38. Devices in the new extraction beamlines and MC-1 building will also need to be connected to the controls system.

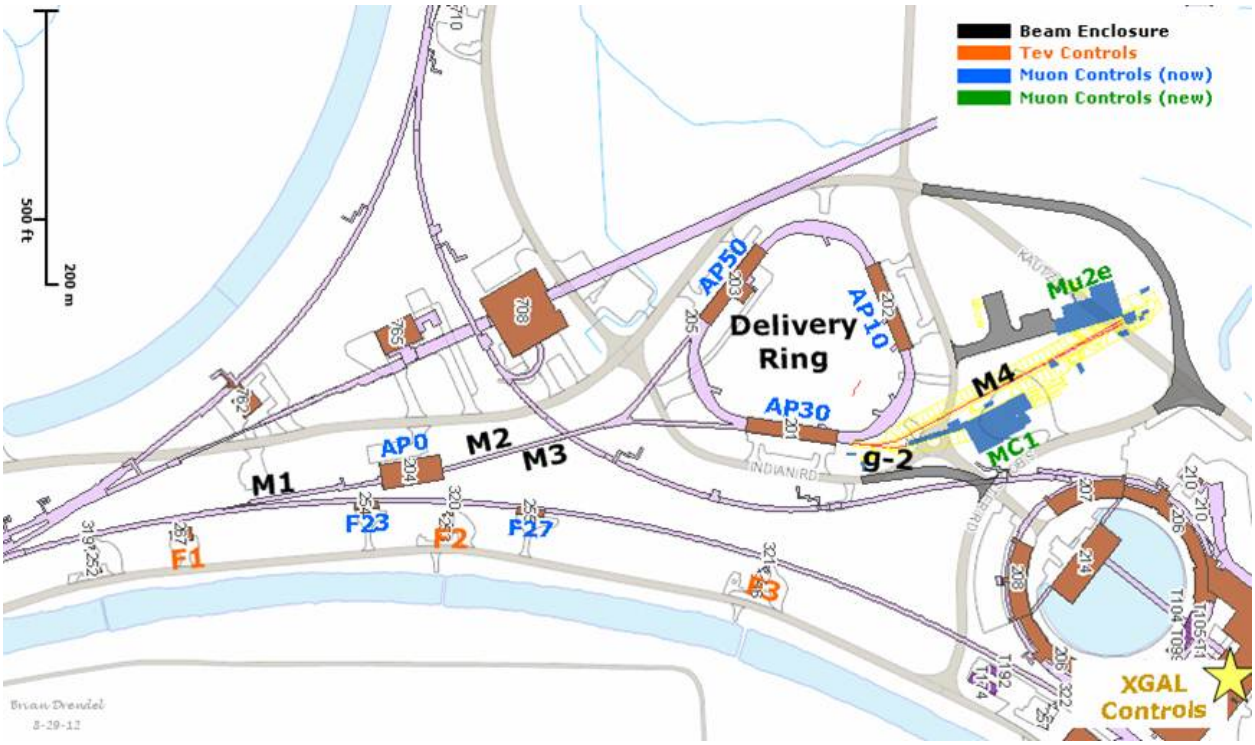

Figure 7.38: Muon Campus service buildings.

CAMAC and links

The existing accelerator service buildings will continue to use the legacy controls infrastructure that is currently in place. These service buildings include all of the Main Injector service buildings, as well as F0, F1, F2, F23, F27, AP0, AP10, AP30 and AP50. Future Muon Campus service buildings, including MC-1 and Mu2e, will be upgraded to a more modern controls infrastructure which will be discussed later in this document. Migration of the existing buildings to the more current controls standard is preferred and is being considered; however, sufficient funding is not available to start the upgrade path and it is believed that the existing infrastructure will be adequate for $(g-2)$ operations.

Computer Automated Measurement and Control (CAMAC) crates exist in each service building and communicate with the control system through a VME-style front-end computer

over a 10 MHz serial link as shown in Fig. 7.39. Both digital and analog status and control of many accelerator devices occur through the CAMAC front ends. There should be no need to install additional CAMAC crates, as there is excess capacity in most of the existing crates. An inventory of existing CAMAC crates in the Muon service buildings shows that about 25% of the slots are unoccupied and could be used for additional CAMAC cards [20]. In addition, further slots have become available that were used to interface devices that became obsolete with the retirement of Collider Run II operations. It is anticipated that there will be ample CAMAC-crate coverage for $(g-2)$ operation in the existing Muon service buildings, and very few crates will need to be added or moved.

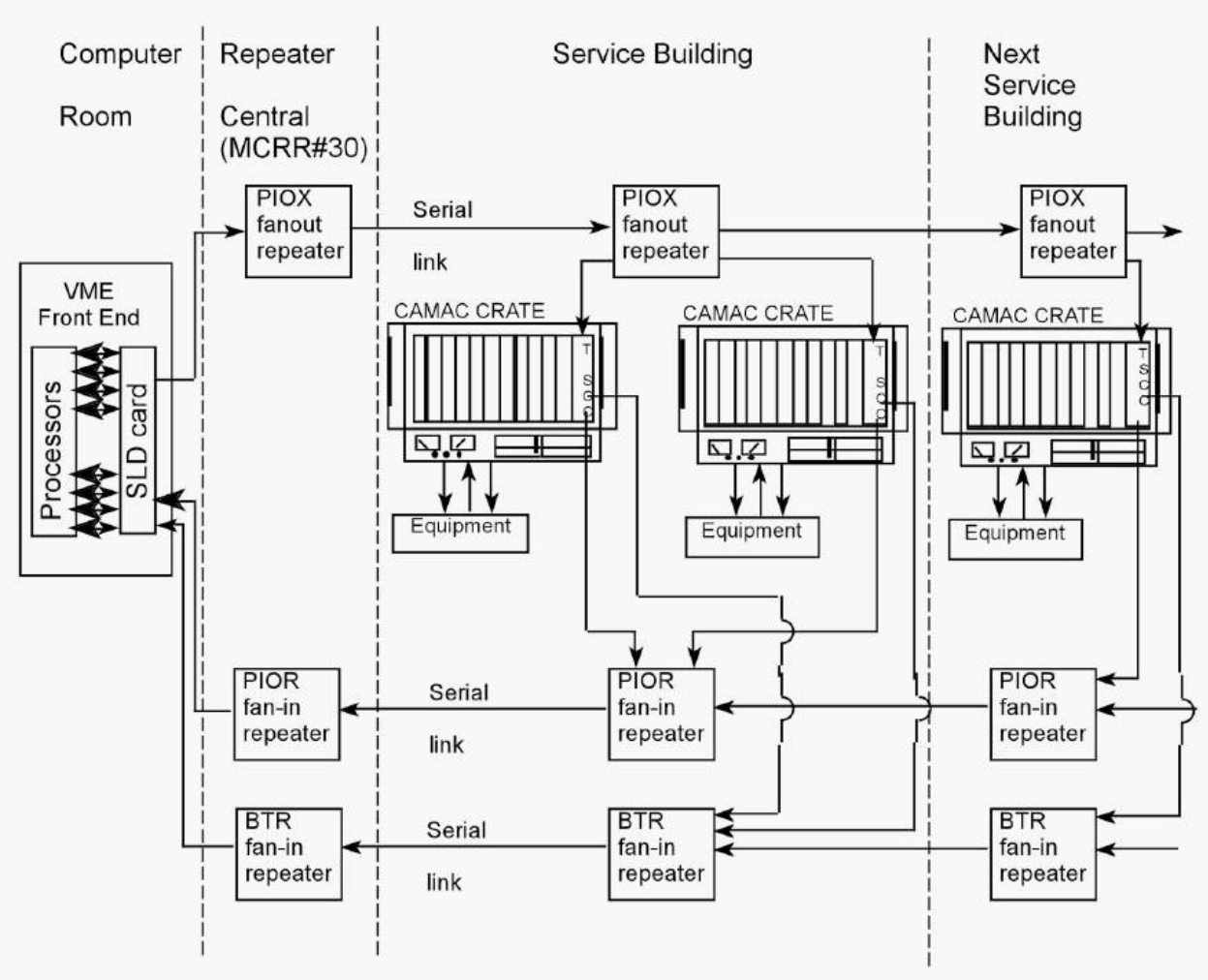

Figure 7.39: Legacy CAMAC crates interfacing VME front ends via serial links provide both analog and digital status and control of accelerator devices, and will continue to be used in existing Muon service buildings.

There are serial links that are distributed through and between the service buildings, via the accelerator enclosures, that provide the necessary communications paths for CAMAC as well as other necessary signals such as clock signals, the beam permit loop, and the Fire and Utilities System (FIRUS). Controls serial links can be run over multimode fiber-optic

cable or copper Heliax cable. Most Muon links that run through accelerator enclosures are run over Heliax, which should function normally in the radiation environment expected for $(g-2)$ operations.

Accelerator device timing that does not require synchronization to the RF buckets will remain on the existing 10 MHz Tevatron Clock (TCLK) system. The existing TCLK infrastructure will remain in existing service buildings and new TCLK link feeds will be run via multimode fiber optic cable from the Mac Room to the new MC-1 and Mu2e service buildings.

Accelerator device timing for devices that require synchronization to the RF buckets will continue to be handled through the Beam Synch Clocks; however, a few changes will be required to maintain functionality. The F0, F1 and F2 service buildings will need both 53 MHz Main Injector beam synch (MIBS) for SY120 operations and 2.5 MHz Recycler beam synch (RRBS) for $(g-2)$ and Mu2e operations. These buildings already support multiple beam synch clocks, so the addition of RRBS will require minimal effort. An obsolete 53 MHz Tevatron beam synch (TVBS) feed in the MI60 control room will be replaced with a 2.5 MHz RRBS feed in order to provide the necessary functionality. The remaining Muon service buildings currently use 53 MHz MIBS, but will require 2.5 MHz RRBS for $(g-2)$ and Mu2e operations. This functionality can be obtained by replacing the MIBS feed at F0 with RRBS and using the existing infrastructure. Further upgrades and cable pulls will only be required if it is later determined that both MIBS and RRBS are required in these service buildings. New beam synch feeds to the $(g-2)$ and Mu2e service building will be run via multimode fiber-optic cable from the Mac Room.

The Delivery-Ring permit loop provides a means of inhibiting incoming beam when there is a problem with the beam delivery system. The Pbar beam permit infrastructure will be used in the existing buildings. The CAMAC 201 and 479 cards, which provide the 50 MHz abort loop signal and monitor timing, will need to be moved from the Mac Room to AP50 to accommodate the addition of the abort kicker at AP50. Existing CAMAC 200 modules in each CAMAC crate can accommodate up to eight abort inputs each. If additional abort inputs are required, spare CAMAC 200 modules will be repurposed from the Tevatron and will only require an EPROM or PAL change. The permit loop will be extended to the MC-1 and Mu2e service buildings via multimode fiber-optic cable from the Mac Room. Abort inputs for these buildings will plug into a Hot-Link Rack Monitor abort card as will be mentioned below.

Operational and permit scenarios are under development. The capability of running beam to the Delivery-Ring dump when Mu2e and $(g-2)$ are down will be needed, as well as the ability to run to either experiment while the other is down.

Hot-Link Rack Monitor

New controls installations will use Hot-Link Rack Monitors (HRMs) in place of CAMAC. A HRM runs on a VME platform that communicates with the control system over Ethernet as shown in Fig. 7.40. Unlike CAMAC, no external serial link is required, minimizing the need for cable pulls between buildings. Each HRM installation provides 64 analog input channels, 8 analog output channels, 8 TCLK timer channels, and 8 bytes of digital I/O. This incorporates the features of multiple CAMAC cards into a single, compact chassis.

Like CAMAC, when additional functionality or controls channels are needed, additional units can be added. As an example, a HRM version of the CAMAC 200 module will be constructed to provide inputs into the Delivery-Ring permit system. One or two HRMs will be installed in both the MC-1 and Mu2e buildings and should provide ample controls coverage for both accelerator and experimental devices.

Figure 7.40: A Hot-Link Rack Monitor is a flexible data acquisition system composed of a remote unit and a PCI Mezzanine card that resides in a VME crate. Each HRM provides provides sixty four 16 bit analog input channels, 8 analog output channels, 8 TCLK timer channels and 8 bytes of digital I/O. HRM.s will eventually replace all of the functionality of CAMAC [21].

HRMs are expected to eventually replace legacy CAMAC systems in the existing buildings. This migration will start by replacing existing 12-bit MADCs and CAMAC 190 cards for analog readings with 16-bit HRM channels. This option was considered for $(g-2)$ operation, but was determined to be impractical considering expected funding, limited legacy Ethernet connectivity in three of the Muon service buildings, and the determination that the existing CAMAC would likely provide adequate performance for $(g-2)$ operations.

Ethernet

Many modern devices have some form of Ethernet user-interface. In addition, many devices and remote front-ends use Ethernet to interface with the control system, instead of using the traditional CAMAC. The results are an increasing demand on the Controls Ethernet. Figure 7.41 is a map of the Muon Controls network. All of the current Muon Ring service buildings have Gigabit fiber-optic connections from the Cross-Gallery computer room to Cisco network switches centrally located in each service building. These will provide ample network bandwidth and connections after the reconfiguration for $(g-2)$ and Mu2e. A central Ethernet switch that fans out to the other Muon Department buildings is currently located in AP10, but will need to be moved to AP30, as will be discussed later in this document.

Ethernet connects between the Muon-Ring service buildings via multimode fiber-optic cable paths that traverse the Rings enclosure on the Accumulator side. The multimode fiber currently in place will remain functional during $(g-2)$ operations. However, in the higher-radiation environments expected during Mu2e operations, these fiber-optic cables will need

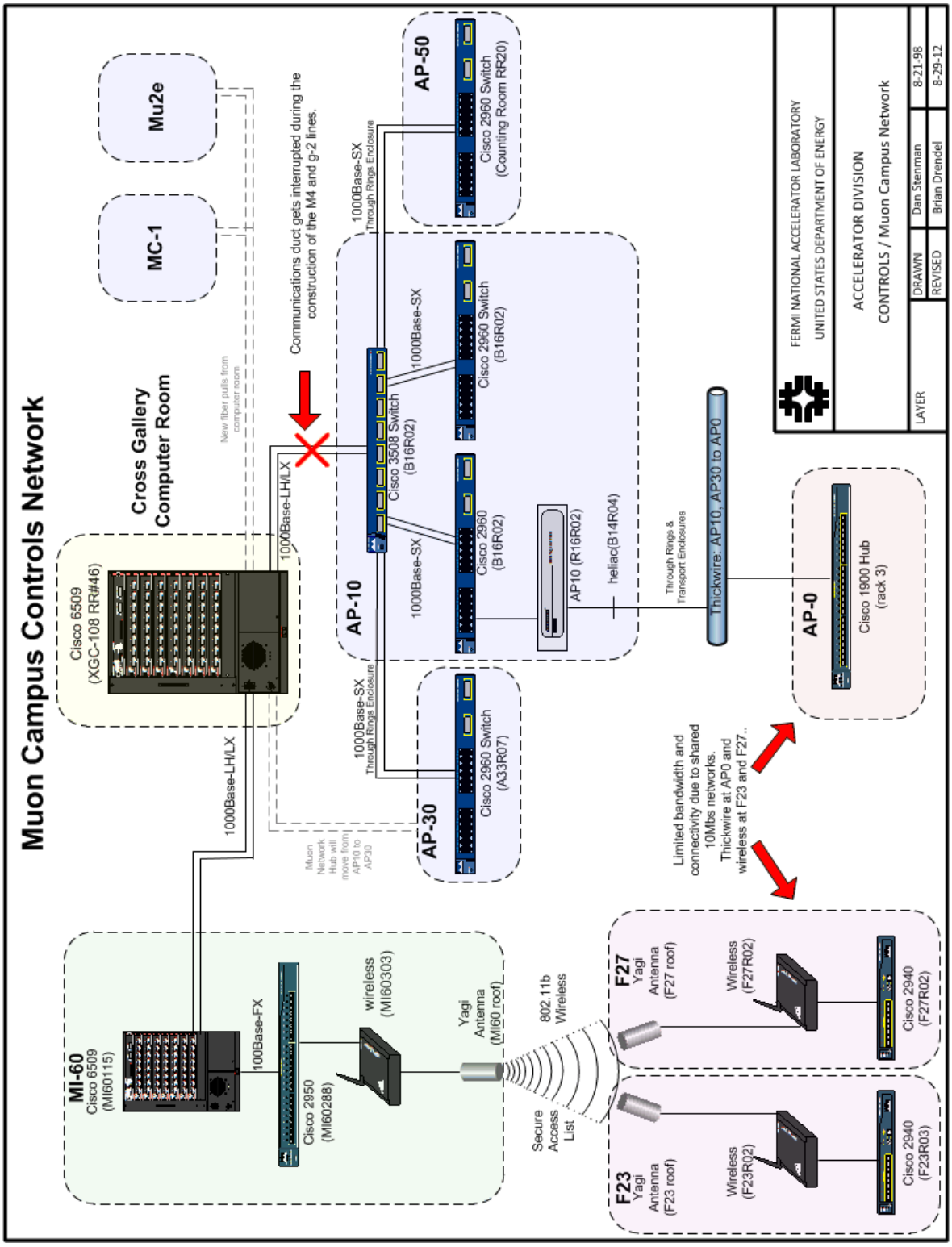

Figure 7.41: Controls Ethernet to the Muon Department service buildings is expected to be adequate for $(g-2)$ operations. The central switch at AP10 will be moved to AP30. Legacy networks at AP0, F23, and F27 have limited bandwidth and connectivity.

to be upgraded to single-mode fiber at a minimum, or to the more costly radiation-hard fiber if radiation rates are too high.

Most beamline service buildings have gigabit fiber connected to centrally located network switches that provide ample network bandwidth and connections. AP0, F23, and F27 are the only three buildings that do not have this functionality. AP0 runs off a 10 Mbps hub that connects to 10Base5 "Thicknet" that runs through the Transport and Rings enclosures back to AP10, while F23 and F27 run off 802.11b wireless from MI60. Both are 10 Mbps shared networks with limited bandwidth and connectivity. It is anticipated that the network in these three buildings may be sufficient for $(g-2)$ operations; however, network upgrade options are being considered, as will be discussed below.

Controls connectivity

Civil construction of the M4 and M5 beamline enclosures will result in the removal of the underground controls communication duct that provides the connectivity between the Accelerator Controls NETwork (ACNET) and the Muon Campus [22]. Included in this communication duct is the fiber-optic cable that provides Ethernet connectivity, as well as 18 Heliax cables that provide the controls serial links and other signals including FIRUS. These cables currently connect from this communications duct to the center of the 20 location in the Rings enclosure, and travel through cable trays on the Delivery Ring side to the AP10 service building. After removal of the communications duct, FESS will construct new communications ducts from the existing manholes. These communications ducts will go directly to AP30, MC-1 and Mu2e service buildings without going through accelerator enclosures. See Fig. 7.42 for drawings of the current and future controls connectivity paths.

Restoring connectivity When the Heliax and fiber-optic cables are cut during the removal of the above-mentioned communications duct, controls connectivity will be lost. The base plan for restoring both Ethernet and controls-link connectivity is to pull new fiber optic cable from the cross gallery, through the MI-8 line communications ducts to AP30. As a result of the new fiber pull, the Ethernet and controls links will fan out from AP30 instead of AP10. This will require some additional controls hardware configuration and labor. Efforts will be made to minimize the disruption by pulling the fiber and staging the new hardware at AP30 before the communication duct is cut. This is especially important for FIRUS which is necessary for monitoring building protection.

More details regarding the base plan and several alternatives, including cutting and splicing the Heliax cable or attempting to keep the fiber and Heliax intact during construction, can be found in Ref. [23].

Establish connectivity to MC-1 New fiber-optic cable will be pulled from the Mac Room to the MC-1 service building. Single-mode fiber is needed for Ethernet and FIRUS, and multimode fiber is needed for the timing links and the abort-permit loop. A bundle of 96 count single-mode and a bundle of 36 count multimode fiber optic cable will be pulled to MC-1. The fiber bundles will share a common path with the fiber bundles headed toward Mu2e from the Cross Gallery to the manhole by Booster West Tower. All three fiber bundles will travel through a single inner duct to the manhole. The Mu2e and MC-1 fiber bundles

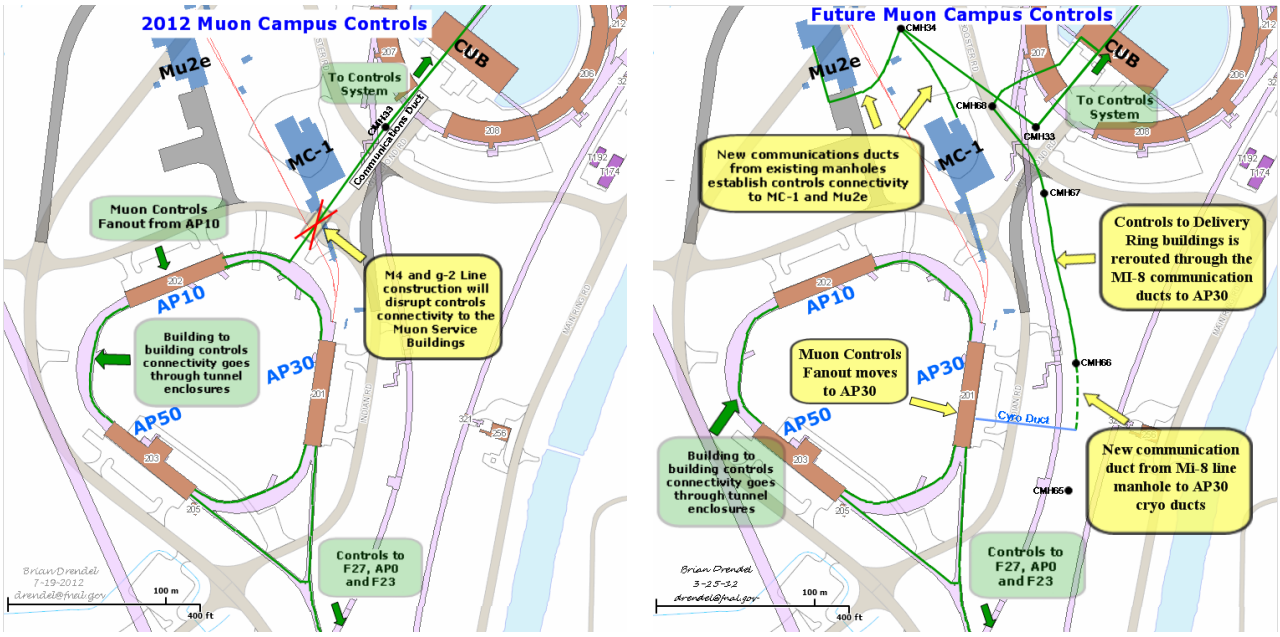

Figure 7.42: Muon campus controls paths. During construction of the M4 and $(g-2)$ beamlines, the communications duct that provides controls connectivity to the Muon Campus will be interrupted. A new communications duct will be built to restore controls connectivity to the Muon service buildings. New controls will need to be established at the MC-1 and Mu2e buildings.

will then branch off to a second manhole inside a common inner duct, and then separate into the new communication ducts to the Mu2e and MC-1 service buildings. The fiber pulls will provide ample connectivity for all Ethernet and controls signals for both the accelerator and experiment. The $(g-2)$ experiment anticipates requiring network rates approaching 100 MB/sec during production data taking which can be handled easily with the proposed infrastructure.

One alternate solution considered was to pull the new fiber along the existing communications duct until it intersected the extraction-lines enclosure. From there, the fiber could be directed along tunnel-enclosure cable trays to the MC-1 service buildings. Though this option would provide MC-1 cable-pull lengths of approximately the same length as the base option, it was eliminated due to the extra complications of pulling fiber through the tunnel enclosures to both Mu2e and AP-30. In both cases, the expected radiation environment would require a more expensive radiation-hard single-mode fiber. In addition, the CAMAC fiber links only run on multimode fiber, so link and clock repeaters would have to be redesigned to run on single-mode fiber, adding additional expense to the project.

Possible upgrades for legacy networks If the legacy Ethernet networks at AP0, F23, and F27 prove to provide insufficient connectivity or bandwidth for $(g-2)$ operations, they can be most cost-effectively upgraded by replacing the current 10Base5 "Thicknet" with single-mode fiber-optic cable. The path would be from the AP30 service building to the Rings enclosure, along the cable trays toward the M3 beamline, and down the Transport

enclosure. From the Transport enclosure, the fiber-optic cable runs can go to F27 and AP0. An additional fiber-optic cable pull from AP0 through the PreVault enclosure provides a path to F23. The largest issue with this upgrade is that the single-mode fiber-optic cable is susceptible to radiation. If the radiation environment in the accelerator enclosures does not allow for single-mode fiber-optic cable, then radiation-hard fiber-optic cable can be pulled, but at a higher cost. Standard 96-count single-mode fiber costs approximately \$1.50/foot, whereas 96-count radiation-hard fiber costs approximately \$22/foot. Upgrading to the radiation-hard cable would add approximately \$50K to the cost of the cable pull. Other fiber-optic cable path options have been considered, but prove to be more costly to implement.

7.6.2 Accelerator instrumentation

Beam types

Beam monitoring can be divided into distinct zones: primary protons, mixed secondaries, proton secondaries, and muon "secondaries" (actually the dominant source of muons should be from the decay of the pion secondaries, so are technically "tertiary"). The locations of each of these areas are shown in Fig. 7.43. The expected beam properties in each of these areas are shown in Table 7.15.

Beam Type	Particle Species	Beam Momentum (GeV/c)	Number of Particles	RF Bucket (MHz)	Bunch Length (ns)	Transverse Emittance (mm-mr)
Primary protons	p	8.9	10^{12}	2.515	120	18π
Mixed secondaries	μ^+, π^+, p, e^+	3.1	10^7 to 2×10^8	2.515	120	40π
Proton secondaries	p	3.1	10^7	2.515	120	40π
Muons	μ^+	3.1	$< 10^5$	2.515	120	40π

Table 7.15: Expected properties of primary proton beam, secondary beam off the target, and muon beam from pion decay relevant to instrumentation designed to measure beam. Transverse emittances are 95% normalized.

Primary proton beam Primary proton beam will traverse the Recycler, P1 stub, P1, P2 and M1 lines. Much of the instrumentation needed to measure the primary proton beam during $(g-2)$ operation already exists, but needs to be modified for use with the faster cycle times and 2.5 MHz RF beam structure. The overall beam intensity is similar to that seen in Pbar stacking operations, and in many cases requires only small calibration changes be made to the instrumentation. Toroids will be used to monitor beam intensity and will be used in conjunction with Beam Loss Monitors (BLMs) to maintain good transmission efficiency in the beamlines. Multiwires and Secondary Emission Monitors (SEMs) will provide beam profiles in both transverse planes. Beam Position Monitors (BPMs) will provide real-time orbit information and will be used by auto-steering software to maintain desired beam positions in the beamlines.

Toroids are beam transformers that produce a signal that is proportional to the beam intensity. There are two toroids in the P1 line, one in the P2 line and two in the M1 line.

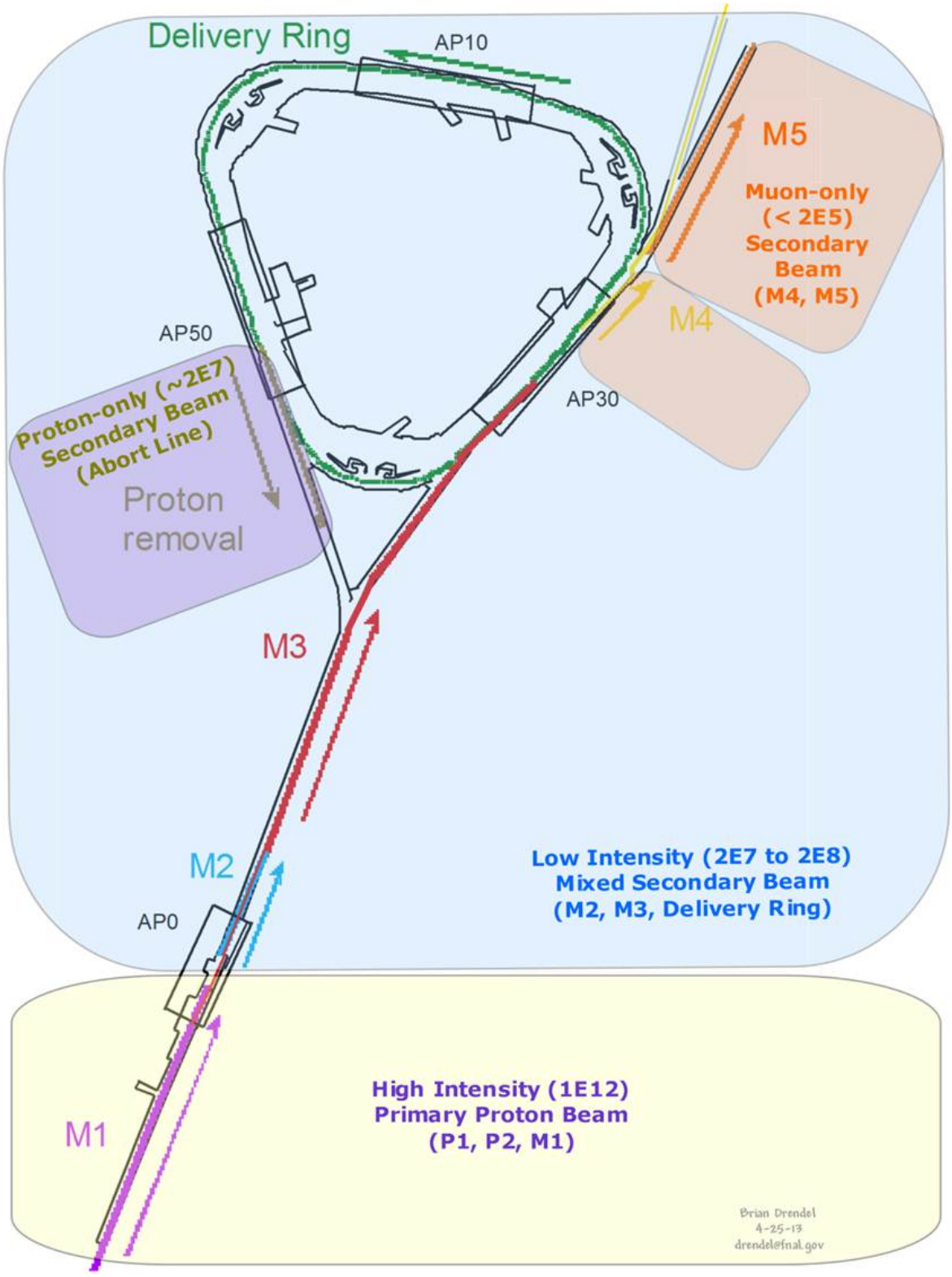

Figure 7.43: Beam monitoring can be divided into four different zones, each with different instrumentation schemes. High-intensity proton beam will be monitored with Toroids, BPMs and BLMs. Low-intensity secondary and proton-only secondary beam will be monitored with Ion Chambers, BPMs and SEMs. Muon-only secondary beam will be monitored with Ion Chambers and SWICs.

They will continue to be used in $(g-2)$ operation to measure the primary proton beam. The electronics for these toroids are comprised of legacy analog processing inside of NIM crates. The base plan, due to funding limitations, is to continue to use the legacy electronics. If funding becomes available, the electronics would instead be upgraded to a VME-based processing environment, repurposing electronics from Collider Run II in order to provide cost savings. The existing toroids provide the majority of the required coverage, though the addition of a second toroid in the P2 line and a toroid in the P1 stub is desirable. The present toroid installation locations will be reviewed and modified as needed to provide adequate coverage. One possible change would be to move the upstream P1-line toroid downstream of the P1 line and P1 stub merge so that it could measure the beam injected into the P1 line from the stub. Filters, chokes, and preamps will be added for analog conditioning. Electronics will be modified, where necessary, to calibrate the toroids for $(g-2)$ operations.

Beamline BPMs provide single-pass orbit-position information with sub-millimeter resolution, and will continue to be the primary beam-position devices in the P1, P2 and M1 lines. All BPMs share the Echotek style of electronics which was built as part of the Rapid Transfers Run II upgrade [24], and is the current standard for beamline BPMs. A functional diagram of the BPM hardware is shown in Fig. 7.44. These BPMs were designed to detect 7 to 84 consecutive 53 MHz proton bunches and four 2.5 MHz antiproton bunches for Collider Run II operations. Minimal electronics modifications will be required to measure the single 2.5 MHz bunches of 10^{12} particles expected during $(g-2)$ operations. Two additional BPMs will be installed in the P1 stub.

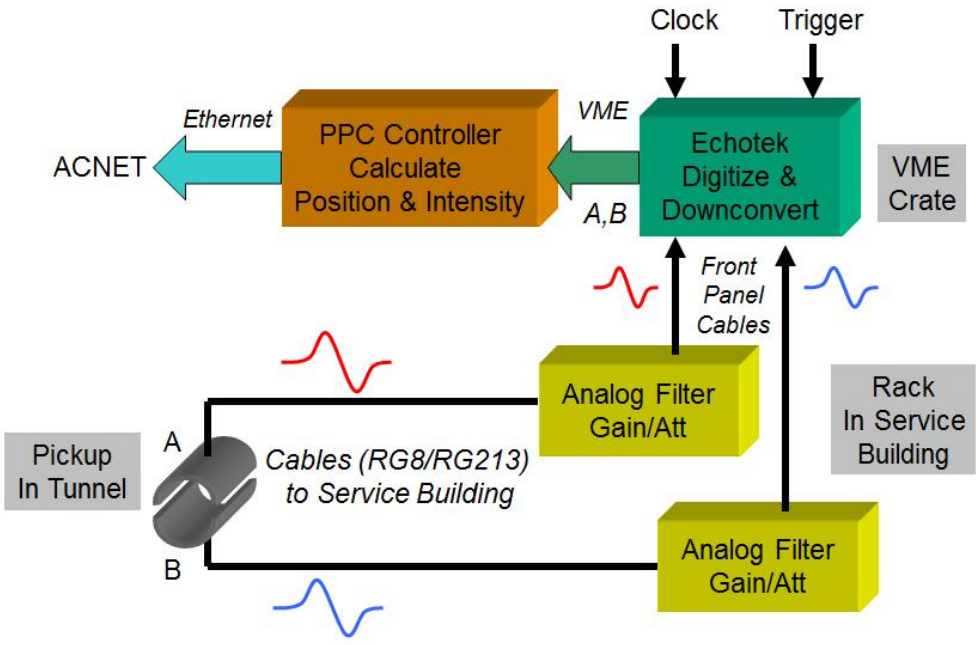

Figure 7.44: BPMs with Echotek processing electronics will be used to measure the transverse beam position of the 2.5MHz primary proton beam in the P1, P2 and M1 lines for $(g-2)$ operations. The BPMs are not sensitive enough to see the low intensity secondary beams downstream of the AP0 target [24].

Beam Loss Monitors are already in place in the P1, P2, and M1 beamlines. Existing ion-chamber detectors will be utilized for Mu2e operation. BLMs will be upgraded to modern BLM log monitor electronics, repurposing unused components from the Tevatron in order to minimize cost. An optional upgrade is being considered that would add snapshot capability to the BLMs. This feature would allow the loss monitors to distinguish losses from individual 15 Hz pulses of beam. However, this option adds significant cost to the BLM system. Two additional BLMs will be installed in the P1 stub.

There are two types of beam profile monitors in the beamlines: multiwires in the P1 and P2 lines, and SEMs in the other beamlines. The profile monitors will primarily be used for commissioning, studies, and documentation of the beamlines. General maintenance will be performed on the hardware and electronics to ensure proper functionality. The current location and wire spacing of the monitors will be reviewed and modified accordingly. Two additional multiwires will be installed in the P1 stub.

Mixed secondaries Mixed-secondary beam will traverse the M2 and M3 lines, as well as the Delivery Ring. Changes to existing instrumentation are required in these areas as a result of the secondary beam being approximately two orders of magnitude lower in intensity than that during the former Antiproton stacking operations. In addition, 2.515 MHz bunch structure and a faster pulse rate must be taken into consideration. Mu2e beam will have beam intensities four to five orders of magnitude higher than $(g-2)$ operations in the M3 line and Delivery Ring, so design upgrades must take into account the vastly different beam intensities required for both experiments. Beam studies have been conducted in order to help determine what instrumentation best suits the low-intensity secondaries of $(g-2)$ operations [3].

Four toroids are available for use in the secondary beamlines and were the primary intensity-measurement device in these lines during Antiproton operations. These will be used for Mu2e operations; however, beam studies show that even with high gain and careful filtering, we were only able to measure beam intensities at levels one order of magnitude higher than $(g-2)$ operational beam [3], as demonstrated in Fig. 7.45. As a result, toroids will likely not be used during normal $(g-2)$ operations, but may still be used with higher-intensity beams during commissioning and studies periods.

A Direct-Current Current Transformer (DCCT) has been used in the Delivery Ring to measure beam intensity. This device will not function at $(g-2)$ operational intensities and cycle time.

Ion chambers will become the primary beam-intensity measurement device for mixed-secondary beam. They are relatively inexpensive devices that can measure beam intensities with an accuracy of $\pm 5\%$ with as little as 10^5 particles. Ion chambers were used in the AP2 line in the past, and work was done during beam studies to recommission the ion chamber that used to be operational near the end of the AP2 line [3]. For $(g-2)$ operations, one or two ion chambers will be implemented in the M2 line. Ion chambers are also being considered for the M3 line and the Delivery Ring; however, these would need to be installed in a vacuum can with motor controls to allow them to be pulled out of the beam during the higher-intensity Mu2e operations. Figure 7.46 shows an ion chamber installation in the AP2 line.

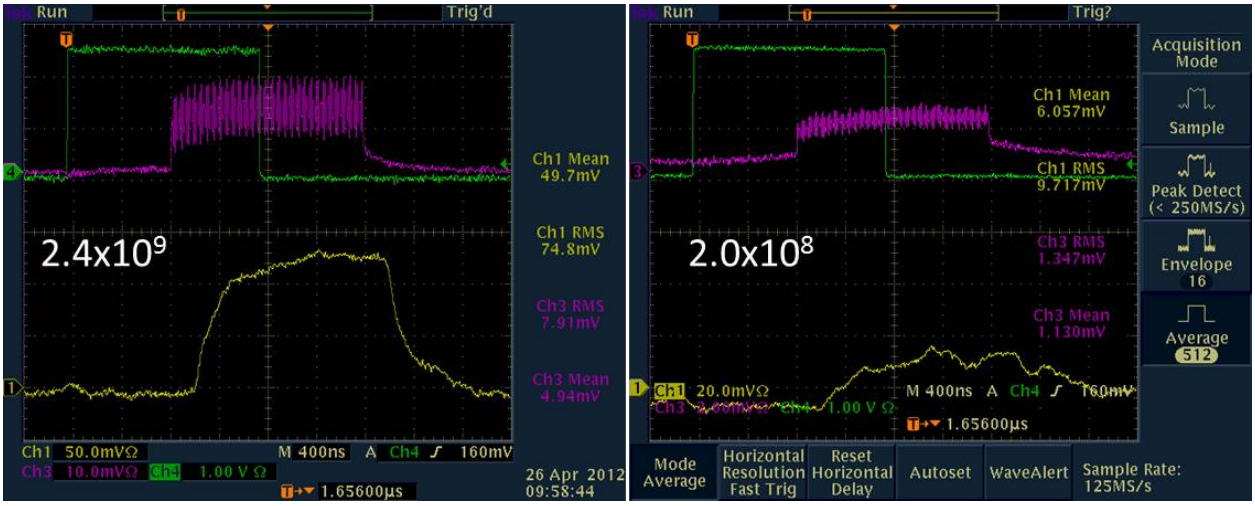

Figure 7.45: The yellow trace on both plots is a calibration test pulse on Toroid 724 in the AP2 line with high-gain preamps and special filtering to look for low-intensity beam. At beam intensities in the low 10^9s, there is an easily-measurable beam signal. However, when the beam intensities are lowered to the level of 10^7-10^8, the $(g-2)$ expected secondary beam intensity range, beam intensities can not be measured.

Wall Current Monitors (WCMs) are an alternative intensity-measurement device being considered for mixed-secondary beam. These devices have the advantage of being completely passive, and not requiring a break in the vacuum, which may make them a better fit in the M3 line where we need to stay compatible with the higher intensities of Mu2e operations, and the Delivery Ring where beam circulates for approximately 56 ms in Mu2e operations. New WCM designs are being considered that would provide accurate intensity measurements for secondary beam during $(g-2)$ operations. The design is based on that of a WCM for Mu2e extraction. Each slice of the slow-spilled Mu2e beam is approximately 2×10^7, which is consistent with the intensity that we would expect in the M3 line and Delivery Ring during $(g-2)$ operations.

BPMs were a key diagnostic in Antiproton-Source operation providing sub-millimeter orbit information in the beamlines and Delivery Ring. BPMs are located at each quadrupole, providing ample coverage. There are 34 BPMs in the AP2 line, 28 BPMs in the AP3 line and 120 BPMs in the Delivery Ring; however, it is believed that the BPMs in these areas will not be able to see the low-intensity 2.515 MHz $(g-2)$ secondary beam.

SEMs will be used to measure beam profiles in the M2 and M3 lines, as well as the Delivery Ring. There are eight SEMs in the AP2 line, seven SEMs in the AP3 line, three SEMs in the D/A line, two in the Debuncher, one in the Accumulator and three spares from the former AP4 line to draw from. SEM tunnel hardware will require some maintenance, and locations where SEMs are moved will require new cable pulls. Beam studies showed that special high-gain preamps will be required to measure the low-intensity secondary beam during $(g-2)$ operations [3]. There are only two working high-gain preamps, so additional preamps will need to be designed and fabricated. Additional SEMs will need to be added to the Delivery Ring from the pool of unused SEMs and spares. A photo of a SEM and its

Figure 7.46: Fixed-position ion chamber in the AP2 line. The ion chamber is separated from the beam pipe by a vacuum window on each side. Fixed-position ion chambers will only be used in the M2 line. In locations like the M3 line and Delivery Ring that will also see Mu2e beam, the ion chambers will be put inside of vacuum cans and made retractable.

profile display are shown in Fig. 7.47.

BLMs (Fig. 7.48) will be used to help maintain good transmission efficiency through the lines. Both Delivery-Ring and AP3 loss monitors will use the existing hardware and electronics for $(g-2)$ operations, but will be replaced for the higher-intensity Mu2e operations. Care will need to be taken to make a BLM plan that allows for switching back and forth between the two separate BLM systems.

Proton Secondaries Proton secondaries will extracted to the Delivery Ring abort line and will have a similar beam intensity to that of the Delivery Ring. Existing instrumentation from the downstream AP2 line will be used. A toroid will be used to measure beam intensity for Mu2e operations, but will be out of its operational range for $(g-2)$. If intensity measurement is needed, a retractable ion chamber will be added to the line. Ion chambers, SEMs and BLMs will be used in the same way they are for the mixed secondary lines.

Muon Secondaries Muon secondaries will traverse the upstream portion of the M4 line and the M5 line. The largest technical challenge will be measuring muon secondary beam, which models show should be on the order of 10^5 muons per pulse. This is two or three orders of magnitude smaller than the upstream mixed-secondary beam. Most diagnostics will not work at these beam intensities.

Beam intensity will be measured with ion chambers that are designed with three signal foils and four bias foils to increase the signal amplification. This design will allow beam

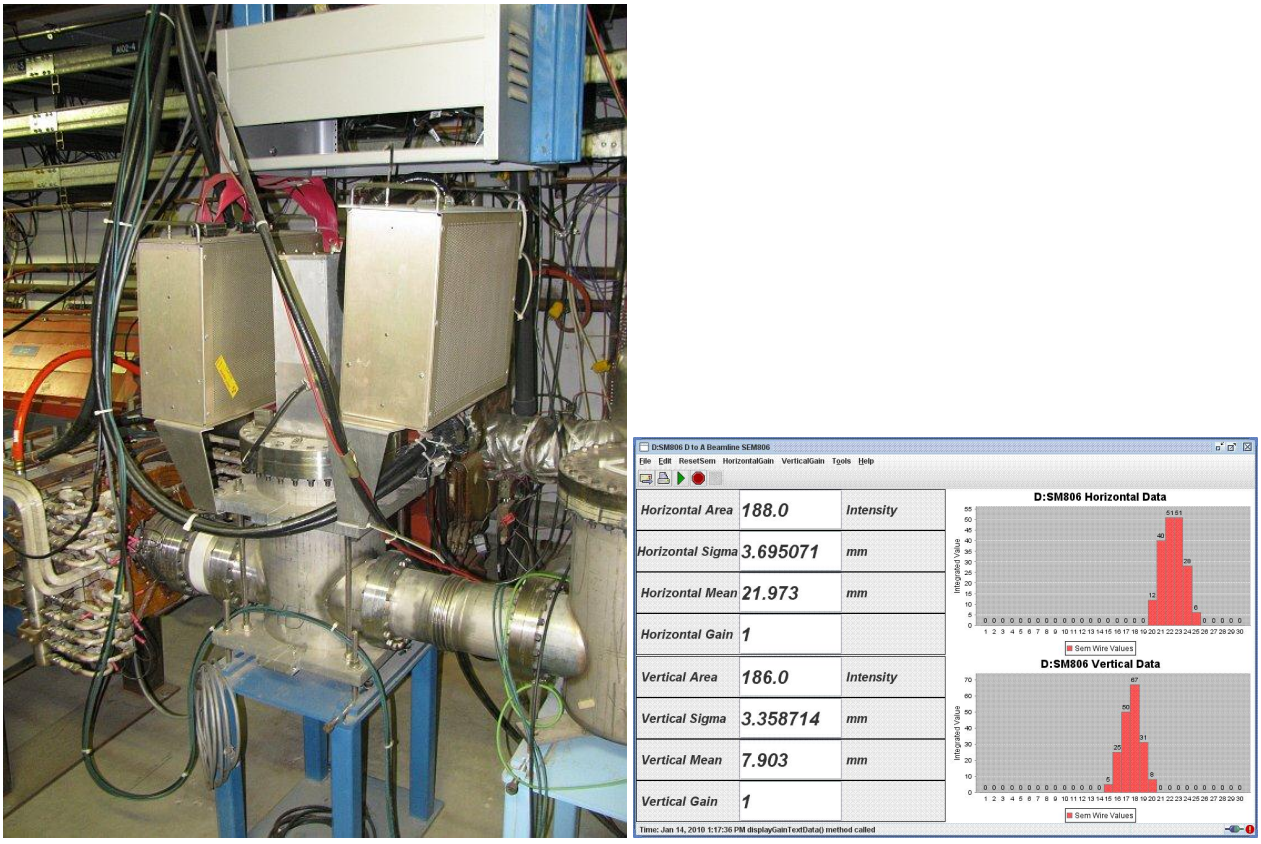

Figure 7.47: SEMs will be used to measure mixed secondary beam profiles. SEM tunnel hardware (left) is pictured. Preamp boxes are mounted next to the vacuum can. The SEM wires can be pulled out of the beam when not in use. SEMs can be used with to measure beam profiles, positions and intensities (right).

intensity measurements down to 10^5 particles. The ion chamber in the M4 line will need to be retractable in order to be compatible with Mu2e operations, while the M5-line ion chambers can be permanently in the beam path. New ion chambers will be designed and built for the M4 line because there is not a pool of available spares to populate these beamlines. Ion chambers for the M5 line will be provided by the repurposed BNL SWICs as will be discussed below. A Wall Current Monitor is another option being considered for beam-intensity measurement in the upstream M4 line. Though this device may be able to measure the Mu2e slow-spill beam intensity, it is not clear if one could be designed that is sensitive enough to see the lower-intensity muon beam expected for $(g-2)$ operations.

The base plan for measuring beam profiles in the upstream M4 and M5 lines are to use Segmented Wire Ion Chambers (SWICs), which are very similar to Multiwires with the exception that the beam goes through $ArCO_2$ gas, which is ionized by the charged-particle beams, creating an amplification that allows measurements of beam intensities down to the 10^4 particle range. This is an order of magnitude lower than the expected $(g-2)$ operational beam. In addition, SWICs are robust enough to handle particle beams several orders of magnitude higher in intensity than are expected during $(g-2)$ operations. This will provide the flexibility of running higher-intensity protons through the M4 and M5 lines

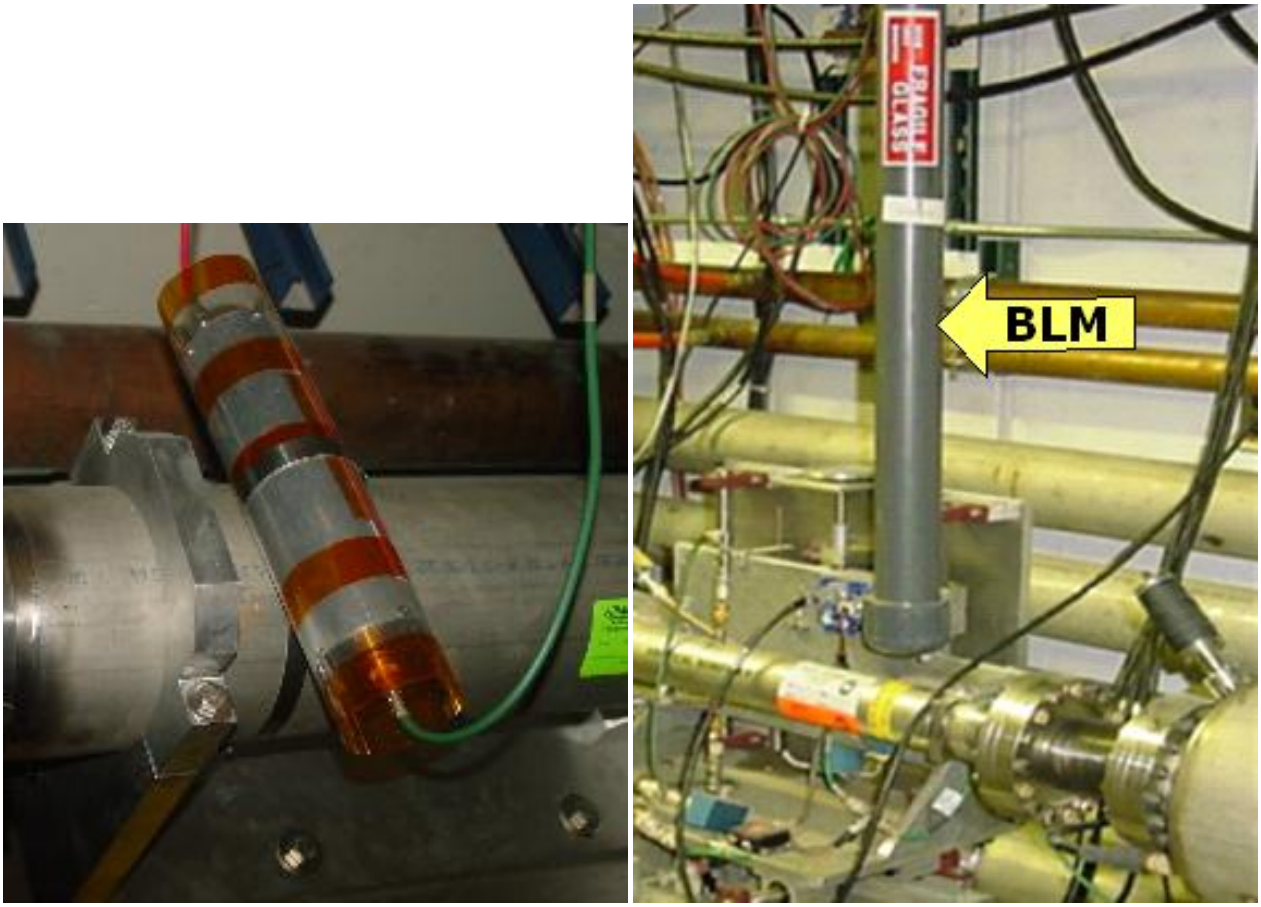

Figure 7.48: Two styles of BLMs will be used. Tevatron-style ion chamber loss monitors (left) will be used in areas of primary beam, and also in the Delivery Ring for Mu2e operations. The Pbar-style ion chamber, which consists of a plastic scintillator and a long light guide connected to a photomultiplier tube shielded from light in PVC, will be used in the Delivery Ring during $(g-2)$ operations.

for commissioning and beam studies. The SWICs in the upstream M4 line will need to be retractable since they are a destructive measurement device. Some vacuum cans can be acquired from other systems to minimize the cost; however, the inventory of spare vacuum cans is not sufficient enough to cover all of the SWICs. The SWICs in the M5 line will combination SWIC and Ion Chamber units repurposed from BNL. These devices allow have both wires for measuring beam profiles as well as foils for measuring beam intensities, but are not retractable and require vacuum windows on both sides of the device.

While maintenance is being performed on the BNL SWICs and interfaces to the FNAL control system are being designed for these devices, three alternate options are being considered for beam profile measurement in the M5 line. The first option is to design and build new SWICs. This would give us the flexibility of making them retractable and not require additional vacuum breaks; however, it would also require us to design and build new Ion Chambers for the line. Similar to the BNL SWICs, newly designed SWICs would measure beam down to the the 10^4 particle range.

A second option that was considered is the Proportional Wire Chamber (PWC). The advantage of the PWC is that it can measure beam down to 10^3 particles, and the wire planes are modular. The major disadvantage is that the wires are easily damaged by higher-intensity pules, limiting the ability to run higher intensity study beam.

The third option that was considered is to design Scintillator Fiber Profile Monitors (SFPMs), which can measure down to 100 particles. These devices are similar to SWICs or PWCs, but the wires are replaced with scintillating fiber. They have been used in the SY120 test-beam lines, and the fibers have been shown to survive long periods of beam operation. The largest disadvantage is that SFPMs cost significantly more than SWICs.

The upstream M4 line will be made compatible with both Mu2e and $(g-2)$ operations. Beam in the M4 line for $(g-2)$ will be at least two orders of magnitude smaller than the individual slices of slow-spilled beam that the line will see in Mu2e operations.

Intensity and profile information will also need to be collected just before and after the inflector, which will likely be achieved with ion chambers and some combination of the profile-measurement devices mentioned above. The two primary factors limiting the instrumentation after the inflector are a much smaller available physical space and potentially lower-intensity beam.

If muon beam profile information cannot be accurately measured with the proposed diagnostics, one option being considered is to develop a tune-up mode. In this mode, protons in the Delivery Ring would not be sent to the abort, but extracted toward $(g-2)$ with the muon beam. This would result in 10^7 particles per pulse in the extraction lines, which is easily measured by ion chambers and SWICs.

Accelerator instrumentation summary

A summary of instrumentation devices which will potentially be used for $(g-2)$ is shown in Table 7.16.

Beamline	Beam type	Intensity	Position	Profile	Loss
Primary protons	P1, P2, M1	toroids	BPMs	multiwires, SEMs	BLMs
Mixed secondaries	M2, M3, DR	ion chambers, WCMs	SEMs	SEMs	BLMs
Proton secondaries	DR abort	ion chambers, WCMs	SEMs	SEMs	BLMs
Muons	M4, $(g-2)$	ion chambers, WCMs	SWICs, PWCs, SFPMs		

Table 7.16: Potential instrumentation to be used in the beamlines for $(g-2)$ operations.

7.7 ES&H, Quality Assurance, Value Management

7.7.1 ES&H

The Accelerator Division ES&H Department has the responsibility for providing Environmental, Safety, and Health coordination and oversight of ES&H throughout the project. As with all Fermilab projects, attention to ES&H concerns will be part of the project management, and Integrated Safety Management will be incorporated into all processes. Line management responsibility for ES&H will be maintained on this project. Safe coordination of installation activities will be accomplished through the Project Management team, Project ES&H Coordinator, Project Engineer, and Task Manager. During installation, the Subcontractors, T&M Crafts, and all Fermilab personnel will utilize Project Hazard Analyzes to plan all work and to mitigate hazards. The Project Manager and Project ES&H Coordinator will audit compliance with all applicable ES&H requirements.

The handling and installation of magnets, vacuum systems, power supplies, and other accelerator components are common tasks within the Accelerator Division, and standard safety practices will be used. If any work falls outside of common practices, job hazard analyses will be conducted in order to ensure that the tasks are performed safely. Detailed procedures exist for handling components in the radioactive target vault, and the activation will be lower after years of not running beam than it was during antiproton production.

7.7.2 Quality Assurance

All aspects of the accelerator work will be periodically reviewed with regard to Quality Assurance issues from Conceptual Design through completion. The following elements will be included in the design and construction effort: an identification of staff assigned to each task with clear definition of responsibility levels and limit of authority as well as delineated lines of communication for exchange of information; requirements for control of design criteria and criteria changes and recording of standards and codes used in the development of the criteria; periodic review of the design process, drawings, and specifications to insure compliance with accepted design criteria.

7.7.3 Value Management

Significant cost savings have been incorporated into the $(g-2)$ accelerator design by utilizing the existing infrastructure from the Antiproton Source. Existing target station components will be reused: target, lens, collimator, and momentum-selection magnet, as well as maintaining the same target-vault layout. A new target-station dump to replace the current one which has an internal water leak will be constructed using the existing design. As many existing components as possible will be reused for the beamlines, including beamline magnets from the previous $(g-2)$ experiment at BNL. New magnets will be based on existing designs, where practical. Much of the beamline instrumentation will also be recycled, with upgraded readout electronics where necessary in order to see the low-intensity $(g-2)$ secondary and tertiary beam.

References

[1] W. Pellico *et al.*, "Proton Source Task Force Report", Beams Doc. 3660 (2010); F. G. Garcia *et al.*, "Fermilab Proton Improvement Plan Design Handbook", Beams Doc 4053 (2012).

[2] D.S. Ayres *et al.*, "NOνA Technical Design Report", NOνA Doc 2678 (2007).

[3] D. Still *et al.*, "$g-2$ Yield Beam Study Results – April 2012", $g-2$ Doc 430 (2012).

[4] I. Kourbanis, "Bunch Formation for $g-2$ experiment", $g-2$ Doc 335 (2012).

[5] M. Xiao, "Transport from the Recycler Ring to the Antiproton Source Beamlines", Beams Doc 4085 (2012).

[6] N. Mokhov, http://www-ap.fnal.gov/MARS.

[7] C. Yoshikawa *et al.*, "Optimization of the Target Subsystem for the New $g-2$ Experiment", IPAC2012.

[8] S. Striganov, "Optimization of $g-2$ Target Parameters", Fermilab Doc GM2-doc-197.

[9] Muons, Inc., http://www.muonsinc.com/muons3/G4beamline.

[10] B. Drendel *et al.*, "Antiproton Source Rookie Book", Beams-doc-2872, June 2010.

[11] ANSYS®, http://www.ansys.com.

[12] R. Shultz, "ANSYS Mechanical Simulation for Lithium Lens", Fermilab Doc GM2-doc-362.

[13] T. Leveling, "An Estimation of Antiproton Source Target Station Performance for Muon $g-2$", $g-2$ Doc 536.

[14] C. Hojvat *et al.*, "The Fermilab Tevatron I Project Target Station For Antiproton Production", Fermilab TM-1175 (March 1983).

[15] D.C. Carey, K.L. Brown, F. Rothacker, FERMILAB-Pub-98/310 (1998).

[16] $g-2$ Doc 484 (2012).

[17] V. Lebedev, $g-2$ Doc 171 (2012).

[18] $g-2$ Doc 252 (2012).

[19] J.P. Morgan, "Power tests for Pbar service buildings", Mu2e Doc 2117 (2012).

[20] B. Drendel *et al.*, "Pbar Controls Reference Material", Mu2e-doc-1161, May 2012.

[21] A. R. Franck *et al.*, "HOTLink Rack Monitor", FERMILAB-Conf-01/342/E.

[22] B. Drendel *et al.*, "Controls to Mu2e/g-2/Muon and Communications Duct Issues", Mu2e-doc-2069, February, 2012.

[23] communications duct details and alternative plans

[24] N. Eddy and E. Harms, "Beamline BPM Upgrade", Beams-doc-1279, September 2004.

Chapter 8

Relocation of the E821 Storage Ring Magnet

The muon storage ring magnet consists of superconducting coils inside their cryostats and the steel yoke and pole pieces. The steel is easily disassembled and shipped by truck, i.e., the time reversal of the process we used twenty years ago. However, the 15m diameter coils were wound in Brookhaven Building 919. In order to maintain the exceptional magnetic field the coils may not be disassembled to the degree that would allow conventional trucking. Special transportation for the very large load is required. Transporting the coils in their horizontal orientation is highly desired in order to prevent extraordinary forces and stresses on the coils.

The largest portion of the coil transport will occur by barge from Long Island, New York to Illinois via the Mississippi River system to the Illinois Waterway. Along the eastern seaboard the barge will travel through the Intracoastal Waterway keeping the barge near ports and in calm waters as compared to open sea travel. An ocean tug will be used from Long Island to New Orleans. A river tug will be used for the remainder of the trip to Lemont, Illinois. A back up plan could route the barge north via the St. Lawrence Seaway and Great Lakes to the Illinois Waterway.

A feasibility study in 2012 studied the best mode of transportation over land for both Long Island and Illinois. The result of the study indicated that the use of a specialized truck and trailer is the best option. Some vendors in the heavy haul industry are capable of performing the work required with a specialized truck/trailer suitable for moving the g-2 coils. A transportation review based on the feasibility study was held at FNAL in September, 2012. One of the recommendations from this review was to be sure that we document the coil/cryostat system before the move. The documentation is given in Fermilab g-2 doc-db references [1], [2], [3], and [4].

A Request for Proposal (RFP) was written at Fermilab and a meeting for the coil/cryostat transportation was held at BNL in November, 2012. Four companies replied to the RFP and attended the meeting; three of these submitted proposals. Emmert International was chosen to perform the work and the contract was signed.

The present plan is to truck the coil/cryostat from Brookhaven National Laboratory to Smith Point Marina in Suffolk County, Long Island. From this port the barge will travel to the Ozinga port on the Illinois Waterway. From the port in Lemont, the coils will travel via

specialized truck/trailer to FNAL this summer.

An analysis has been performed by Emmert International to determine the deflection of the shipping fixture arms while supporting the coils. This has been determined for various support conditions that the fixture will undergo during the phases of the shipment. The results of the Emmert calculations have been verified at Fermilab. The expected forces and deflections have also been imposed on the coils in a Finite Element Analysis at Fermilab. The stresses imposed on the coils are seen to be low on the order of a few hundred psi. The coils and other internal components of the cryostats are not expected to be damaged as a result.

The shipment of the coils will be performed using a quality assurance plan. The plan will provide a means of assuring that the coils will not see stresses above those that we plan for. Severe storms will be avoided. Distant storms that cause higher than normal wave motion will be monitored. The shipment will be monitored with accelerometers capable of transmitting a signal. For wave motion approaching our limits, the barge will be called to safe harbor. A safe harbor plan will be a part of this quality assurance plan. The accelerometer readings will be recorded for later analysis as well.

8.1 Preparations for Shipping

Figure 8.1 shows a recent picture of the cryostats and the mostly disassembled steel. In this photo the upper yoke plates have been removed as well as much of the spacer plates. The coils will be removed for shipment before most of the lower yoke and the remaining spacer plates will be moved.

The following are the important activities occurring (or in process of occuring) in preparation for the move:

- Replacing all the G10 radial stops with Aluminum stops. The G10 stops do not touch the mandrel when warm, only when cold. The Aluminum stops are longer and are designed to touch the mandrel. This prevents the coil from moving sided-to-side.

- For the outer coil, vertical bolts at the hangar locations will be inserted through the cryostat's top surface, and engage the mandrel. This is additional protection to prevent the mandrel from moving side-to-side. FEA simulations of this item and of the first item, show that these safeguards are sufficient for handling the worse case of 0.7g side load.

- The exposed (unpainted) surfaces of the yoke steel was coated with Cosmoline to prevent rusting.

- A structure has been designed to support the interconnect and the hardware outside the outer cryostat (see reference [5]). This is to minimize the stress on both the coils and cryostat walls.

- A shrink wrap will cover the cryostats during the move.

- During the move, dry nitrogen will be flowing through the cryostat to keep it dry.

Figure 8.1: Coils/Cryostats at BNL.

8.2 The Coil Shipping Fixture and Transportation

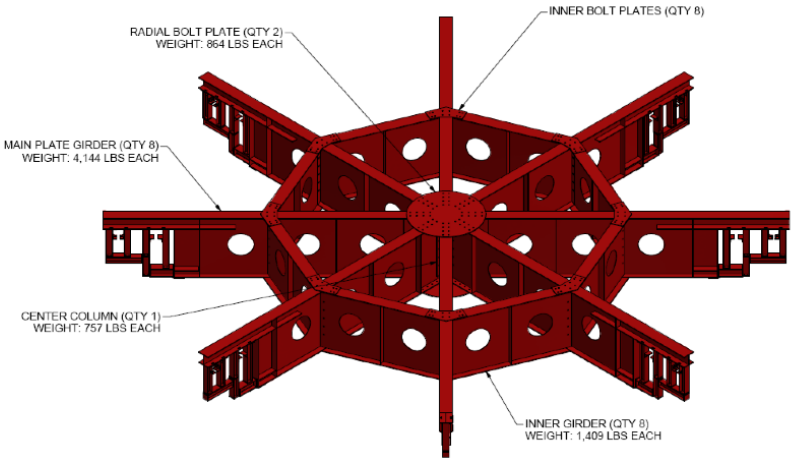

Figure 8.2: The shipping fixture.

Figure 8.2 shows the shipping fixture as specified by Fermilab and designed and built by Emmert International per the criteria to carry the coils. The coils will remain very flat during the shipment to limit the stress imposed onto the coils.

Figure 8.3 shows an engineering drawing of the mover and support fixture. Overall length of this rig is in excess of 117 feet. The trailer has three hydraulic zones to keep the load level and to distribute the weight to the wheels evenly. The truck will move slowly over the roadways ranging from walking speed to a maximum of 10 mph depending on the terrain and the proximity of obstacles along the path. The shipment will move over public roadways during night time hours to limit disruption to public traffic.

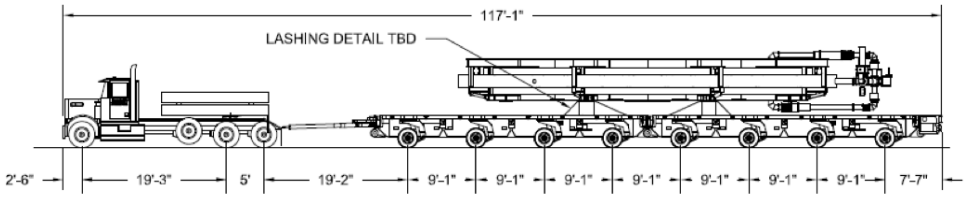

Figure 8.3: Specialized Truck and Trailer for Coil Shipment.

Figure 8.4: Scaled model showing the specialized truck and trailer holding the coils.

Figure 8.4 shows a model of the mover and support fixture. The 50 foot diameter coils require roughly the width of four traffic lanes to traverse the roadways in Long Island and Illinois.

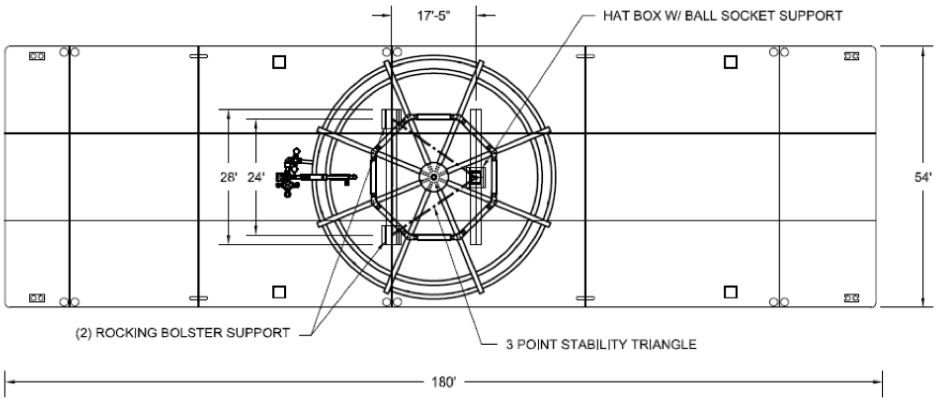

Figure 8.5: Shipping fixture with coils shown secured to the barge.

Figure 8.5 shows a drawing of the shipping fixture with coils secured to the barge. The

barge that we plan to utilize has a 54 foot width by 180 foot length. This barge size is chosen to limit the maximum roll, pitch, and heave the coils will experience over the water.

References

[1] E821 Muon Storage Ring Coil Resistance Benchmark. g-2 DocDB note 499-v1.

[2] Coil Resistance to Ground Measurements. g-2 DocDB note 352-v1.

[3] Cryostat Vacuum System Documentation. g-2 DocDB note 314-v1.

[4] E821 Interconnects. g-2 DocDB note 302-v1.

[5] Erik Voirin, g-2 Cryostat Interconnect Support for Transportation. g-2 DocDB note 979-v1.

Chapter 9

The Muon Storage Ring Magnet

9.1 Introduction

As emphasized in Chapter 2, the determination of the muon anomaly a_μ requires a precise measurement of the muon spin frequency in a magnetic field ω_a, and an equally precise measurement of the average magnetic field felt by the ensemble of precessing muons, $\langle B \rangle$. We repeat the spin equation given in Eq. 3.11, since it is central to the design of the storage-ring magnet.

$$\vec{\omega}_a = -\frac{Qe}{m}\left[a_\mu \vec{B} + \left(a_\mu - \left(\frac{m}{p}\right)^2\right)\frac{\vec{\beta}\times\vec{E}}{c}\right]. \tag{9.1}$$

As explained in Chapter 2, the need for vertical focusing and exquisite precision on $\langle B \rangle$ requires that: either the muon trajectories be understood at the tens of parts per billion level, and the magnetic field everywhere be known to the same precision; or the field be as uniform as possible and well-measured, along with "reasonable knowledge" of the muon trajectories. This latter solution was first employed at CERN [1] and significantly improved by E821 at Brookhaven [2]. The uniformity goal at BNL was ± 1 ppm when averaged over azimuth, with local variations limited to ≤ 100 ppm.

Fermilab E989 will use the storage-ring magnet designed and built for Brookhaven E821, with additional shimming to further decrease the local variations in the magnetic field. This requires the relocation of the ring from BNL to Fermilab, which is described in detail in the following chapter. While the magnet steel comes apart and can be moved by conventional trucks, the 14.5 m diameter superconducting coils will need to be moved as a package, on a custom designed fixture that can be pulled by a truck to travel by road, and put on a barge to travel by sea, and then again by road to get it to the Fermilab site.

The storage ring is built as one continuous superferric magnet, an iron magnet excited by superconducting coils. A cross-section of the magnet is shown in Fig. 9.1. The magnet is C-shaped as dictated by the experiment requirement that decay electrons be observed inside the ring. The field, and hence its homogeneity and stability, are determined dominantly by the geometry, characteristics, and construction tolerances of the iron. Although both copper and superconducting coils were considered, the use of superconducting coils offered the following advantages: thermal stability once cold; relatively low power requirements; low voltage, and hence use of a low-voltage power supply; high L/R time constant value

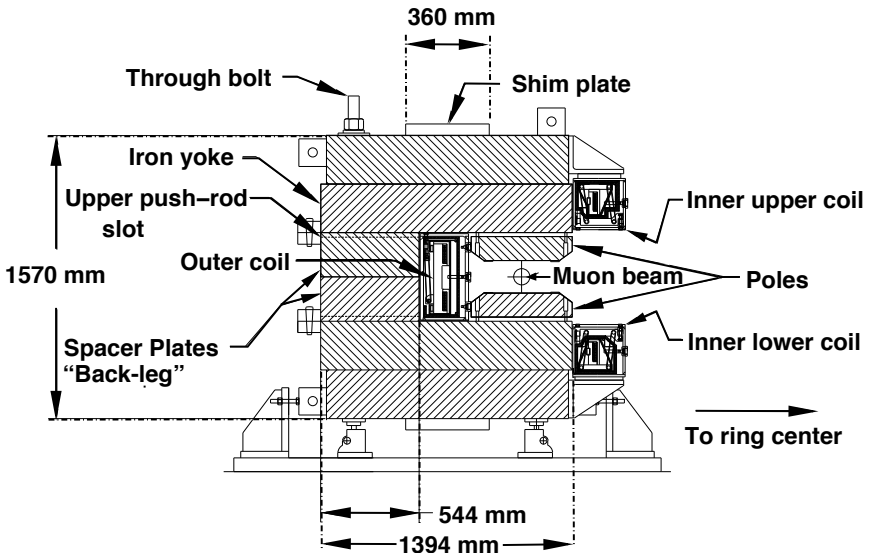

Figure 9.1: Cross section of the E821 storage-ring magnet. The yoke is made up of 12 azimuthal sections, each of which consists of six layers of high quality magnet steel provided by Lukins Steel Corporation. The pole pieces were provided by Nippon Steel Corporation.

and hence low ripple currents; and thermal independence of the coils and the iron. The main disadvantage was that the coils would have a much larger diameter and smaller height than any previously built superconducting magnet. However, since the E821 magnet team could not identify any fundamental problems other than sheer size, they decided to build superconducting coils.

To obtain the required precision in such a large diameter magnet with an economical design is an enormous challenge. The magnet had to be a mechanical assembly from sub-pieces because of its size. With practical tolerances on these pieces, variations up to several thousand ppm in the magnetic field could be expected from the assembled magnet. To improve this result by two to three orders of magnitude required a design which was a "shimable kit".

Because of the dominant cost of the yoke iron, it was an economic necessity to minimize the total flux and the yoke cross-section. This led to a narrow pole, which in turn conflicts with producing an ultra-uniform field over the 9 cm good field aperture containing the muon beam.

A simple tapered pole shape was chosen which minimized variations in the iron permeability and field throughout the pole. The ratio of pole tip width to gap aperture is only 2/1. This results in a large dependence of the field shape with the field value B. However, since the storage ring is to be used at only one field, $B = 1.45$ T, this is acceptable. Because of dimensional and material property tolerance variation, the compact pole piece increases the necessity for a simple method of shimming.

Experience with computer codes, in particular with POISSON [4], had demonstrated that, with careful use, agreement with experiment could be expected at a level of 10^{-4} accuracy. POISSON is a two-dimensional (2D) or cylindrically symmetric code, appropriate

for the essentially continuous ring magnet chosen for the $(g-2)$ experiment. Computational limitations, finite boundary conditions, and material property variations are all possible limitations on the accuracy of "paper" designs.

We will briefly discuss the design features that are relevant to E989, especially to moving the ring, but not repeat all the details given in Danby et al. [3], and in the E821 Design Report [5]. The parameters of the magnet are given in Table 9.1

Table 9.1: Magnet parameters

Design magnetic field	1.451 T
Design current	5200 A
Equilibrium orbit radius	7112 mm
Muon storage region diameter	90 mm
Inner coil radius - cold	6677 mm
Inner coil radius - warm	6705 mm
Outer coil radius - cold	7512 mm
Outer coil radius - warm	7543 mm
Number of turns	48
Cold mass	6.2 metric tons
Magnet self inductance	0.48 H
Stored energy	6.1 MJ
Helium-cooled lead resistance	6 $\mu\Omega$
Warm lead resistance	0.1 mΩ
Yoke height	157 cm
Yoke width	139 cm
Pole width	56 cm
Iron mass	682 metric tons
Nominal gap between poles	18 cm

9.2 Yoke Steel

E989 will reuse the yoke steel manufactured for the E821 experiment. The yoke pieces have been surveyed and disassembled at Brookhaven and are in the process of being shipped to Fermilab. The design and construction of the magnet has been documented and published in NIM [3] as well as the final report in Phys. Rev. D [2]. We summarize the main design features and issues here, with a discussion of potential improvements in Section 9.4.

Ideally, the $g-2$ magnet would be azimuthally symmetric. To ease the fabrication and assembly processes, the magnet was built with twelve 30° sectors. Each sector consists of an upper and lower yoke separated by a spacer plate as shown in Fig. 9.1. Due to the large thickness of the yoke (54 cm), the individual plates were fabricated separately and welded together after machining. The spacer plate is also split at the midplane to allow for the installation of beam pipes and other services after the lower section is in place but prior to

the installation of the upper yoke. The yoke plates and spacers in each sector are all fastened together with eight long high-strength steel bolts that cover the full 1.57 m tall yoke. The total sector mass is $\approx$ 57,000 kg, which results in a total magnet mass of $\approx$ 680,000 kg.

Significant quality control efforts were taken during the manufacturing process to ensure that the magnet had sufficiently uniform permeability and the appropriate geometric shape. Both of these parameters have strong effects on the uniformity of the magnetic field in the storage region.

High-quality plates were manufactured by hot-rolling AISI 1006 iron to minimize magnetic voids in the material. These plates were manufactured with $< 0.08\%$ of carbon and other impurities. The finished plates were inspected ultrasonically to detect voids and inclusions, and analyzed chemically to understand the composition.

Although the yoke steel is partially magnetically isolated from the storage region by an air gap near the pole pieces, strict machining specifications are required to minimize non-uniformities in the storage region field. The surfaces of the yoke plates closest to the storage region were milled flat within 130 μm and 1.6 μm finish. Similarly, the spacer plate surfaces were milled flat within $\pm$130 μm, with a thickness accurate to $\pm$130 μm. These surfaces are parallel within 180 μm. The radial tolerance for each yoke plate and the spacer plates was $\pm$130 μm. When constructed, the vertical yoke gap had an rms deviation of $\pm$90 μm, or 500 ppm of the total air gap of 20 cm, and a full-width spread of $\pm$200 μm.

Each of the 12 sectors need to be connected smoothly to achieve azimuthal symmetry. To achieve azimuthal continuity, each sector end has four radial projections for bolts to fasten adjacent sector ends to each other. When the sectors are fitted to each other, shimmed, and the bolts tightened, relative motion of adjacent sectors is minimized. The average azimuthal gap between sectors was 0.8 mm, with an rms deviation of $\pm$0.2 mm.

When we begin to reconstruct the storage ring, we will clean the yoke steel and remove any rust that has developed. It will be important to do this in a non-destructive manner that maintains the high-level of precision achieved during manufacturing.

9.3 Poles and Wedges

E989 will reuse the pole pieces and wedge shims that were manufactured for the E821 experiment. The pole pieces and wedges have been removed from the storage ring at Brookhaven and have already been shipped to Fermilab where they are awaiting reassembly.

9.3.1 Poles

More stringent quality requirements are placed on the machining of the pole pieces than the yoke steel. The air gap between the yoke and pole pieces decouples the field region from non-uniformities in the yoke. Thus, irregularities in the pole pieces dominate the field aberrations. Ultra-pure continuous vacuum cast steel with $< 0.004\%$ carbon impurities is used for the pole pieces. The fabrication process greatly minimizes impurities such as ferritic inclusions or air bubbles.

A dimensioned view of the pole pieces is shown in Figure 9.2. Each 30° yoke sector contains three pole pieces (azimuthally). The pole pieces are 56 cm wide (radially), with

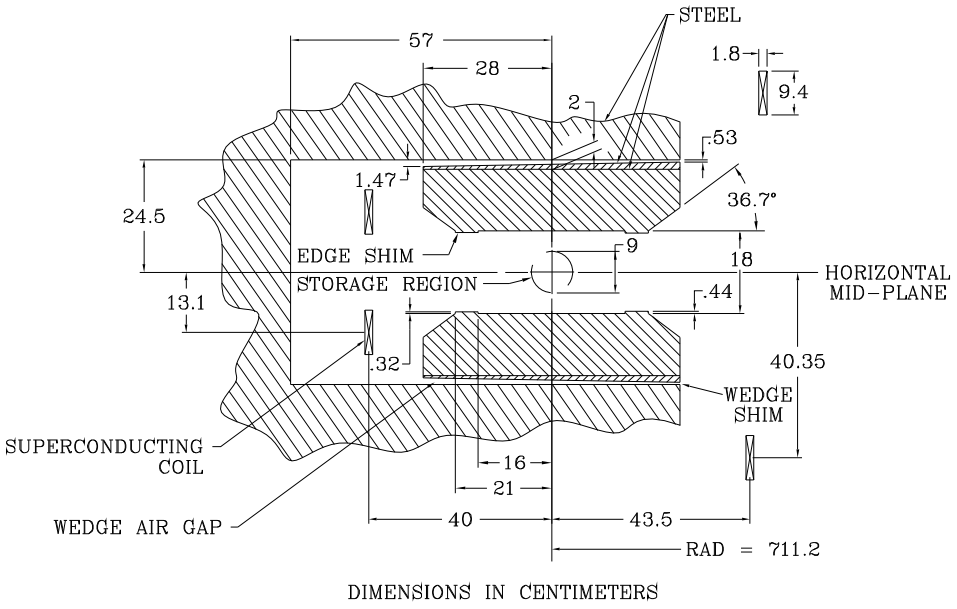

Figure 9.2: Cross section view of the magnet gap region.

a tolerance of 50 μm. The thickness (vertical) of each piece is 13.3cm with a tolerance of 40 μm. The pole faces which define the storage ring gap have tight machining tolerances. Each face has a flatness tolerance of 25μm, leading to upper and lower faces being parallel within a 50 μm tolerance. The surface finish is 0.8 μm. These machining tolerances are so stringent due to the large quadrupole moment introduced by non-parallel surfaces. An OPERA-2D simulation of the magnet has determined that a 100 μm tilt of the pole piece over its width corresponds to > 100 *ppm*. This is in good agreement with the 2D POISSON calculations performed for the E989 simulations.

Each yoke sector contains three pole pieces. Vertically, the pole pieces are mounted to the yoke plates with steel bolts. The outer two pieces are each machined radially, parallel to the yoke sector. The middle pole piece in each sector is interlocking, with an angle of 7° with respect to the radial direction. The pole pieces were isolated azimuthally by 80 μm kapton shims, which served two purposes. First, the kapton shims helped position the pole pieces at the correct azimuth. Second, the kapton electrically isolated the poles from each other. If the poles were all in contact with each other, large eddy currents would develop around the entire circumference of the ring during field ramping leading to distortions of the magnetic field

The pole gap distance was measured using a capacitive sensor, as described in Section 15.4.2. The gap was 18 cm with an rms variation of $\pm$23 μm, and a full range of 130 μm. As the magnet is powered, the induced torque causes the open side of the C-magnet (inner

radius) to close slightly. Thus, during the installation, the poles were aligned with an opening angle of 80 μrad. A precise bubble level was used to achieve 50 μm precision over the length of the pole piece. Pole realignment will be part of the shimming process described in Section 15.4.2.

9.3.2 Wedges

The gaps between the yoke and poles isolate the yoke steel from the poles and provide a region where shims can be inserted to fine-tune the magnetic field. Steel wedges that are sloped radially (see Fig 9.2) are inserted to compensate for the intrinsic quadrupole moment produced by the C-magnet. There are 72 wedges in each 30° yoke sector. The induced quadrupole term depends on the slope of the wedge, which was calculated to be 1.1 cm over the 53 cm width for E821. This wedge angle was verified empirically, and no additional grinding was needed. The radial position of the wedges can be adjusted to change the total material in the gap, affecting only the dipole moment (see Section 15.4.3).

During the ramping of the main coil current, the thick end of the wedge attracts more field lines, leading to a torque. To prevent the wedges from deflecting vertically, an aluminum "anti-wedge" is used to fill the air gap between the wedge and the pole piece.

E989 will reuse the wedge-spacer combination as is. Fine tuning of the quadrupole moment can be achieved with active current shims, as discussed in Section 15.4.3.

9.4 Thermal Effects

Temperature variations in the experimental hall are expected to be controlled within $\pm 1\,^{\circ}$C during the course of data taking. This will change the shape of the magnet, which will in turn change the magnetic field. We produced thermal simulations with ANSYS to quantify the geometric distortions, which are then input into the OPERA-2D model of the storage ring.

E821 used 3.5" of fiber glass insulation around the bulk of the yoke and 3/8" foam rubber insulation near the poles pieces, as shown in Figure 9.3 (a). Reasonable thermal film coefficients in the range of 5-25 W/m^2C were used at the surfaces of the magnet. Thermal oscillations based on day-night temperature cycles are imposed on the $g-2$ magnet system and modeled with ANSYS. The air temperature is assumed to be spatially uniform throughout the hall. The model indicates that this will lead to thermal fluctuations at the yoke and pole pieces of a few tenths of a degree, as shown in Figure 9.3 (b). The pole pieces are constrained mechanically to prevent sliding, thus, in response to the thermal variations, they bend.

Figure 9.4 shows the response of the magnet under the $1\,^{\circ}$C hall fluctuations. The contours show the maximum extent of the deflection for the both radial shifts (Figure 9.4 (a)) and vertical shifts (Figure 9.4 (b)). The deflections are on the order of 1 μm per degree C change in the hall temperature. The parallelism of the pole faces is known to affect the higher-order multipole components of the magnetic field. Figure 9.5 plots the relative change in the pole gap as a function of radius for the thermal changes described above.

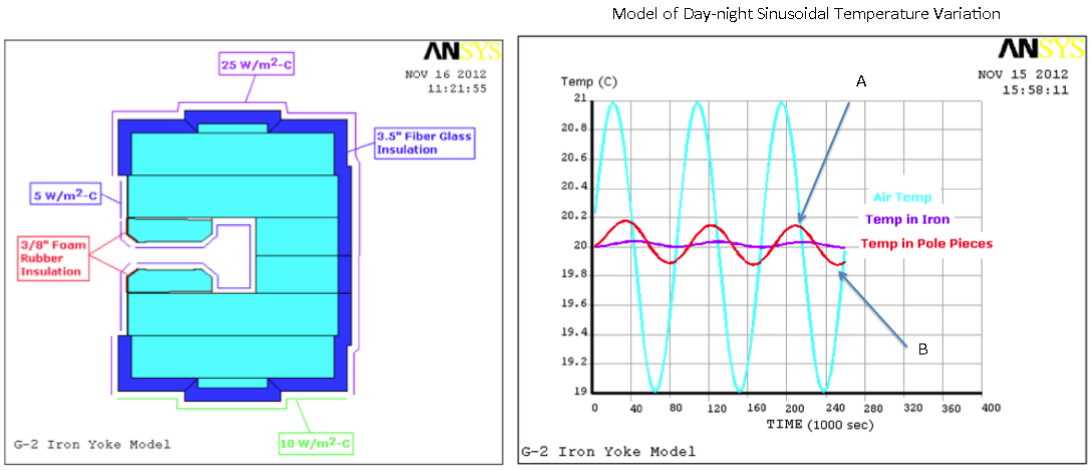

(a) (b)

Figure 9.3: (a) An ANSYS model of the $g-2$ storage ring includes the thermal insulation used in E821. (b) Thermal oscillations based on day-night temperature cycles are imposed on the $g-2$ magnet system assuming a $\pm 1\,^{\circ}$C. The temperature variations of the the yoke (purple) and pole (red) are overlaid.

Two different thermal contact resistances of the pole foam rubber insulation were modeled. In both cases, the gap distortion leads to a change of about 1 μm. The pole gap distortions were input into the OPERA-2D magnetic field simulation. Distortions on there order of a few tenths of a *ppm* were observed in the sextupole and octupole moment with a change of 1 μm in the pole gap. Because the monitoring of the higher order multipole moments is done primarily with the trolley runs, extrapolation of the field map from the fixed probes during the main data collection will rely on stable magnet geometry.

The ANSYS and OPERA tools nicely complement each other and allow us to understand the effects of magnet deflections in E989. We plan to repeat these studies with varied insulation thickness and with additional insulation around the inner superconducting coils. With a high quality temperature control system stabilizing the experimental hall and better thermal isolation of the steel, E989 will have significantly smaller time-dependent magnet distortions than E821. This will lead to more stable multipole components.

9.5 WBS 476.03.02.03 The Superconducting Coil System

9.5.1 Overview

The coil design was based on the TOPAZ solenoid at KEK [6]. TOPAZ conductor was used, with pure aluminum stabilizer and niobium-titanium superconductor in a copper matrix. Conductor characteristics are given in Table 9.5.1. At full field the critical temperature of the outer coil is 6.0 K. The magnet typically operates at 5.0 K. This represents 76% of

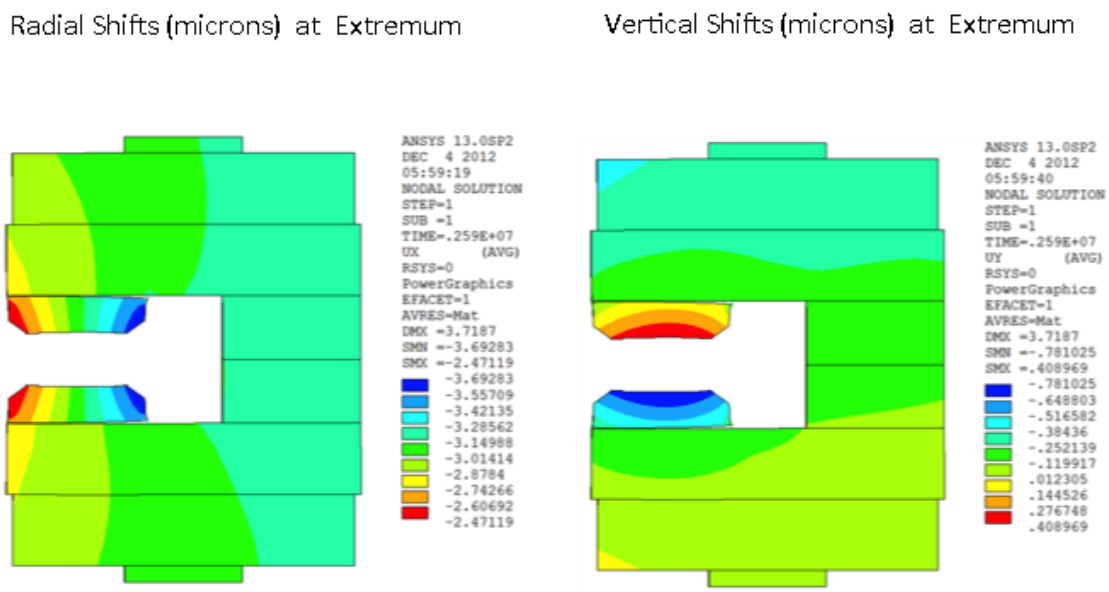

(a) (b)

Figure 9.4: The thermal fluctuations depicted in Figure 9.3 are imposed on the magnet, causing distortion of the magnet, as modeled in ANSYS. The deflections are decomposed in (a) the radial and (b) the vertical dimensions for the worst-case scenario.

the superconductor limit. Each coil block is effectively a very short solenoid with 24 turns, and one layer. The coils are wound from the inside of the ring so that, when powered, the coils push out radially against a massive aluminum mandrel. Cooling is indirect with helium pipes attached to the mandrels. The coil turns, coil stack and insulation are epoxied together, forming a monolithic block. The coils hang from the cryostat with low heat load straps, and the shrinkage and expansion of the coils is taken by the straps. The coils are located using radial stops on the inner radius. For the outer coil the stops transfer the force from the coil to the cryostat box, and push rods from the iron yoke transfer the force from the box to the iron (see Fig. 9.7). For the inner coils, pins replace the pushrods.

When the coils are cooled, they contract down onto the radial stops into a scalloped shape. When powered, the Lorentz force pushes the coils outward, increasing the force against the mandrel, which provides cooling. This feature, the result of winding on the inside of the mandrel, reduces the risk of cooling problems even if the coil were to separate from the mandrel during transport citeyamamoto-pc.

A ground plane insulation band of 0.3 mm thickness was built from a sandwich of three layers of 50 μm kapton, epoxy coated, between two layers of epoxy-filled fiberglass. The insulation assembly was fully cured and placed into the mandrel. A 0.1 mm layer of B-stage epoxy film was placed between the mandrel and kapton laminate, and between the kapton laminate and the conductor block after winding. A 4.8 mm thick G-10 piece was placed on the winding ledge, and on top and on the inner radius of the completed coil block. The insulation protected against a local failure in an insulation layer and against creep failure

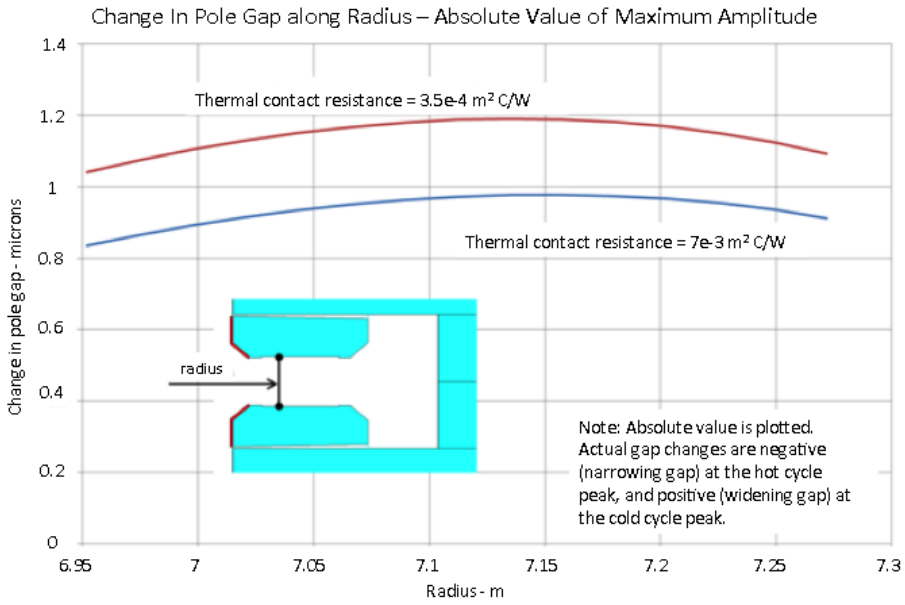

Figure 9.5: The deflections of the pole pieces under thermal variations are quantified in ANSYS simulations as a function of the radial coordinate. Typical fluctuations of 1 °C will produce micron scale distortions. Two different thermal contact resistances are shown.

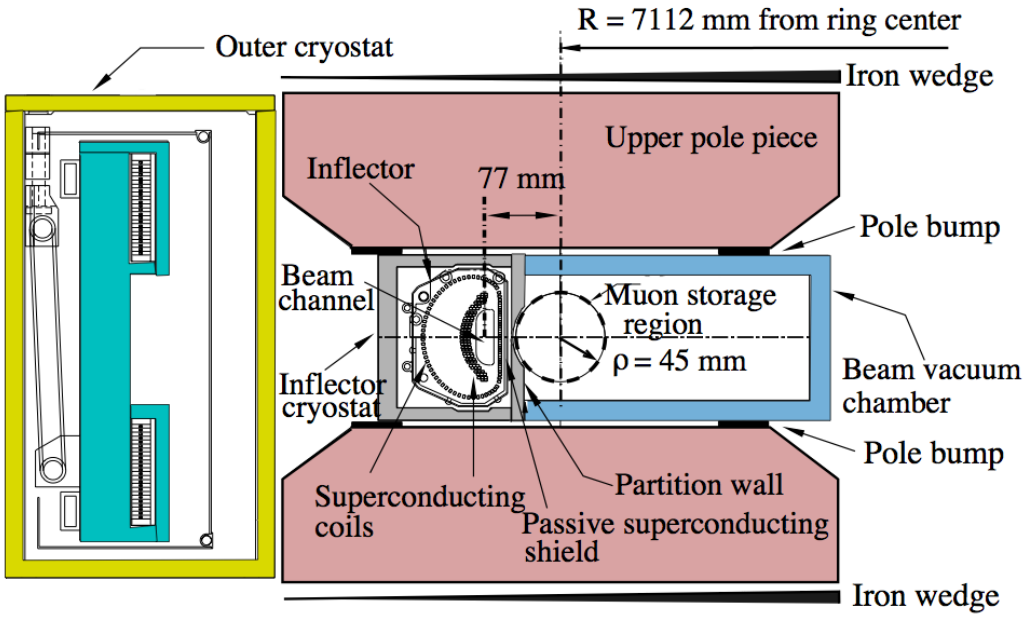

Figure 9.6: The arrangement of the pole pieces, shimming wedges and the inflector cryostat, showing the downstream end of the inflector where the beam exits. The beam is going into the page, and the ring center is to the right.

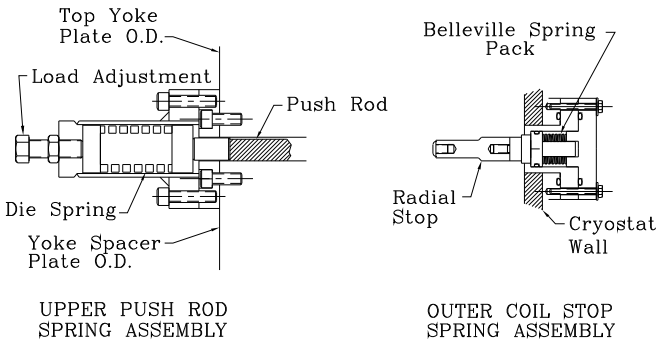

Figure 9.7: The spring-loaded radial stop and push rod. The stops are attached to the cryostat inner wall. The push rods preload the outer cryostat, attaching to the yoke at the outer radius, passing through a radial slot in the yoke to the outer cryostat.

3967 along a surface. The epoxy-filled fiberglass in the ground plane insulation sandwich improved
3968 heat transfer between coil and mandrel.

Table 9.2: Superconductor parameters

Superconductor type	NbTi/Cu
Nominal dimensions	1.8 mm × 3.3 mm
NbTi/Cu ratio	1:1
Filament 50 μm	
Number of filaments	1400
Twist pitch	27 mm
Aluminum stabilizer type	Al extrusion
Ni/Ti composite dimensions	3.6 mm × 18 mm
Al/(NbTi + Cu) ratio	10
RRR (Al)	2000-2500
RRR (Cu)	120-140
I_c	8100 A (2.7 T, 4.2 K)

3969 The coil was then wound using a machine that wrapped the superconductor with three
3970 overlapping layers of 25 μm of kapton and fiberglass filled with B-stage epoxy, 19 mm in
3971 width, laying the conductor into the mandrel with a compressive load as described in Ref. [3].
3972 The wrap was tested at 2000 V DC during the wind. Aluminum covers were added after the
3973 coil was wound, and the entire assembly heated to 125° C to cure the epoxy. See Fig. 9.8.
3974 The outer coil contains two penetrations, one to permit the beam to enter the ring, and
3975 one which which could have permitted high voltage to be fed to a proposed electrostatic

muon kicker. It was decided at the time to make this "kicker penetration" in the outer coil, but not to make a hole through the magnet yoke until it was shown that this kicker could be built (which was not demonstrated).

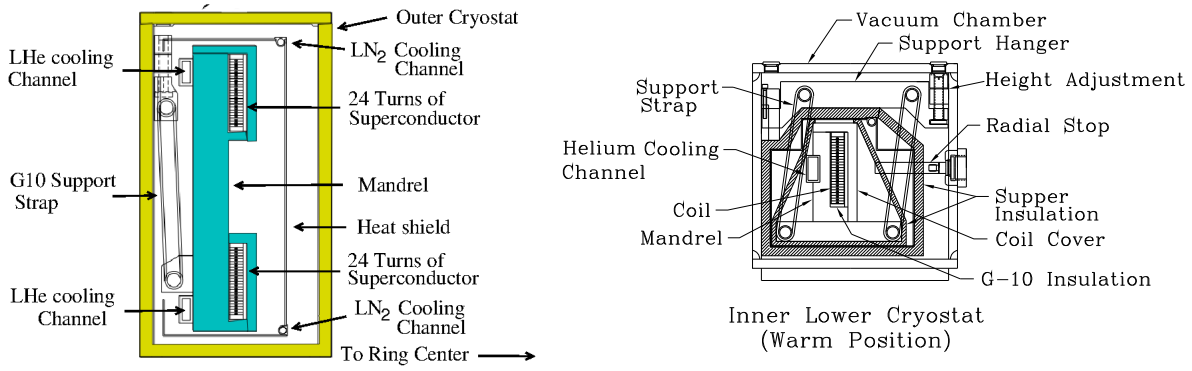

(a) Outer Coil (b) Inner Coil

Figure 9.8: The outer and inner coil structures. Both are shown in their warm configuration.

The coils are indirectly cooled with two-phase He flowing through channels attached to the mandrel, as shown in Fig. 9.8. The two-phase helium cooling avoids the increase in temperature that would occur in a circuit cooled with single-phase helium. The operating temperature of the coils is within 0.2 K of the coldest temperature in the cooling circuit. The advantages of two-phase cooling are: (1) the helium flows in well-defined flow circuits; (2) the total amount of helium that can be flashed off during a quench is limited to the mass of helium in the magnet cooling tubes; and (3) the location of the helium input and output from the cryostat and the location and orientation of the gas cooled leads are not affected by the cooling system [8].

The key to the operation of a two-phase helium cooling circuit is a helium dewar (the control dewar) that contains a heat exchanger. This heat exchanger sub-cools the helium from the J-T circuit before it enters the magnet cooling circuits. This isobaric cooling provides a higher ratio of liquid to gas with a higher pressure and lower temperature than the refrigerator J-T circuit alone would provide. This feature is important for the long cooling channels in the magnet cooling circuits. The use of a heat exchanger in the control dewar reduces the helium flow circuit pressure drop by a factor of two or more. The control dewar and heat exchanger also have the effect of damping out the oscillations often found in two-phase flow circuits. The helium in the control dewar acts as a buffer providing additional cooling during times when the heat load exceeds the capacity of the refrigerator.

The $(g-2)$ cooling system was originally designed to have three separate cooling circuits: a 218 m long cooling circuit that cools all three mandrels in series, the lead and coil interconnect circuits that are 32 m long (the gas-cooled leads are fed off of this circuit), and a 14 m long cooling circuit for the inflector magnet. Later the cooling system was modified to permit each of the mandrels to be cooled separately. Ultimately, the $(g-2)$ cooling system operates with parallel cooling circuits for the coils, inflector, and lead cooling. Electrically, the three coils are connected in series so that the two inner coils are in opposition to the

outer coil to produce a dipole field between the inner and outer coils. The magnet is powered through a pair of tubular gas-cooled leads developed for this application. Each lead consists of a bundle of five tubes. Each tube in the bundle consists of three nested copper tubes with helium flow between the tubes. The copper tubes used in the leads are made from an alloy with a residual resistance ratio of about 64. The lead length is 500 mm. A typical cool down from 300 to 4.9 K takes about 10 d. Once the control dewar starts to accumulate liquid helium, it takes another day to fill the 1000 l dewar. In operation, the pressure drop across the magnet system is about 0.02 MPa (3.0 psi). We initiated several test quenches and had one unintentional quench when the cooling water was shut off to the compressors. The peak measured pressure during a 5200 A quench was 0.82 MPa (105 psig). Other places in the cooling circuit could have a pressure that is 40% higher. The quench pressure peak occurs 11 s after the start of the quench. The quench pressure pulse is about 12 s long compared to current discharge time constant at 5200 A of 31 s. The outer coil mandrel temperature reaches 38 K after the quench is over. Re-cooling of the magnet can commence within 5 min of the start of the quench. After a full current quench, it takes about 2 h for the outer coil to become completely superconducting. The inner coils recover more quickly.

Table 9.3: Estimates of cryogenic heat leaks

		4.9 K load (W)	80 K load (W)
Magnet system heat load	Outer coil cryostat	52	72
	Two inner coils	108	77
	Inflector	8	5
	Interconnects	11	46
	Magnet subtotal	**179**	**200**
Distribution	Helium piping	19	
	Control dewar	5	
	Interconnects/valves	33	32
	Nitrogen piping		34
	Distribution subtotal	**57**	**66**
Lead gas (1.1 g/s)	Equivalent refrigeration	114	
Total refrigeration		351	266
Contingency		70	51
Cryogenic design	**Operating point**	**421**	**308**

Both persistent mode and power supply excitation were considered. The total flux, $\int \vec{B} \cdot d\vec{s}$, is conserved in persistent mode. However, room temperature changes would result in changes in the effective area. Thus although the flux, is conserved, the magnetic field in the muon storage region is not. Persistent mode would also require a high-current superconducting switch. Power supply excitation with NMR feedback was chosen, although no feedback was used for the 1997 run. This method gives excellent control of the magnetic field and allows the magnet to be turned off and on easily. The power supply parameters are shown in Table 9.5.1.

Table 9.4: Power supply parameters

Rating	5 V, 6500 A	
Rectifier	480 VAC input, 12 pulse (Two ±15°, 6 pulse units in parallel)	
Output filter	0.4 F	
Regulator	Low-level system	0.1 ppm stability with 17 bit resolution
	Power section	Series regulator with 504 pass transistors
Cooling	Closed loop water system with temperature regulation	
Regulation	Current-internal DCCT	±0.3 ppm over minutes to several hours
	Field-NMR feedback (current vernier)	±0.1 ppm (limited by the electronics noise floor)
Manufacturer	Bruker, Germany	

Both persistent mode and power supply excitation were considered. The total flux, $\int \vec{B} \cdot d\vec{s}$, is conserved in persistent mode. However, room temperature changes would result in changes in the effective area. Thus although the flux, is conserved, the magnetic field in the muon storage region is not. Persistent mode would also require a high-current superconducting switch. Power supply excitation with NMR feedback was chosen, although no feedback was used for the 1997 run. This method gives excellent control of the magnetic field and allows the magnet to be turned off and on easily. The power supply parameters are shown in Table 9.5.1.

The quench protection design parameters were determined by the requirements of magnetic field stability and protection of the magnet system in case of a quench. When the energy is extracted, eddy currents are set up in the iron which oppose the collapse of the field. This can cause a permanent change in the magnetic field distribution [9]. This is sometimes called the 'umbrella effect, since the shape of the change over a pole resembles an umbrella. The eddy currents are minimized if the energy is extracted slowly. There will also be eddy currents in the aluminum mandrels supporting the coils. Electrically, this can be represented by a one turn shorted transformer. These eddy currents will heat the mandrels and can cause the entire coil to become normal. This is called quench-back. This has several beneficial effects. The part of the stored energy that is deposited in the coil is deposited uniformly over the entire coil and mandrel assembly. Also, once quench-back occurs, the energy extraction process is dominated by the quenchback and not by the specifics of where the quench occurred. Therefore, the effects of a quench on the reproducablility of the magnetic field should be minimal.

The energy extraction system consists of a switch, resistor, and quench detection electronics. An energy extraction resistor of 8 m) was chosen. Including the resistor leads,

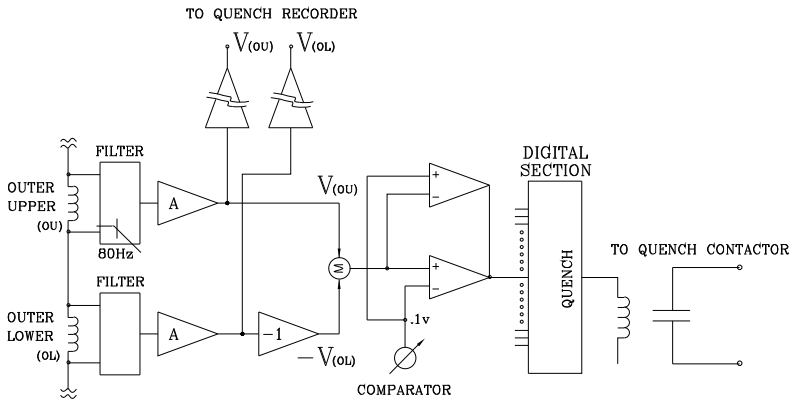

Figure 9.9: Diagram of the quench protection circuit.

the room temperature resistance is 8.8 m). This gives an /R time constant of 1 min. The actual time constant varies due to the temperature increase of the coil and dump resistor and the effect of eddy currents in the mandrels during the energy extraction (see below). This resistance value was calculated to cause quenchback in the outer mandrel within 2 s at full current. The quench protection circuit is shown in Fig. 9.9. The energy extraction trigger for a quench which originates in one of the coils is the voltage difference between matching coils; for example, $V(\text{outer} - \text{upper}) - V(\text{outer} - \text{lower})$. Since the inductance is effectively the same, the voltages should be equal even while charging the magnet, unless a quench develops in one coil. This quench threshold is set at 0.1 V. However, the coil interconnects are thermally coupled together with the helium tubes. It is possible that a quench in an interconnect could propagate to both coils almost simultaneously. Therefore, a voltage threshold of 10 mV was chosen for each interconnect. The outer upper to lower interconnect is only 1 m long. This threshold was set to 5 mV. The thresholds were determined by the requirement that the quench be detected within 0.2 s. The gas-cooled leads develop a voltage of typically 15 mV at full current. If the lead voltage exceeds 30 mV, the energy is extracted.

9.5.2 Preparations Prior to Transportation

No significant changes will be made to the design, and nearly all components are reused from E821. The WBS sections below describe the steps to reassemble and recommission the items above. We will not need to fabricate any parts, other than to replace old components or to build spares.

Prior to the coil transportation, room temperature tests were performed to verify as much as possible the working state of the system. These were:

- Electrical verification of the instruments connected to the coil and/or mandrel. These refer to the temperature probes, voltage taps for quench detection, and strain gauges. The instruments connected to the cryostat consists of thermometers, voltage taps, and strain gauges. There are as indicated in figures 9.10 and 9.11. The strain gauges are attached to the straps, which counteract the Lorentz forces, and the radial stops, which counteract the shrinking of the radial stops due to cooling.

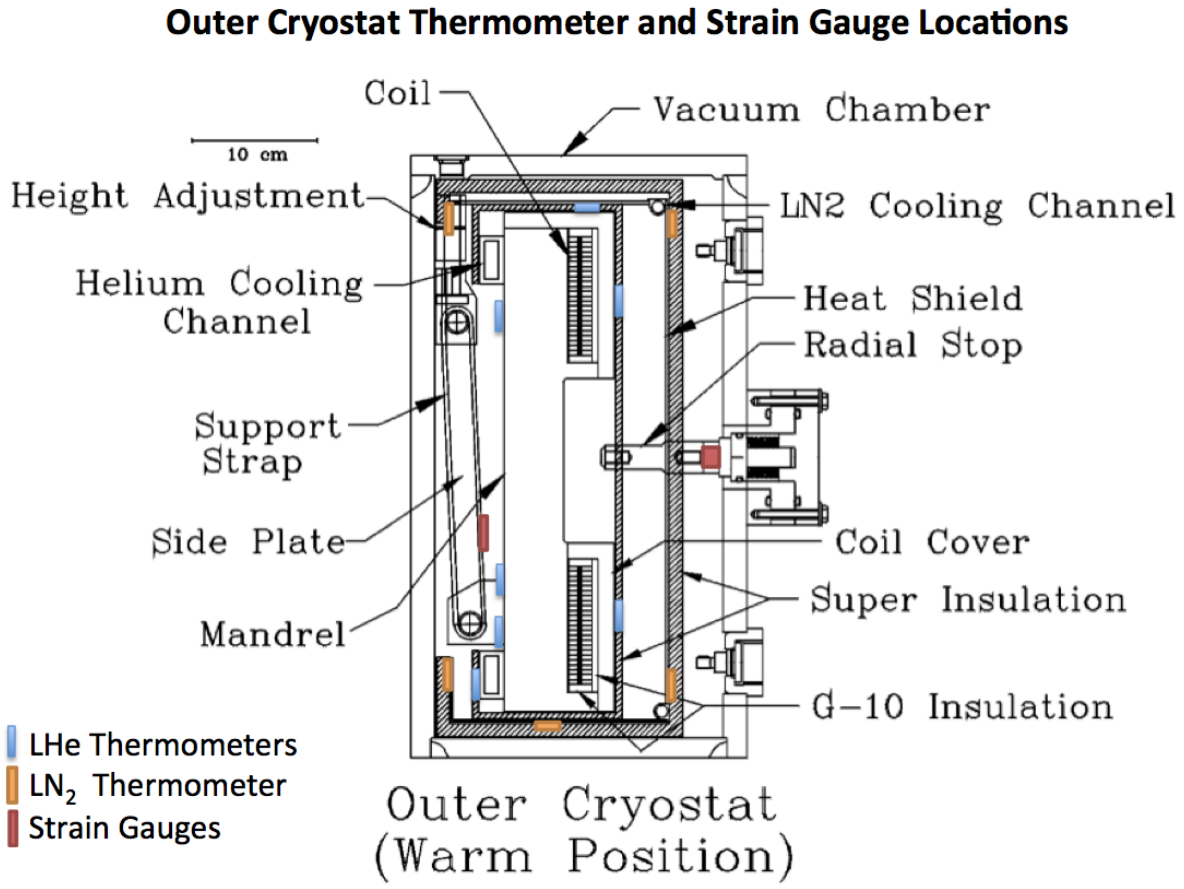

Figure 9.10: Location of outer coil instrumentation, showing the LHe LN_2 thermometers, and strain gauges. For the thermometers, there are typically 8 locations in azimuth at each locations indicated.

- Resistance measurements of the coil at room temperature, which agree with measurements performed in 1995 (see table 9.5).

- The resistance between the coil leads and ground was measured to be a few kohms, where as an open resistance was expected. Further tests showed the 'short-to-ground' occurring at the connection between the inner lower coil and the power supply (see

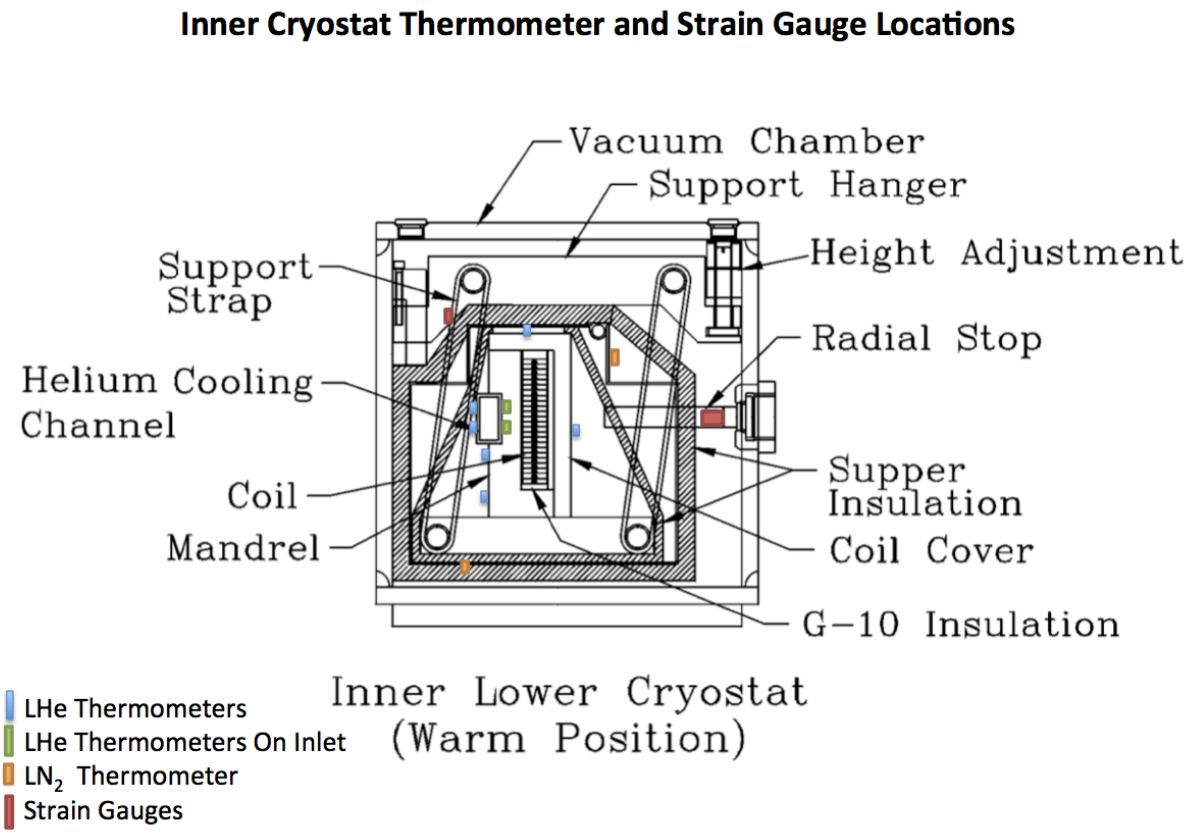

Figure 9.11: Location of the lower inner coil instrumentation, showing the LHe and LN_2 thermometers, and strain gauges. The instrument locations are symmetrically placed for the upper coil instruments. For the thermometers, there are typically 8 locations in azimuth at each locations indicated.

figure 9.15), and is a straight-forward repair. There is no short within the coils themselves. This short was likely present during E821 running, and would have contributed a 0.01 mA current-to-ground, out of a total of 5200 amps. This is 2 ppb effect and would not have been seen in E821 (see references [11] and [12]).

Following this verification, the interconnections between the three coils (see figure 9.12) were separated by a grinding wheel. The temperature was monitored and kept well below 100°C during the process to minimize degradation to the Aluminum resistance and the NbTi current-carrying capacity. Figures 9.13 and 9.14 shows the detail of the welds that were cut in this region.

9.5.3 WBS 476.03.02.03.01 Cryostat Vacuum Chambers

This WBS consists of the vacuum chambers that provide the thermal insulation for the coils. After the interconnects have been rewelded (see section 9.5.7), the vacuum flanges enclosing that region will be reconnected.

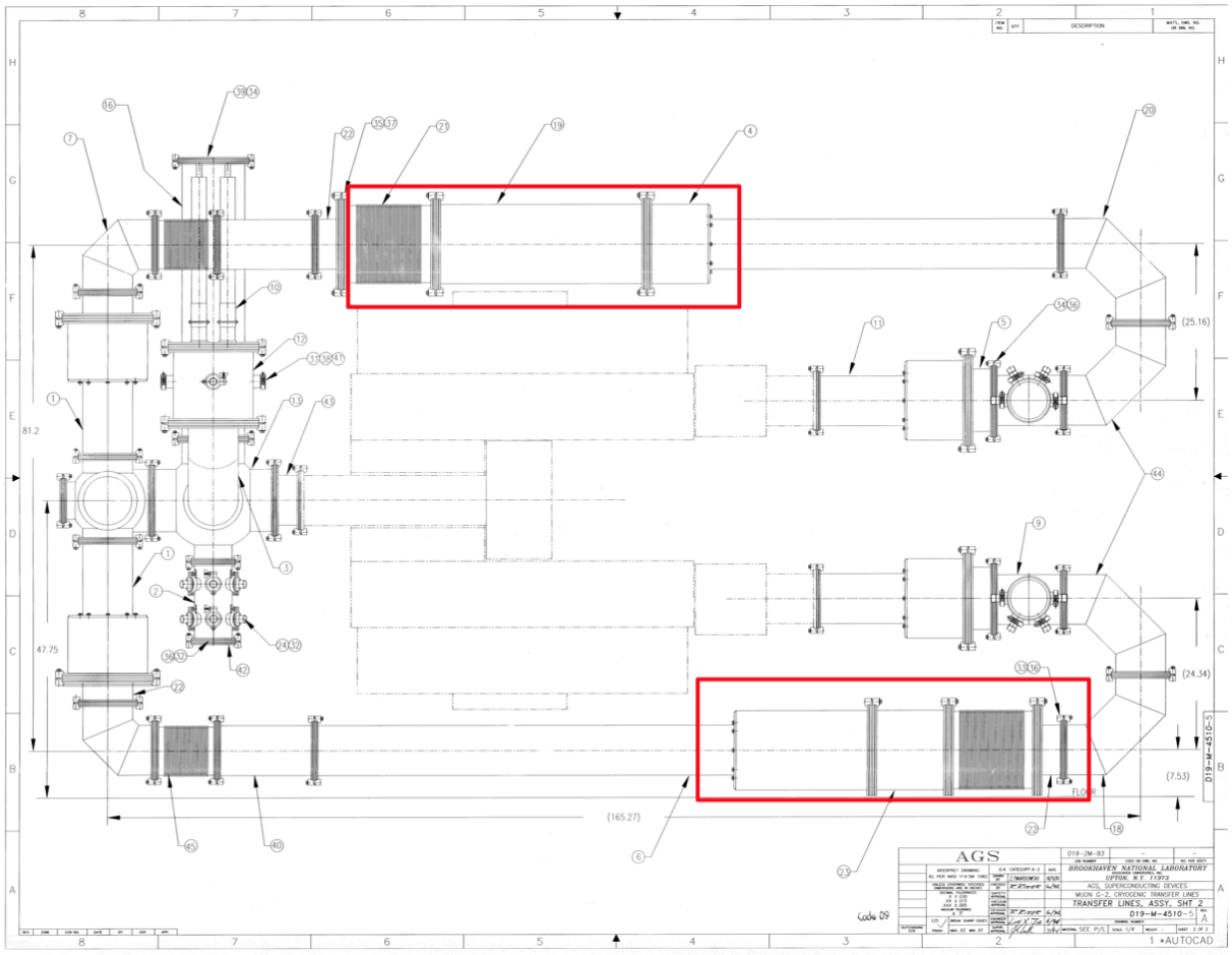

Figure 9.12: The connection between the three coils are indicated. The upper(lower) red box is the connection between the outer-upper (outer-lower) coil and the inner-upper (inner-lower) coil.

For transportation, a vacuum port connected to the outer cryostat will be cut in order to gain clearance. Therefore, this pipe will be rewelded upon reassembly at Fermilab.

9.5.4 WBS 476.03.02.03.02 Vacuum Pumps

New or refurbished 'dry' vacuum pumps will used to pump down the cryostat vacuum chambers. The pumps must remain a few meters away from the storage beam region in order to not perturb the precision magnetic field. The vacuum quality needed is about 10^{-4} Torr (check with Del).

E821 implemented a mechanism described below to deal with a potential failure mode called the 'cold cryostat problem'. In the event of loss of cryostat vacuum while the coils are cold, the cryostat walls will also become cold and therefore will shrink. Such could happen if the cryogenic lines leaked cryogens into the vacuum. However, the cryostat positions are firmly attached to the yoke steel in order to have a well-defined coil position. Therefore, the cryostat wall at the attachment point would experience stresses exceeding the allowable

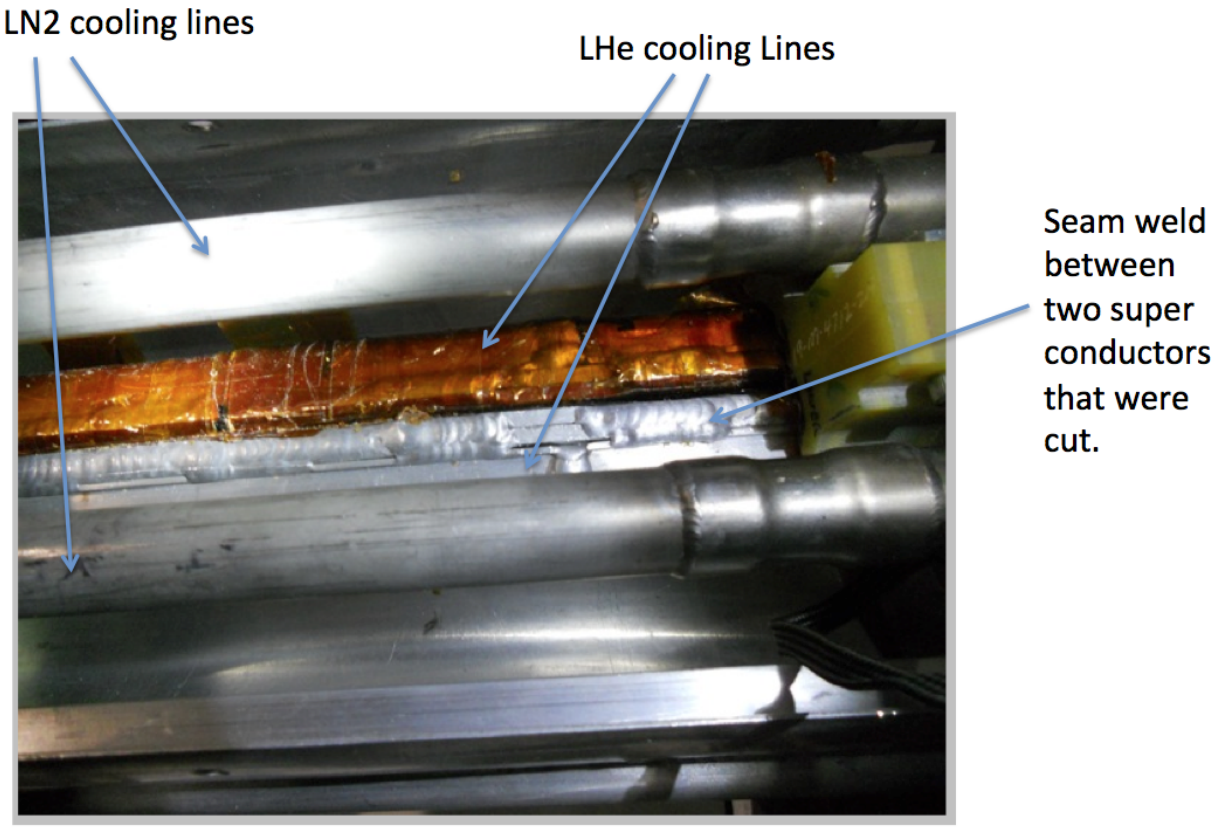

Figure 9.13: Photograph of the region of the interconnection, indicating welds and cooling lines.

value for Aluminum.

For this potential failure scenario, E821 implemented a scheme to trigger a large Roots blower vacuum pump to rapidly evacuate the vacuum chamber.

9.5.5 WBS 476.03.02.03.03 Power Supply and Quench Protection

The power supply for the main ring will be the same unit use in E821 and as described in reference [3]. Therefore the design and specifications will be the same. Once moved to Fermilab, the power supply will be refurbished, tested, and then commissioned for installation and use. A similar process will be used for the quench protection circuitry and components. The voltage taps and quench detection circuitry are located as shown in figures 9.15 and 9.16.

Once the hardware examination and the necessary replacement procedures have been completed, the power supply unit will be tested in stages. This testing process will be done in a staging area and not connected to any other component:

- Stage 1: AC power will be applied to the separate modules of the unit. This is to first check out operation of readout and controls.

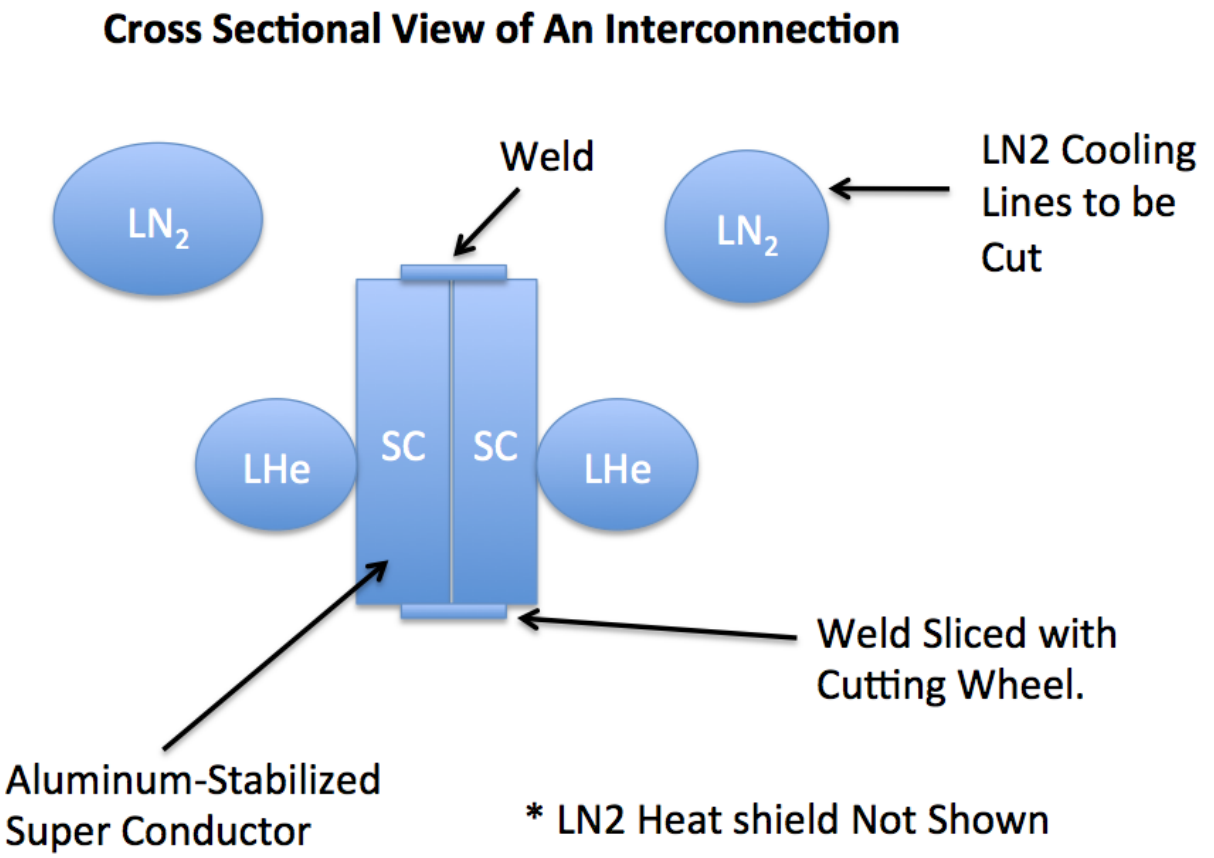

Figure 9.14: Diagram of the region of the interconnection, indicating welds and cooling lines that were cut, in order to facilitate the transportation.

- Stage 2: AC power will then be applied to the complete unit with no DC load connected. This is designed to observe and check out the initial operation and to exercise the controls.

- Stage 3: Once the controls operation is verified, a partial DC load (10-20%) will be applied to exercise the output and to check for stability.

- Stage 4: Add parallel DC loads to the output to slowly bring up the power supply to full power. Once the initial checkout is done, this step will be repeated.

The quench detection voltage threshold used for E821 was 100 mV across the coils, and 10 mV across each interconnect between the outer and inner coils, and 5 mV across the outer upper and outer lower coils. The thresholds were determined by the requirement that the quench be detected within 0.2 s. The gas-cooled leads develop a voltage of typically 15 mV at full current. If the lead voltage exceeds 30 mV, the energy is extracted.

In a similar manner to that used for the power supply, the quench protection circuitry will be examined and refurbished to its original operational state. Testing will also be in stages until the completed unit, along with the transfer switch and dump resistor, operates

Coil	Resistance (ohms) Sept-1995	Resistance (ohms) Dec-2011
Inner Upper	0.429	0.430
Inner Lower	0.426	0.430
Outer Upper	-	0.483
Outer Lower	-	0.476
Outer Upper + Lower	0.952	0.958

Table 9.5: Room temperature coil resistance (ohms) measurements, showing consistency between Sept-1995 and Dec-2011.

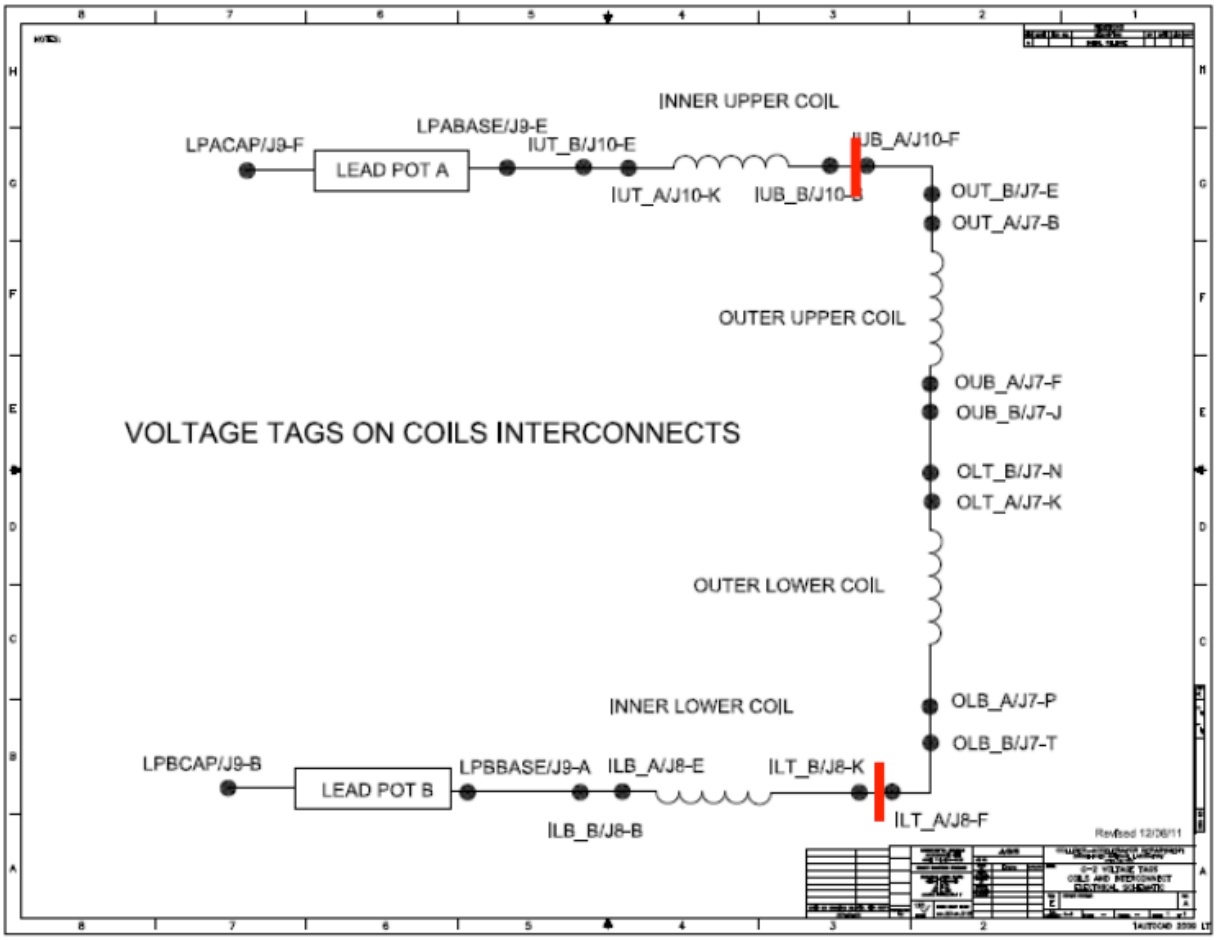

Figure 9.15: Voltage tap locations for quench detection. The red bars indicate the location of the cuts needed for transportation.

as originally designed. This testing will also be in stages and not connected to any ring components.

Similar to E821, the dump resistor will be located outdoors. During energy extraction, approximately 6 MJoules of energy will be dissipated into the dump resistor. If the dump resistor was located indoors, it would raise the air temperature by approximately 2°C. While

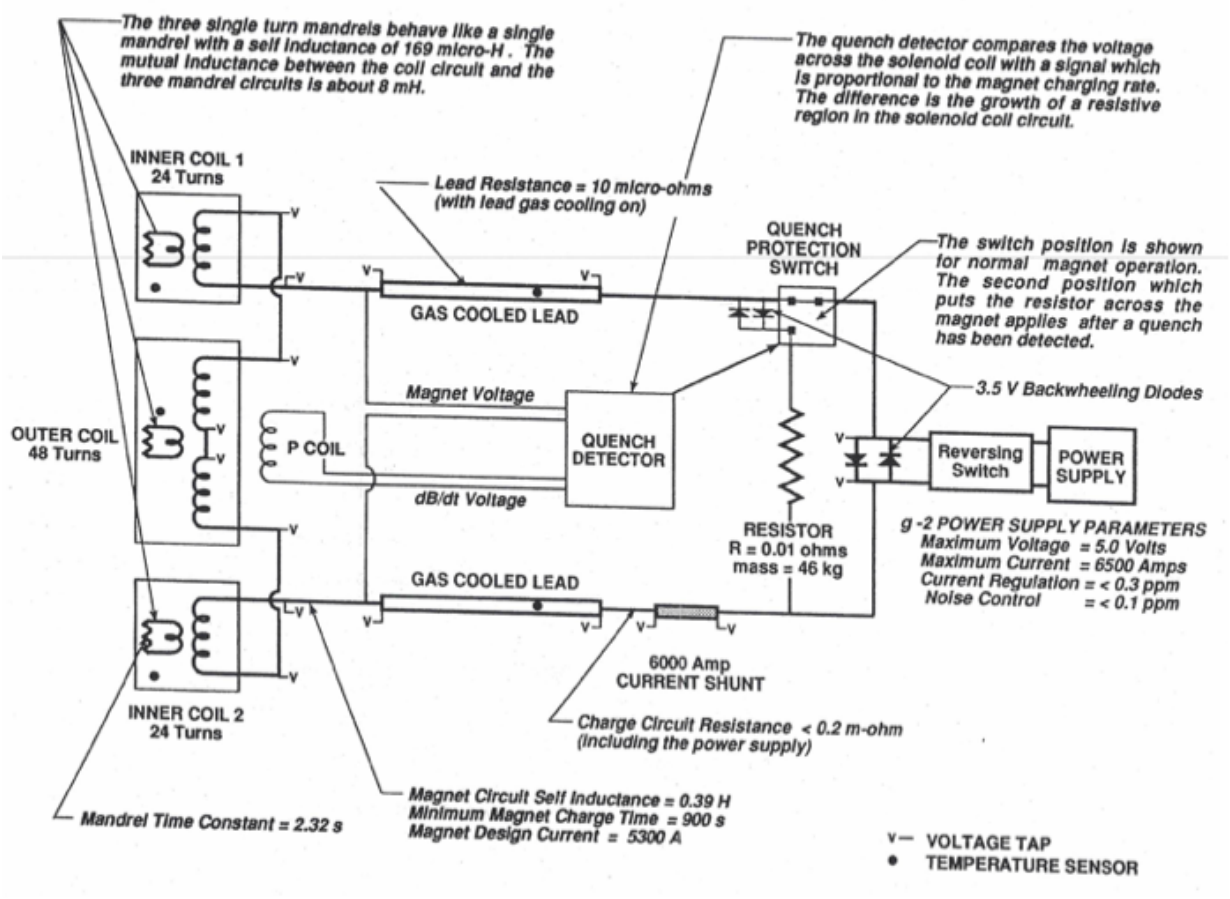

Figure 9.16: Quench detection and power supply diagram.

that can be handled by the building HVAC, it would produce unwanted temperature non-uniformity in the hall.

Once the four main components, power supply, quench protection unit, transfer switch, and dump resistor have been tested individually, reconnection of these components will be done in the staging area. At this time, specific procedures will be developed for reconnection. These procedures will be fully tested and reviewed prior to connection to the main ring coils. A simulated load will be used to mimic operation of the ring coils. At first, this load will be resistive or active linear loads. A desired, but not necessary next step would be to use an existing magnet coil to test all operation.

After these tests are completed satisfactorily, the components will then be moved to the g-2 hall for final assembly and commissioning. The commissioning process will be dependent on the assembly of the main ring. Again, this process should be done in stages of operation (low to medium power, warm to cold coil operation) but these stages need to be defined once the risk to the main ring connections can be identified and reasonably mitigated.

9.5.6 WBS 476.03.02.04 Cryogenics

This WBS refers to the cryogens (LHe and LN_2) required to cool the coils to 4.9K, the cooling lines, the heat shields cooled to LN_2 temperatures, and the flow control valves. The E821 will be reused as much as possible, especially the 1000 liter dewar. The E821 cryogenic flow diagram is shown in figure 9.17.

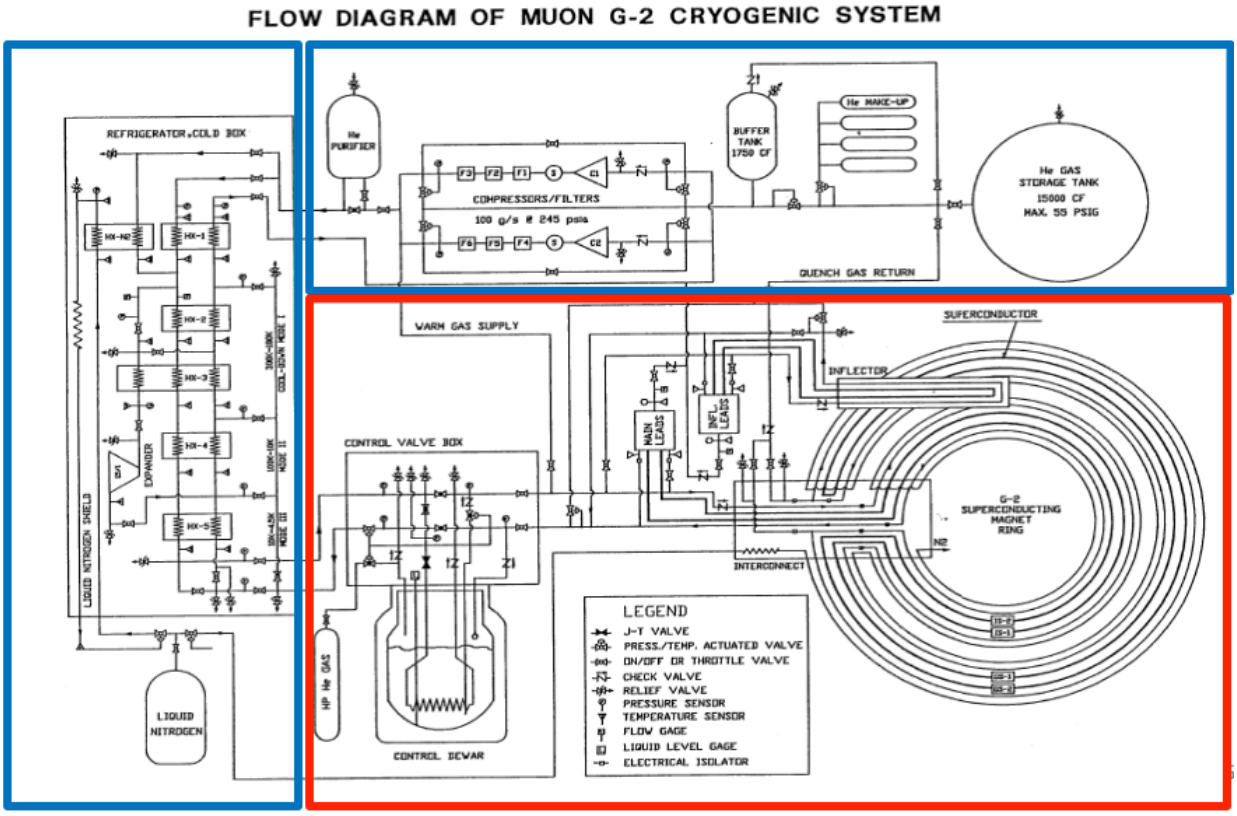

Figure 9.17: The cryogenic plant and its connection with E821 (G-2). The red box outlines the flow within building 919 at BNL. The upper (left) blue box outlines the LHe (LN_2) cryogenic plant.

While no design changes will be made, this WBS requires considerable verification, reanalysis, and documentation due to the significant hazard and stored energy, and the potential for the 'cold cryostat' problem as described in the section above.

The documentation were generated for E821, and will be reaccessed for E989. Attention will be given to:

- Heat load of the system. There will be a slight increase due to the rewelding of the coils at the interconnection (see section 9.5.7) and a slightly longer run between the cryogenic plant and the LHe dewar.
- Flow diagram, pressure drops, and flow rates. These are specified to be identical to that of E821.
- Cool-down and warm-up procedure.

- Connection to the Controls and Instrumentation WBS.

The Fermilab Accelerator Division (AD) will provide two dedicated refrigeration system for E989. An important difference between E821 and E989 is that the latter will share aspects of the cryogenic plant with the Mu2e experiment[13]. Mu2e and g-2 helium gasses are mixed together, and therefore share a common compressor. The AD design includes a cryo adsorber to trap contamination.

9.5.7 WBS 476.03.02.05 Super Conducting Coils

After the steel yoke pieces and coils have been reinstalled into the correct position, the recommissioning activities can begin. The key recommissioning activities for this WBS consists of:

- Performing electrical continuity tests of the instruments such as thermometers and strain gauges.
- Performing electrical continuity tests on the coils. This also verifies unwanted thermal shorts.
- Rewelding the coil interconnects using pure Aluminum filler using the TiG (Tungsten inert Gas) welding technique.
- Rewelding the LHe and LN_2 cooling lines in the interconnection region.

During the interconnect cutting and the TiG rewelding process, a small amount of degradation to the pure Aluminum stabilizer is to be expected due to work hardening. Work hardening will cause a resistance increase of the Aluminum, therefore adding to the heat load at 4.9K and a small local heating at the interconnection region.

It also reduces the critical current capacity (I_c) before the superconductors become normal. For the welding that took place during the E821 construction, the SC coil heating due to welding was modeled. The maximum temperature seen by the SC coils due to welding is 350°C[3]. Degradation of NbTi critical current of $< 5\%$ was measured for a 2T field for an annealing time of 10s at 400°C[9].

For E821, the coil current and temperature were approximately 5200 amps and 4.9K respectively. The magnetic field at the coil was approximately 2T. The critical temperature was estimated to be 6.2K, giving a safety margin of 1.2K[10]. However, the magnetic field at the interconnect is estimated to be < 1T, and so the safety margin at the interconnect is even greater.

E821 also welded a test overlap joint, and measured a cold resistance of $16 \cdot 10^{-9}$ ohms at 2T. At the current of 5200 Amps, the heat load is 0.43 Watts at 4.9K, as compared to the heat load of 351W at 4.9K (see table 5 of reference [3]).

In summary, the coils were designed with a rather large safety margin. No quenches were observed to have taken place at the interconnects. To be conservative, we will measure the resistance properties of an overlap weld, cut it and reweld, and remeasure the resistance properties. Finally, work hardening of the Aluminum is strongly anti-correlated with yield strength[14]. Therefore, room temperature tests can be performed to gauge the level of work hardening.

9.6 ES&H, Quality Assurance, Value Management, Risks

9.6.1 Yoke, Pole, and Shims

The hazards will be in the stored mechanical energy of these very heavy items during the use of the crane during installation. While the magnet is powered, the super bolts will be stressed (stretched) to counteract the magnetic forces' tendency to close the pole gaps. The stored electro-mechanical energy is approximately 6 MJoules. The storage region magnetic field of 1.45T is also a hazard.

Mitigation would be to train the collaboration in proper procedures, controlling access to the area, and implementing a mechanism for detecting high magnetic susceptibility materials so that they are kept away from the high field area.

Quality assurance, value management, and risks concerns are minimal since these items have been built and worked to specifications for E821. They are also passive material and have high mechanical strength. Since considerable E989 machinery has already developed to model the magnetic field, temperature, we can simulate all alignment requirements.

9.6.2 Power Supply and Quench Protection System

Hazards

The hazards during the testing processes will be primarily electrical. There will be an arc-flash hazard based on the incoming 480 VAC power feed and at 60-amps. A complete hazard analysis can be made once the units are received and initially examined. The mitigations for these hazards are:

- In the staging area, a safety disconnect switch will be used to provide emergency shut-off of power to the power supply.
- No operation of any component will be done unattended. There will always be 2 persons minimum present during any operation and testing.
- Only properly trained persons, Electrical NFPA-70E and LOTO II at a minimum, will be allowed to work on the equipment.
- Proper PPE and distances will be observed during operation and testing, especially during initial power up and during full-load operation. The level of PPE will be determined once the staging area is set up.

Risks

Risks to the successful completion of the tasks:

- Use of Obsolete Components: Level-Medium. This risk involves the use of relatively old electronics. Therefore, component failure probability (based on hours of previous operation and power cycles, will need to be assessed for critical components of the power supply. Mitigation, at a minimum, will be to list these components and acquire

spares in case of failure. To minimize the effect this risk will have on the schedule, the component list will be generated in parallel with the other operations. Initial costs will be incurred to acquire these spare components.

- Catastrophic Failure During Testing: Level-Low to Medium. The units have operated before and they operated as initially designed. Therefore, testing of the components and of the units in stages should provide early indications of failure and allow replacement before the start of connection and commissioning.

- Difficulty in Acquiring the Proper Testing Equipment: Level-Low. At this time, most equipment needed for testing, is, or should be, readily available on site. Therefore, purchases of new equipment will be at a minimum.

- Catastrophic Failure During Commissioning: Level-Low. The risk here would be the most critical since failure of any component while connected to the ring coils would also present risk to the coils themselves. Mitigation here would be the exhaustive testing of components prior to connection to the ring and the powering up of the ring in stages of load and cooling. In addition, specific procedures for connection to the rings leads will be repeatedly and continuously reviewed.

Quality Assurance

The assurances that the units will operate as required are two-fold: First, the design is already done. Redesign should be at a minimum. Second, there will be exhaustive testing of each component prior to re-assembly. These testing procedures will be continuously reviewed during and after each stage of testing. Again, the primary process for all this is the initial examination followed by testing in stages as opposed to a one-time, massive final test. The staged testing allows deficiencies or problem areas to be identified at the earliest possible point in the task schedule. This again stresses the importance of the initial examination for the results of this will determine, in large part, the testing schedule.

Value Management

As much reuse of components will be implemented throughout these processes. Also, preliminary examination will serve to spot questionable components. Overall, the refurbishment process is used to minimize the need to purchase or redesign components and systems. Since the design is already done and it did operated as designed, the risk and extra effort in developing a new design can be kept to a minimum.

9.6.3 The Cryogenic and Related Systems

The hazards are related to the use of LHe and LN_2 cryogenics: thermal energy and ODH. As described above, if the cooling lines in the vacuum cryostat leak, there is potential for the 'cold-cryostat' scenario (see above). These can be mitigated in the same fashion as E821. The cooling lines and vacuum chambers can be pressure tested at room temperature, following delivery from BNL and prior to use.

Quality assurance, value management are minimal since these items have been built and worked to specifications for E821. Should the items fail during recommissioning, they can be easily replaced since they are commercially available items of reasonable cost. These are vacuum parts and cryogenic lines. The only outstanding technical skills required are Aluminum welding and vacuum leak-testing.

There are inherent risks in nearly all cryogenic systems since these are usually very complex and have long time scales. Even though E821 operated a successful system, significant engineering is required for recertification. A mitigating factor is that similar systems have been built at Fermilab, and is inline with the expertise of the project mechanical engineer.

9.6.4 The Superconducting Coil System

The coils system do not present a significant health hazard. Quality assurance and value management concerns are minimal since these items have been built and worked to specifications for E821.

The risks are not considerable. The risk of damage to the coils, straps, heat shields, glue joints are minimal since the stresses expected during transportation is at least 4x smaller than the maximum allowable stress. The expected stresses and deflections due to transportation have been simulated by FEA.

However, we itemize them here since the replacement cost of the coils is beyond the scope of the project:

- The coil windings are on the inside radial surface of the mandrel, rather than on the outside. During power up, the coils push against the mandrel, thereby enhancing the thermal cooling. Therefore, the system can tolerate failures of the glued interface, which is designed to enhance thermal conductivity.

- Failure of the straps, though unexpected, can be detected as we slowly energize the coils. If a strap fails, it can be detected as a shift in the coil vertical position. It can be repaired by cutting an access hole in the vacuum cryostat. The downtime would be of order 2 weeks.

- Failure in the heat shield can be detected as the system taking too long for cool down. Failure of the cooling lines can be detected as loss of vacuum. These are repaired via cutting access holes into the vacuum cryostat. However, it will be difficult to locate the point of failure.

- There is a very slight risk of the Aluminum resistance at the interconnection becomes too high during the reweld. We will prototype the rewelding process and study the correlation of resistance with yield strength. We can anneal the interconnection to improve the resistance.

References

[1] Bailey J, et al. Nucl. Phys. B150:1 (1979).

[2] Bennett GW, et al.(The Muon $(g-2)$ Collaboration) Phys. Rev. D, 73:072003 (2006).

[3] G.T. Danby, et al., Nucl. Inst and Meth. **A 457**, 151 (2001).

[4] Reference Manual for teh POISSON/SUPERFISH group of codes, LANL, LA-UR-87-126.

[5] Design Report, BNL E821, A New Precision Measurement of the Muon $(g-2)$ Value at the level of 0.35 ppm. 3rd edition, D.H. Brown et al. B.L. Roberts Editor, March 1995.

[6] A. Yamamoto, H. Inoue, H. Hirabayashi, J. Phys. 45 (1984) C1-337.

[7] A. Yamamoto, private communication.

[8] M.A. Green et al., Operation of a two-phase cooling system on a large superconducting magnet, Proceeding of the Eighth International Cryogenic Engineering Conference, Genoa, Italy, June 1980, IPC Science and Technology Press, 1980, p. 72.

[9] Th. Schneider and P. Turowski, Thirteenth International Conference on Magnet Technology, Victoria, Canada, September 1993, Paper R-J-07.

[10] Bill Morse, Characteristic of the E821 Interconnects, GM2-doc-302-v1.

[11] Bill Morse, Coil Resistance to Ground Measurements, GM2-doc-352-v1.

[12] Bill Morse, Coil Resistance to Ground Measurements, GM2-doc-976-v1.

[13] Del Allspach, Vacuum and Cryogenics Presentation at g-2 December 2012 Collaboration Meeting, GM2-doc-615-v1.

[14] T. Tonogi et. al., Aluminum Stabilized Superconductor for the Atlas Central Solenoid Magnet, Hitachi Cable Review No. 18, V87.

Chapter 10

The Superconducting Inflector Magnet

In this chapter we first introduce the E821 inflector magnet, which is our baseline starting option. We then describe the shortcomings of this magnet, as well as the characteristics and the benefits that an improved inflector would have. Any new design will require significant R&D and opera simulations to arrive at a new inflector design.

10.1 Introduction to the Inflection Challenges

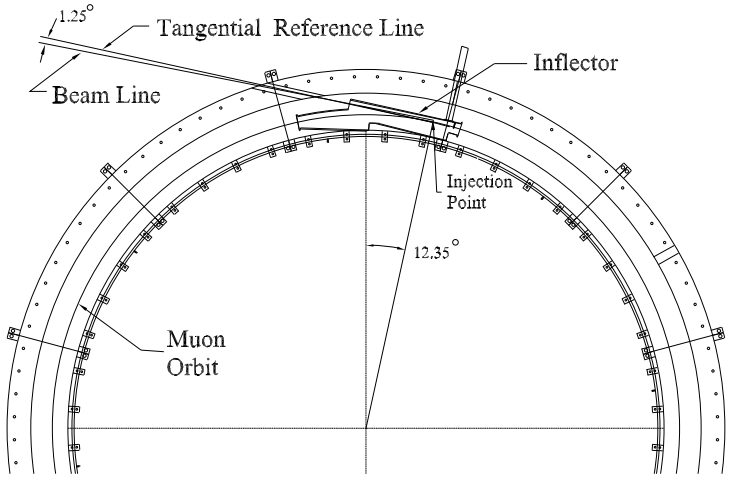

Figure 10.1: Plan view of the beam entering the storage ring.

The usual storage ring is composed of lumped beamline elements such as dipoles, quadrupoles, sextapoles, etc., which leaves space for injection, extraction, and other beam manipulation devices. For the measurement of a_μ, the requirement of ± 1 ppm uniformity on the magnetic field, which in E989 must be known to $\leq \pm 0.07$ ppm, prohibits this usual design. Instead, as described in Chapter 9 the $(g-2)$ storage ring is designed as a monolithic magnet with

no end effects. The "C"-magnet construction shown in Fig 9.1 presents several obstacles to transporting a beam into the storage ring: There must be holes through the back-leg of the magnet and through the outer coil cryostat and mandrel for the beam to enter the experiment. These holes must come through at an angle, rather than radially, which complicates the design, especially of the outer-coil cryostat.

A plan view of the beam path entering the storage ring is given in Fig. 10.1. Since the beam enters through the fringe field of the magnet, and then into the main 1.5 T field, it will be strongly deflected unless some magnetic device is present that cancels this field. This device is called the inflector magnet.

The injection beam line is set to a 1.25° angle from the tangential reference line (Fig. 10.1). The inflector is aligned along this reference line and its downstream end is positioned at the injection point. The point where the reference line is tangent to the storage ring circumference is 77 mm radially from the muon central orbit. The main magnet fringe field, upstream of the inflector, bends the incoming beam by about 1.25°, so that the beam enters the inflector nearly parallel to the inflector axis.

The requirements on the inflector magnet are very restrictive:

1. To a good approximation it should null the storage ring field such that the muons are not deflected by the main 1.5 T field.

2. It should be a static device *to prevent time-varying magnetic fields correlated with injection*, which could affect $\int \vec{B} \cdot d\vec{\ell}$ seen by the stored muons and produce an "early to late" systematic effect.

3. It cannot "leak" magnetic flux into the precision shimmed storage-ring field that affects $\int \vec{B} \cdot d\vec{\ell}$ at the sub-ppm level.

4. It cannot contain any ferromagnetic material, which would distort the uniform magnetic field.

5. The inflector angle in the cryostat should be variable over the full range permitted by the constraints of the space available.

10.2 The E821 Inflector Design and Operation

Three possible solutions were considered in E821: A pulsed inflector, a superconducting flux exclusion tube, and a modified double $\cos\theta$ magnet. The pulsed inflector proved to be technically impossible at the repetition rate necessary at BNL. Furthermore it violates item 2 above. Naively one could imagine that a superconducting flux exclusion tube would work for this application. However, an examination of Fig. 10.2 shows that in the vicinity of the tube, the magnetic field is perturbed on the order of 10%, or 100,000 ppm [1], an unacceptable level. Attempts to figure out how to mitigate this problem were unsuccessful. This is because the large eddy currents needed to shield the 1.45 T field are large enough to affect the uniformity of the field seen by the muons contained in the red semicircle. However, this principle will re-appear in the discussion of how to shield the 200 G (20 mT) residual magnetic field from the truncated double $\cos\theta$ design employed in the E821 inflector. The properties of the E821 Inflector are summarized in Table 10.1

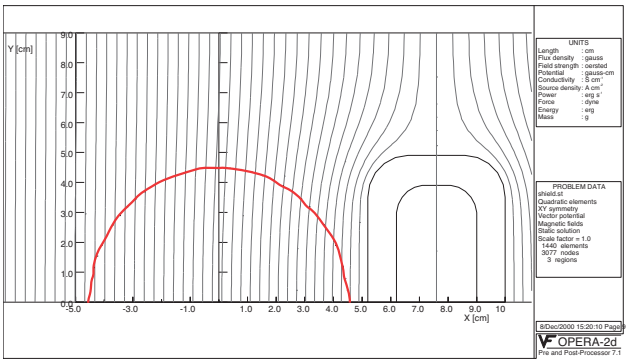

Figure 10.2: The calculated magnetic field outside of a superconducing flux exclusion tube placed in a 1.45 T magnetic field. The red circle is the muon beam storage region. (From Ref. [1])

Table 10.1: Properties of the inflector superconductor.

Overall dimension	110(W)× 150(W)×2025(L) mm^3
Magnetic length	1700 mm
Beam aperture	18 mm (W) × 56 mm (H)
Design current	2850 A (with 1.45 T main field)
Number of turns	88
Channel field	1.5 T (without main field)
Peak field	3.5 T (at design current, with main dipole field)
Inductance	2.0 mH
Resistance	1.4 Ω (at 300 K)
Cold mass	60 kg
Stored energy	9 kJ (at design current)

Table 10.2: Properties of the inflector superconductor.

Configuration (NbTi:Cu:Al)	1:0.9:3.7
Stabilizer	Al (99.997% RRR = 750
Process	Co-extrusion
NbTi/Cu composite	Diameter 1.6 mm monolith
NbTi filament	Diameter 0.02 mm
Number of filaments	3050
Twist pitch	31 mm
Conductor dimension	2×3 mm^2
Insulated conductor dimension	2.3×3.3 mm^2

10.2.1 Magnetic Design of the E821 Inflector

Only the double $\cos\theta$ design[2] satisfied the three criteria listed above. The double $\cos\theta$ design has two concentric $\cos\theta$ magnets with equal and opposite currents, which outside has negligible field from Ampère's law. A double $\cos\theta$ design provides a 1.5 T field close to the storage region, and traps its own fringe field, with a small residual fringe field remaining. However, what is needed for the $(g-2)$ beam channel is a septum magnet. This is achieved by truncating the two $\cos\theta$ distributions along a line of constant vector potential A [2]. The truncation method is shown in Fig. 10.3, taken from Ref. [2], which should be consulted for additional details.

Aluminum-stabilized superconductor was chosen for the BNL $(g-2)$ inflector: (a) to minimize the interactions of the incoming pion/muon beam at both upstream and downstream ends of the coil with no open apertures for the beam, and (b) to make the coils and cryostat design compact, so that the conductive cooling (without liquid helium containers surrounding the coils) can be achieved effectively. An existing Al-stabilized superconductor was supplied by Japan KEK (fabricated by Furukawa Co.). This conductor was developed for ASTROMAG (Particle Astrophysics Magnet Facility) [3, 4]. Fig. 10.4 shows the cross-

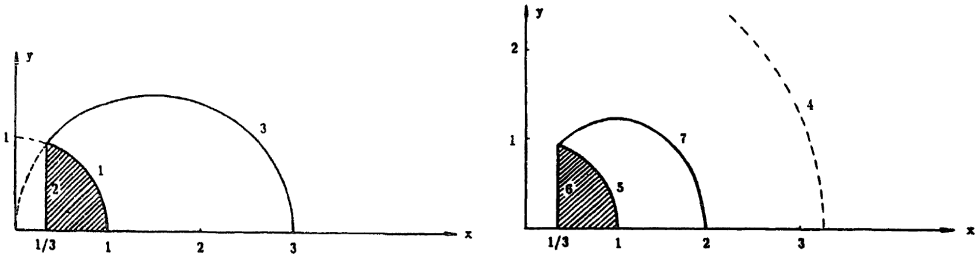

(a) Truncated Single $\cos\theta$ (b) Double Truncated $\cos\theta$

Figure 10.3: (a) The principle of the truncated single $\cos\theta$ magnet. (b) The principle of the truncated double $\cos\theta$ magnet.

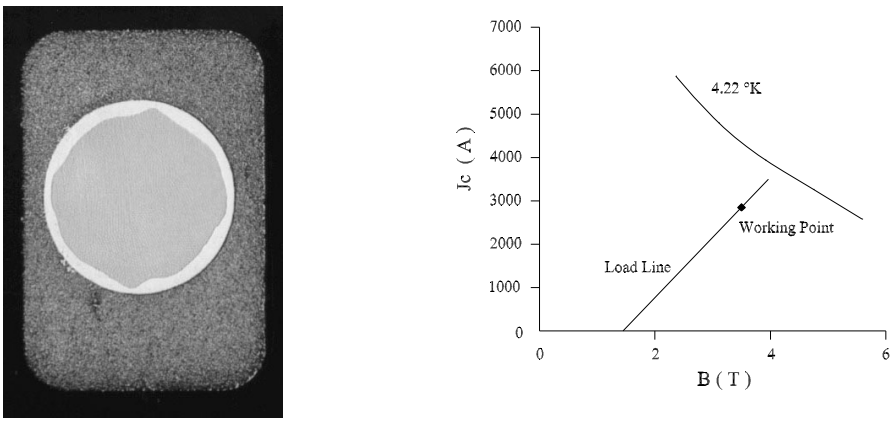

(a) SC cross-section (b) Inflector Load Line

Figure 10.4: (a) The inflector superconductor cross-section. (b) Superconductor characteristics and the inflector load line in the environment of 1.45 T magnetic field.

section of this conductor. The basic parameters are listed in Table 10.2. From computer calculations, the peak field seen by the by the inflector conductor filaments reaches 3.5 T; if the self-field effect [5] is taken into account. This is due to the superposition of the return flux and the main field. Short sample tests showed that the critical current of this superconductor is about 3890 A at 4.6 K and 3.5 T. In the $(g-2)$ storage ring, the inflector sees 1.45 T field (from the main magnet) even at zero operating current. From the conductor characteristics, the inflector operates at around 73% of the full load (at 4.6 K). The short sample test data and the inflector load line (in the storage ring field environment) are shown in Fig. 10.4(b).

The result is a magnet with conductors arranged as shown in Fig. 10.5(a). The conductors are connected in series, with an equal number with current into and out of the page. In Fig. 10.5(a) the current is flowing out of the page in the backward "D" shaped pattern of conductors, and into the page in the "C" shaped arrangement of conductors. The field from

the inflector magnet is vertical up in the beam channel and downward in the return area, as shown in Fig 10.5(a). With the main storage ring field vertical, there is no field in the beam channel and $\simeq 3$ T field in the return area. With this design and the ASTROMAG conductor, it is difficult to open up the beam channel very much because moving the "C" arrangement of conductors to the left would quickly exceed their critical current.

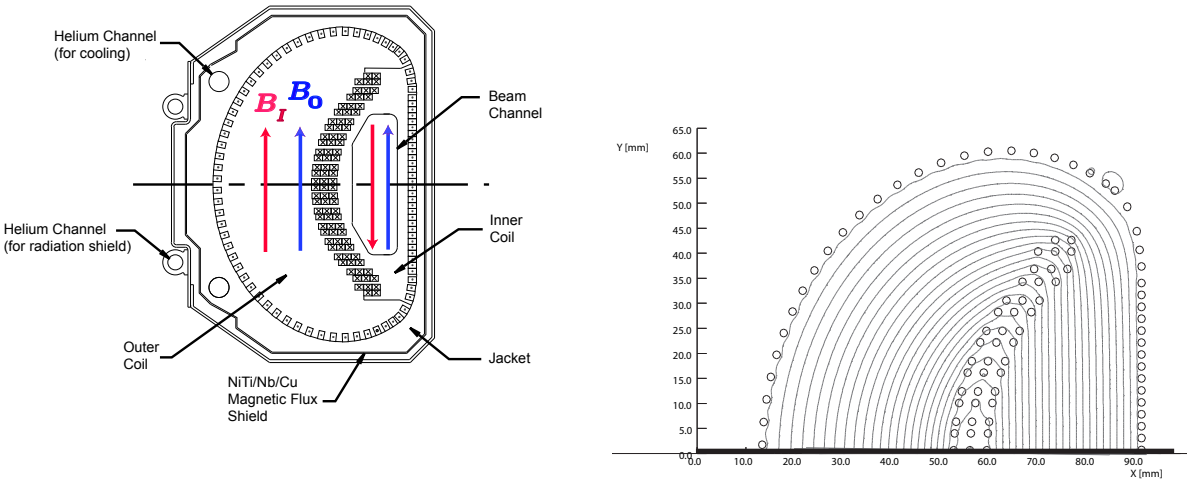

(a) Inflector Conductor Arrangement (b) Calculated Field

Figure 10.5: (a) The arrangement of conductors in the inflector magnet, showing the direction of the inflector field B_I and the main field B_0 for a beam of positive muons going into the page. The current in the inner "C" is into the page and is out of the page in the backward "D". (b) The magnetic field generated by this arrangement of conductors. The beam aperture is 18×56 mm^2.

There are two sources of magnetic flux that from the inflector that can leak into the storage region. Because the field is produced by discrete conductors, rather than a continuous current distribution, some flux does leak out of this arrangement of conductors, see Fig. 10.5(b). The inflector lead configuration is also important, and when it was necessary to produce a second inflector, the lead configuration was changed to reduce this effect.

The coil was wound in two different pieces indicated by "inner" and "outer" coils in Fig. 10.5(a). One end of the coil is shown in Fig. 10.6(a) The choice was made to wind the coil over the beam channel, because this configuration would have less flux leakage, and was thought to be more stable from quenches. However, a 0.5 m prototype was constructed with one open and one closed end, which are shown in Fig. 10.6. This prototype inflector was operated in the earth's field, and then in an external 1.45 T field without incident.

The inner coil and the outer coil are connected in series. The joint is located inside the downstream end of the coils; and is made by soldering the superconductors without removing the aluminum stabilizer. The joined leads were placed inside a U-shaped groove, as shown in Fig. 10, attached to the coil end structure. Cooling tubes run through the extender

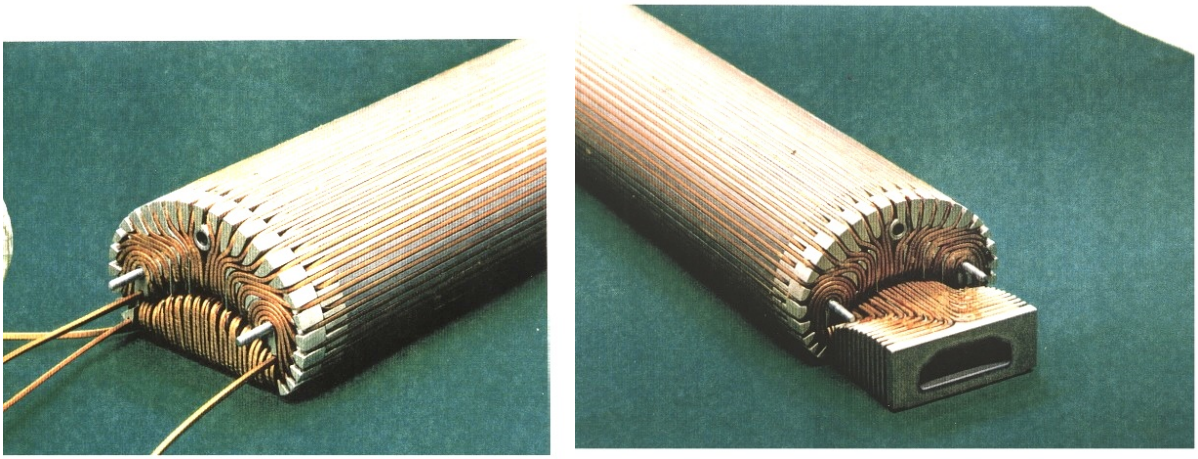

(a) Closed Inflector End (b) Open Inflector End

Figure 10.6: (a) The prototype closed inflector end. (b) The prototype open inflector end.

(aluminum block). One temperature sensor was mounted near the joint to monitor the local ohmic heating.

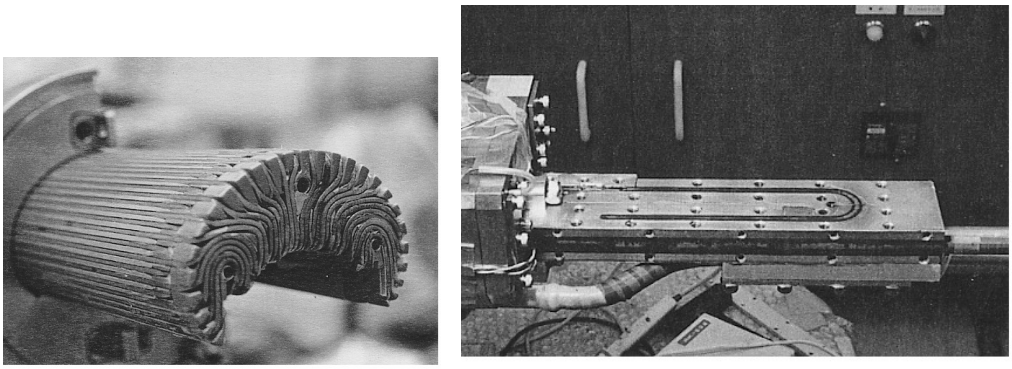

(a) Outer Inflector Coil (b) Coil Interconnect

Figure 10.7: (a) The arrangement of conductors in the inflector magnet.(b) The joint and lead holder for the interconnect.

The geometry of the inflector cryostat is complicated by the proximity of the outer-coil cryostat, the pole pieces and the muon beam. A sketch of the beam path through the outer coil is shown in Fig. 10.8(a). The complicated arrangement where the inflector entrance nests into the concave wall of the inflector cryostat is shown in Fig. 10.8(b). Fig. 10.9 shows the combined inflector cryostat and beam vacuum chamber. The cryostat region and beam region have different vacuums, so the inflector can be cooled, independent of whether the beam vacuum chamber is evacuated or not.

The exit of the inflector magnet is shown in Fig. 10.10, which clearly indicates the accelerator physics issue. The incident beam is contained in the red 18 mm $\times$ 56 mm "D"-shaped

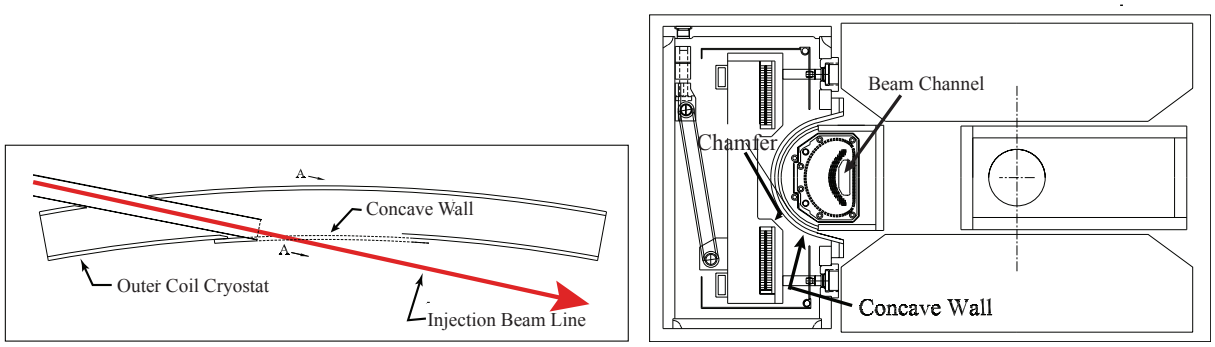

(a) Outer Coil Penetration (b) Inflector Entrance

Figure 10.8: (a) A plan view of the beam penetration through the outer coil and cryostat. (b) An elevation view of the inflector entrance showing the concave wall of the outer-coil cryostat where the beam exits the outer coil-cryostat.

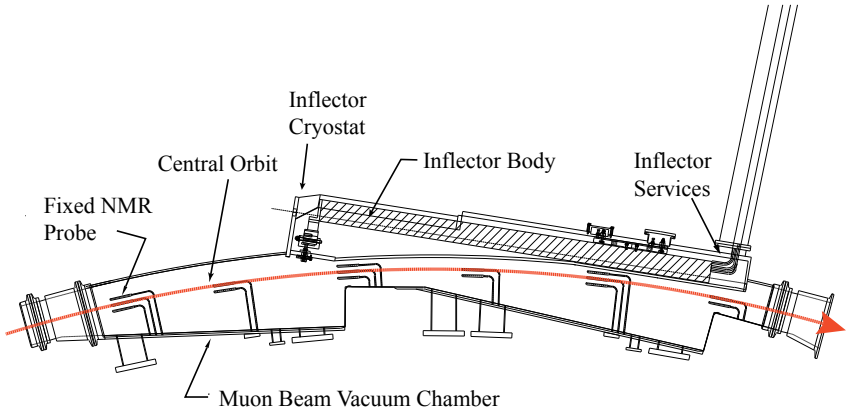

Figure 10.9: Plan view of the combined inflector cryostat-beam vacuum chamber arrangement. The inflector services (power, LHe and sensor wires) go through a radial hole in the back-leg outside of the storage-ring magnet. The NMR fixed probes are in grooves on the outside of the vacuum chambers, above and below the storage region. The red arrow shows the muon beam central orbit.

channel, while the stored beam is confined to a 45 mm diameter circular aperture. Thus it it impossible to match the β or α functions between the ring and the muon beamline. The result is a "β wave" that causes muon losses after the beam is injected.

10.2.2 Shielding the residual fringe field

At the design current, the maximal fringe field within the muon storage region was calculated to be about 200 G (1.4%) near the outer edge. The fringe field behaves in such a way that it is a rapidly varying function along the transverse direction, i.e. the radial direction of the

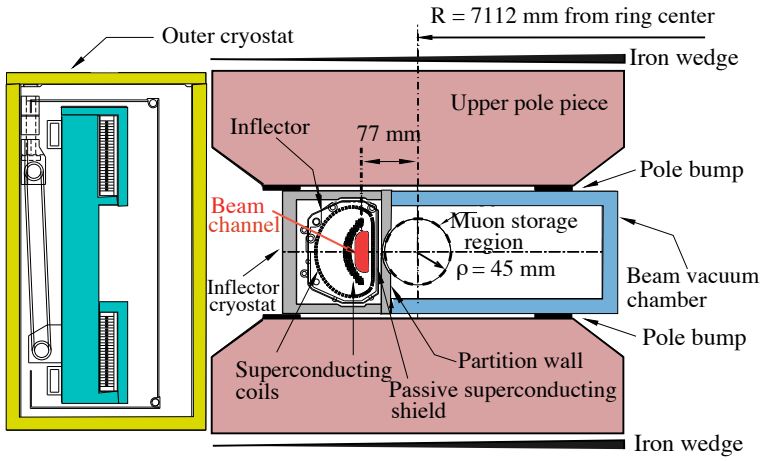

Figure 10.10: The inflector exit showing the incident beam center 77 mm from the center of the storage region. The incident muon beam channel is highlighted in red. (Modified from Fig. 9.6)

storage ring, and essentially gives a negative disturbance. The fringe field of the inflector is opposite to the main field at the outer radius of the storage ring, and changes sign while crossing the central orbit.

The consequence of such a fringe field is severe. The high gradient of the field would be beyond the working range of the NMR probes, so that the magnetic field map of the storage region would be incomplete, directly impacting the error of the measurement precision of the muon magnetic moment.

Conventional magneto-static shimming studies to reduce this fringe field using computer simulations were carried out. The iron compensation must be located outside the muon storage region. Its contribution to the central field will be a slowly varying function in this space, which is not able to cancel the larger gradient fringe field to an acceptable level [10]. The best way to eliminate a multipole fringe field is to create an opposite multipole current source with the same magnitude. The best such current source is the super-current generated inside a superconducting material due to the variation of the surrounding field. A method of using SC material to shield the inflector residual fringe field was studied and developed. The fringe field specification was then satisfied.

A test sheet of a superconducting shield was developed that contained 30 layers NbTi, 60 layers Nb, and 31 layers Cu. The Cu layers greatly improved the dynamic stability against flux jumping [7]. The Nb layers act as barriers, which prevent the diffusion of Ti into Cu. The diffusion could form hard inter-metallic layers and create difficulties for the rolling process. Fig. 10.11 shows the typical cross section of the sheet. Based on successful tests, Nippon Steel Corp. developed large, thin pieces of sheet especially for the $(g-2)$ inflector, to cover its 2×0.5 m^2 surface and to fit into the limited space between the storage region and main magnet coil. The shielding result was extremely satisfactory.

The steps in using the shield are as follows:

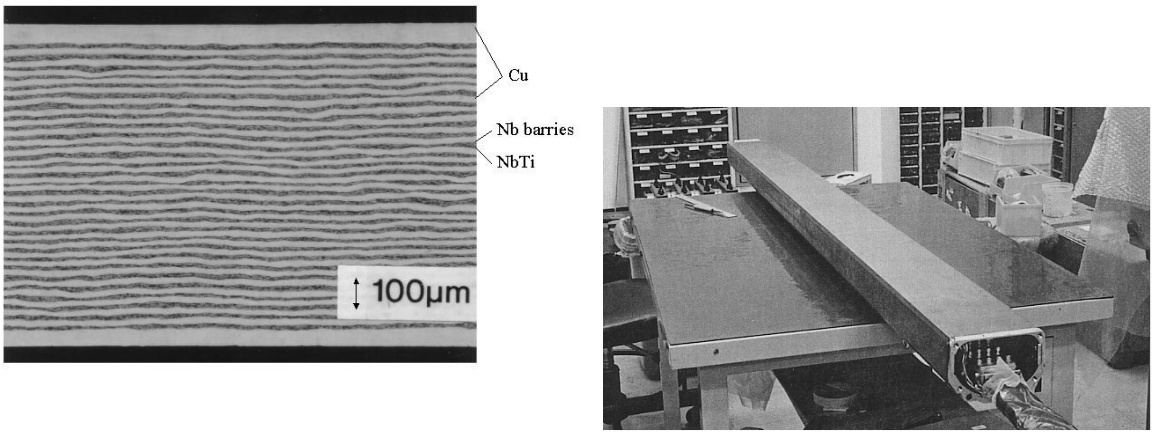

(a) SC shield X-section

(b) SC shield installed

Figure 10.11: (a)Cross section of the multi-layer superconducting shield sheet. (b)The superconducting shield installed around the body of the inflector.

1. With the inflector warm ($\sim$ 20 K) the storage ring magnet is powered and allowed to reach equilibrium.

2. The inflector is then cooled to superconducting. The shield material is a Type-II super conductor, where $H_{C1} = 0.009$T for NbTi is the maximum field for the Meissner effect to occur. Therefore, as it is cooled down to the superconducting state, the shield is not able to expel the external field. Rather, the external field will fully penetrate the shield. and the shield traps the main field

3. The inflector is then powered. In this superconducting state, the shield will exhibit perfect diamagnetism, and will resist any change in the flux penetration through its surface.

10.2.3 Performance of the E821 Inflector

Two full-size inflectors were produced. To emphasize the importance of the superconducting shield, we relate what happened when the shield on the first inflector was damaged. In the testing of the first inflector, an accident occurred, where the interconnect shown in Fig. 10.7(b) was melted, leaving a few centimeters of undamaged cable outside of the inflector body. In order to repair it, the superconducting shield was cut to give access to the damaged superconductor. After the repair, an attempt was made to apply a patch to the shield. Unfortunately this attempt was not completely successful. The resulting fringe field reduced the storage-ring field by 600 ppm (8.7 G) over a 1° azimuthal angle, resulting in unacceptable magnetic-field gradients for the NMR trolley probes closest to the inflector body. It was also realized that a significant fringe field came from the inflector leads. An average field map from the 1999 run using the damaged inflector, and from the 2001 run using the new inflector

are shown in Fig. 10.12. The field in the region with large gradients had to be mapped by a special procedure following data taking. This large fringe field introduced an additional uncertainty into the average field of ±0.20 ppm in the result [12]. While this additional error in the 1999 result, which had a 1.3 ppm total error, it would have been completely unacceptable for the subsequent runs.

The damaged inflector was replaced in mid 1999, well before the 2000 running period. Two modifications were made to the new inflector design: The superconducting shield was extended further beyond the downstream end; The lead geometry was changed to reduce the fringe field due to the inflector leads. Both of these improvements were essential to the excellent shielding obtained from the second inflector. For both the 2000 and 2001 running periods, the fringe field of the inflector was immeasurably small [15, 16].

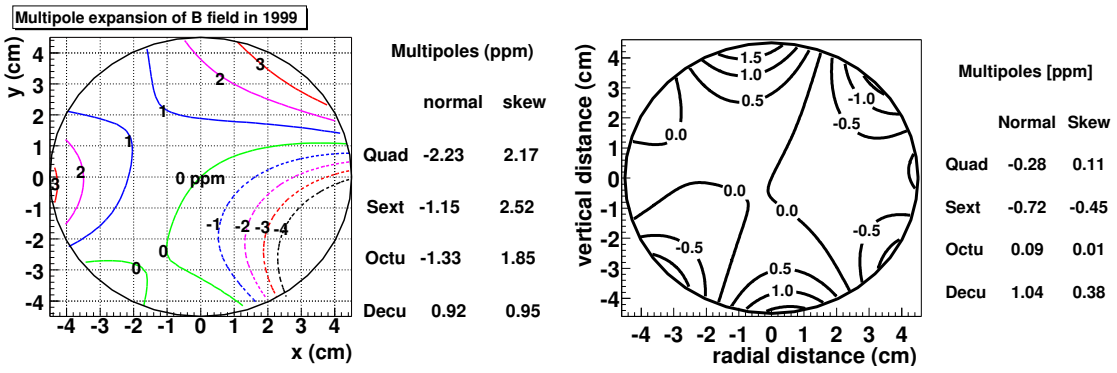

(a) 1999 Data Set (b) 2001 Data Set

Figure 10.12: The average magnetic field $\langle B \rangle_{azimuth}$ (a) with the damaged inflector (1 ppm contours) (b) and with the second inflector (0.5 ppm contours). Note that the large disturbance in the average field was from a 600 ppm disturbance in the field over 1° in azimuth.

10.3 Lessons for E989 from the E821 Inflector

The most important single lesson from the E821 inflector came from the flux leakage from the damaged inflector, and the realization that the first design of the inflector leads also contributed to this problem (see Fig.10.12). The ±0.2 ppm systematic error from this problem is three times the E989 magnetic field error budget of ±0.07 ppm. The highly localized 600 ppm perturbation at the location of the "repaired" superconducting shield simply could not be shimmed away. The second issue that must be addressed is the mismatch in the E821 inflector aperture and the storage ring's. The third issue is to open the ends, and to open the size of the beam channel.

The guiding principles going forward are:

- *The flux inside of the inflector must be confined inside of the inflector and not permitted to leak into the storage region.*

- *Any new inflector design must have a horizontal (radial) aperture significantly larger than 18 mm; as close to 40 mm as possible.*

- *The ends of the inflector need to be open, rather than have coil windings across them.*

The latter two conditions could increase the number of stored muons by almost a factor of four.

The muon injection efficiency achieved in E821 was around 2%. Early simulations predicted that it should be 5 - 7%. Opening the ends of the inflector would have doubled the number of stored muons. So it becomes clear that a new open-ended inflector with a larger aperture, perhaps as large as 30 to 40 mm diameter, is desirable and possible. Given the time that will be needed to develop a new inflector, it is impractical to have a new inflector ready by mid-2015 when the shimming program would be ready to install vacuum chambers and the inflector.

Going forward, we need: (i) To open both ends of the inflector; (i) A larger aperture than the E821 inflector; Careful lead design to minimize stray field; A passive superconducting shield that prevents flux leaking from the inflector into the precision magnetic field.

10.4 A New Inflector

Several concepts have been considered to replace the existing inflector. Any new design is constrained by the injection geometry shown in Figs. 10.1, 10.8 10.9 and 10.10. A passive superconducting shield to remove any leakage flux from the new inflector will be essential.

The small aperture of the E821 inflector, and the coil windings over the beam channel make matching the beamline to the storage ring impossible. While it worked well enough in E821 to reach ± 0.54 ppm, and there would have been no issues in reaching the ± 0.35 ppm goal, had the running at BNL not been terminated. Since E989 plans to accumulate 21 times the data of E821, it is necessary to revisit the inflector aperture issue. Opening the radial aperture to a 3 - 4 cm would come close to matching with the incoming beam, and permit many more muons to be stored. The trade-off is as the aperture gets larger, a larger kick will be needed to place the beam on orbit. Shielding a large open end will also be challenging.

In E989 the knowledge of the average magnetic field needs to be improved by a factor of three over E821. While the plan to improve the magnetic field measurement and control is discussed in Chapter 15, this plan is meaningless if any device in the experiment spoils the field by introducing extraneous magnetic flux into the storage region. The damaged inflector in E821 demonstrated how a 0.2 ppm problem can easily be introduced.

Two possible suggestions have been proposed for a new inflector:

- A double coil structure that is either the double-cosine θ design, or another double magnet that cancels the storage ring field.

- An elliptical double dipole magnet

Any of the powered magnet solutions would need a passive superconducting shield that traps whatever flux might leak from the magnets, preventing this leakage flux from changing the magnetic field seen by the muons while they are stored in the ring.

10.4.1 A New Double Cosine Theta Magnet

This option needs study. The truncated double cosine theta design encased in a multi-layer superconducting shield worked well in E821, albeit with the limitations discussed above. Certainly any new design must have open ends, since the multiple scattering makes it impossible to correctly match the incoming beam to the ring. The open ends will certainly produce issues for shielding the fringe field, which are common to the other wound magnets discussed below.

Fortunately our UK colleagues at the Rutherford-Appleton Laboratory (RAL) have suggested studying how to make such a double-cosine theta magnet using modern superconductor, with an increased aperture. A target would be going from the 18×56 mm^2 E821 aperture to 40×56 mm^2.

10.4.2 Double magnet, using the serpentine winding technique

Brett Parker at Brookhaven has developed a new technique to wind superconducting magnets, using CNC techniques [17], which permits multi-layer coils of rather complicated current distributions to be fabricated. An example of a quadrupole magnet is shown in Fig. 10.13. A visit to his lab at BNL was very informative, and he has confirmed that he could wind elliptical dipoles, as well as circular ones.

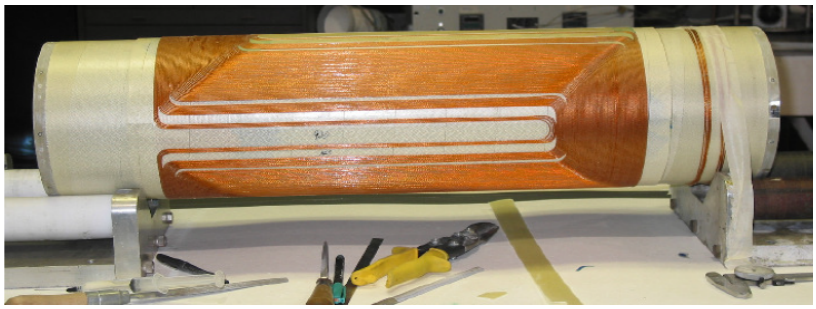

Figure 10.13: Coil for a superconducting quadrupole

An examination of Fig. 10.10 shows the problems. A circular cross section moves the beam center further away from the center of the storage region, thus requiring a much stronger kick. An elliptical cross section would significantly open the beam aperture, permit a larger vertical aperture, while reducing the extra kick needed to store the beam. the cross section of such a coil is shown in Fig. 10.14. Parker says that to achieve the fields needed in E989, it would be necessary to have four layers. There would also have to be the canceling magnet outside, and a superconducting shield to remove any residual flux.

10.4.3 Inflector Superconducting Passive Shield

While the exact fringe field will be modeled by computer simulations, and made as small as practically possible, our baseline goal for the shield is that it should be able to cancel a fringe field < 1 kG ($H_{MAX} = 1000$ Oersted).

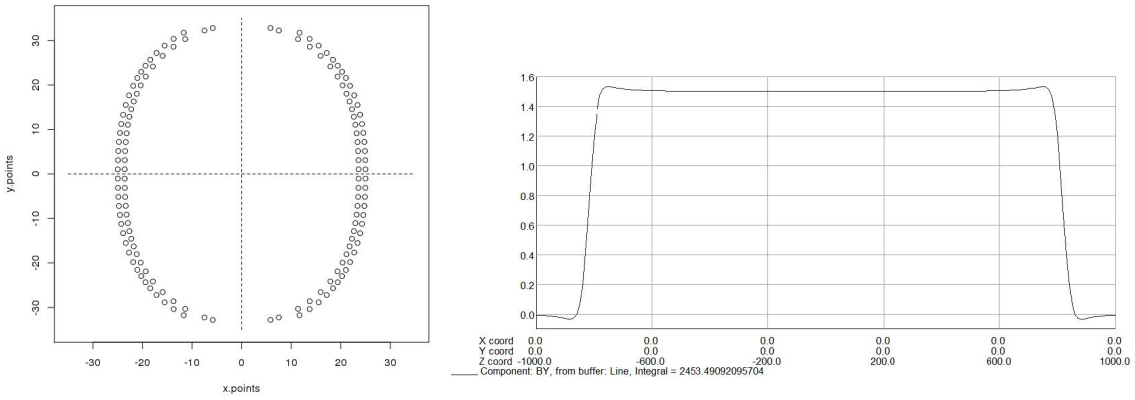

Figure 10.14: (a) An elliptical coil arrangement. (b) The calculated longitudinal magnetic field from this coil arrangement.

The shield will surround the inflector coils. The shield should be as large and as long as possible, while still fitting within the inflector cryostat. The open end of a new inflector will present additional challenges for the shield, and will need to be studied in simulations. From this constraint, the shield diameter will be approximately 12 cm. It extends 26 cm downstream of the inflector coils. Upstream, it is flush with the coils due to space limitations.

We have several options for shield material supply: (1) reuse the shield from existing working shield, (2) reuse the shield from spare (but broken) inflector, and (3) contact industry to fabricate a new shield.

Option (1) is not preferred, since we need to preserve a working inflector. Option (2) is possibility. The shield was epoxied to the inflector mandrel. We should be able to melt the epoxy to remove the shield.

For option (3), we have contacted and are in discussion with MTI Metal Technology[20] and ATI Wah Chang[21]. We have not been able to contact Nippon Steel, the original maker of the shield.

In principle, a shield can be fabricated from smaller overlapping pieces. However, care must be taken to provide sufficient cooling. We should prototype, test, and verify that the overlapping region functions properly as a shield. Given the issues with the attempt to repair the damaged shield on the original inflector, overlapping shields, rather than one continuous one, is by no means a viable option.

10.5 Muon Storage Simulations Using a New Inflector

Several aspects of a new superconducting inflector magnet are simulated to study their impact on the fraction of muons transmitted into the storage region. The options studied are the following with the E821 setting shown in parentheses: *a*) open-end vs closed-end (E821) geometry, *b*) 30 or 40 mm vs 18 mm (E821) horizontal aperture, *c*) sensitivity to beam phase-space matching. Results of the simulation are presented as improvement factors defined as the fraction of stored muons with the new inflector divided by the baseline E281

inflector. The baseline E821 storage rate is also presented. Assuming all improvements add coherently, a new open-ended inflector with a 40 mm horizontal aperture is expected to increase the fraction of stored muons by **X.Y** compared to the E821 inflector.

10.5.1 E821 Inflector Simulation

The E821 inflector magnet is simulated using a GEANT4-based software, which allows particle tracking beginning at the inflector and into the storage region. Within this framework, the closed ends of the inflector are constructed using distinct volumes of aluminum (1.58 mm), copper (0.39 mm), and niobium-titanium (0.43 mm). An additional 4 mm of aluminum is added to each end to model the window, flange, and cryostat. Between the end-caps, a "D"-shaped vacuum beam channel is constructed to approximate the double cosine theta geometry. The magnetic field within the beam channel is the vector sum of the main magnet fringe field and the 1.45 T field ($\int \vec{B} \cdot d\vec{\ell} = 2.55$ Tm) produced by the inflector magnet leading to a net cancellation of the impulse caused by the main magnetic field.

The E821 muon beam is simulated by uniformly populated a phase space ellipse bounded such that the area defined as $A = \varepsilon \times \pi = 40\pi$, where ε is the beam emittance. The phase space axes are determined by the beam TWISS parameters, α and β in both horizontal (x) and vertical (y) directions. The nominal TWISS parameters are determined by maximizing the transmission rate through the inflector and shown in Table 10.3 when the beam is localized at the "downstream"-end of the inflector (*i.e.* nearest to the ring). The beam momentum, $|P|$, is generated by sampling a Gaussian distribution with mean equal to the magic momentum P_{m} and width $\delta P/P = 0.5\%$. The longitudinal width of the beam, or equivalently, the width in time is 25 ns. The orientation of the inflector angle with respect to the ring tangent was set to -3 mrad to optimize transmission. These settings approximate those of the 1997 E821 run at BNL.

Table 10.3: Nominal muon beam Twiss parameters.

Direction	Emittance (ε)	α	β
Horizontal (x)	40	-0.544	2.03
Vertical (y)	40	-0.0434	19.6

All muons passing into the storage region are given a "perfect kick" to place them onto a stable orbit. This kick is modeled by applying a 220 Gauss magnetic field throughout the kicker volume for the first revolution. Finally, the storage rate is defined as the fraction of muons surviving 100 revolutions around the storage ring. No muons are allowed to decay in this simulation.

10.5.2 Open-ended vs. Closed-ended Inflector Geometry

The E821 inflector magnet was constructed with a closed end (*i.e.* the superconducting coils wrapped around the end of the magnet) because this greatly reduced magnetic flux leakage

into the muon storage region. The impact of the closed end on the horizontal and vertical emittance was studied analytically and with the GEANT tracking software. In the analytic approach, the fraction of muons traversing the inflector ends is studied by comparing the horizontal and vertical beam widths (σ_x, σ_y) after multiple scattering in the material. In this study, a beam filling the horizontal aperture of 18 mm grows to a size of $\approx$ 35 mm, suggesting that approximately half $(18/35 = 51\%)$ of the beam will fail to exit the inflector aperture. Of course, with two closed ends the net effect is to lose between $50 - 75\%$ of the incoming beam.

The tracking simulation approach removes the end coils, flange, and window from the GEANT inflector material without altering the magnetic fields. Table 10.4 summarizes the muon storage rates assuming an open and a closed inflector magnet. The beam parameters and inflector aperture are identical in both simulations. Values within parentheses show the results of an incoming beam with a momentum spread of 2% instead of the nominal 0.5%.

Table 10.4: Summary of E821 Inflector Simulations.

Inflector Geometry (Upstream-Downstream)	Muons Generated	Muons Surviving	Storage Fraction
Open-Open	5000 (20000)	664 (691)	**13.2±0.3 (3.4±0.1)**
Closed-Open	5000 (20000)	522 (593)	**10.4±0.3 (2.8±0.1)**
Closed-Closed	5000 (20000)	323 (395)	**6.5±0.3 (1.9±0.1)**
Improvement Factor ≡ Open-Open/Closed-Closed			
	5000 (20000)	-	**2.1× (1.7×)**
Improvement Factor ≡ Closed-Open/Closed-Closed			
	5000 (20000)	-	**1.6× (1.5×)**

10.5.3 Sensitivity to Beam Phase-space Matching

A consequence of the limited inflector aperture is gross phase space mismatching into the storage region. This is seen by studying the amplitude of the muon beam (A), which is defined as $A = \sqrt{\beta\varepsilon}$. The maximum horizontal size of a beam clearing the inflector is ±9 mm, thus, a beam with $\varepsilon = 40$ mm-mrad must have $\beta_x < 2.5$ m and $\beta_y < 19.6$ m. As this beam propagates into the storage region the horizontal β-function subsequently undergoes large oscillations with $\beta^{\max} = 28$ m and $\beta^{\min} = 2.5$ m. This corresponds to a modulation of the horizontal beam amplitude (A) of $r = \sqrt{\frac{\beta^{\max}}{\beta^{\min}}} = 3.4$.

An alternative to these large oscillations is to perfectly match the β-functions into the storage ring. Assuming a drift space within the inflector $(\vec{B} = 0)$, then the β-function at the inflector is defined as $\beta^{\inf} = \beta^{\text{ring}} + s^2/\beta^{\text{ring}}$. The resulting β-functions ($\beta_x^{\inf} = 7.6$ m and $\beta_y^{\inf} = 19.2$ m) requires the incoming beam to be 2.38 times larger than the inflector aperture. Thus, only $1/2.38 = 42\%$ of the beam will clear the inflector. This conclusion follows the GEANT-based tracking result, which shows 53% of the beam clearing the inflector aperture.

10.5.4 Increased Horizontal Aperture

The E821 inflector was constructed with a ±9 mm horizontal aperture in part due to the double cosine theta magnet geometry and the limited space between the outer main magnet cryostat and the muon storage region. The horizontal aperture also constricts the available phase space in the muon storage region, whose aperture is ±45 mm.

An augmented inflector "D"-shaped aperture of $\pm 20 \times \pm 28$ mm^2 is modeled in the `GEANT` tracking software. In this study, the main magnet fringe field is assumed to be identically canceled within the inflector beam channel for simplicity. The horizontal beam size is increased allowing for ideal matching to the storage ring β-function, corresponding to $\beta_x = 7.6$ m. The horizontal and vertical α Twiss parameters are set to zero in this scenario.

Table 10.5 summarizes the muon storage rate for the two apertures (18 vs 40 mm) and the two end coil inflector geometries (open vs closed) [1].

Table 10.5: Summary of E821 Inflector Simulations. The "D"-shaped aperture shown in Fig. 10.5(a) was used. The vertical aperture was 56 mm, the horizontal (radial) aperture was 18 mm, or 40 mm.

Inflector Aperture (Open or Closed ends)	Muons Generated	Muons Surviving	Storage Rate
18 mm Aperture ($A_{\pm 9}$)			
(open ends)	120000	11444	**9.5±0.1**
(closed ends)	120000	5117	**4.2±0.1**
40 mm Aperture ($A_{\pm 20}$)			
(open ends)	120000	19161	**15.9±0.1**
(closed ends)	120000	8706	**7.2±0.1**
Improvement Factor $\equiv A_{\pm 20}/A_{\pm 9}$			
(open ends)	-	-	**1.7**×
(closed ends)	-	-	**1.7**×
Improvement Factor $\equiv A^{\rm Open}/A^{\rm Closed}$			
(18 mm Aperture)	-	-	**2.2**×
(40 mm Aperture)	-	-	**2.2**×
Improvement Factor $\equiv A^{\rm Open}_{\pm 20}/A^{\rm Closed}_{\pm 9}$	-	-	**3.8**×

10.6 ES&H

The superconducting inflector is in a cryostat that includes one section of muon beam tube. The cryostat vacuum is separate from the beam vacuum chamber, so that the inflector can be operated independently of whether the muon beam chamber is evacuated. The

[1] Note that these storage rates are computed with a different muon beam and therefore can not be compared directly to the rates in the previous sections.

cryogenic system, and its operation will follow all Fermilab safety standards for cryogenic and vacuum system operations. This includes, but is not limited to Extreme Cold Hazard, Oxygen Deficiency Hazards. The cryogens involved are liquid helium and liquid nitrogen. No flammable liquids or gases will be employed. The existing E821 inflector was operated at Brookhaven National Laboratory where similar safety requirements were in place.

10.7 Risks

10.7.1 Relocation Risk

There is a small risk that in the de-installation at Brookhaven and shipping to Fermilab of the E821 Inflector that some problem is introduced that compromises the inflector performance. We will seek to minimize this risk by careful dissassembly and shipping. As soon as cryogenic capability is available in MC-1, we would set up a test stand in the experimental area outside of the ring to cool and power the inflector.

10.7.2 Other Risks

There is the possibility that some mechanical aspect of the E821 inflector has deteriorated in the 12 years since it was operational, causing the magnet to quench repeatedly before reaching full current. This risk is probably small, since it was tested at KEK, shipped to BNL, installed, and was brought to full current with only a few training quenches. It was very robust in subsequent operation at BNL. The plan to test it as soon as possible at Fermilab will clarify this risk.

A helium leak in the valve box or lead-pot will need to be located and repaired. There is a small risk that the leak was in the magnet itself, but this is viewed as extremely unlikely by Akira Yamamoto, who supervised the engineering design and construction, and Wuzheng Meng, who did the magnetic design and was responsible for its operation at BNL.

The most sensitive part of the re-installation is reconnecting the inflector leads. Our technician Kelly Hardin was involved in the disassembly at BNL, and understands the issues involved in the reconnection very well.

10.8 Quality Assurance

Proper quality assurance is essential in the transport and reassembly of the inflector magnet. The mechanical aspects, heat shield, etc. will be carefully examined for issues, once the inflector arrive at Fermilab. It will be determined as quickly as possible whether the inflector meets the Muon g-2 requirements for performance and reliable operation. Quality Assurance will be integrated into all phases of the transport and reassembly work. including design, procurement, fabrication, and installation.

10.9 Value Engineering

The baseline is to begin the experiment by re-using the existing E821 Inflector. A new inflector with a much larger horizontal aperture could permit three to four times as many muons to be stored. A gain of this factor would significantly improve the statistical reach of the experiment, and permit more beam time to be used for systematic studies. This presents a significant opportunity to improve the experiment and to use running time more effectively. At present we plan that our UK collaborators at the Rutherford-Appleton Laboratory will produce a new inflector. If they are unable to obtain funding, we will explore the possibility that a larger-aperture inflector can be produced in collaboration with Brett Parker at BNL.

References

[1] A. Yamamoto, et al., Nucl. Inst. Meth. **A 491**, 23 (2002).

[2] Frank Krienen, Dinesh Loomba and Wuzheng Meng, Nucl. Inst. Meth. **A238**, 5 (1989).

[3] A. Yamamoto, Nucl. Instr. and Meth. A 453 (2000) 445.

[4] Y. Makida, et al., IEEE Trans. Magn. 27(2) (1991) 1944.

[5] M. Garber, A. Ghosh, W. Samson, IEEE Trans. Magn. 25 (2) (1989) 1940.

[6] Y. Saito, et al., Development of beam inflection superconducting magnetevaluation of prototype, Tokin Technical Review, No. 20.

[7] M.N. Wilson, Superconducting Magnets, Oxford Science Publications, Oxford, 1983.

[8] A. Yamamoto, Status of the inflector, Internal Meeting Minutes, 1992; W. Meng, K. Woodle, Superconducting shield test on $(g-2)$ inflector magnet, $(g-2)$ Note, No. 210, 1994.

[9] M.A. Green, W. Meng, IEEE Trans. Appl. Supercond. 5 (2) (1995) 667.

[10] G.T. Danby, W. Meng, W. Sampson, K. Woodle, IEEE Trans. Magn. 30 (4) (1994) 1766.

[11] I. Itoh, T. Sasaki, IEEE Trans. Appl. Supercond. 3 (1993) 177.

[12] H.N. Brown, et al, Phys. Rev. Lett. **86** 2227 (2001).

[13] F. Krienen, et al., IEEE Trans. Appl. Supercond. **5** (2) (1995) 671.

[14] W. Meng, K. Woodle, Superconducting shield test on g-2 inflector prototype, g-2 Note, No. 210, 1994.

[15] The $g-2$ Collaboration: G.W. Bennett et al., Phys. Rev. Lett. **89**, 101804 (2002); Erratum-ibid. **89**, 129903 (2002).

[16] Bennett GW, et al. (The $g-2$ Collab.) Phys. Rev. Lett. 92:161802 (2004)

[17] http://www.bnl.gov/magnets/Staff/Parker/

[18] Brett Parker, private communication, March 2013.

[19] Lance Cooley, Fermilab. Private Communication.

[20] Steve Smith at MTI Metal Technology. http://www.mtialbany.com/

[21] Tony Nelson at ATI Wah Chang. http://www.atimetals.com/

Chapter 11

WBS 476.03.04 Beam Vacuum Chambers

The muon storage volume, which lies within the 1.45T magnetic field, is evacuated in order to minimize multiple scattering of muons and positrons. This is accomplished by a set of aluminum vacuum chambers, which also provides mechanical support for:

- the beam manipulation systems: the electrostatic plates of the quadrupole system, the collimators, and plates of the magnetic kicker system.
- the positron detection systems: the trace-back straw trackers and auxiliary detectors such as the fiber harp.
- the magnetic field measurement systems: 400 fixed NMR probes surrounding the storage volume, a set of rails for the trolley NMR system, and the plunge probe system.

The chambers from BNL E821 will be reused for E989, and we will make changes as described in the section below. The chamber design is detailed in the BNL E821 design report[1], and so only a brief discussion is given here. Figure 11 shows the layout. The systems comprises mainly of 12 large vacuum chambers, separated by 12 short bellows adapter sections.

A simplied FEA model of a large vacuum chamber is shown in figure 11.2, showing the 15 grooves for mounting the NMR probes. The 15 grooves on the bottom and flange ports are not shown. The FEA model predicts that the top and bottom surfaces deflect by 0.453 mm under vacuum load[2]. This is agreement with the measurement of 0.45 mm[3]. The FEA model reconfirms that the chamber has reasonable factors against buckling, and the wall stresses are below 12000 psi, as required by the ASME Pressure Vessel Code for pressure vessels for Aluminum 6061-T6.

The 12 vacuum chambers and 12 bellow adapter sections are bolted together and placed in between the upper and lower pole pieces. The average radius of this structure is mechanically fixed and cannot be adjusted. There are thin dielectric sheets in between vacuum sections to prevent low frequency eddy currents from traveling in between the sections. Finally, all chamber materials including bolting hardware are non-magnetic.

Figure 11.3 and 11.4 shows the cage system and how it resides inside a vacuum chamber. The cage system holds the quadrupole plates, kicker plates, and the rails used by the trolley.

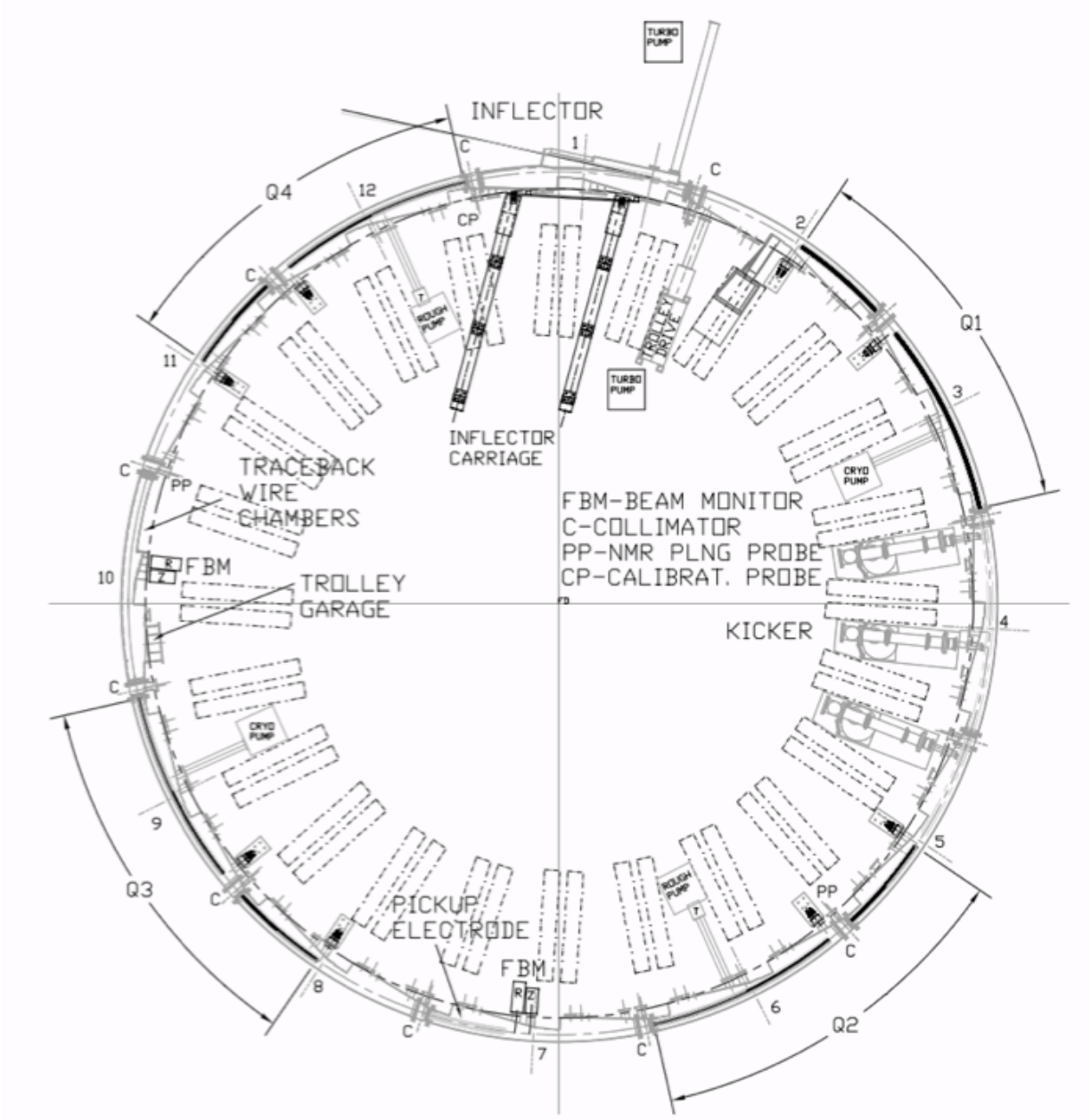

Figure 11.1: Layout of the BNL E821 beam vacuum chamber system.

Screws allow for adjusting the position of the cage within the vacuum chamber system. The position of the cage system plays an important role, and has the following requirements. (1) The rail system from neighboring vacuum sections must line up to allow smooth motion of the trolley as it travels between sections. And (2), since the quadrupole plates and kicker plates positions define the beam storage region, these devices should place the beam in the most uniform portion of the magnetic field. The beam center should be at the geometrical center between upper and lower pole faces. A critical period occurs after installing the chambers and before vacuum pump down. During this time, the vacuum flanges are open

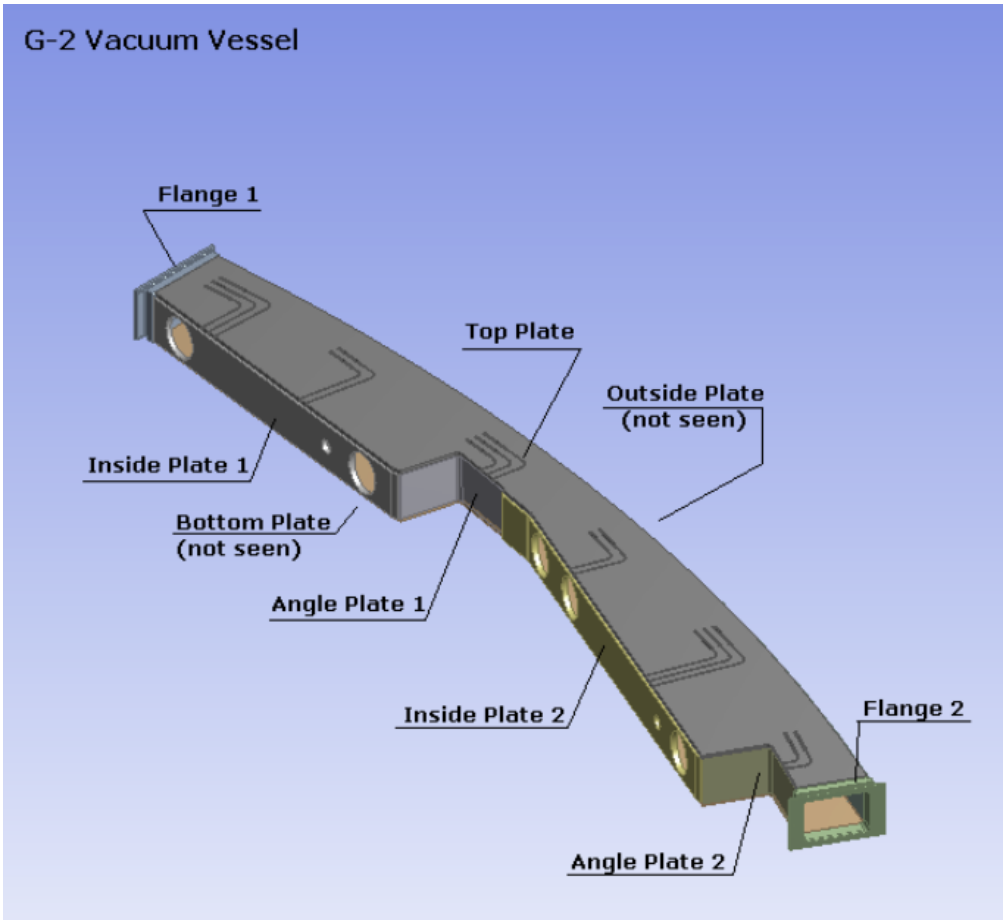

Figure 11.2: Simplified mechanical model for stress and strain analysis.

and so will allow access to the adjustment screws.

11.1 Changes to the E821 Design

For E989, we are proposing to make the following changes. We will add fixed NMR probes to the mid plane ('mid plane probes') of the beam storage region. A concept is shown in figures 11.6 and 11.7, showing the probes mounted to the cage system. The mid plane probes will have the long axis aligned in azimuth, and should lie as close as possible to the edge of the beam region. But they must be remain sufficiently far from the quadrupole and kicker plates in order to prevent sparking and signal pickup. The probes will be in vacuum, and the probe coax cables attach to commercially-available vacuum SMA electrical feed throughs. As shown from simulations, the magnetic field values should be within the mid plane probe operating range.

For E821, a small fraction of the upper and lower fixed probes were too close (in azimuth) to the boundary between two pole pieces. In this region, the magnetic field gradient is generally larger due to gaps and steps (of order < 25 microns) between two pole pieces, and therefore degrades the probe's S/N. Simulations show that maintaining a distance of O(5

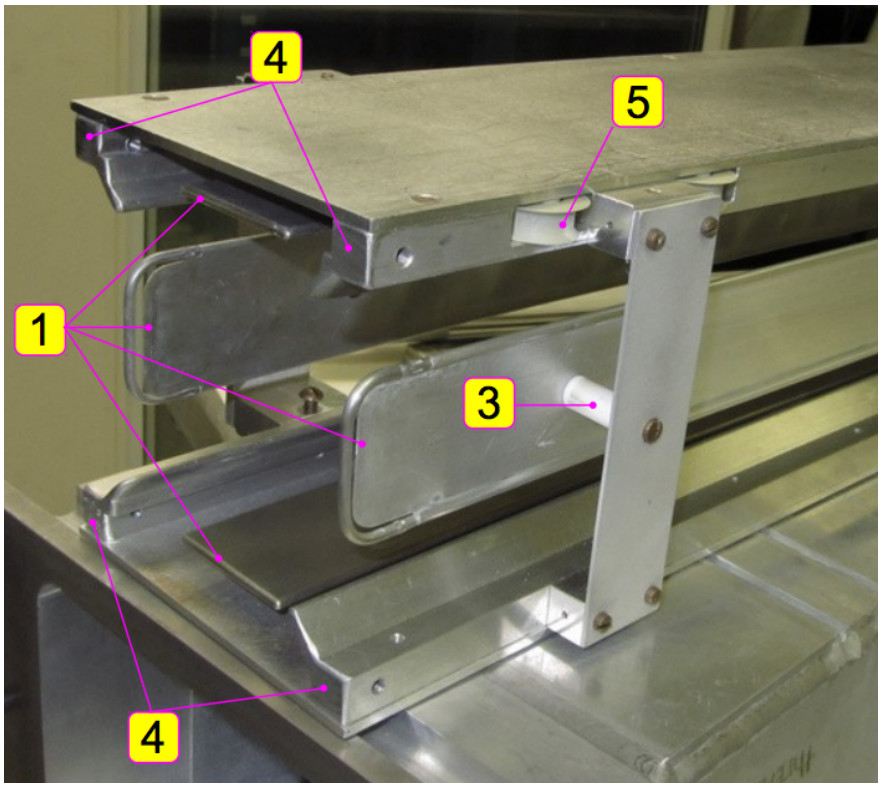

Figure 11.3: Picture of a cage system showing the (1) quadrupole plates, (3) macor (insulator) supports, (4) trolley rails, and (5) a wheel for guiding the cable that pulls the trolley

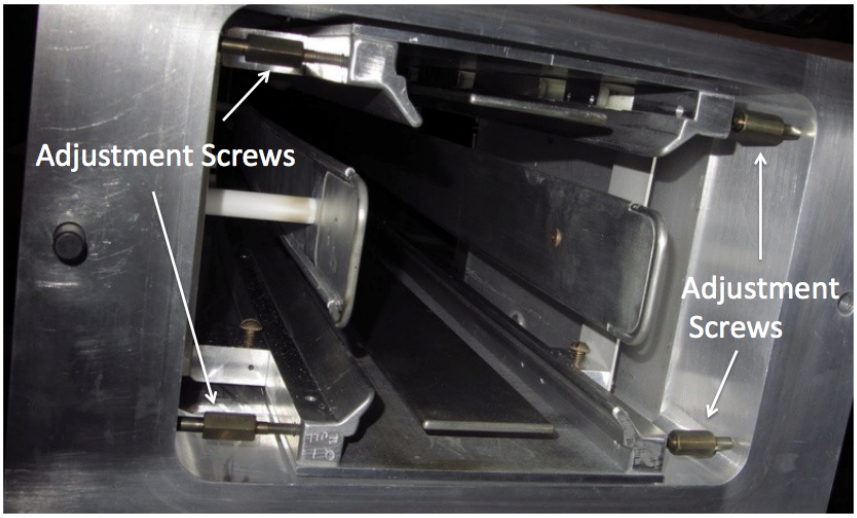

Figure 11.4: Picture of a cage system inside a vacuum chamber showing the adjustment screws to center the quadrupole plates to the geometrical center of the pole pieces.

cm) (*check this*) will recover the required S/N. For E989, we will either lengthen or cut new grooves to optimize probe placement.

In E821, the trace back system operated in air and was located in vacuum chamber sector

10, which was modified to be without a 'scallop'. For E989, the straw trace back system will be in vacuum, and vacuum chamber sector 10 will have its scallop shape reinstalled. A second straw station will be placed in sector 8. The inner radius vertical side walls of sectors 8 and 10 will be modified to accept the straw chamber flange. Figure 11.8 shows the locations of the proposed changes.

The kicker occupies chamber sectors 4 and 5. The magnetic kicker firing will cause eddy currents, which compromises physics data at beginning of injection and reduces the kicker field strength. Opera simulations are being done to see whether the top and bottom surface of the vacuum chamber can be redesigned to reduced eddy currents. A concept for this modification is shown in figure 11.5.

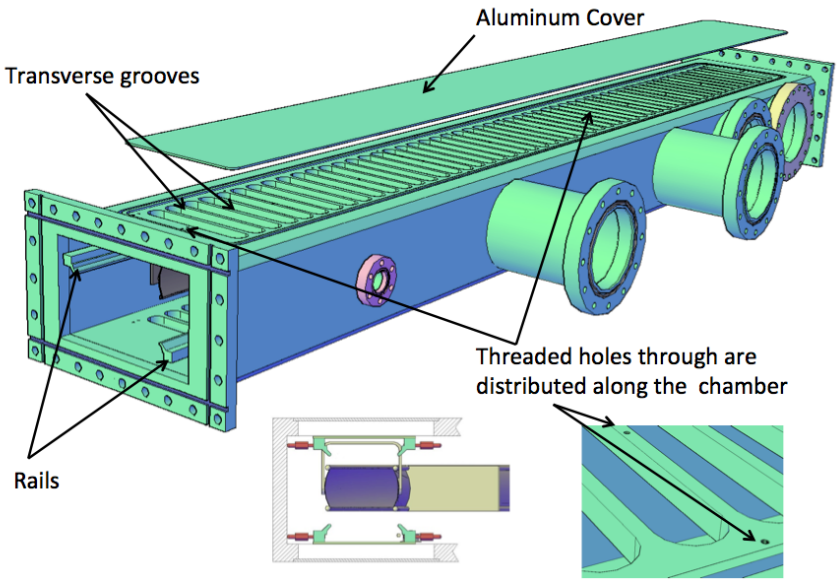

Figure 11.5: Concept for modifying chamber sectors 4 and 5 to reduce eddy currents induced by the kicker system.

Finally, the vertical inner radius surface of the vacuum chamber will be lined with insulation. This will improve the thermal stability of the magnet iron.

11.2 WBS 476.03.04.02 Vacuum Chambers

This WBS refers to the actual chambers, the small bellows, the piping to the pumps, and the bolting hardware. We are exploring major modifications to sectors 8, 10, 4, and 5. This WBS also covers the reassembly labor effort.

Chamber sectors 10 and 8 would be re-machined to accept the new in-vacuum straw trace back chambers. For sector 10, the 'scallop' portion must be reinstalled. Chamber sectors 4 and 5 would have the top and bottom plates modified to install transverse grooves to reduce eddy currents.

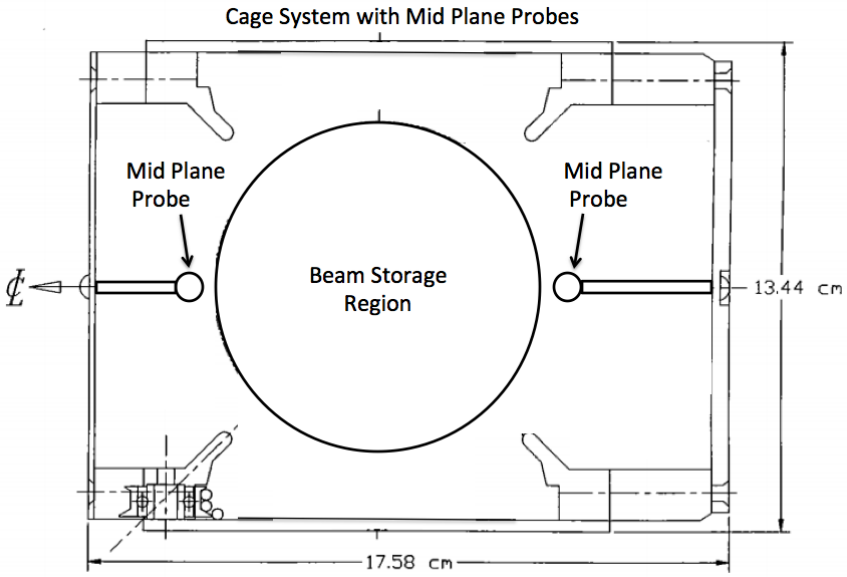

Figure 11.6: Concept for placement and attachment of mid plane probes within the cage systems that do not contain quadrupole and kicker plates. Signal coax cables attach to commercially available vacuum SMA electrical feed throughs.

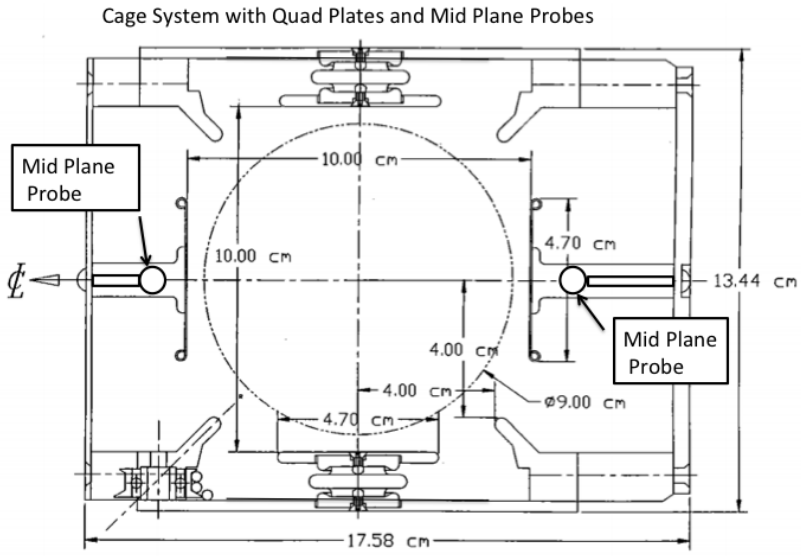

Figure 11.7: Concept for placement and attachment of mid plane probes within the cage system in the quadrupole plate region. The mid plane probes are farther from the beam center. They are offset and do not interfere with the macor quadrupole plate support stands. Signal coax cables attach to commercially available vacuum SMA electrical feed throughs.

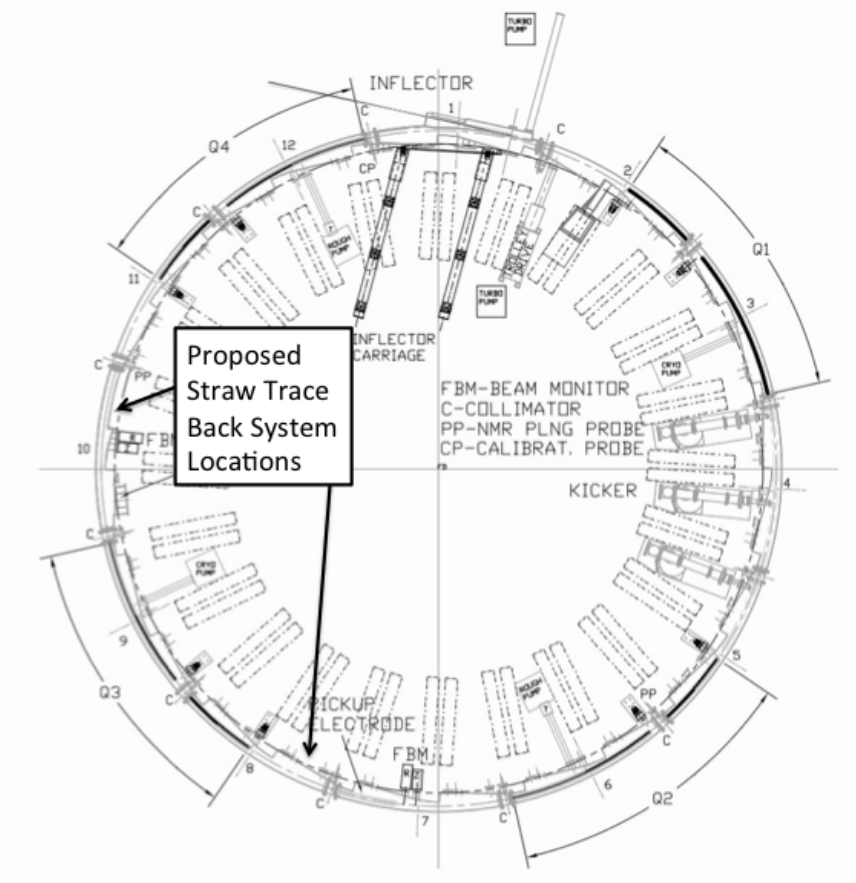

Figure 11.8: Proposed locations for in-vacuum straw trace back chambers.

11.3 WBS 476.03.04.03 Vacuum Pumps

The vacuum level must be less than 10^{-6} Torr in the region of the quadrupoles. This is to minimize the trapping of ionized electrons due to the residual gas. However, there is a vacuum load of < 100 liters/sec at 10^{-6} Torr from each of the two straw tracker trace back system (*Check with Mandy and Brendan Casey*).

From this requirement alone, the minimum pumping speed is 100 liters/sec at 10^{-6} Torr. However, each pump is attached to the vacuum chamber through a large pipe. As the pumps will likely contain ferromagnetic material and generate transients that would affect the magnetic field uniformity, they must remain sufficiently far from the vacuum volume. For E821, this distance was 1-2 meters. Therefore, extra piping will increase slightly the pumping speed requirement. The exact minimum pumping speed will be determined by engineering calculations. For E821, the pumping speed was 2000 liters/sec at 10^{-6} Torr, accomplished by 3 pumps spaced uniformly over the ring.

Finally, the vacuum chamber system should remain clean, as the quadrupole and kicker plates carry high voltage and the high current, respectively. We will ensure this by utilizing dry (oil-free) roughing and turbo pumps.

11.4 WBS 476.03.04.04 Mechanical Interface

As mentioned above, the vacuum chambers must provide the mechanical interface for several systems. This WBS covers the following activities needed for the NMR system:

- Modifications to the upper and lower grooves to improve the S/N of fixed probes near the boundary between pole pieces.
- Adding additional commercially available vacuum SMA connections to readout the in-vacuum mid plane probes. The exact number and location will be estimated by Opera simulations.
- Calibration of the trolley position in absolute space: for a given motor or position encoder reading, what is the actual position of fiducial marks on the trolley in absolute space.
- Calibration and operation of the positions of the plunge probe motors. Calibration refers to converting a given motor encoder reading to an actual position (in absolute space) of the probe head.

The mechanism to move the plunge probe is shown in figure 11.9. This mechanism bolts to vacuum flanges at positions shown in figure 11. The probe itself is in air. There is a vacuum bellows in which the probe is inserted. The probe is moved radially by piezo electric motors. We expect no changes are needed for the plunge probe mechanism, other than connection to a different computer.

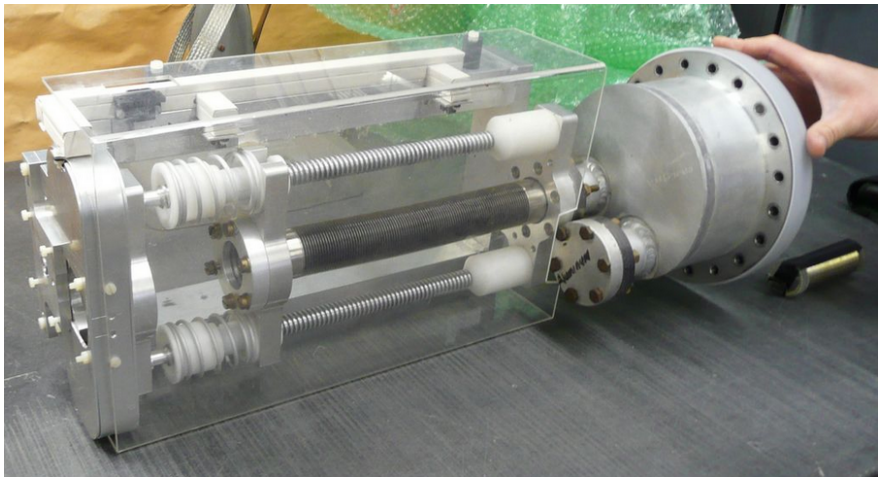

Figure 11.9: The plunge probe mechanism.

References

[1] BNL E821 Design Report

[2] GM2 Doc-417-V1

[3] BNL E821 Muon G-2 Note 248

Chapter 12

The Fast Muon Kicker

Injected muons exit the downstream end of the inflector magnet, and enter the good field region of the main dipole. The trajectory of the muons exiting the inflector is a circle displaced 77 mm radially outward the closed orbit of the storage ring. The path of the muons that emerge without having been scattered in the coil end of the inflector will be tanjential to that displaced circle. On exiting the inflector, muons are within the full 1.41 T field of the ring dipole. The muons cross the closed orbit of the storage ring, that is the orbit at the magic radius, about 90° azimuthally around the ring from the end of the inflector. The circular trajectory of the muons intersects that closed orbit at an angle of $\theta_0 = 10.8$mrad. Indeed the minimum crossing angle, namely $\theta_0 = 10.8$mrad obtains for trajectories that are tangential at the inflector exit. Any angle, positive or negative, with respect to the tangent line results in crossing angle greater than the minimum. Therefore muons that scatter in the inflector coil end will necessarily cross the closed orbit with a larger angle. The crossing angle is related to the scattering angle α according to

$$\theta \sim \left(\theta_0^2 + \alpha^2\right).$$

The contribution to beam divergence angle due to multiple scattering in the coil end is estimated to be about 4.6 mrad. Divergence due to the finite emittance of 40 mm-mrad is about 4 mrad. The result is that the mean angle at which muons cross the closed orbit is $\theta \sim 12.4$ mrad. Simulation that includes energy spread of the injected muons and scattering in the quadrupole plate indicates that the mean angle is nearly 14 mrad. Our specification for the system is a 14 mrad kick.

The azimuthal angle at which the muons cross the closed orbit, and the crossing angle are computed using a `GEANT4` simulation of the E821 experiment. This result, however, assumes three properties of the muon beam which are not realized in the experiment. First, the beam must have zero emittance (i.e., $|p| = p_z$), momentum localized around the magic momentum (i.e., $\delta p/p << 1$), and no multiple scattering as it traverses the outer quadrupole plates and standoffs. Varying each of these properties changes the azimuthal position and the crossing angle as seen in Table 12.1. Assuming a realistic beam with 40π emittance, $\delta p/p = 0.5\%$, and allowing for multiple scattering through the quadrupoles plates, the required kick increases from 10.8 mrad to 13.7 ± 3.9 mrad. Distributions of the azimuthal crossing point and crossing angle θ under these assumptions are shown in Fig. 12.1.

Table 12.1: Summary of Kicker Requirements for Different Beam and Ring Properties.

Beam $\delta p/p$ (%)	Emittance [mm · mrad]	Multiple Scattering	Azimuthal Crossing Point [degrees]	Crossing Angle [mrad]
0	0	OFF	89 ± 0	10.8 ± 0
0.5	0	OFF	88 ± 17	12.4 ± 2.7
0	40	OFF	86 ± 10	11.3 ± 3.3
0	0	ON	76 ± 7.8	15.1 ± 1.8
0.5	40	ON	**85±21**	**13.7±3.9**

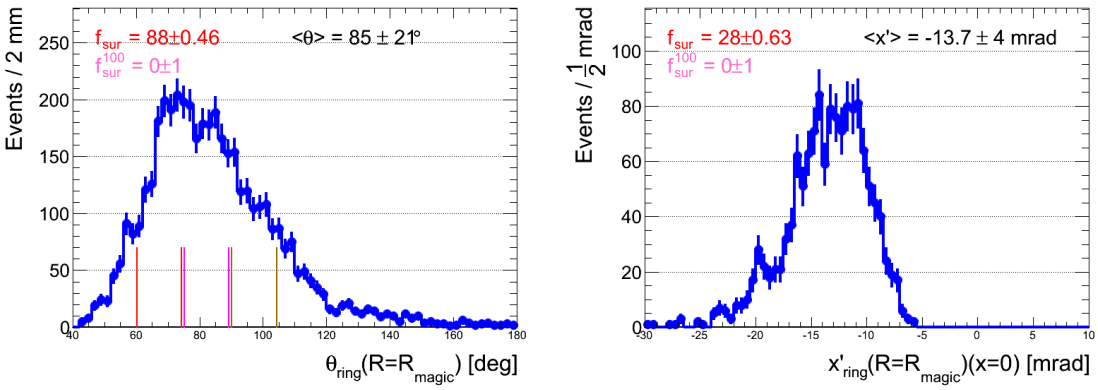

Figure 12.1: (a) Azimuthal crossing angle in degrees (b) Required kick x' in milliradians.

The fast kicker is a pulsed magnet with vertical field that directs the muons, onto the ideal orbit by compensating the crossing angle. Ideally, the centroid of the injected bunch, on exiting the field of the kicker plates will coincide with the closed orbit of the storage ring, thus ensuring maximal capture efficiency and minimum residual coherent betatron oscillation. The 10-14 mrad kick requires an integrated vertical field of 1.1 - 1.4 kG-m. The kicker is comprised of three independent 1.7m long magnets, each with dedicated pulse forming network. Muons are delivered to the storage ring in pulses with transverse emittance near 40π mm-mrad, pulse length of about 120ns and at a repitition rate of up to 100Hz. The ideal kicker field maintains a flat top at about 220-280 Gauss, for the full 120ns, and then returns to zero before the lead muons complete a single revolution and re-enter the kicker aperture 149ns later.

The injection of muons into the storage ring is complicated by several requirements:

1. Since the magnet is continuous, any kicker device has to be inside of the precision magnetic field region.

2. The kicker hardware cannot contain magnetic elements such as ferrites, since they will spoil the uniform magnetic field.

3. Any eddy currents produced in the vacuum chamber, or in the kicker electrodes, must

be negligible by 10 to 20 μs after injection, or must be well known and corrected for in the measurement.

4. Any kicker hardware must fit within the real estate occupied by the E821 kicker, which employed three 1.7 m long devices.

5. The kicker pulse should be shorter than the cyclotron period of 149 ns

12.1 Requirements for the E989 Kicker

The need for a fast muon kicker was introduced in Section 3.2. Direct muon injection was the key factor that enabled E821 to accumulate 200 times the data as the preceeding CERN experiment. Since E989 needs more than twenty times as much data as E821, it is critical that the limitations of the E821 kicker be eliminated. The layout of the E821 storage ring is repeated in Fig 12.2. The three kickers magnets are located approximately 1/4 of a betatron wavelength around from the inflector exit.

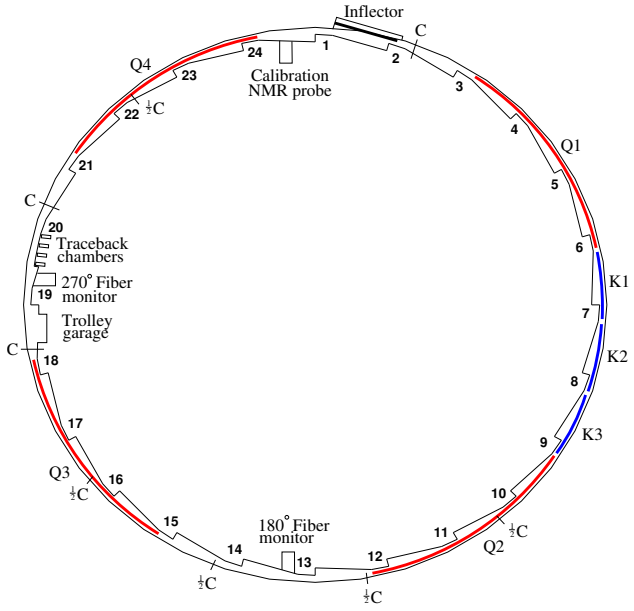

Figure 12.2: The layout of the storage ring, as seen from above, showing the location of the inflector, the kicker sections (labeled K1-K3), and the quadrupoles (labeled Q1-Q4) (Fig. reffg:ring repeated here for convenience).

12.1.1 The E821 Kicker and its Limitations

The E821 kicker [1] consisted of three identical sectors with 1.7 m long parallel plates carrying current in opposite directions, located as shown in Fig. 12.2. Each section was powered by a pulse forming network where a HV capacitor was resonantly charged to $\simeq$ 95 kV, and then shorted to ground by a deuterium thyratron, giving a characteristic damped LCR oscillating

current and magnetic field. The resulting LCR pulse is shown in Fig. 12.3. Unfortunately the LRC pulse was much wider than the beam width, in fact significantly longer than the cyclotron period of 149 ns. This is emphasized by the series of red gaussians which are separated by the 149 ns revolution period. Thus the beam is kicked several times before the LCR pulse dies away.

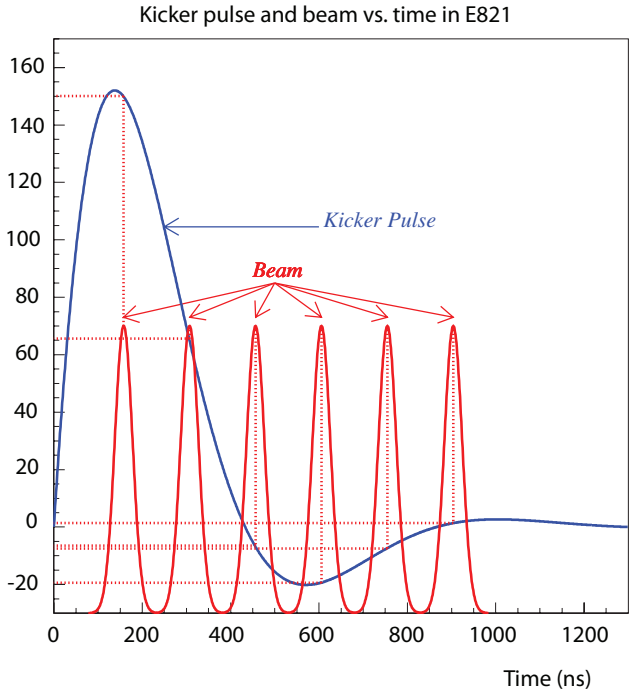

Figure 12.3: The E821 kicker LCR waveform (blue). The red pulses represent the injected beam, which has a cyclotron period of 149 ns.

The kicker units began sparking around 95 kV, and each section had a different voltage defined as 100%. The number of muons stored vs. kicker high voltage is shown in Fig. fg:stored-v-HV. Unfortunately, at the maximum voltage possible, the number of stored muons did not turn over. It is not clear how many muons might have been stored if it had been possible to increase the voltage until the maximum number of stored muons was reached.

12.2 New Kicker Design

The design of the kicker for E989 attempts to address the shortcomings of the E821 kicker, specifically, the pulse shape and pulse amplitude. We are developing a pulse forming network based on a Blumlein triaxial transmission line as an alternative to the E821 LCR PFN. The kicker plates are redesigned to yield a spatially more uniform field and with somewhat higher efficiency in terms of gauss per unit current through the plates. The kickers consist of 1.7m long plates as shown in Figure 12.5

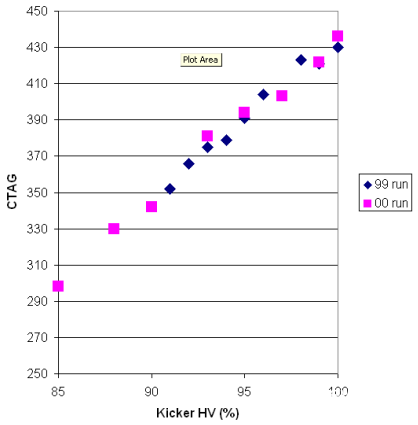

Figure 12.4: The number of stored muons versus kicker high voltage (arbitrary units).

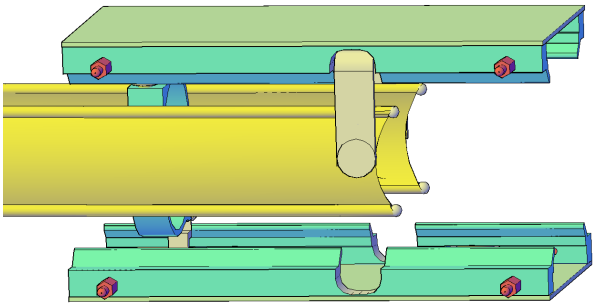

Figure 12.5: The kicker plates for E989. The current pulse is fed to the 1.7m long plates at the far end to the left of the plot. A jumper connecting the plates at the near end that closes the circuit is shown.

The proposed implementation is a variation on a transmission line PFN driving a matched load. We consider each 1.7 m long pair of kicker plates a load (each pair of plates is a transmission line in its own right) with impedance Z_L, and imagine, at least conceptually, that each kicker is terminated with a resistive load $R = Z_L$. If the impedance of the PFN transmission line matches the impedance of kicker plates and load, then the we anticipate a rectangular current pulse with width $\tau = 2L/c$ where L and c are the length and group velocity of the PFN, and current $I = V/Z$, where V and Z are the peak charging voltage and the impedance of the line respectively. With such a configuration we expect that the rise and fall time of the pulse will be limited by the turn on/off time of the thyratron switch of about 20-30ns.

We estimate the impedance of the kicker plates to be nearly 600 Ω. The current required to achieve the requisite $\sim$ 250 G field is about 3kA corresponding to the impractically high charging voltage of 1.8MV if the impedance of the PFN is matched to the impedance of the kicker plates. Furthermore it would be awkward to terminate the kicker plates with

a resistor. We propose alternatively to place a load resistor with resistance of only 25 Ω. between the pulse forming network and the kicker plates. The PFN transmission line is then matched to the load resistor. The reflections that will inevitably arise from the imperfect match at the junction of load resistor and kicker plates, will be confined to the plates, and dissipated on the timescale of the plate transit time of about 6ns. We thus deliver the desired current with ∼87kV charging voltage. At the transition through the load resistor to the kicker, the transmission line is tapered to mitigate the mismatch.

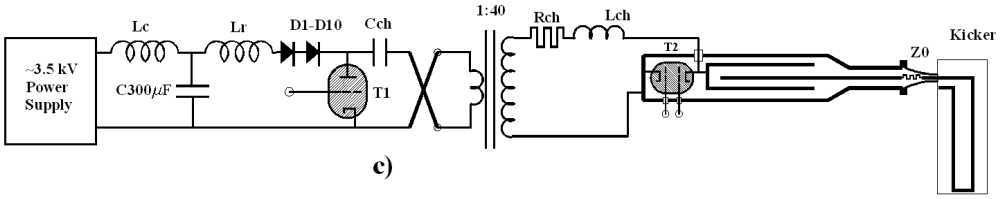

Figure 12.6: Schematic of the kicker, pulse forming network and charging circuit. The Blumlein, resistive load (Z_0) and kicker are in series to the right of the figure. In the final installation the load resistor is mounted near the vacuum chamber coupling directly to the kicker plates. The blumlein connects to the resistor via high voltage coax.

12.3 New Pulseforming Network

The pulse forming network that we are developing for the kicker is a Blumlein triaxial transmission line. The Blumlein is shown schematically in Figure 12.7. The LCR circuit used in E821, and a coaxial transmission line are included in the Figure for comparison. The equivalent circuit for a Blumlein is a pair of series bi-axial lines with a shared conductor and it is so rendered blumlein in Figure 12.8.

The width of the pulse

$$\tau = \frac{2L}{v} = 2L\frac{\sqrt{\mu\epsilon}}{c}.$$

For the bi-axial line the voltage at a matched load is half the charging voltage. For the Blumlein, output voltage and charging voltage are one and the same[2]. Another advantage of the Blumlein as compared to a bi-axial transmission line is that the base of the thyratron can be fixed at ground potential. A bi-axial pulse forming network would require that the base of the tube float to high voltage when the thyratron is switched. The Blumlein PFN under development at Cornell is shown in cross section in Figure 12.9. The middle conductor is connected through a large resistance and inductance to the high voltage power supply. Current flows through the load Z_L off of the central conductor during the charging cycle. The thyratron (T) shorts the middle conductor to the outer conductor and after a delay of $T/2$, where T is the width of the current pulse generated by the line, the current flows through the resistive load and into the kicker.

Some details of our implementation of the Blumlein are shown in Figure 12.10. The left and right drawings correspond to configurations with characteristic impedance of 25Ω

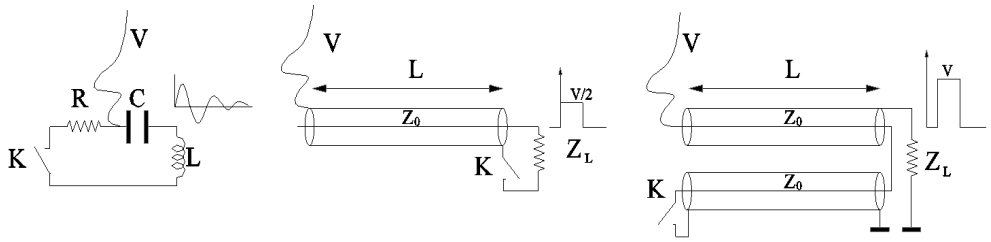

Figure 12.7: The overdamped LCR circuit at left was use in E821. The line labeled "V" indicates the charging voltage and K the thyratron switch. At center is a coaxial transmission line PFN. The Blumlein equivalent circuit is at the right. The corresponding pulse shape is shown for each of the configurations. Note that for both coaxial and triaxial lines, pulse width is proportional to twice the line length. Voltage across a matched load for the blumlein is twice that of the coax. The Blumlein pulse is delayed by half of the pulse width.

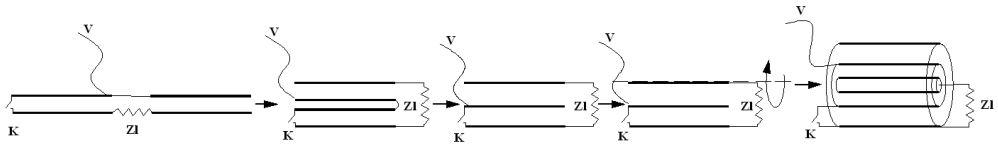

Figure 12.8: Topological modification of series coaxial lines into a tri-axial blumlein transmission line. (One can choose the rotation axis coinciding with the lower plate).

and 12.5Ω respectively, (assuming 561 silicon oil with $\epsilon = 2.7$). We have modeled the basic electrical properties of the pulser with an equivalent circuit using SPICE. Each of the two series coaxial lines are modeled with discrete elements as shown in Figure 12.11. The kicker load is represented with characteristic capacitance and inductance. The current pulse through the kicker when the switch is closed, as computed with SPICE, is shown in Figure 12.12.

The impedance of the triaxial line is equivalent to the sum of the impedances of the series bi-axial lines. The middle conductor in Figure 12.9 that is charged to high voltage serves as the inner conductor for one bi-axial line and the outer conductor for the other. The impedance of each of these bi-axial components is 12.5Ω. The output of the PFN is coupled to the load with a pair of parallel 50Ω high voltage coaxial cables, with combined impedance of 25Ω. The transition hardware is shown in Figures 12.13 and in an exploded view in 12.14.

A schematic of the Blumlein pulser connected via high voltage coax to the kicker inside the muon ring vacuum chamber is shown in Figure 12.15. Also shown is the electronics rack with 1500 V power supply, thyratron driver, and thyratron trigger pulser. The cylindrical container sitting on the floor beside the rack is the oil tank with high voltage transformer. The single high voltage transformer will charge the three Blumleins for each of the three kickers. Figure 12.16 is a rendering of the 5m long Blumlein with coupling to charging transformer at the right and transition to a pair of coaxial cables at the left. The thyratron

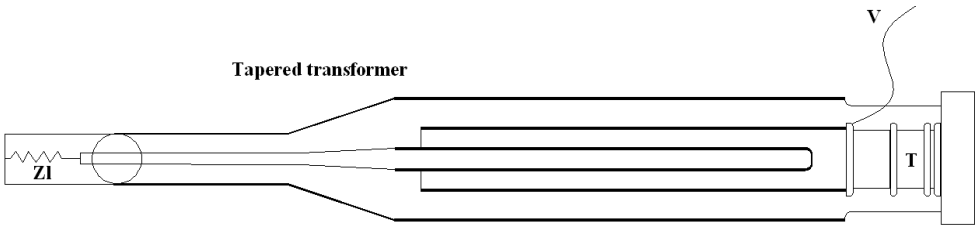

Figure 12.9: Middle conductor is charged to high voltage via the line labeled "V". The centermost conductor is coupled via a high voltage coaxial cable to the resistive load that is mounted directly to the input of the kicker. (The kicker is not shown here.) The thyratron (T) shorts the middle conductor to ground. The volumes between conductors, around the thyratron and load are all filled with transformer oil.

is housed in the section at the extreme right.

12.4 New Kicker Plate Design

The geometry of the kicker plates will be optimized for better uniformity over the storage volume and higher efficiency. We show the field profile for the proposed plate geometry in Figure 12.17(Left) as compared to the E821 geometry in Figure 12.17(Right). A proper calculation of the magnetic field generated by the time dependent current pulse has not yet been completed. But in the limit of steady state current and neglecting the effect of eddy current in the vacuum chamber and plates themselves, the new plate geometry provides at least 33% more magnetic field per unit current than the old design. Distancing the kicker plates from the vacuum chamber also mitigates the effect of induced field in the aluminum. We estimate that a current of 3500A will be requred to achieve a 14mrad kick, corresponding to a charging voltage of 87.5 kV, ($\sim$10 kV below the breakdown voltage of the E821 kicker system).

Whereas in the E821 configuration, the kicker plates served as rails for the NMR trolley, those functions will be separated in the new implementation as can be seen in Figure 12.18. The kicker plates will be suspended from the top of the vacuum chamber as shown in Figure 12.19. Care must be taken to ensure the stability of the plates with respect to the time dependent forces associated with the current pulse. At the same time it is desireable to minimize the thickness of the plates and scattering of decay electrons.

12.5 Kicker R&D at Cornell

A laboratory has been outfitted at Cornell to build and test a prototype Blumlein pulse forming network and fast kicker magnet. The electronics that has been recovered from the E821 experiment and re-assembled includes: high voltage power supply, high voltage charging transformer, thyratron driver, trigger pulser and thyratron. We have fabricated a prototype 5 meter Blumlein and tests with a resistive load are in progress. Figure 12.20 shows two

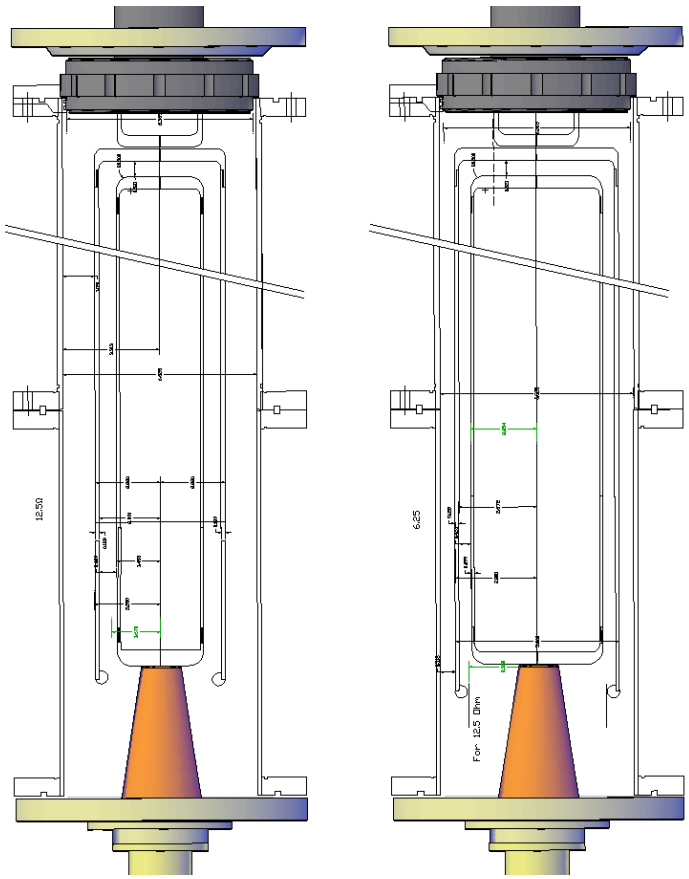

Figure 12.10: Cross section of 25Ω (left) and 12.5Ω (right) Blumlein. The central conductor couples through the orange transition at the bottom of the figure to the load resistor and kicker. The middle conductor connects through the U bracket near to the top to the klystron (not shown). The penetration of the high voltage charging line through the outer conductor to the middle conudctor is not shown.

views of the prototype Blumlein. The downstream, business end of the Blumlein is shown in Figure 12.21. For the test in progress, the line is terminated in a 25Ω resisitive load. The Figure also shows the current pulse through the load as measured with both E-field antenna and B-field current monitor. The rise and fall time of the E-field pulse is dominated by the thryatron turn on and off time. The limited bandwidth of the B-field further degrades the apparent rise time. The base width of the E-field pulse is about 100 ns and the rise time is 30ns, not atypical for a 10 year old, 4-gap tube. (We plan to experiment with other 4-gap thyratron and are investigating the possibility of a 2-gap tube. The required standoff voltage is somewhat less than 100kV, and we have identified a two-gap tube that at least according to its specifications is a viable alternative.

The prototype vacuum chamber is shown in Figure 12.22. Ports have been added to the top and bottom of the chamber to provide a path for the laser light for the Faraday effect field measurement. Macor high voltage standoffs are mounted to the ceiling of the chamber. The new plates will hang from the standoffs. (The laser light ports and macor standoffs are

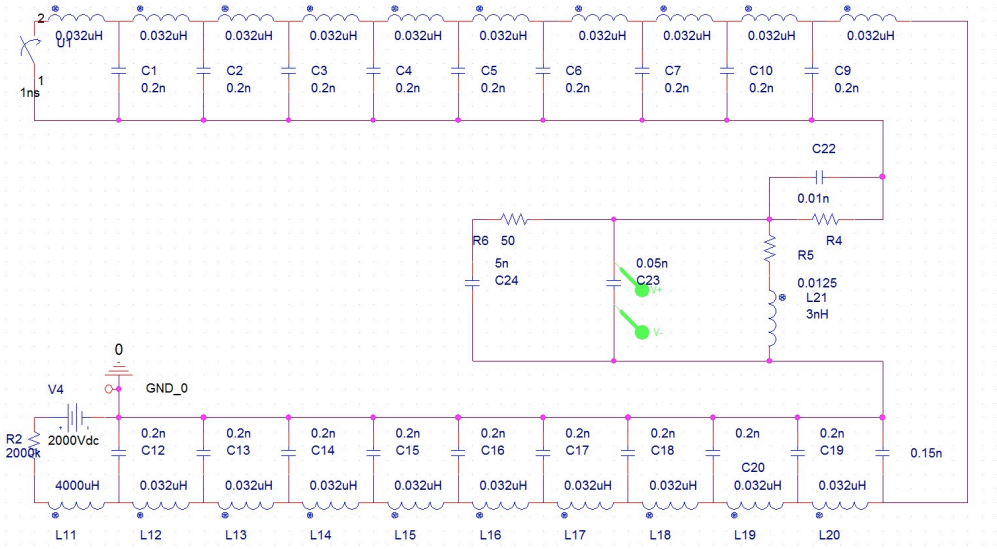

Figure 12.11: Discrete circuit element of the Blumlein that is shown as the right hand schematic in 12.7. Each of the two transmission lines is assembled with lumped inductance and capacitance. The kicker load is represented as inductance with small capacitance.

not visible in the Figure)

The coaxial coupling of the Blumlein to the prototyp vacuum chamber is shown in Figure 12.23.

The kicker lab is equipped to test and modify and test again the PFN and the kicker plate assembly as required to meet the design specifications.

12.6 Kicker Field Measurement

Measurement of the time dependent field of the kicker will ultimately determine the effectiveness of the design choices. Furthermore, it is essential to measure, and ideally eliminate, fields due to the eddy currents in the vacuum chamber and kicker plates, that are generated by the kicker pulse. If the eddy currents have a long decay time, any persistent field will introduce a systematic shift in a_μ.

We plan to implement a Faraday rotator to measure the time dependence of the kicker field and associated persistent fields modeled on the device used in E821. We have machined ports into the prototype vacuum chamber for transmitting polarized laser light through a birefringent crystal that will be mounted between the plates in the laboratory. It is desireable to repeat field measurements in-situ during the course of the experiment and we are exploring the possibility of implementing a Faraday rotator for that purpose.

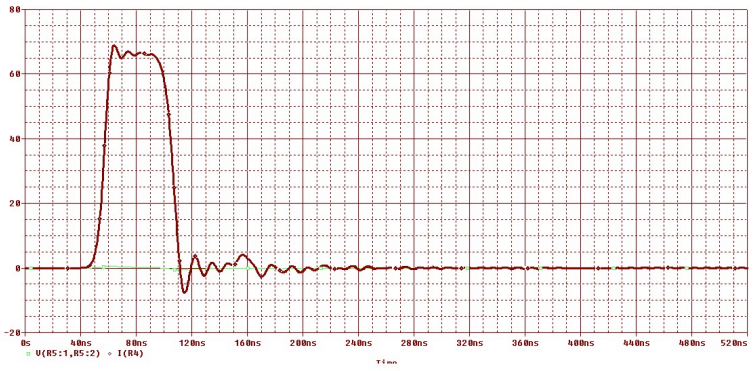

Figure 12.12: Pulse generated by blumlein equivalent circuit in Figure 12.11. Width of the "flat" top is about 70 ns. (Major ticmarks (solid lines) along time axis are every 50 ns.)

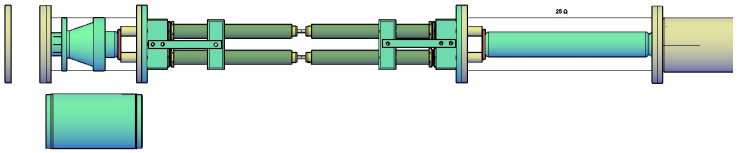

Figure 12.13: Transition from Blumlein to load. The green cylinder at the right couples to the centermost conductor of the Blumlein. With the outer conductor in place (not shown in this view), this short coax will have an impedance of 25Ω. The 25Ω coax couples to a pair of 50Ω high voltage coax cables. At the load end of the cables, there is a transition back to a single 25Ω coax and to the load resistor through the exponential impedance transformer.

12.7 Risks

12.7.1 Performance Risk

The kicker system will be designed to provide an integrated field of 1447 G-m for the duration of the length of the injected muon pulse ($\sim$ 120ns), and then drop to zero field, 149ns after the first muons entered the ring. Failure to achieve the specified field value will result in reduced muon capture efficiency and increased coherent betatron oscillation of the muons that are captured. Failure to turn off after 149 ns will likewise compromise capture efficiency and contribute to coherent betatron motion. The risk of less than optimal system performance are increase in statisical error (fewer muons) and additional systematic error (increased coherent betatron motion). The risk will be mitigated by extensive system testing and optimization prior to installation.

A failure of the thyratron tube, a breakdown internal to the Blumlein-PFN, or a break-

Figure 12.14: Exploded view of the impendace transformer in Figure 12.13 is shown at left. Two possible implementations of the load resistor, that is located on the axis of the transformer, are shown at right.

down of the plates inside the vacuum chamber would have more catastrophic consequences, as very few muons will store without an operational kicker. We plan to operate the system continously at the design repitition rate before installation into the muon ring to establish reliability. We note that the system is designed to operate at 87 kV, approximately 10 kV below the level at which the E821 system was limited by breakdown.

There is some risk that the kicker will excite a long lived eddy current in the vacuum chamber that will in turn generate a lingering magnetic field that will alter the muon precession frequency. We plan to calculate and more importantly measure the parasitic fields generated by the kicker pulse and if we are unable to eliminate them entirely, to account for them in the analysis. We are developing instrumentation for an in-situ monitor of the long lived field.

12.8 Quality Assurance

The quality of the kicker system will be assured by extensive testing in advance of installation into the ring.

12.9 ES& H

The kicker system will operate at high voltage $\sim$ 90kV, however there will be no explosed high voltage. All external surfaces of the Blumlein will be fixed at ground potential. As there are no diodes in the charging circuit, the time constant for dissipation of stored charge

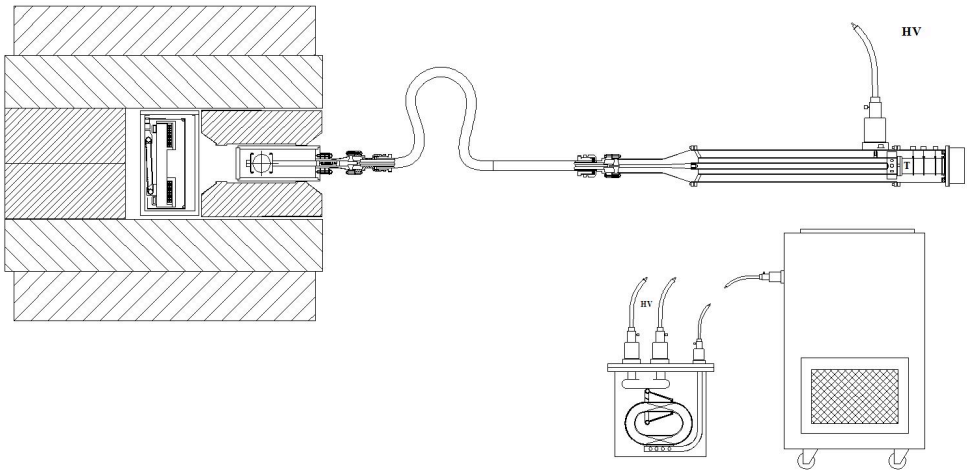

Figure 12.15: Blumlein is coupled through a pair of 25Ω high voltage coaxial cables to the kicker magnet inside the ring vacuum chamber. (Only a single coax is shown). High voltage power supply and thyratron driver are in the electronics rack at right. The 1:84 high voltage transformer that provides charging voltage to the PFN is in the oil tank to the left of the electronics rack.

is a few seconds. A procedure for de-energizing in the event that dissassembly is required will be established. Each of the three Blumlein tri-axial lines will be filled with non-flammable and nontoxic 561 silicon transformer oil. While there is the danger of a spill, (75 liters/line), the oil itself is not hazardous.

12.10 Value management

We are reusing as much as possible, components from E821, in particular, the thyratron tubes.

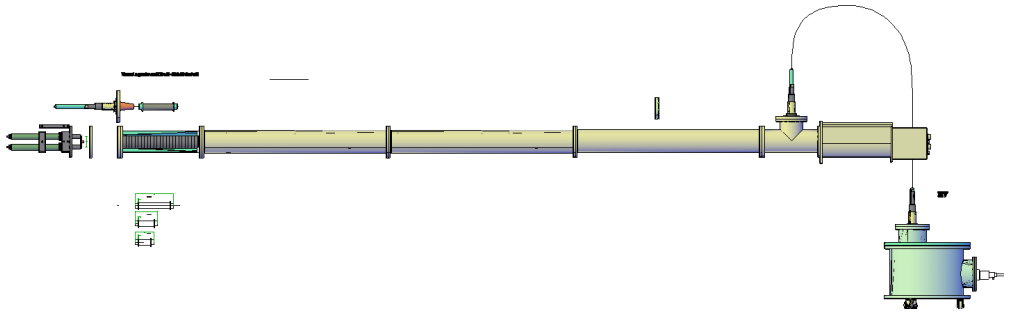

Figure 12.16: Blumlein connected to high high voltage charging transformer. Transition to dual coaxial lines is at the left.

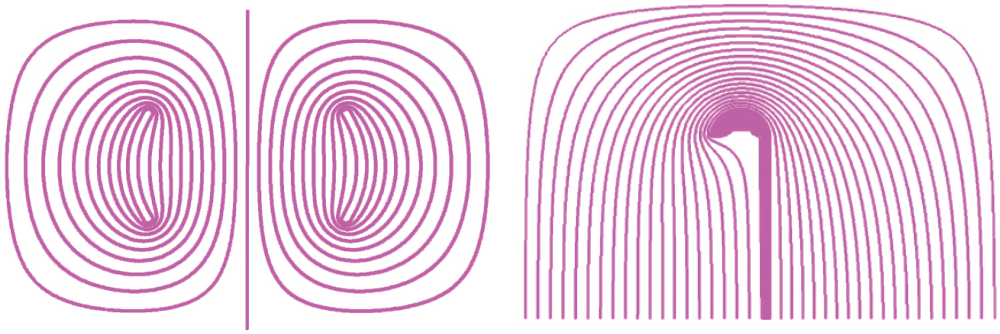

Figure 12.17: (Left) Proposed kicker plate geometry and magnetic field lines computed with MERMAID. (Right) One quadrant of the E821 kicker plate geometry and field lines. The boundary condition at the vacuum chamber surface is set to mimic effect of induced currents due to fast rise time. Note high density of field lines at the edge of the plate that also serves as the trolley rail.

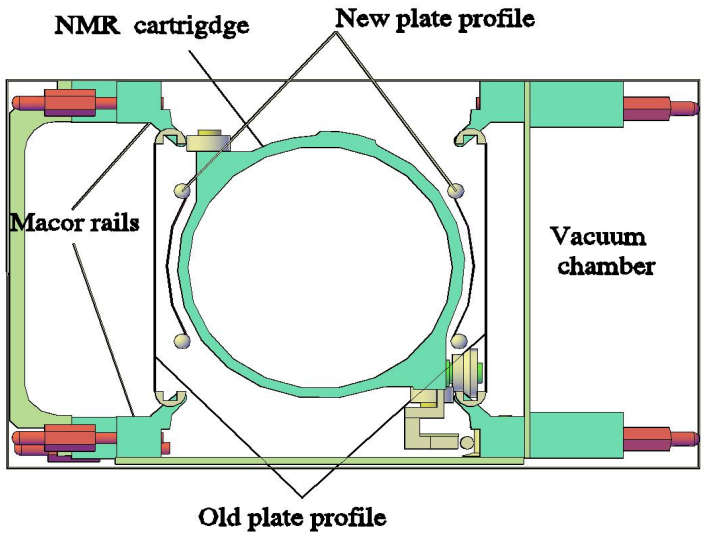

Figure 12.18: E821 kicker plates, new plates, NMR trolley, and new rails are shown in the vacuum.

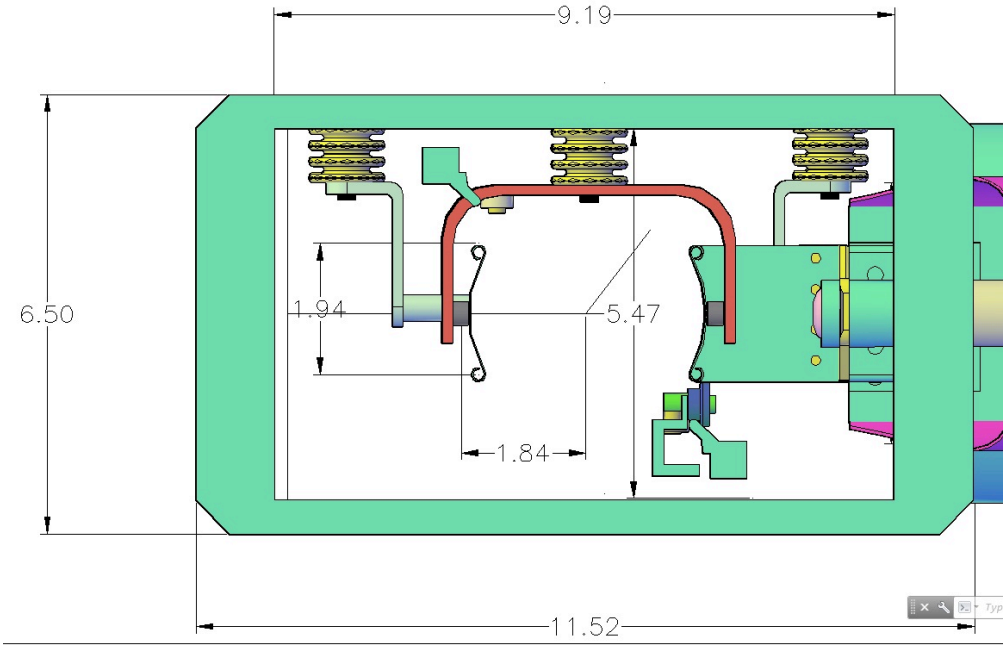

Figure 12.19: The new kicker plates hang from macor standoffs mounted on the top of the vacuum chamber. The crossover from inner to outer plate at the far end of the kicker is also shown.

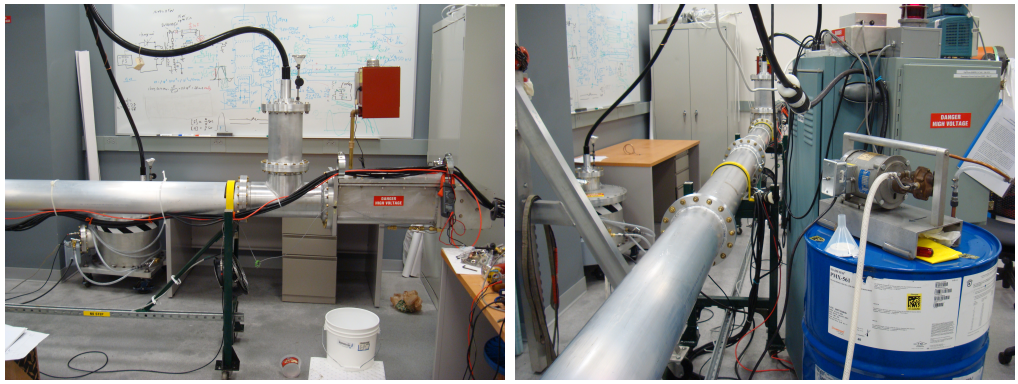

Figure 12.20: (Left) Upstream end of Blumlein. The black cable attached at the top of the transition delivers the charging current. The thyratron is mounted horizontally in the far right module with the red High Voltage warning lable. The space between the conductors of the Blumlein and the volume around the thyratron is filled with transformer oil. (Right) Looking from the business end of the Blumlein upstream towards the thyratron.

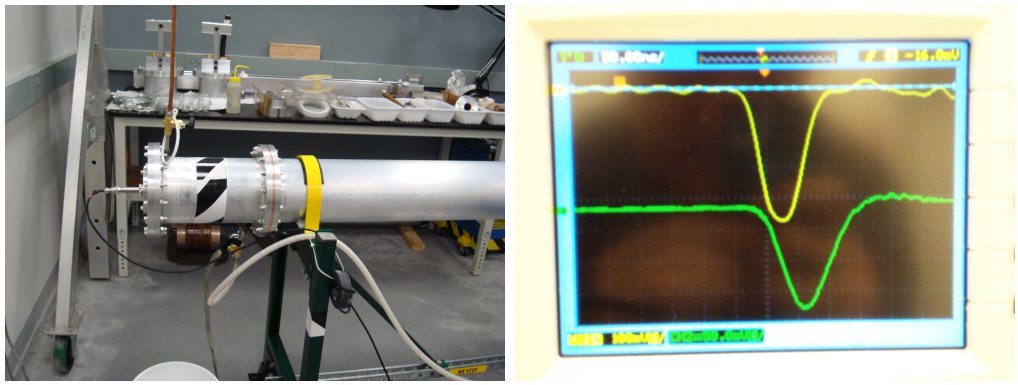

Figure 12.21: (Right) Pulse generated with Blumlein, discharged through a resistive load that is in the end section of the Blumlein(Left). The horizontal scale (hard to see) is 50 ns/division. The base of the yellow pulse is about 100 ns and the rise time 30ns. The nominal pulse width, for the 5m line and ideal switch is 50ns. The width of this pulse is dominated by the thyratron switching time. The yellow signal is from an antenna probe and the green from a somewhat slower current monitor. With 561 oil, ϵ= 2.7 the pulse width $\sim$ 50 nsec, with Castor oil,ϵ= 4.7, the pulse width $\sim$ 66 nsec. and with addition of Ferrofluid, $\mu_{eff} \sim 3$, the pulse width $\sim$ 112 nsec.

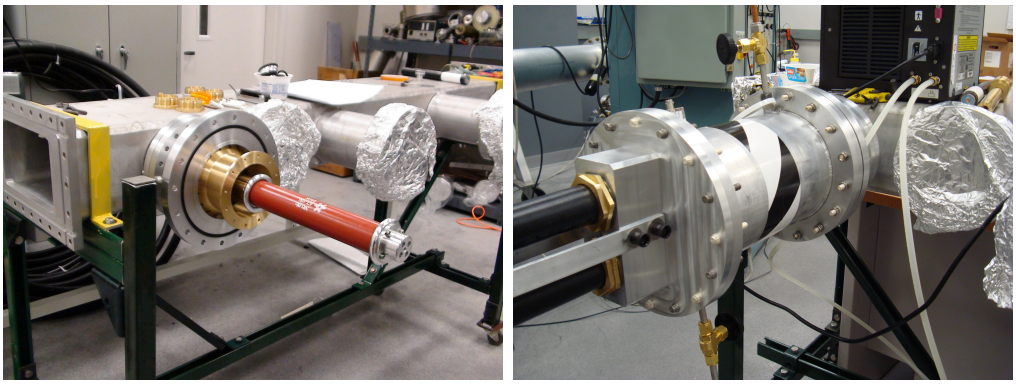

Figure 12.22: (Left)Load resistor at vacuum chamber port. (Right) The pair of coaxial cables links the Blumlein output to the load resistor (located inside the chamber with the black and white tape) and then to the kicker plates inside the vacuum chamber.

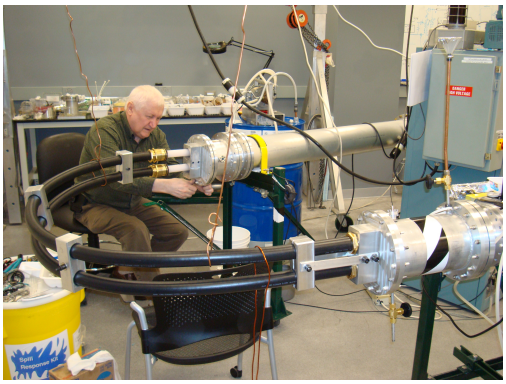

Figure 12.23: A pair of 50Ω coaxial cables couples Blumlein (background) to input to vacuum chamber (foreground)

References

[1] Efstathiadis E, et al. *Nucl. Inst. and Methods Phys. Res.* A496:8-25 (2002)

[2] A.D. Blumlein, Apparatus for Generating Electrical Impulses, U.S. Patent No. 2,496,979 Feb 7(1950).

Chapter 13

The Electrostatic Quadrupoles

13.1 Introduction

One of the ways to be able to store a significant number of muons in the storage ring is to use electric focusing quadrupoles (ESQ) and muons at their magic momentum of about 3.09 GeV/c. At that momentum the radial E-field precesses the muon momentum and the muon spin vectors at exactly the same rate and thus it does not influence the $(g-2)$ precession frequency. The method was first used in the last muon $(g-2)$ experiment at CERN [1], and in E821, the muon $(g-2)$ experiment at BNL [2]. We have also decided to use it for E989, the FNAL experiment, after we have carefully considered alternatives, e.g., weak magnetic focusing, and alternating skew electrostatic quad focusing. However, we found the present scheme, used in E821, to be preferable.

The principal characteristics of the design are similar to the E821 ESQ described in [3]. In the present document we are going to describe them and include the main points that aim to improve the muon ring acceptance and reduce muon losses as well as certain systematic errors associated with the coherent betatron oscillation frequencies. Fig. 13.1 shows a schematic of the top view of the muon $(g-2)$ ring and the vacuum chambers indicating the azimuthal coverage of the quadrupoles in E821. The total azimuthal coverage is kept at 43%, keeping a four-fold symmetry with segment names of Q1, Q2, Q3, and Q4. Each quad segment consists of a "short" quad of 13° and a long one of 26°, see Fig. 13.2, for two reasons: 1) to make every quadrupole chamber independent of others, facilitating their development, testing, etc., and 2) to reduce the extend of low energy electron trapping. Therefore there are two high voltage vacuum-to-air interfaces for each segment.

The maximum voltage we used during the muon runs on the ESQ of E821 was 25.4 kV resulting to a field focusing index of 0.144. We now plan to raise the maximum voltage to 32 kV for a field focusing index of $n = 0.18$. At 0.18 the following things we expect to happen:

1. Increase the ring admittance and most likely the muon storage efficiency.
2. Reduce the muon losses during storage.
3. Reduce the coherent betatron oscillation (CBO) systematic error.

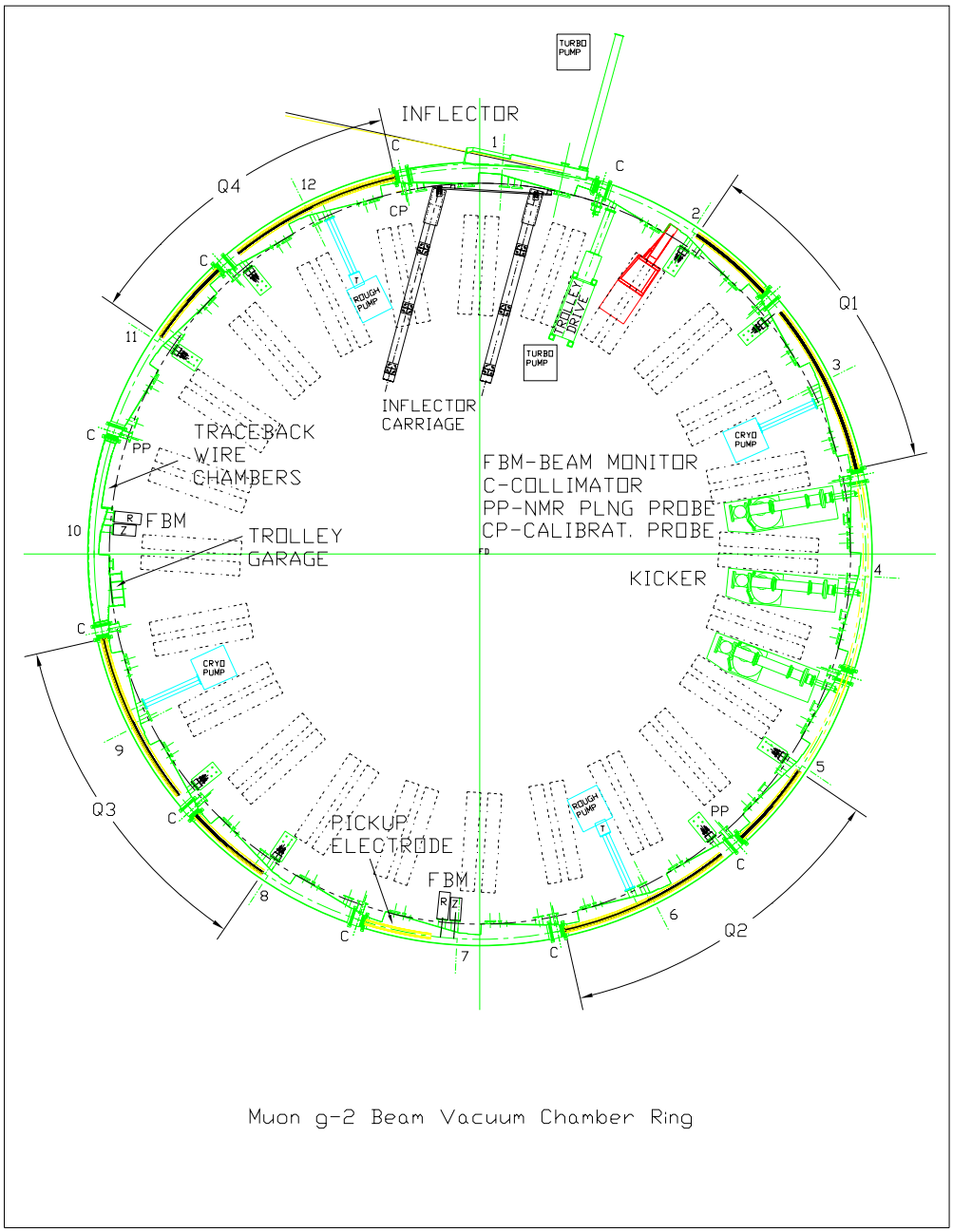

Figure 13.1: A schematic of the muon $(g-2)$ ring as well as the location of Q1, Q2, Q3, and Q4, the four-fold symmetric electrostatic focusing system.

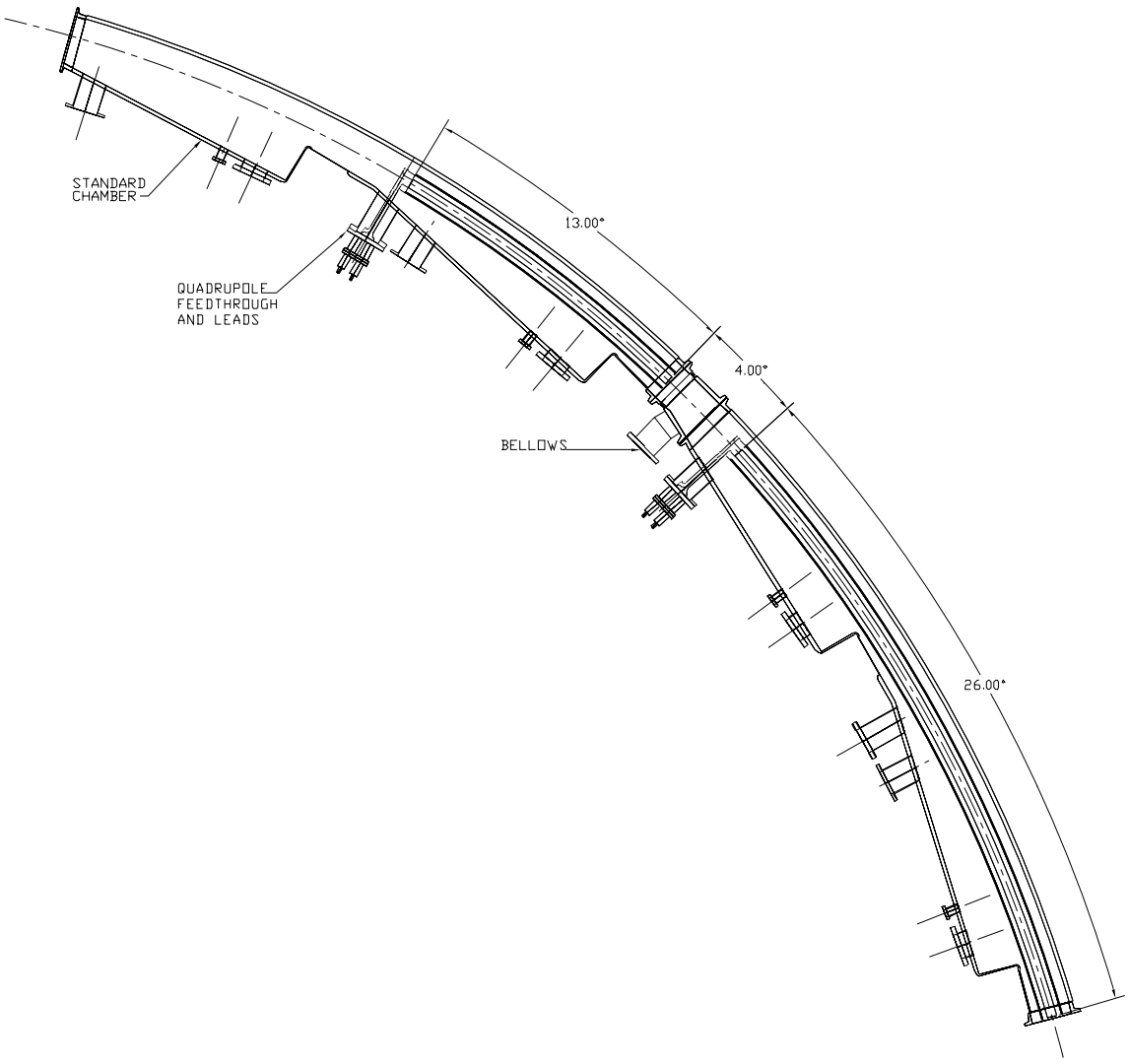

Figure 13.2: A schematic of a short quad of 13°, and the adjacent long one of 26° is shown here. The high voltage feeding leads break the quad symmetry at the upstream end of the plates to quench the low energy electron trapping and guide them outside the magnetic field region, where they can be released. Some of the bellows were equipped with collimators where the muon beam was scrapped immediately after injection.

We will test the quads up to 35 kV, about 10% higher voltage than the anticipated nominal voltage level, in order to substantially reduce the required number of pulses to be applied for a successful testing. A large number of improvements will be implemented to the new system based on the experience we accumulated running the quadrupole system for E821. They are discussed later on in this chapter.

13.2 E821 Design and Limitations

The cross-section of the quadrupoles is shown in Fig. 13.3 with the various dimensions indicated in the figure. The ESQ consist of four aluminium plates symmetrically placed around the muon storage region. The placement accuracy was 0.5 mm for the horizontal (top/bottom) quad plates, and 0.75 mm for the vertical (side) quad electrodes. When measured by the surveyors they were found to be well within those values.

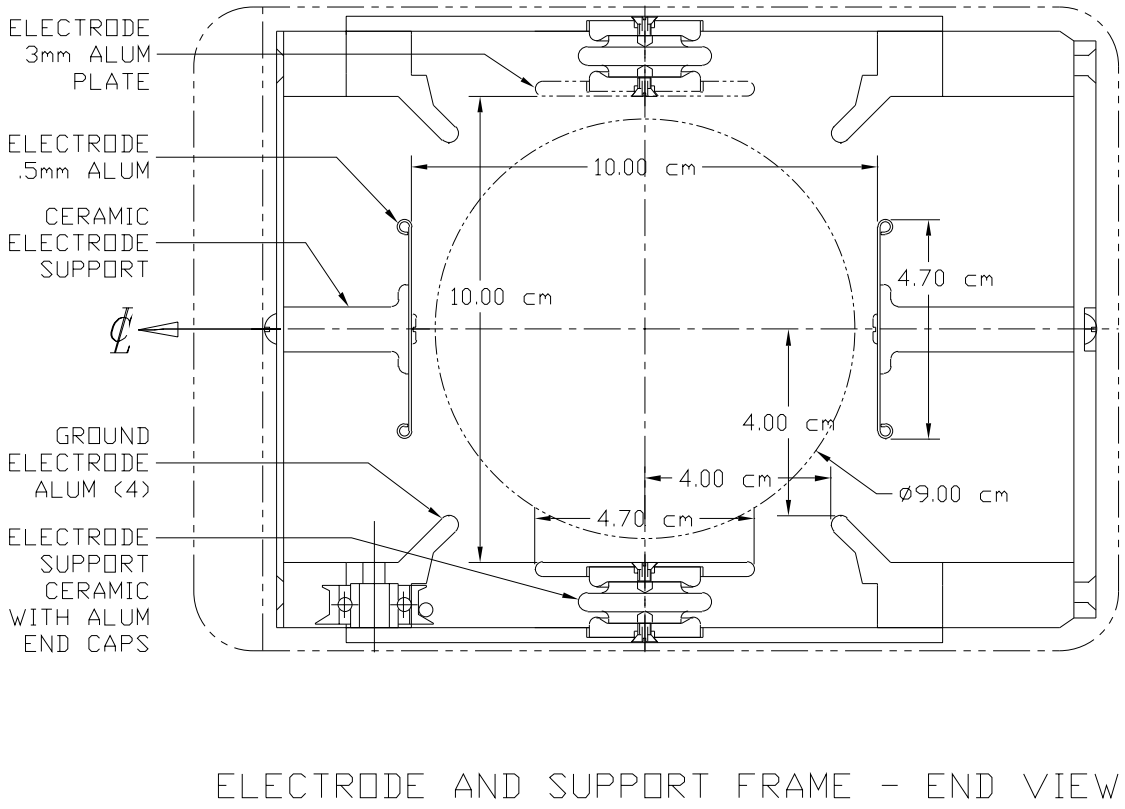

Figure 13.3: A schematic of the quadrupole cross-section. The rails in the corners are kept at ground potential. Most of the support insulators are replaced with uniform diameter insulators of 0.5 cm.

Fig. 13.4 shows a picture of the quadrupoles at the downstream end of one chamber. The main issue in E821 was to be able to hold the high voltage without sparking for about

1 ms. This is a very demanding task, especially for storing negative polarity muons, due to low energy electron trapping in the quad region. We were able to achieve this task by designing the HV feeding leads in a way to quench the low energy electron trapping, see Figs. 13.5, 13.6, 13.7.

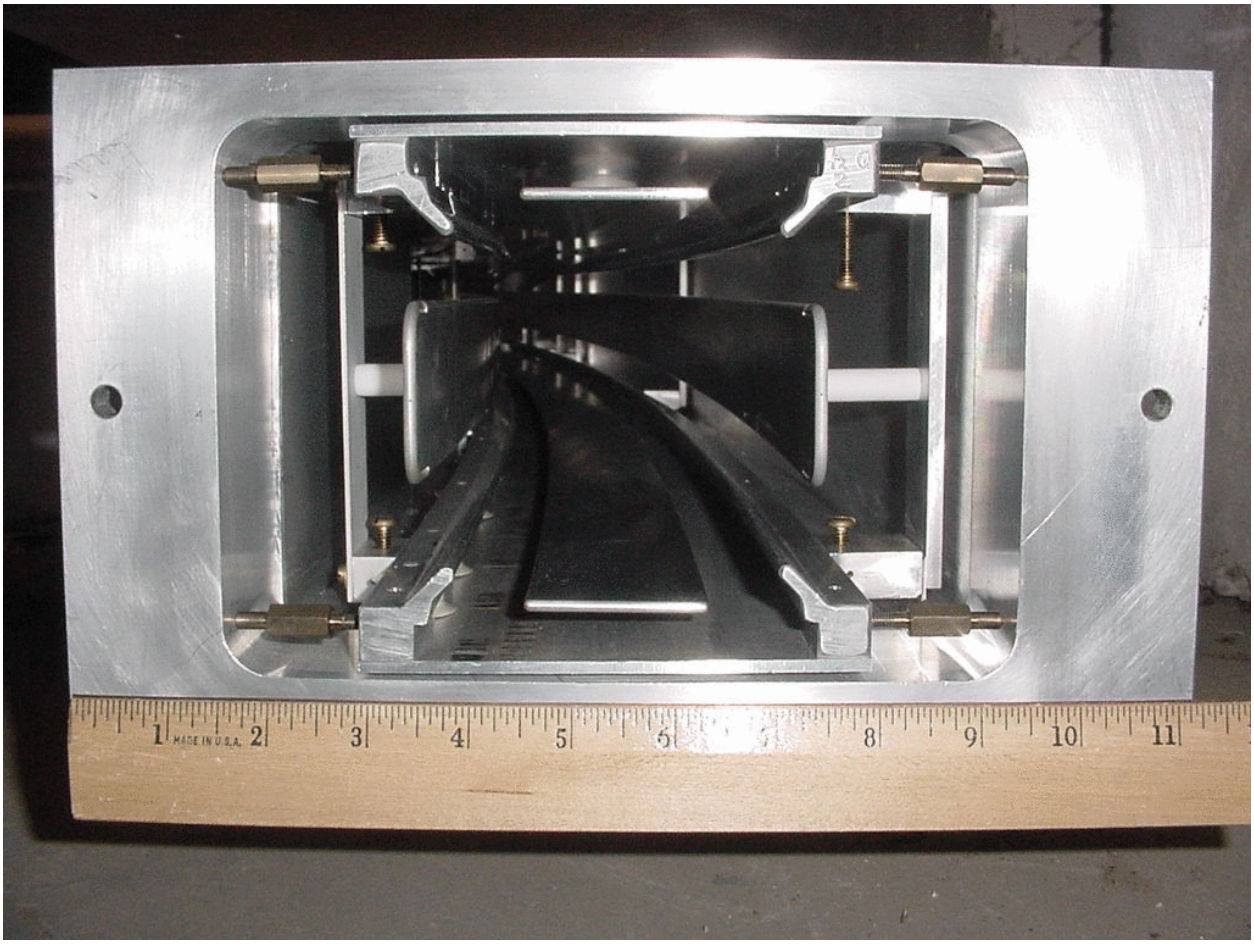

Figure 13.4: A photograph of the downstream end of a vacuum chamber with the cage and quads showing.

Fig. 13.8 shows the schematic of the HV pulsing system. Two of the quadrupoles were used to scrape the injected beam horizontally, by moving the beam sideways [3], while all the quadrupoles were used to scrape the beam vertically [3]. The HV monitor location is also indicated. Fig. 13.9 shows the (home-made) HV monitors output waveforms as recorded by an oscilloscope.

The great success of the quadrupole system is based on the fact that it allowed the storage of positive and negative muons for more than 0.75 ms in the storage ring, even though the azimuthal quad coverage was almost half that of the last muon $(g-2)$ experiment at CERN. The vacuum requirements were in the low 10^{-6} Torr for the positive muons and low 10^{-7} Torr for the negative muons. Higher vacuum pressures were tolerated for limited operation periods. Those requirements allowed a speedy recovery after any unavoidable opening up of the vacuum chambers during the initial stages of the runs, related mostly to

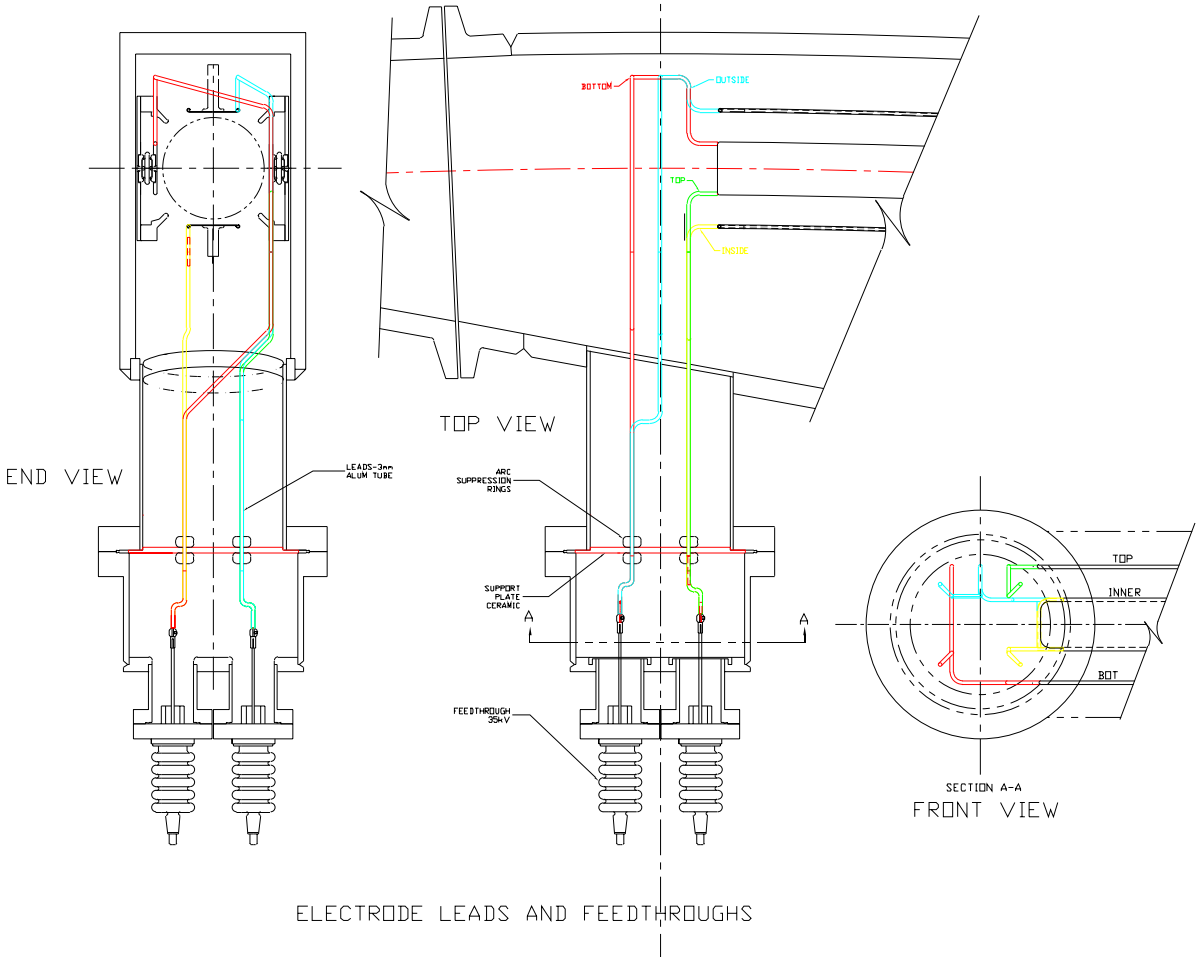

Figure 13.5: Various aspects of the quadrupole high voltage feeding lead geometry, designed to minimize low energy electron trapping.

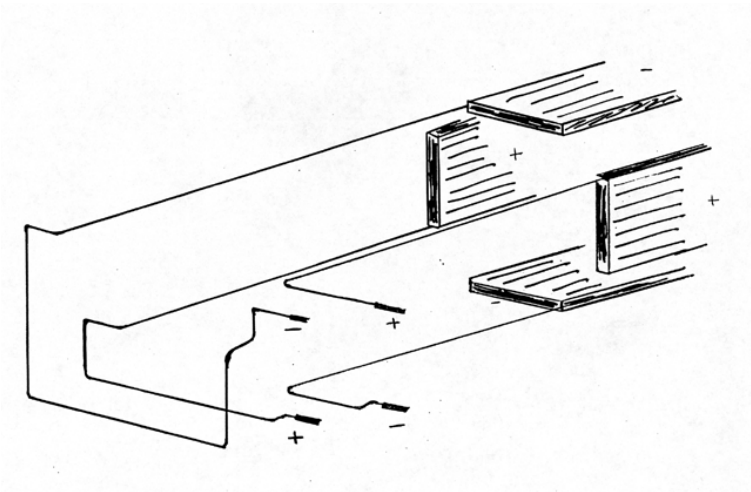

Figure 13.6: Early stages of a hand drawing indicating the high voltage feeding lead geometry.

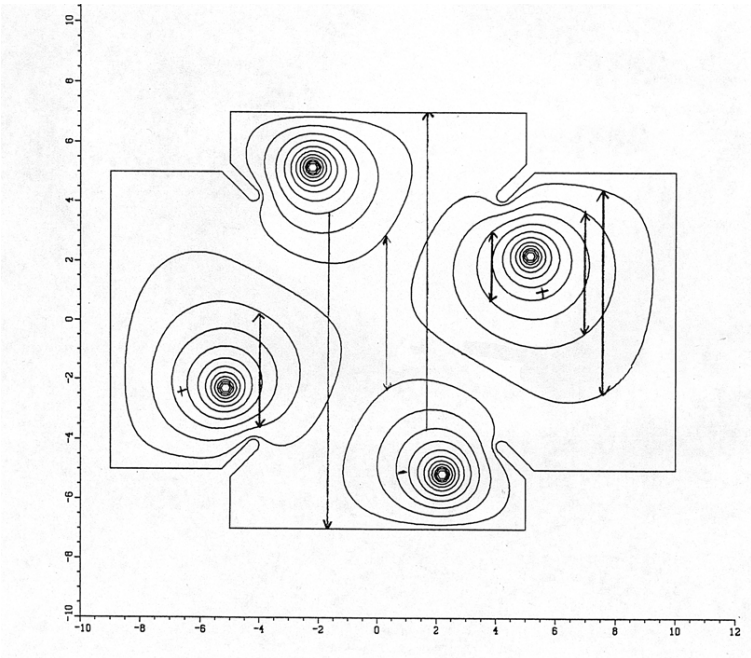

Figure 13.7: A cross section of the lead geometry (vertical [cm] vs. horizontal [cm]). The schematic showing the equipotential lines as well as the low energy electron trapping regions. The lead-geometry was designed to optimize the quenching of the electron trapping for the negative muon storage polarity.

issues other than the quadrupole operations.

For E989 we focus on positive muon storage only, due to the following advantages:

- It allows us to improve the E-field quality by restoring the normal quadrupole field in the lead region. The plan is now to connect the leads at the center of the plates, expose the E-field from the leads for a couple of centimeters, and then hide them behind a ground shield. The aim is to shield the muon storage region from the E-field generated by the leads. Space is very tight at this location, so we will work very carefully to avoid sparking.

- We will be able to raise the high voltage and keep it there for longer times, which may have an impact on the muon lifetime measurement or other systematic error measurements.

- For E821 the quadrupoles required a lengthy conditioning period (a couple of hours, depending on pressure) after every trolley run. For positive muon storage plus an automated conditioning system we expect to minimize this recovery time by a factor of two to three. Quadrupole conditioning is much more straight forward in the positive polarity than in the negative polarity. The main reason is that in the negative polarity the support insulators are intercepting the low energy trapped electrons, which, depending on the trapping rate, could cause sparking. The conditioning process in the negative polarity was very delicate and lengthy. One of the possible models why it even

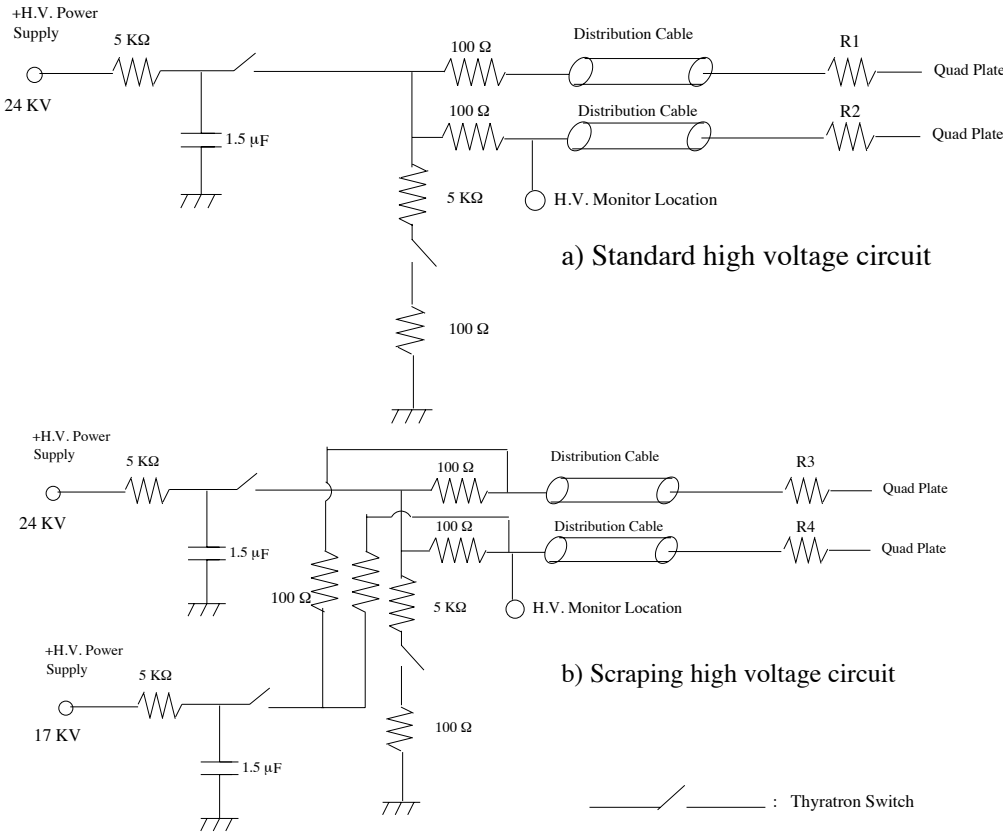

Figure 13.8: A schematic of the scraping and normal HV pulsing systems. The Thyratron switch model used in E821 was the CX1585A from eeV, good to 40 kV.

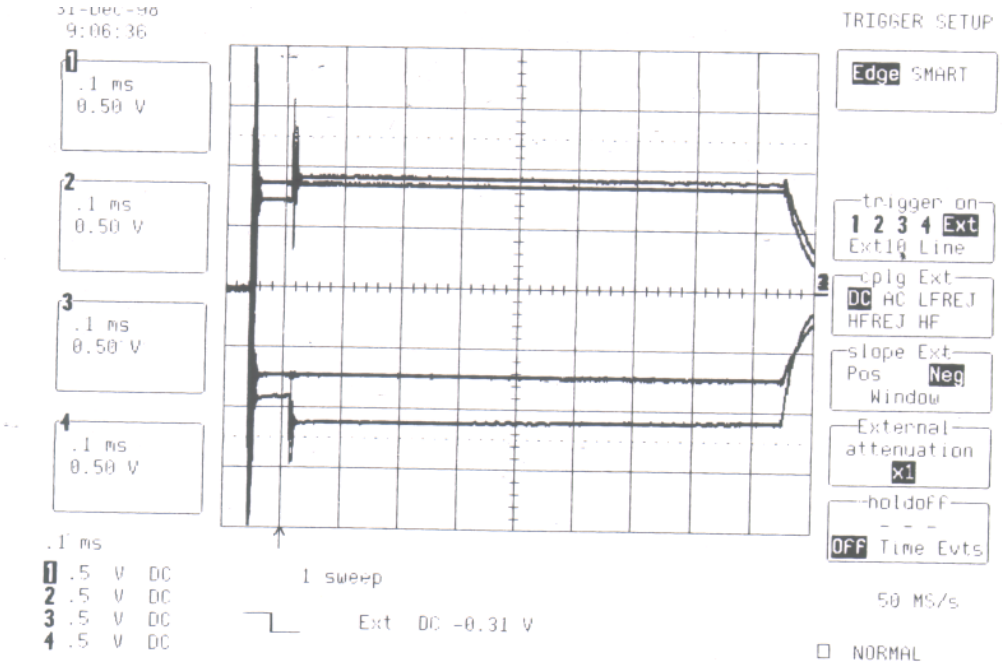

Figure 13.9: The output of the HV monitors as recorded by the oscilloscope.

worked was that the slow conditioning creates a thin conducting layer on the insulator surface, allowing them to slowly move and thus avoid accumulating a critical level. For the positive polarity there are no insulators in the way of the trapped electrons. We will write a computer software program that will be able to condition the quadrupoles taking into account the vacuum pressures and sparking history.

- For positive muon storage we expect the voltage on the plates to be more stable as a function of time and from pulse to pulse.

Table 13.1: Comparison of high-n and very high-n values.

Parameter	**n=0.142**	**n=0.18**
ν_x	0.926	0.906
ν_y	0.377	0.425
$f_{\rm CBO}$	495 kHz	634 kHz
$f_{\rm CBO}/f_a$	2.15	2.76
$1/(f_{\rm CBO}-2f_a)$	27μs	5.7μs
HV	25 kV	32 kV

For E989 we require improvements in a number of areas:

1. Operate the quadrupoles at a higher n-value to primarily change the horizontal coherent betatron oscillations (CBO) frequency away from near twice the muon $(g-2)$ frequency. The CBO frequency, being very close to twice the $(g-2)$ frequency, see Table 13.1, pulled the $(g-2)$ phase and was a significant systematic error that required special attention during data analysis. We target to operate at $n=0.18$ to reduce it by more than a factor of three. Other improvements, e.g., properly matching the beam-line to the storage ring (requiring a proper inflector channel) is expected to reduce it by at least another factor of three. Overall the CBO systematic error can be reduced to a level required by E989.

2. Reduce the muon losses by more than an order of magnitude to reduce the muon losses systematic error. We will achieve this goal by moving the operating point to $n=0.18$, beam scraping by 2 mm in the horizontal and vertical directions after injection, and by keeping the radial B-field below 50 ppm (this level of radial B-field displaces the average vertical position by about 2 mm). The region around $n=0.18$ is more resonance free than the previous n-values we ran with, see Fig. 13.10. We will refine the quadrupole operating mode by running precision beam dynamics tracking simulations to more accurately predict the muon population phase-space after scraping.

3. Shield the muon storage region from the modified quadrupole field due to the HV feeding lead geometry. This region is less than 5% of the good quad coverage around the ring, but it can still influence the muon loss rate.

4. The quadrupole voltage monitors were home-made with limited success in achieving an adequate frequency compensation. We now plan to equip every quad plate (32 in

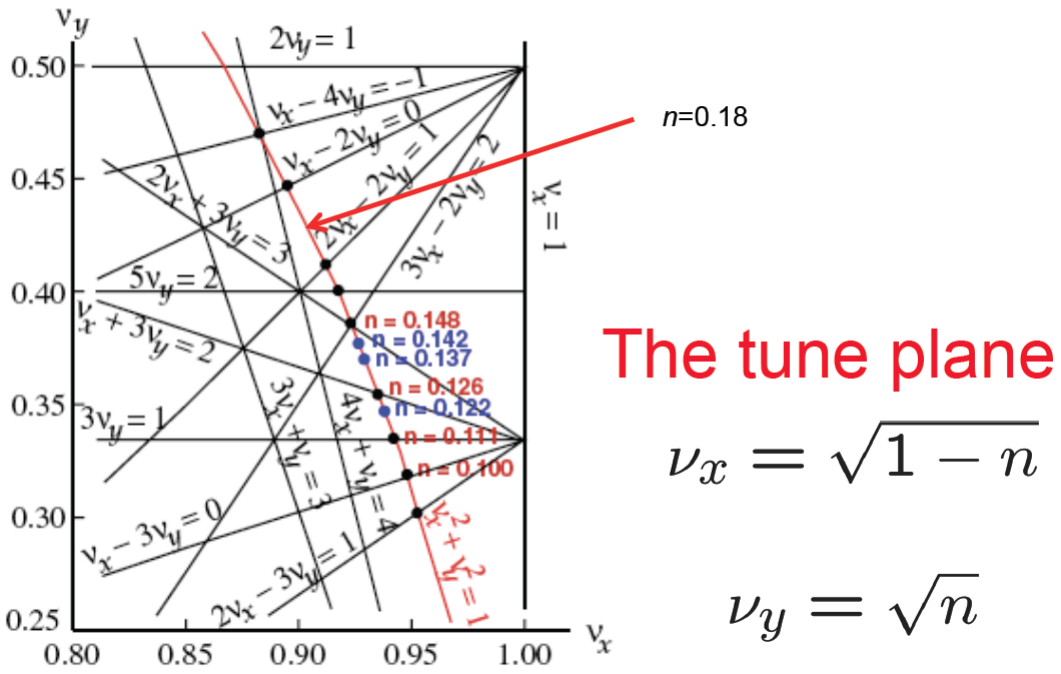

Figure 13.10: The vertical vs. horizontal tune plane together with a number of potential resonance points. The value $n = 0.18$ is on the red line and in the middle between the resonance lines $\nu_x - 2\nu_y = 0$ and $2\nu_x - 2\nu_y = 1$.

total) with a commercially available frequency compensated HV monitor. This will improve the voltage stability readout by an order of magnitude. In addition, we will cross-calibrate the frequency compensation of each monitor with the electric field in the quad region measured using the Kerr effect.

5. Improve the reliability of the HV-vacuum interface regions with a goal of reducing sparking by at least an order of magnitude. The base design is to cover the interface in oil capable of holding high electric fields. Alternative design calls for increasing the spacing between positive and negative leads in the air side of the interface.

6. The outer Q1 plate and support insulators are estimated to have reduced the stored muon population by about 40%. We now plan to address the muon loss issue by a number of alternative modifications. Currently the baseline is to relocate the outer Q1 from $x = -5$ cm to $x = -7$ cm to allow for the uninhibited injection of the muon beam. Fig. 13.11 shows the `OPERA` model of the quadrupole plates in a quadrupole cage. The plate width is adjusted so that only the normal quadrupole field is dominant, and the 20-pole is kept at the 2% level. Every other multipole is below 0.1%, including the sextupole, octupole, etc. Fig. 13.12 shows the current plan for providing a "massless" outer Q1 plate, by placing it outside the muon path. In order to restore an acceptable field quality, the plate voltage also needs to be raised by about a factor of two, see Fig. 13.13. Another parameter we can use to improve the field quality is to work with the plate geometry (width, shape, etc.). The requirement of increasing the voltage by

a factor of about two we believe we can achieve in the positive muon polarity and we will test it with the setup planned at BNL.

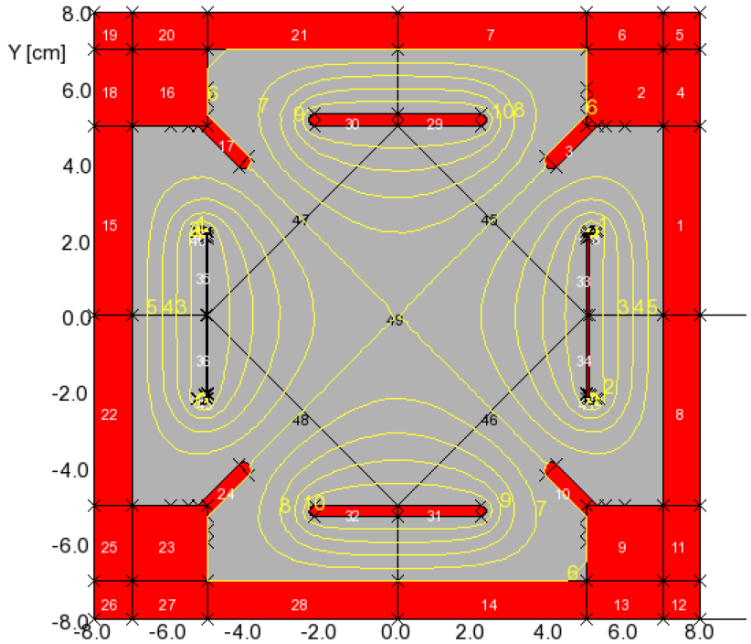

Figure 13.11: An OPERA model of the (normal: Q2, Q3, and Q4) electrostatic quadrupole plates. The top/bottom plates are at a positive voltage and the side electrodes are at (the same) negative voltage. The yellow curves represent the equipotential lines.

7. Measure the plate vibration during pulsing and stiffen the plate support as needed.

13.3 Improvements that Permit Higher n-Value Operation

Quad upgrade and testing with the aim to produce an ESQ focusing system that maximizes muon statistics and minimizes potential systematic errors. Fig. 13.14 shows one segment of the muon $(g-2)$ electrostatic quadrupoles at BNL outside its vacuum chamber.

Vladimir Tishchenko is the L3 manager for the ESQ system and Yannis Semertzidis was the former L3 manager for the same system. The ESQ system currently consists of 8-chambers, 4-pulser systems, 6-HV-power supplies, and a HV monitoring system:

- Refurbish the H.V. pulsers to operate at a maximum voltage of ± 35 kV, from the present ± 25 kV used in E821. The side insulators are all varnished during the negative muon operation at BNL, see Fig. 13.15. The insulators will be either cleaned or will be replaced by new ones.

- Utilize a C-magnet at BNL to imitate the conditions of running the ESQ in the muon $(g-2)$ magnet as closely as possible. For practical reasons we can only test the half-scale

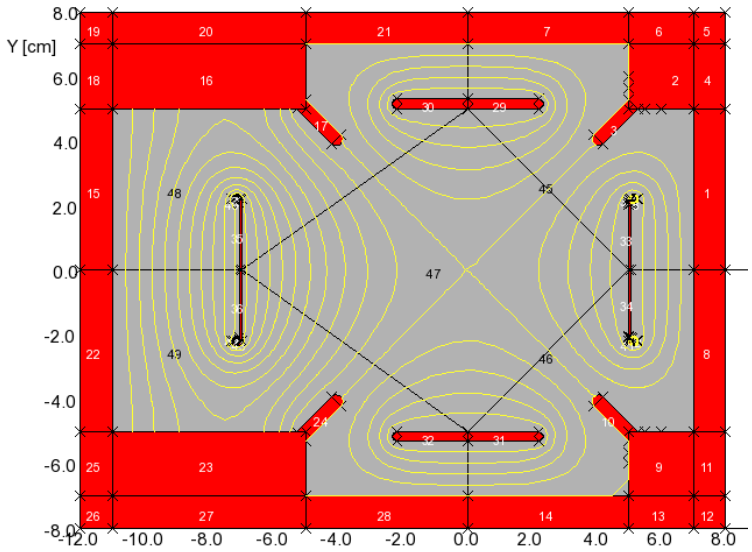

Figure 13.12: An OPERA model of the electrostatic quadrupole plates for Q1. The left plate is displaced to the outside by 2 cm to allow the muons to enter the storage region without having to cross the plates or the support insulators. In order to restore a good field quality (indicated by the symmetric equipotential lines in the center region), the voltage on the left plate is about twice that on the right plate.

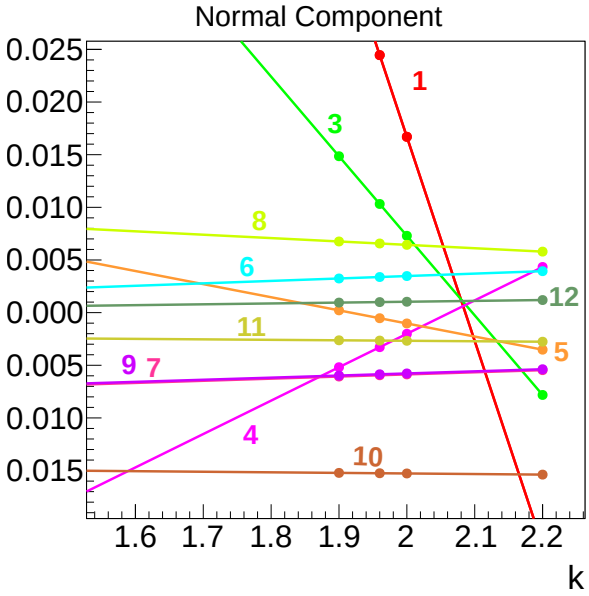

Figure 13.13: Results from OPERA as a function of the voltage multiplication factor for the displaced (outer Q1) plate. Most of the multipoles are below 0.5% but not all. Next we will study the effect of the plate shape on the multipoles.

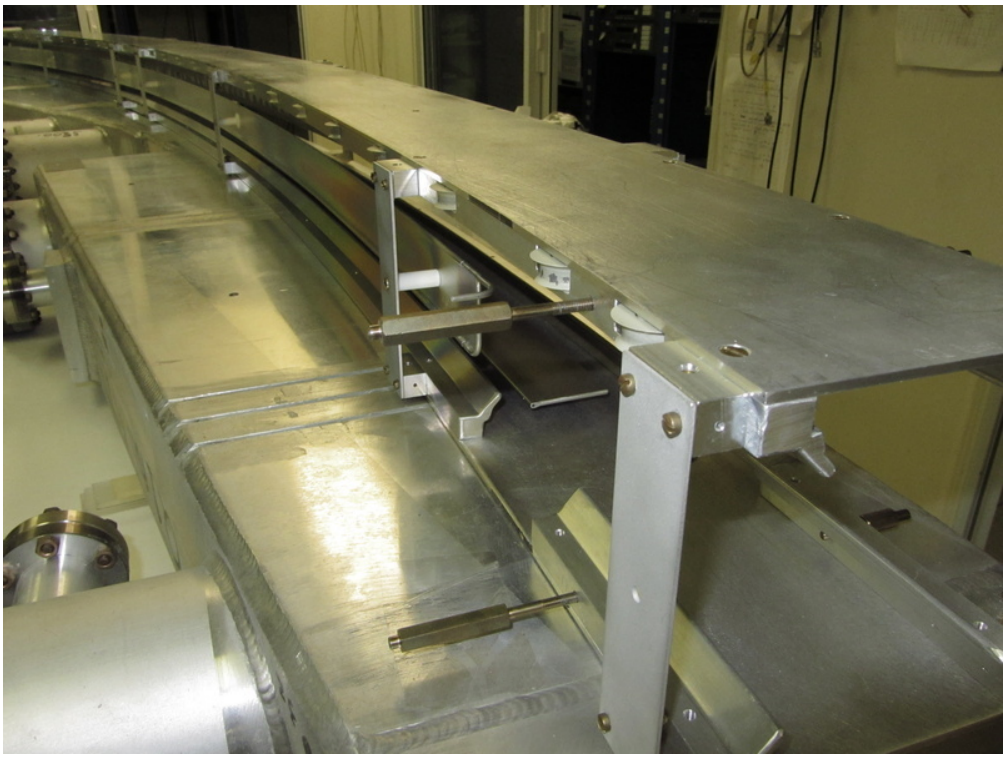

Figure 13.14: One cage (placed here up-side-down) that holds the plates of the electrostatic quadrupoles of the muon $(g-2)$ experiment.

quadrupoles, as the (straight) C-magnet under consideration could not accommodate the full scale quads, see Fig. 13.16. We will be able, however, to extrapolate to the full quads by placing stricter requirements on the vacuum pressure.

- Optimize the ESQ for positive polarity muon storage. The leads will be re-configured to quench the low energy electron trapping more efficiently aiming to achieve higher electric field gradient by 30% compared to E821. Achieving this goal will help eliminate the CBO systematic error as well as substantially reduce muon losses.

- Expand the H.V. vacuum chamber/air interface tube aiming to significantly reduce the sparking in the vacuum side of the leads.

- Modify the geometry of the H.V. -vacuum interface to reduce sparking in the air side of the H.V. lead system or immerse it in oil that can withstand the E-field strength. The later is applied routinely in H.V. applications but it is harder to gain access to it. The sparking rate in the positive polarity in E821 was dominated by sparks at those locations (approximately one spark per 0.5-1 million pulses).

- Shield the electric field generated by the leads from the muon storage region.

- Measure or place strict limits on the magnetic field generated by the trapped electrons.

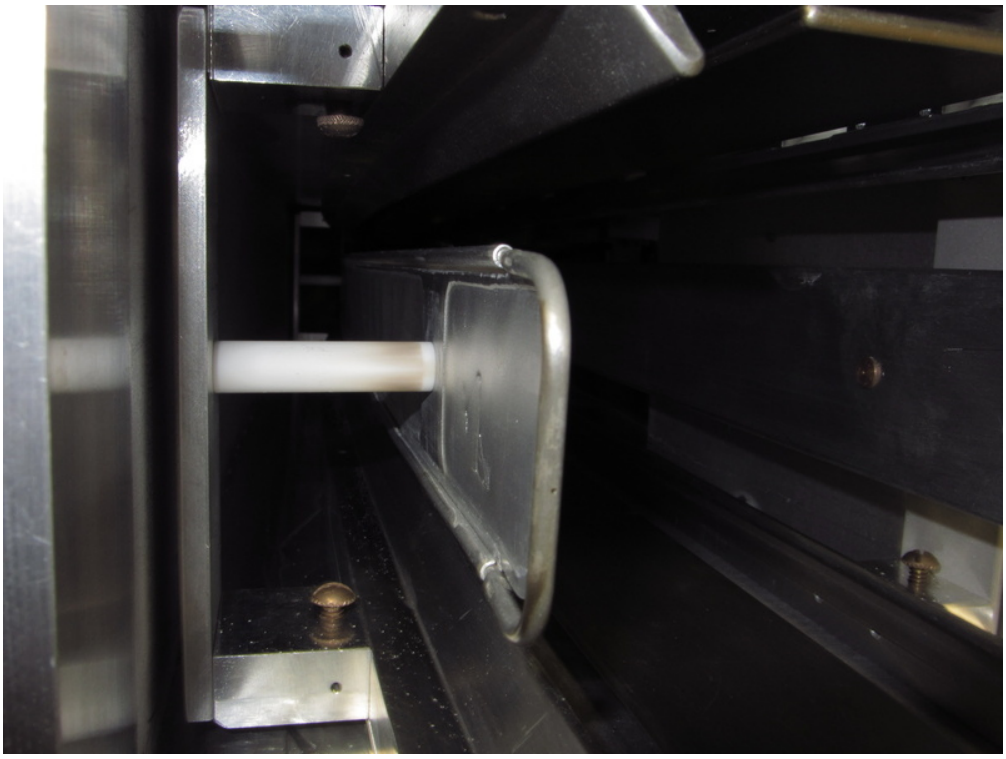

Figure 13.15: The side support insulators are varnished due to trapped electron obstruction during negative muon operations at BNL.

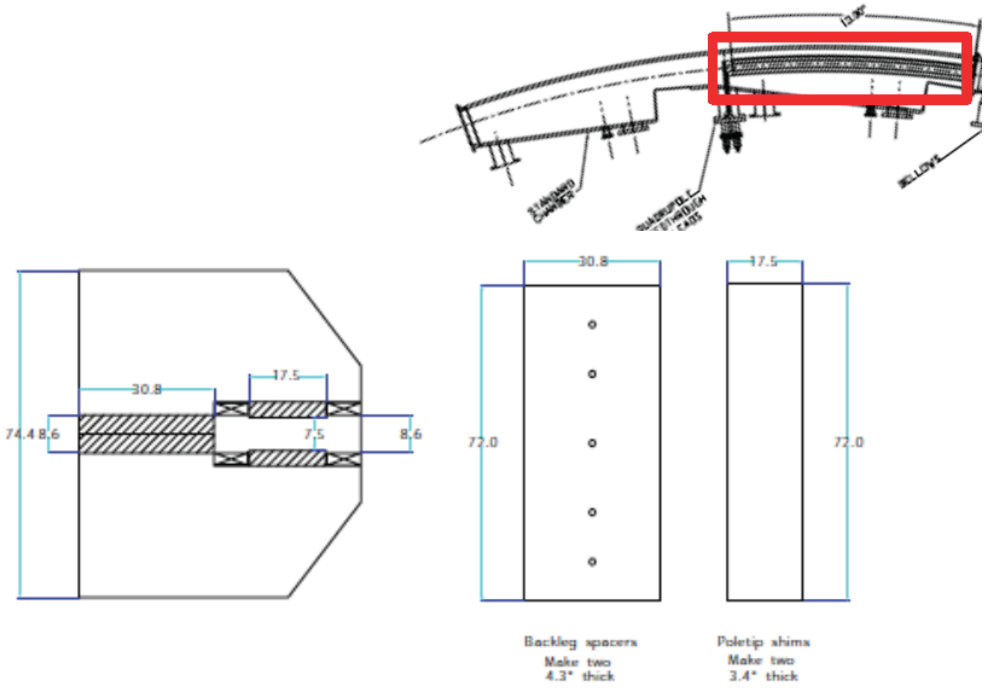

Figure 13.16: A C-magnet is being prepared at BNL for testing the quad upgrades. The magnet can fit the short quads but it requires shortening the plates by about 20 cm (for testing purposes only).

- Calibrate the pulse shape output of the commercial H.V. monitors by measuring the electric field generated by the plates using the Kerr effect. The bandwidth (BW) of the Kerr effect measurement is in the GHz range and therefore it is not limited by the level of frequency compensation due to the large capacitance of the components involved.

- Measure the vibration parameters of the quadrupole plates when pulsed using a laser light and a split diode detector. The quad plates can flex under the electromagnetic forces when pulsed. This flexing is (crudely) estimated that it can be of order of 10 mm if the pulse duration is of order 1 s. However, for 1 ms the plates can only move by about 10 μm, much below our specs. We will setup a laser system to measure the plate motion due to the impulse of the electrostatic pulse.

13.3.1 Coherent Betatron Oscillations

The average position and width of the stored beam can vary as a function of time as the beam alternately focuses and defocuses in the ring. This is the result of a mismatched injection from the beam-line into the $(g-2)$ ring via a narrow line, the so-called inflector magnet. This imposes an additional time structure on the decay time spectrum because the acceptance of the detectors depends on the position and width of the stored muon ensemble.

The CBO frequency in E821 was close to the second harmonic of ω_a, so the difference frequency $\omega_{\rm CBO} - \omega_a$ was quite close to ω_a, causing interference with the data fitting procedure and thereby causing a significant systematic error. This was recognized in analyzing the E821 data set from 2000. In the 2001 running period the electrostatic focusing field index was adjusted to minimize this problem. This greatly reduced the CBO systematic uncertainty. We will follow this strategy again but this time we will increase the quad voltage by another 30% to decrease the CBO systematic error by more than a factor of three, see Fig. 13.17.

In addition, the anticipated new kicker pulse shape will better center the beam on orbit. On the detector side, we plan to increase the vertical size of the detectors compared to E821 (from 14 to 15 cm). This reduces the fraction of lost electrons passing above or below the detector, and therefore the sensitivity of the detector acceptance to beam position and width.

In an ideal world, where the detector resolution is uniform around the ring, the CBO systematic error averages to zero when all the detected positron pulses are summed up. However, for E821 the kicker plate geometry broke significantly the detector resolution symmetry around the ring resulting to a non-zero average. With the new design we expect to significantly restore this symmetry.

The combined efforts should reduce the CBO uncertainty by at least a factor of 4 to well below 0.02 ppm. If a new, more appropriate inflector with wider horizontal aperture is used, then it is feasible to eliminate the CBO systematic error to well below our sensitivity level.

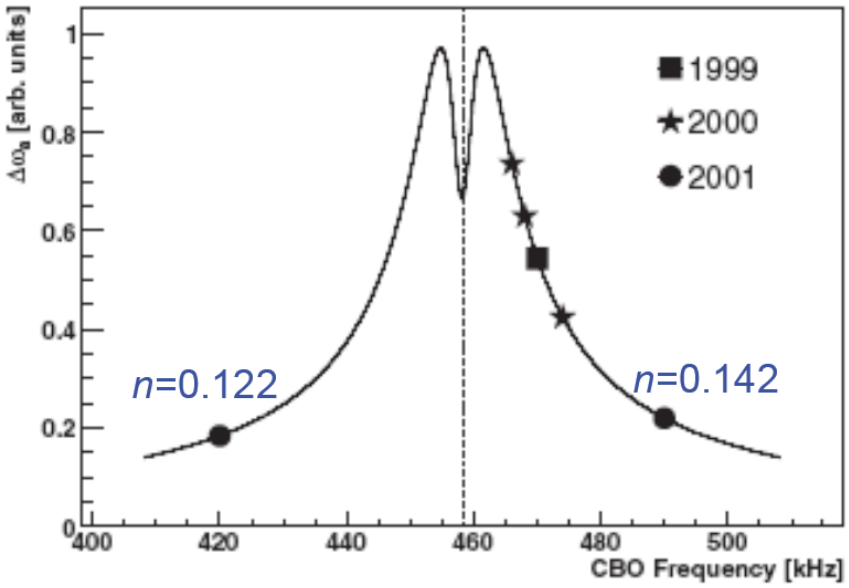

Figure 13.17: The CBO systematic raw error (arbitrary units) as a function of CBO frequency. The year notation indicates the frequencies ran with in E821. For E989 we plan to use much higher field focusing index (see quad section) with a projected CBO frequency of 634 kHz. This frequency will significantly reduce the CBO systematic error.

13.3.2 Electric Field and Pitch Correction

With a vertical magnetic field B_y and radial electric field E_r, the precession frequency is given by

$$\omega_a = -\frac{q}{m}\left[a_\mu B - \left(a_\mu - \frac{1}{(\gamma^2-1)}\right)\beta E_r\right]. \tag{13.1}$$

If B_y and E_r vary with position, the time averages $\langle B_y\rangle$ and $\langle E_r\rangle$ should be used. At exactly the magic momentum the effect from E_r is zero. Muons of slightly higher momentum δp have an equilibrium orbit

$$x_e = \frac{R_o}{1-n}\cdot\frac{\delta p}{p}.$$

As they oscillate about this equilibrium orbit they experience a mean electric field $\langle E_r\rangle = n\,(\beta B_y/R_0)\,x_e$ and their deviation from the magic momentum is proportional to x_e. This leads to a correction to ω_a proportional to x_e^2. In this experiment n is measured from the observed horizontal betatron frequency, and the distribution of muons with respect to x_e is found from the modulation of counting rate by the rotation frequency of the muon bunch. The observed value of $< x_e^2 >$ was confirmed by simulation. The correction is +0.46 ppm.

With electric focusing, the plane in which the muon spin is precessing oscillates vertically, exactly following the oscillation of the muon momentum. When the orbit is inclined at angle ψ to the horizontal, ω_a is reduced by the factor $(1-\frac{1}{2}\psi^2)$. If ψ_m is the angular amplitude of the vertical oscillation, the average over the ensemble of muons is $(1-\frac{1}{4}\langle\psi_m^2\rangle)$ where the brackets indicate an average over the muon population, $\langle\psi_m^2\rangle = n\langle y_m^2\rangle/r_o^2$ where y_m is the amplitude of the vertical oscillation.

Information on $\langle\psi^2\rangle$ is obtained by simulation in which a representative set of muons is tracked around the ring from the inflector exit, via the kicker magnet, for many turns. The discrete quadrupole structure and aperture defining collimators are included as well as the calculated deviations from a pure quadrupole field. The pitch correction is +0.29 ppm.

A combined (correlated) electric field and pitch correction uncertainty of 0.05 ppm was used in E821. We expect to improve on our knowledge of the electric field and pitch corrections by use of a new muon traceback system that can better image the beam motion versus time at a number of azimuthal positions around the ring. Furthermore, our simulation effort has improved, which is essential to some of these corrections. It is expected to reduce the uncertainty on these important corrections and we estimate a final combined error of less than 0.03 ppm.

13.4 Collimators and Lost Muon Systematic Error

The E821 lost muon systematic error was 0.09 ppm. In this section we discuss how we will decrease the lost muon rate with an improved storage ring/collimator system. The distortions of the vertical and horizontal closed orbits due to radial and vertical magnetic field distortions are:

$$\Delta y_{\rm CO} = \sum_{N=0}^{\infty} \frac{R_0}{B_0} \frac{B_{RN}\cos(N\Theta + \phi_{yN})}{N^2 - Q_y^2} \tag{13.2}$$

$$\Delta x_{\rm CO} = \sum_{N=0}^{\infty} \frac{R_0}{B_0} \frac{B_{yN}\cos(N\Theta + \phi_{xN})}{N^2 - Q_x^2} \tag{13.3}$$

For E821, B_{R0}/B_0 drifted by typically 40 ppm per month, which was correlated with temperature changes. About once a month B_{R0} was adjusted with the current shims to maximize the number of stored muons, i.e., centering the beam vertically in the collimators. From equ. (13.2) $B_{R0}/B_0 = 40$ ppm changes the vertical closed orbit by 2 mm. At FNAL we plan much better temperature control compared to E821. B_{y1}/B_0 was shimmed to < 20 ppm, which distorted the horizontal closed orbit by < 1 mm. For the FNAL experiment, we want both of these components < 10 ppm. Other components are less important since $Q_y^2 \approx 0.18$ and $Q_x^2 \approx 0.82$ are closest to the integers 0 and 1, respectively (see Table 13.2). For E821 we used $Q_y^2 \approx 0.13$ and $Q_x^2 \approx 0.87$.

The E821 collimators were circular with radius 45 mm. The E821 beta functions vs. ring azimuth are shown in Fig. 13.18. The FNAL experiment collimators will be oval with the x and y axes modulated by the square root of the beta functions, i.e., ± 0.8 mm in x and ± 0.7 mm in y.

Fig. 13.19 shows the E821 collimator ring placement. Since the E821 kick extended over many turns, we needed "half" collimators just after the kicker and at π radial betatron phase advance, so that the muons would survive enough turns to get the full kick. The FNAL kicker is being designed to give the full kick on the first turn. Thus we can go from 3 full collimators and 5 half-collimators to eight full collimators.

We purposely distorted the vertical and horizontal closed orbits by 2.6 mm during scraping for the first 10^2 turns, but 2.6 mm was not large compared to the above effects. Indeed,

Table 13.2: Distortion of the closed orbits for E821 (FNAL) tune values and B_{RN}/B_0 and $B_{yN}/B_0 = 10$ ppm.

N	y_{CO} (mm)	x_{CO} (mm)
0	0.53 (0.40)	0.08 (0.09)
1	0.08 (0.09)	0.53 (0.40)
2	0.02 (0.02)	0.02 (0.02)
3	0.01 (0.01)	0.01 (0.01)

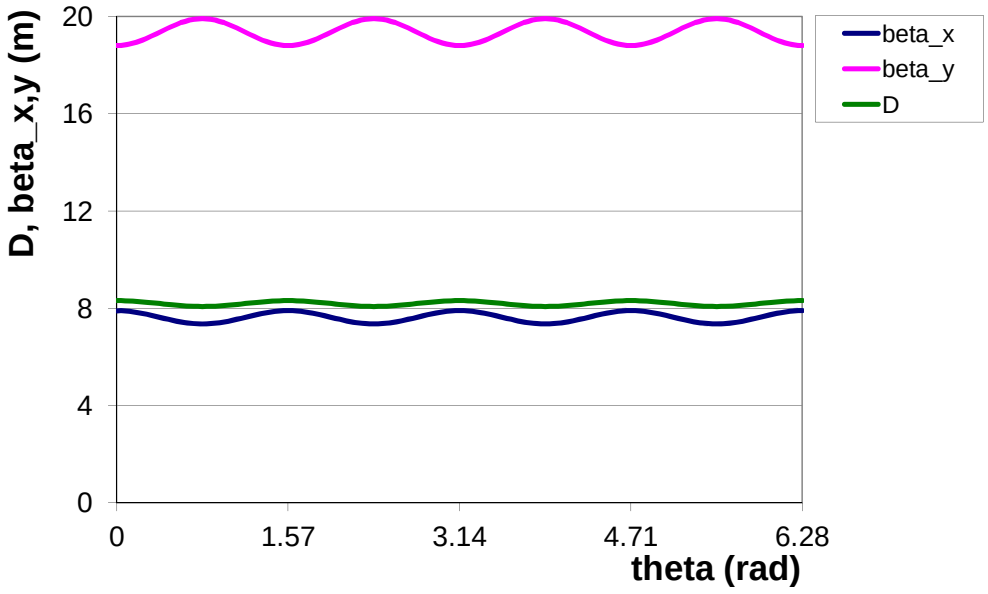

Figure 13.18: E821 horizontal and vertical beta functions.

when there were large temperature variations, we sometimes observed that the lost muon rate went *up* after scraping ended! With better control over the horizontal and vertical orbit distortions due to B_{R0} and B_{y1}, oval collimators to match the ring beta functions, and eight full collimators, we anticipate a lost muon rate at FNAL which will be about ten times lower than E821. The exact lost muon rates will be calculated with tracking simulation. The collimators should be surveyed to better than 0.2 mm. The coefficient of expansion of steel is 1.3×10^{-5}/C; multiplying times the radius of 7.1 m gives 0.1 mm/C.

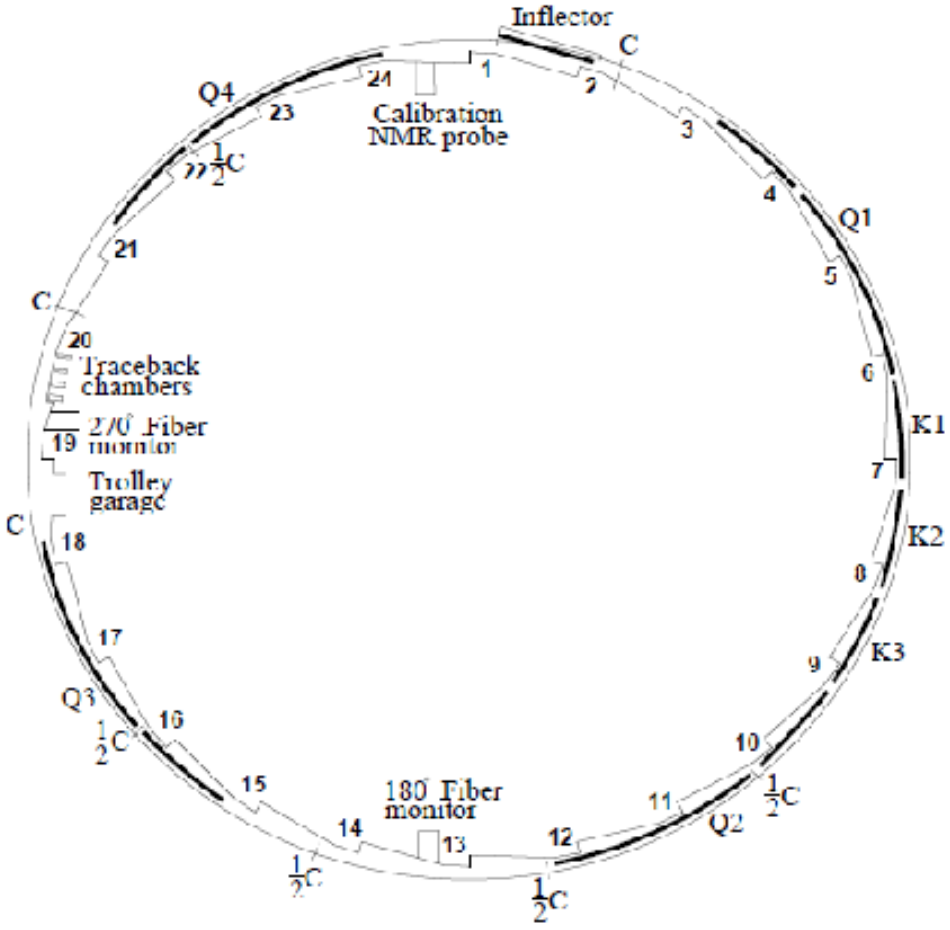

Figure 13.19: Schematic diagram of the E821 ring showing the location of the half and full collimators. For the FNAL experiment, there will only be full collimators.

13.5 ES&H

Potential hazards of the ESQ system are power system and X-rays.

The system contains both low voltage, high voltage (up to 75 kV) and high current circuits. There are no exposed electrical terminals. All electrical connections are bolted

and enclosed. Cables will either be run along the floor in cable tray or in double-grounded conduit. The power supplies and the thyratrons are fused. We will use lock out/tag out when servicing the unit. When the power supplies are disabled, the storage capacitors will also be shorted to ground with a safety relay. We do not anticipate that we will need to work on the unit hot. There are no requirements for emergency power. There will be a remote control unit in the control room. The operation of ESQ will be limited to system experts and trained personnel.

Soft X-rays can be produced in the system in spark discharges. Even though the ESQ system is designed to have no sparks during normal running conditions, sparks are most likely to occur during conditioning of the system. The ESQ plates are enclosed in 1-cm-thick Al vacuum chambers, which will provide shielding against X-rays emission. Safety expert at BNL will conduct calculations of the effect for the Test Stand which will be used at BNL for R&D studies and development. The equipment will be checked for the production of X-rays during a discharge. The results will be applicable to the $(g-2)$ experiment. It is unlikely that X-rays will be a serious hazard in the experiment, but depending on the recommendation of the safety expert additional safety measures may follow. Irrespective of the outcome, all personnel will be required to wear TLD badges in the experimental hall.

One of the alternative designs of the outer plate of Q1 quadrupole includes beryllium foil. Beryllium is ideal material for such purpose due to its mechanical, electrical and magnetic characteristics. Most importantly, muon scattering in beryllium will be significantly reduced in comparison with aluminum plate due to lower Z of beryllium. However, beryllium is a significant health hazard. We are not planning to machine beryllium. The foil will be produced and, presumably, assembled by a certified commercial company. During running the beryllium plate will be enclosed in vacuum chamber inaccessible to regular personnel. Only certified persons will be allowed to perform work on ESQ Q1.

13.6 Risks

The baseline design is to displace the Q1 outer plate by about 2 cm (the needed displacement will be determined more accurately by R&D studies). If the baseline design cannot be achieved for various reasons, we will consider the following alternatives for Q1 outer plate, *i)* a plate made from a thin beryllium foil, *ii)* a plate made from a thin wire mesh, *iii)* a plate made from a thinner aluminum foil, *iv)* a plate from other alternative materials (e.g. fiber carbon). This will lead to the following consequences to the Project

- More effort will be needed for R&D studies of alternatives.
- Muon scattering in any material will reduce the fraction of stored muons and hence increase the time required to reach the statistical goal of the experiment. The preferable material is beryllium.
- Beryllium foil will increase the cost of the Project. The cost of the beryllium material for the plate is about \$16 k per meter. Thus, to cover a 5-m-long quadrupole plate at least \$90 k in addition will be required not including the manufacturing and assembling expenses.

- Beryllium is a hazardous material. Special handling requirements will complicate ESQ plate installation and adjustment procedure.

The baseline design is to increase the operating voltage of ESQ to ±35 kV. The CBO systematic error will be more challenging to address if this goal is not reached. This will also increase muon losses.

The ESQ system requires good vacuum to operate properly (10^{-6} Torr or better). Bad vacuum conditions may lead to inability of ESQ to operate at nominal voltage. One potential source of vacuum leak is the tracker system. Two to four additional vacuum pumps may be needed to pump the vacuum chambers equipped by the tracker system. If high vacuum conditions are not met with installation of additional vacuum pumps, we may consider taking production data without tracker system and taking special runs with the tracker system to measure the distribution of muons in the storage ring. The disadvantage of such a mode of operation is that the tracker runs will be excluded from the production dataset.

References

[1] Bailey J, et al. Nucl. Phys. B150:1 (1979)

[2] Bennett G.W., et al., Phys. Rev. D 73, 072003 (2006)

[3] Y. K. Semertzidis et al., Nucl. Instr. Meth. Phys. Res., A 503 (2003) 458-484

Chapter 14

WBS 476.03.07 Ring Instrumentation and Controls

This chapter gives a preliminary description of the g-2 cryogenic and vacuum control system. This control system will be a copy of the typical Siemens S7-400 PLC (Programmable Logic Controller) control system as deployed by the Fermilab mechanical department.

The g-2 cryogenic and vacuum system will be located on the Muon campus in the MC1 building, Muon g-2 experimental hall. This area is classified as ODH class 0 area and has several large cryogenic and gas components. Cryogens include liquid Helium and Liquid Nitrogen.

This cryogenic system has approximately 300 electronic input sensing devices and 50 output devices. Input devices include temperature sensors, pressure transmitters, vacuum gages, level probes, and strain gages. Output devices include solenoid valves, control valves, and vacuum valves and pumps.

All electronic and electrical control system equipment is air cooled and does not require any forced air cooling or water cooling. Cabinet air vents are provided for certain devices where appropriate.

The control system equipment components are all commercially available products which are UL listed. The cryogenic control system has been designed and will be built following all the required rules and standards such as the NEC and NFPA 70E. All premises wiring is to be installed by Fermi Electrical contractors and licensed electricians.

14.0.1 Cryogenic/Vacuum Control System

Programmable Logic Controller

The g-2 cryogenic/vacuum system will be controlled by a Siemens S7-400 PLC with S7-300 associated I/O modules (or equivalent industrial controls system) networked on a Profibus network. This PLC system will be programmed using the Siemens S7 engineering programming software (or equivalent software meeting IEC 61131-3 standard). Siemens S7-400 PLC systems are currently in use at several Fermilab projects: LAPD, LBNE 35 Ton, Super CDMS, and NML/CMTF. A diagram of the typical PLC in use at Fermilab is given in figure 14.1

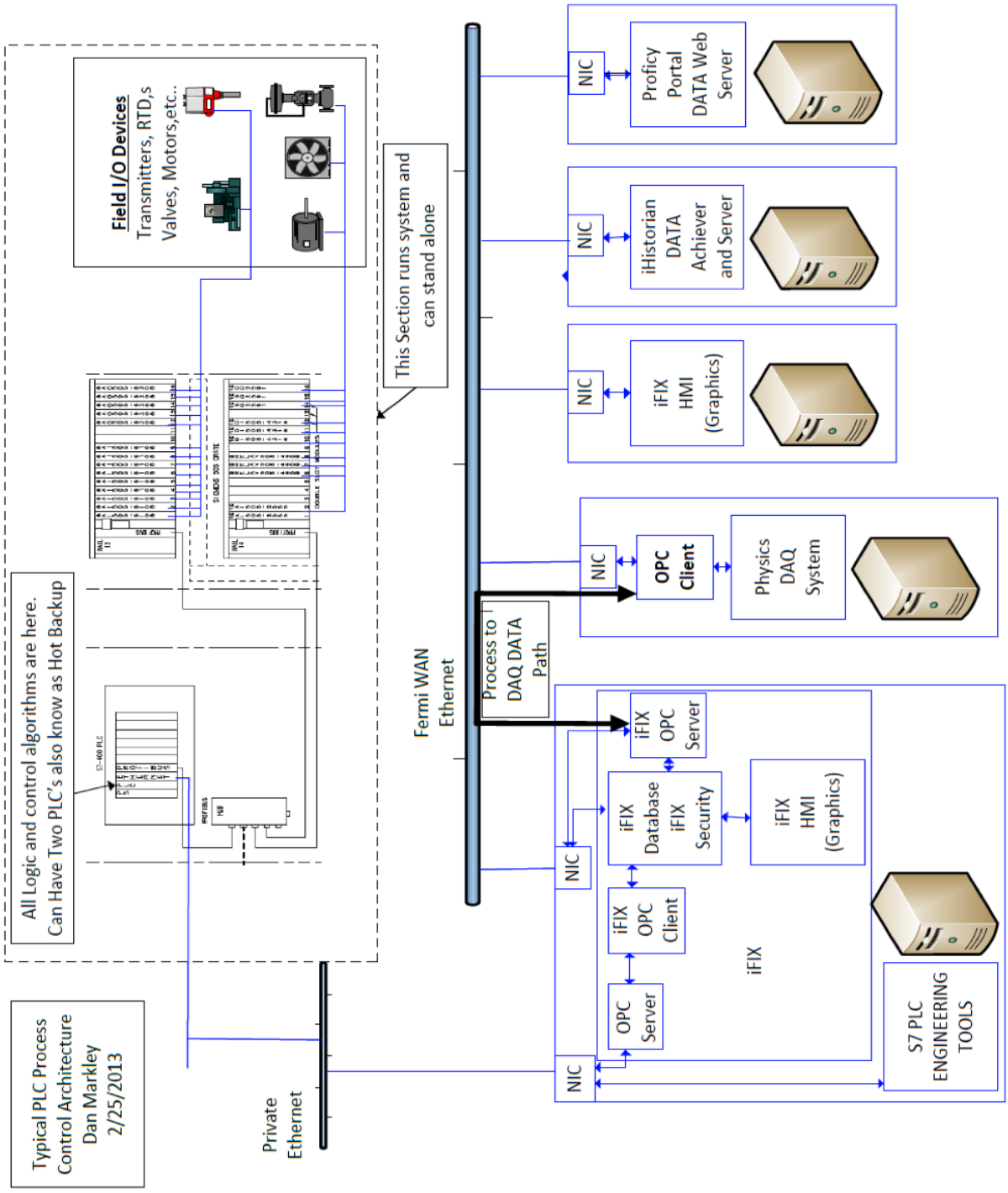

Figure 14.1: Diagram of a typical PLC in use at Fermilab.

Human Machine Interface

Human Machine Interface (HMI) controls will be provided through GEFANUCs iFIX software. iFIX connects to the S7-400 through Private Ethernet using an OPC driver purchased

from Kepware. iFIX will handle all operator security, computer alarming, and remote operator controls via the PPD-iFIX server. iFIX will also provide historical data through the PPD-iFIX historian. This historical data will be viewable in iFIX picture displays or on the web through the iFIX Proficy portal server. An example of a HMI for the LAPD experiment is shown in figure 14.2.

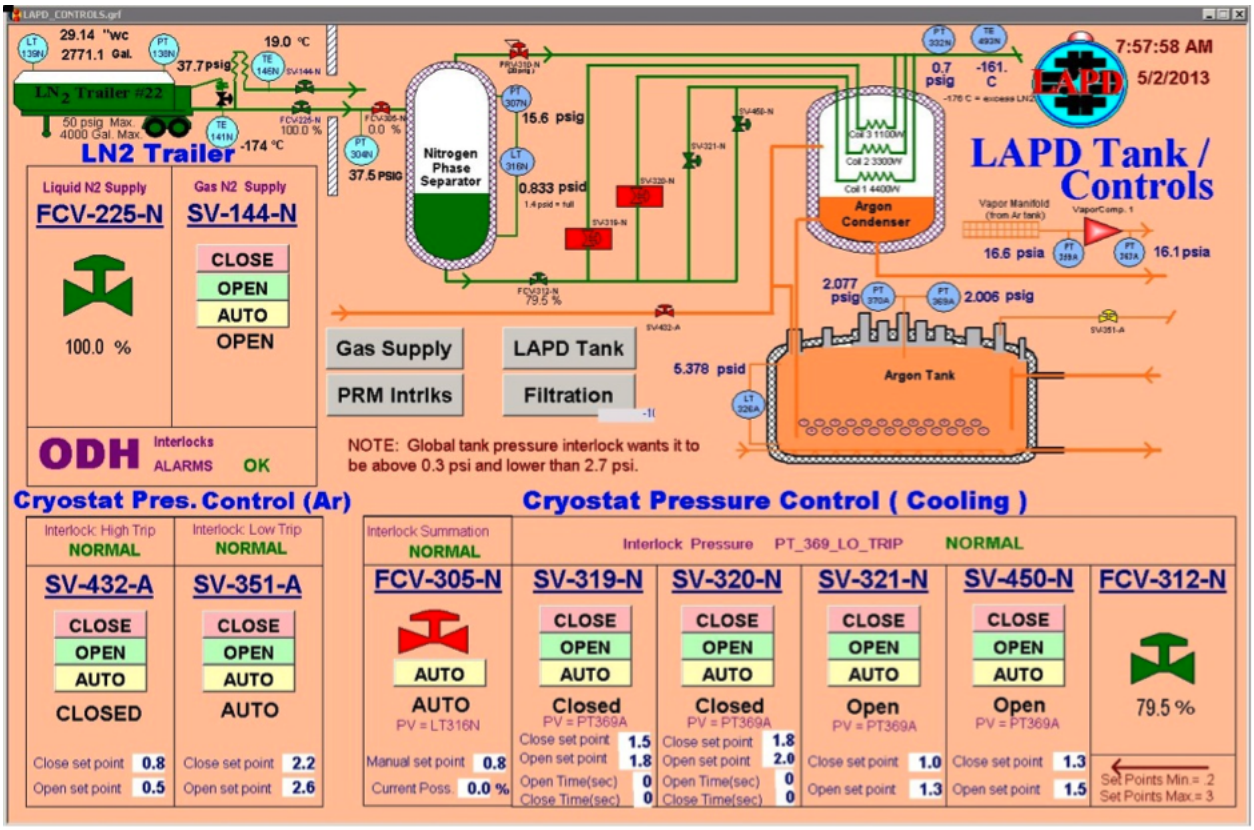

Figure 14.2: Human Machine Interface for the LAPD experiment.

14.0.2 Life Safety and System Reliability

ODH Control System

The ODH system will utilize four MSA O2 heads. Two O2 heads will be located near the ceiling of the g-2 experimental hall, with another two O2 sensors located near the floor of the hall. There will be an ODH warning horn and strobe lamp. These will be centrally located in the hall. There will be two ventilation fans used to maintain the ODH risk class zero status in the g-2 hall. One fan will exhaust air out of the g-2 hall at the ceiling venting it outside. The second fan will supply fresh air to the building near the floor outside of the rings. These fans are controlled by the S7 PLC and can also be run locally using a switch mounted at the fan controls. The ODH system is hardwired to both fans such that during an ODH alarm both fans run.

The O2 Sensors are MSA model A-UltimaX-PL-A-14-03D2-0000-100 and have a span of 0-25%. Each O2 sensor is to be wired to an MSA electronic controller which provides an

analog output signal wired to the S7 PLC. This MSA electronic unit also provides relays which have three O2 level alarms thresholds, 18.5%, 18%, and 17.5%. The relay output that is set at 18.5% is wired directly to the ODH warning horns and strobe lamps located in MC1 and FIRUS. The MSA electronic unit also provides a trouble relay output which is also wired to the PLC and FIRUS. The trouble output is wired in a failsafe manner, such that loss of power or blown fuse to the ODH controls will generate a trouble alarm.

The MSA equipment is wired directly to its own self-contained control circuitry in its own enclosure. This self contained enclosure has its own power supply which is independent of the PLC control system, allowing the ODH system to function independently of the PLC control system. The power for this ODH system comes from a U.P.S.

Uninterruptible Power Supply (U.P.S.)

The control system U.P.S. is to be a commercial unit such as those manufactured by Best power. The U.P.S. input power is fed from a premises powered outlet using the U.P.S. input line cord. This U.P.S. system will be diesel generator backed. The diesel generator will be auto start with auto switchover on commercial power loss. There may be other loads on this generator as well.

The U.P.S. has standard outlets located on the rear of the cabinet. An APC surge protector is located on the U.P.S. and its input power cord is plugged into the U.P.S output outlets. All relevant control system loads are plugged into the APC surge protector output outlets.

PLC Reliability and Redundancy

Siemens SIMATIC (S7 PLC and ET200M I/O modules) components meet all relevant international standards and are certified accordingly. Temperature and shock resistance are defined in the SIMATIC quality guidelines, as are vibration resistance or electromagnetic compatibility. The Siemens S7 PLC system equipment can be redundant at many different levels, from the PLC CPU (Hot Backup) to the module and instrument level. The level of redundancy, if any, has not yet been determined for the g-2 control system.

References

[1] Electrical Design Standards for Electronics to be used in Experiment Apparatus at Fermilab.

[2] EED/Infrastructure Doc. No:H011228A.

Chapter 15

The Precision Magnetic Field: ω_p

In this chapter we present the requirements on the storage ring magnetic field and field measurement, with a conceptual design for fulfilling these requirements. We first consider the field measurement requirements and the recommended design. The requirements on the storage ring magnetic field and recommended design are then discussed.

15.1 Precision Magnetic Field Measurement

15.1.1 Relation between a_μ and ω_p

In an idealized experiment, the anomaly a_μ could be extracted by measuring the difference frequency ω_a between the muon spin ω_s and cyclotron frequencies ω_c for a muon in a storage ring with a perfectly homogeneous magnetic field $\vec{B}$ with no focusing (see Eqn. 3.11):

$$\vec{\omega}_a = -\frac{Qe}{m_\mu} a_\mu \vec{B}. \tag{15.1}$$

The magnetic flux density $|\vec{B}|$ could be in determined in Tesla through proton nuclear magnetic resonance (NMR) measurements via $\omega_p = \gamma_p |\vec{B}|$, where ω_p is the free proton precession frequency and $|\vec{B}|$ is the lab-frame magnetic field which governs muon motion in the storage ring. The free proton gyromagnetic moment ratio γ_p is currently known to 24 ppb [1]. The muon charge to mass ratio appearing in Eq. 15.1 can be expressed in terms of (m_e/m_μ) known to 25 ppb and (e/m_e) known to 22 ppb [1]. Even with measurements of ω_a and ω_p at the ppb level of precision, a_μ could only be extracted to 41 ppb due to uncertainties on these auxilary ratios. Fortunately it is not necessary to determine the field in Tesla. The anomaly a_μ is dimensionless and can instead be extracted from the same measurements in terms of a ratio of frequencies and a dimensionless ratio of magnetic moments :

$$a_\mu = \frac{\omega_a/\omega_p}{\mu_{\mu^+}/\mu_p - \omega_a/\omega_p}. \tag{15.2}$$

This is derived from Eq. 15.1 based on relations between fundamental constants, with the requirement that ω_p refers to the free proton precession frequency in the same flux

density $\vec{B}$ seen by the muons. The additional input, μ_{μ^+}/μ_p = 3.183 345 24(37) (120 ppb) is determined from the E1054 LAMPF measurement of Zeeman ground state hyperfine transitions in muonium (Mu) [2, 1]. The result is based solely on measured quantities, the validity of the Breit-Rabi Hamiltonian to describe the experiment, and a small (17.6 ppm) bound-state QED correction to the g factor for a muon in muonium (where the uncertainty on the correction is sub-ppb).

Alternatively, the same experiment measured the ground state hyperfine interval in muonium, $\Delta\nu_{\rm Mu}$(E1054) = 4 463 302 765(53) Hz (12 ppb), where the theoretical prediction is given by [1]:

$$\Delta\nu_{\rm Mu}({\rm Th}) = \frac{16}{3} cR_\infty \alpha^2 \frac{m_e}{m_\mu}\left(1+\frac{m_e}{m_\mu}\right)^{-3} + \text{higher order terms} \quad (15.3)$$

$$= 4\ 4634\ 302\ 891(272)\ \text{Hz (61 ppb)}. \quad (15.4)$$

The theory uncertainty has a 101 Hz contribution from uncertainty/incompleteness in the theory calculation, but is dominated by the uncertainty in the mass ratio m_e/m_μ which appears as a parameter in the prediction.

The hyperfine interval is dominated by QED contributions, but there is a weak contribution $\Delta\nu_{\rm Weak} = -65$ Hz from Z^0 exchange, a hadronic contribution $\Delta\nu_{\rm Had} = 236(4)$ Hz, and a hadronic light-by-light contribution of 0.0065 Hz (see references in [1]).

Setting $\Delta\nu_{\rm Mu}$(E1054) = $\Delta\nu_{\rm Mu}$(Th) can determine the mass ratio (m_μ/m_e) to 25 ppb, which in turn can determine $\mu_\mu/\mu_p = 3.183\ 345\ 107(84)$ to 26 ppb since

$$\frac{m_\mu}{m_e} = \frac{\mu_e}{\mu_p}\,\frac{\mu_p}{\mu_\mu}\,\frac{g_\mu}{g_e}, \quad (15.5)$$

where the uncertainty on μ_e/μ_p is 8.1 ppb and the uncertainty on g_μ/g_e is less than 1 ppb [1]. This determination, which is nearly 5 times more precise than μ_μ/μ_p extracted directly from measurement, requires that the Standard Model fully describes $\Delta\nu_{\rm Mu}$. However, theories predicting new contributions to the muon anomaly might also lead to new contributions to $\Delta\nu$ that should be considered.

Given that the difference between $a_\mu^{\rm E821}$ and $a_\mu^{\rm SM}$ is roughly twice the weak contribution to a_μ, a comparable contribution to $\Delta\nu$ would imply the current theory uncertainty might be underestimated, as would be the 26 ppb uncertainty on μ_μ/μ_p. A more precise, independent measurement of μ_μ/μ_p, planned at J-PARC, would be very helpful. Note however, that even in the absence of a new measurement, any BSM theory can be tested against E989 at the 0.14 ppm level as long the BSM contributions to $\Delta\nu$ are considered simultaneously and the uncertainties are at the level of 25 ppb or less.

15.1.2 Physics Requirements on ω_p

Based on the above approach for a_μ, our requirement for the total uncertainty on ω_p in E989 is $\delta\omega_p \leq 0.07$ ppm, roughly a factor of three smaller than was achieved in E821. Here $\tilde{\omega}_p$ refers to the free proton precession frequency weighted by the muon distribution in the storage ring.

15.2 Recommended Design

E989 will largely use the principles and hardware originally developed at Universität Heidelberg and Yale, that were employed successfully in E821 (and E1054 at LANL). The E821 field measurement electronics and the underlying physics are described in [3]. The calibration of the field measurements in terms of the equivalent free proton precession frequency using an absolute calibration probe is described in [4]. Details of the E821 field analysis, systematics, and of the hardware are described in the final E821 paper [5], and in several theses [6, 7, 8].

While E821 achieved an uncertainty $\delta\tilde{\omega}_p \approx$ 0.17 ppm, E989 will have to implement specific changes to the hardware and techniques to reduce the systematic errors to a final goal of $\delta\tilde{\omega}_p \approx 0.07$ ppm. The recommended E989 hardware, techniques, and changes from E821 will be discussed in the rest of this chapter, A table of estimated contributions to the systematic uncertainty on ω_p is presented at the end of the chapter.

15.2.1 Overview of field measurement using NMR

Nuclear magnetic resonance (NMR) is at the heart of the magnetic field shimming, measurement, and control, since it can measure magnetic fields to absolute accuracies of tens of parts per billion (ppb).

The pulsed NMR hardware developed for E821, which produced and detected the free induction decay (FID) signals from protons in water, has already demonstrated single shot accuracy at the level of 10 ppb [3], and absolute calibration in terms of the free proton precession frequency at the level of 35 ppb [4]. The challenge of the field measurement is to effectively transfer this absolute calibration to the many NMR probes required to monitor the field in the large volume and over long periods in which muons are stored.

There are four major tasks required from the NMR system: (1) Monitoring the field when muon data are being collected; (2) Providing feedback to the storage ring power supply when muon data are collected; (3) Mapping the storage ring field when the beam is off; (4) Providing an absolute calibration relating field measurements to the Larmor frequency of a free proton.

15.2.2 The Fixed Probe NMR system

The fixed probe system consist of the fixed NMR probes and the accompanying VME system, DAQ, pulser, mixer, multiplexers, and digitizers. Its purpose it to accomplish the first task of monitoring the field continuously while muon data are being collected. A block diagram of the recommended system is shown in Fig. 15.1.

The recommended design consists of a set of 378 NMR probes at 72 locations in azimuth around the ring. The number of probes at each azimuthal position alternates between two probes at radii of 7112 and 7142 mm, or three probes at radial positions of 7082, 7112, and 7142 mm, where the probes are placed in grooves on the upper surface of the storage ring vacuum chambers. In addition, probes matching in azimuth and radius are placed in grooves on the lower surfaces of the vacuum chambers. From this geometry the fixed probes provide

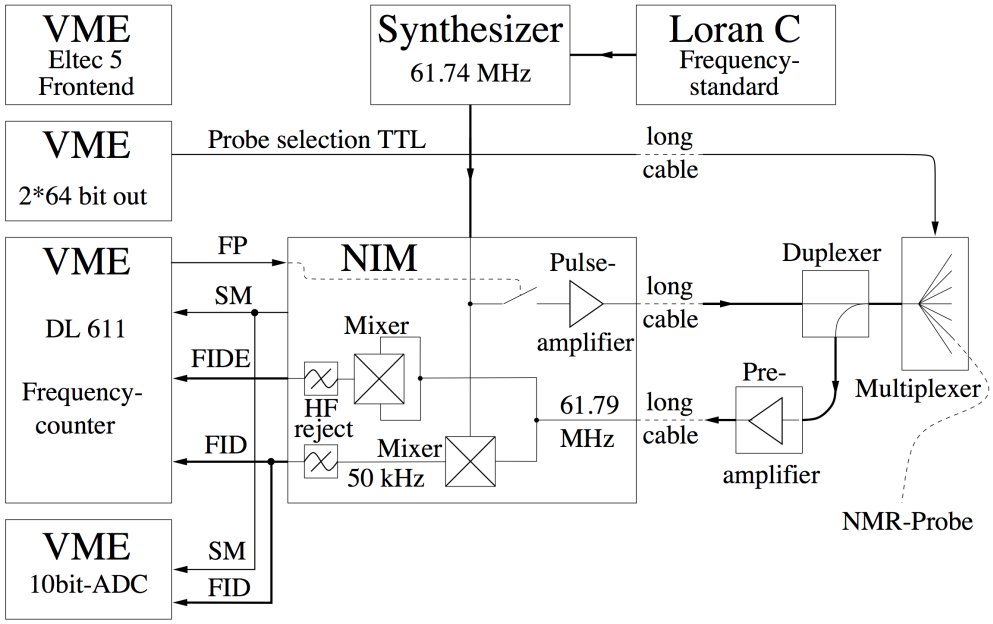

Figure 15.1: A schematic of the fixed probe system. The system consists of a set of NMR probes close to the muon storage volume connected to multiplexer boxes that sit on the storage ring magnet. The multiplexers are connected to NIM modules and a VME system and DAQ that sit in the counting house. The functions of each element are described in the text.

a good monitor of the dipole field around the ring, with some sensitivity to changes in the skew and normal quadrupole components.

In E821, roughly half of these fixed probes were used to monitor the storage ring field. Of the remainder, some probes were noisy, and a significant number of fixed probes were located in regions near the pole-piece boundaries where the local magnetic field gradients were sufficiently large to reduce the free induction decay time in the probe. This limited the precision of the frequency measurement. In E989 several steps will be taken to increase the number of useful probes.

First, finite element analysis of the vacuum chambers indicates that the grooves containing the probes can be extended without significantly increasing the deflection of the chambers under vacuum. This will allow probes to be moved farther from pole boundaries, increasing the number of useful probes. Second, in E821 the majority of the NMR samples in the fixed probes were cylinders of water. Over the course of the experiment, the water samples could evaporate. In E989, the possibility of replacing the water samples with petrolatum (CAS 8009-03-8) will be explored. Petroleum jelly was observed in E821 to have several advantages over water: low evaporation, a proton NMR signal comparable in magnitude and frequency to water, and a temperature coefficient smaller than that of water, which is better for our experiment. In addition, it has favorable relaxation times; preliminary measurements at U. Michigan indicate T_2 of order 40 ms. Third, during the refurbishment of the probes for E821 (see below), any intermittent electrical contacts will be improved. Finally, the NMR

electronics of E821 which extracted precession frequencies by counting zero-crossings of FIDs mixed down to the 50 kHz range, will be supplemented with a high-performance set of digitizers. The 16 bit (13 bits effective), 20 MS/sec digitizers (Struck SIS 3302) will allow useful information to be extracted from probes with short signals. In addition, higher resolution is possible by interpolating the positions of zero-crossings, and fitting the signals around zero crossings can help when dealing with probes with poor signal to noise. Digitizers will allow the lineshape (and changes in the lineshape) to be extracted from the Fourier transform of the signals. This may allow a more robust extraction of the average field compared to counting zero crossing when the digitization noise is comparable or less than the signal to noise of the FID, since the zero-crossing rate itself is time-dependent when the lineshape is asymmetric.

15.2.3 Fixed Probes for E989

The same basic probe design from E821 is recommended for E989, and is shown in Figure 15.2. Materials used to construct the probes, mostly aluminum and PTFE, have low susceptibility and the coax cable has copper conductors instead of the more common copper plated steel. The probe's outer aluminum shell has a diameter of 8 mm which fits in grooves machined into the outside surface of the top and bottom plates of the vacuum chamber. The probe's outer shell and the inner body form the capacitor C_s, which in series with L_s makes a resonant circuit. C_s is adjusted by moving a PTFE sleeve in and out to tune the circuit to the frequency ω_p. The circuit quality factor $Q \approx 30$ corresponds to a bandwith of 3% which is the range over which the magnetic field can be measured without retuning the probes. A coil in parallel, L_p, allows for tuning the impedance of the probe to 50 Ω's for optimal transmission.

Resurrecting the existing E821 measurement system requires a complete working set of probes provided either by refurbishing existing ones or constructing new ones.

Refurbishing existing probes: In E821 the sample volume was filled with water with $CuSO_4$ added to decrease the relaxation time and allow for shorter measurement times. In some of the probes the water has leaked and corroded part of the probe. These probes need to be rebuilt. Tests on about 40 fixed probes from E821 indicate that about 1/4 are in this category. The coil wire and coax cable shield are bonded to the aluminum parts with low temperature solder. These connections require inspection and all broken connections require re-soldering. All the other probes will be refilled with petroleum jelly, tuned and checked for correct functioning.

An existing dipole magnet at University of Washington (UW) has been re-purposed to provide the 1.45 Tesla field required for testing the probes. Its field is uniform to 1000 ppm/cm but will be shimmed to 100 ppm uniformity over the active volume of the probe to increase the duration of the NMR signal. A Metrolab PT 2025 Teslameter with 10 ppm accuracy is used to independently map the field in the magnet. A test facility to provide the $\pi/2$ pulse, send/receive duplexer switch and preamplifier that does not require the E821 electronics has been set up at UW.

Constructing new probes: Any new probes constructed must meet the above geometry

and materials requirements including any solders used to bond the wires. The probes will be reverse engineered and CAD drawings produced. In consideration of the quantity, new parts will be produced using numerically controlled machines at the UW machine shop. Metric sized aluminum tubing 8 mm x 0.5 mm and 7 mm PTFE rods are available in the European market. After the parts are completed the coils will be wound and the same procedure as for refurbishing will be followed.

Testing the probes: For each probe, the resonant circuits are tuned to 61.79 MHz and 50 Ω impedance using a vector impedance meter. The resonance is then excited in the probe and if the free induction decay FID is observed with sufficient signal to noise ratio SNR, the probe passes the test. In the E821 system the SNR at the beginning of the decay was ≈ 300:1.

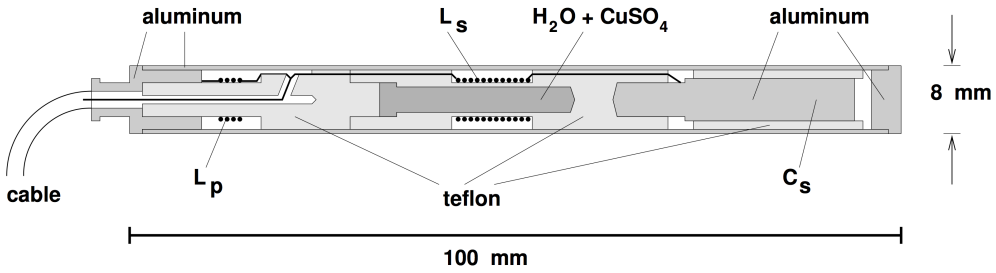

Figure 15.2: NMR fixed probe containing a cylindrical water sample. The resonant circuit is formed by the two coils with inductance L_s and L_p and a capacitance C_s made by the Al-housing and a metal electrode. The active water volume has a diameter of 2.5 mm and a length determined by the coil L_s of 15 mm.

15.2.4 Multiplexers

Groups of up to 20 fixed probes are connected to a single multiplexer located a few meters away in the experimental hall. The multiplexer is a self-contained electronic module that selects one of 20 NMR probes based on the bit pattern of 5 TTL-levels which are set in the counting house, and which arrive on a DB-9 connector. The TTL signals control PIN diodes in the multiplexer and direct an RF $\pi/2$ pulse, from NIM modules in the counting house and used to tip the spins, to the single selected NMR probe. To improve the isolation of open switches effective-$\lambda/4$ lines are incorporated. A duplexer (basically a transmit/receive switch) in the multiplexer steers the output of the RF pulse towards the NMR probe. The same duplexer steers the pulse away from the sensitive low-noise preamplifier, but sends the low-level precession signal to a low noise preamplifier after the pulse, with an overall gain of 60 dB. The module requires an external source of power, +15 Volts at 0.3 Amperes. The switches, duplexer, and TTL integrated circuits are realized with discrete surface mount components and replacements are readily available. The preamplifier uses two RF amplifier modules UTO-101 and GPD-201. The multiplexer design in described in [3, 6].

The preamps for E821 were made by Avantek, a company no longer in existence. An important characteristic of these amplifiers is their rapid recovery from an overload condition as experienced when the probe is excited. While some Avantek products are still sourced at Teledyne-Cougar (www.teledyne-cougar.com), future supplies are not guaranteed. For existing modules we will procure spare Avantek products if available. In constructing new multiplexer modules for E989, a new preamplifier design will be considered.

15.2.5 Pulser and Mixer

Each of the 20 multiplexers is connected to a single width NIM module located in the counting house. These function as the receiver and transmitter (pulse generator) for the NMR fixed probes. The pulse generator creates the 4μs $\pi/2$ pulse of $\omega_{ref} = 61.74$ MHz and sends it through a custom made 10-watt class C amplifier to the multiplexer. In the receiver part of the module, the amplified NMR signal at the Larmor frequency ω_L from the multiplexer is mixed with the frequency synthesizer output; a signal of well defined frequency ω_{ref} close to the NMR frequency $\omega_L \approx$ 61.79 MHz. From the mixing products the difference frequency $\omega_L - \omega_{ref}$ is selected by a low pass filter and further amplified. This signal (at roughly 50 kHz) is referred to as the FID (free induction decay) of the NMR probe. In a second branch of the receiver the envelope of the NMR signal, called FIDE, is constructed by multiplying the preamplifier output by itself and discarding the $2\omega_L$ component. A TTL SM (signal measure) pulse is generated in the NIM module roughly 10 μs after the end of the RF pulse. This pulse goes the the custom Heidelberg DL611 frequency counter module in the NMR VME crate (discussed below) to start the zero crossing counter. The delay accomodates deadtime in the multiplexer preamplifier, and transients such as from ringdown of the L_s coil and decay of the transient response in the low-pass filter.

The inputs to the NIM module are the TTL FP (fire pulse) which starts the RF pulse generator. The FP signal is generated in the DL611 frequency counter modules in the VME crate. A second input is the the synthesizer reference at 61.74 MHz, and the NMR probe signal from the multiplexer preamplifier. The outputs are the $\frac{\pi}{2}$ pulse, a TTL signal whose width is the dead time of the receiver (the SM signal), the FIDE and two channels of the FID (one for the zero-crossing counter in the VME crate, one for a digitizer in tbe crate).

For the most part this module contains surface mount and integrated circuit components and replacements are readily available. The exceptions are 5 amplifiers GPD-201, GPD-202, and 3 GPD-462 made by Avantek, which no longer exists. The most likely point of failure in the 10 watt class C amplifier is a DU2820S MOSFET that is still available and could be replaced if necessary with little difficulty. Replacement amplifiers exist but they tend to be wide band class A amplifiers which are less efficient. In constructing new pulser/mixer modules, using a class A or class AB amplifier would require that it be mounted external to the NIM module to dissipate the additional heat. Modular high performance commercial RF amplifiers are available from Amplifier Research and other vendors.

15.2.6 NMR VME System and DAQ : Requirements and Recommended Design

The fixed probe NMR system will be controlled by a VME crate in the counting house, performing similar functions as in E821 but with updated hardware for E989.

The NMR VME system is required to (1) send a bit pattern to each multiplexer that encodes which NMR fixed probe to use (2) Send FP (fire pulse) signals to the NIM modules in an adjacent crate, (which send the RF $\pi/2$ pulses to the fixed probes) (3) Count zero crossings of the FIDs from the NIM modules (4) Send the zero crossing data and a timestamp to a PC to be recorded.

The Eltec 9 VME crate controller used in E821, which ran the realtime operating system OS9, no longer works and must be replaced. The original E821 NMR VME crate, which was customized with the addition of -5V power supply to run the Heidelberg DL611 frequency counter modules, is still operational.

For E989 the recommended design replaces the Eltec controller with a Struck SIS1100 VME crate controller which connects via a fiber optic cable to a Struck SIS3104 PCIe card on a PC running Scientific Linux. The new controller is compatible with the VMEbus IEEE-1014 standard E821 crate, and with the faster 2eVME bus cycles of VME64x systems.

To accomplish task (1) above, a 5-bit pattern using TTL levels must be set in each of the 20 multiplexers, and is used to select which of the 20 fixed NMR probes is to be used. In E821 these levels were set by two custom VME modules made at Heidelberg (module number DL620). These modules still work, but a commercial solution will be sought as replacement in the case of failure and to allow more multiplexers to be added easily. Possible solutions include an Acromag AVME9660 VME carrier card for up to 4 IP-EP201 FPGA Digital I/O modules with 48 TTL lines each. FPGA I/O modules using high-speed USB or PCIe interfaces are also possible but a VME-based solution is preferred. The latter is more portable (modules reside in a single crate) and flexible (allows the VME crate to placed in the experimental hall and controlled by the PC over a single fiber optic cable), and the software should be easier with just a single interface to deal with.

To accomplish task (2), the fire pulse (FP) TTL signal can be issued by the Heidelberg DL611 frequency counter modules. There are 5 DL611 modules, and each one can issue 4 independent FPs, allowing 20 NIM modules to be controlled. These DL611 modules still function and will be used as is in E989. New modules acting as spares based on the DL611 design will be made at the Center for Experimental Nuclear Physics and Astrophysics (CENPA) at the University of Washington. These additional modules will allow more multiplexers to be controlled if more fixed probes are added. Note that the new digital I/O cards could also be used to issue the FP signals.

Task (3) which involves counting the FID zero crossings will be accomplished with the existing DL611 modules and with the spares that are constructed The DL611 modules, which are described in [3], count the zero crossings, k, of the FID till the FIDE signal falls below an adjustable threshold or until a maximum time has elapsed. Over the same interval the ticks, N, of an external clock at $\nu_{\rm clock}$=20 MHz are counted. This 20 MHz clock signal is an input on the front panel of each DL611, and comes from a stabilized frequency synthesizer. For both counters the start and stop coincide with a positive zero crossing of the FID. The frequency of the FID is $\nu_{\rm FID} = k \times \nu_{\rm clock}/N$. For FID signals exceeding 1 ms, the uncertainty

on the frequency due to the discretization of the clock counts is roughly 8 ppb or less. The uncertainty on the frequency due the finite signal-to-noise of the FID (typically $S/N \approx 100$ when FIDE falls below threshold) is roughly the signal linewidth/(S/N). This is typically of order 25 ppb on a single NMR FID above threshold for a ms or more [3]. Any new design for the multiplexer preamps, NIM module electronics, and DL611 modules will need to meet or exceed this specification which is achieved by the existing hardware. The option of performing the frequency determination with fast, high-accuracy digitizers will be explored (see next section).

Recording the results of the frequency measurement, task (4), is accomplished by reading the contents of the DL611 VME addresses containing the zero-crossing and clock counts, and writing them to disk on the DAQ PC. In E821, roughly 100 fixed NMR probes were read per second, and data rates were much less than 100 kB/second. Another custom VME module from Heidelberg provided a timestamp to be recorded with the measurements. For E989 the preliminary design replaces the Heidelberg timestamp module with a Hytec 2092 VME module. This module has an antenna input to receive GPS timing signals and provides a timestamp with an absolute accuracy better than 100 ns with respect to UTC (Co-ordinated Universal Time). This is more than adequate for NMR signals which are typically 1 ms in length or longer. The advantage of this scheme is that potential external influences on the storage ring field from booster operations at 15 Hz, pickup at 60 Hz and harmonics, coordination with muon fills of the storage ring (which are typically asynchronous with the NMR readings) and other external events can be investigated when all NMR signals have a reliable, high-resolution absolute time stamp. Finally, the Hytec module produces a GPS-derived 1 pps TTL output which will be used to stabilize a Rb frequency reference producing a 10 MHz reference for the NMR and ω_a frequency synthesizers. There is other hardware for obtaining GPS-derived 1 pps references and reliable computer timestamps - the Hytec module is recommended as part of the conceptual design since it accomplishes several goals in a single module.

Finally we note that low level software for the Struck controller has been developed to control the original Heidelberg clock, DL620 probe selector, and DL611 frequency counter modules. It can be recommended for use in E989 over alternative controllers because it has already been shown to work.

15.2.7 Digitizer

Struck SIS3302.

15.2.8 Frequency Reference

The $(g-2)$ experiment is essentially a measurement of the ratio $\omega_{\rm a}/\omega_{\rm p}$. Its goal is to achieve relative uncertainties of 0.07 ppm for both of these frequencies. Frequency references are necessary for both of these measurements, and the contribution to the uncertainty budget from uncertainties in the reference should be made negligible.

The NMR system requires a frequency synthesizer at 61.74 MHz which is amplified and pulsed for manipulating the proton spins in the NMR probes. The FID at the Larmor frequency (typically 61.79 MHz) is mixed down by subtracting the 61.74 MHz reference,

and the frequency of the resulting 50 kHz signal is determined by counting zero crossings with respect to a 20 MHz clock (for the fixed probe) or the 61.74 MHz reference clock (for the probes in the trolley) from a digitizer. The accuracy goal for the ω_p determination requires that the 61.74 MHz and 20 MHz clocks be accurate at the ppb level. Since the NMR clocks and the clock used by the waveform digitizers to determine the muon spin precession frequency are phase-locked to the same master clock, the variations in the master clock frequency drop out to first order, and the ppb-level accuracy requirement is reduced to be less than about 10^{-5}. Nevertheless, to simplify the study of systematic uncertainties in the magnetic field in the ring, our goal is to have relative uncertainties in the reference clock frequencies to be less than 1 ppb.

This uncertainty is required to be achieved short-term, that is, for a single NMR measurement that takes about a few ms where phase noise is the limiting factor. It is also a limitation on the long-time drift over the course of the experiment, that is, several years.

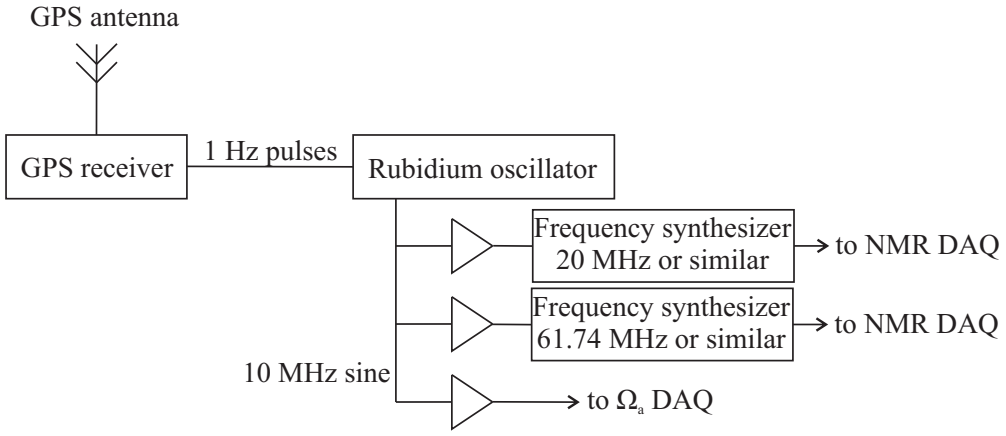

Figure 15.3: Scheme for common master-clock.

Figure 15.3 shows how the reference frequencies are generated. The master clock is planned to be an atomic rubidium oscillator that is disciplined by GPS for better long-term stability. It generates a master frequency that is a sine wave, usually at 10 MHz. The master frequency is distributed to the data acquisition system for $\omega_{\rm a}$, where frequency synthesizers are used to transfer the master clock frequency to the clock frequency needed by the waveform digitizers. It is also used as input for the frequency synthesizer responsible for the reference frequency $\omega_{\rm ref}$, and for another synthesizer responsible for the fixed 20 MHz frequency signal. Frequency synthesizers in both systems should have resolutions of about 1 ppb, to allow for some variability in the frequency that can be used for blinding schemes and for tests of systematics. It is the synthesized frequencies that have to fulfill the accuracy requirement discussed above. Master clock and synthesizers that fulfill the requirements given above are available from vendors like Precision Test Systems, Symmetricon, Agilent, and Stanford Research Systems. Amplifiers from vendors like Stanford Research Systems and Mini-Circuits can distribute master clock and the needed reference frequencies to the places where they are needed. There is experience in the collaboration from the BNL-$(g-2)$ experiment and, more recently, from the clock system used for the MuLan experiment at

PSI in Switzerland in the specification and use of these systems.

15.3 Trolley

The in-vacuum NMR trolley system shown in Fig. 15.8(a) has the purpose of precisely mapping the magnetic field distribution over the muon storage aperture around the ring. From this distribution, the multipole composition of the field averaged over the ring azimuth is extracted in order to subsequently fold it with the multipole expansion of the measured stored muon beam profile. Because the trolley measurements prohibit the injection of muons, the mapping of the field around the entire storage ring happens intermittently with the spin precession frequency measurement. During these typically 2 hour runs with the trolley, a cross-calibration of the field observed by the fixed probes to the field measured by the trolley probes is performed. This is an important ingredient due to the fact that the magnetic field encountered by the stored muons can only be inferred from the fixed probes.

In the following sections, we will first specify the requirements for E989 and then discuss the conceptual design of future upgrades and efforts related to the trolley system.

15.3.1 General requirements

As can be seen from Table 15.2, trolley related systematic errors in the BNL E821 experiment were of sizeable amount and require significant improvement to meet the physics goals in E989. The two main sources of uncertainty stem from the calibration procedure of the trolley probes to the plunging probe (0.09 ppm) and errors related to position uncertainties during the actual trolley runs (0.05 ppm). Additional smaller effects (like temperature or voltage drifts) were grouped into one systematic error (Others) together with non-trolley related systematics in the field measurement. For the new E989 experiment, the trolley system will be used in a very similar fashion as in E821. Given the required improvements in the overall systematic errors for the field measurement, we will need some changes for the new system.

The requirements for the actual measurement during a single trolley run remain the same. An individual NMR frequency measurement will have a precision at least as good as 20 ppb as was achieved in E821. The field will be measured at 6000 points around the ring for each probe. A single trolley run should be accomplished in at most two hours. While about 1 hour is required for the mapping of the 6000 data points for each probe, the return trip can be sped up to reduce the interruption of the spin frequency measurement. Trolley runs should be repeated more frequently than in E821 where an interval of 2-3 days was typical. Increased frequency of trolley measurements will reduce the error associated with the fixed probe interpolation and allow for a complete mapping over all temperature changes in the storage ring.

As mentioned above, transverse and longitudinal position uncertainties coupled with field gradient are a major systematic error category in the measurement. While we plan on having improved overall shimming in E989 and hence reduced gradients, we will also put effort into reducing the position uncertainties. The longitudinal position knowledge during the trolley field mapping was inferred from a combination of the measurement of the cable unwinding by means of optical rotary encoders in the drums and by the observed change in the NMR

frequency in the fixed probes due to the small but measurable changes in the magnetic field induced by the trolley (maximally in the vicinity of the onboard electronic). The overall longitudinal position knowledge was estimated to be on the order of 1 cm corresponding to a 50 ppb systematic error. Together with the better shimming in the azimuthal direction (see section 15.4), we aim to reduce the position uncertainty to 5 mm to significantly improve on this error contribution.

During its movement the trolley rides on two rails which determine the transverse position of the trolley with respect to the center of the muon distribution. The requirements on the precision alignment of the trolley rails remain the same as in E821. A maximal deviation from their circular, ideal position of ± 0.5 mm will keep the associated systematic error below 10 ppb. The rails were not continuous at the vacuum chamber interjoints. Slight misalignment of neighboring rails at these gaps led to possible tranverse deviations of the trolley's center introducing an estimated systematic error of 10 ppb. In E989, we will reduce these misalignments and precisely verify the deviation of the rails from their nominal position around the full azimuth. Here, we will employ two methods, namely i) optical survey with laser systems or other precision metrology observation equipment and ii) the introduction of known, transverse gradients by means of the pole surface coils during dedicated special trolley runs.

During the calibration with the plunging probe in a specially shimmed region in the storage ring, relative position uncertainties between the plunging and trolley probes added contributions to the overall systematic error. In E821, the transverse reproducibility was estimated to be 1 mm whereas the relative position uncertainty in azimuth was determined to 3 mm. This resulted in contributions of 20 ppb and 30 ppb, respectively. For E989, we aim to cut these contributions in half (at least in the azimuthal direction) by a more precise alignment of the probes in a repeatable way. For this, we plan to introduce a mechanical stop for the trolley in the calibration region, by allowing a positioning of the plunging probe in all three directions and by testing the calibration transfer carefully in a homogeneous solenoid test magnet before data taking.

Other effects contributed to the E821 result with a summed contribution of 50 ppb. These included the temperature and voltage dependence of the NMR measurement and an estimate of the influence of higher multipoles. The dependence of the supply voltage of the trolley was derived to be 0.27 ppm/V and a voltage stability of 50 mV was achieved. In the new experiment, a modern power supply will significantly reduce the voltage drift and make this contribution totally negligible. We will reduce the effects of a temperature change on the extracted NMR frequency. One possibility is to use petroleum jelly instead of water for the NMR probes due to the reduced temperature coefficient of the jelly. In addition, an increase in the heat dissipation of the trolley would reduce the change of its temperature during the measurement. Overall, the effect should be negligible in the E989 experiment and we can carefully study it in the solenoid test magnet under controlled temperature conditions. The 30 ppb systematic error in E821 stemming from the folding of higher multipoles with the muon distribution can be improved by a modification of the current trolley probe arrangement shown in figure 15.8(b). There is room to further move the probes to an outer position closer to the 4.5 cm aperture of the muon storage region. In addition, a reconfiguration of the overall probe distribution can help to get a better handle on the measurement of the sextupoles and higher multipoles.

It should be noted that any additional modifications should respect the strict requirement that the field at the NMR probes is disturbed as minimally as possible. The maximal distortion of the field by the trolley electronics in E821 was about 2 ppm and future changes cannot introduce any major additional magnetic contribution compared to this level.

In the following sections, we will detail our specific conceptual design for future upgrades and activities that are aimed to meet the above outlined requirements for the E989 experiment.

15.3.2 Garage

The trolley garage shown in Fig. 15.4 serves the purpose of storing the trolley inside the vacuum outside the muon storage aperture during the main periods of spin precession measurement. A set of three rods driven by a non-magnetic piezo motor provides the mechanism to move cut-outs of the rails into the muon storage region and retract them. The in-vacuum requirements and a lack of motion stops have possibly put stress on these mechanics over the course of the E821 operation. The overall integrity of the system will need inspection to understand if the system is suited for the extended operation over the two years of data taking in E989. Future improvements might include the replacement of the rods, the addition of non-magnetic limit switches to smoothly stop the rail movement when in place, or even a re-design of the garage with a switchyard solution. While ideally the garage could be operated as is in E989, the exact measures to improve will be decided after detailed inspection in the near future at Brookhaven and later at Argonne.

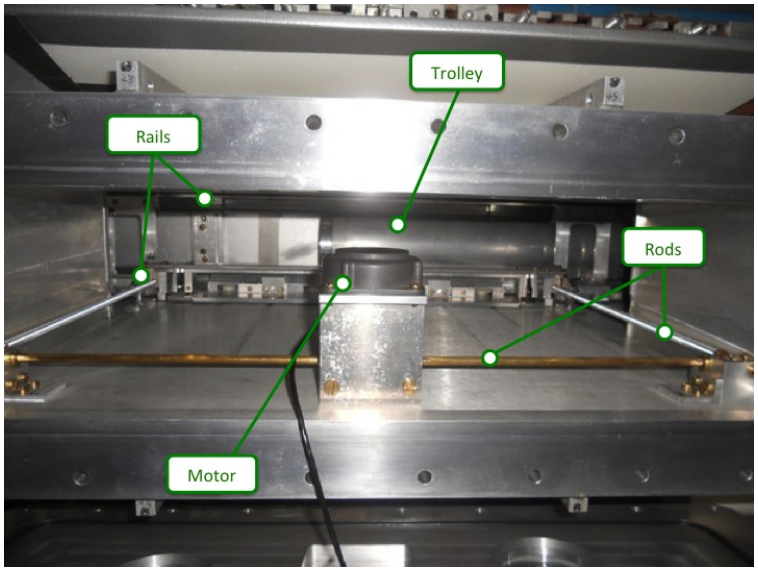

Figure 15.4: Trolley garage with the piezo motor, the driving rods, the rails and the trolley partially in the parking position where it can retracted from the storage region.

As can be seen in Figure 3.4, the trolley garage is attached to one of the 12 vacuum chambers. Since the general upgrades to other systems (like the alignment of the trolley

rails) will require collaborators to work on the vacuum chambers, the upgrade activities with respect to the garage will be coordinated over the course of the next two years.

15.3.3 Drive

The trolley drive mechanism shown in Figure 15.5 is located about 120° degree away from the garage. It is connected to one of the vacuum chambers and sits on the inner side of the storage ring (see the 1 o'clock position in Fig. 11. The cable drums together with the driving piezo motors are outside the vacuum. Two 1.5 m-long tubes guide the two cables from the drive to the vacuum chamber and provide the vacuum feedthrough. Two cables are required to pull the trolley a full 360 degrees in each direction during its NMR measurement and its return trip. Since the cables remain attached to the trolley during the storage in the garage, one of the two cables runs through the kicker region. To prevent any damage to the onboard electronics from electronic pickup on the cable from the kicker pulses, this cable is a non-conducting fishing line. The other cable is an all-copper double-shielded cable with an outer coating suitable for in-vacuum operation. This cable allows the feeding of the power and reference frequency signal as well as the communication with the trolley microcontroller.

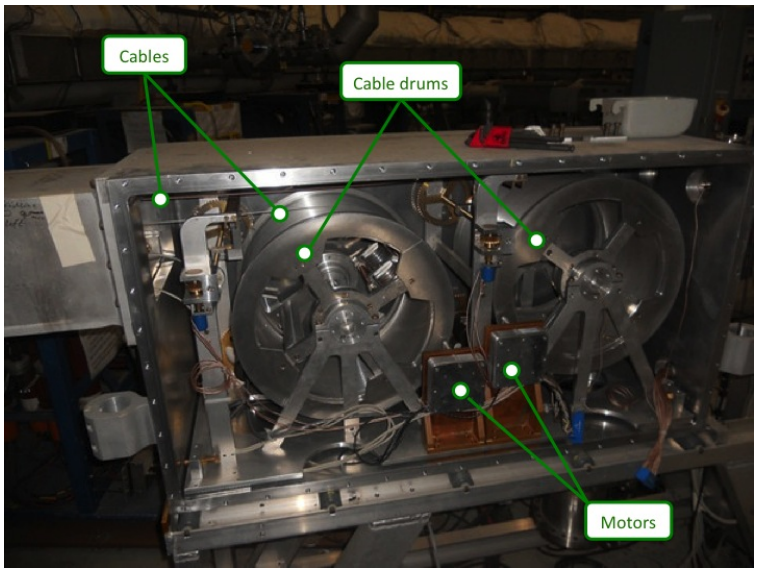

Figure 15.5: Trolley drive with the cable drums, motors and cables.

The cable drive mechanism will need refurbishment and inspection of its functional integrity. In general, we expect it to be used mainly as is since the overall wear in E821 was small and the mechanical parts should survive another 2 years of operation during the E989 experiment. In order to speed up the return trip of the trolley to minimize interruption of the spin precession frequency measurement, an upgrade of one of the motors is anticipated. We also plan to relocate two optical rotary encoders that monitor the unwinding of the cables to minimize some non-linearities in their readback values with respect to the actual cable unwinding length. For full operation of the drive, the motor controller needs to be brought back into operation. Its central component is an Infineon SAB80C535 microcontroller that

facilitates the communication with the remote DAQ. Its refurbishment should mainly require compilation and uploading of the Pascal software code which is available to us.

15.3.4 Position Measurement

The measurements of the trolley's position in both the longitudinal and transverse directions relative to its motion plays an important role in the evaluation of several systematic error sources. Uncertainties in the trolley's position convoluted with the local field gradients give rise to a shift in the measured B fields during both the relative calibration with the plunging probe and the mapping of the field around the full azimuth.

As stated in the requirements section 15.3.1 above, some improvements in the determination of the trolley's position compared to the E821 experiment are necessary. Together with the better shimming of the magnet (c.f. section 15.4) and hence reduced field gradients, this will give the overall reduction of the position related systematic errors required for E989.

During the calibration procedure of the trolley probes in a specially shimmed region in the ring, the plunging probe and the trolley probes need to be positioned repeatedly at the same position. The uncertainty in E821 for the relative azimuthal alignment was estimated to be 3 mm. As the trolley was positioned visually, we foresee improvements by means of a well-defined stop mechanism or an external laser beam on a fine positioning grid through the viewing port. The plunging probe currently has only limited directional movement and addition of its azimuthal adjustment inside the vacuum should also help in reducing this position uncertainty.

While the trolley moves on the rails around the ring, the transversal position of the 17 NMR probes relative to the central muon orbit is mainly defined by the precision alignment of the rails. An average radial and vertical deviation of the rails of less than $\pm$ 0.5 mm would be sufficient to keep the associated systematic error negligible. While mechanical improvements of the rail fixture, curvature, and positioning inside the vacuum chambers will be performed in conjunction with other work on the cages, a precise verification of this stringent alignment requirement needs to follow. We anticipate a combination of two measurements to have a consistent cross-check of the trolley's transversal movement. The first verification will be based on optical (or other suitable) survey techniques with the trolley riding on the rails. This technique should work on individual vacuum chambers in air. Once all chambers are mounted in the storage ring and evacuated, optical inspection of the trolley's movement could only happen via ports on the radial inner side of the chambers (see figure 3.4). However, the sole inspection of the trolley's movement inside a non-evacuated chamber might be sufficient since FEA modeling and measurements show that the deflection of the chamber walls is small. A second technique will make usage of imposing radial and vertical gradients using the surface coils to observe the changes in the NMR probe readings around the ring.

The longitudinal position measurement of the trolley was achieved by a combination of optical rotary encoders and potentiometers monitoring the cable unwinding as well as the response spikes in the NMR frequency of the fixed probes due to the passing electronics of the trolley. The overall estimate of the longitudinal uncertainty was on the order of a centimeter. We aim to reduce this uncertainty to 5 mm or better by refurbishing an onboard barcode reader that was mostly unused in E821 due to its overheating in the vacuum environment. As can be seen in Figure 15.6, the vacuum chambers are equipped with marks around the ring.

The continously spaced marks have a spacing of 2.5 mm while the larger spaced irregular codes serve as abolute reference marks. A reduction of the power consumption by usage of more efficient LEDs and light sensitive detectors or by increasing the heat dissipation capabilities of the reader head would then give a direct longitudinal measurement of the trolley at the required precision level.

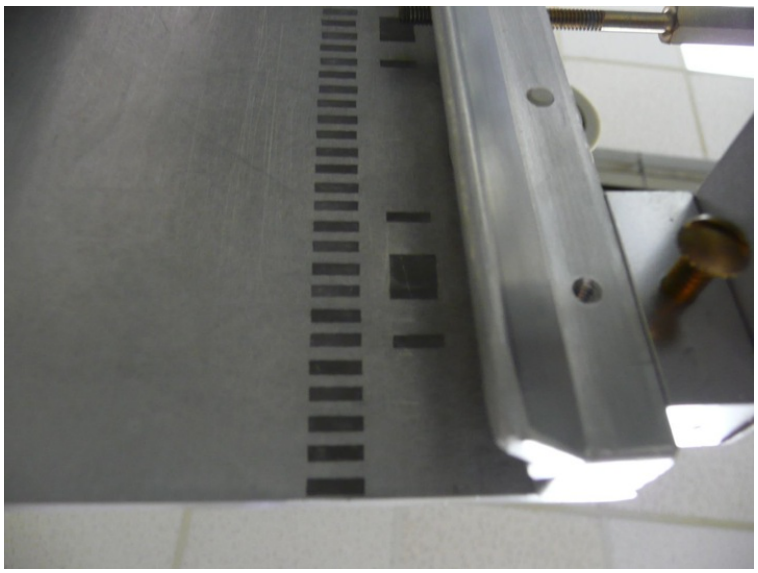

Figure 15.6: Trolley bar code marks on vacuum chameber plate

15.3.5 Probes

The 17 trolley NMR probes (c.f. Figure 15.9(b)) are identical to the fixed probes. No major work should be necessary for future usage in E989 except for a standard refurbishment procedure performed by collaborators from the University of Washington. These activities will include the refilling with the NMR substance (either water or petroleum jelly), resoldering of broken wire connections, tuning of the probes Q-value and impedance matching to the 50 Ω cable as well as testing of a normal NMR response at 1.45 T. Replacement of parts of the probe would also be handled in these steps.

As can be seen in the Figure 15.8(b), the outermost radius covered by the trolley probes is 3.5 cm. The folding of the muon distribution with the magnetic field multipole expansion is performed over the entire muon storage aperture with radius 4.5 cm. In E821, the estimate of the contribution from the sextupole and higher multipoles were obtained from data with a special shimming trolley in 1998 and amounted to a systematic error contribution of 0.03 ppm. Since a different arrangement of the 17 NMR probes, especially moving towards outer radii, could be beneficial to reduce this contribution, we will study the gains. The implementation would require two new teflon holder plates inside the trolley with a new hole configuration for the probe placement.

15.3.6 Frequency Measurement

The NMR frequency measurement for the 17 NMR trolley probes is currently all integrated into the onboard electronics. At its heart sits the Motorola 68332μC microcontroller with a multitude of functionality. Power, RS232 communication, and the NMR reference frequency are brought in over a single double-shielded cable. The remaining NMR components (RF pulse amplifier, multi- and duplexer, signal preamplifier and frequency counter) are all integrated into the trolley housing. Additional temperature and pressure sensors and the barcode reader are also available. The development of this minimally magnetic, low power and noise system was a major effort in E821. As future changes to the internal electronics come at the risk of a failure and could cause the need of significant engineering resources, we will avoid such activities as much as possible.

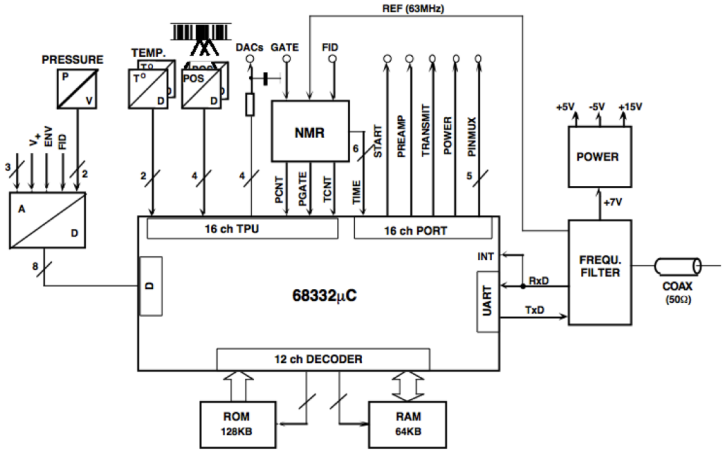

Figure 15.7: Schematics of central electronics on board of the trolley.

Even the low electric power of less than 1 W leads to changes in the temperature of the trolley electronics and the probes of a few degrees °C over the course of a trolley run. As the measured NMR frequency is temperature dependent, minimization of the temperature changes will help to reduce the associated systematic error. While we will also study the temperature dependence carefully in a test solenoid, we will investigate whether the heat dissipation via radiation to the vacuum chamber walls could be increased by increasing the surface emissivity of the trolley's aluminum shell or if an additional heat sink could stabilize the temperature sufficiently long enough.

15.3.7 DAQ

The communication with the onboard microcontroller happens via the pulling cable over the RS232 communication protocol. A new standard DAQ computer will be established to perform this functionality in the future E989 expreiment and to provide all necessary user interfaces to execute commands on the trolley microcontroller. The same DAQ infrastructure will be used to communicate with the trolley drive which is similarly interfaced via a

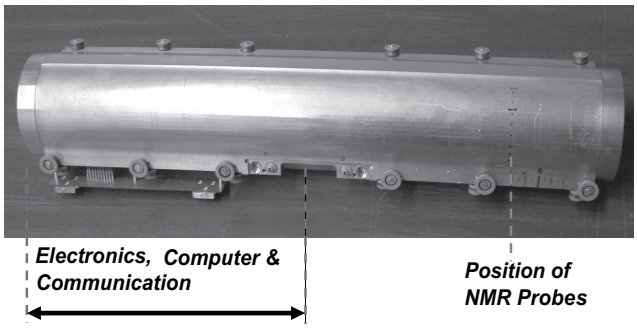

(a) NMR Trolley

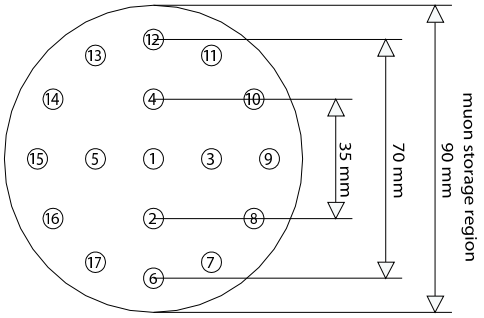

(b) Distribution of NMR probes

Figure 15.8: (a)Photograph of the NMR trolley, which measures the magnetic field in the storage ring. The array of 17 NMR probes, which are located inside the trolley housing, 82(1) mm behind the front of the trolley. Electronics occupies the back part of the device. At the location of the probes, the field perturbation by these materials is less than 2 ppm and is accounted for by the calibration method. (b)The probe numbers and placement are given by the schematic.

microcontroller. The plunging probe mechanism shares the same microcontroller concept and could be operated from this computer, too. If possible, we will also operate the garage retraction mechanism from here.

To map the storage ring magnetic field when the beam is off we will use a beam-tube trolley.

A central element of the system is a field-mapping trolley, shown in Fig. 15.8(a) that mapped the field at several thousand points around the ring. This trolley contains 17 NMR probes arranged in concentric circles as shown in Fig. 15.8(b).

The magnetic field is measured and monitored by pulsed Nuclear Magnetic Resonance of protons in water samples [3]. The free induction decay (FID) is picked up by the coil L_S in Fig. 15.9 after a pulsed excitation rotates the proton spin in the sample by 90° to the magnetic field. The proton response signal at frequency $f_{\rm NMR}$ is measured by counting its zero crossings within a well-measured time period the length of which is automatically adjusted to approximately the decay time (1/e) of the FID. It is mixed with a stable reference frequency and filtered to arrive at the difference frequency $f_{\rm FID}$ chosen to be typically in the 50 kHz region. The reference frequency of $f_{\rm ref} = 61.74$ MHz is obtained from a frequency synthesizer, which is phase locked to a LORAN C secondary frequency standard [9], and it is chosen such that always $f_{\rm ref} < f_{\rm NMR}$. The very same LORAN C device also provides the time base for the ω_a measurement. The relationship between the actual field $B_{\rm real}$ and the field corresponding to the reference frequency is given by

$$B_{\rm real} = B_{\rm ref}\left(1 + \frac{f_{\rm FID}}{f_{\rm ref}}\right). \tag{15.6}$$

The field measurement process has three aspects: calibration, monitoring the field during data collection, and mapping the field. The probes used for these purposes are shown in

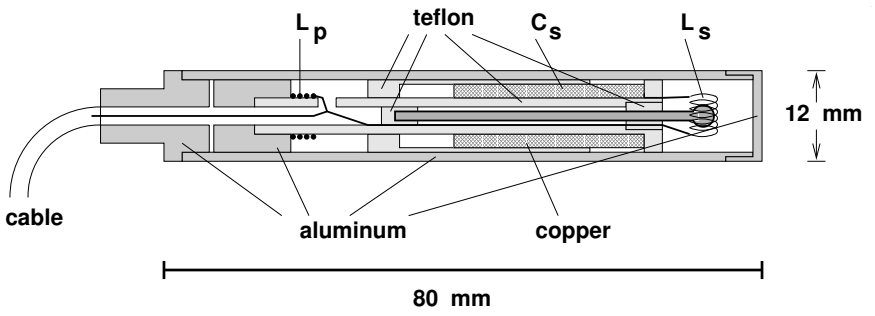

(a) Plunging probe

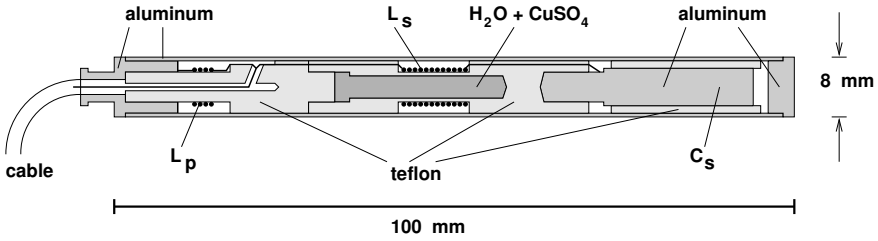

(b) Trolley and fixed probe

Figure 15.9: (a) Plunging probe, which can be inserted into the vacuum at a specially shimmed region of the storage ring to transfer the calibration to the trolley probes. (b) The standard probes used in the trolley and as fixed probes. The resonant circuit is formed by the two coils with inductances L_s and L_p and a capacitance C_s made by the Al-housing and a metal electrode.

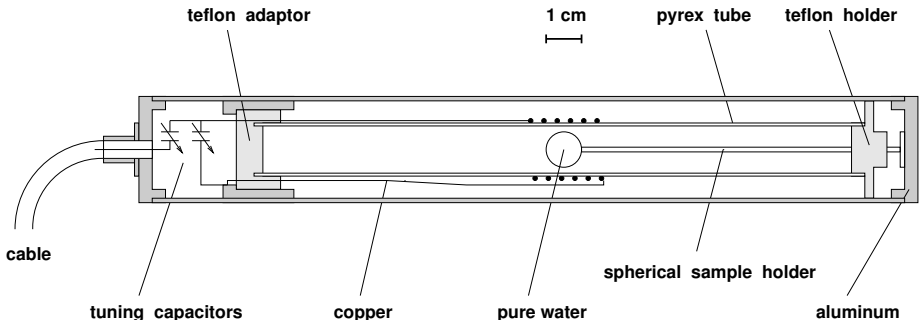

(a) Absolute calibration probe

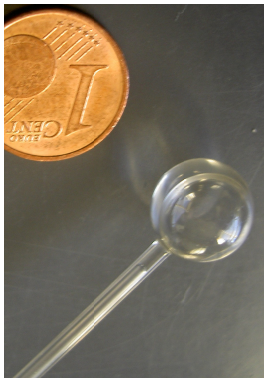

(b) Spherical Pyrex container

Figure 15.10: The different NMR probes. (a) Absolute probe featuring a spherical sample of water. This probe and all its driving and readout electronics are the very same devices employed in reference [19] to determine λ, the muon-to-proton magnetic-moment ratio. (b) The spherical Pyrex container for the absolute probe.

Fig. 15.9 To map the field, an NMR trolley [7] was built with an array of 17 NMR probes arranged in concentric circles, as shown in Fig. 3.8. While it would be preferable to have information over the full 90-mm aperture, space limitations inside the vacuum chamber, which can be understood by examining Figs. 3.8, prevent a larger diameter trolley.

The trolley is built from non-magnetic materials and has a fully functional CPU on-board which controls a full FID excitation and zero crossing counting spectrometer. It is pulled around the storage ring by two cables, one in each direction circling the ring. One of these cables is a thin co-axial cable with only copper conductors and Teflon dielectric and outside protective coating (Suhner 2232-08). It carries simultaneously the dc supply voltage, the reference frequency $f_{\rm ref}$ and two-way communication with the spectrometer via RS232 standard. The other cable is non-conducting nylon (fishing line) to eliminate pickup from the pulsed high voltage on the kicker electrodes.

During muon decay data-collection periods, the trolley is parked in a garage (see Fig. 3.4) in a special vacuum chamber. Every few days, at *random times*, the field is mapped using the trolley. During mapping, the trolley is moved into the storage region and over the course of 2 hours is pulled around the vacuum chamber, measuring the field at some 100,000 points by continuously cycling through the 17 probes while moving. Data were recorded in both possible directions of movement. During the approximately three-month data-collection runs, the storage-ring magnet remains powered continuously for periods lasting from five to twenty days; thus the conditions during mapping are identical to those during the data collection.

To cross calibrate the trolley probes, a two-axis non-magnetic manipulator made from aluminum and titanium only, including titanium bellows, and driven by non-magnetic piezo motors was developed. It was placed at one location in the ring and it permits a special NMR plunging probe, or an absolute calibration probe with a spherical water sample [4], to plunge into the vacuum chamber. In this way the trolley probes can be calibrated by transferring the absolute calibration from the calibration probe shown in Fig. 15.9 to individual probes in the trolley. These measurements of the field at the same spatial point with the plunging, calibration and trolley probes provide both relative and absolute calibration of the trolley probes. During the calibration measurements before, after and occasionally randomly during each running period, the spherical water probe is used to calibrate the plunging probe, and with this then the trolley probes. The absolute calibration probe provides the calibration to the Larmor frequency of the free proton [11], which is called ω_p below.

The magnetic field data consist of three separate sets of measurements: The calibration data taken before, after, and occasionally during each running period; maps of the magnetic field obtained with the NMR trolley at intervals of a few days at random hours; and the field measured by each of the fixed NMR probes located in the vacuum chamber walls. For the latter measurements groups of 20 probes were connected via one of 20 analog multiplexers to one of 20 readout channels, each consisting of a frequency mixer and a custom-designed FID zero crossing counting device [3]. The plunging probe and the calibration probe [4] were also connected to one of the multiplexer inputs. The probes of each group were sequentially excited and their FID was read in full cycles repeated approximately every 5 seconds all throughout the experimental periods and whenever the magnet was energized. The data taken concurrent with the muon spin-precession data were tied to the field mapped by the trolley, which were used to determine the average magnetic field in the storage ring, and

subsequently the value of ω_p to be used in Eq. (3.21).

Calibration of the trolley probes

The errors arising from the cross-calibration of the trolley probes with the plunging probes are caused both by the uncertainty in the relative positioning of the trolley probe and the plunging probe, and by the local field inhomogeneity. At this point in azimuth, trolley probes are fixed with respect to the frame that holds them, and to the rail system on which the trolley rides. The vertical and radial positions of the trolley probes with respect to the plunging probe are determined by applying a sextupole field and comparing the change of field measured by the two probes. The field shimming at the calibration location minimizes the error caused by the relative-position uncertainty, which in the vertical and radial directions has an inhomogeneity less than 0.2 ppm/cm, as shown in Fig. 15.11(b). The full multipole components at the calibration position are given in Table 15.3.7, along with the multipole content of the full magnetic field averaged over azimuth. For the estimated rms 1 mm-position uncertainty, the uncertainty on the relative calibration is less than 0.02 ppm.

The absolute calibration utilizes a probe with a spherical water sample (see Figs. 15.9(a), 15.9(b)) [4]. The Larmor frequency of a proton in a spherical water sample is related to that of the free proton through [10, 14]

$$f_{\rm L}({\rm sph}-{\rm H_2O},T) = [1-\sigma({\rm H_2O},T)]\, f_{\rm L}({\rm free}), \tag{15.7}$$

where $\sigma({\rm H_2O},T)$ is from the diamagnetic shielding of the proton in the water molecule, determined from [11]

$$\begin{aligned}\sigma({\rm H_2O},34.7^\circ C) &= 1-\frac{g_p({\rm H_2O},34.7^\circ C)}{g_J(H)}\frac{g_J(H)}{g_p(H)}\frac{g_p(H)}{g_p({\rm free})} &(15.8)\\ &= 25.790(14)\times 10^{-6}. &(15.9)\end{aligned}$$

The g-factor ratio of the proton in a spherical water sample to the electron in the hydrogen ground state ($g_J(H)$) is measured to 10 parts per billion (ppb) [11]. The ratio of electron to proton g-factors in hydrogen is known to 9 ppb [15]. The bound-state correction relating the g-factor of the proton bound in hydrogen to the free proton are calculated in References [16, 17]. The temperature dependence of σ is corrected for using $d\sigma({\rm H_2O},T)/dT = 10.36(30)\times 10^{-9}/^\circ{\rm C}$ [18]. The free proton frequency is determined to an accuracy of 0.05 ppm.

The fundamental constant $\lambda_+ = \mu_{\mu^+}/\mu_p$ (see Eq.(3.21)) can be computed from the hyperfine structure of muonium (the μ^+e^- atom) [14], or from the Zeeman splitting in muonium [19]. The latter experiment used the very same calibration probe as well as the essential NMR field monitoring and mapping devices and techniques, including all the driving and readout electronics, as we used in our $(g-2)$ experiment. The magnetic environments of the two experiments were slightly different, so that perturbations of the probe materials on the surrounding magnetic field differed by a few ppb between the two experiments, which can be neglected at our level of accuracy. We have therefore a direct robust link of our magnetic field to the muon magneton (proton NMR has only the role of a fly wheel), which is independent of possible future changes in fundamental constants in the regular adjustment procedures [14], unless the muon magneton will be remeasured experimentally.

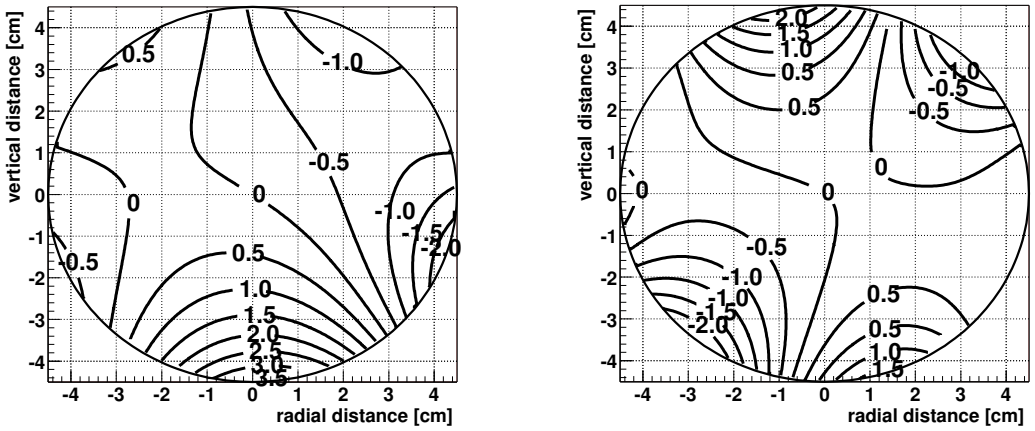

(a) Calibration position

(b) Azimuthal average

Figure 15.11: Homogeneity of the field (a) at the calibration position and (b) for the azimuthal average for one trolley run during the 2000 period. In both figures, the contours correspond to 0.5 ppm field differences between adjacent lines.

The errors in the calibration procedure result both from the uncertainties on the positions of the water samples inside the trolley and the calibration probe, and from magnetic field inhomogeneities. The precise location of the trolley in azimuth, and the location of the probes within the trolley, are not known better than a few mm. The uncertainties in the relative calibration resulting from position uncertainties are 0.03 ppm. Temperature and power-supply voltage dependences contribute 0.05 ppm, and the paramagnetism of the O_2 molecules in the air-filled trolley causes an experimentally verified 0.037 ppm shift in the field.

Table 15.1: Multipoles at the outer edge of the storage volume (radius = 4.5 cm). The left-hand set are for the plunging station where the plunging probe and the calibration are inserted. The right-hand set are the multipoles obtained by averaging over azimuth for a representative trolley run during the 2000 period.

Multipole	Calibration		Azimuthal Averaged	
[ppm]	Normal	Skew	Normal	Skew
Quadrupole	-0.71	-1.04	0.24	0.29
Sextupole	-1.24	-0.29	-0.53	-1.06
Octupole	-0.03	1.06	-0.10	-0.15
Decupole	0.27	0.40	0.82	0.54

Mapping the magnetic field

During a trolley run, the value of B is measured by each probe at approximately 6000 locations in azimuth around the ring. The magnitude of the field measured by the central probe is shown as a function of azimuth in Fig. 15.12 for one of the trolley runs. The insert shows that the fluctuations in this map that appear quite sharp are in fact quite smooth, and are not noise. The field maps from the trolley are used to construct the field profile averaged over azimuth. This contour plot for one of the field maps is shown in Fig. 15.11(b). Since the storage ring has weak focusing, the average over azimuth is the important quantity in the analysis. Because the recorded NMR frequency is only sensitive to the magnitude of B and not to its direction, the multipole distributions must be determined from azimuthal magnetic field averages, where the field can be written as

$$B(r,\theta) = \sum_{n=0}^{n=\infty} r^n \left(c_n \cos n\theta + s_n \sin n\theta\right), \tag{15.10}$$

where in practice the series is limited to 5 terms.

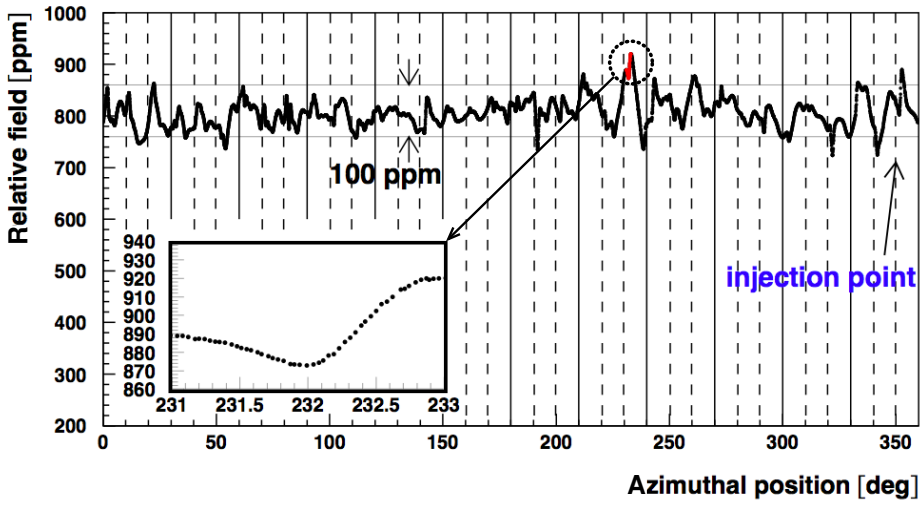

Figure 15.12: The magnetic field measured at the center of the storage region vs. azimuthal position. Note that while the sharp fluctuations appear to be noise, when the scale is expanded the variations are quite smooth and represent true variations in the field.

Tracking the magnetic field in time

During data-collection periods the field is monitored with the fixed probes. To determine how well the fixed probes permitted us to monitor the field felt by the muons, the measured field, and that predicted by the fixed probes is compared for each trolley run. The results of this analysis for the 2001 running period is shown in Fig. 15.13. The rms distribution of these differences is 0.10 ppm.

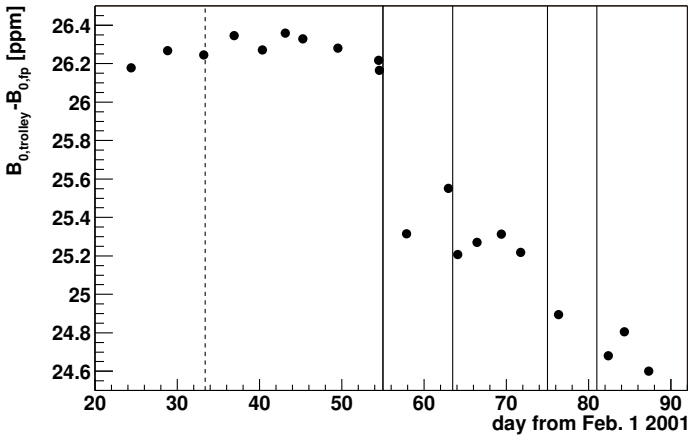

Figure 15.13: The difference between the average magnetic field measured by the trolley and that inferred from tracking the magnetic field with the fixed probes between trolley maps. The vertical lines show when the magnet was powered down and then back up. After each powering of the magnet, the field does not exactly come back to its previous value, so that only trolley runs taken between magnet powerings can be compared directly.

Determination of the average magnetic field: ω_p

The value of ω_p entering into the determination of a_μ is the field profile weighted by the muon distribution. The multipoles of the field, Eq. (15.10), are folded with the muon distribution,

$$M(r,\theta) = \sum [\gamma_m(r)\cos m\theta + \sigma_m(r)\sin m\theta], \tag{15.11}$$

to produce the average field,

$$\langle B \rangle_{\mu-\mathrm{dist}} = \int M(r,\theta) B(r,\theta) r dr d\theta, \tag{15.12}$$

where the moments in the muon distribution couple moment-by-moment to the multipoles of $\vec{B}$. Computing $\langle B \rangle$ is greatly simplified if the field is quite uniform (with small higher multipoles), and the muons are stored in a circular aperture, thus reducing the higher moments of $M(r,\theta)$. This worked quite well in E821, and the uncertainty on $\langle B \rangle$ weighted by the muon distribution was ± 0.03 ppm.

The weighted average was determined both by a tracking calculation that used a field map and calculated the field seen by each muon, and also by using the quadrupole component of the field and the beam center determined from a fast-rotation analysis to determine the average field. These two agreed extremely well, vindicating the choice of a circular aperture and the ± 1 ppm specification on the field uniformity, that were set in the design stage of the experiment. [5]

Summary of the magnetic field analysis

The limitations on our knowledge of the magnetic field come from measurement issues, i.e. systematics and not statistics, so in E821 the systematic errors from each of these sources had to be evaluated and understood. The results and errors are summarized in Table 15.2.

15.3.8 Principles of Calibration

Ideally the frequency ω_p is the average over space and time of the Larmor-precession frequency of free protons having the same distribution as the muons within the storage ring. This, of course, cannot be directly measured, and we therefore rely on a set of measurements of protons in water or other proton-rich material (e.g. petrolatum/ petroleum jelly) and a calibration chain traceable to the Bohr magneton/μ_μ. The magnetic field measurement system and calibration chain consists of the following elements:

1. Fixed proton-NMR probes permanently mounted onto the vacuum chambers in grooves milled into outer surfaces of the aluminum. There are 360 available fixed probes.

2. Mid-plane proton-NMR probes permanently mounted in reentrant tubes near the vertical center of the muon storage volume. These are under consideration with the number to be detemined.

3. The trolley consisting of (17) proton-NMR probes that periodically maps the field in the muon storage region to correlate with fixed and mid-plane probes. The trolley probes do not span the entire muon-storage volume, and redesign is under consideration.

4. Plunging probe to transfer proton-NMR calibration corrections to the trolley probes in a calibrated and mapped magnetic field in vacuum.

5. Calibration probes (proton-NMR and/or ^{3}He) used for absolute calibration of the plunging probe, trolley probes and transfer to the fixed probes.

The frequency ω_p is thus estimated from a set of *fixed probe* frequency measurements, and can be expressed as

$$\omega_p = \sum_i \sum_j W_i(t_j)\omega_i(t_j) = \sum_{ij} W_{ij}\omega'_{ij}, \tag{15.13}$$

where i labels the specific fixed probe, j labels the time of the measurement and ω'_{ij} is the frequency measured by the fixed probe i at the time t_j during data taking *corrected to the calibrated trolley frequency averaged over the muon distribution estimated at time* t_j and the W_{ij} are weights that vary, for example due to the statistical weight of the w_a data at time t_j or quality of data from the fixed probe. For example, if the experiment consists of 10-measurements of ω_a with equal statistical weight ($j = 1...10$), and all 360 fixed probes provide data of equal quality, then the weight W_{ij} would just be $\frac{1}{3600}$ for all i and j. In practice, the weight for a particular probe could be zero, in fact only about 120 probes were used in E821 due to the poor quality of signals from probes in the inhomogeneous magnetic field near the breaks in the iron flux return.

The corrections to the frequency measured at a fixed probe are determined from the calibration chain and consist of an additive and a multiplicative component, i.e. $\omega'_{ij} = \alpha_i j \omega_i j + \delta\omega_i j$. The multiplicative component α arises due to corrections to the probe frequency due to diamagnetism and bulk effects, while the additive shift arises due to spatial (and temporal) separation of the fixed probe measurements and the measurements in the muon storage volume. The multiplicative α can be written

$$\alpha = \sigma_{\mathrm{H_2O}}(T) + \delta_b + \delta_p + \delta_s, \tag{15.14}$$

where $\sigma_{\mathrm{H_2O}}(T) = (25.790(14) + 0.010(05)(T - 34.7°C) \times 10^{-6}$ [11, 12] is the temperature-dependent diamagnetic shielding factor for protons in water, where the temperature is measured in $°C$. For ^{3}He, $\sigma_{^3\mathrm{He}} = 59.924(2)\times 19^{-6}$ [13], and $\mu_{^3\mathrm{He}'}/\mu_{p'} = 0.7617861313(33)$ with $\mu_{p'}$ the magnetic moment of protons in water and $\mu_{^3\mathrm{He}'}$ the magnetic moment of the ^{3}He nucleus - the hellion - in gaseous ^{3}He. The factor δ_b is the bulk correction given by $(\epsilon - \frac{4\pi}{3})\chi$ with $\epsilon = \frac{4\pi}{3}$ for a sphere and $\epsilon = 2\pi$ for a cylinder with axis perpendicular to $\vec{B}$ (the orientation of the fixed probes and trolley probes). For a water-filled probe that is nearly spherical, such as shown in Figure .. the bubble requires an additional correction [11]. The factor δ_p accounts for paramagnetic impurities in the sample and magnetic materials in the probe, respectively. Using pure, deionized distilled water in the calibration and field-mapping probes minimizes impurity effects and can be monitored by measuring the magnetization time-constants T_1 and T_2 using appropriate pulse sequences. Careful selection of calibration-probe materials using a protocol of testing materials, for example through our collaboration with PTB-Berlin and Technical University of Munich, is essential. An additional shift of the calibration arises due to the mirror effect of the iron, i.e. an image of the magnetized samples due to reflection of field lines at the high-mu iron of the pole pieces.

The chain of calibrations begins with the absolute determination of the magnetic field in a section of the ring in which the field has been trimmed to be as uniform as possible. The field should be measured over a volume encompassing the set of trolley probes and referenced to a spherical calibration probe located near the center of the volume, i.e. an array of probes will be used to map the field. For E821, a plunging probe that could be translated along the vertical axis was used. We envision modifying the plunging probe to provide 3-dimensional mapping. Alternatively an array of probes distributed similar to the trolley probes (number to be determined); however the probes consist of nominally spherical samples (trolley probes and fixed probes have cylindrical samples). Unlike the trolley, the array of 18 probes can be rotated (e.g. set into a V-block providing 90° rotations) and flipped front-to-back to exchange probe positions and account for differences in the probes. (See figure...). The field-mapping probes can be either pure water or ^{3}He as discussed below. The calibration and field mapping measurements will be done in an oxygen-free atmosphere or vacuum to eliminate the paramagnetism of O_2.

Figure ... shows the distribution of the 17 E821 trolley probes along with frequency deviations (in ppm) of the measured frequency from the central position of the calibration and plunging probes. These deviations are due to a combination of the field distribution and differences of the probes. The field distribution can be separated from probe differences with field-mapping. The stability of the field and the magnetometers is crucial and will also be monitored enabling interpolation, i.e. the calibration and mapping will be performed

before and after the frequencies of the trolley probes are measured. For E821, the trolley calibration systematic error was 0.09 ppm. This will be improved to 0.06 ppm or better by making use of the mapping probe and eliminating the O_2.

For a trolley run, the trolley is pulled around the muon-storage volume, rolling on rails. The 17 calibrated probes are monitored during the approximately 2-hour measurement providing about 100,000 measurements, which are used to map the field and determine ω_p for the trolley run. For E821, the systematic error on ω_p from the trolley runs was 0.05 ppm, which will be improved to 0.02 ppm (HOW?). Simultaneously, the fixed probes are monitored so that the corrections α and $\delta\omega$ can be determined for each fixed probe. The fixed-probe corrections are interpolated in time between trolley runs. For E821, the systematic error due to interpolation was 0.07 ppm, which will be improved to 0.06 ppm or better with more frequency trolley runs. (See trolley improvement section).

15.3.9 Fixed-probe improvements

Petrolatum/Petroleum Jelly samples

For E821, the fixed probes and trolley probes, illustrated in Figure ..., had samples of $CuSO_4$ dopped water. The $CuSO_4$ is paramagnetic and is typically used in NMR to shorten the magnetization recovery time (T_1) so that more frequent measurements can be made. For pure H_2O, $T_1 \approx 3.5$ s, so consistent free -indiuction-decay NMR measurements can be taken only every 10-15 seconds. As noted in equation 15.14, paramagnetic impurities lead to a shift of the measured frequency, and changes in the $CuSO_4$ concentration, for example due to slow evaporation of the water will affect the stability of the measurement. We are therefore investigating the use of petroleum jelly in place of the $CuSO_4$-dopped water. Preliminary investigations are reported in the PhD dissertation of R. Prigl[6]. We have recently measured the NMR relaxation times of a sample of petrolatum at 0.4 T using saturation-recovery (for T_1) and standard spin-echo sequence (for T_2). We find $T_2 \approx T_1 \approx 40$ ms. The temperature dependence of the diamagnetic shielding is crucial, and we are currently preparing a measurement at 1.5 T using a warm-bore superconducting solenoid magnet at Michigan. A temperature controlled plug containing a fixed probe with a petrolatum will be place in the bore, which is thermally isolated from the superconducting coil to measure the temperature dependence.

15.3.10 ^{3}He Magnetometry

A second absolute calibration probe being considered will contain polarized ^{3}He. Such a probe has the advantage that the NMR frequency does not depend on the shape of the ^{3}He volume, unlike the water sample which has to be spherical, and depends on a number of external quantities discussed above.

NMR with hyperpolarized ^{3}He produced by laser optical pumping is practical because the NMR signal per atom is of order 10^5 times larger than protons at 1.5 T, compensating for the much lower concentration in the gas phase. There are several potential advantages to using hyperpolarized ^{3}He in place of distilled water in the calibration/field-mapping probes leading to reduced systematic uncertainties. From equation 15.14, the diamagnetic shielding

factor $\sigma_{^3\mathrm{He}} = 50.924(2) \times 10^{-6}$, though larger than for H_2 and H_2O, has about 100× smaller temperature coefficient for gases [27]. Additionally, motional narrowing eliminates line-shape distortion and the FID produces a Lorentzian line shape whose center is well defined. For H_2O the line shape must be analyzed in the same way as reference [11] in order to accurately transfer the calibration. Our experience with hyperpolarized xenon suggests that that signal-to-noise is comparable to the E821 H_2O calibration sample. Additionally, the samples can be made smaller, e.g. 5 mm diameter and thus average over a smaller volume, though cell-shape effects, discussed in the next paragraph, are more difficult to deal with in smaller cells.

Hyperpolarized ^{3}He can be provided from a spin-exchange (SEOP)[29, 28] or metastability-exchange (MEOP)[30, 31] set up. We have extensive experience with SEOP and have worked closely with MEOP systems and will cooperate with expert groups at Ecole Normal Superieur and Simon Fraser to develop an effective system. The MEOP approach has advantages for the calibration because it can be applied at room temperature and therefore in-situ in the probe. In the MEOP scenario, a turnkey 1083 nm laser light from a fiber laser (e.g. http://www.keopsys.com/index.php/en/products-n-services/cw-laser/cyfl/cyfl-giga-series.html) is distributed to each of the probe cells by a fiber. A discharge is struck in the cell to produce the excited state. Polarization of 10% or more is expected in a few minutes. A second option is hyperpolarized ^{3}He produced in a separate cell and transferred to the calibration cells through PFE tubing similar to the polarizers we have used for medical imaging work [32]. In either scenario, the dominant corrections will arise due to cell-shape effects (δ_b in equation 15.14), i.e non-sphericity of the cell, but more importantly the polarized gas in any tubing or pull off used in cell filling.

High-field hyperpolarization magnetometry using the MEOP technique will be developed at Michigan working with long-term collaborators from our EDM [33] and medical-imaging work [34]. One of the challenges is effecting high magnetization at high field (signal-to-noise is proportional to magnetization, i.e. the product of polarization and gas density). High-field MEOP polarization of ^{3}He has been recently studied by the ENS group [35, 36], who show that, due to higher polarization rates, nuclear polarization, of 80% at 1.33 mbar and 25% at 67 mbar, have been achieved. The magnetization at 67 mbar is essentially identical to protons in H_2O at 1.5 T, though the signals may be slightly smaller due to the difference of gyromagnetic ratios (32.4 MHz/T for ^{3}He and 42.6 MHz/T for protons).

The development work at Michigan will make use of our 1.5 T field and will enable probe development, polarization and studies of temperature dependence similar to those planned for petrolatum. SEOP polarized samples are also under consideration, and we have significant experience in these techniques and equipment.

As a basis for discussion, the systematic errors from E821 are listed below in Table 15.2.

15.4 Magnet Shimming

15.4.1 Overview

The main technical objective of the $g-2$ storage ring shimming is to produce a field that is extremely uniform when averaged over azimuth. Both the muon distribution and the average field can be described by multipole expansions (see Sec 15.1). Care should be taken

Table 15.2: Systematic errors for the magnetic field for the different run periods. †Higher multipoles, trolley temperature and its power supply voltage response, and eddy currents from the kicker.

Source of errors	R99 [ppm]	R00 [ppm]	R01 [ppm]
Absolute calibration of standard probe	0.05	0.05	0.05
Calibration of trolley probes	0.20	0.15	0.09
Trolley measurements of B_0	0.10	0.10	0.05
Interpolation with fixed probes	0.15	0.10	0.07
Uncertainty from muon distribution	0.12	0.03	0.03
Inflector fringe field uncertainty	0.20	–	–
Others †	0.15	0.10	0.10
Total systematic error on ω_p	0.4	0.24	0.17
Muon-averaged field [Hz]: $\widetilde{\omega}_p/2\pi$	61 791 256	61 791 595	61 791 400

to minimize higher-order multipoles in the field. Improved field uniformity at any local azimuthal position is also desirable since the performance of the NMR probes relies on keeping the field gradients as small as possible in order to optimize the measurement of the free induction decay (FID) signal.Furthermore, small field gradients reduce the uncertainty contribution from the position uncertainty of the probes. Since the probes sample the field over a non-negligible volume, the requirements on knowledge of the position are relaxed if the field gradients are minimized.

Before shimming, the magnet was designed to produce a field uniformity in the muon storage region of better than a few parts in 10^4. This was achieved by using high-quality steel for the magnet yoke, and ultra-low carbon steel (ULCS) for the pole pieces. Upon assembly, the field uniformity is improved by more than two orders of magnitude through a shimming sequence. The general shimming strategy implemented in E821 was two-fold: passive shimming via precision alignment of ferromagnetic materials and active shimming utilizing current distributions. We will base our general shimming procedure on that of E821 and the experience gained therein. The $g-2$ superconducting coils, yoke, pole pieces, and shims has been simulated with OPERA-2D as well as OPERA-3D. The results of these simulations are compared both with the POISSON simulations and results obtained during the development of E821 [20, 21, 22, 23, 24, 25, 26]. One critical aspect of the simulation is the use of realistic B-H magnetzation curves. Although the steel is not fully saturated at 1.45 T, the response is not perfectly linear. This non-linearity is partially responsible for generating higher-order multipole moments in the shimming simulations, and must be recognized during the actual shimming procedure. Our OPERA simulations will allow for a sophisticated shimming plan that improves the overall uniformity of the field in E989.

15.4.2 Passive Shims

Passive shimming refers to the set of mechanical adjustments that are performed during the assembly of the ring and remain fixed during a long running period. The general strategy is

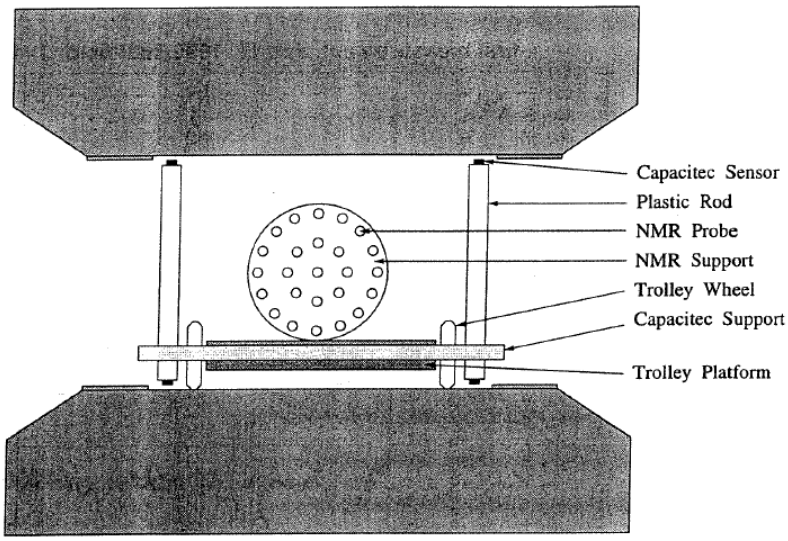

Figure 15.14: Schematic depiction of the NMR shimming trolley situated on a platform. Capacitive sensors on plastic rods help measure the pole piece alignment.

to begin with adjustments far from the muon storage region and work towards it with finer and finer adjustments. The principle passive shimming controls consist of the following:

1. Iron pieces on the yoke
2. Alignment of the pole faces
3. Wedge shims in the air gap between the pole piece and yoke
4. Edge shims in the gap between upper and lower pole faces
5. Iron pieces in the azimuthal gaps between adjacent pole faces

Throughout the physics measurement, the NMR trolley described in Section 15.3 will travel around the ring to map out the magnetic field. However, prior to the installation of the vacuum chambers, more space is available between the pole pieces and a larger trolley can be used. This shimming trolley (see Figure 15.14) consists of 25 NMR probes; one is at the center of the muon storage region, eight are at a radius of 2.25 cm, and 16 are at a radius of 4.5 cm. This allows a mapping that extends to the outer radius of the muon storage region. The shimming trolley was positioned on the end of a ≈ 7 meter turntable arm positioned about the center of the storage ring. Rotating the turntable allowed the shimming trolley to map the field at various azimuthal positions.

The platform on which the shimming trolley rests also allows for a precision measurement of the vertical gap between the upper and lower pole faces. Plastic rods with capacitive sensors (model Capacitec HPB-150A-A-L2-10-B-D) on each end allowed for a determination of the relative parallelism between the poles [26]. By rotating the assembly by 180° about the vertical axis, any systematic error due to the relative length of the rods was eliminated.

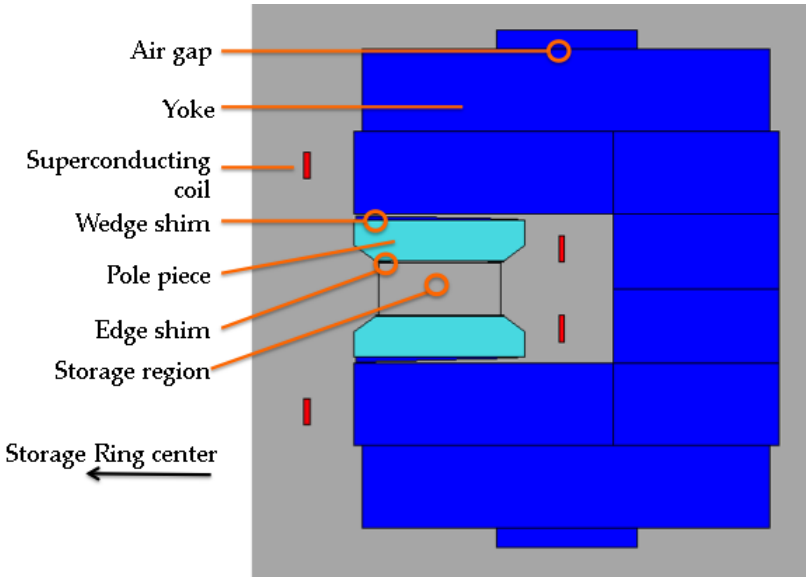

Figure 15.15: OPERA-2D model of the $g-2$ magnet. The yoke and wedge shims are steel and shown in blue. The yoke (cyan) is made from ultra-low carbon steel (ULCS). The current in the superconductor coils is into the page for the inner coils and out of the page for outer coils.

The analysis of the data from the shimming trolley provided feedback during each stage of the shimming procedure.

Procedure

A two-dimensional slice of the $g-2$ magnet simulated in OPERA-2D is shown in Figure 15.15.

Yoke Iron The yoke is subdivided into twelve 30° sectors, as described in Section 9.2. Long wavelength azimuthal variations in the field uniformity can be addressed by adjusting the positioning of pieces of iron on the outer surface of the yoke. In particular, an increase in the air gap between the top piece of steel (labeled 7 in figure 15.15) and the upper yoke plate (labeled 5) leads to an increase the overall reluctance of the magnetic circuit. In this manner, rough adjustments to the dipole field can be achieved on a sector by sector basis. In other regions of the ring, steel shims will be added to the outside of the yoke in order to compensate for holes that are required for items like vacuum feedthroughs, the inflector, etc.

Pole Piece Alignment The Capacitec sensors mounted to the shimming trolley apparatus will be able to measure the gap to a precision of < 0.25 μm. An increase in the gap size of 25 μm corresponds to a 100 *ppm* decrease of the dipole field. A 50 μm tilt over the length of the pole corresponds to a change in the quadrupole moment of 120 ppm. Thus the information from the shimming trolley will be used to properly align the pole pieces.

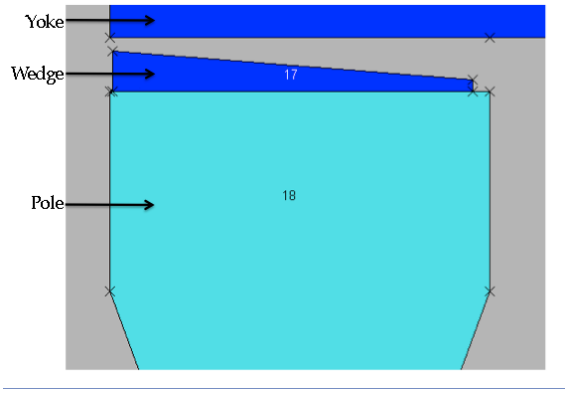

Figure 15.16: OPERA-2D model of the $g-2$ magnet, zoomed in on the air gap between the yoke and pole pieces. The wedge shims are radially adjustable.

Wedge Shims Wedge shims are inserted into the 2-cm air gap between the pole piece and the yoke, as depicted in Figure 15.16. The gap is designed to isolate the high-quality precision pole pieces from the yoke steel, which contains some magnetic inhomogeneities. Each 30° sector contains 72 wedge shims, which are 9.86 cm wide (azimuthally) and 53 cm-long (radially)[3]. This is shorter than the 56 cm-long pole pieces (radially), to accommodate radial adjustments. At the inner radius, the wedge shims are 1.65 cm thick, while at the outer radius, they are 0.5 cm thick. Viewed from above, each wedge shim is rectangular. Thus the space between adjacent wedge shims increases as the radial coordinate increases.

The angle of the wedge shims was calculated to be 20 milliradian in order compensate for the intrinsic quadrupole moment produced by the C-shaped magnet. Due to the asymmetry in the C-magnet, the field lines would tend to concentrate in the gap near the return yoke. The dipole field is determined by the average thickness in the air gap above the storage region. The average wedge thickness is adjusted by translating the radial position of the wedge shims. Because of the shallow angle of 20 mrad, a radial movement by 50 μm changes the gap by 1 μm, allowing fine control for the dipole field. OPERA-2D simulations show that inserting the wedges into the air gap (towards the return yoke) radially by 50 μm produces a 5.4 *ppm* increase in the dipole field. The quadrupole and higher-order multipoles are each affected by less than 0.1 *ppm* for this adjustment.

Edge Shims Each of the 36 pole pieces has four removable edge shims mounted on the surface closest to the muon storage region, as shown in Figure 15.17. Each shim is 5 cm wide (radially), spans one pole piece (10° azimuthally), and is positioned at either the inner or outer edge of the pole faces. Variation of the thickness of the edge shims can produce (and thus counteract) predictable multipole moments.

In E821, the shims were ordered oversized (3.2 mm for the outer shims and 4.4 mm for the inner shims) and then ground down to tune the quadrupole through octupole moments. A first pass was performed to uniformly grind the shims as a function of azimuth. A final pass optimized the thickness of the edge shims pole piece by pole piece.

We have studied the effect of systematic shim thickness variations in OPERA-2D. Since

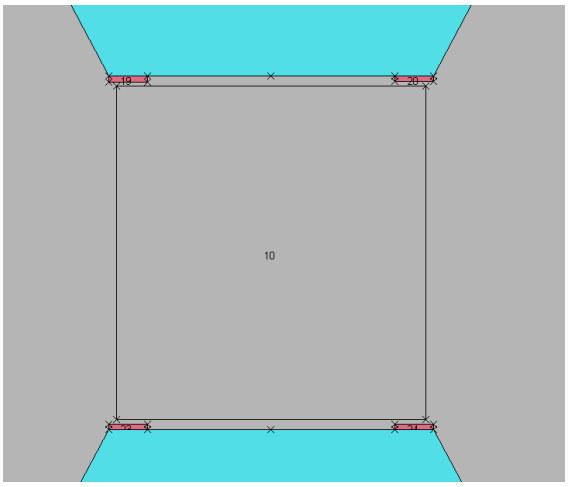

Figure 15.17: OPERA-2D model of the $g-2$ magnet, zoomed in on the storage region. Edge shims are mounted on the pole pieces. "Inner" refers the shim at smaller radius (closest to the center of the ring), while "outer" refers to the shim at the larger radius (closest to the return yoke).

the model assumes vertical symmetry, the upper and lower edge shims are always adjusted simultaneously. Symmetrically increasing the thickness of both the inner and outer edge shims affects primarily the sextupole moment. We found that a 100μm increase in the edge shim thickness in all four corners increases the sextupole moment by 10.8 *ppm*. Asymmetric thickness adjustment leaves the sextupole moment unchanged and allows fine tuning of the quadrupole and octupole moments. Increasing the outer edge shim thickness by 100μm while decreasing the inner edge shim thickness by the same amount increases the quadrupole and octupole moments by 13.2 *ppm* and 5.6 *ppm*, respectively. Although the simulation utilized vertical symmetry, this model can be extended to up-down and diagonal (skew) asymmetries.

We plan to use a similar shimming strategy in E989. We will order oversized edge shims, map the field, grind, and repeat. Based on the experience of E821 and the extensive OPERA simulations, we believe this phase of the shimming will require only two iterations.

Gap shims Azimuthally, significant variations in the magnetic field occur at the boundaries between adjacent pole pieces, as shown in figure 15.18. The effect is even more pronounced at the pole piece surface than in the storage region, jeopardizing the effectiveness of the fixed probes located near the inter pole piece gaps. In E989, we plan to reduce the azimuthal variations in the field by shimming the gaps with thin iron plates. The basic concept would be to span the surface of adjacent pole pieces with high quality steel plates varying from 10 to 100 μm. Simulations show that a local change of 10μm in the air gap between the pole pieces results in a 40 *ppm* shift in the dipole field. This should be a fairly short wavelength affect that will reduce the local field gradients and improve the performance of the fixed NMR probes mounted in the vacuum chambers.

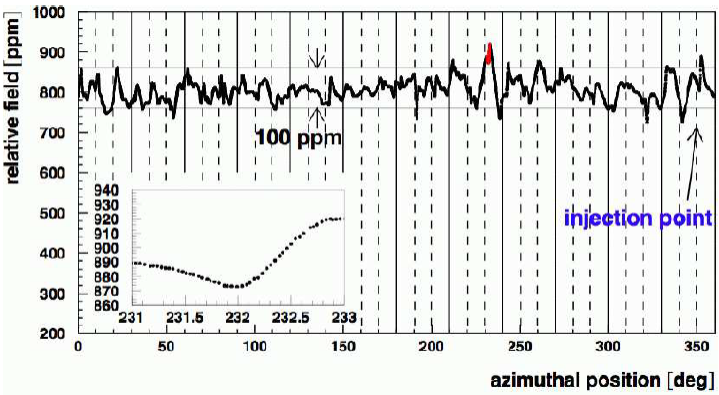

Figure 15.18: The magnetic field determined by the center NMR trolley probe versus azimuthal position in the storage ring during one trolley pass (reproduced from Ref [5]). The solid vertical lines denote boundaries between the 12 yoke sectors. The dashed vertical lines denote the pole piece boundaries.

Radial Field

An auxiliary measurement of the radial component of the magnetic field was performed during the passive shimming phase prior to the installation of the vacuum chambers. In the storage region, the direction of magnetic field is principally vertical. The presence of a radial field component has a significant impact on the muon storage beam dynamics, affecting both the mean vertical position and the vertical betatron oscillations. Quantitatively, the radial field component needs to be measured to ≈ 10 *ppm*. However, the NMR probes only measure the total magnitude of the magnetic field without providing information about the separate vertical and radial components. In E821 an auxiliary measurement using Hall probes was implemented to quantify the radial component of the field. We plan to reproduce this procedure.

Figure 15.19 shows a schematic representation of the setup used to measure the radial field. Two Hall probes (BH-206, F.W. Bell) were vertically aligned to measure the radial magnetic field, with the Hall currents running in the z and y directions. To ensure alignment of the setup with respect to the gravitational vertical direction, electrolytic tilt sensors (RG33A, Spectron Systems Technology, Inc.) were mounted to the support structure. Finally to account for potential misalignment of the Hall probes with respect to the support structure, the measurements were repeated after rotating the entire structure by 180° about the vertical axis and taking the difference of the Hall voltages.

Figure 15.20 shows the data from the Hall probes overlaid on the expected radial field as calculated from the multipole expansion of the absolute field measurement. The overall precision of the radial field measurement was significantly better than the required 10 ppm. Figure 15.21 shows the radial field measurement (dots) from the Hall probe as a function of the azimuthal position around the ring. The line in this plot represents the measured pole tilt derived from the capacitive sensor data described above. The tracking of these two curves demonstrates the qualitative dependence of the radial field on the pole alignment.

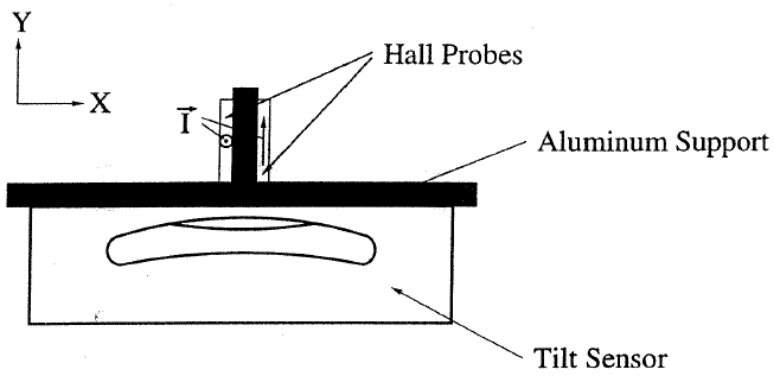

Figure 15.19: (a)A schematic representation of the radial field measurement configuration. Two Hall probes are mounted to measure the radial component of the field (x) with Hall currents oriented in the z and y directions. The rigid configuration is equipped with a tilt sensor. Rotating the entire setup 180° about the y-axis isolates the radial component.

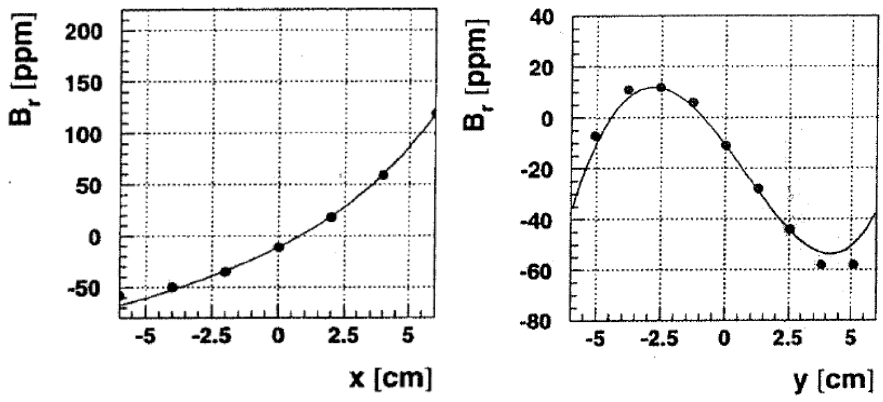

(a) (b)

Figure 15.20: Radial component of the magnetic field in ppm as a function of (a) radial position x and (b) vertical position y. The dots show the data from the Hall probe, while the solid lines represent the field variation expected from the multipole coefficients calculated from the absolute field measurement.

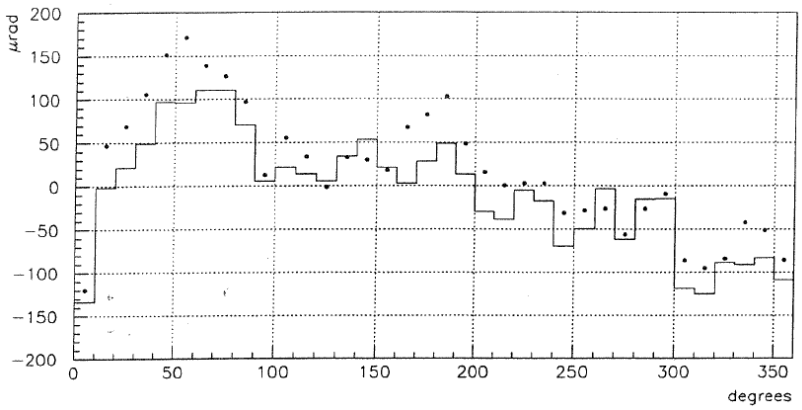

Figure 15.21: (a)The radial field measurement (dots) from the Hall probe and the average pole tilt (line) from the tilt sensor are shown as a function of the azimuthal position around the ring.

15.4.3 Active Shims

Active shimming refers to the adjustment of current distributions to eliminate any residual field non-uniformities that remain after the passive shimming is complete.

The principle active shimming controls consist of the following:

1. Control of the main superconductor current
2. Surface correction coils on printed circuit boards between the pole face and the vacuum chamber
3. Dipole correction loops in the gap between the wedge shim and the yoke
4. Gap correction loops in the azimuthal gaps between adjacent pole faces

Main Current

NOTE: DO WE WANT THIS TO BE IN THIS SECTION AT ALL? IT IS A DIPOLE SHIMMING PARAMETER IN A SENSE BUT IS PROBABLY BEST COVERED ELSEWHERE The central value of the dipole field is determined primarily by the current in the main superconducting coils. The nominal current is 5200 Amp per turn. OPERA simulations show that an increase of 1 A increases the field in the storage region by about XX *ppm*. During beam-on data collection periods, the field is monitored by the fixed NMR probes. The shape of the magnet gets distorted due to temperature variations, so a feedback loop is utilized to stable the dipole field.

Surface Correction coils

Correcting coils on the surface of the poles permit ultimate fine control of static, and slowly varying errors. The surface coils can be used to correct lowest multipoles to tens of ppm, thus

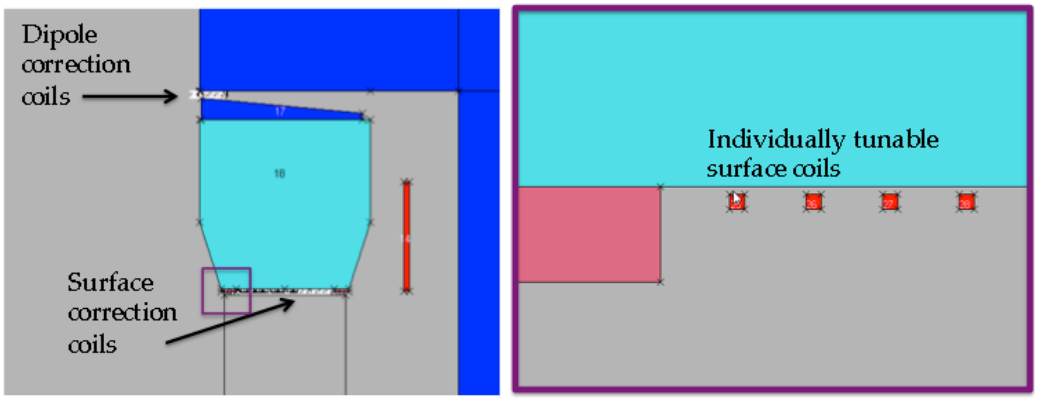

(a) (b)

Figure 15.22: An OPERA-2D depiction of the dipole correction coils and the surface correction coils. (a) Schematic overview showing the positions of the current traces on the printed circuit boards. The purple box is zoomed in and displayed in panel (b). Individual traces are adjusted to tune various multipole contributions.

providing significant overlap between the iron shimming and the dynamic shimming. These coils have been constructed to generate moments over the entire 360° azimuth. The coils were designed with printed circuit boards, with 120 wires running azimuthally around the ring on the top and bottom pole surfaces facing the storage ring gap, and spaced radially 2.5 mm apart, to avoid lumpy effects which generate higher multipoles. The boards must be thin enough to fit between the pole faces and the vacuum chamber. We have studied the surface correction coils in OPERA-2D (see Figure 15.22) and verified that the various multipole contributions can be compensated for with the appropriately applied current distributions. A summary of the principle current distributions is shown in Table 15.4.3. E821 used these coils successfully to shim out the final few ppm for the higher order multipoles.

Table 15.3: Current distributions needed to correct for various multipole components, and the maximum range that can be corrected with less than 1 Amp. The currents are calculated at the fixed vertical position of the boards (y=a=9 cm).

Multipole	K(x) (y =a)	Maximum range (ppm)
Quadrupole	a	20
Sextupole	$2ax$	10
Octupole	$3ax^2 - a^3$	8
Decupole	$4ax(x^2 - a^2)$	6
Duodecupole	$5a(x^4 - 2x^2a^2 + a^4/5)$	4
Quattuordecupole	$2ax(3x^4 - 10x^2a^2 + 3a^4)$	2

For E989, we plan to fabricate 12 new printed circuit boards at Fermilab that extend over each sector. Because these coils extend azimuthally around the entire ring, interconnects between adjacent boards must be designed. We will study the trace spacing and radial

range to ensure our solution provides fine enough tuning without drawing too much power. Currents are expected to be limited to about 1 Amp. Finally, we will explore the option of using the bottom of the boards for active current shims in the gaps between pole pieces.

Dipole correction loops

The "continuous" ring was built with 10° pole sections, 36 of which form an almost continuous ring. Dipole correction coils are located in the air gaps for each 10° pole, as depicted in Figure 15.22 (a). These coils are a pancake design with 50 turns of copper wire wound in a rectangular shape. The dipole correction coils will be capable of tuning each pole section independently. E821 used active NMR feedback loops to stabilize the field by adjust the main superconductor current. It is possible that the field could be stabled in each pole piece separately by using the local NMR feedback to adjust the dipole correction currents. This would be particularly useful if temperature gradients over the 14 m diameter ring lead to different field distortions in different locations.

Gap correction loops

We want to minimize the azimuthal variation of the magnetic field, as explained in Section 15.4.2. Thus, E989 will use OPERA-3D to study the possibility of adding small loops to the bottom of the surface correction coil boards at the azimuthal positions between adjacent poles. We would primarily have control over the dipole moment, with limited ability to modify the higher order multipoles.

15.4.4 E821 results

E821 successfully implemented many of the passive and active shimming techniques described above. Table 15.4.4 shows the historical progression of the uniformity of the field as a function of time during the commissioning phase of the experiment. As they worked towards the storage region, the higher order became more controlled. The final column shows the principle changes that were implemented at that step. We plan to use this experience to compress the shimming schedule for E989.

15.5 Alternatives

The determination a_μ in terms of $\omega_a/\tilde{\omega}_p$ and μ_μ/μ_P requires the storage ring magnetic field be measured in terms of the muon distribution weighted free proton precession frequency, $\tilde{\omega}_P$. In principle this could be done by injecting a 3.1 GeV/c polarized proton beam into the storage ring with a proton spin analyzer (polarimeter) in the ring based on the spin dependence of p-carbon elastic scattering. The anomalous precession frequency would be close to 40 MHz, and the phase space of the protons and muons would have to be matched or measured to mm precision. Proton beam measurements of the field distribution would have to alternate with muon injection. Developing a polarized proton source, 3.1 GeV/c accelerator, polarimeter, proton beam position monitoring hardware etc. would add significant cost and technical challenge to the experiment, and it's not clear that the field determination could be made

Table 15.4: If time permits, convert this to a plot that shows the evolution of these moments vs time. Quadrupole (Q), Sextupole (S), Octupole (O), and Decupole (D) multipoles, broken down into normal(n) and skew(s) components, in *ppm*, evaluated at the storage radius (r = 4.5 cm).

Date	Q_{n}	S_{n}	O_{n}	D_{n}	Q_{s}	S_{s}	O_{s}	D_{s}	Action
Jun 1996	-169.12	112.03	-34.16	23.71	27.06	5.82	3.12	0.46	Initial configuration
Nov 1996	5.52	3.19	-1.11	1.95	9.13	5.32	0.85	0.45	Edge shims ground uniformly
Jul 1997	5.26	2.94	-1.03	1.45	12.26	2.78	0.36	0.25	Edge shims ground in each pole piece+ pole alignment
Aug 1998	7.73	-5.29	-2.79	0.38	-2.07	-0.02	-0.25	0.71	Final passive shimming
Sep 1998	-2.54	-1.25	-2.70	0.34	-2.39	-0.18	-0.28	0.42	Active shimming commissioned
PRD	0.24	-0.53	-0.10	0.82	0.29	-1.06	-0.15	0.54	something

to 70 ppb. Further, during periods of muon injection, an NMR-based system of fixed probes outside the storage volume would still be required to monitor the field and provide feedback to the power supply to stabilize the field. A similar NMR system would be required to shim the magnet.

Other field measurement technologies such as Hall probes have been considered. One advantage is that a 3-axis device could make measurements of B_x, B_y, B_z. However, Hall probes have a significant temperature dependence ($\leq 20 ppm/^{\circ}\mathrm{C}$), resolutions at the 1 ppm level (versus 20 ppb for NMR), and fluctuating offsets. Commercial technology is currently inadequate for the level of accuracy sought in E989. Further, they would require frequent calibration in terms of an equivalent free proton precession frequency, so an NMR-based absolute calibration probe would still have to be developed and tested.

Finally we note that pulsed NMR is preferred over CW techniques since the latter typically requires a small field modulation coil that perturbs the local field, introduces image fields in the iron poles and yokes, and is potentially difficult to calibrate at the precision sought in E989. In addition, the lineshape analysis required in CW techniques to achieve ppb levels of precision is substantially more difficult than the analysis methods required for analyzing pulsed NMR FIDs.

15.6 ES&H

15.7 Quality Assurance

It is necessary to test the NMR hardware before shimming and installation in the g-2 storage ring. This requires the development of independent test-stands that include a set of NMR probes, NMR electronics, DAQ, and a magnet. We have located at least 4 magnets suitable for these purposes, where the requirements on the magnet depend on the hardware component being tested.

To test the fixed probes requires a vector impedance meter or network analyzer and a magnet at 1.45 T with field gradients less than 20 ppm/cm. The latter is sufficient to ensure an FID of ms duration, sufficient to confirm the probe works. An electromagnet suitable for testing fixed probes and basic functioning of the NMR hardware is being prepared spring 2013 at the University of Washington.

Precision tests of the NMR hardware - such as single shot frequency resolution, temperature dependence of NMR signals, reference frequency dependence of the electronics, aging effects, measurements of T_2, etc. require magnets with stability of 0.01-0.1 ppm per hour and field gradients of <0.2 ppm/cm. Such a magnet is available to the group at Univ. of Michigan (with access to a large bore persistent mode MRI magnet). The Univ. of Massachusetts group has unrestricted access for several years to a small bore (89 mm) peristent mode superconducting magnet from Cryomagnetics, with better than 0.01 ppm/hr stability and a shim set to achieve sub-ppm/cm homogeneity over an 8 cm^3 volume. The small bore cannot accomodate the E989 NMR probes (it can only accomodate the plunging probe), but many sensitive tests of the NMR electronics and behavior of the NMR probe samples (temperature effects etc.) can be measured at the 10 ppb level using custom probes.

Finally, we require a large bore superconducting persistent mode magnet at Fermilab for local tests of the hardware. The LANL Biological and Quantum Physics group agreed to transfer to FNAL the Oxford Magnet Technology Unistat 41443 MRI solenoid used by E1054 at Los Alamos. This solenoid has measured stability of better than 0.1 ppm/hour, a shim set for ppm-level homogeneity over a 10 cm diameter volume, and a 910 mm bore diameter, essential for extensive performance tests of the NMR trolley in advance of installation in the g-2 storage ring. This will also be essential for determining the magnet influence of the calorimeter and tracker hardware on the storage ring field. (Early tests of basic performance of the trolley will be made with a large gap electromagnet at BNL).

Extensive early testing of the NMR hardware should allow identification of problems and the implementation of solutions in advance of installation in the g-2 ring. By having several absolute calibration probes, repeated calibration of the trolley probes, and extensive investigations of potential systematics, we intend to produce a robust result on ω_p.

15.8 Value Management

References

[1] P. J. Mohr, B. N. Taylor, and D. B. Newell, Rev. Mod. Phys. **84**(4), 1527 (2012).

[2] W. Liu *et al.*, Phys. Rev. Lett. **82**, 711 (1999).

[3] R. Prigl, *et al.*, Nucl. Inst. Methods Phys. Res. **A374** 118 (1996).

[4] X. Fei, V. Hughes and R. Prigl, Nucl. Inst. Methods Phys. Res. **A394**, 349 (1997).

[5] G. Bennett, *et al.*, (Muon $(g-2)$ Collaboration), Phys. Rev. **D73**, 072003 (2006).

[6] Ralf Prigl, doctoral thesis, Universität Heidelberg (1994)

[7] Alex Grossmann, doctoral thesis, Universität Heidelberg (1998)

[8] Huaizhang Deng, doctoral thesis, Yale University (2002)

[9] LORAN-C User Handbook, OMDTPUB P16562.6, available at http://www.navcen.uscg.gov/loran/handbook/h-book.htm

[10] see A. Abragam, "Principles of Nuclear Magnetism", Oxford U. Press, (1961), pps. 173-178.

[11] W.D. Phillips *et al.*, Metrologia **13**, 179 (1977).

[12] B.W. Petley *et al.*, Metrologia **20**, 81 (1984).

[13] J.L. Flowers *et al.*, Metrologia **30**, 75 (1993).

[14] P.J. Mohr and B.H. Taylor, Rev. Mod. Phys. **77**, 1 (2005).

[15] P.F. Winkler, D. Kleppner, T. Myint, and F.G. Walther, Phys. Rev. **A5**, 83 (1972).

[16] W.E. Lamb Jr., Phys. Rev. **60**, 817 (1941).

[17] H. Grotch and R.A. Hegstrom, Phys. Rev. **A4**, 59 (1971).

[18] B.W. Petley *et al.*, Metrologia **20**, 81 (1984).

[19] W. Liu et. al., Phys. Rev. Lett. **82**, 711 (1999); D.E. Groom, et al, (Particle Data Group), Eur. Phys. J. **C15**, 1 (2000).

[20] G.T. Danby and J.W. Jackson, E821 Muon $g-2$ Internal Note No.1, 1(1987).

[21] K. Woodle, E821 Muon $g-2$ Internal Note No.44, 1(1990).

[22] S. Redin, E821 Muon $g-2$ Internal Note No.51, 1(1990).

[23] X. Fei and V.W. Hughes, E821 Muon $g-2$ Internal Note No. 86 (R), 1(1991).

[24] M.J. Fischer, E821 Muon $g-2$ Internal Note No. 114, 1(1992).

[25] G.T. Danby and J.W. Jackson, E821 Muon $g-2$ Internal Note No.180, 1(1993).

[26] R. Prigl, Internal Note.

[27] Yu. I. Neronov, A.E. Barzakh, Sov. Phys. JETP, 769-778 (1978); R. V. Reid, Phys. Rev. A, **11**, 403 (1975).

[28] M. A. Bouchiat, T. R. Carver, and C. M. Varnum, Phys. Rev. Lett. **5**, 373 (1960).

[29] T.E. Chupp, K.P. Coulter, Phys. Rev. Lett. **55**, 1074 (1985); M. E. Wagshul and T. E. Chupp, Phys. Rev. A **40**, 4447 (1989).

[30] F.D. Colgrove, L.D. Schaerer, G.K. Walters, Phys. Rev. **8** 439 (1962).

[31] ENS MEOP

[32] M. S. Rosen, T. E. Chupp, K. P. Coulter, R. C. Welsh, S. Swanson, Rev. Sci. Instrum. **70**, 1546 (1999).

[33] S.R. Nuss-Warren et al., Nucl. Inst. Meth. A **533**, 275 (2004).

[34] S. D. Swanson, M. S. Rosen, B. W. Agranoff, K. P. Coulter, R. C. Welsh, T. E. Chupp, Magn. Reson. Med. **38**, 695 (1997).

[35] M. Abboud, A. Sinatra, X. Maitre, G. Tastevin, P.-J. Nacher, Europhys. Lett., **68**, 480 (2004).

[36] M. Abboud, PhD thesis, "Pompage optique de lhlium-3 forte pression dans un champ magntique de 1.5 Tesla" University of Paris VI (2005).

[37] G.T. Danby *et al.*, Nucl. Inst. Meth. A **457**, 151 (2001).

Chapter 16

The ω_a Measurement

The anomalous spin precession frequency ω_a is one of the two observables required to obtain the muon anomalous magnetic moment, a_μ. In order to reach the experiment's proposed goal of 0.14 ppm precision in a_μ, the targeted error budget allows for a 0.1 ppm statistical uncertainty combined with equal 0.07 ppm systematic uncertainties from the ω_a and ω_p analyses. This chapter summarizes the procedure for the ω_a measurement, with subsequent Chapters 17-22 elaborating upon the design of each subsystem. First the decay kinematics are reviewed and the encoding of the muon spin information into the data set is explained (Section 16.1). From that basis several complementary methods are explained (16.1.2). Then a review of uncertainties is presented, first the statistical (Section 16.2) and then the systematic uncertainties intrinsic to the detector (Section 16.3). Finally the detector system organization is explained and broken down into subsystems (Section 16.4). These subsystems include: stored muon monitoring, electron decay tracking, electron calorimeter, signal digitization, data acquisition, and slow control systems.

16.1 Measurement Overview

The anomalous precession frequency, ω_a, is the difference between the ensemble-averaged muon spin precession and the cyclotron frequency. The weak decay of the muon is parity violating, with the consequence that the emitted electron energy is correlated—on average—with the muon spin direction[1]. Therefore by measuring the decay electrons and analyzing their energy a measurement of the muon spin is possible. The angle between the boost from the muon center-of-mass frame (CM) to the lab frame and the muon spin acts as an analyzer. As the spin rotates relative to the boost direction the rate observed modulates at the frequency ω_a. That modulation is observed over several boosted muon lifetimes and fit to extract ω_a.

16.1.1 Muon Decay and Boost Kinematics

The angular distribution of emitted electrons from an ensemble of polarized muons at rest is

[1] The discussion which follows is extracted in part from Ref. [1].

$$dn/d\Omega = 1 - a(E)\left(\hat{S}_\mu \cdot \hat{P}_e\right). \tag{16.1}$$

Where $\hat{S}_\mu$ is the muon spin direction and $\hat{P}_e$ is the electron momentum direction. The asymmetry a depends on electron energy (E) and is such that the higher-energy electrons have the strongest correlation to the muon spin.

The decay electron energies in the laboratory frame are related to the CM energy by

$$E_{e,lab} = \gamma(E_e^* + \beta P_e^* \cos\theta^*) \approx \gamma E_e^*(1 + \cos\theta^*). \tag{16.2}$$

The starred quantities indicate CM frame, $\gamma = 29.3$, and θ^* is the angle between the rest frame electron momentum and the boost direction. The maximum energy in the lab frame occurs when the electron momentum is aligned with the boost direction and the decay energy is the maximum. Therefore by applying a threshold to lab frame electron energy only the highest energy muon rest frame decay electrons are observed. Thus capturing the important relationship that the electron *energy* in the lab frame is correlated to the emitted *angle* and therefore muon spin in the CM frame.

16.1.2 Analysis Methods Summary

The simplest analysis procedure is to identify individual decay electrons and plot the rate of their arrival versus time using only events having a measured energy above a threshold. This is dubbed the T (time) method; it was the dominant analysis technique used in the Brookhaven experiment and it is fairly robust against systematic uncertainties.

The rate of detected electrons above a single energy threshold E_{th} is

$$\frac{dN(t; E_{th})}{dt} = N_0 e^{-t/\gamma\tau_\mu}\left[1 + A\cos(\omega_a t + \phi)\right]. \tag{16.3}$$

Here the normalization, N_0, asymmetry, A, and initial phase, ϕ, are all dependent on the threshold energy. The time spectrum of detected electrons from a portion of the data from Brookhaven E821 is shown in Figure 16.1. This is the type of distribution from which the anomalous precession frequency will be extracted.

While the T Method is sufficient to reach the experimental goal, additional analysis techniques can also be used. Weighting the events by their average asymmetry or by their energy increases the statistical power for the same data set as the cost of more stringent systematic requirements. As in the T method, the data stream from the calorimeters must be first deconstructed into individual events, which are then processed into histograms akin to what was shown in Figure 16.1. The uncertainties here are largely based on the stability of the deconstruction process vs. time in the storage ring fill.

There is an additional experimental method that involves identical hardware to the T Method but a different data acquisition philosophy. The Q method, does not require event by event reconstruction. Instead simply integrates the detector current (energy for a linear device) vs. time in fill.

- ***T* Method:** Events are individually identified and sorted. The events vs. Time-in-Fill histogram is built from all events with reconstructed energy about a threshold. All

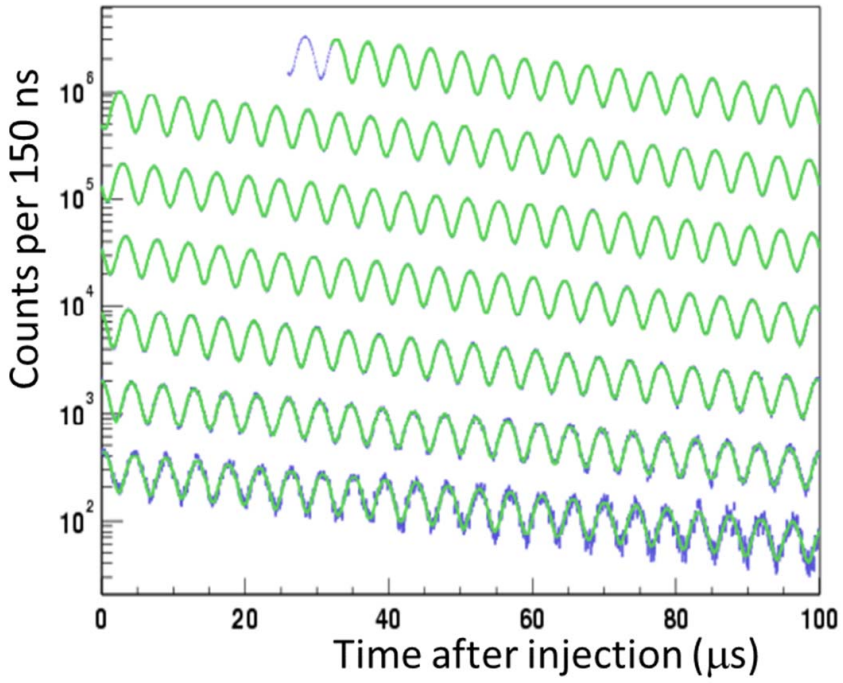

Figure 16.1: Example precession frequency data (blue) and fit (green) from Brookhaven E821. The calorimeter data must be analyzed to determine the energy and time for each event. The plotted time is modulo 100 μs.

events in the histogram are given equal weight. The acceptance-modified figure-of-merit (FOM, defined to be equal to 1.0 here) is optimized at $y \approx 0.6$, corresponding to an electron energy of 1.8 GeV. The quantity ω_a is obtained from a fit to a pileup-subtracted histogram. This is the standard method used in E821 and the benchmark for determining the statistical and systematic requirements for the E989 experiment.

- ***E*-Weighted Method:** Identical to the T method except that the histogram is built by incrementing a time bin with the value of the energy of an event, not by each count, therefore producing the Energy vs. Time-in-Fill histogram. The bin weight in the fit varies over one full $g-2$ cycle and it can be determined reliably by an analysis of late-time events that are not plagued by pileup effects. The FOM maximum is realized at a slightly lower threshold than the T Method. This method will be more vulnerable to gain- or energy-scale variations compared to the T method.

- ***A*-Weighted Method:** Identical to the T method except that the histogram is built by incrementing a time bin with the value of the asymmetry for that electron energy. The weight for each bin must be determined separately. This is potentially a powerful method, but the systematics are unknown. Further study is warranted.

- ***Q* Method:** Events are *not* individually identified. Energy vs. Time-in-Fill histograms are built by summing the energy of a all digitized waveform samples vs. time for a

calorimeter station. The application of appropriate zero-suppression will have to be introduced to minimized the noise contribution. No attempt to correct for pileup is necessary in the fit; only a low-threshold makes sense here. The acceptance-corrected FOM is nearly identical to the standard T method.

16.2 Statistical Uncertainty

The T, energy-weighted, asymmetry-weighted, and Q methods of analysis all lead to histograms similar to what is shown in Figure 16.1, albeit with different bin weights and asymmetries. A fit is then performed using Equation 16.3 and the relevant parameter ω_a is obtained. The optimization of the experimental system follows from minimizing the uncertainty on that parameter, namely $\delta\omega_a$. A detailed study of the statistical methods used in the E821 experiment that gives guidance to the statistical power of any data set built using various weighting methods was published in Ref. [2]. That publication parameterizes the uncertainty on ω_a as

$$\delta\omega_a = \sqrt{\frac{2}{N(\gamma\tau_\mu)^2} \cdot \frac{\langle p^2\rangle_y}{\langle pA\rangle_y^2}}, \tag{16.4}$$

where N is the integrated number of decay electrons in the analysis, p is the weight function and therefore is method dependant, and $\langle f\rangle_y$ is the value of f averaged over all detected electron energies above threshold. The parameter y is the fractional decay electron energy with respect to a maximum value; therefore y ranges from 0 to 1, where $y = 1$ corresponding to approximately 3.1 GeV.

In the following, care must be paid to whether distributions shown vs. y are differential or whether they represent the integrated value from threshold y. For example, Fig. 16.2 shows *differential* plots of N, A and NA^2 vs. energy for a uniform acceptance detector. The plots illustrate the importance of the higher-energy electrons that have the greatest asymmetry. he asymmetry is negative for lower-energy electrons; thus, a single low threshold can be expected to dilute the average asymmetry. If, on the other hand, data are sorted by energy bin and then fit (using possible weighting schemes by energy or asymmetry), the overall statistical power of the data set can be improved. Importantly, the modification of the ideal curves owing to finite detector acceptance is non-negligible as the detector placement greatly favors the higher-energy events because low energy electrons can curl between detectors and be missed. The acceptance impacts the values of N and A, which are functions of the energy-dependent detector acceptance, and modified significantly the idealized curves of Fig. 16.2. In the T method each event carries the same weight ($p = 1$) and the uncertainty $\delta\omega_a$ following Eq. 16.4 reduces to

$$\delta\omega_a = \frac{1}{\gamma\tau_\mu}\sqrt{\frac{2}{NA^2}}. \tag{16.5}$$

The boost factor $\gamma = 29.3$ is fixed by the magic momentum requirement. The figure of merit (FOM) that should be maximized to minimize $\delta\omega_a$ is NA^2. The value of the threshold that maximizes the FOM corresponds to $A \approx 0.4$ and an energy of 1.8 GeV. Therefore the

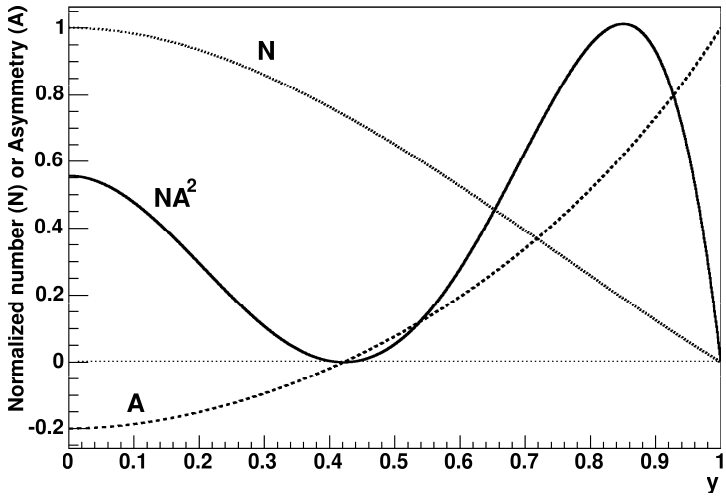

Figure 16.2: The differential distributions: normalized number of events (N/N_{total}), asymmetry (A), and the figure of merit (NA^2). Note, this plot assumes uniform detector acceptance across the full energy spectrum.

relative uncertainty in ω_a is

$$\frac{\delta\omega_a}{\omega_a} = \frac{1}{\omega_a} \cdot \frac{\sqrt{2}}{\gamma\tau_\mu A} \cdot \frac{1}{\sqrt{N}} \approx \frac{0.0385}{\sqrt{N}}. \tag{16.6}$$

For a statistical uncertainty on $\delta\omega_a/\omega_a$ of 0.10 ppm, $N = 1.5 \cdot 10^{11}$ fitted events would be required, stemming from a 100% polarized stored muon beam.

For the energy-weighted ($p = y$) and asymmetry-weighted ($p = A(y)$) analysis methods the computation of $\langle p^2\rangle_y/\langle pA\rangle_y^2$ in Eq. 16.4 is non-trivial. Figure 16.3 (left panel) shows the figure of merit for different analysis technique assuming a uniform detector acceptance [2]. The gain from performing a weighted analysis is potentially as high as 10% for the energy-weighted and 20% for asymmetry-weighted analyses. We conducted a simulation that included the finite detector acceptance to determine the FOM for the T and energy-weighted techniques. The right panel of Fig. 16.3 is to be compared to the uniform acceptance case. Notice that the FOM for the energy method does not fall as fast at low threshold because the detector preferentially selects events having higher energy.

A tacit assumption in the methods described is that each event can be treated as if it is identified accurately for energy and time of arrival at the detector. The events are then sorted and placed into histograms with appropriate weights. When the rate is high events can overlap in time and space such that some fraction of them cannot be resolved into individual occurrences. High-rate, asymmetry-based experiments (e.g, parity-violating electron scattering) encounter this problem regularly and solve it by simply integrating the current on a detector as a function of time (or beam burst). Here, the same concept can be employed. By integrating the light yield from the calorimeters as a function of time, one obtains an unresolved "energy" method, or charge method, we call Q. The method makes no effort to record anything other than a histogram of energy in the detector vs. time. As shown in Fig. 16.3, this corresponds to the "weighted method" plotted for the

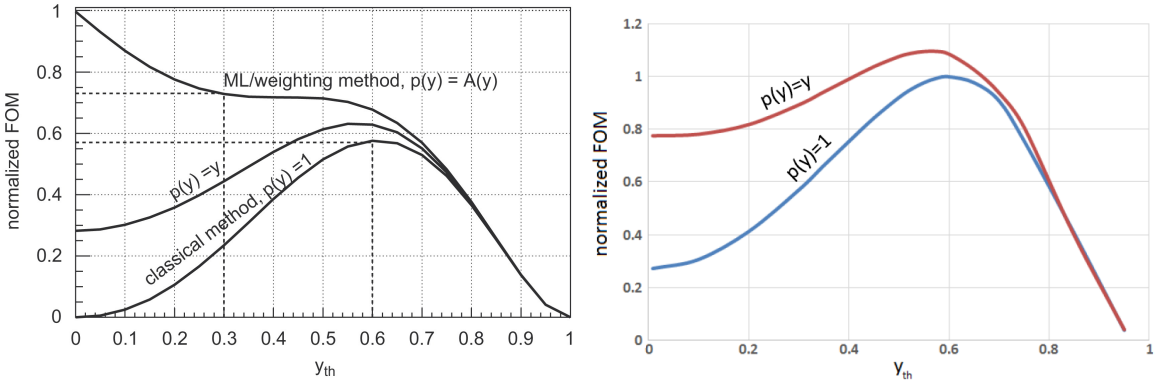

Figure 16.3: Left: Figure of merit as a function of energy threshold. These curves were calculated analytically [2] with uniform acceptance in energy space assumed. What is labeled "classical" method is the T method; the $p(y) = y$ is the energy-weighted method, and the $p(y) = A(y)$ is the asymmetry method. The right hand panel shows the T and energy-weighted distributions produced as the output of a detailed analysis using simulated data and finite detector acceptance. Of particular interest is the low-threshold behavior of the energy-weighted method, which remains high in the real model.

finite acceptance simulation with a threshold approaching $y = 0$. The method provides a statistical power approximately equivalent to the T method and it does not involve pileup subtraction. We have studied this method using Monte Carlo simulations to determine the proper weighting to place on the bins in the fit; they vary over the $g-2$ cycle, but can be easily determined using a sample of late-time data that can be evaluated using individual events to build a pseudo-Q-method histogram in the absence of pileup. We plan to incorporate this alternative data-taking and analysis method in the new experiment. Figure 16.4 shows a fit to Monte Carlo data generated with the full ring simulation in terms of muon spin and time dependence and the finite acceptance of the detectors. Here, the beam polarization is assumed to be unity and an event is accepted at its defined energy if the the electron hit anywhere on the front face of the calorimeters. The ω_a value represented by R is 116 in the truth and the units of R are ppm. Both T and Q methods give similar statistical precision.

It was not possible in E821 owing to the high energy threshold and lack of memory in the digitizers. These technical limitations are easily overcome with today's large memories in such devices). We are also actively exploring the types of systematic uncertainties associated with the Q method. Note that the data sets in the T and Q method are not identical, but substantial overlap exists. For example, in the T method, all events below $\sim$ 1.8 GeV do not contribute and all events above are weighted with $p = 1$. The Q includes all events that strike the detector and weights each by its energy, $p = y$. Therefore, a combination of the results of the two methods will enable an overall reduction in the final uncertainty of ω_a; but more importantly, the two methods will serve as important cross checks that systematics are under control.

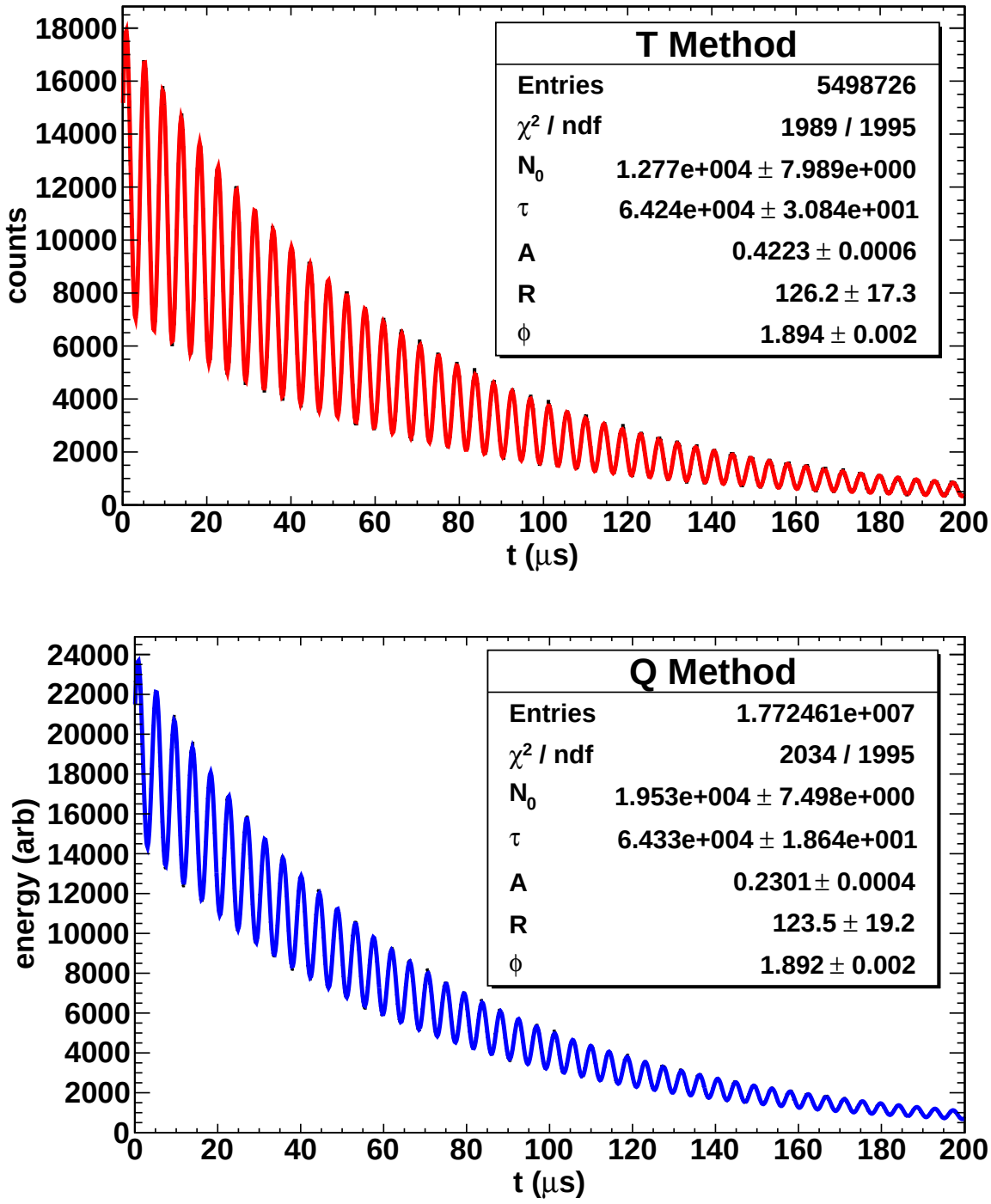

Figure 16.4: Top: Monte Carlo data analyzed using the T method with a threshold cut at $y = 0.6$. Bottom: Same data analyzed using the Q method. Detector acceptance is included. The asymmetry A is much higher for the T method, however the Q method has many more events (N). The ω_a central value is listed as R in the fit table with $R = 116$ in ppm the truth. Both methods give similar statistical uncertainty.

Table 16.1: Detector-specific systematic uncertainties in E821 and proposed upgrade actions and projected future uncertainties for E989.

E821 Error	Size [ppm]	Plan for the New $g-2$ Experiment	Goal [ppm]
Gain changes	0.12	Better laser calibration; low-energy threshold; temperature stability; segmentation to lower rates	0.02
Pileup	0.08	Low-energy samples recorded; calorimeter segmentation; Cherenkov; improved analysis techniques	0.04

16.3 Detector-related Systematic Uncertainties

In this section we discuss the systematic error issues related to the Detectors, Electronics, DAQ and the Offline Analysis. Table 16.1 lists the Gain and Pileup uncertainties and projections for improvements in the new $g-2$ experiment. The traditional T method analysis is assumed because uncertainties can be reliably projected based on our considerable experience in these analysis efforts. Since the Q method is new, we have not included its positive and partially independent impact on the final statistical result, nor are we presently able to fully project associated systematics. This topic is an active study in the collaboration. One key attractive feature of the Q method is pileup immunity; there is no correction necessary so that systematic uncertainty is absent. Comparing the analysis results using both T and Q methods will provide a valuable confirmation that systematic errors are understood.

16.3.1 Gain Changes and Energy-Scale Stability

The hardware gains of the E821 detectors [3] were determined to be stable to $\approx$0.15% from early-to-late times within a storage ring fill. This limit was established by plotting the average energy for each $(g-2)$ period versus time after the PMTs were switched on. The gating circuitry in the tube base that allowed the PMTs to be turned off to avoid the initial burst of pions entering the ring, also resulted in a small variation in the gain. For gain variations like this one, where the time constant is long compared to the $(g-2)$ oscillation period, the coupling to the ω_a frequency is small and, after correction, the residual systematic error is less than 0.02 ppm.

Several aspects of the current plan will be different. The first is that we will use silicon photo-multipliers (SiPMs), which can be saturated from a light burst and then recover with the same time constant as they might do for a low-light pulse. Each pixel is "on" or "off" and recovers with a common time constant. Importantly, we do not intend to switch off these devices during injection because the anticipated hadronic-based flash will be (largely) absent. The initial pion flux at the target location will be reduced the factor $\exp(-x/173)$, where 173 m is the pion decay length for 3.1 GeV/c. The path from target to storage ring, including 4 trips around the muon Delivery Ring (DR) is approximately 2000 m; thus primary pions are reduced by a factor of 10^5. Essentially no pions will enter the ring. Similarly, beam protons[2]—which travel slower than pions at the magic momentum— will be eliminated in

[2]positive beam will run first and protons out of the target are a large component of the beam guided by

the DR using a kicker system timed to fire when the muon and proton bunches are well separated in space.

If the gain oscillates at a frequency ω_a, with an amplitude that varies in time, and with a phase that differs from that of the ω_a oscillation of the electron sample, then a direct error on the measured value of ω_a is produced. The average rate at which energy is deposited into the calorimeters oscillates with frequency ω_a, and therefore any rate dependence in the gain of the detectors produces gain oscillations. We were able to demonstrate that the gain dependence on rate was small enough that its effect on ω_a was typically less than 0.03 ppm. In the new experiment, the slightly increased beam rates will be offset by increased detector segmentation and our proposed monitoring system will be greatly improved compared to that employed in the past.

In E821, a UV-laser system was used to periodically pulse the scintillator in the detectors and thus monitor the complete gain and reconstruction chain during data collection against an out-of-beam reference counter. Unfortunately, the light distribution system included too many branches and only one upstream reference detector. Small fluctuations cascaded so that gain stability could be monitored to no better than a few tenths of a percent. The system being designed for E989 is based on the experience with cascaded systems having multiple monitors. This is described in Chapter 17, Section 17.2.4.

The largest contribution to the gain systematic error in E821 came from artificial gain oscillations at the ω_a frequency, introduced by the data reconstruction software. Here, the "energy-scale" stability is related to software reconstruction of waveforms, not to the hardware. When a signal was above the waveform digitizer (WFD) hardware threshold, a pre-set minimum number of sequential samples was recorded. These data were fit offline for the peak plus linear background to deduce the energy and time of the electron. But, if the trigger pulse was followed or preceded closely by another pulse, both pulses were fit together with a common background term, and the fitting region becomes longer compared to that used for a single pulse. The fitted energy was found to depend slightly on the length of the fitting region and the fitting samples were fixed in number by hardware. Because the data rate oscillates at frequency ω_a, and is higher at early than at late decay times, it follows that the fitting region length oscillates at ω_a and is, on average, longer at early times compared to late times. This produces a small, effective gain oscillation with frequency ω_a whose amplitude decreases with time, leading to a systematic error on ω_a. Given the current capabilities in data throughput, the new electronics will record all samples in place of isolated islands, thus removing the source of this reconstruction bias. In summary, the larger of the gain systematic pieces will be eliminated by design and the smaller contribution will be monitored more precisely.

16.3.2 Pileup

The unresolved pileup fraction scales linearly with rate in each segment of the detectors. The effective size of the segment depends on the geometric extent of the shower. Our simulations demonstrate that an array of PbF_2 crystals, having 54 independent segments (see Chapter 17), and a smaller Molière radius compared to the Pb/SciFi used in E821, will

the FODO channel and into the DR.

provide an effective three-fold reduction in the intrinsic pileup based on the implementation of a very simple and robust shower separation routine and a 9-element cluster algorithm. The simulation includes a representative stored muon ensemble in the ring and correct spin physics in precession and decay.

While the final stored muon rate increase will depend on the actual implementation of several options discussed in earlier chapters on the Beam and Ring, we work here with the expectation of a 50% increase compared to E821 and design for a range of up to a factor of 3 higher. We will use a factor of 3 below as it represents an upper limit of what might be expected.

With a 3-fold rate increase compared to BNL, the intrinsic pileup rate for the same two-pulse resolution time resolution of 5 ns is expected to be largely the same as in E821., owing to the segmentation. What can be improved is the uncertainty associated with the correction for unresolved pileup. We will characterize the two-pulse resolution by an applied artificial deadtime (ADT). The ADT is the time established in the analysis software below which two pulses are not resolved (even if they can be). The analysis proceed by sorting data using a series of ADT values beginning with the true, device-specific minimum, and extending to much larger values that exaggerate the pileup. The extraction of ω_a is then done for each data set, and ω_a will be plotted as a function of ADT. The true value occurs at the zero-ADT extrapolation point. We have spent considerable laboratory bench time and offline pulse-reconstruction efforts to determine and optimize the minimum hardware ADT that our detectors will permit. Our laboratory tests demonstrate that pulses separated by 5 ns or more can easily be resolved for most pulse-amplitude ratios expected. We have even demonstrated resolved pulses with Δt between them as low as 2.5 ns. On the analysis procedure side, we have carried out a precision muon lifetime analysis with a pileup correction algorithm based on this ADT extrapolation concept. The work is well documented [4].

In the past, an artificial pileup spectrum was constructed from individual pulses in the data, then subtracted from the raw spectrum. In the pileup construction, it is necessary to use pulses with pulse heights below as well as above the hardware threshold. Because of the relatively high hardware threshold and limited storage of the E821 WFD system, those pulses below threshold were only found by searching during the relatively short period of continuous WFD digitization following the trigger generated by the presence of a large pulse above threshold. Consequently, the sample size for pileup events was limited and somewhat biased, since they had to always ride on the tails of larger pulses. In the new scheme, described in the following Chapters on Electronics and Data Acquisition, it will be possible to significantly improve the pileup construction process. Continuous digitization, with local software sorting of data streams including T-method, Pileup T-method and Q-method datasets, is anticipated. Pulses of all heights can be searched for, independent of whether there is a nearby large pulse that fired a hardware trigger.

The contribution of pileup to the error in ω_a for E821 was divided into three components. The first two are correlated and add linearly. The third is not correlated so it is added in quadrature to the other two.

1. Pileup efficiency, 0.036 ppm. This is due to an estimated 8% uncertainty in the amplitude of the constructed pileup spectrum.

2. Pileup phase, 0.038 ppm. This is the error due to the uncertainty in the phase of the

constructed pileup spectrum.

3. Unseen pileup, 0.026 ppm. This is the error due to pulses so small that they cannot be reconstructed and therefore they are not included in the pileup construction.

We expect that the segmented detectors, better laser calibration, more complete waveform record storage, and the use of our more modern extrapolation algorithms will lead to a comprehensive pileup correction with minimal uncertainty. We assign up to 0.04 ppm here to account for any difficulties in the anticipated analysis. As mentioned earlier, the Q method is complementary to the traditional T method and has different sources of systematic errors. The most significant difference is the effect of pileup—it will be greatly reduced for the Q method.

16.4 Detector Systems Overview

Three principle detector systems are central to the ω_a measurement: Calorimeter, Electronics, Data Acquisition. They each have their own chapter in this report. The Tracker System and Auxiliary detectors contribute to systematic uncertainty determintion. Figure 16.5 illustrates the various subsystems within the direct ω_a measurement framework, organized to illustrate how we define our work plans and distributed effort.

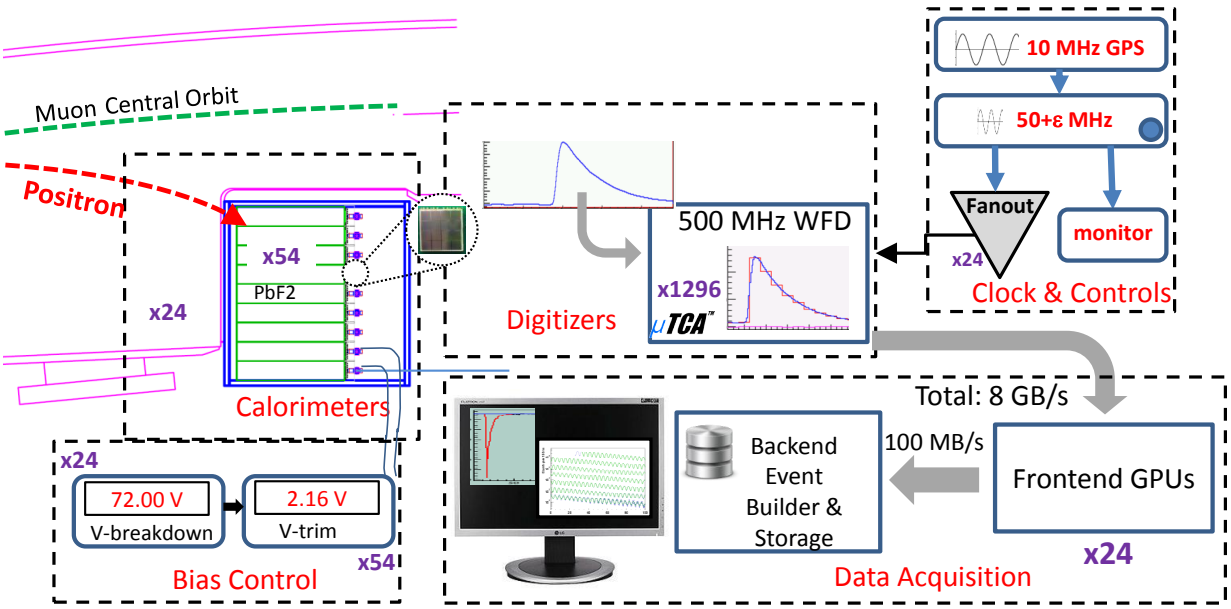

Figure 16.5: Schematic of the ω_a instrumentation organized by dedicated systems.

16.4.1 Calorimeter Subsystem Considerations

The decay electrons have momenta below the muon storage momentum and therefore they curl to the inside of the ring through the opening in the C-shaped magnet. Electromagnetic

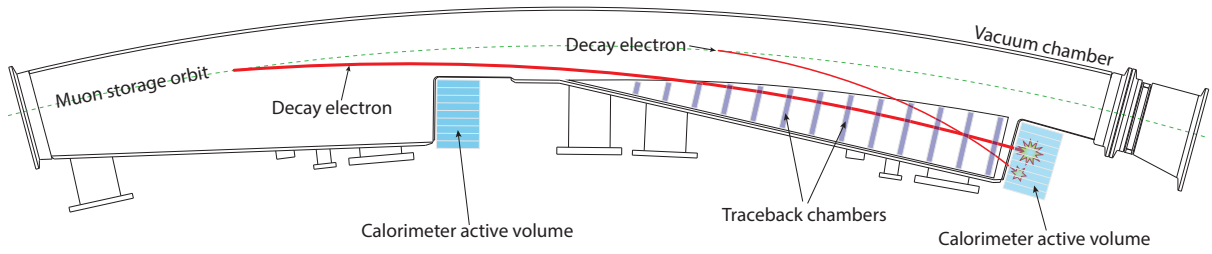

Figure 16.6: Scalloped vacuum chamber with positions of calorimeters indicated. A high- (low-) energy decay electron trajectory is shown by the thick (thin) red line, which impinges on the front face of the calorimeter array.

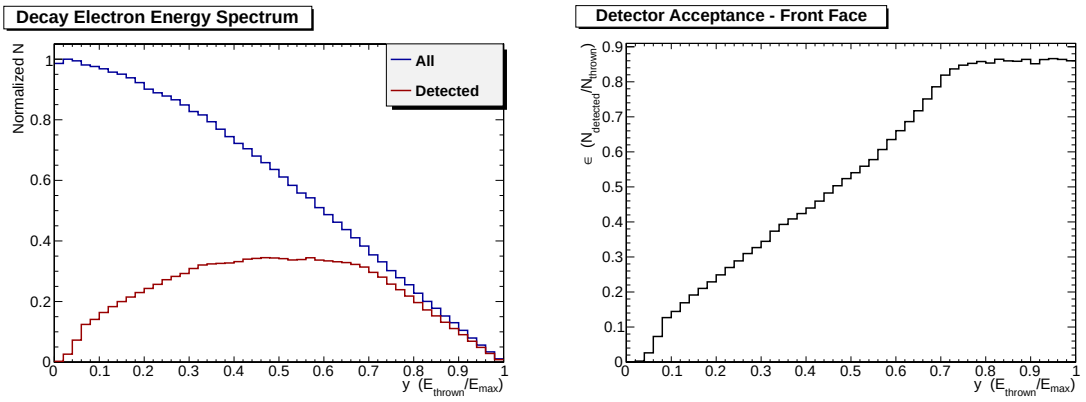

Figure 16.7: Left panel: Number of decay events vs. y in the laboratory frame (upper curve) and those that intercept the front face of a calorimeter (lower curve). Simulation uses full geometry, including pre-showering effects. Right panel: The differential acceptance of the 24 calorimeters vs. energy (the ratio of the two curves in the left panel). This is the fractional acceptance of events that hit the front face of the calorimeter array only.

calorimeters are used to intercept the electrons and provide a measurement of energy and time of detection. The time of flight is different depending on their energy, see Fig.16.6.

The calorimeters will be placed adjacent to the storage ring vacuum chambers, and located at 15 degree intervals around the ring. The 24 stations and their locations are constrained by the plan to reuse the E821 vacuum chambers, see Fig. 16.6. These parameters were optimized in a study preceding E821 construction and the conclusions remain valid for E989.

The number of emitted decay electrons vs. fractional energy is shown in the left panel of Fig. 16.7. The upper curve is all decay electrons. The lower curve are only the electrons that that strike the front face of one of the calorimeters. The right panel shows the ratio of detected to thrown electrons vs. fractional energy. The geometry is designed to favor the high-energy electrons that carry the maximum spin correlation information. Low-energy electrons will often curl in between calorimeter stations and be lost. The design of the new calorimeters is constrained by the unusual experimental demands. It is important to emphasize that the relevant time scale for most systematic uncertainties is one 700 μs long

measuring period. The instantaneous event rate of several MHz drops by almost five orders of magnitude during the 700 μs measuring period; thus, any rate-dependent detector or readout response changes must be accurately known. The overall measurement system must be extraordinarily stable for each short-term storage ring fill; however, long time scale drifts can generally be tolerated. As an example, consider a gain function G that varies from the beginning of a fill to the end of a fill; that is, $G \rightarrow G(t)$. When coupled to a fixed energy threshold, the population of accepted events will then vary throughout the fill. Because the asymmetry A and phase ϕ are functions of energy, the extracted ω_a will vary throughout the fill. If this occurs systematically during each fill (as it might if the gain change is coupled to rate), and is unaccounted for, then ω_a might be incorrectly determined. Similarly, a time shift Δt owing to the clocking system or other influence can also change the fitted frequency. Our experience in E821 established that the stability conditions that ensure less than a 0.05 ppm shift to ω_a can be characterized by the requirement that $\Delta G < 0.1\%$ and $\Delta t < 10$ ps over a 200 μs interval.

Two low-energy electrons, arriving close together in time, can be interpreted as one equivalent high-energy electron, a type of "pileup" event. Because the low-energy electrons have a shorter flight path to the detector compared to higher-energy electrons, they correspond to muons having a slightly greater muon phase advance. Therefore, if such incorrect interpretations of high-energy electrons are made more often early vs. late in a storage ring fill, the ensemble average phase will shift, which is equivalent in the fit to a shift in ω_a. Unaccounted for, pileup will produce this effect, since the rate of fake high-energy electrons coming from coincident low-energy electrons has a $\sim e^{-2t/\gamma\tau}$ time dependence. This means the pileup rate falls twice as fast as the muon population decays. To minimize pileup, the calorimeter response must be fast (few ns) and the readout system must record information to enable the distinction between closely occurring pulse pairs, which strike the same detector elements. This information should also provide a mechanism to correct the data, on average, by removing the pileup events. Furthermore, if the detector segmentation is optimized, many simultaneous lower-energy electrons will be recorded in independent area of a calorimeter station and thus will not be interpreted as a pileup event. The goal in the detector design is to reliably resolve same-element pulses separated by 5 ns or more, to segment the detector to minimize pileup, and to accurately subtract unresolved pileup.

The calorimeter resolution must be moderately good near 1.8 GeV to provide adequate energy discrimination. However, it also must be compact to avoid a preponderance of electrons that strike the inside face of the detector. Usually higher density materials imply lower resolution, so an optimization must be made. For E989, we are aiming for improved resolution compared to E821 at BNL by a factor of 2. This will aid in the pileup analysis, but is not particularly critical to the simple T method threshold analysis in the absence of pileup.

16.4.2 Electronics and Data Acquisition Subsystems Considerations

To guarantee deadtime-free calorimetry readout, the signal from each of the 1296 active calorimeter channels will be continuously digitized for every 700 μs muon fill. Those wave-

forms are then transferred to the DAQ system for data reduction – isolation of the time windows containing electromagnetic showers – and storage. The DAQ must apply an energy threshold to identify showers within a station, so the 54 waveforms from that station must be summed to keep the threshold independent of the incident electron position in a crystal. All 54 WFD waveforms must therefore be transferred to the same frontend DAQ system, which will use the waveform sum to perform data reduction on the digitization stream: identification of time islands with activity (T-method) and time rebinning of the waveform (Q-method).

The energy range of interest for an individual calorimeter element is 25 to 3100 MeV for single events. Allowing pileup, suggests pushing the upper limit close to 5000 MeV. A digitizer with 12-bit depth (4096), is ideal. It will allow good pulse definition, important for the energy resolution requirements, and it will not saturate for the highest energy events. As discussed in Chapter 17, the pulse shape risetime is approximately 2-4 ns and we are actively working to reduce it. The laboratory tests done to date suggest that a minimum of 500 MHz sampling will be required to accurately fit the pulses, subject to optimizing pileup rejection. Therefore, each digitized waveform is therefore 350K 12-bit words for each muon fill.

A precision oscillator ("clock") will provide the timebase from which the ω_a frequency is measured. It must be controlled to provide negligible error compared to the anticipated 0.1ppm uncertainty on ω_a. In order to achieve this, the clock must have jitter that is significantly less than the 2 ns sampling period of the waveform digitizers. It must also have very low (< 10 ps) systematic shift across the time of a single fill. This latter requirement is important because of the large variation in event rate within a fill. A systematic time-slew that is correlated with muon or positron intensity would bias the result. The clock system must also enable a convenient blinding scheme such that the actual precise clock frequency cannot be known to the data analyzers.

The data acquisition system must provide a deadtimeless readout of calorimeter segments using the waveform digitizers. Onboard memories in the digitizers will buffer the raw data and allow its asynchronous readout, thus decoupling the data acquisition cycles from storage ring fills. A frontend layer of multicore CPUs/GPUs will process the digitized records of each fill from every calorimeter segment into T-method, Q-method and other derived datasets. A backend layer of multicore CPUs/GPUs will handle the assembly of event fragments from the frontend layer and transfer of assembled events to the mass storage. Each stored event will represent a complete deadtime-free history of the entire activity in the detector system for every fill cycle.

References

[1] D. W. Hertzog and W. M. Morse, Ann. Rev. Nucl. Part. Sci. **54**, 141 (2004).

[2] G. W. Bennett *et al.* [Muon G-2 Collaboration], Nucl. Instrum. Meth. A **579**, 1096 (2007).

[3] Sedykh SA, et al. *Nucl. Instrum. Meth. A*455:346 (2000).

[4] V. Tishchenko *et al.* [MuLan Collaboration], Phys. Rev. D 87, 052003 (2013) arXiv:1211.0960 [hep-ex].

Chapter 17

Calorimeter

This chapter illustrates the design concept for the electron calorimeter. The primary purpose of the electron calorimeter is to measure the energy and time of arrival of decay electrons from stored muon decay. First the physics goals and subsequent requirements are reviewed. Then the recommended design is presented broken down by subsytems which include: Absorber, Photodetection (SiPM), Bias Control, Laser Calibration, and mechanical. Alternative designs are also presented. The chapter ends with a discussion of: ES&H, risks, quality assurance, and value management.

17.1 Introduction

17.1.1 Physics Goals and Requirements

The energy and timing information from the electron calorimeter introduces possibly two major sources of systematic errors to ω_a:

1. Unidentified pileup events, i.e. simultaneous electron showers in the same calorimeter station that cannot be resolved.

2. Rate-dependent effects that couple to the spin precession frequency (e.g. a rate-dependent gain change).

To meet the new FNAL E989 goal, the electron calorimeter must be able to resolve two simultaneous showers by either the timing information or spatial separation. For two electron showers hitting the same calorimeter with a time separation of more than 5 ns, the new calorimeter must allow to separate these at 100% efficiency. For showers that occur closer in time than 5 ns, the new design must allow for a separation of the two shower signals for $\approx 66\%$ of these pileup events. Therefore, the new calorimeter must have improved spatial resolution compared to the former design employed at the BNL E821 experiment [1].

The requirement of stable gain G leads to the design goal of a maximally allowed gain change of $\frac{\delta G}{G} < 0.1\%$ within a 200 μs time period in a fill. In addition, the arrival of a pulse should not affect the gain for a second pulse arriving a few nanoseconds later on the same channel, unless that change is understood and can be applied to the interpretation of a following pulse in a reliable manner. The long term gain stability ($>$ seconds) is more

relaxed and we aim at $\frac{\delta G}{G} < 1\%$. To verify the overall gain stability, each of the 24 stations needs to be equipped with a calibration system that monitors the gain continually during the muon spills with a precision of $\frac{\delta G}{G} \sim 0.03\%$.

17.1.2 Evaluation Methodologies: Test Beams and Simulations

The recommended design follows extensive testing and simulation efforts. Prototype detectors were built. Various silicon photomultiplier (SiPM) and photomultiplier tube (PMT) candidates were tested and several iterations of the electronics boards needed to operate the SiPMs were built and tested. We also employ simulations to study detector performance, sensitivity to ω_a and pulse-shape fitting. A brief summary is given next for context.

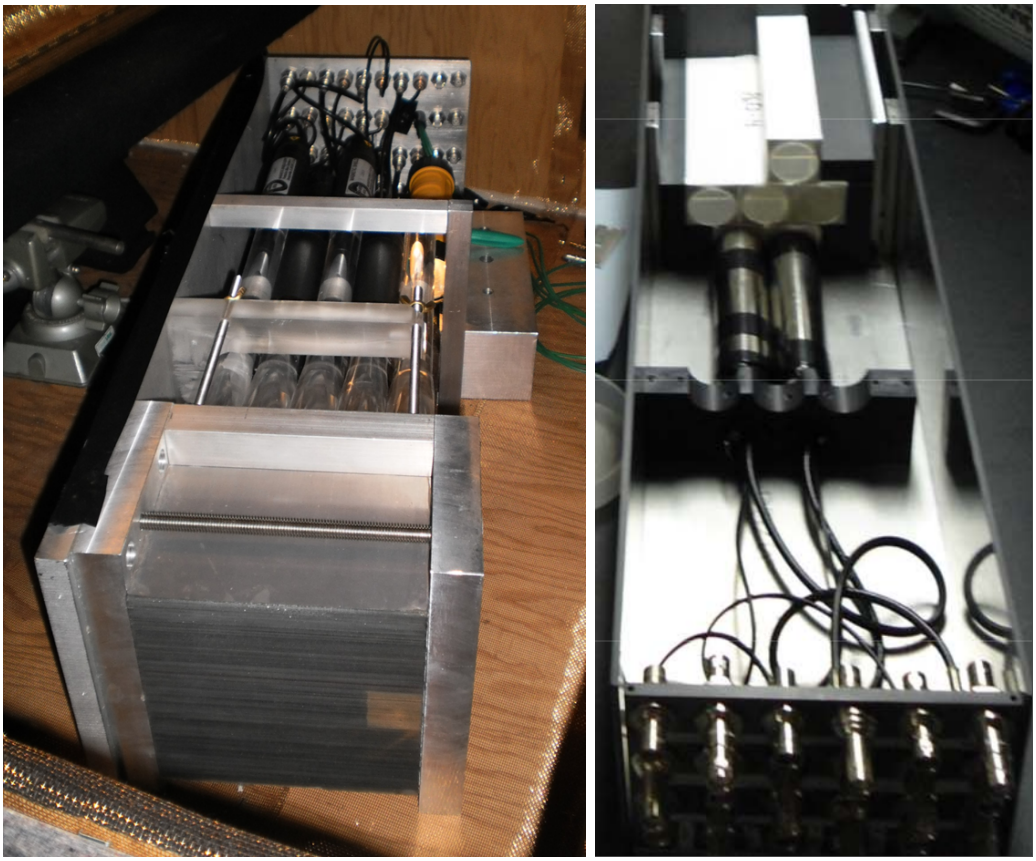

Figure 17.1: left: Monolithic block of W/SciFi having 0.5 mm thick pure tungsten plates alternated with 0.5 mm diameter ribbons of blue scintillating fiber. The readout side is divided into 25 individual elements. Tapered lightguides direct the light from a 3×3 cm^2 area to a PMT. right: Crystals being prepared for test beam. Here, PMTs are used for the outer elements and a SiPM will be placed on the center crystal and alternatively a very fast Hamamatsu R9800 PMT for comparison.

The Fermilab Test Beam Facility (FTBF) was used several times to evaluate prototype calorimeters. In particular, our first effort with a mixture of 0.5-mm pitch tungsten plates alternated with 0.5-mm layers of scintillating fiber resulted in a publication [2]. A larger

prototype was then built and tested, see left panel of Fig. 17.1. Finally, the recommended design based on PbF_2 crystals was tested using a $2 \times 3 \times 2$ array. The April 2012 FTBF period was used to directly compare these crystals to the W/SciFi detector and to a custom $PbWO_4$ crystal. The right panel of Fig. 17.1 shows the arrangement of PbF_2 crystals during assembly and Fig. 17.2 displays a front view of the full test setup. Various readout methods, wrappings and couplings were employed.

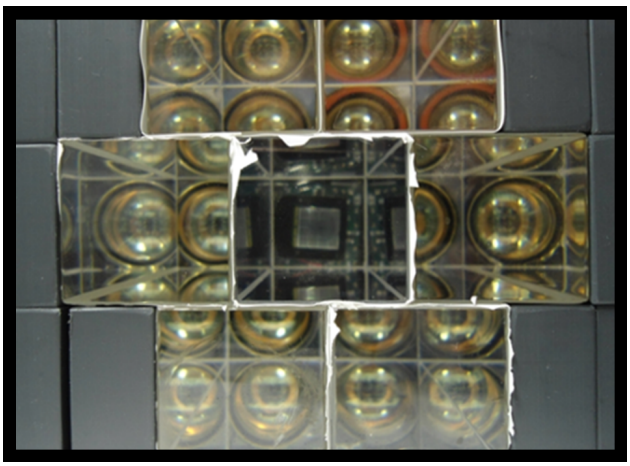

Figure 17.2: Front picture of the 7-crystal test array used in the FTBF. In this configuration, a SiPM is visible on the center channel, while PMTs are used on the remaining elements. These crystals were wrapped in white millipore paper.

We also used simulation tools to evaluate performance and optimize parameters. GEANT-4 simulations were used to study light collection in crystals and to evaluate crystals shape, wrapping, and light yield. They were used to study array size and cluster formation. A realistic muon storage simulation was used to produce decay events having the correct energy, spatial, and temporal distributions on the calorimeters. Finally, we developed custom software to build pulse-shape libraries from controlled lab test and to use the libraries to fit individual events and two-pulse events. The results of these efforts are described in line with the design recommendation topics.

17.2 Recommended Calorimeter Design

The Calorimeter System includes the following subsystems: Absorber, Photodetection, Bias Control, Calibration, and Mechanical. Over the past several years, the calorimeter design has gone through an extensive down-select process from considered absorber and readout technologies. Briefly, each of the 24 calorimeter stations will consist of a 6×9 array of lead-fluoride (PbF_2) Cherenkov crystals. Each crystal will be read out by a 16-channel Hamamatsu MPPC (Multi-Pixel Photon Counter, but more generically, these have been dubbed "SiPMs" or silicon photomultipliers). Custom supporting electronics amplify the summed signal and convey it to the digitizers following a hardware pole-zero correction to shape the output. SiPM gains are very sensitive to bias and temperature. A precise and stable bias voltage control system is being developed and a temperature-stable operating

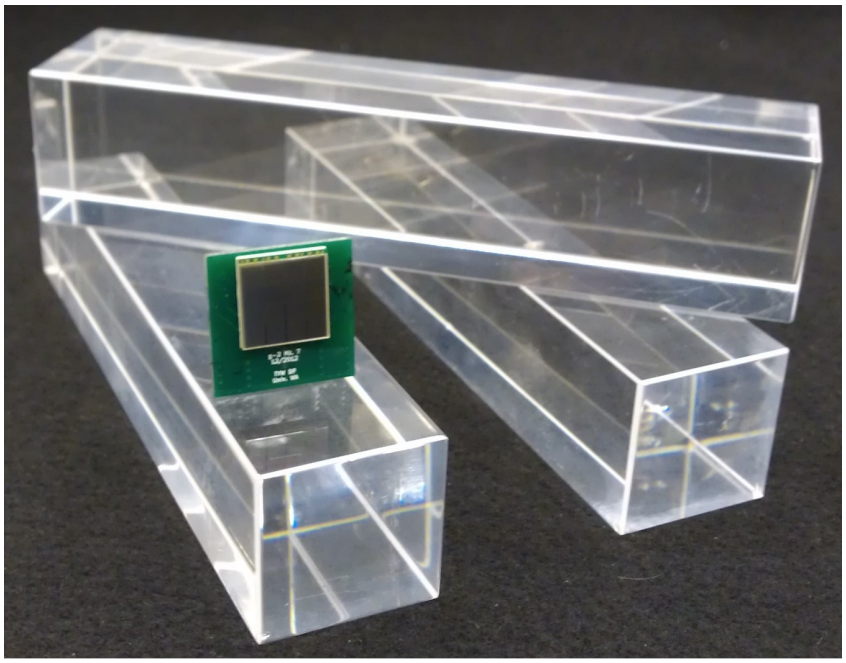

Figure 17.3: Sample $3 \times 3 \times 14$ cm^3 PbF_2 crystals together with a 16-channel Hamamatsu SiPM mounted to our Mark VII, resistive summing, voltage amplifier board. (Note, these crystals are larger than in the conceptual design.)

environment has been designed. Both systems will help to maintain high gain stability, which addresses a leading source of systematic uncertainty. A state-of-the-art laser-based distributed calibration system has been designed. It will permit precise monitoring of gain vs. time-in-fill for the nearly 1300 crystals. A photo of the prototype crystals and 16-channel surface-mount SiPM is shown in Fig. 17.3.

Several factors that influenced the technology choice are:

- Each of the 24 calorimeter stations will be located in the fringe field of the central storage ring, directly adjacent to the muon storage volume in a cutout of a scalloped vacuum chamber (see Fig. 16.6). The space is highly constrained vertically (17 cm) and longitudinally (owing to vacuum interconnects and flanges). Strict limits exist on the allowed magnetic field perturbation from the absorbers, electronics and mechanical housings.

- The absorber must be dense to minimize the Molière radius and radiation length. The latterand to minimize the number of electrons entering the side of the calorimeter.

- The intrinsic signal speed must be very fast with no residual long-term tail, thus minimizing pileup.

- The resolution should be good—it is used to select events—but it need not be "excellen." A resolution of $\approx 5\%$ at 2 GeV is the required benchmark and improves upon the E821 calorimter system by a factor of 2.

Table 17.1: Properties of lead-fluoride crystals

Crystal cross section	2.5×2.5 cm^2
Crystal length	14 cm ($> 15X_0$)
Array configuration	6 rows, 9 columns
Density of material	7.77 g/cm^3
Magnetic susceptibility	-58.1×10^{-6} cm^3/mol
Radiation length	0.93 cm
Molière radius R_M	2.2 cm
Molière R_M (Cherenkov only)	1.8 cm
$KE_{threshold}$ for Cherenkov light	102 keV
Expected photo-electron yield* / GeV (White wrapping)	1765
Expected photo-electron yield* / GeV (Black wrapping)	685
*using 1.2 cm^2 SiPM on rear face; light integrated over several crystals to have full shower containment	

17.2.1 Absorber Subsystem

The default material choice following an extensive comparative evaluation program (see Sec. 17.3) is lead-fluoride crystal (PbF_2). This crystal exhibits good energy resolution and a very fast Cherenkov signal response. It is (essentially) non-magnetic, have a radiation length of $X_0 = 0.93$ cm, and a Molière radius of 1.8 cm. We used a precise ($\delta P/P \sim 1\%$) Frascati 500 MeV electron beam to verify the resolution and light yield that had been documented [3] by a Mainz Collaboration, that built a large PbF_2 array for their experiments. They found $\sigma/E \sim 3.5\%/\sqrt{E}$ and about 1.7 p.e/MeV. A summary of the properties of the crystals is given in Table 17.2.1.

The Shanghai Institute of Ceramics (SICCAS) provided the prototype crystals and an attractive quote for the 1350 elements required for the full system (plus spares). We own and have used instrumentation to measure the spectral response of the crystals over the range 230 nm to 800 nm, see Fig. 17.4. We have also made AFM measurements on a crystal to determine the surface quality that we might properly represent it in our light-propagation simulations. The crystal procurement plan involves a 1st-stage quality control check by the Shanghai University members of the collaboration, who are local to the vendor. Next, the crystals will be sent to the University of Washington team for wrapping and assembly. PbF_2 crystals are relatively easy to handle; they are only slightly hydroscopic.

Detailed GEANT ray-trace simulations and direct laboratory measurements have been used to study the light collection efficiency of the crystals subject to various wrapping schemes and couplings to the photo-sensitive readout. We have focussed on two extremes, namely an all-black tedlar absorptive wrapping, and a diffuse reflective white millipore paper wrapping. The black wrapping largely transmits only the direct Cherenkov light cone, while the white wrapping allows light to bounce multiple times within the crystals eventually leading to a higher overall photon yield. Both wrappings have advantages. For the shortest pulse occupancy time, the black wrapping excels. For the greatest light yield, the white wrapping is better. Shorter-duration pulses improve pileup rejection; higher light yield

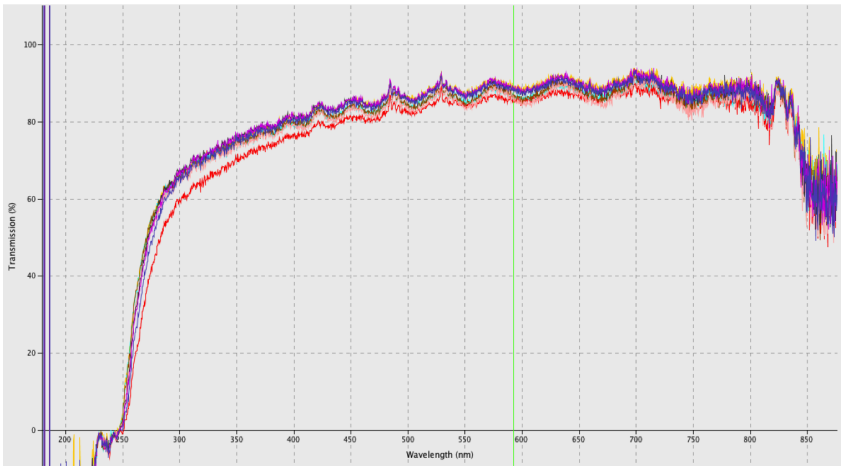

Figure 17.4: Transverse transmission efficiency vs. wavelength through a 3-cm-thick PbF_2 prototype crystal. The four curves correspond to rotations of the crystal with respect to the light source from an Ocean Optics spectrometer.

improves resolution. We have tested both wrappings and an aluminum foil wrapping in a test-beam using a standard 29-mm Photonis PMT for readout. The left panel of Fig. 17.5 shows the results with the amplitudes normalized. The tedlar wrapped FWHM is limited here by the PMT. The right panel compares PbF_2 to alternative design options discussed in Sec. 17.3. Here we observe the true full width of 4 ns for the PbF_2 crystal as measured using a fast Hamamatsu R9800 PMT.

Table 17.2.1 includes two entries that compare absolute light yield in photo-electrons as would be detected by our default photo-sensitive detectors. The simulation generates the correct Cherenkov light distribution (by wavelength) from a 2 GeV incident electron and it uses the correct crystal dimensions and surface reflectivity parameters. Optical-grease coupling is assumed as is the photo-detection efficiency of the readout device as a function of wavelength. The yield of white paper wrapping is 2.5 times greater than the black paper, which is consistent with laboratory tests we carried out with cosmic rays. The pulse duration is also measured and largely agrees with the measurements. We intend to repeat the light yield test in a beam with a better control of the pe/channel of the photo-sensitive readout.

GEANT-4 simulations have been used to study to optimize the individual crystal size and the array matrix configuration. A visualization of a typical 2 GeV electron shower is shown in Fig. 17.6. A driving specification for an array of crystals is the reduction in pileup to be realized by spatial separation. Candidate arrays of 5×7 and 6×9 (height by width) segmentation using 3×3 cm^2 or 2.5×2.5 cm^2, $15X_0$-deep crystals, respectively, will fit the space constraints. A simulation with full showering and cluster reconstruction using a simple and robust two-shower separation algorithm was used to choose the best arrangement. Not surprisingly, the higher-granularity array is best. We find that it will provide at least a 3-fold reduction in pileup compared to a monolithic design. These conclusions were arrived at form a combination of simulation and direct measurement using the FTBF.

Energy sharing among neighbor crystals is shown in Fig. 17.7 for a shower that strikes the center of the middle crystal. The simulation is calibrated against the test-beam measure-

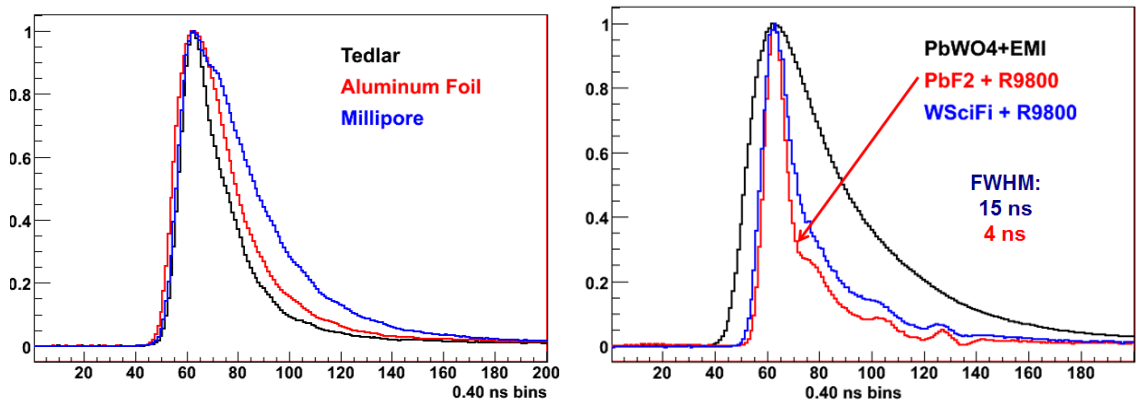

Figure 17.5: Left panel: Normalized response of PbF_2 crystal wrapped in absorptive black tedlar, reflective aluminum foil, and a bright, white millipore paper. A standard 29-mm Photonis PMT was used. Right panel: Comparison of three pulse shapes from PbF_2, using a very fast Hamamatsu R9800 PMT, to W/SciFi using the same PMT and to $PbWO_4$ using an EMI PMT.

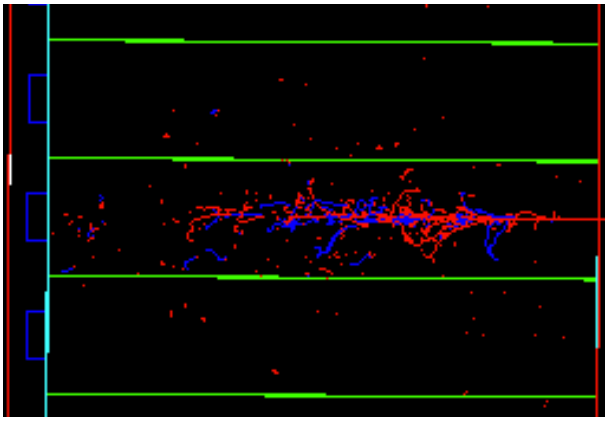

Figure 17.6: A single shower showing secondary positrons and electrons in a 2.5×2.5 cm^2, by $15X_0$ deep PbF_2 crystal, subject to a 2 GeV incident electron.

ments in which an electron beam was directed into a crystal at various known positions and the ratio of neighboring crystal responses was recorded. Fig. 17.7 also shows a histogram of data vs. the simulation prediction. The agreement is excellent and verifies the model used to optimize array size and to evaluate pileup by shower separation. The simulation was then used to study the spatial separation efficiency for two simultaneous showers. The left panel of Fig. 17.8 shows schematically the shower deposition by color. The right panel is a systematic study of two-shower events as distributed on the calorimeter based on the full muon storage and decay simulation. From the simulation we see that the 6×9 configuration will enable a reduction in pileup by a factor of 2/3 compared to a monolitic array.

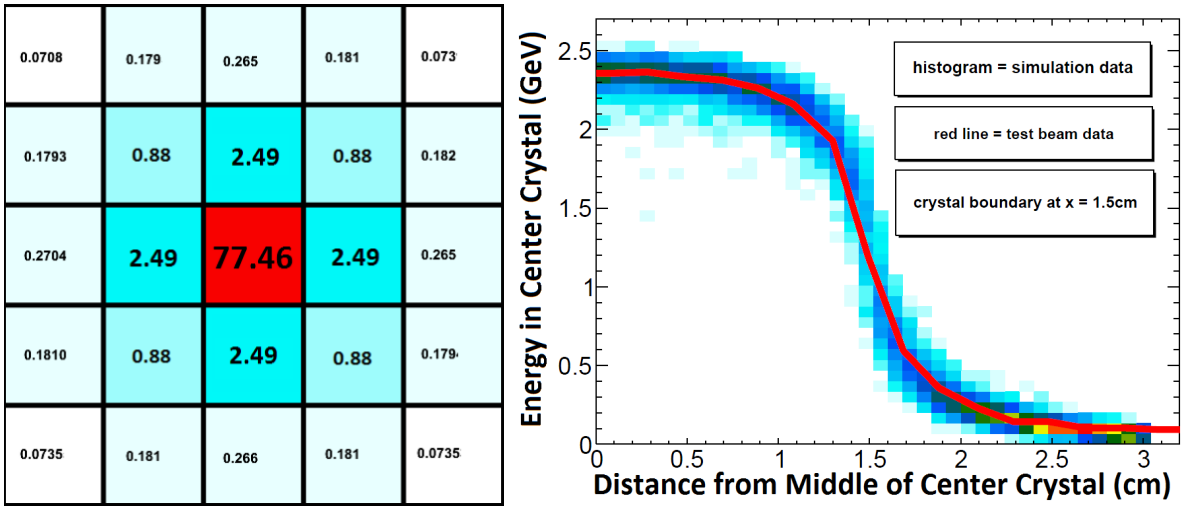

Figure 17.7: Left: Schematic representation of energy deposition in a section of the segmented electromagnetic calorimeter. Each cell is one crystal with dimensions (2.5 x 2.5 x 14 cm^3). The numbers represent the percentage of the kinetic energy deposited in each crystal. This data was produced from a GEANT-4 simulation with an electron incident on the center of the central crystal. The results do not change for electrons in the range of 0.5 GeV to 3 GeV. Right: A comparison of test beam data and simulation data. This plot shows the shower leakage into neighboring crystals as a function of beam incidence position.

17.2.2 Photodetection - SiPM - Subsystem

Silicon photomultipliers (SiPMs) are assumed in the baseline design to read out the crystals. While challenging and relative new devices, they are increasingly becoming the standard substitute for traditional PMTs in many nuclear and particle physics applications. As such, the body of experience in their use is growing rapidly and the variety of SiPM devices from many manufacturers is increasing. They work as pixelated Geiger-mode counters. The default SiPM we are considering has 57,600 50-μm-pitch pixels on a 1.2×1.2 cm^2 device. When a photon strikes a pixel, it can cause an avalanche that is summed together with the other stuck pixels in a linear fashion to produce the overall response. Quenching resistors are intrinsic to the device to arrest the avalanche and allow the device to recover with typically 10's of ns time constant. Those pixels that are not struck, meanwhile, remain ready for a next pulse. In general, the concept is to have a pixel count that greatly exceeds the highest photon count that would strike the device. For example, for our crystals, a working number is 1 pe/MeV (where pe represents a converted photon). With a range of up to 3100 MeV for single events, the occupancy fraction remains no more than about 5%, which is in a near-linear regime and allows for a good measurement of any closely trailing second pulse.

The selection of SiPMs over PMTs is pragmatic. They can be placed inside the storage ring fringe field, thus avoiding the awkward, long lightguides that would be needed for remote PMTs. They have high photo-detection efficiency, they will not perturb the storage ring field, and they can be mounted directly on the rear face of the PbF_2 crystals. The cost of large-area SiPM arrays is rapidly falling and their performance characteristics continue to improve. We have spent the last 2 years developing lab tests to evaluate these devices. The

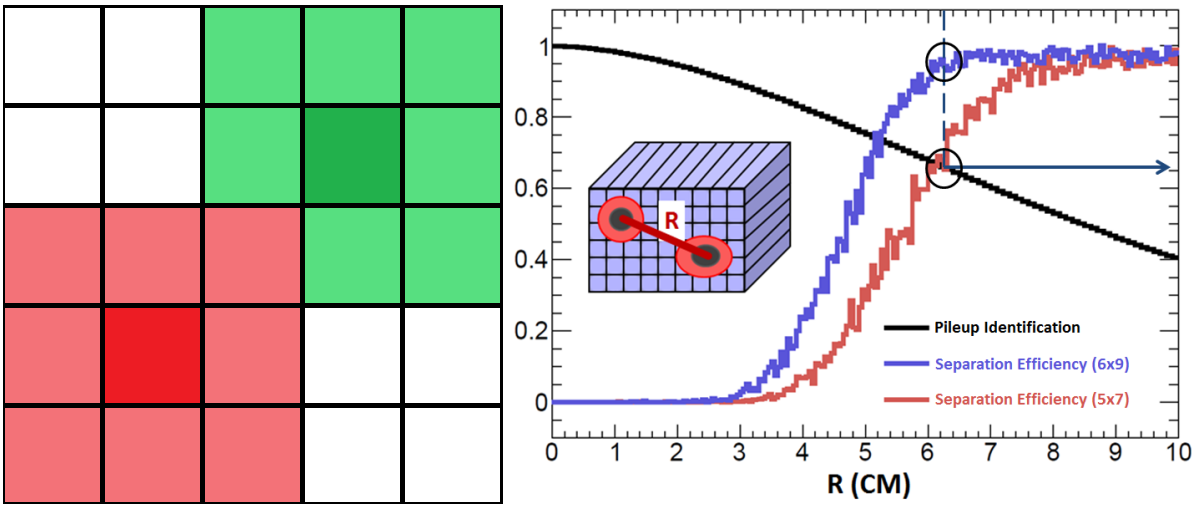

Figure 17.8: Left panel: Schematic representation of energy deposition in a section of the segmented electromagnetic calorimeter. Red represents the primary cluster reconstructed by the analysis software. Green represents the secondary cluster. The dark cells dictate the seed of each cluster. Right panel: Pileup separation efficiency curves for two different crystal segmentations, 6x9 (blue) and 5x7 (red), which correspond to 2.5 cm and 3 cm crystals, respectively. The black curve represents the amount of pileup rejected for a certain R value. The variable R is the distance between the two incident electrons and is shown graphically in the inset.

collaboration has designed and built a series of custom pre-amplifier and summing amplifier boards. The most recent version features low-power consumption and an intrinsic short pulse when coupled to a pole-zero correction circuit that eliminates the long RC time-constant tail of the device.

Large-area SiPM devices are packaged as arrays of smaller individual channels. While the market is constantly evolving, we are presently using a Hamamatsu surface-mount 16-channel MPPC having 57,600 50-μm pixels in a 1.2×1.2 cm^2 active area. It is reasonably well-matched to the surface 2.5×2.5 cm^2 crystal face. Figure 17.9 shows the Hamamatsu 16-channel surface-mount MPPC (SiPM). This board is based on a the concept of a passive sum and voltage amplifier. The output of a SiPM from a photo-electron event is a pulse

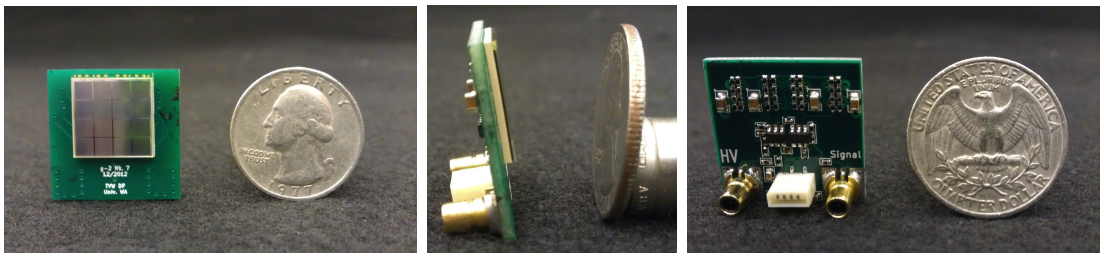

Figure 17.9: Surface-mount 16-channel MPPC. The coaxial connections represent the signal out and the common bias voltage in. The board low voltage is supplied through the white edge connector.

of current, with a fast rising, sub-ns, edge and a longer tail on the order of tens of ns, which is converted to a voltage by a load resistor. In our present design, this is followed by two stages of voltage amplification provided by high speed op amps. We are constantly improving our circuit and watching the field to learn about new devices and techniques. Our development will likely cycle through 2 or more iterations prior to final purchase of components in order to take advantage of the latest offerings. We have also begun a dialog with University of Washington EE and Medical Physics research groups who are developing an ASIC design having many overlapping features of common interest. Considering this dynamic environment, the baseline conceptual design has been demonstrated to function well enough for $g-2$, but we are confident that improvements will be made based on announcement of new products from the vendors and from the rapid advancement in the electronics designs.

One of the challenges of using SiPMs is their particular sensitivity to temperatures. Figure 17.10 (left panel) shows the gain change of our SiPM device vs. temperature. The slope of about $4\%/\deg C$ implies that we must keep the board temperature stable during a fill to 1 part in 40. While short-term shifts are unexpected, the overall SiPM environment must be maintained at a fairly constant temperature in order to simplify the global calibration of gain during the running period. The response of a SiPM is also quite sensitive to the bias voltage stability above Geiger-mode breakdown threshold. The right panel of Fig. 17.10 shows a lab measurement of our SiPM and voltage amplifier board vs. bias voltage. Around the working bias of 72.5 V, the slope is steep, leading to the need to have a separate bias control subsystem, which we describe in Subsection 17.2.3.

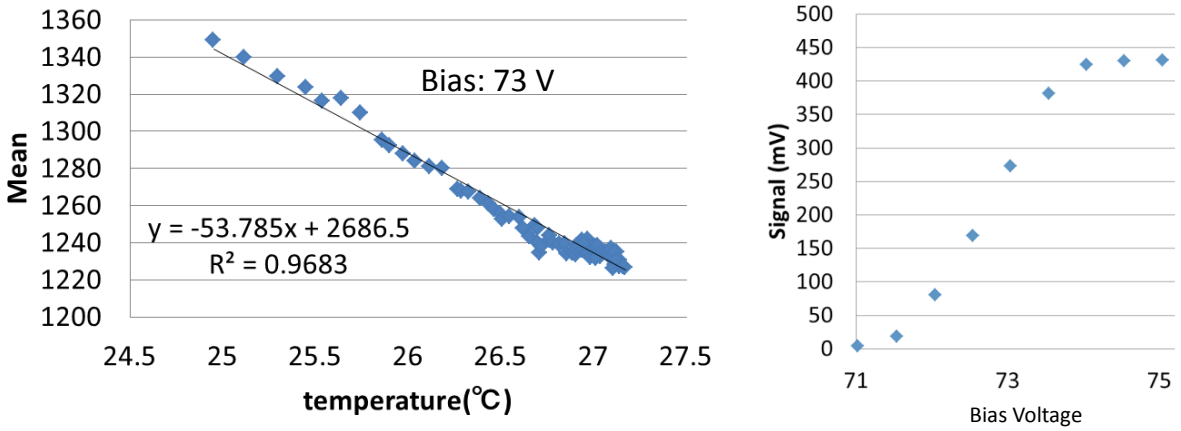

Figure 17.10: Left: Gain vs. temperature for 16-channel SiPM array. Right: Gain vs. bias voltage.

Given the working electronics board described above, simulations were carried out to determine pulse-shape characteristics and, most importantly, two-pulse separation. We used a 5 GSPS digitizer to record a series of pulses in which a SiPM was excited by a 600 ps pulse-length N_2 laser (337 nm) light burst. The intrinsic fast risetime of a SiPM is slowed somewhat by our circuit and the quenching resistance and internal capacitance determined the exponential recovery time constant. Because the pulse shape is predictive, a pole-zero

correction can be applied, post-amplifier, to produce the final recorded pulses. The left panel of figure 17.11 shows the intrinsic raw SiPM pulse with its long recovery time. The same pulse is seen with the pole-zero correction circuit applied. A series of pulses is used to develop a pulse-shape library. The right panel then shows a representative single pulse fit using the library template. This procedure is the basic element of our eventual analysis protocol.

The analysis of two-pulse waveforms is critical for pileup rejection. Both simulated and measured studies were made, following many of the protocols we developed for the MuLan 1-ppm muon lifetime experiment. In that effort, unresolved pileup had to be subtracted at the per mil level to avoid distortions to the lifetime [4]. It is less severe here, but still important. Our two-pulse resolution software was adopted for the new $g-2$ situation, which has different pulse shapes and a much wider range of amplitude ratios for the two nearby pulses. At present, we find that two pulses separated by 5 ns or more can be reliably separated. An active area of our laboratory work is to systematically map out the two-pulse separation function with varying pulse-to-pulse amplitude ratios and time separations. As an example, Fig. 17.12 shows the waveform from laboratory tests in which the laser pulse was split with one leg delayed by exactly 5 ns with respect to the second. Further details regarding the digitization the these pulses are given in Chapter20.1. The lab setup allows both to be measured individually and then the sum together. The figure clearly shows resolved pulses. Tests are ongoing to map the efficiency of two-pulse resolution vs. Δt and R_{12}, the ratio of amplitudes for pulse 1 and pulse 2. Additionally, we intend to map out the function $G2(\Delta t, R_{12})$, which is the fidelity of the gain of the second pulse amplitude versus the time separation and amplitude ratio. Because pixels are struck (and therefore temporarily disabled) from the leading pulse, the trailing pulse effectively see a "smaller" device, but in a predictable manner.

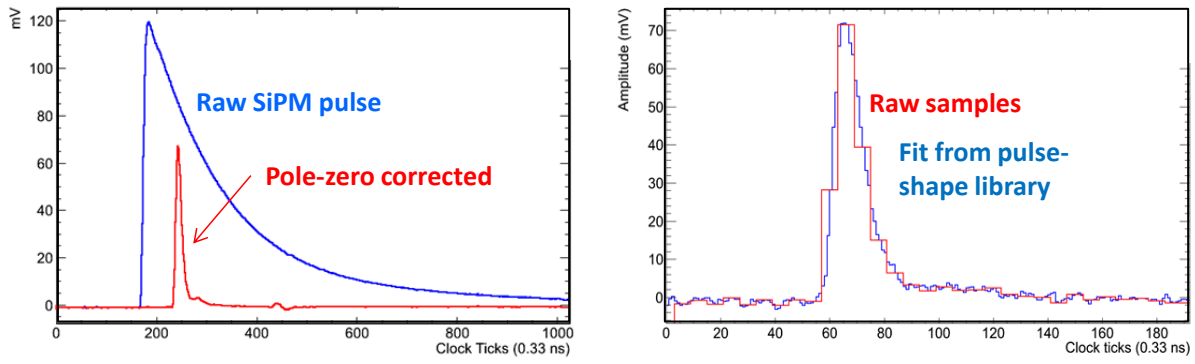

Figure 17.11: Left: Raw Laboratory measurement of raw 16-channel SiPM pulse using voltage amplifier. Same pulse with post-amplifier, pole-zero circuit included. Right: Single pulse and fit using pulse-shape template library and current pulse-finding analysis software.

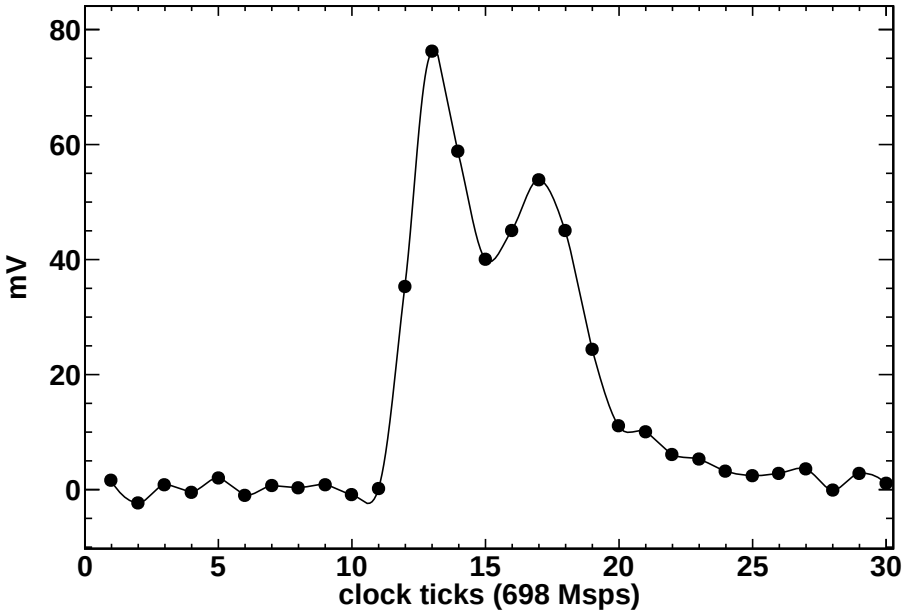

Figure 17.12: Digitized samples for a pair of pulses laser pulses striking the SiPM array 5 ns apart.

17.2.3 Bias Control Subsystem

The bias voltage control system will provide the operating voltage setpoint for the SiPMs. Key design aims are that each of the 1296 installed boards must be adjustable in mV increments over a range of $\pm 2.5\,\mathrm{V}$ around the nominal HV bias of $\sim$72 V, just above the Geiger mode breakdown voltage. Further, the system must maintain a high degree of bias voltage stability and deliver an average current of up to $50\,\mu\mathrm{A}$ per channel. These are unusually strict benchmarks that are established to minimize any offline gain correction procedures. At this time, no commercial device satisfies these requirements and the need for distribution to the 24 "satellite" locations around the ring. Hence, the system will be built by the UVa and JMU groups. It will conform to global $g-2$ slow control protocols and provide control and readback functions based on the new Midas Slow Control Bus (MSCB) standard. The system will consist of a stabilized DC power supply, HV boards, readback and control (16 channels/board), 5 V DC power, shielded twisted pair ribbon HV cables, and RS485 serial bus for the MSCB. These will be packaged together as a single unit capable of providing 64 channels of HV into a single module. Twenty five modules will be built and tested.

17.2.4 Laser Calibration Subsystem

A high performance calibration system is required for the on-line monitoring of the output stability of each individual tower in all calorimeter stations. It is estimated that the detector response must be calibrated with relative accuracy at sub-per mil level to achieve the goal of the E989 experiment to keep systematics contributions to the accuracy on the measured observables at 0.02 ppm level. This is a challenge for the design of the calibration system because the desired accuracy is at least one order of magnitude higher than that of all other

existing, or adopted in the past, calibration systems for calorimetry in particle physics.

Almost 1,300 channels must be calibrated during data taking; the proposed solution is based on the method of sending simultaneous light calibration pulses onto the readout photo-detector through the active sections (crystals) of the calorimeter. Light pulses must be stable in intensity and timing to correct for systematic effects due to drifts in the response of the crystal readout devices. A suitable photo-detector system must be included in the calibration architecture to monitor any fluctuation in time of the light source intensity and beam pointing as well as any fluctuation of the transmitted light along the optical path of the light distribution system, which could occur due to mechanical vibrations or optics aging.

Some guidelines are defined to select the light source(s) and to design the geometry of the light distribution and monitoring; the following criteria are adopted to select the light source type:

- Light wavelength must be in the spectral range accepted by the detector and determined by the convolution of the spectral density of the Cherenkov signal produced by electrons in PbF_2 crystals with the spectral transmission of the crystals, and with the spectral quantum efficiency (Q.E.) of the photo-detector; Q.E. is peaked around 420 nm for SiPMs.

- The luminous energy of the calibration pulses must be in the range of the electron deposit in the crystals, typically 1-2 GeV; this corresponds to a luminous energy on each tower of a calorimeter station of about 0.01 pJ, or to about 0.013 nJ for simultaneous excitation of all calorimeter readout channels (1300). The numbers quoted above are merely indicative of the order of magnitude and they are derived by assuming that the readout of each crystal will produce up to 2 photo-electrons per MeV with 50% P.D.E. (Particle Detection Efficiency) for SiPMs and with 40% coverage of the crystal readout face.

- The pulse shape and time width must be suitable to infer on the readout capability in pile-up event discrimination; pulse rise/trailing time must be of the order of some hundred of picoseconds, the total pulse width should not exceed 1 ns. This implies a peak power per pulse at the source of about 1 Watt (1 nJ in a 1 ns wide pulse), assuming the conservative value $T \simeq 0.01$ for the total intensity transmission factor of the calibration system.

- The pulse repetition rate must be of the order of 10 KHz; this value will be tuned to obtain the best compromise between the need of having enough calibration statistics in the time interval (some tens of microseconds after the muon injection in the ring) when the maximum rate is achieved in the readout devices and the need to avoid saturation of the DAQ bandwidth.

A number of commercial diode lasers cope with the criteria listed above, and have been considered as a source for the calibration pulses. The final choice will be made after the completion of all tests required to qualify, in terms of light transmission and time stability, all other optical elements of the calibration system. Guidelines for designing the light distribution chain are listed below:

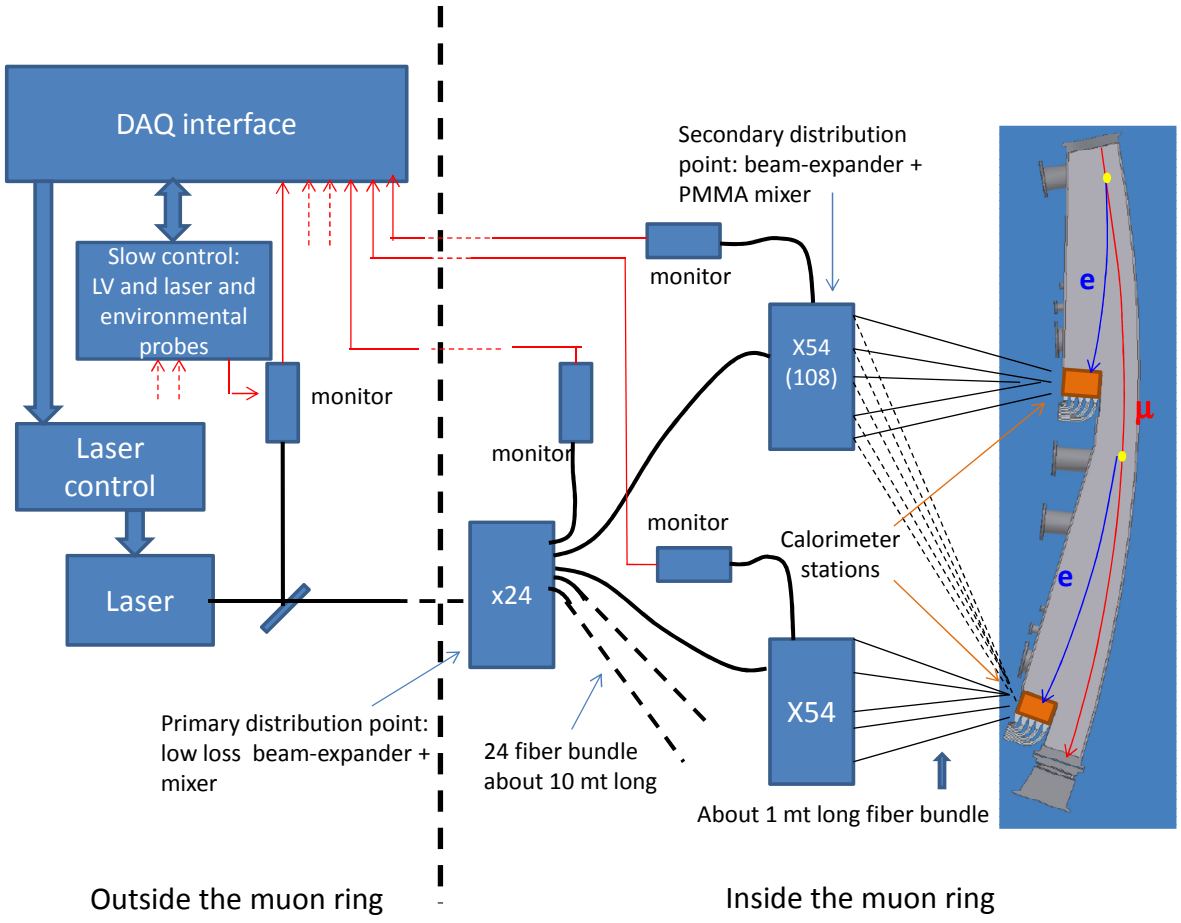

Figure 17.13: Calorimeter calibration system: sketch with the main components.

- High sensitivity monitors of the transmitted light at the end-point of each individual section of the distribution chain must be used to ensure online control of the system stability and to have information for applying feed-back correction to the source operation parameters, if needed.

- The optical path must be minimized in order to limit the light loss due to self-absorption in the optical fibers; the number of cascade distribution points must be also minimized to reduce the unavoidable light loss in the couplers between different sections;

- The laser source and its control electronics should be located outside the muon ring in order to avoid e.m. perturbations of the local field induced by the current flow used to excite the laser. Consequently, a suitable geometry should include a primary light distribution point outside the ring, a bundle of fibers about 20 meter long and used to feed light from the primary distribution point to the secondary ones, and secondary distribution points located close to each calorimeter station; from the secondary distri-

bution points, short fibers, about 1 meter long, feed the light to the individual towers of each calorimeter station.

- Optical fiber selection: silica fibers (20 dB/Km attenuation at 400 nm) are the best solution for long path light transmission and in terms of robustness against solarization or other aging affects due to large values of transmitted light intensity. For the shorter fiber bundles, where the transmitted intensity is at least one order of magnitude lower, also PMMA clear fibers (200 dB/Km attenuation at 400 nm) can be considered to save money.

A possible geometry fulfilling all the requirements set by the guidelines listed above is shown in Figure 17.13; light generated by a laser source is fed onto a primary distribution device located in the center of the muon ring; quartz fibers (about 10 meter long, one per calorimeter station plus spares for monitoring purposes) route the light to secondary distribution devices located near the calorimeter stations, each distributor serving one or two close stations. A small fraction of the light exiting the source and the light distributors is routed to monitors whose analog signal is returned to the DAQ system for on-line checking of the system stability. Interface with DAQ is also required for slow control signal recording and communication with the timing signal controls is used to trigger the electronics of the laser driver.

Qualification tests of the individual components will include comparison measurements of different options; apart the fiber type, alternative approaches are considered for:

- laser source; as an alternative to a single, powerful laser light source, the possibility to use two or four lower power, synchronized, lasers can be considered; the latter solution would have the advantage that, in case of laser failure, no calibration stops will occur during data acquisition; moreover, lower power lasers have, in general, better stability characteristics. Issue for the multi-source option is to demonstrate that the different pulses can be synchronized at the desired level, some tens of ps.

- light distributors; baseline solution uses custom designed beam-expanders with light mixers inside; this feature is required to guarantee intensity stability of the distributed light against geometrical effects due to beam-pointing instabilities. Integrating spheres are an alternative and offer a high degree of output uniformity at the price of a higher factor in intensity loss (up to 100). Beam-splitters made with the linear circuit technology could also be considered if commercial devices, nowadays widely used only in the IR range for telecommunication, will be produced for the near-UV/visible range.

17.2.5 Mechanical Subsystem

Each calorimeter station will comprise a number of individual crystals which are made out of dense material which is usually also brittle. In addition, the detector including the photosensitive device needs to be in a light tight encapsulation. A typical set of crystals and photodetectors forming one calorimeter station weighs $\approx 40\,\mathrm{kg}$. The housing must provide the light tightness, proper stability to carry the weight, feedthrough for cables, and a mechanism for easy lifting of the entire box and insertion into or out of the ring in the radial direction (e.g, rails).

The locations of the 24 calorimeter experiment are fixed by the design of the scallop-shaped vacuum chambers. Several vacuum ports, bellows and the magnet's pole gap impose spatial limitations on the design. Specifically, the length of the calorimeter station along the electrons trajectory cannot exceed 38 cm. The pole gap limits each station to less than 17 cm. There are no tight limiting factors in the radial dimension that we can see would constrain the calorimeter station.

For installation, maintenance and access to the vacuum chamber or the magnet, each calorimeter station needs to be easily removable. We will determine later the degree of alignment necessary, but a system of pins should allow for a reproducible position. The absolute position is less critical. The calorimeter housing and retractable platform must allow for routing of a variety of cables (detector signals, bias voltage, control signals, monitoring signals) and service lines (e.g. water cooling pipes). The mechanical design must incorporate space for the readout electronics crates to be placed on-board to be compatible with the moving mechanism.

A mechanical housing system was built for the test beam and a full-scale version has been designed by CENPA engineers and costed for the experiment. It ensures a light-tight environment, provides cooling as necessary, includes patch panels for cable runs and has a front-end that will mate to the calibration interface plate described above. The housing has serviceable doors that will allow easy access to the crystals and readout devices. Figure 17.14 shows three engineering drawings of the proposed system. Modifications will be made once the decision on the signal and bias cabling is finalized. The front panel of the light-tight housing holds the calibration plate. Figure 17.15 shows our current design in perspective. This system will couple to the rest of the enclosure in a manner that allows easy removal for servicing.

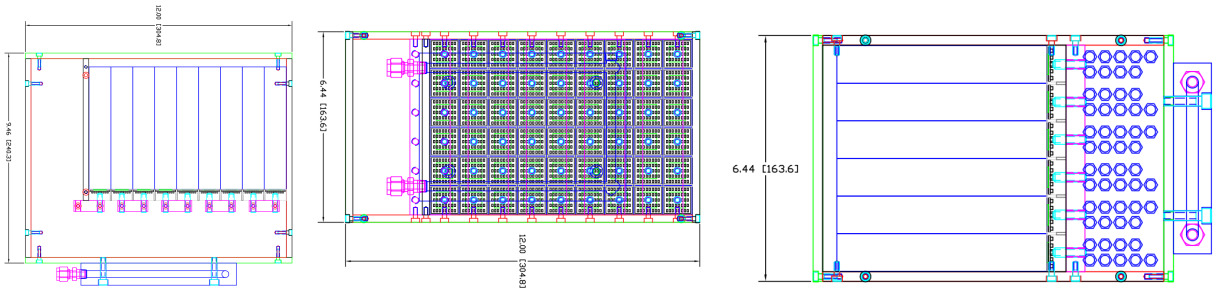

Figure 17.14: Proposed calorimeter light-tight housing. Left: Top view of 9 crystal columns. The storage ring is on the right. The extra space on the left side is used for panels, cooling, servicing. The rear part of the box includes a cooling channel. The front accommodates the calibration plate (not shown here). Mid: Side view of 6 rows of crystals. The conceptual plan for the signal feedthroughs is indicated. Right: Rear view showing the 54 SiPM pre-amplifier / amplifier summing boards.

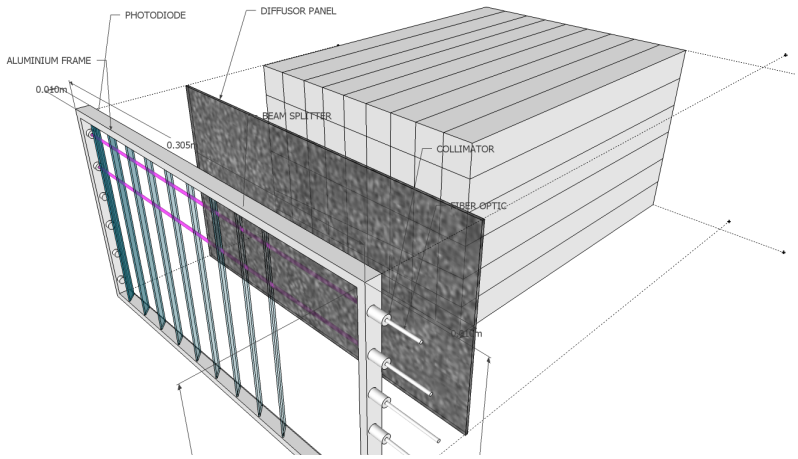

Figure 17.15: Proposed front calibration plate. Six optical fibers penetrate from the inner radial direction. The light is split using a series of beam splitter plates. A diffusor panel spread the light across the crystal front faces. This system is being prototyped.

17.3 Alternative Design Considerations

Two alternative calorimeter material options and one alternative readout option were tested using the Fermilab test beam facility. These included a home-built tungsten-scintillating fiber sampling calorimeter, which is dense ($X_0 = 0.7$ cm), and has a fast-scintillator signal response [2]. Unfortunately, it did not exhibit acceptable resolution in the as-built W:SciFi 50:50 ratio and necessary modifications would reduce the density. Next we tested a custom undoped lead tungstate ($PbWO_4$) crystal. The idea was to reap the benefits of the higher light yield of $PbWO_4$, but to avoid the slow scintillator light component that is prohibitive long for our application. Although its resolution was excellent, the intrinsic pulse FWHM of 15 ns greatly exceeds the 4 ns width measured for PbF_2. There were no benefits of this crystal from cost or other perspectives. A comparison of the pulse shapes from W/SciFi and $PbWO_4$ to our default design of PbF_2 is shown in the right panel of Fig. 17.5.

We also evaluated fast photomulplier tubes as alternatives to SiPMs. The Hamamatsu 9800 is an excellent PMT, having a fairly compact footprint and intrinsic fast response. We are using it regularly to benchmark the intrinsic light output time distribution from our crystals. Unfortunately, it is not a good choice for full implementation in the experiment owing to the need to place these PMTs at least 1.5 m from the calorimeter arrays. Because of the rear-face readout from the geometry, the guides would require a rapid 90-degree bend toward the radial direction and then a second bend to put the PMTs out of plane. The high cost of the PMTs (about 5 times higher than the SiPMs) and the awkward lightguide constraint were deemed to be major issues compared to the development of SiPMs that can be located onboard the crystals.

We are also actively evaluating SiPMs made by different companies, including the latest blue sensitive SiPMs from SensL, STMicroelectronics and other vendors. Hamamatsu has also announced new devices with attractive features such as silicon vias and lower quench resistance. One option to increase the fractional readout area on the rear face of the crystals (presently 144 mm^2 / 625 mm^2 for the 16-ch MPPC) is to use larger area arrays of tileable

SMT packaged SiPMs on custom-designed PCBs. For example, an ideal 5×5 array of 3 mm^2 can be made using devices, which are competitively priced, from STMicroelectronics. Larger area coverage would allow the use of smaller, thus faster pixels, while maintaining sufficient overall photon detection efficiency. We are exploring these options prior to freezing the final design.

17.4 ES&H

The 1300 SiPMs all receive a low-current $\sim$ 70 V bias voltage, which is delivered to the enclosed housing through coax cables from a custom-built bias control system. A laser system will be used to distribute calibration pulses. Apart from the laser hut, the light will be entirely contained in optical fibers, with no possibility of escaping under normal use. The laser hut will be upstairs in the main MC-1 building and appropriate safety requirements will have to be developed to isolate the room and limit access to trained experts. The mechanical weight of the calorimeters is only 40 kg each and they will be supported on railed housings. There is no vacuum insertion, but these detectors will be placed near the storage ring magnetic field and, as such, care must be taken when servicing them to ensure that no magnetic tools are used (a general requirement for any access to the storage ring area).

17.5 Risks

17.5.1 Performance Risks

If the gain stability of the system in actual use fails to meet the specifications, other analysis techniques will have to substitute. This situation happened in E821, where the laser system did not meet the performance goals. Instead, the stability of the gain was able to be determined from the data itself. It is not ideal, but did mitigate the risk.

17.5.2 Schedule Risks

An NSF Major Research Instrumentation proposal was submitted in February, 2013. This proposal would fund the costs of the detector, electronics and data acquisition systems. A substantial matching component was arranged from the domestic and international universities involved. Separately, the Italian groups await approval from INFN for their production of the calibration subsystem. If either of these proposal fail, a greater burden on the Project budget will follow, with possible delays in the schedule.

The production of large numbers of crystals and the procurement of SiPMs and the design and assembly of the bias control system all could encounter vendor or design delays. We do not anticipate this, given the quoted 18-month production time for the longest lead-time item (crystals), but any delay in funding, coupled with a slower production rate could impact the schedule. The demanding performance parameters applied to the bias control and laser gain monitoring system could require revision cycles that impact the schedule. We will try to get ahead of this curve with an aggressive R&D program.

17.6 Quality Assurance

Our local Shanghai University collaborators will inspect the crystals at the factory before acceptance of the products. The crystals will then be shipped to the University of Washington where a sample of them will be tested for transmission efficiency. The crystals will then be wrapped. The SiPM boards will be build and tested using a custom light scanner that can calibrate each device. Finally, the assembly of complete crystal-SiPM blocks will be assembled into an array and tested with a calibrated laser front panel plate. We have a SiPM test laboratory to evaluate the production SiPM boards and will prepare a program using undergraduate students to evaluate each piece in the assembly line.

17.7 Value Management

Competitive quotes have been obtained in order to prepare the MRI Proposal. Local fabrication at universities with largely overhead-free labor will keep costs in check. We are continuing an aggressive program of SiPM vendor evaluations and board designs to obtain a higher fractional readout coverage at competitive cost.

17.8 R&D

We have used test beam opportunities repeatedly as necessary. We intend to use the new SLAC electron test beam to make final measurement of the light yield of crystals with two wrappings and the final SiPM device. In 2013, the Detector Team intends to build a 25-element array (5 x 5) and take it to the test beam for a full evaluation with all systems operational, including prototype digitizers and data acquisition.

We continue to use our local laboratory tools to evaluate SiPM performance and have several student projects ongoing to map out gain functions and other performance characteristics.

References

[1] Sedykh SA, et al. *Nucl. Instrum. Meth. A*455:346 (2000).

[2] R. McNabb, *et al.*, Nucl. Instrum. Meth. A **602**, 396 (2009) [arXiv:0910.0818 [physics.ins-det]].

[3] P. Achenbach, *et al.*, Nucl. Instrum. Meth. A **465**, 318 (2001).

[4] V. Tishchenko *et al.* [MuLan Collaboration], Phys. Rev. D 87, 052003 (2013) arXiv:1211.0960 [hep-ex].

Chapter 18

Tracking Detectors

18.1 Physics Goals

The primary physics goal of the tracking detectors is to measure the muon beam profile at multiple locations around the ring as a function of time throughout the muon fill. This information will be used to determine several parameters associated with the dynamics of the stored muon beam [1]. This is required for the following reasons:

- Momentum spread and betatron motion of the beam lead to ppm level corrections to the muon precession frequency associated with the fraction of muons off the magic momentum and the fraction of time muons are not perpendicular to the storage ring field.

- Betatron motion of the beam causes acceptance changes in the calorimeters that must be included in the fitting functions used to extract the precession frequency.

Uncertainty	E821 value (ppm)	E989 goal (ppm)	role of tracking
Magnetic field seen by muons	0.03	0.01	Measure beam profile on a fill by fill basis ensuring proper alignment
Beam dynamics corrections	0.05	0.03	Measure beam oscillation parameters as a function of time in the fill
Pileup correction	0.08	0.04	Isolate an event library with more than one positron hitting the calorimeter
Calorimeter gain stability	0.12	0.02	Better tracking resolution and E/p measuerments

Table 18.1: Systematic uncertainty goals for the Muon g-2 experiment. Information from the tracking detectors will be used to constrain these in several ways as indicated in the final column. For the first two rows, the tracker plays a primary role. For the last two, the tracker plays a supporting role.

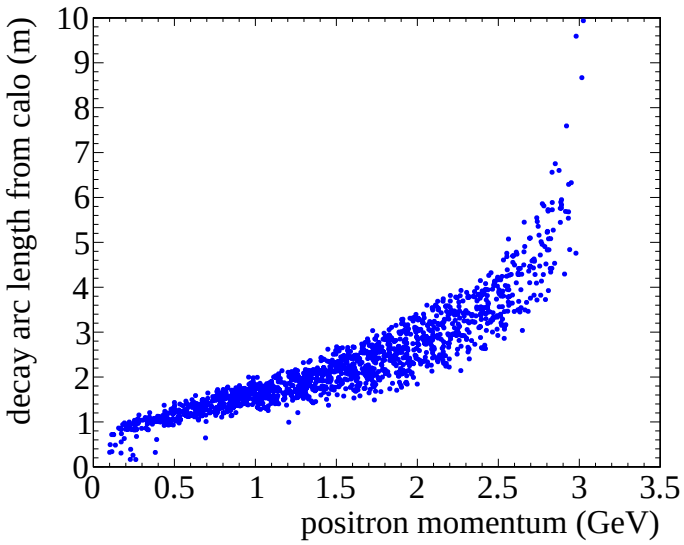

Figure 18.1: Arc length between the calorimeter and the muon decay point as a function of positron momentum.

- The muon spatial distribution must be convoluted with the measured magnetic field map in the storage region to determine the effective field seen by the muon beam.

The tracking detectors also play an important roll in understanding systematic uncertainties associated with the muon precession frequency measurement derived from calorimeter data. In particular, the tracking system will provide a library of time windows that have multiple positrons hitting the calorimeter within a short time period and will provide an independent measurement of the momentum of the incident particle. This will allow an independent validation of techniques used to determine systematic uncertainties associated with calorimeter pileup, calorimeter gain, and muon loss based solely on calorimeter data. The goal for the systematic uncertainties that can be directly determined or partially constrained using tracking information are listed in Table 18.1.

The tracking detectors will also play a leading role in the search for a permanent electric dipole moment (EDM) of the muon. A muon EDM causes the precession plane to tilt out of the horizontal plane. This leads to a time dependent asymmetry in the positron angle that can best be measured using a tracking detector [2].

18.2 Requirements

Requirements for the tracking detectors have been documented elsewhere [3] and are summarized here. The DC nature of the muon beam requires that the tracker perform well over a large momentum range and for muon decay points up to 10 meters in front of the first tracking plane. The arc length between the calorimeter and the muon decay point as a function of positron momentum is shown in Fig. 18.1. The tacker must measure the vertical and

radial profile of the muon beam to much better than a centimeter leading to requirements of below 100 μm resolution per measurement. The long extrapolation from the tracking detector to the muon decay point requires that multiple scattering be minimized and that the material associated with each tracking plane be below 0.1% radiation length.

The trackers are required to reside in vacuum chambers in a vacuum of approximately 10^{-6} Torr and have either a vacuum load on the system below 5×10^{-5} Torr l/s or include a local increase in pumping speed near the tracker. The readout electronics must also be in the vacuum chamber to minimize the need for excessive feedthroughs. The tracker must be located as close to the stored muon beam as possible without interfering with the NMR trolley.

Any perturbations to the magnetic field due to material or DC currents must be below 10 ppm at the center of the storage region over an azimuthal extent of greater than 2°. Any perturbations due to transient currents on time scales below 1 ms must be below 0.01 ppm since these cannot be detected or monitored with NMR [4]. The requirements are summarized in Table 18.2.

18.3 Recommended Design

The recommended design is an array of straw tubes in UV configurations with alternating planes oriented 7.5° from the vertical direction. The DC nature of the beam requires a tracker with multiple planes spread out over as long a lever arm as possible. The required number of planes, along with the need to minimize multiple scattering lead to the choice of a gas based detector. The requirement to place the detectors in the vacuum leads to the choice of straws since the circular geometry can hold the differential pressure with minimal wall thickness.

Parameter	value	comments
Impact parameter resolution	$\ll 1$ cm	set by RMS of the beam
Vertical angular resolution	$\ll 10$ mrad	set by angular spread in the beam
Momentum resolution	$\ll 3.5\%$ at 1 GeV	set by calorimeter resolution
Vacuum load	5×10^{-5} Torr l/s	assumes 10^{-6} Torr vacuum and E821 pumping speed
instantaneous rate	10 kHz/cm^2	Extrapolated from E821
Ideal coverage	16×20 cm	Front face of calorimeter
number of stations	≥ 2	required to constrain beam parameters
Time independent field perturbation	< 10 ppm	extrapolation from E821
Transient (< 1 ms) field perturbation	< 0.01 ppm	invisible to NMR

Table 18.2: Summary of the major requirements and environmental considerations for the tracking detectors.

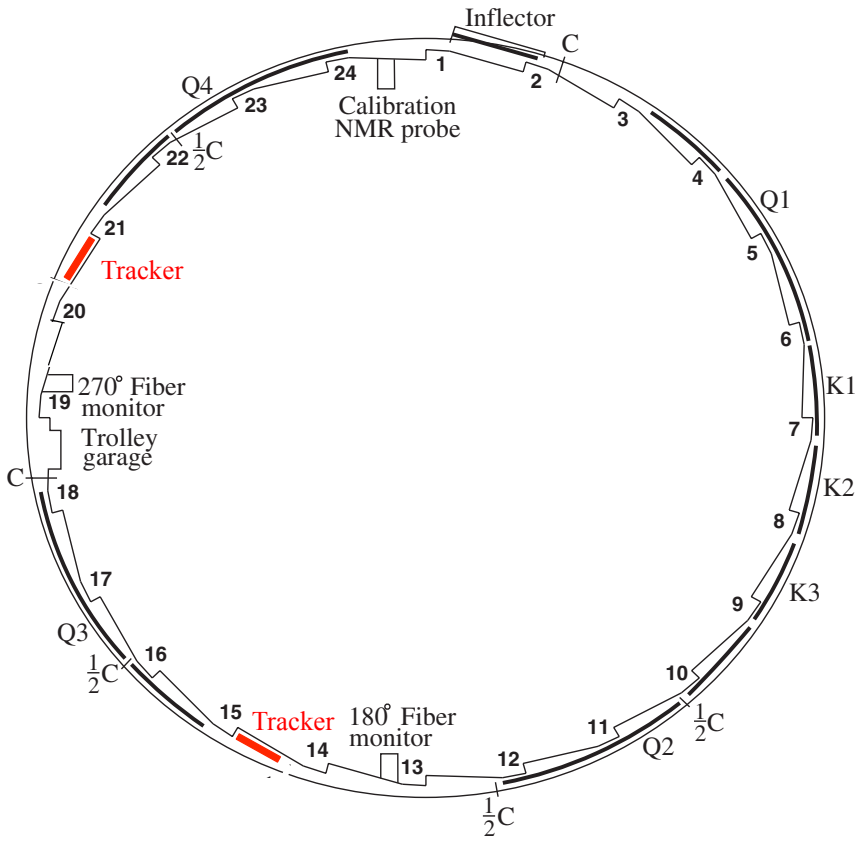

Figure 18.2: Placement of the tracking detectors in the muon storage ring. The detectors can be seen in front of calorimeter stations 15 and 21.

18.3.1 Mechanical Design

The design is two have two tracking detectors placed at approximately 180 and 270 degrees from the injection point as shown in Fig. 18.2. These locations have a clear line of sight to

Material	Aluminized Mylar
Thickness	15 μm
Wire	25 μm gold plated tungsten
length	12 cm
sterio angle	$\pm$ 7.5° from vertical
gas	80:20 Argon:CO_2
pressure	1 Atm
Operating voltage	1400 V

Table 18.3: Summary of the properties of the tracking detectors.

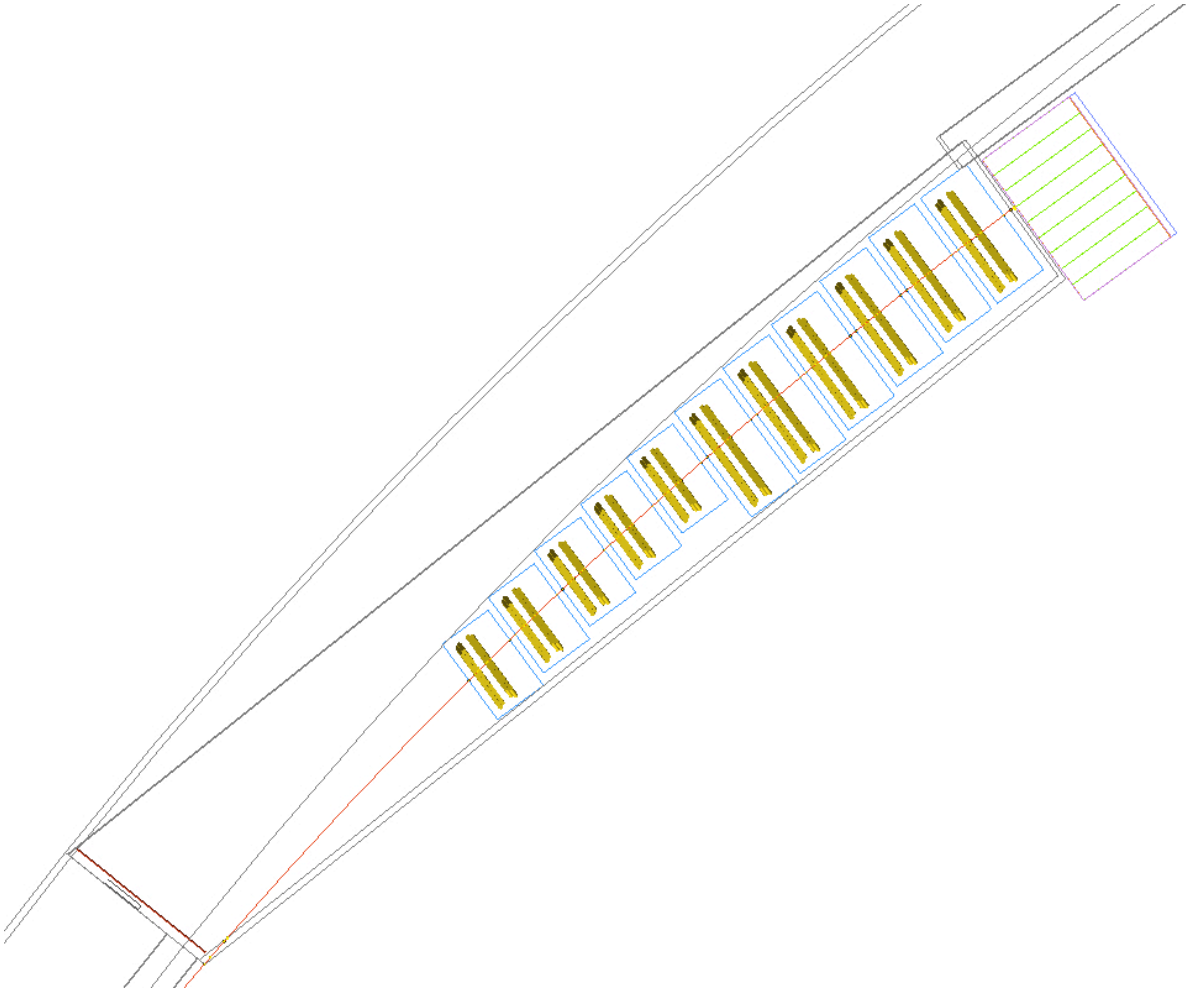

Figure 18.3: Placement of the straw tracking stations in the scalp region of the vacuum chamber.

the muon beam. The vacuum chambers in these locations will be modified to contain large flanges that allow for installation and servicing of the tracking detectors.

Each tracking detector consisting of 11 tracking stations as shown in Fig. 18.3. Each tracking station station has two planes of straws. The planes are in a UV configuration oriented $\pm 7.5^{\circ}$ from the vertical direction. Each plane consists of a closed pack doublet of straws.

There are two types of station to account for the decreasing area in the scalloped region of the vacuum chamber. The first station is 10 cm wide and contains 64 channels. The second type is 14 cm wide and contains 96 channels. The total channel count including prototypes and spares is listed in

A diagram of the largest station is shown in Fig. 18.4. The active hight of each station is 10 cm. A 2.5 cm high gas manifold sits above and below the the straws and houses the readout electronics. The stations are self supporting and sit on the bottom of the vacuum chamber on a thin aluminum plate that locks the stations in place controlling the station

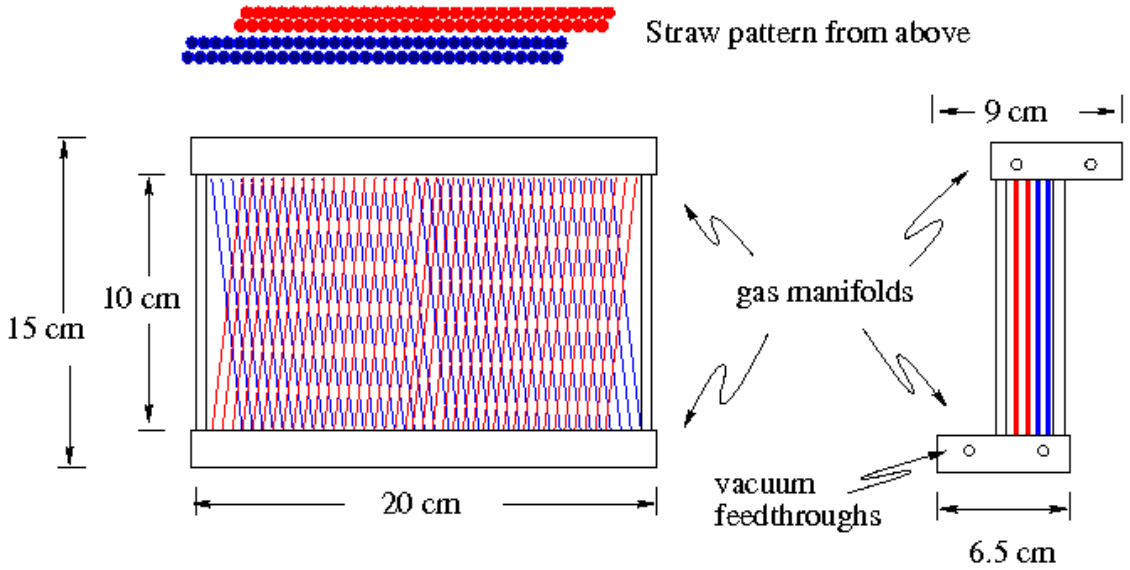

Figure 18.4: Diagram of the largest tracking station. The station is 32 straws wide. The figure on the left is the vertical-radial view. The figure on the right is the vertical azimuthal view. Needs to be updated to a 24 station

alignment.

add table for straw count

We have chosen a system based on Mu2e straws [5]. Each straw is 5 mm diameter and 12 cm long. The straw wall is made of two layers of 6 μm Mylar, spiral wound, with a 3 μm layer of adhesive between layers. The total thickness of the straw wall is 15 μm. The inner surface has 500 Å of aluminum overlaid with 200 Å of gold as the cathode layer. The outer surface has 500 Å of aluminum to act as additional electrostatic shielding and improves the leak rate. The straws are attached to the manifolds at the ends and tensioned to 50 grams to compensate for expansion under vacuum. The straw parameters are summarized in Table 18.3.

Add paragraph and table for material budget.

The sense wire is 25 μm gold plated tungsten centered on the straw. The wire is tensioned to 10 grams and supported on the ends. The wire will be held at a voltage of 1400 V. The drift gas is 80 : 20 Argon:CO_2. The requirements of the best position resolution and the relatively low rates per straw allow us to not require a fast, flammable gas.

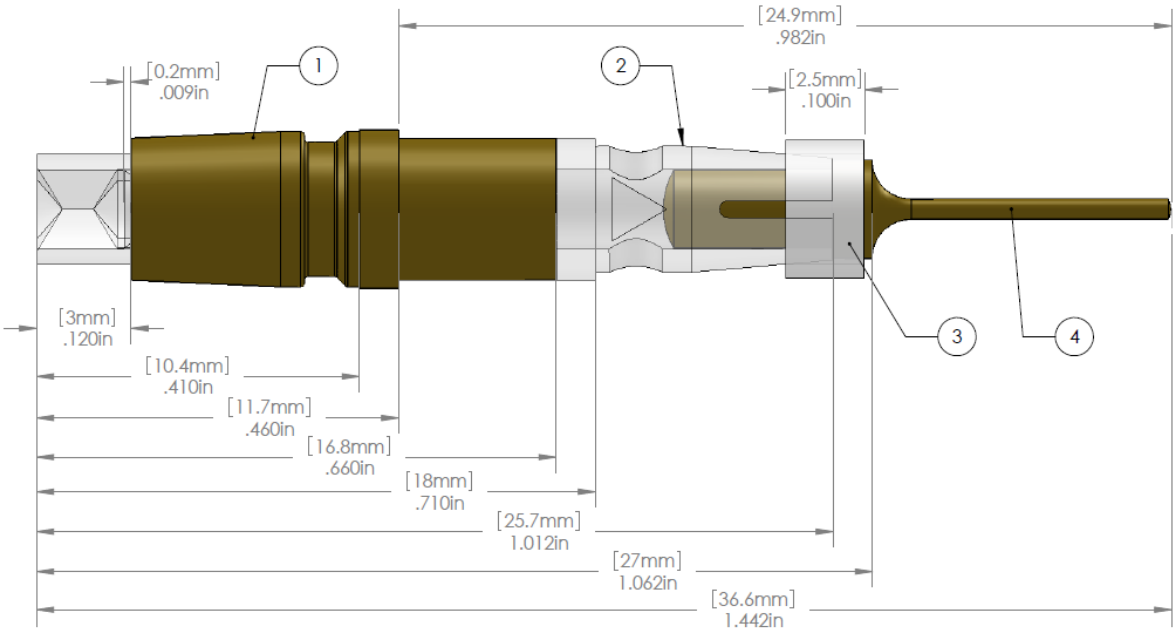

Figure 18.5: Straw terminations.

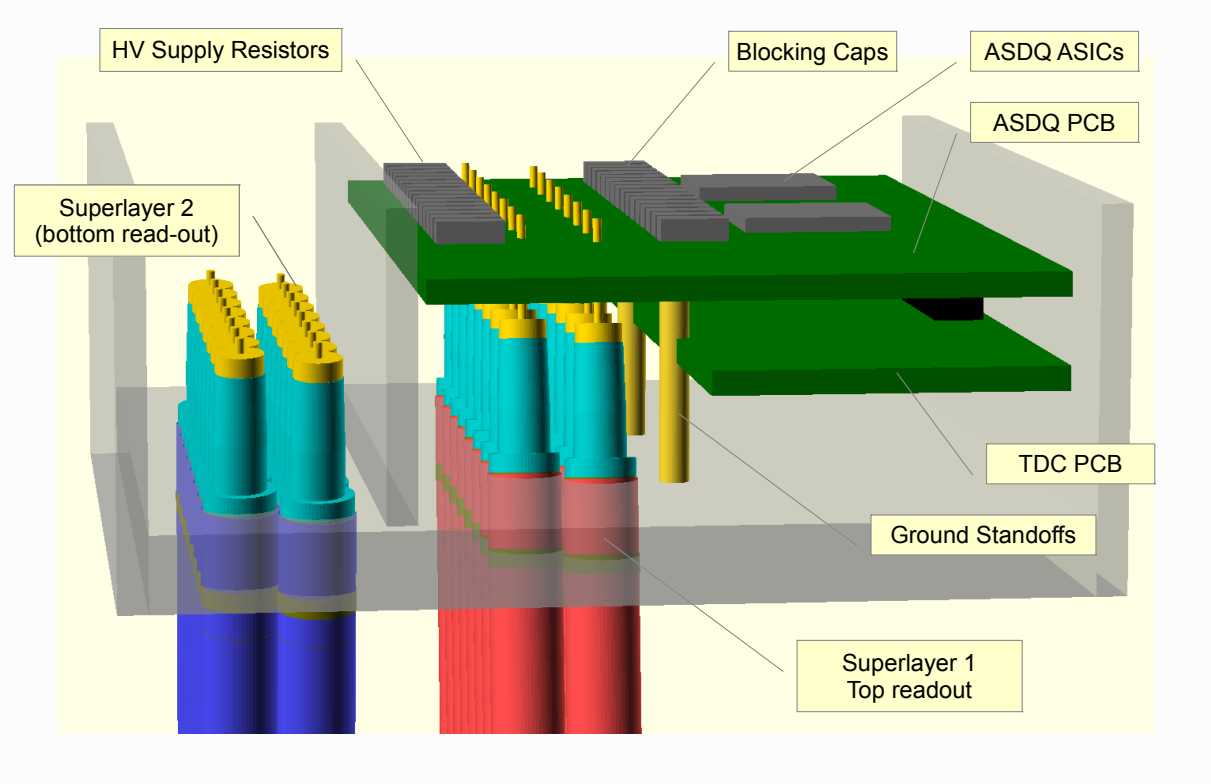

Figure 18.6: Gas manifold and electronics housing for the straws.

The straw terminations are shown in Fig. 18.5 are an iteration of the terminations successfully deployed by the Brookhaven E781 experiment [6] and consist of an aluminum collar with an injection molded ULTEM insulator. The insulator contains a V groove to position the wire and an aluminum pin crimps the wire in place and holds the wire tension.

The straw is attached to the collar with a bead of silver epoxy to provide the electrical connection and a bead of standard epoxy to provide mechanical strength. A similar blend is used to connect the straw terminations to the manifolds.

The gas manifolds for the straws are shown in Fig. 18.6. They are approximately 2.5 cm high and contains separate gas paths for the U and V straws. The gas is brought into the manifold through a vacuum penetration through the flange and the manifold. The gas flows through the straws and then over the readout electronics. The gas is required to dissipate approximately 5 Watts from the readout electronics. The gas then flows out a wide 5/8 in tube that also carries 2 twisted pair cables that carry low voltage, high voltage and control signals to the readout electronics and carry the digitized signals out of the straws.

18.3.2 Readout Electronics

Channels per readout board	32 or 48
Gas Gain	4×10^4
Number of Primary Electrons (P.E.) for a typical track	41 pe
Signal amplitude for a typical track	256 fC
Operating threshold in P.E.	10 pe
Operating threshold	32 fC
Capacitance	1 pF

Table 18.4: Tracker Readout parameters

The basic instrumentation parameters which drive the design of the readout are given in Table 18.4. The readout electronics for a stereo layer pair consists of two stacked PC boards, a readout board and a TDC board. The readout board contains two or more ASDQ ASICs[7] which provide amplification, shaping, discriminator and charge measurement for eight straws. The ASDQ outputs are digitized by a TDC implemented in a field-programmable gate array (FPGA).

The tracker wire connection diagram is shown in Figure 18.8. The HV terminal provides high voltage (1400V nom.) to each tube through a 100k current limit resistor. HV is blocked by a 2kV SMT capacitor (value *t.b.d*). A protection circuit consisting of four Schottky diodes in a 2x2mm DFN package provide bipolar protection for both the primary and inverting ASDQ inputs. A 10 ohm series resistor limits peak current.

The ASDQ provides eight channels of full analog signal processing between the chamber and the TDC. Though developed for the CDF Central Outer Tracker, it provides a good match to the muon g-2 tracking detector requirements. It provides fast charge collection ($\approx$ 7ns), good double pulse resolution of $\approx$ 30ns, low power ($\approx$ 40 mW/ch) and low operational threshold ($\approx$ 2 fC). Baseline restoration and ion tail compensation using the pole-zero cancellation technique are provided. The output of the ASDQ is eight digital differential

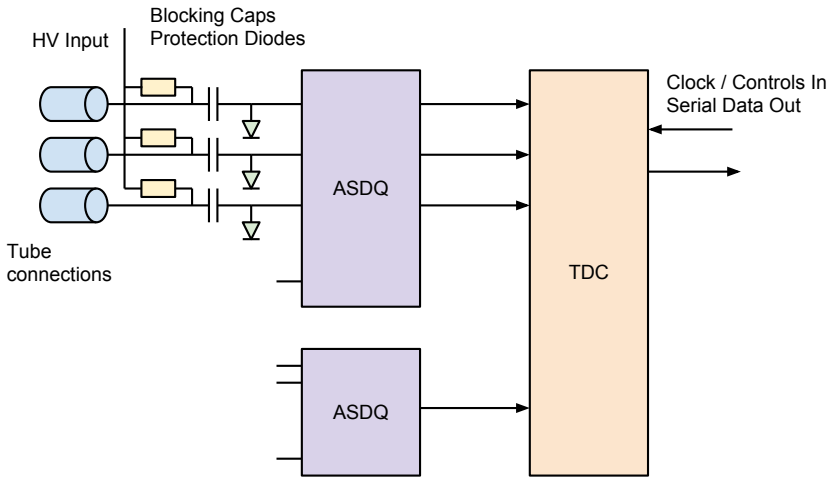

Figure 18.7: On-Chamber Electronics Overview

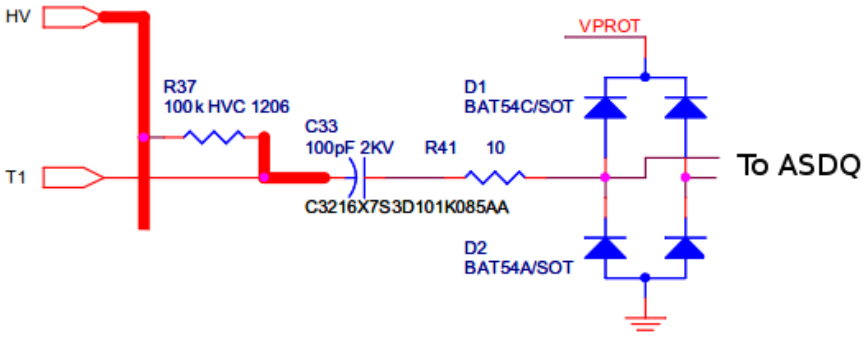

Figure 18.8: Input Schematic Detail

signals, with leading edge representing the threshold crossing time and the pulse width proportional to input charge.

A 16-channel TDC with 625 ps LSB is implemented in an Altera EP3C5F256C6 FPGA, with the initial design using about 50% of the FPGA logic resources. A reference clock of 10 MHz is provided externally on an LVDS signal pair with multiplexed trigger and control signals. The clock is multiplied internally to a four-phase 400 MHz clock for time measurement and internal operation. Up to 2k TDC hits are stored on-chip and read out over a single serial link at 25 MHz.

Power, clock, control and readout for each chamber is provided by a tracker readout module (TRM), implemented as an advanced mezzanine card[8] (AMC) and mounted in a MicroTCA[9] crate. A block diagram is shown in Figure 18.10. An FPGA in the TRM receives clock and control signals from the MicroTCA crate controller via the MicroTCA backplane and distributes them to each station. DAQ data is received from the chambers and decoded and buffered in the FPGA, which also provides a gigabit Ethernet interface via

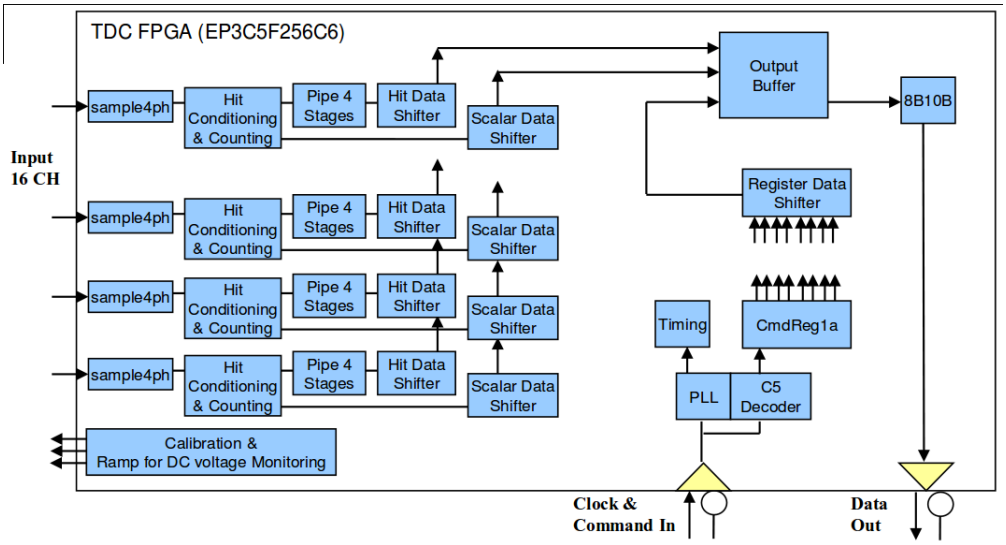

Figure 18.9: TDC Block Diagram

the MicroTCA hub controller. Cables carry DC power from the TRM to the top and bottom of each chamber's readout electronics, along with clock, control and readout signals. Power for the on-chamber electronics is switched and current-limited on the TRM.

Up to 12 TRM modules are mounted in a MicroTCA crate, as shown in Figure 18.11. Control and configuration commands are provided to all modules by a commercial MicroTCA hub controller (MCH) module via switched gigibit Ethernet and intelligent platform management bus (IPMB)[10] interfaces. A custom AMC13 module[11] developed for the CMS experiment distributes clock and timing signals and reads out data from the TRMs.

18.4 Performance

The expected performance of the tracker conceptual design is determined by a simulation. The performance of a single straw is determined using GARFIELD [12]. This program simulates the propagation of electrons and ions in a gas in the presence of electric and magnetic fields. The geometry of the system is determined using a full GEANT4 [13] model of the g-2 storage ring that includes the proper physics model to simulate muon storage, precession, and decay. The performance of the tracker is determined using a fast tracking software package that takes the positron hit positions from the GEANT4 simulation, applies resolution from GARFIELD and multiple scattering corrections, determines the positron trajectory, and extrapolates back to the point of tangency to determine the muon decay position.

The $x - t$ relation and single straw resolution determined from GARFIELD are shown in Fig. 18.12. The average resolution is found to be approximately 100 μm. The efficiency to reconstruct at least 5 hits as a function of momentum and as a function the muon decay distance is shown in Fig. 18.13. There is sufficient coverage at all momenta that can be used to determine beam parameters. The loss of efficiency at lower momenta is due to the fact that the lowest momentum positrons originate very close to the calorimeter and it is difficult to fit

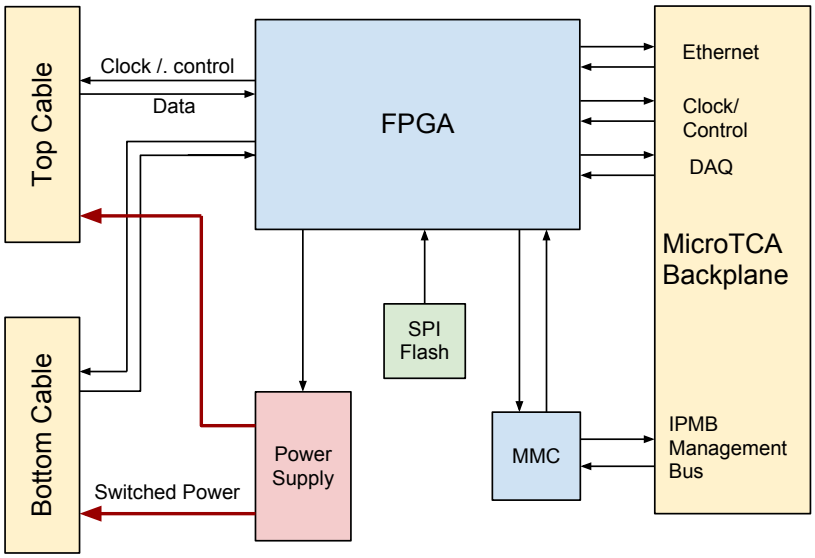

Figure 18.10: Tracker Readout Module Block Diagram

enough tracking stations close enough together. The distance between stations is currently dominated by the area necessary for the readout PCBs. In the final design iteration we will investigate different geometries that could increase this efficiency.

The momentum resolution, muon decay position, and positron vertical angle resolution are shown in Figs. 18.14,18.15,18.16, and 18.17. The muon decay position resolution is roughly 3 mm in the radial direction and 2 mm in the vertical direction. Both resolutions become significantly worse above 2.6 GeV. In this region, the muons are decaying between 5 and 10 meters from the first tracking plane and the large lever arm makes a more precise determination impractical. The momentum resolution is lower than for a typical gas based system but is well below the resolution of the calorimeter which satisfies the requirements. The vertical angle resolution is also well below the requiements.

A single straw prototype has been constructed to verify key features of the GARFIELD simulation and to gain experience with the assembly procedure. The straw is read out using an ASDQ chip that has an analog output after directly before the discriminator. The straw is illuminated with an Fe^{55} source with produces on average 230 primary electrons in our gas mixture. The signal peak after amplification and shaping is shown in Fig 18.18. The turn-over in the plot is due to clipping in the readout electronics. From this we expect that a typical positron depositing 41 primary electrons will correspond to a signal peaking at about 16 mV at an operating voltage of 1400 V which should be well above noise.

The mechanical integrity of the design is modeled using ANSYS. Particular attention was given to the grounding plate in the manifold. The plate should be as thin as possible to maximize the vertical acceptance of the detectors and the straw pitch should be as close to the straw diameter as possible to avoid large gaps. However, the plate must be thick enough to hold the straw tension and the 1 ATM pressure differential.

The final conceptual design calls for a x mm plate thickness and a 5.5 mm straw pitch.

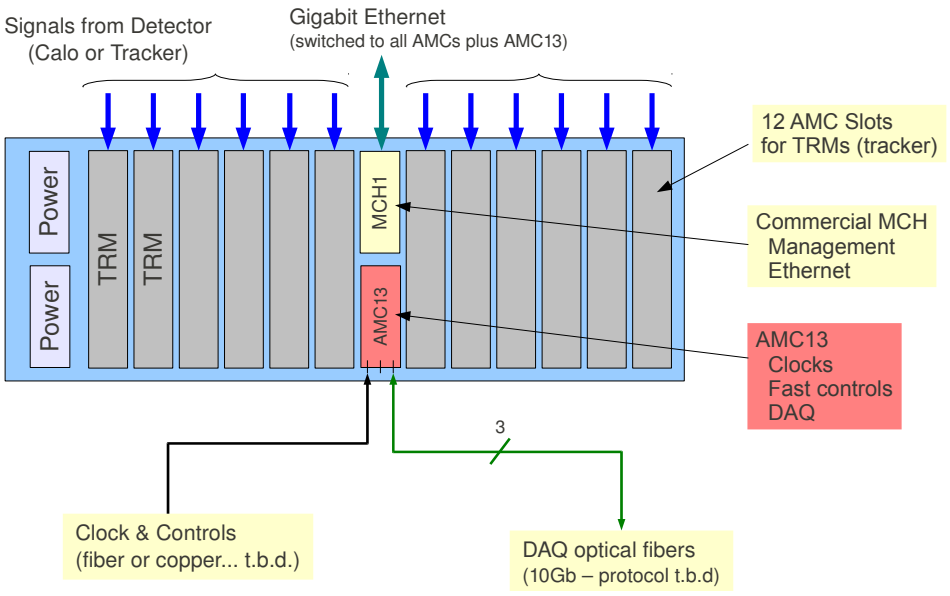

Figure 18.11: MicroTCA Crate

The stresses on the manifold are shown in Fig. 18.19. The model indicates that the manifold can safely hold the stresses but the current deflection gradient needs to be reduced. This will most likely be accomplished in the next design iteration by adding a rib structure to the inside of the large manifold.

The front end electronics are based on the ASDQ chip which has been used in several experiments and the performance is well documented. A first version of the TDC code exists and an LSB of 0.6 ns has been achieved. The specifications for data size and transfer rates are well below the limits of the micro-TCA crate specifications.

Add EDM paragraph here.

18.5 Alternatives

The two leading alternatives to a straw based system for the tracker are both Silicon based. The first would use 300 μm Hamamatsu single sided strip sensors. These sensors were purchased for the Dzero Run IIb detector upgrade but never used. Sufficient sensors are in hand to build the g-2 tracker. The readout would be based on the FSSRII chip originally designed for BTeV and now being used for instrumentation upgrades for the JLab 12 GeV program. Tracking stations could be made with two sensors at a small stereo angle for a total material budget of 0.5% X_0 per station.

The second alternative would use the 50μm thick Mimosa 26 pixel sensor that has been developed with ILC R&D funding. There is about 25% dead space on the chip which would

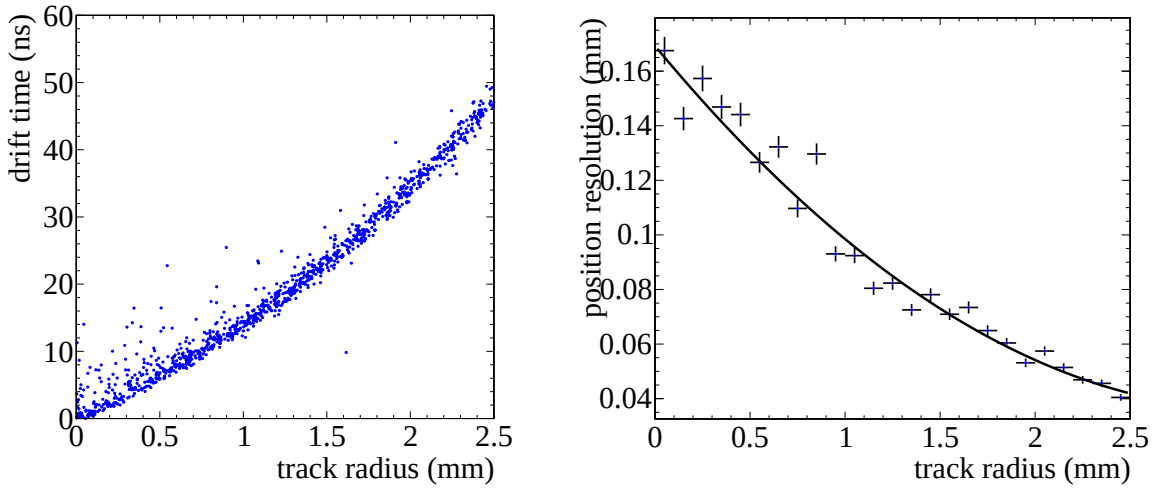

(a) (b)

Figure 18.12: (a): Time versus distance relation in a single straw predicted by GARFIELD. (b): The position resolution determined from GARFIELD for a single straw using the derived x-t relation.

require a doublet structure. Material is also needed in the active region for cooling and for flex cables. A thermal model of the device indicates that heat can be adequately dissipated if the two layers are mounted on blocks of 2.5 mm thick Si foam. After the Si foam and flex cables are added, the material budget is also close to 0.5% X_0 per station.

If we had a well defined interaction point and could build something like a 4 layer detector, either of these two alternatives would be preferable to straws. However, the DC nature of the beam requires us to have a multi layer device to sufficiently cover the momentum spectrum of the positrons. Building this out of the Silicon options above would add far too much material and the effects of multiple scattering would severely compromise our ability to extrapolate the positron trajectories all the way back to the muon decay position.

For the amplifier, besides the ASDQ chip, we explored using desecrate components or building an ASIC. Discrete components were ruled out due to space considerations and also due to power consumption. An ASIC is an expensive alternative particularly since the ASDQ chips are free, but it has the advantage that we could control all material used in the chip to avoid magnetic components such as tin. However we brought the ASDQ and FPGA chips to a 1.5 T test magnet at the Fermilab Technical division and determined that these chips have magnetic properties well below our specifications.

For the TDC, we considered commercially available products such as the 128 channel CAEN 767 or 1190 model multi hit TDCs. This would require bringing all signals out of the vacuum through some sort of feedthrough system. We investigated the feedthroughs being designed for liquid Argon but these would have difficulty operating at the g-2 vacuum of 10^{-6} Torr. The current design of an FPGA based TDC is much more simple and cost effective.

For the station geometry, we considered a more closed packed system that could be constructed using existing vacuum ports without requiring modifications to the existing

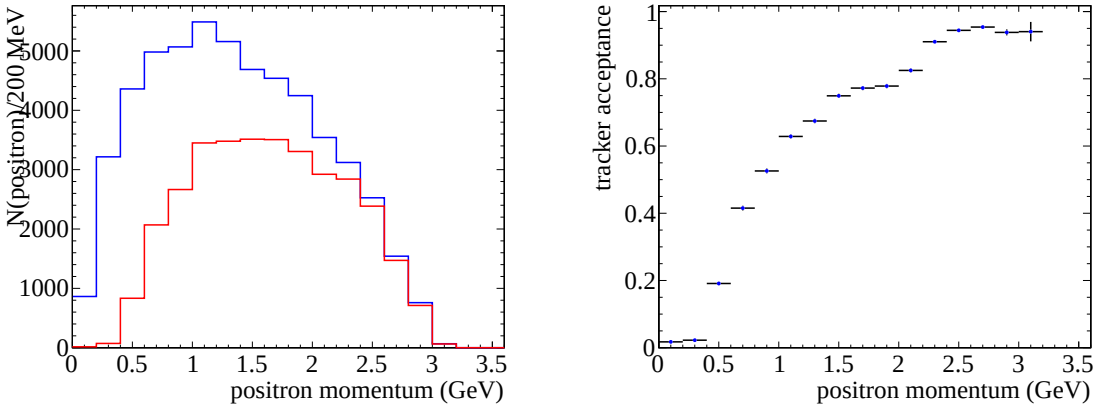

(a) (b)

Figure 18.13: (a): The positron momentum spectrum for positrons incident on the front face of the calorimeter (blue) and also with sufficient hits in the tracking detector to form a track (red). (b): The ratio of the two distributions giving the relative efficiency between the tracker and the calorimeter as a function of positron momentum.

vacuum chambers. A working solution was found for a detector that would have a total length of 0.5 meters. However, simulation indicates that the 1 meter lever length we have now is required to gain useful information on the higher momentum tracks that have the longest extrapolation back to the muon decay point.

There are two alternatives still under consideration. The conceptual design calls for a closed packed doublet geometry with each layer offset by half a straw diameter. Once the required gap between straws is considered and the fact that the resolution is worst at the center of the straw, we would like to consider alternative offsets between layers. One option we will consider is having the two layers offset by 1/3 a straw diameter.

The tracking simulation studies indicate that we have better resolution on the vertical parameters of the beam than the radial parameters. In general, the radial parameters have a greater effect on the g-2 systematic uncertainties since they directly effect the acceptance of the calorimeters. The original stereo angle was chosen based on calculations of the error on parameters by hand. The full tracking simulation indicates that we may be able to reduce the stereo angle and improve the vertical resolution without adversely effecting the horizontal resolution.

18.6 ES&H

The g-2 tracker is similar to other gas-based detectors that are commonly used at Fermilab and are identical in many cases to the Mu2e system. Potential hazards include power systems and compressed gas. The gas will permeate at a small level inside the g-2 vacuum and come in contact with the quadrupole high voltage. Any gas leak in the experimental hall with also bring the gas in contact with the high voltage stand-offs and feed-throughs of the kicker and

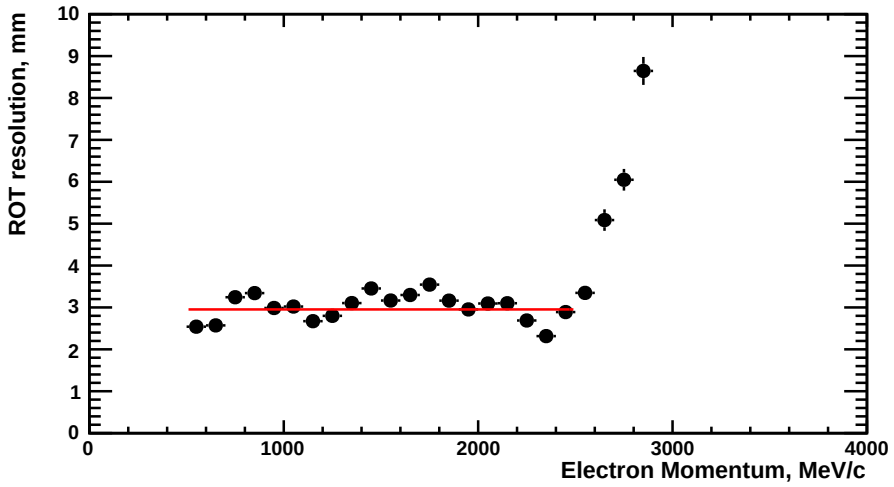

Figure 18.14: Resolution on the radius of the positron at the point of tangency to the central muon orbit as a function of positron momentum. The red line is a fit to the points in the region below 2.5 GeV.

quadrupoles. Because of this, and because using non-flammable gas appears to work, we are precluding the use of flammable gas. These and all other hazards have been identified and documented in the Muon g-2 Preliminary Hazard Analysis.

The detector requires both low voltage, high current an high voltage, low current power systems. During normal operation, the tracker will be inaccessible inside the storage ring. Power will be distributed to the tracker through shielded cables and connectors that comply with Fermilab policies. Fermilab will review the installation prior to operation.

Gas that will be used for the tracker will be kept in DOT cylinders in quantities limited to the minimum required for efficient operation. The cylinders will be stored in a dedicated location appropriate to the type of gas being used. The storage area will be equipped with fire detection and suppression system. The installation, including all associated piping and valves, will be documented and reviewed by the Fermilab Mechanical Safety Subcommittee.

The detector itself does not have any radioactive sources. However, Fe^{55} sources will be used to measure the gain of the straws before installation. Usage of radioactive sources will be reviewed to ensure adherence to Fermilab safety policy. In particular, the sources will be monitored and stored and we see no opportunity for producing mixed waste.

Solvents such as ethanol will be used to clean components before assembly and epoxy resins will be used in the assembly process. All chemicals will be clearly labeled and stored in approved, locked storage cabinets and will adhere to the Fermilab safety policy.

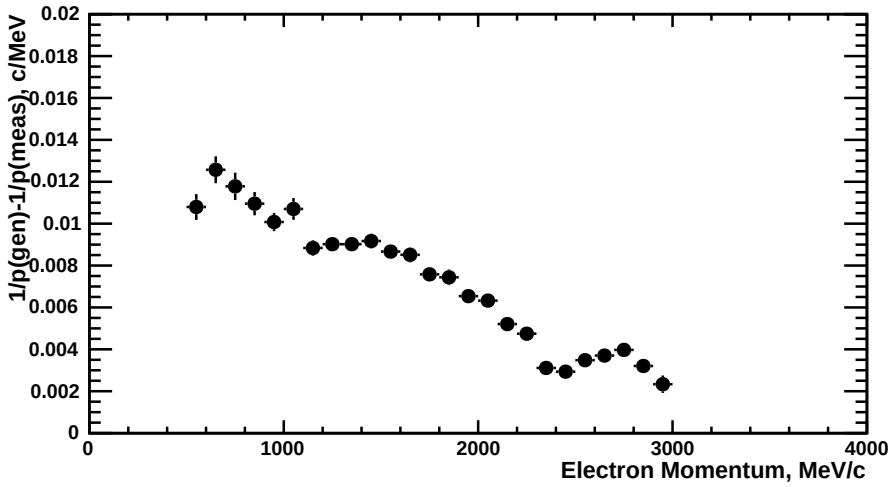

Figure 18.15: Resolution on the radius of the track curvature as a function of positron momentum.

18.7 Risks

18.7.1 Performance Risk

The performance of the system relies on the single straw resolution. Simulation indicates that the resolution is adequate to meet the goals of the experiment however the final performance will be a factor of many variables, particularly how well the system is assembled. This risk is being mitigated by perfuming cosmic tests of prototypes and a beam test of a full station prototype in Fall 2013. This will give a very good indication of the single straw resolution in a real system and will give us sufficient opportunities to make adjustments to the design before the project is baselined. Several quality control procedures will be put in place such as x-raying the detectors to determine proper positioning of the wires to insure that the resolution is not compromised during assembly.

The detector will require precise alignment with respect to the central muon orbit. Poor alignment could easily become the dominant source of error in the tracking measurement. The alignment can be determined in-situ using positrons but this can take a long time and can not be used to monitor alignment in real time. This risk will be mitigated by taking complete trackers to a beam test before final installation to determine the relative alignment between stations. Dedicated muon fills will also be taken on a regular basis where the muon losses are intentionally increased. These muons are essentially straight when they go through the tracker and can be used to verify the inter-station alignment as well as determine the alignment of the system with respect to the beam. We are also investigating adding 3-D Hall probes inside the gas manifolds for the tracking stations. The precision field is known well enough so that any change in the Hall probe readout would constitute a change in the tracking station position.

The tracker has been designed assuming a max instantaneous rate of 10 hKz/cm^2. This value is extrapolated from measurements at the Brookhaven experiment. The Brookhaven

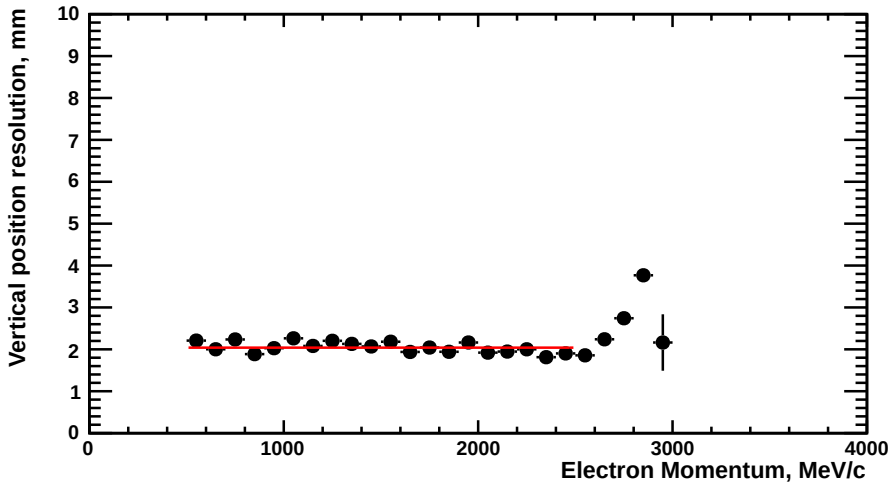

Figure 18.16: Resolution in the vertical muon decay position as a function of positron momentum. The red line is a fit to the distribution below 2.5 GeV.

experiment had significant contamination from pions that lead to a large hadronic flash at the beginning of the fill. This pion contamination has been removed from the Fermilab experiment but there is still a possibility that there will be some unaccounted for background that leads to unacceptable rates. The straws have been designed to operate with CF_4 so a after gas could be used to deal with this. We are also investigating using a circuit to reduce the gain of the straws during injection. This is complicated and would require electrical engineering resources to design if we are required to go down that path.

The system of collimators used to scrape the muon beam after injection is partially in the line of sight of the tracking detectors. This would limit the acceptance of the tracker and potentially cause high backgrounds early in the fill. To mitigate this risk, we are perfuming studies to determine alternative locations for the collimators and working closely with the groups associated with the collimator system.

18.7.2 Technical and Operational Risk

The greatest technical risk is that the tracking system will in some way effect the precision magnetic field of the storage ring. This risk is being mitigated in several ways:

- All scientists, engineers, technicians, students, and vendors involved in the design and construction of the system are educated on the importance of the magnetic properties of the system.

- The specifications are clearly stated in terms of the static and dynamic effects on the field. These have been documented and agreed on by the collaboration.

- Individual components are taken to an existing 1.5 T test magnet and their static magnetic properties are verified to be within specifications.

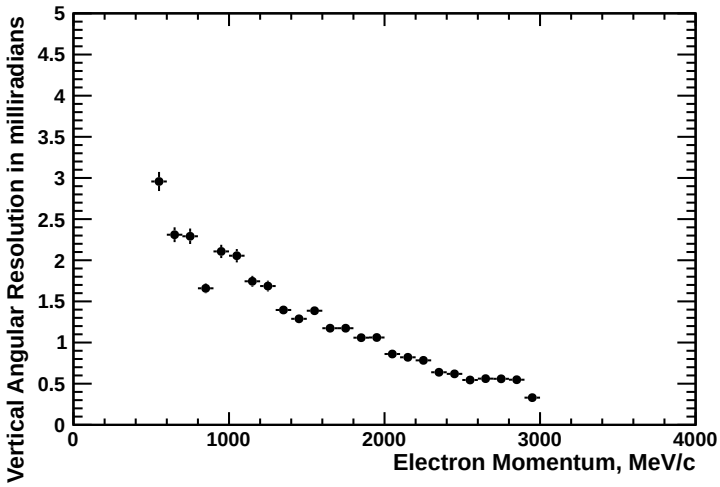

Figure 18.17: Resolution on the vertical positron angle as a function of positron momentum.

- Full magnetic simulation of the detector using OPERA is added to the existing storage ring OPERA simulation to verify that any static effects can be shimmed out of the field using the existing shimming kit.
- The full detector will be tested in a test solenoid that is being shipped from LANL to Fermilab specifically for this purpose.
- A fast coil will be designed to measure the size and time structure of any transient magnetic fields being produced by the electronics.

The vacuum specifications for the g-2 storage ring are set by the electrostatic quadrupoles inside the storage ring. The combination of the electric field from the quads and the magnetic field from the g-2 magnet leads to regions where photoelectrons can be captured in Penning traps. These electrons can eventually interact with residual gas molecules leading to avalanche and sparking. This is the number one factor influencing the lifetime of the quadrupole plates.

For μ^+ operation, a vacuum of 10^{-6} Torr is required. If μ^- running is required or if the quadrupoles are operated at a greater HV to move to a different tune point, the vacuum may need to be decreased to 10^{-7} Torr. The leak rate of the straws has been measured by Mu2e and indicates that 10^{-6} Torr can be achieved. To mitigate the risk of needing to operate at a higher vacuum we are designing the ability to add higher capacity to the pumping speed near the tracking detectors.

Contaminated gas is a serious risk for any drift chamber. This risk is mitigated in several ways. First, Ar:CO_2 is one of the least prone gasses to harmful contaminants. Second, by performing a detailed analysis on each batch of gas. Finally, monitoring chambers will be included in the system and will be illuminated with radioactive sources to give early warning of problems.

A broken wire will cause an entire plane of a station to be inoperable. A broken straw will cause an entire station to be inoperable. To mitigate this risk, the system is being designed

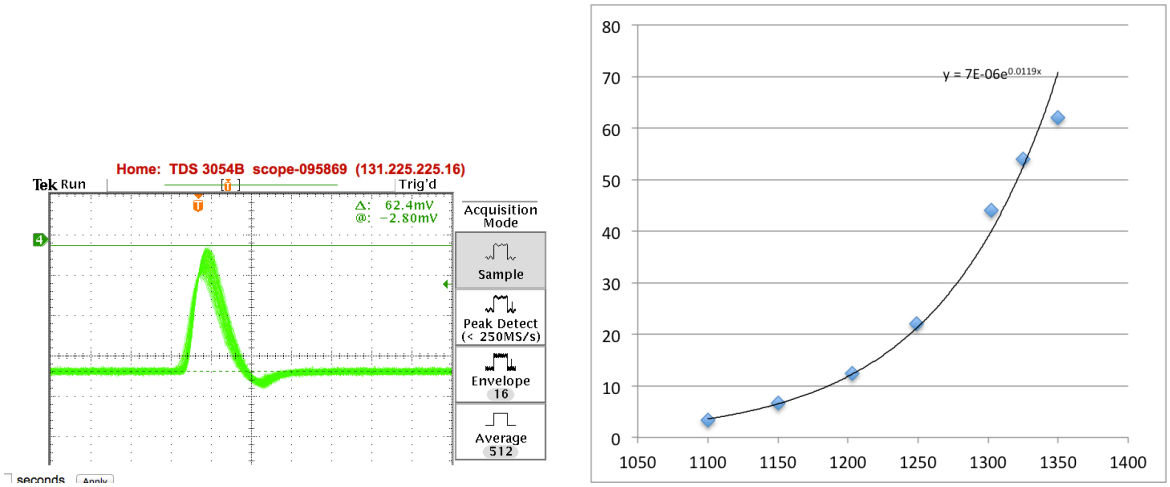

(a) (b)

Figure 18.18: (a): The signal from a Fe^{55} source after amplification and shaping corresponding to 230 primary electrons at an operating voltage of 1400 V. (b) The peak voltage of the Fe^{55} signal as a function of applied voltage.

in a way so that a damaged station can be easily removed and replaced with a spare with approximately 1 day lost to reestablishing the vacuum. We anticipate breaking vacuum at least once every several months to service the NMR trolly so as long as the frequency of problems is much less than this, there is no risk to the run schedule.

18.8 Quality Assurance

Proper quality assurance is essential yo construct a tracking detector that meets the Muon g-2 requirements for performance and reliable operation. Quality Assurance will be integrated into all phases of the tracker work including design, procurement, fabrication, and installation.

Individual straws must be leak tight, straight, and have the proper wire tension. The straws will be leak tested before being installed. The straws will be connected to a clean gas system and over-pressured. The leak rate will be measured over an appropriate time interval by measuring the pressure drop. After the assembly of a station, the entire station will be leak tested again.

The straws must maintain their shape and be mounted at the proper stereo angle to operate efficiently and to maintain an appropriate distance between the wire and the grounded Mylar surface to avoid breakdown. Straws will be visually inspected for roundness and straightness before assembly. Flawed straws that escape detection during visual inspection can be identified by non-uniform gas gain and resolution. This will be done as part of the wire position measurement.

The appropriate tension must be applied and maintained in a straw for efficient, stable operation. Tension is applied through calibrated mechanical force but can be lost through

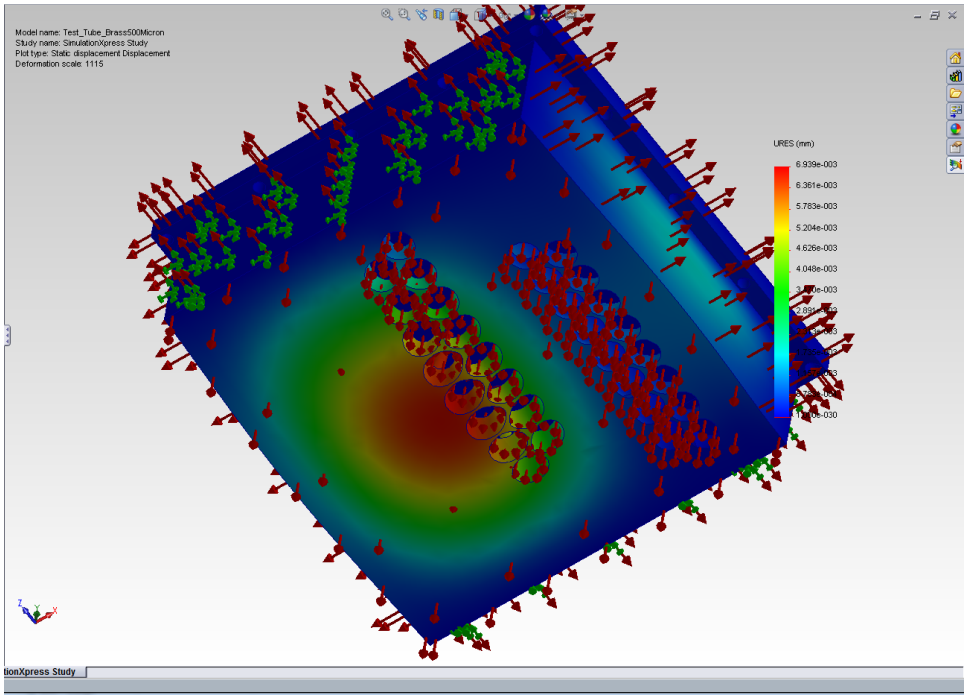

Figure 18.19: ANSYS model of the stresses in the gas manifold due to the straw and wire tension and the 1 ATM differential pressure.

relaxation mechanisms. Both wire and straw tension will be measured after assembly using vibrational resonance techniques appropriate to our short straws.

All electronics components will be tested prior to installation on the tracking stations including a suitable burn-in period. The high voltage circuits will be tested for leakage current. The threshold characteristics of each channel will be tested with a threshold scan. A noise scan will be performed for various threshold settings to identify channels with large noise fractions. The FPGA TDCs will be validated by comparing their output to commercial TDC devices with higher resolution.

18.9 Value Management

The tracker technology for Muon g-2 is well established and has been implemented in other high energy and nuclear physics experiments. Value management principles have been applied over time during the development of the technology. Value management moving forward is mainly related to labor costs since the straw tracker assembly will be labor intensive. We have identified collaborating institutions with students who can perform a large fraction of the assembly work at minimal cost. This requires more work up front in engineering to design parts that do not require highly skilled technicians for assembly but this is in any case part of best practice engineering.

We are subcontracting engineering to university engineering departments and using Fermilab engineering resources to perform independent design reviews before production or

procurement. This keeps the overall engineering costs low while maintaing the standards of Fermilab engineering.

We are also in the process of performing a full analysis of determining the beam parameters from the tracking system. While the default configuration calls for two tracking stations around the ring separated by 90 degrees, this study may indicate we need more than two stations or that the information from one station is sufficient.

The back-end readout electronics and data acquisition for the tracker are equivalent to those used for the calorimeters. This simplifies the design and operation of the system. However, once the final specifications are known, we will investigate possible cost savings by using different system components. Current FPGA technology is sufficient to meet the needs of the tracker electronics. These will be purchased once they are no longer the most current devices which should lead to significant cost savings. Sufficient spares will be purchased to ensure the stock for the lifetime of the experiment.

The straw terminations require injection molded pieces. The cost of these pieces is almost entirely driven by the cost of the mold and so design iterations are costly. To mitigate this, we intend to first produce all injection molded pieces with a 3-D printer and construct straws with the printed pieces to validate the design before the molds are procured.

18.10 R&D

Work is well underway on straw termination, tensioning, and alignment procedures. Three, 4 to 8 channel prototypes have been constructed to gain experience with proper handling and assembly procedures. A full type-8 station is currently under construction that will include a prototype ASDQ readout board and an FPGA evaluation board. This will be tested in-vacuo using cosmics and in a beam test scheduled for Fall 2013.

References

[1] G. W. Bennett *et. al.* (Muon $g-2$ Collaboration) Phys. Rev. D 73, 072003 (2006).

[2] G. W. Bennett *et. al.* (Muon $g-2$ Collaboration) Phys. Rev. D 80, 052008 (2009).

[3] B.C.K. Casey, GM2-doc-512-v1.

[4] B.C.K. Casey, D. Kawall *et. al.* GM2-doc-xxx-vy.

[5] R.E.Ray, Mu2e-doc-1169-v21

[6] S. Graessle *et. al.*, Nucl. Inst. Meth. A 367, 138 (1995).

[7] T. Affolder *et. al.*, Nucl. Inst. Meth. A 526, 249 (2004).

[8] "AdvancedMC$^{\text{TM}}$Mezzanine Module" AMC.0 Rev 2.0, PICMG.

[9] "MicroTCA®" Rev MTCA.0 Rev 1.0, PICMG.

[10] Intelligent Platform Management Interface.

[11] Evolving design.

[12] The appropriate reference for Garfield.

[13] S. Agostinelli *et. al.* Nucl. Inst. Meth. A 506, 250 (2003).

Chapter 19

Auxiliary detectors

19.1 Fiber harps

19.1.1 Purpose

The fiber beam monitor (FBM) system is designed to serve two primary purposes:

- As a commissioning instrument, to determine the radius and angle of the beam in its first turns, and
- To observe and directly characterize periodic beam motion, notably the modulation of beam centroid position and width by coherent betatron oscillations.

On the other hand, the FBM is not suited to a determination of the equilibrium radius of the stored beam. A GEANT4 simulation showed that energy loss in the fibers moves the average radius inward by $\sim$0.1 mm/μs, so it will be altered before equilibrium can be established. Even an order of magnitude less energy loss would still be unacceptable for this measurement, so it is not plausible that any system that intercepts the beam would be useful for it.

19.1.2 Existing system

The FBMs were originally built for E821 by a group at KEK that is not part of the Fermilab collaboration [1, 2]. We intend to refurbish and reuse all components from the existing system that remain suitable.

Each FBM holds a "harp" of seven scintillating fibers of 0.5 mm diameter, each 90 mm long and separated from its neighbors by 13 mm, as shown in Figure 19.1(a). There are a total of four devices, and they are deployed near the 180° and 270° positions in the ring. The 180° FBM should observe an image of the beam as it was injected at the inflector, while the 270° FBM should map the inflector angle into position. At each position, one FBM has the fibers suspended vertically to measure in x, and the other arranges them horizontally to measure in y. The fibers stay inside the beam vacuum, and they can be plunged into the beam path. They can be also rotated into a horizontal plane, where all fibers see the same beam, for calibration, or upright for measurement. Because ferromagnetic material cannot

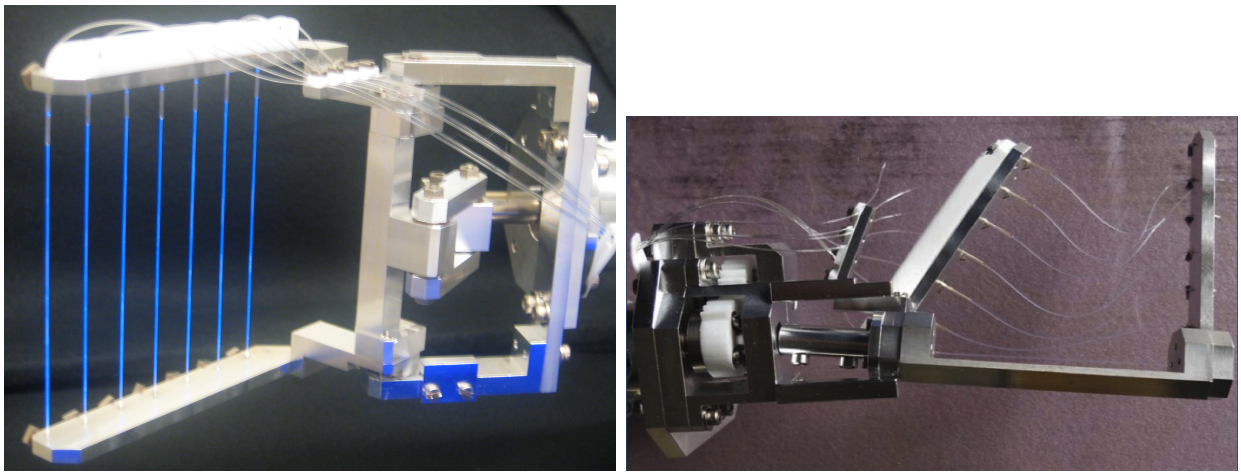

(a) (b)

Figure 19.1: (a) The 180° x profile monitor, glowing under ultraviolet illumination in the laboratory. (b) The 270° y profile monitor, which was found to be damaged when it was removed from the Brookhaven E821 storage ring.

be placed this close to the precision magnetic field, aluminum motors and actuators driven by compressed air are used for this motion.

Each scintillating fiber is bonded to a standard optical fiber that connects it to a vacuum feedthrough. At that point, a ∼3 m long fiber connected each fiber to an Amperex XP2202/B photomultiplier tube (PMT) that was located in a cable tray above the storage ring in a location where the magnetic fringe field could be shielded with mu-metal. The signals were small enough that various models of LeCroy linear amplifiers in an adjacent NIM crate were needed to drive the long cables to the counting room.

19.1.3 Refurbishment and upgrade plans

All of the FBMs have been dismantled from E821, and three of the four appear to be in good condition. One FBM was found to be damaged, with a snapped fiber and some bent frame components, as shown in Figure 19.1(b). The observed muon loss rate in E821 when the fiber harps were inserted suggests that this damage may have existed at that time. At a minimum, this frame will need to be straightened and realigned, and the broken fiber will need to be re-bonded.

We will clean and lubricate the parts of the system that were outside the vacuum, and we will test the compressed-air driven motion control system, making any necessary repairs. Similarly, we will test and assure the vacuum integrity of the system.

The PMTs and voltage divider bases that were used in E821 had already been reused from a previous project, and they are clearly aging devices that are in need of replacement. Replacement by SiPMs mounted directly on the fiber harps will allow the long fiber to a remote PMT to be eliminated. SiPMs also have higher photon detection efficiency than conventional PMTs.

Initial SiPM tests have been conducted with the Hamamatsu S10362-11-050C, for which we have developed a readout board with a simple two-stage voltage preamplifier. It has a 1×1 mm^2 area that is suitable for fiber readout applications. It also seems to be an appropriate match to the estimated number of photoelectrons. An initial GEANT4 simulation indicated that the most probable energy deposit is 0.06 MeV in each interaction, leading to approximately 6 photons at the SiPM. This SiPM, with ∼65% quantum efficiency and 61.5% fill factor, would therefore yield 2.4 photoelectrons per interaction. Approximately 1% of stored muons should interact with a typical fiber in each turn. Extrapolating from E821, we anticipate approximately 7000 stored muons in each fill, which would lead to 170 photoelectrons. This is comfortably near the center of the dynamic range of 400 available pixels on the SiPM. The maximum dark count rate of 800 kcps would give one photoelectron of noise every 8 fills.

We have acquired a quantity of 30 of this model of SiPM from unused spares from a previous project at Argonne National Laboratory, more than the 28 that are required. We will refine the readout board so that one printed circuit board will provide both mechanical support and preamplification for all seven SiPMs on each device.

19.2 Entrance counters

19.2.1 Purpose

The time at which the muon bunch enters the ring must be subtracted from the time of each decay electron in order to align data from different fills properly. The relative intensity of each fill is also monitored. An entrance counter, positioned just outside the inflector, is needed to record the time and intensity of each fill.

In E821, "flashlets" of beam that leaked from the AGS onto the target during the measuring period were a potential systematic error. The primary method of monitoring the rate of flashlets was to suppress the firing of the electrostatic quadrupoles periodically, preventing the injected muon bunch from being stored. Any signals that appeared in the calorimeters during these fills were presumed the be from flashlets. However, a dedicated flashlet counter was also deployed at times just outside the inflector.

19.2.2 Existing system

In E821, the primary entrance ("T0") counter consisted of a 1 mm thick, 10 cm diameter volume of Lucite that produced Cerenkov light. It was coupled to a two-inch Hamamatsu R1828 photomultiplier. This existing T0 counter appears to be in good condition. It will be tested and repaired as needed. Because it will be among the only traditional photomultipliers in the experiment, a single-channel high voltage supply will need to be procured for it.

The flashlet counter was a plastic scintillation detector that was only used in early runs of E821. The photomultiplier was configured to be gated off at the primary beam injection time by reversing the voltages on two dynodes. Consequently, the gain could be set to observe small amounts of beam entering at later times. This detector is also believed to be in working condition and to require only a suitable high voltage power supply.

19.3 Alternatives

Initially, we evaluated reusing the conventional photomultipliers that were used with the fiber beam monitors in E821. However, an initial inspection showed that they were in poor condition and unsuitable for future use. It would have been necessary to develop a new light conversion system, whether or not we moved to SiPM technology. Given the collaboration's familiarity with SiPMs from their extensive use in the calorimeter development, their compactness, and their comparatively low cost, there was a clear choice.

We also briefly considered diagnostics that would remain continuously deployed in the storage ring. However, any detector that intercepts the muons would degrade the beam lifetime unacceptably, and the E821 experience with pickup electrodes was unsatisfactory; they were paralyzed by the pulsed high voltage devices.

19.4 ES&H

The most significant hazards associated with the auxiliary detectors are electrical. The bias voltages needed for the SiPM readout of the fiber beam monitors will be approximately 70 V. To mitigate this hazard, a current-limited power supply will be used, with the current limit set to the lowest value that allows the devices to operate. The photomultipliers required by the entrance counters require a voltage of approximately 2000 V. Again, an appropriately current-limited high voltage supply will be used. All electrical devices will be subject to Fermilab's standard design review and operational readiness clearance processes.

The fiber beam monitors will be powered by compressed air at less than 150 psi. Requirements for appropriate personal protective equipment, such as eye protection, when working around compressed air lines will be determined in consultation with Fermilab ES&H experts. Similarly, the fiber beam monitors interface with the ultra high vacuum system, and they are within the large fringe field of the storage ring magnet. We will work with Fermilab ES&H to establish appropriate procedures to mitigate these hazards.

19.5 Risks

There is a risk of hidden damage, or degradation over time, to the fiber beam monitors that might require more repair work than anticipated. This damage may not be discovered until mechanical, vacuum, and light output tests are completed. There is also a risk that, after testing, we may find that the SiPMs that we were able to acquire at no cost are not suitable for the application and that we need to procure another model.

However, the only risk that would be expected to increase the project cost by $40k or more would be the destruction or damage beyond repair of one or more of the existing fiber harp devices by an accident in shipping, storage, or testing. Because much of the original knowledge of the system has been lost, to re-create an FBM from scratch would require a significant level of unplanned engineering cost in addition to the precision machining work.

Because the fiber beam monitors interface with the ultra high vacuum system, any leak could cause downtime for the experiment. The motion control system could potentially fail in a way that would not allow them to be retracted, which would also cause downtime,

requiring the entire storage ring to be brought up to atmospheric pressure to remove them. We intend to minimize these risks by careful testing before installation.

19.6 Quality Assurance

We will test the motion and vacuum integrity of the fiber beam monitors with extensive exercises in a test chamber in the laboratory before they are installed in the storage ring. We will also check the output of each fiber, and therefore the functionality of each SiPM channel, with a set of light pulsers and radiation sources.

19.7 Value Management

The auxiliary detectors represent a successful application of value management principles. All components that are suitable for reuse from Brookhaven E821 will be reused. The primary upgrade to the fiber beam monitor devices will be a SiPM readout system. For that installation, suitable unused SiPM devices (spares from a previous project) were identified and made available by Argonne National Laboratory.

19.8 R&D

Extensive R&D work on the auxiliary detectors will begin in earnest in summer 2013. Several undergraduate students will have summer research projects related to the fiber beam monitors. One will develop an improved version of our SiPM readout circuit and will use it to test the light output from each fiber. Another will re-establish the motion of the devices and will set up a vacuum test stand to check for leaks. A third student will begin to define the interface between the motion controller and the MSCB-based slow control system.

References

[1] Y. Mizumachi and T. Sato, E821 Muon $g-2$ Internal Note No. 192, 1(1994).

[2] Design Report, BNL E821, A New Precision Measurement of the Muon $(g-2)$ Value at the level of 0.35 ppm. 3rd edition, D.H. Brown et al. B.L. Roberts Editor, March 1995.

Chapter 20

Anomalous Precession Frequency Measurement Backend Electronics

20.1 Backend Electronics

The backend electronics for E989 encompass the systems for the distribution of the clock and synchronization signals to the experiment, and for the digitization of the waveforms from each channel of electromagnetic calorimetry.

20.1.1 Physics Goals

The clock system must provide a frequency stabilized and blinded clock signal that provides the time basis for determination of ω_a and a second frequency-stabilized clock, tied to the same master clock, for the determination of ω_p.

The waveform digitizers (WFD) must convert the analog waveforms to digital while retaining the signal fidelity necessary to meet the calorimetry requirements on energy resolution and pileup differentiation. The system must convert the distributed clock frequency to the required sampling frequency range while maintaining the timing requirements, without allowing circumvention of the experimental frequency blinding. The digitized waveforms must be transferred without loss to the DAQ front ends for data reduction. The system must also provide the support and infrastructure to capture samples for pedestal determination, gain monitoring and correction, and for stability cross checks of the gain monitoring system.

20.1.2 Requirements

Clock and synchronization distribution

To avoid systematic biasing of ω_a, the distributed clock must be held stable against systematic phase shifts or timing drifts to under 10 ps over the 700 μs fill. To help maintain signal fidelity, the random timing jitter should be much smaller than the ADC signal sampling window (the ADC's aperture delay), which is of order $100 - 200$ ps for the required digitization rates. The frequency up-conversion within the WFDs must maintain these requirements.

Synchronization signals such as start-of-fill and reset must be distributed to each front-end electronics channel. These signals must perform two distinct functions. First, to allow precise time alignment of signals from each channel within a calorimeter to allow for rapid summation on the DAQ front-end data reduction algorithms, they should be delivered to each channel within a calorimeter with a relative precision commensurate with the ADC aperture delay.

Second, across the entire experiment, the the synchronization signals will flag the specific the clock cycle on which to begin data acquisition for each muon fill. This requires signal delivery to the detector stations within a time window somewhat smaller than the digitization period.

Waveform Digitization

Signal requirements The energy resolution budget (5% near the 1.5 GeV threshold for fitting) determines the waveform digitizer (WFD) minimum bit depth. Assuming a typical 3×3 array of crystals summed to determine the energy, having 8 bits at 1.5 GeV would already contribute 1.2% to the energy resolution. This energy is about 1/2 the maximum energy range, and the system should have the overhead for complete study of the pileup energy distribution, which requires 10 effective bits. The effective number of bits is typically between 1 and 2 bits lower than the physical ADC bits. We therefore requires a digitization depth of at least 12 bits.

The signal separation characteristics will be determined by a combination of the crystal wrapping, the choice of which the GEANT4 Cherenkov light simulation (section 17.2.1) shows can cause the rise time to vary from 1 to 3 ns, the SiPM and amplifier response (see Figure 17.11), and the total cable and WFD bandwidth. The WFD bandwidth must be large enough to avoid significant stretching of the pulse shapes, with the rise time remaining under 2 ns (if the final wrapping choice allows). The overall pileup requirement for the experiment (see section 17.1.1), that the system must be able to distinguish pulses separated by 5 ns, drives the specification for the digitization sampling rate. Laboratory tests at 700 megasamples per second (MSPS) show clear separation of pulses with this separation (see figure 17.12). Figure 20.1) shows the fits for two pulses measured in the lab with 5 and 10 ns separations at 500 MSPS sampling rate. We can clearly resolve even the 5 ns separation at 500 MSPS, but we will lose fidelity at lower sampling rates. We still have some headroom to separate pulses separated less than 5 ns, which will help ensure our pileup separation requirement, and therefore require a minimum digitization rate of 500 MSPS.

Physical requirements The WFD crates will be located about 1 - 1.5 m from the dipole field of the storage ring, where the fringe field is of order 100 gauss. Ideally, the resulting magnetization of the materials in each WFD station would perturb the storage ring field by well under a part per million. We can make rough limit on magnetic materials assuming a magnetized sphere of material in a uniform magnetic field with static perturbations under 10^{-7}. A predominantly aluminum chassis would be no problem – 15 kg would result in a perturbation under 0.1% of this limit. For ferromagnetic materials, however, the total mass must kept under about 200 g, which may require the power supplies to be located farther away. WFD prototype studies will determine whether shielding will be required to suppress dynamical field perturbations.

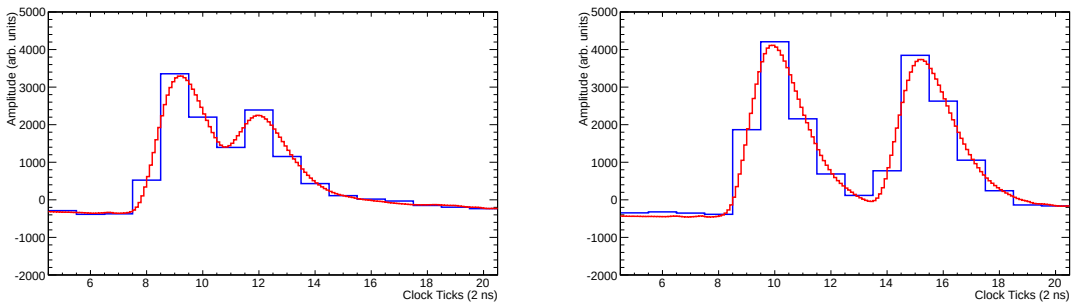

Figure 20.1: Fits to test data (see Section 17.2.1) with two pulses separated by 5 ns (left) and 10 ns (right) with a 500 MSPS sampling rate. The fits (red) clearly resolve the two peaks in the data (blue), even for the 5 ns separation.

DAQ requirements During experimental running, muons will be stored in the storage ring for 700 μsec fills. The basic fill structure will be four groups of four fills, with the fills within a group occurring at 12 msec intervals and the groups of four occurring at 132 msec intervals. This basic structure repeats every 1.3 sec., for an average fill rate of 12 Hz.

To eliminate dead-time, the 700 μsec waveform for each calorimeter channel will be digitized and transferred to the DAQ front-end system for data reduction. Each WFD station must provide adequate buffering and throughput to support the average data rate, assuming a 500 MSPS digitization rate, of 3 Gbit / s. The rates will require high speed serial lines, which must be quiet during each fill to avoid introducing potentially rate-dependent noise. There must therefore be a begin-of-fill synchronization signal that arrives early enough to allow any WFD $\rightarrow$ AMC13 block data transfers to complete before the fill starts.

20.1.3 Recommended Design

Clock distribution

The Clock System will distribute a high-precision clock and synchronization signals to each front-end crate. It will provide timing that is fully independent of accelerator timing to insure that the ω_a measurement is not biased by synchronous events.

The Clock System follows a similar strategy to that which was used in E821 and MuLan. This system will primarily consist of off-the-shelf components. The primary clock signal will be produced by a Meridian Precision GPS TimeBase, a GPS-disciplined oscillator. We have recently purchased an initial module and are currently evaluating its properties. The Meridian module will be supplemented by their "Low-Phase-Noise" output module to minimize jitter. The GPS TimeBase will be used as the clock source for both the ω_a and ω_p measurements. The utilization of the clock in the ω_p measurement is described in Sect. 15.2.8. The GPS clock produces a 10 MHz output signal. This will be fed to a Fluke 6160B frequency synthesizer that will shift the ω_a clock to 50 MHz plus a small offset that will be blinded. The $50 + \epsilon$ MHz clock, where ϵ is the blinded offset that will be kept constant, will then be distributed to the calorimeter front end crates. An AMC13 board, originally designed for

the CMS μTCA on each calorimeter μTCA crate will receive the clock signal and put it on the μTCA backplane. Once received by each waveform digitizer, the clock frequency will be shifted up to the 500 MHz sampling frequency.

To minimize pickup from other sources, particularly sources that might be synchronous with within a fill, the clock will be delivered to each front end crate on double-shielded RG-142 cable.

Monitoring of the clock system will occur at several stages. We will continuously monitor the source and frequency synthesizer for any systematic shifts in frequency. At the receiving end, the AMC13 will verify clock functionality with an internal counter compared to a local oscillator. Further, direct tests on time slewing and other systematic effects will be performed using the clock signals as seen by the waveform digitzers.

The Clock System will also receive and distribute timing signals from the Fermilab accelerator system. For example, the "Recycler Ring beam sync" signal will identify the time of Recycler beam extraction. This signal, after time-alignment, will serve as the "begin fill" signal that will synchronize all front ends (provide a common $t = 0$) and initiate data acquisition. We will deliver accelerator synchronization signals to each calorimeter crate differentially on shielded, twisted pair cable.

In order to perform system testing at all sites participating in this proposal, we will construct a μTCA "Test Clock" emulator board that will deliver a realistic set of clock and synchronization signals to the AMC13 board. The Test Clock will not have the timing precision of the final system, but it will permit development and testing to go on at remote sites under realistic DAQ system conditions. This increases the likelihood of a smooth transition to full scale system assembly at Fermilab.

Waveform digitization

The proposed system draws heavily on a DAQ upgrade underway for the CMS experiment at the Large Hadron Collider (LHC), which utilizes μTCA technology. The WFDs for each calorimeter station will reside in a single Vadatech VT892 μTCA crate as a set of 5 channel Advanced Mezzanine Cards (AMCs). The crate accommodates 12 full height AMC cards. Eleven AMCs will instrument the 54 calorimeter channels for one calorimeter station, leaving one channel for the pin diode signal that monitors the laser calibration intensity delivered to the station. A twelfth WFD AMC will reside in the crate as a hot spare. The μTCA choice brings a robust system designed for remote operation and monitoring, with cooling, power distribution and clock distribution capabilities already designed in.

CMS has already prototyped the AMC13 as part of its hadronic calorimeter DAQ upgrade (Figure 20.3), and Cornell has begun assembling a μTCA test bench for the WFD AMC development.

VadaTech has previous experience in migrating other μTCA chassis from their standard steel-based configuration to an aluminum chassis. They will provide us with a custom aluminum chassis for the full order, and will send us preliminary versions of the chassis for magnetics characterization before filling the full order. They are currently working with us to identify and control other areas of the crate and modules that contain ferromagnetic materials.

Readout will be controlled by a CMS-designed AMC card that replaces a second (re-

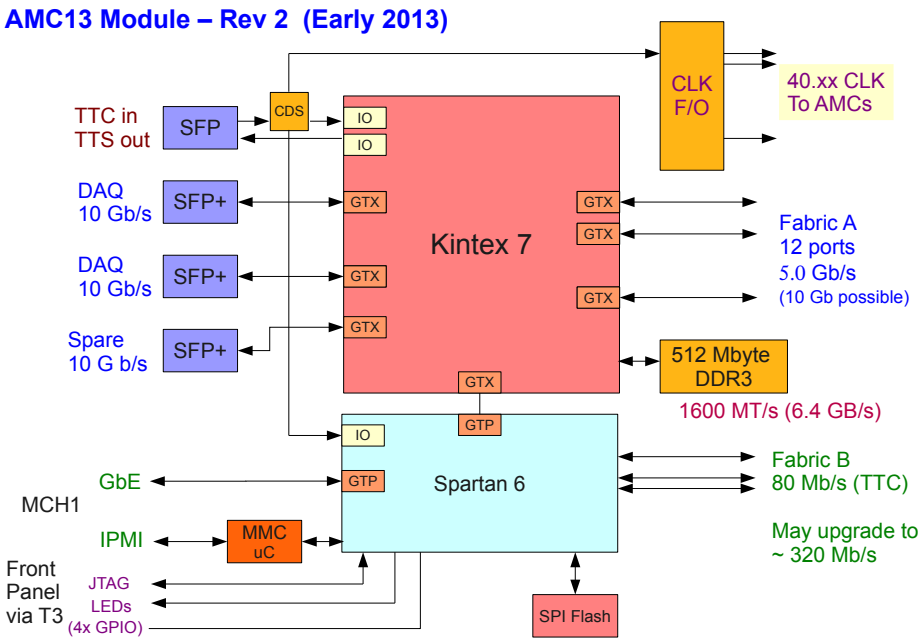

Figure 20.2: Block diagram of the CMS-designed AMC13 μTCA card that will control the $g-2$ WFD readout.

dundant) μTCA Carrier Hub (MCH) in the μTCA crate. This AMC13 card [1] is shown in block diagram form in Figure 20.2. The μTCA backplane connects each of the 12 WFD AMC cards in a star topology (Figure 20.4). These connections, managed by the Kintex 7 FPGA, allow parallel readout of the 12 WFDs at rates up to 5 Gbit / second. The current CMS firmware introduces overhead that maintains backwards compatibility with some of their subdetectors, but currently limits the throughput to 2.5 Gbit / second. This overhead will be eliminated through reprogramming of the Kintex 7, with no hardware modifications.

The AMC13 itself can provide buffering of several seconds of calorimeter waveform data on its 512 MB on board memory the AMC13 by taking advantage of lossless encoding / decoding. This encoding can easily be accommodated by the Kintex 7 on the fly. This buffering alone will allow the AMC13 to communicate with the external DAQ system at the average data rate of 3 Gbit / second, though the individual WFD channels will provide deeper buffering. The AMC13 includes 3 10 Gbit optical links for communicating with the DAQ front-end computers, though $g-2$ needs only one of these links. We will support a TCP/IP protocol on standard 10 Gbit ethernet, so the DAQ system will communicate with the WFD system via a standard 10 Gbit optical NIC.

The AMC13 has substantial on-board processing capability in the Kintex 7 device which could be used to form time islands for the T method or accumulate histograms for the Q method. This would substantially reduce the required bandwidth between the AMC13 and the DAQ front ends, as well as relieving processing requirements on the DAQ, if needed.

The baseline WFD design is centered on the TI ADS5463, a 500 MSPS 12 bit ADC with

Figure 20.3: Left: VadaTech 892 with CMS AMC13 under testing for CMS HCAL DAQ upgrade. Right: Core μTCA equipment under setup at Cornell to begin testing for $g-2$.

an input bandwidth of 300 MHz, and will be based on the successful 300 MSPS design [2] (see Fig. 20.5) used for the CESR-TA project at the Cornell Electron Storage Ring (CESR). The block diagram for the five-channel AMC card is also shown in Fig. 20.5. Each channel will have a Kintex 7 FPGA to control the data flow out of the ADC and to / from an 64M x 16 bit SDRAM memory buffer. At an average 12 Hz fill rate, this buffer can hold over 15 seconds of data.

A sixth Kintex-7 FPGA provides the interface to the μTCA fabric. The BU engineering group, which has designed the AMC13 for CMS, will provide the FPGA firmware block that supports the 5 Gbit/s transfer link from our WFD AMC to the AMC13 Kintex-7. This Kintex-7 will transfer data out of the five channels sequentially, communicating with the each channel's FGPA over a dedicated high speed serial line. For the 500 MSPS 12 bit baseline design, the data from one fill can be transferred from the five-channel card in 4 msec over the 5 Gbit link.

The AMC card must frequency lock on the distributed $50 + \varepsilon$ MHz clock and upconvert to a near-500 MHz clock for the ADCs. The WFD cards will receive the 50 MHz clock via the μTCA backplane, which is distributed by the AMC13 via the FPGA-free LVDS clock path shown in Fig. 20.6. The full clock path will need significant testing to verify that it will have highly stable% duty cycle, slew and wander within the phase stability specifications over a fill, and no differential nonlinearities. The engineer responsible for the clock for operation of the Cornell Electron Storage Ring (CESR), which also has stringent timing requirements, does not anticipate any intrinsic difficulty in meeting the $g-2$ stability specification. On timescales of several hundred μsec, a more important issue is typically environmental noise. We must ensure, for example, that the clock supplied to the ADC will be immune in particular to noise sources correlated with the fill structure, such as the firing of the kicker. Because environmental noise is an issue, we are planning a single package clock management, based on the TI LMK04010 or similar chip, rather than a discrete component solution. This chip can up convert the 50 MHz input clock to the 500 MHz range, distribute it over five output channels with a programmable delay on each line. The programmable

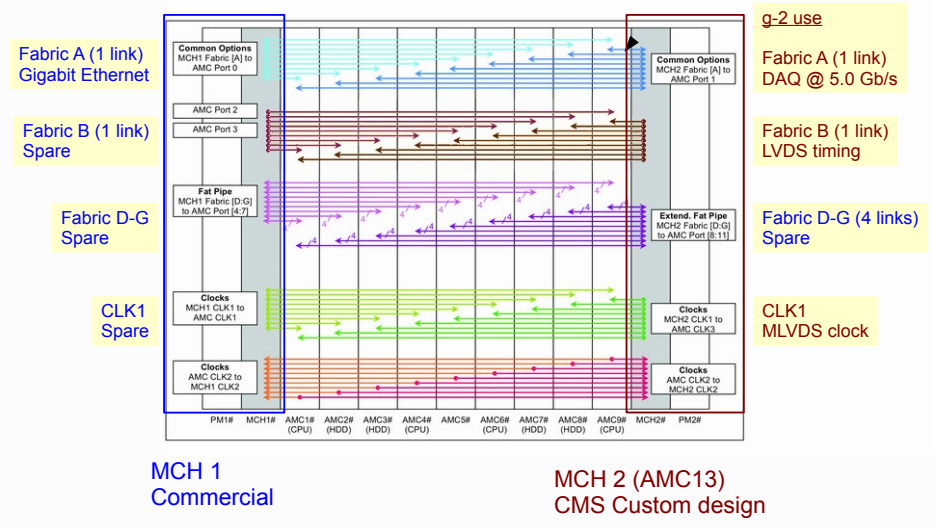

Figure 20.4: Dual-star backplane configuration for use with g-2 AMC13. High speed data transfers proceed over Fabric A. Timing and synchronization proceed via Fabric B.

delay will allow correction of channel by channel timing differences in signal path lengths from the photodetectors at the sub-clock-cycle level. The single package device will be far less immune to external noise than a discrete component solution, and has much better overall jitter specifications (under 200 fs) than a discrete component solution.

We will operate the WFDs following the CESR-TA implementation: the ADC chips will sample continuously, and data collection will be gated during the fill, triggered by the synchronization signal. There will also be options for dedicated operation to collect pedestal and gain data.

Bench testing the clock distribution from the AMC13 to the ADC will be the highest priority testing we will launch with the one-channel prototype under development. These studies will include sensitivity to environmental noise sources. We are also considering design options for the final system that would incorporate monitoring of the final ADC clock. Options could include onboard comparison to a second independent stabilized clock signal generated locally on each station's MCH.

20.1.4 Performance

The proposed baseline will meet the basic energy, pulse separation, readout rate and random jitter requirements. As noted above, the level of control of systematic timing trends over the 700 μs fill times with the expected fill structure must still be characterized, but we do not expect a serious problem.

The proposed solution also provides the experiment with significant flexibility. The system is capable of readout of the data from a fill in the 11 msec inter fill period, even at a 1 GSPS sampling rate. Should the opportunity arise, for example, for a higher average rate of muon fills, there is no intrinsic limitation from the μTCA-based solution outlined here.

With the TI ADC, we expect each station to consume approximately 500 W of power,

Figure 20.5: Left: A single-channel 300 MSPS ADC mezzanine card with on board buffering developed for the CESR-TA program. Right: Block diagram of the five-channel WFD AMC card.

which is safely below the maximum power of the 792 W power module available for the VadaTech crate

The μTCA solution also provides a natural platform for the tracker readout boards 18.

20.1.5 Alternatives and Value Engineering

We considered a PCIe-based system to host the WFD's as an alternative to μTCA. Under this scenario, the WFD's would become PCIe cards that plug either directly into a PCIe-based motherboard or into a PCIe expansion chassis. We would need to engineer all of the timing, cooling, power, mechanical and remote monitoring elements that are already engineered into a COTS μTCA system, escalating the risk. Data throughput rates would require a PCIe backplane with enough 16 lane slots to accommodate all of the WFDs, which were difficult to locate. Finally, the solution did not scale easily from the 35 channel calorimeter considered early on to the 54 channel baseline. As our initial estimates indicated that the solution was only about 10% less expensive, but carried significantly more risk, particularly for the 54 channel calorimeter.

We also considered COTS waveform digitizers. When approaching Struck, however, the reply we received was "For an application in the 1500 channel count I tend to assume, that a custom card may be advised to optimize performance and cost to the application." We continued on the path of developing our own.

We considered two other 12 bit 500 MSPS ADC chips as alternatives to the TI ADS5463, the e2v AT84AS001 and the Analog Devices AD9434-500. All chips had a similar cost / part. The e2v AT84AS001 has a much larger footprint than the other chips, which would complicate the layout in an already dense board, so we eliminated it from consideration. The TI chip had slightly better noise and bandwidth specifications, while the AD chip consumed considerably less power and space. We may have opted for the AD9434-500, all else being equal, but TI offered to donate all 1600 ADCs needed for prototype WFD development and final WFD production.

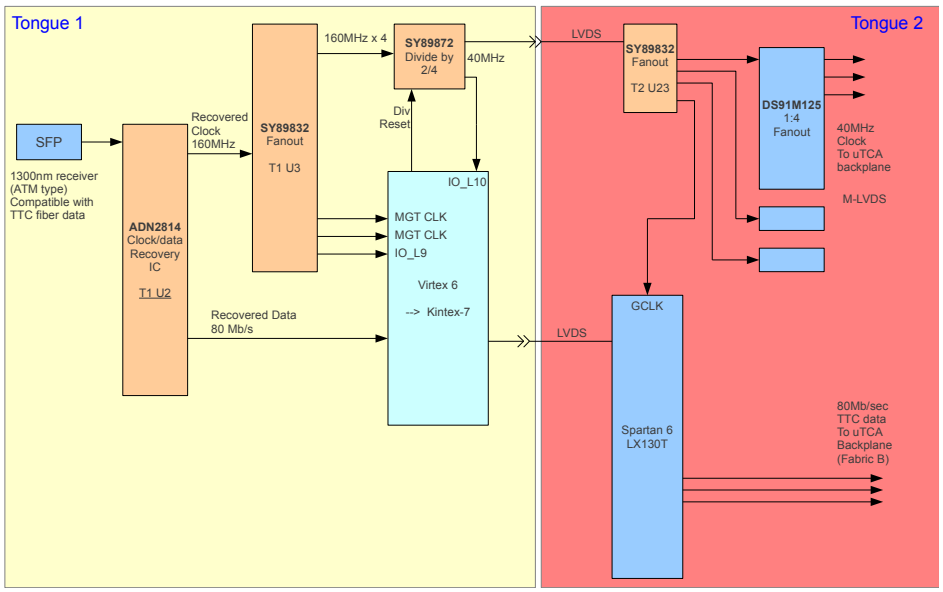

Figure 20.6: Right: Timing paths through the AMC13 for the LHC. The $g-2$ experiment will utilize the FPGA-free LVDS path, which distributes the 40 MHz clock shown for CMS, but in principle can support any frequency in the range from 10 to several hundred MHz. The $g-2$ baseline design utilizes 50 MHz.

We also explored the 1 GSPS versus 500 MSPS digitization rate, but find the cost prohibitive at this time. Currently, the price differential for native 1 GSPS ADCs alone would double the cost of the WFD system, even before considering the additional engineering required for the increased clock stability and higher rate data movement between ADC and buffer memory. Interleaving two 500 MSPS TI chips would also essentially double the WFD system cost. The power requirement would almost double, and we are already near the maximum we would consider given the power the crate can deliver. Hence we would need two μTCA crates per system, as well as additional parts and FPGAs. Interleaving the AD ADCs is feasible from a power perspective, but would forego the TI donation. The incremental system cost would exceed $500,000 in that scenario.

We have investigated discrete component circuitry on the WFD AMC card based on the AD9510 or another similar clock synthesizer. The design included a clock delay line for each channel that can correct for differences in signal path lengths from the photodetectors at the sub-clock-cycle level. Such a design would have significantly more inherent jitter, several tens of picoseconds, and would have greater sensitivity to environmental noise.

As we move forward, we will continue to evaluate performance / cost issues for emerging μTCA MCH options, component options for the WFD AMC cards, for power supplies for the μTCA crates, and elsewhere as the opportunity arises.

For the Clock System, we have considered alternate clock sources. The clock for E821 was disciplined by the LORAN-C signal which is now obsolete. Undisciplined Rubidium oscillators would likely deliver the precision necessary, however the GPS disciplined oscillator provides long term stability as well as additional features like time-stamps which are of

particular use to the field measurement. Options for the frequency synthesizer are limited by the 50 MHz signal necessary for the WFD.

20.1.6 ES&H

The μTCA crate for each calorimeter station will weigh approximately 30 pounds and will be supported by the calorimeter housing (see section 17.4). Power to each crate will be supplied by a 60 – 70 V supply that connects to an in-crate power module that maintains the stable 48 V on the backplane. When fully populated with the WFDs, the each station will draw approximately 500 W of power. If the magnetic field requirements allow, the power supply will be resident on the crate. If not, the supplies will be located more centrally in the ring, with a few meter cable run and the supply voltage closer to 70 V.

The latter configuration in particular involves high voltage with several amps of current. We will ensure that all our equipment and installation conforms to the Operational Readiness Clearance criteria.

20.1.7 Risks

The largest risk in the WFD project regards the distribution of the clock signal through the AMC13 and μTCA backplane, and in particular, whether that path will meet the frequency and phase drift requirements. To mitigate risk to the project, we will design the WFD AMC cards to allow timing and synchronization inputs via the front panel. We can then engineer a standalone distribution system to the AMC modules that meets the final specifications. This alternative would also require a modified clock fan-out and cabling scheme. Total differential cost to the experiment should be under $40K for engineering and production. Biases in the clock translate directly into biasing of ω_a, so the clock must meet its stability requirements.

20.1.8 Quality Assurance

Cornell is establishing a test station to assess the performance of the μTCA platform, of the AMC13 modules and the WFD AMCs themselves. We plan two major stages of prototyping: and initial one channel design to verify the fundamental per channel performance without facing the board density issue simultaneously. The second stage will move the one channel design to the full five channel design with the denser component layout. The plans for each stage include two versions of AMC prototype, and both versions will undergo significant testing to assure that the baseline requirements for $g-2$ are met.

We will produce enough of the second five channel prototype to fully populate the μTCA crate, as planned for the experiment, so that we can ensure the entire system under full load can meet the specifications, and that we do not encounter unanticipated cross talk or clock biasing with the full system. This system will also be deployed in the 25 channel test beam planned to stress test the entire calorimeter through DAQ design.

Production of the WFD AMC modules and delivery of the μTCA crates should complete a year in advance of the start of the experiment. Burn-in and stress-testing of the production components will continue at Cornell as we receive the components, and can continue for several months thereafter before moving the equipment to FNAL for installation.

The Illinois group will test and evaluate each component of the clock system prior to installation. In addition, we will perform detailed in-situ timing for each path in the final experimental configuration. This "timing-in" is necessary to insure that the synchronization signals are delivered to each location simultaneously.

20.1.9 References

References

[1] Amc13 development project, http://www.amc13.info.

[2] N.T. Rider, J.P. Alexander, J.A. Dobbins, M.G. Billing, R.E. Meller, M.A. Palmer, D.P. Peterson, C.R. Strohman, *Development of an X-Ray Beam Size Monitor with Single Pass Measurement Capability for CESRTA*, Proceedings of the 2011 Particle Accelerator Conference (PAC 11) , 687 (2011).

Chapter 21

Data Acquisition System

21.0.10 Physics Goals

The data acquisition system must read, process, monitor and store the data produced by the various detector systems in the muon g-2 experiment. Most importantly, the DAQ must provide a distortion-free record of the detector signals originating from the decay positrons during the 700 μs-long spills from the muon storage ring. Additionally, the system must record all data required to perform the corrections from effects such as pulse pileup, gain instabilities and beam dynamics. Furthermore, the system must permit the monitoring needed to guarantee the overall integrity of data taking and record-keeping needed to document the experimental conditions during data taking.

21.0.11 Overall Requirements

The DAQ must handle the accelerator-defined time structure of the data readout from the detector systems. Under normal operations we anticipate a 12 Hz average rate of muon spills that comprises sequences of four consecutive 700 μs spills with 11 ms spill-separations for each booster batch received by the muon g-2 experiment. The procedures for reading, processing, monitoring and storing these data must introduce no time-dependent losses or time-dependent distortions of the detector signals during the muon spills.

The DAQ must handle the readout, processing, monitoring and storage of the data obtained from the 1296 channels of 500 MHz, 12-bit, waveform digitizers instrumenting the individual PbF_2 crystals of the twenty four calorimeters. For each spill the raw data will consist of 1296 channels of 700 μs-long streams of continuously-digitized ADC samples. The DAQ must process these raw data into derived datasets including: T-method data (*i.e.* individual islands of digitized pulses), Q-method data (*i.e.* accumulated histograms of calorimeter spectra), and other calibration, diagnostic and systematic data. At a 12 Hz spill rate the readout (*i.e.* raw) data rate will be about 8 GB/s and the stored (*i.e.* derived) data rate will be about 50 MB/s.

The DAQ must also handle the readout, processing, monitoring and storage of the data obtained from the two positron tracking stations. This system consists of roughly 2000 channels of straw tubes with associated amplifier-discriminator-TDC electronics. The raw data – consisting of time stamps and spill numbers from individual straw tubes – is expected

to yield a roughly 2 MB/s time-averaged data rate.

Additionally, the DAQ must handle the readout, processing, monitoring and storage of data from the auxiliary detector systems. These systems include the muon entrance detector, fiber harp detectors and electric quadrupole monitors and involve both instrumentation that is operated during normal data taking (the muon entrance detector) and instrumentation that is operated during dedicated data taking (the fiber harp detectors). The read out for the muon entrance detector, fiber harp detectors and electric quadrupole monitors will use an existing system of custom-built, fast-sampling, VME-based, waveform digitizers. The expected data rates from auxiliary detector systems are: (i) 17 MB/s during dedicated data taking with the fiber harp detectors and (ii) 3 MB/s during normal data taking with the muon entrance detector and the electric quadrupole monitors.

The DAQ must coordinate the acquisition of data by the frontend readout processes with the accelerator-defined spill cycles. This coordination involves both readout systems where data is transferred synchronously with spill cycles (direct memory transfer from VME-based electronics) and readout electronics where data is transferred asynchronously with spill cycles (network packet transfer from micro-TCA based electronics).

The DAQ must assemble the individual fragments of spill-by-spill data from networked readout processes into complete, deadtime-free, records of each muon spill. This includes assembling the data banks of T-method and other datasets from the twenty four calorimeters stations as well as the data from the two tracker stations and the auxiliary detector systems. In total the event builder must match and assemble the fragments originating from roughly thirty frontend processes at an expected rate of about 50 MB/s. The resulting fully-assembled spill-by-spill events must be transferred to the Fermilab computing facilities.

The DAQ must provide the local / remote run control for data taking as well as facilities for configuration and read-back of parameters such as high voltages, digitizer configurations, *etc*. The system must provide the monitoring of data integrity and data quality and a comprehensive database of the experimental conditions and configuration parameters during data taking. The system must additionally provide for local storage of sufficient data for online analysis tasks.

21.0.12 Recommended Design

The major challenge for the data acquisition is the combination of the high data rates with the requirement of avoiding any time-dependent losses or time-dependent distortions of detector signals during muon spills. In addition, the system must provide: the monitoring of data integrity, cataloging of experimental conditions, and flexibility for diagnostics measurements.

The DAQ will acquire data in deadtime-free blocks that correspond to individual muon spills from the storage ring. Each event will represent a complete deadtime-free history of the entire activity in the detector systems for a complete spill – rather than events corresponding to individual positrons. This scheme will utilize the on-board memories in waveform digitizer and multi-hit TDCs to temporarily buffer the recorded data before its data transfer to the data acquisition. The design will be implemented as a modular, distributed computer system on a parallel, layered array of networked, commodity processors with graphical processing units (GPUs). The DAQ group have developed and operated very similar architectures [1] for the MuLan, MuCap and MuSun experiments at the Paul Scherrer Institute.

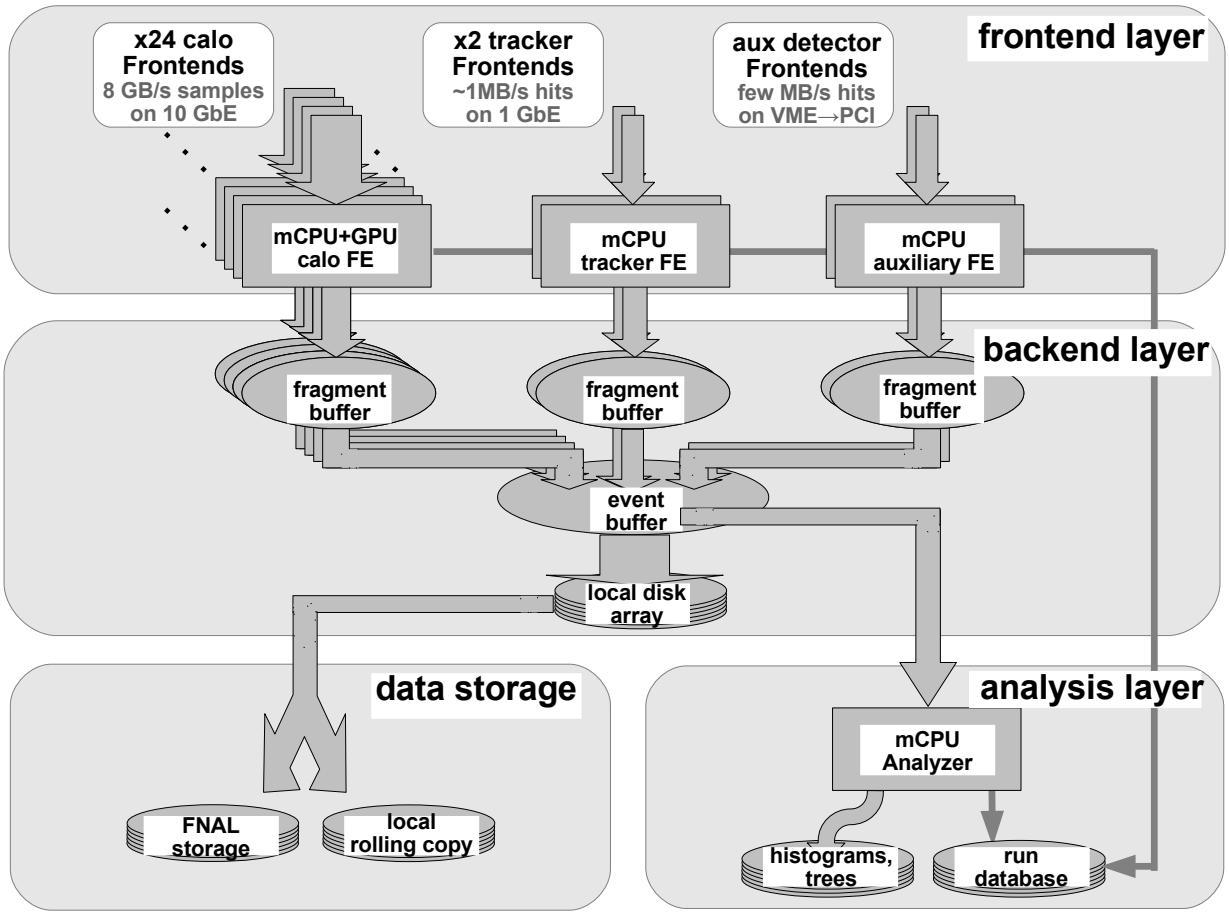

Figure 21.1: Conceptual design of the g-2 data acquisition. The figure shows: (i) the frontend layer for readout and processing of data from the calorimeter stations, tracking stations and auxiliary detector systems, (ii) the backend later for event building and data storage, (iii) the analysis layer for monitoring data quality and recording run-by-run experimental conditions, configuration parameters, *etc.*, and (iv) data storage. The layers comprise arrays of networked commodity processors.

The data acquisition system is depicted schematically in Fig. 21.1. It shows a frontend processor layer responsible for readout and processing of waveform digitizer and multihit TDC data, a backend layer responsible for event assembly and data storage, a slow control layer responsible for control and read-back, and a data analysis layer responsible for monitoring data integrity. The DAQ hardware will comprise a networked cluster of high performance processors running Scientific Linux. The DAQ software will be based on the MIDAS data acquisition package [2], ROOT data analysis package [3], and NVIDIA's parallel computing platform CUDA. To maximize bandwidth, one network will handle traffic between the frontend layer and the backend layer and another network will handle traffic between the backend layer and the analysis layer.

The calorimeter readout consists of one frontend processor per calorimeter station. Each

frontend processor will read out the 54 waveform digitizer channels associated with the 9×6 PbF_2 crystals of a single calorimeter station. Each group of 54 waveform digitizer channels will occupy a single micro-TCA crate. The digitizers are configured via a commercial MCH controller [] with a 1 GbE link and read out via a custom AMC13 controller [] with a 10 GbE link. For each spill the raw calorimeter data will consist of $24 \times 54 = 1296$ channels of 700 μs-long streams of continuously-digitized, 500 MHz, 12-bit, ADC samples – a total of 680 MB per spill. The processors are designed to provide the necessary performance to compress the continuously-digitized ADC samples into the T-/Q-method datasets at the software level in the frontend CPU/GPUs. The T-method datasets will consist of individual "islands" of above-threshold calorimeter signals and the Q-method datasets will consist of histograms of consecutive spills of continuously-digitized samples. The algorithms for constructing the T-/Q-method datasets involve copying, masking and summing data arrays and therefore are well suited to GPU-based parallelization using standard algorithms. The scheme will offer the flexibility to implement other datasets – such as pile-up datasets (*e.g.* by summing fills before storing islands) and diagnostic datasets (*e.g.* by storing prescaled fills of fully-digitized samples) – as needed. Each calorimeter frontend processes will finally zip, pack and dispatch the various derived datasets as MIDAS-format databanks over the frontend network to the event builder.

The positron tracking system consists of two tracking stations that each comprise about 1000 individual channels of straw tube detectors. The raw data – derived from amplifier-discriminator-TDC electronics that instrument each straw tube detector – are transferred to custom AMC modules housed in a single micro-TCA crate for each tracking station. The AMC modules are configured and read out via a commercial MCH controller with a 1 GbE link. Each tracker frontend process will receive the raw data – *i.e.* hits defined by a time stamp and a spill index – and then zip, pack and dispatch the tracking station data as MIDAS-format databanks over the frontend network to the event builder.

The auxiliary detector systems comprise the muon entrance detector, fiber harp detectors and electric quadrupole monitors. Their read out will be based on existing electronics of custom-built, high-speed, 8-bit, waveform digitizers [] with 512 kByte on-board FIFO memories. These digitizers are configurable for different sampling rates and different triggering / gating modes and therefore suitable for the read out of the different detector systems. The digitizers are housed in 6U VME crates and readout using Struck Innovative Systeme SIS3100/1100 VME-to-PCI interfaces. The muon entrance readout will use a single digitizer channel operating at 500 MHz sampling rate to record continuous ADC samples. The fiber harp detector read out will use 28 channels of waveform digitizers operating at a 500 MHz sampling rate with an external gate signal to record continuous streams of ADC samples during the initial 100 μs of the muon spill. The electric quadrupole monitors will be read out using 32 channels of waveform digitizers operating at a 25 MHz sampling rate with an external gate signal to record continuous streams of ADC samples during the entire 700 μs of the muon spill.

The DAQ design incorporates a master frontend process and hardware control logic in order to synchronize the data acquisition readout cycles with the accelerator-defined spill cycles. Importantly, the master frontend and control logic must accommodate both the spill-synchronous data transfer from the VME crates via Struck SIS 3100/3300 interface modules and the spill-asynchronous data transfer from the micro-TCA crates via 1/10 GbE network

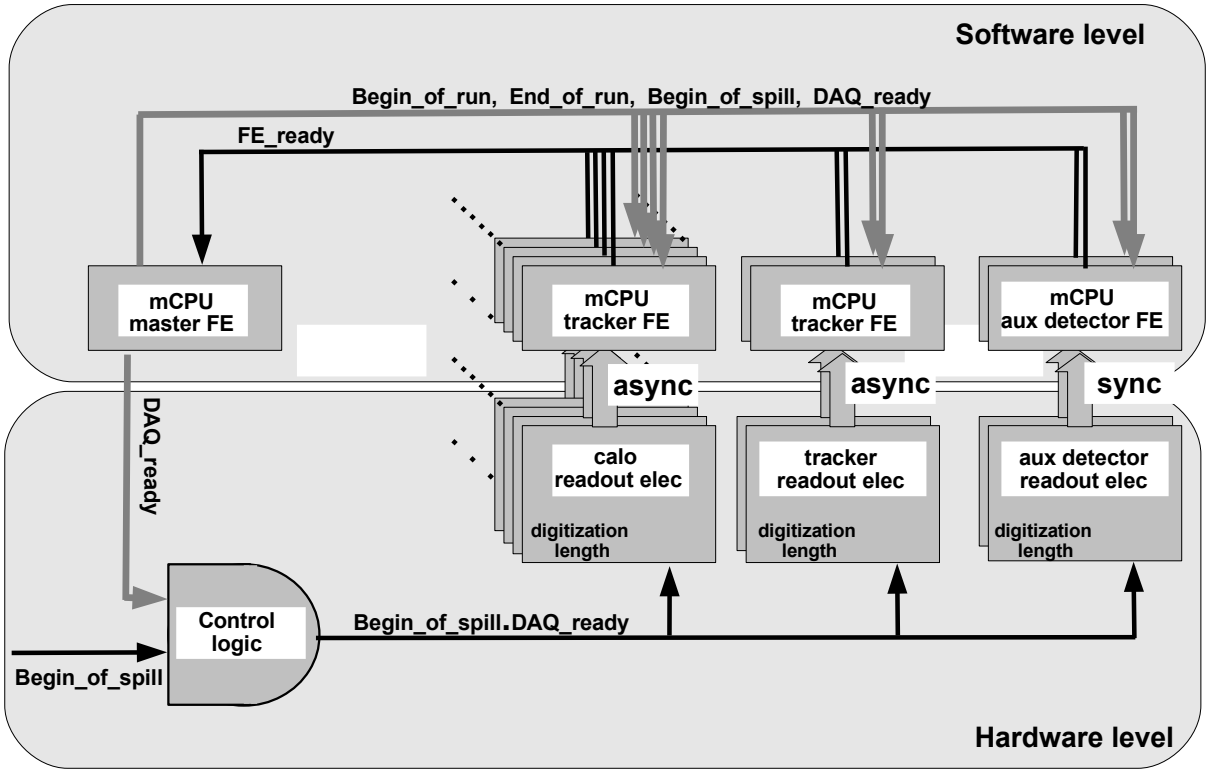

Figure 21.2: Conceptual design of the g-2 control logic. The controls signals involve a accelerator-defined begin_of_spill signal and a process-defined DAQ_ready signal. Control signals are distributed across the readout processes by remote procedure calls (the upper software level) and across the read electronics by the control logic module (the lower hardware level).

links.

The conceptual design of the logic to coordinate the fill cycles and readout cycles is given in Fig. 21.2. The design involves two control signals – a begin_of_spill signal and DAQ_ready level – that are distributed to the readout electronics via the hardware control logic and distributed to the frontend readout processes by the master frontend process. On run start-up, after completing their initialization, each enabled readout process will transmit a FE_ready signal via a remote procedure call to the master frontend process. On receipt of all FE_ready signals from all enabled readout processes the master processes sets the DAQ_ready level "high" in the control logic. The next begin_of_spill signal then: propagates through the control logic to initiate the digitization by readout electronics, propagates to the readout processes to initiate any software begin_of_spill functions, and resets the DAQ_ready level "low". The digitization time range for each detector system is a configuration parameter

set in the readout electronics by the data acquisition. Synchronous frontend processes, which require the readout of data between spills, will identify the end of digitization by a polling scheme and report the completion of read out via a FE_ready remote procedure call. Asynchronous frontend processes, that receive their data as network packets from frontend electronics, do not report the spill-by-spill completion of read out cycles. After receiving the FE_ready signals from all synchronous readout processes, the master processes again sets the DAQ_ready level "high" in the control logic – thus continuing the data taking. Note we plan to use a PCI-based GPS synchronization card [5] to GPS timestamp the digitized spills to facilitate later coordination between the detector system readout and the magnetic field readout.

Each frontend readout process will transmit its spill-by-spill data fragments as MIDAS-format databanks across the frontend network to the backend processor. Initially, the data fragments from the twenty four calorimeter processes, two tracking system processes and various auxiliary detector processes, are transferred to individual shared memory segments on the backend machine. After matching the MIDAS serial numbers and muon spill indexes of event fragments the event builder process assembles all data fragments into single events representing a complete record of each spill. The spill events are then written by the event builder process to a final memory segment known as the system memory segment and are available for data storage tasks, data analysis tasks, *etc.*

The backend layer will use a two step procedure to permanently store a full copy of the data on the Fermilab Computing facilities and temporarily store a rolling copy of the recent data on our analysis layer. First, the data will be transferred from the system memory segment to a temporary disk file on a local redundant disk array on the backend processor. Next, the temporary data files on the backend processor will be asynchronously migrated to both the Fermilab computing facilities for permanent storage and the DAQ analysis layer for local analysis projects. This approach will minimize any delays in data taking due to latencies associated with the permanent archiving of the experimental data and make the current data available for local analysis projects.

The DAQ analysis layer will provide both integrity checking and online histogramming. The online analyzer will receive events over the network from the system memory segment on the backend layer. These events will be received "as available" in order to avoid introducing any delays into the read out or the data storage. The online analysis will utilize the MIDAS analyzer package and a modular, multistage approach to the analysis tasks. Specifically, the different analysis tasks are implemented as individual analyzer modules and switched on / off as needed. Each analysis module had access to a global structure that contains both the raw MIDAS databanks from the readout processes and any derived MIDAS databanks from the preceding analysis modules. Low-level modules will be responsible for unpacking the databanks and checking their integrity. Intermediate-level modules will be responsible for various histogramming to ensure the correct operations of detector systems. High-level modules will be responsible for online "physics" analysis such as fits to the precession signal.

The data acquisition system will incorporate database support to provide a comprehensive run-by-run record of the experimental conditions, configuration parameters, *etc.*, during data taking. The run-by-run database will store information derived from the MIDAS online database such as run start time, run stop time, operator run-time comments, the number of events, and hardware settings including the high voltage setting, digitizer configuration pa-

rameters, multhit-TDC configuration parameters, *etc.* In addition, the database will record such quantities as detector gains, pedestals, *etc.*, fitted frequencies, lifetimes, *etc.*, that are derived from the analysis layer. These metadata are foundations for the offline data analysis.

The DAQ will be housed in the computer room in the MC-1 building. 10 GbE optical fiber links (64 cables) and 1GbE copper Ethernet (48 cables) will provide the connections between the detector sub-systems in the experimental hall and the data acquisition in the control room. The DAQ will require clean, uninterruptible power of roughly 50 kiloWatts total power with appropriate power distribution for roughly thirty rackmount computers and associated network switches, mass storage devices, *etc.* The control room will require air circulation for appropriate temperature and humidity control with temperature, humidity and air velocity sensors with digital readout. It will require a reliable, fast network connection between the MC-1 computer room and the Fermilab data storage facilities that is capable of a sustained data rate of roughly 100 MB/s.

21.0.13 Design Performance

The DAQ is designed to operate at 12 Hz average spill rate with muon spills that comprises sequences of four consecutive 700 μs spills with 11 ms spill-separations. It must handle the readout, processing and storage of the raw data rates from the twenty four calorimeter stations, two tracking station, and the auxiliary detector systems

During normal data taking at 12 Hz spill rate, the time-averaged data rate of raw calorimeter ADC samples will be 340 MB/s per individual station and 8.2 GB/s for all twenty four stations. Overall – to achieve both manageable rates and reasonable volumes of stored data – the data processing by calorimeter frontends must achieve at least a 100-fold compression of continuously-digitized ADC samples into T-/Q- and other method datasets. During normal data taking at 12 Hz spill rate, the tracking system raw data rate is expected to be roughly 2 MB/s. and the auxiliary detector systems raw data rates are expected to be roughly 3 MB/s.

The experiment will require the Fermilab data storage facilities to handle a sustained data rate of up to 80 MB/s during the operating periods of the g-2 experiment. Based on about one year of total running time, the experiment will require a permanent data storage capacity from Fermilab data storage facilities of 1-2 Petabytes.

21.0.14 Alternatives and value engineering

The collaboration considered two alternative data acquisition frameworks: the CODA DAQ package that is used at JLab and the Art-DAQ framework that is under development at Fermilab. One advantage of using the MIDAS is that collaboration members have already developed very similar DAQ architectures with the MIDAS framework for other experiments. The g-2 DAQ can therefore profit from the software/hardware development for the earlier experiments. Another advantage of MIDAS is the availability of an extensive range of DAQ tools including an event builder, an analysis framework, a slow control system, a data alarm system, data storage and database tools, as well as large collections of device drivers for readout hardware. MIDAS has a active community of software developers and is widely used at numerous nuclear and particle laboratories.

Several alternatives were considered for processing the raw calorimeter data into T-, Q- and other method datasets. In particular, the collaboration considered the possibilities of deriving the T-/Q- method datasets at either the software level in the frontend processors or the hardware level in the digitizer FPGA electronics. An advantage of the software implementation is the greater flexibility to modify or add new datasets as needed during the design, commissioning and running phases of the experiment. An advantage of the firmware implementation is the lower data rates from the readout electronics to the frontend processors.

Different architectures and parallelization schemes were also considered for the calorimeter frontend processors. In one parallelization scheme using multicore CPUs the frontends process individual spills in separate CPU threads in order to achieve the necessary data compression bandwidth. In another parallelization scheme using many core GPUs the frontends process individual samples in separate GPU threads in order to achieve the necessary data compression bandwidth. The GPU-based approach is better suited to paralleling the tasks involved in deriving T-/Q-method datasets and takes advantage of standard algorithms for such operations.

Two different NVIDIA GPU architectures – the newer Kepler architecture and the older Fermi architecture – will be evaluated for the frontend processors. The Kepler architecture may permit faster data transfer between the CPU and the GPU and thereby improve the rate performance for data compression.

In addition to T-/Q-method data compression we plan to evaluate the loss-less compression of digitizer data using standard libraries (*e.g.* ZLIB library [6]). For continuously-digitized ADC samples that consist of occasional pulses the loss-less algorithms should offer efficient compression.

21.0.15 ES&H

The components of the data acquisition do not involve either hazardous materials or unusual electrical / mechanical hazards. The system will comply with standards fur use of power strips and will require appropriate temperature, humidity and air velocity sensors.

21.0.16 Risks

The largest risk in the data acquisition system is the corruption or the distortion of the positron time spectra (the calorimeter readout involves computation of derived T-/Q-method datasets from continuously digitized ADC samples). Another risk is delays in the software development of the data acquisition that would impact schedules for detector commissioning and data taking. A further risk is insufficient performance of the data acquisition hardware/software that would impact rates of data accumulation during running periods. The DAQ is assembled from commodity computing hardware so procurement and delivery is not a risk.

21.0.17 Quality Assurance

Kentucky has established a test stand for DAQ development, testing and quality assurance. Our first stage of prototyping for calorimeter readout and event building is underway using simulated data. A second stage of prototyping will begin this summer with the acquisition of micro-TCA crate with MCH/AMC13 cards and continue this fall with the acquisition of a single prototype digitizer. Other DAQ groups at UIUC and Oxford will also establish test stands for DAQ development, testing and quality assurance for the tracker readout and the DAQ control system.

An important milestones for DAQ development is a single calorimeter test run planned for SLAC in spring 2014 and a tracker sub-system test run planned for Fermilab in fall 2013. Stress tests and integrity tests of the DAQ components will be conducted using the test stands at the various institutions. Software and support will be provided to other institutions responsible for readout electronics and detector systems.

21.0.18 R&D

The collaboration has conducted a number of R&D projects to test the design components. In particular, a number of R&D projects were conducted on the hardware / software implementation of the: (i) frontend processing of raw calorimeter ADC samples into T-/Q-method datasets, (ii) event builder tasks of event fragment matching and event fragment assembly, and (iii) coordination between the accelerator-controlled spill cycles and the the computer-controlled readout cycles. In addition, a DAQ system was developed for beam tests of calorimeter prototypes and evaluation tests of waveform digitizer systems.

The MIDAS-based DAQ platform for R&D projects is shown in Figs. 21.3 and 21.4. It comprises a network of three frontend processor and one backend processors. The backend processor hosts the MIDAS server process MSERVER that manages inter-process communications, the MIDAS web daemon MHTTPD that provides run control, the MIDAS event builder MEVB, as well as MIDAS data storage and analysis tools. Frontend processor FE01 comprised two quad-core Intel Xeon X5550 CPUs and a 1024-core, NVIDIA Tesla C1060 GPU. A calorimeter emulator in that enabled processor FE01 was used for development work on GPU-based T-/Q-method processing of continuously-digitized ADC samples. A GbE interface to two 12-bit, 500 MHz Struck SIS3350 waveform digitizer modules [4] was used for both DAQ development work and prototype calorimeter tests. Another frontend processor FEMB was connected to a XiLinx FPGA-based programmable pulser and used to emulate the accelerator-defined spill cycles. Another frontend processor FEMB was used for the synchronization between the spill cycles and the readout cycles. The platform was arranged as a local network of disk-less, frontend processors with a backend server.

Fig. 21.5 shows a typical spill of simulated data – *i.e.* $3.5{\times}10^5$ ADC samples of 700 μs continuous-digitization – that was Monte-Carlo generated by the calorimeter emulator. In building streams of ADC samples, the decay positrons were generated with the appropriate energy-time distributions for 3.094 GeV/c decays and the calorimeter hits were generated with appropriate x-y distributions and pulse shapes. The raw data were "read out" and processed into T-/Q-method datasets in the DAQ frontend layer and then analyzed and histogrammed in the DAQ analysis layer. Representative plots of T-method energy and

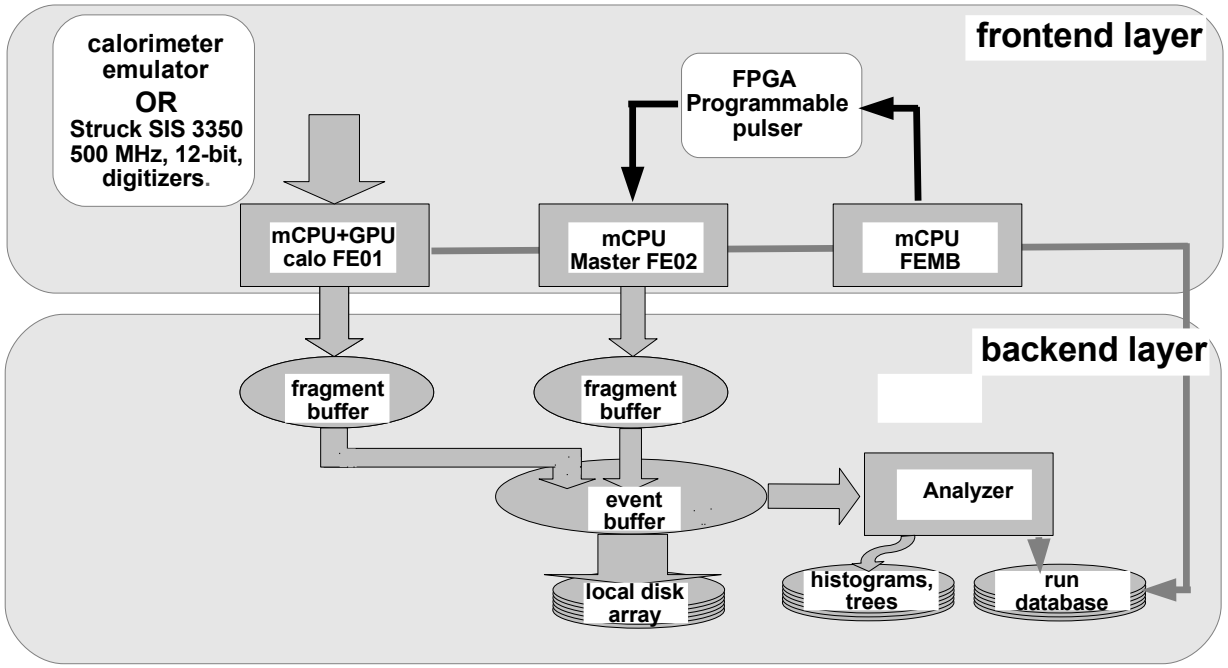

Figure 21.3: Layout of MIDAS-based DAQ-platform for R&D projects. The frontend FE01 incorporates both readout of emulated continuously-digitized ADC samples from a calorimeter simulation thread and real continuously-digitized ADC samples from a Struck SIS3350 digitizer system. The frontend FEMB emulates the Fermilab accelerator control signals and the frontend FE02 provides the software synchronization of spill-by-spill readout. The system also includes an event builder layer and data monitor layer.

time distributions of decay positrons are shown in Fig. 21.6.

Results from frontend timing tests of the GPU-based, T-/Q-method processing of the simulated calorimeter data are shown in Fig. 21.7. After completing the read out of each spill of ADC samples the raw data are transferred from the CPU memory to the GPU memory. The GPU then initiates a sequence that involves: derivation of the segment-summed calorimeter samples from the individual crystal segment samples, identification of the T-method above-threshold pulses in the summed calorimeter samples, assembly islands of the T-method above-threshold islands with pre-/post-samples, and transfer of the resulting T-method data from the GPU memory to the CPU memory. Additionally, a Q-method dataset was constructed by summing consecutive blocks of 32 ADC samples of digitizer data and then copied from the GPU memory to the CPU memory. Finally, the T-/Q-method

Figure 21.4: Photograph of the DAQ test stand at the University of Kentucky,

datasets are packaged into MIDAS databanks and transferred to the backend layer.

Also conducted were timing tests of event building on simulated databanks in the backend layer of the data acquisition. The tests showed the rate limitations in event building were largely governed by memory copy operations during event fragment assembly. For the backend processor in the R& platform – a six core, Intel i7 processor with 8 GBytes of high-bandwidth DDR3 memory – the DAQ was able to handle a 80 MB/s data rate of event building without introducing time delays.

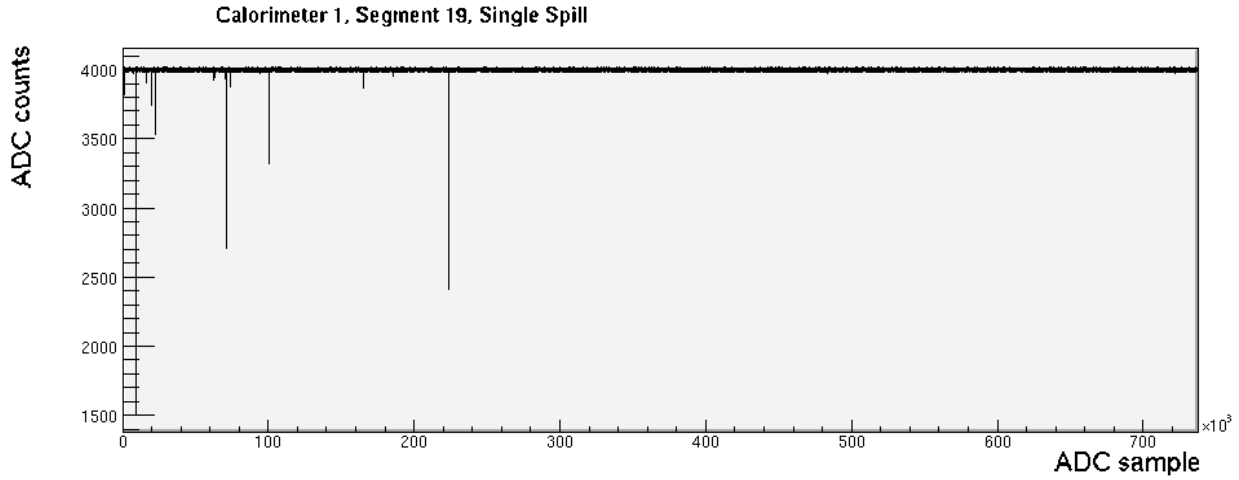

Figure 21.5: A representative single spill of simulated data generated by the calorimeter emulator. The data correspond to 3.5×10^5 ADC samples of 700 μs continuous-digitization for one segment of one calorimeter.

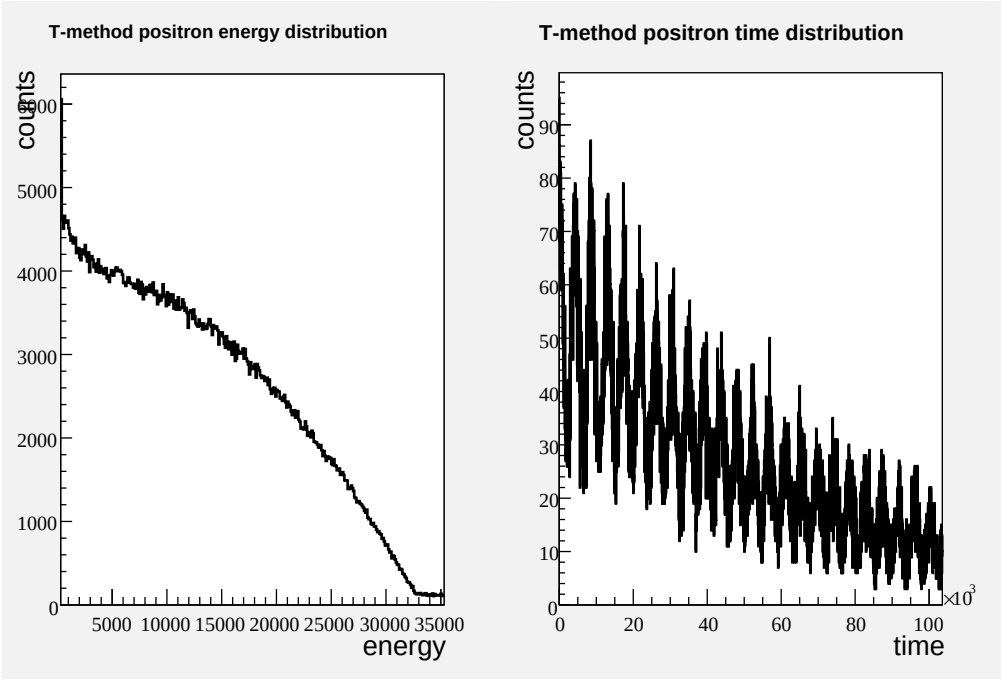

Figure 21.6: Energy distribution (lefthand plot) and time distribution (righthand plot) of energy / times of positron hits. The data were generated as continuous-digitization spills by the calorimeter emulator, were processed into T-Method datasets in the calorimeter, and histogrammed in the analysis layer. The energy distribution shows the positron endpoint energy and the time distribution shows the anomalous precession frequency.

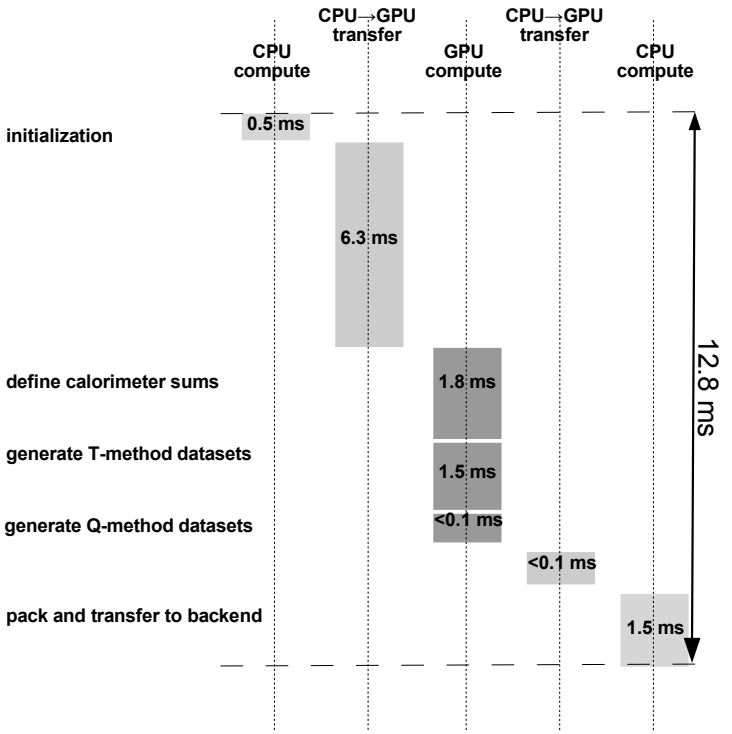

Figure 21.7: Schematic diagram of frontend processing of T-/Q-method datasets from simulated data of continuously-digitized ADC samples.

References

[1] V. Tishchenko, S. Battu, S. Cheekatmalla, D. B. Chitwood, S. Dhamija, T. P. Gorringe, F. Gray and K. R. Lynch *et al.*, Nucl. Instrum. Meth. A **592**, 114 (2008) [arXiv:0802.1029 [nucl-ex]].

[2] E. Frlez *et al.*, Nucl. Instrum. Meth. **A526** (2004) 300; see also http://midas.psi.ch/.

[3] Rene Brun and Fons Rademakers, Nucl. Instrum. Meth. **A389** (1997) 81; see also http://root.cern.ch/.

[4] Struck Innovative System, Harksheider Str. 102A, 22399 Hamburg, Germany; see also http://www.struck.de/.

[5] For example see http://www.spectracomcorp.com/ProductsServices/TimingSynchronization, Spectracom Corporation, 1565 Jefferson Road, Suite 460, Rochester, NY 14623.

[6] D. A. Huffman, Proceedings of the Inst. of Radio Engineers, **40** (1952) 1098; see also http://www.zlib.net/.

Chapter 22

Slow Controls

22.1 Overview and general requirements

The g-2 muon storage ring experiment is a complex system that involves many subsystems for which adequate sensoring and control during normal operation is required. The purpose of the slow controls and its data acquisition system is to set and monitor external parameters such as (high) voltages, currents, gas flows, temperatures etc. These tasks are essential for operation of the experiment over many months of data taking. The immediate online feedback allows to monitor the quality of the incoming data and react to changes in the running conditions. In addition, some of these variables can be extremely helpful in understanding trends in the analysis and relate shifts in the main observables to the change in running conditions. For example, unprecedented gain stability via precise control of bias voltages for the silicon photo-multiplier readout of the electron calorimeter is required to meet the systematic error budget for ω_a. While the gain stability of these photo-detectors will be monitored at the 10^{-3} level or better via a dedicated laser calibration system, immediate feedback on the two parameters (bias voltage and temperature) determining the gain of these devices is achieved via such continuous monitoring. There are plenty of other cases where such external parameters will be useful in this high precision measurement to establish a full understanding of all systematic errors.

For setting and read-back of parameters, the slow control system must provide sufficient sensors or control units which will either be directly integrated into the design of new subsystems or come as external devices. Most of these systems will connect to the slow control DAQ via the Midas Slow Control Bus (MSCB) which is a cost effective field bus developed at the Paul Scherrer Institute (PSI), Switzerland. This very mature system has been successfully employed in other similar experiments and allows for easy integration into the envisioned data acquisition framework MIDAS. The slow control DAQ will also include communication interfaces to other external systems like the main g-2 storage ring controls (iFix) and the Fermilab accelerator over ACNet to allow for the exchange of data. Other external devices like the μTCA crates for the readout electronics of the electron calorimeter will need to be interfaced as well as to monitor their operational status.

The demand and read-back values for all parameters controlled by the slow control system need to be stored in a convenient database such as MySQL or PostgreSQL. While a local copy

of the data will be available for online monitoring and analysis, the copy will be transferred to a Fermilab database server for long-term storage. For efficient usage of the read-backs during data taking, user friendly visualization tools have to be provided in order to easily access the stored database information. A web browser based framework will be developed to display the large amount of different channels monitored by the system. Such script based tools are easy to expand and offer an interface for users without the need of installation of special software tools.

Critical subsystems of the detectors might require special handling in case of unsafe running conditions. A stand-alone alarm systems will provide necessary interlocks and other measures for such situations. For example, the gas flow of the straw tracker will be monitored and shutdown in case of flow read-backs that are out of a specified normal range. Other critical systems like the cryogenic and vacuum controls of the g-2 ring will be embedded in a special PLC system. In the current design, no direct communication between the two systems has been designed but it is anticipated that the two systems might be interlinked. The alarm system within the slow control system will provide all measures in case of unsafe running conditions to comply with possible regulations.

22.2 Recommended Design

22.2.1 Software and hardware architecture

The slow control will comprise a variety of sensors and control units described in more detail in the following section. Some of these systems will be purchased as single units (like power supplies) and interfaced via serial or parallel standard (like RS232, GPIB). Other subsystems will be custom-built and their design requires integration of an appropriate slow control interface. The usage of field buses like CAN, Profibus and LON are not justified as their integration requires significant effort. Instead, we will employ the Midas Slow Control Bus (MSCB, http://midas.psi.ch/mscb) which is a field bus developed at PSI. This system was optimized for the environment of a typical physics experiment and cost-efficiency (typically $20 per node). In addition, it conveniently integrates into the MIDAS data acquisition (http://midas.psi.ch) which is the basic design choice for the slow control computing infrastructure.

The MSCB as a mature system will be the default choice for all sensors and control units that are custom built for the g-2 experiment. The MSCB is based on the RS485 protocol which is similar to RS232 except for employing differential signals for superior noise immunity. RS485 is a multidrop half duplex so that many nodes can be connected to the same bus but only one can send data at a time. Hence, a single submaster can facilitate the communication between the MIDAS host computer and up to 256 individual MSCB nodes. In fact, by employing a layer of repeaters up to 65536 nodes can be operated on a single bus with up to a few km long cables. The MSCB requires two signal wires for the differential signal and a ground wire. Three additional lines provide power ($+5\,\mathrm{V}$, $\pm 12\,\mathrm{V}$). The usage of a 10-wire flat ribbon cable provides four additional digital lines for application specific usage. Figure 22.1(a) shows one of the available submasters that can be purchased from PSI. Given the simple MSCB protocol, a typical node remains relatively compact like for example the

SCS100 shown in Fig. 22.1(b) that contains DACs, ADCs and an integrated temperature sensor for the on-board micro-controller. For g-2 specific applications, the development of new nodes is a viable option which we will employ for some systems in the g-2 setup (e.g. the bias voltage module for the electron calorimeter). The alternative is to purchase the more integrated SCS2000 unit with appropriate MSCB daughter cards for various applications. This possibility will be explained in more detail in the section 22.2.2 below.

(a) MSCB ethernet submaster

(b) SCS100 MSCB node with DACs, ADCs and integrated temperature sensor.

The MSCB protocol is byte oriented and uses the bit 9 from RS232 for addressing purposes. As this bit usually cannot be switched on and off fast enough in the UART of a PC, simply using RS232-RS485 converters is not sufficient. This can be overcome by employing a submaster on the computer side with a micro-controller to provide the handshake with the PC and enough memory to avoid data loss. In this scheme, bit rates of up to 345600 baud are sustainable.

As mentioned before, the MIDAS software framework will be used for the slow control data acquisition computer(s). Straightforward integration of MSCB based hardware is already provided by appropriate drivers integrated into the software package. The end user has to provide an application specific frontend module to control the specific sensor or control unit, i.e. to set and readout parameters of the hardware system. Setting of the parameters such as detector voltages or the readout rates of sensors are handled by corresponding settings in the online database (ODB) on the slow control computer. A backend main server will handle the collection of the readout data with an adapted event builder provided in the MIDAS software. The assembled MIDAS events from all slow control subsystems are then handed off to a data logger module which will store the data in an SQL based database locally as well as transfer it to the Fermilab long-term storage server.

Figure 22.1 shows the basic layout of the slow control system in the g-2 experiment indicated by the solid colored boxes. A single slow control backend host (brown box) manages the communication with all MSCB nodes (blue boxes) via the MSCB submaster (green box). Non-MSCB based sensor and control nodes (purple boxes) will communicate directly with the backend server via appropriate interfaces (e.g. USB, RS232, ...). During the development

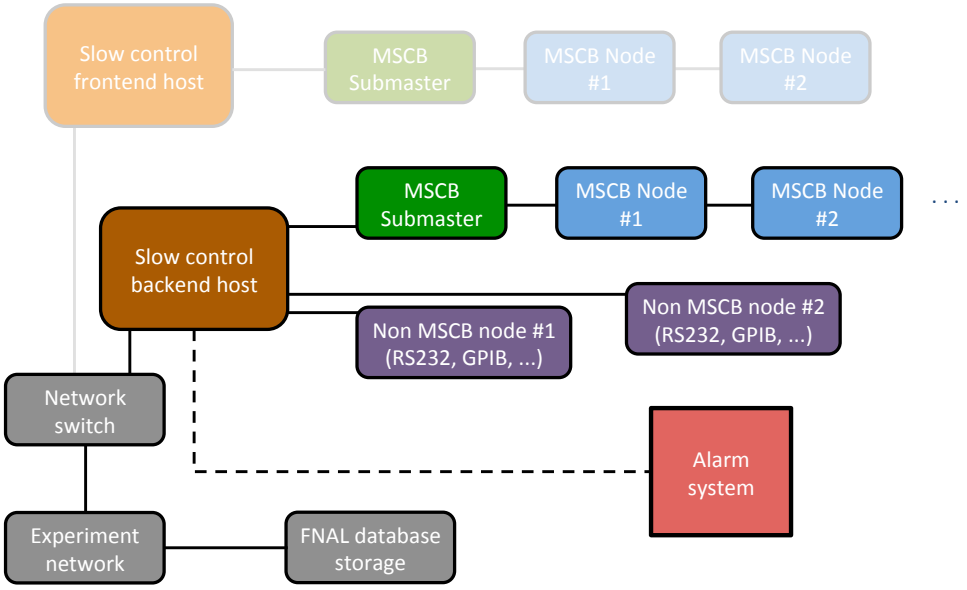

Figure 22.1: Slow control system for the g-2 experiment: The basic layout includes a backend host (brown box) which manages the communication with all MSCB nodes (blue boxes) via the MSCB submaster (green box). Non-MSCB nodes (purple boxes) directly connect to the backend via the appropriate interface (USB, RS232, ...). Lightly shaded boxes refer to possible frontend computer(s) with their own MSCB bus and nodes for dedicated applications which would communicate and exchange data with the backend server via ethernet network. The stand-alone alarm system (red box) will provide adequate measures to handle unsafe running conditions.

phase of the g-2 experiment, we expect several institutions to setup their own MIDAS and MSCB host computers for testing of individual components (e.g. the MSCB interface for the SiPM bias voltage control). Although a single main PC and submaster would be sufficient to handle all MSCB nodes in the g-2 experiment, these additional available host computers with their MSCB submaster and nodes could be easily integrated into the slow control system. Therefore, the final implementation in E989 might involve additional MSCB frontend hosts to control special subsystems as indicated by the light shaded chain of boxes in Fig. 22.1. Data exchange between a frontend computer and the slow control backend computer happens via ethernet network. This scheme adds redundancy to the system in case of maintenance or failure of one of the computers since MSCB nodes and their appropriate MIDAS software frontend can be easily moved from one to another computer. The system is completed by a stand-alone alarm system (red box) to provide appropriate actions in case of unsafe operating conditions of various subsystems.

In the following subsection, we will describe the sensors and control units, their requirements and the institutional responsibility. Thereafter, the conceptual design of the alarm system, the backend server and the data storage are outlined.

22.2.2 Sensors and controls

The g-2 experiment will employ a variety of systems to facilitate the overall measurement of the muon anomalous magnetic moment. Figure 22.2 displays the current required functionality for a variety of systems (as depicted by the individual nodes). Solid boxes denote systems that are currently known to have direct interfacing to the slow control whereas lightly shaded nodes are currently interfaced by the fast calorimeter DAQ system (see 21).

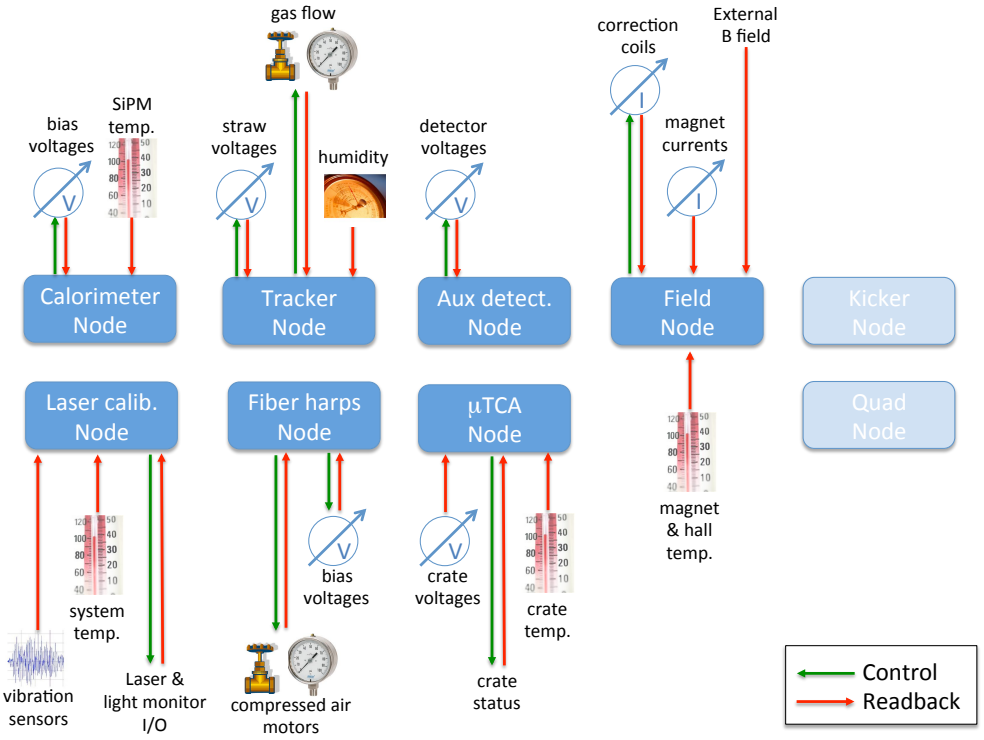

Figure 22.2: Schematic breakdown of the individual slow control nodes with individual control of parameters and sensor read-backs. More details are given in the text.

The corresponding table 22.1 lists the actual parameters set and monitored via the slow control. The read-back precision, rates and channel counts are preliminary estimates as far as they are known today and will be subject to change with advancing design of each system. The photo-readout of the electron calorimeter for the spin precession frequency will be based on silicon photo-multipliers (see section 17). The design incorporates a surface mount SiPM on a readout board integrating the bias voltage supply and an amplification of the readout signal. Since the experiment requires high gain stability, a stabilization and monitoring of the two external parameters that determine the SiPM gain, namely the bias voltage and temperature, is required. While the bias voltage of each SiPM channel is set and monitored separately for each channel, the temperature sensors will only be placed at a few locations inside each calorimeter station. The associated laser calibration system which monitors absolute gain changes will require a monitoring of the laser and light distribution system's temperature at several locations. Due to the usage of diffusing spheres for the laser

distribution and their sensitivity to small mechanical movement, a vibration monitor is most likely needed during operations. It would consist of a 3-axis inclinometer and be integrated over a second so that readout rates of the order of less than 1 Hz are required. In order to control and enable the system, a few I/O channels will be necessary. Depending on the final implementation of the laser system, somewhere between 2 and 48 channels for each input and output are necessary. Finally, some of the available lasers under consideration have a serial (USB, RS232) interface to control and read-back the laser status.

The tracker system comprises two stations of in-vacuum straws located in two scallop regions. The slow control will provide readings for ambient temperature, humidity, and pressure at the two locations. It will also monitor the gas flow and temperature as well as currents and high voltages for the 36 individual substations. The system will provide the setting of the high voltage demand values as well as their read-backs. The stand-alone alarm system (see section 22.2.4) will provide interlocks for immediate shutdown of gas and HV in case of irregular running conditions.

Table 22.1: List of control and read-back parameters in g-2 handled by the slow control unit with anticipated read-back precision and rates, channel counts and the institutional responsibility for the implementation of the actual devices.

Parameter	**Read-back precision**	**Read-back rate**	**Channel count**	**Responsibility**
Calorimeter				
SiPM bias voltage	∼mV	0.1 Hz	1300	UVa, JMU
preamp voltage	0.1 V	0.01 Hz	24	UVa, UW
SiPM temperature	0.1° C	0.1 Hz	∼ 75	ANL, UW
Laser calibration				
Laser temperature	< 0.5 °C	< 1 Hz	< 10	INFN, ANL
Vibration monitor		< 1 Hz	∼ 10	INFN
Output signals (enable)			< 48	INFN
Input signals			< 48	INFN
Serial laser interface	–		< 10	INFN
Tracker				
Voltage	∼ 1 V	< 1 Hz	36	FNAL
Current		< 1 Hz	36	FNAL
Amb. pressure		< 1 Hz	2	FNAL, ANL
Amb. temperature	< 0.5 °C	< 1 Hz	2	FNAL, ANL
Amb. humidity		< 1 Hz	2	FNAL, ANL
Gas flow		< 1 Hz	36	FNAL
Gas temperature		< 1 Hz	36	FNAL
Fiber harps				
SiPM bias voltage	few mV	0.01 Hz	2	Regis
preamp voltage	0.1 V	0.01 Hz	2	Regis
SiPM temperature	0.1° C	0.1 Hz	4	ANL

Table 22.1 – *Continued from previous page*

Motor control	-	-	4	Regis, ANL
t_0 & flashlet counter				
PMT HV	~ 1V	0.01 Hz	2	Regis
General				
Yoke temperature	$< 0.5\,^{\circ}$C	< 0.01 Hz	~ 20	ANL
Hall temperature	$< 0.5\,^{\circ}$C	< 0.01 Hz	~ 5	ANL

The fiber harp detectors will be equipped with high and low voltage power supplies that have some serial interface for the communication so that remote control and readback of the voltages is possible. As the SiPMs for the readout of the fibers are grouped in 4 rows of 7, we anticipate monitoring the SiPM temperatures with one probe per row so that four sensors are required. As the fiber harps are rotated into the beam by compressed air actuators, 2 control channels and readbacks of these must be available.

The auxiliary detectors node in Fig. 22.2 includes all future additional counters that might be added to the g-2 setup. At this moment, it only comprises the so-called t_0 flashlet counter which is a scintillator paddle with standard PMT readout that requires a single channel HV power supply with a serial interface for remote communication.

The μTCA node comprises the communication between the slow control DAQ and the μTCA crates via the Remote Management Control Protocol to monitor the status of each crate. As we are mainly reading status parameters provided by the crate, most likely no additional sensors will be required. Some more details about this communication interface will be covered in the following section 22.2.3.

The field node in Fig. 22.2 includes possible readouts of the main magnet and the correction coil currents as well as external fluxgate monitors. While these readbacks will be recorded, they are currently not explicitly listed in Table 22.1 since it is most likely that these are stored by the DAQ for the fixed NMR probes.

Many of the systems described above include temperature readout channels. In addition, we will monitor the ambient hall and magnet yoke temperatures at approximately 25 additional locations. Since changes in the magnet temperature are the main driver for changes in the field homogeneity, a monitoring of the temperature will allow detection of any irregular temperature trends which could be caused by a deterioration of the magnet insulation. Overall, we expect a total of $\sim$100 temperature probes with a readback precision of at most 0.1° C. Since we are mostly sensitive to temperature changes, the absolute accuracy is of less importance. For the implementation of these temperature sensors, we plan to use the available general purpose SCS2000 unit[1] shown in Fig. 22.3(a). The SCS2000 provides the MSCB communication over Ethernet via the MSCB submaster with the PC. The unit has an on-board programmable logic device (CLPD, Xilinx XC2C384) which handles the MSCB protocol on one side. On the other end, there are slots for 8 independent MSCB daughter cards which are each accessed by the CLPD via a 2-lane SPI and a parallel 8-bit bus. The available daughter cards come with a multitude of different functions. Examples are shown in

[1] At the time of the expected purchase, the successor SCS3000 will be available which provides the same functionality but adds a graphics display for direct user interaction and immediate status feedback.

Fig. 22.3(b) and the complete set of these daughter cards comprises functions like standard I/O channels, 24-bit ADCs, current sources, valve controls, and many more. This system is successfully employed in the MEG experiment at PSI and therefore, the set of typical slow control functionality is available. Because the MSCB protocol and communication is handled by the central CPLD in the SCS2000, the layout of the daughter cards is pretty simple and the whole package offers a relatively cost-efficient solution. For the above mentioned ∼100 temperature channels, we plan on using an existing 8-channel temperature daughter card based on the Analog Device AD590 2-terminal temperature transducer. Since each channel senses the current in the AD590, long cables of more than 10 m can be used so that the SCS2000 unit(s) may be located at the center of the ring. Unused card slots in the two SCS2000 can be used for additional other functionality.

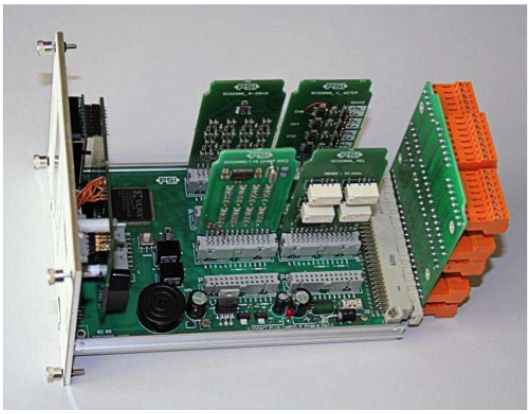

(a) SCS-2000 general purpose control unit.

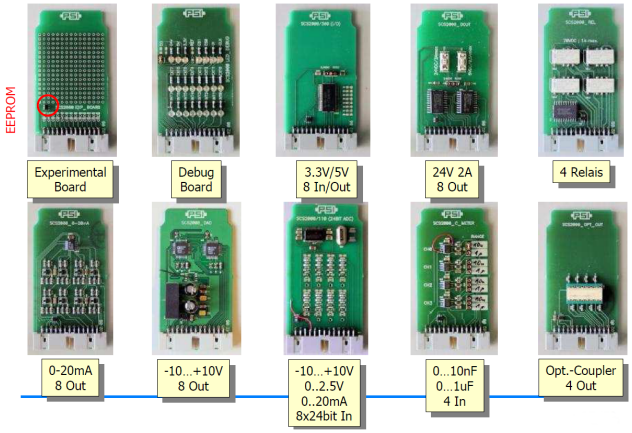

(b) Examples of available SCS200 daughter cards.

Figure 22.2 also shows two nodes (Kicker and Quads) in a lighter color indicating that these are currently not foreseen to be integrated into the slow control system. Since both systems operate at the frequency of the muon injection, the readback of these is handled by the fast DAQ (described in section 21) which has fill-by-fill synchronization. This scheme eliminates the need for a precise timestamp synchronization of the slow control DAQ with the muon fills.

22.2.3 Communication with external systems

The slow control DAQ will not only retrieve data from the various sensors described above but also communicate with other systems in the g-2 experiment and the Fermilab accelerator infrastructure. As of now, there are a total of three such systems. Communication will need to be established with the main ring control system, the Fermilab accelarator complex, and the μTCA crates for the readout of the electron calorimeter stations. In the following we will shortly describe some more details about the three communication methods to the extent relevant for the conceptual design of the slow controls.

The ring control system for the cryogenics and vacuum is based on PLC interfaces which are accessed via the human machine interface iFix. Figure 14.1 shows the schematic layout for this complex system. As can be seen in the figure, the communication path (thick double

arrow) between the iFix server (bottom left rectangle) and the slow control computer (bottom middle computer labeled "Physics DAQ system") will be facilitated via an OLE for Process Control (OPC) server integrated into iFix. The communication on the slow control DAQ side is handled by an OPC client which is available as commercial or open-source products for the Linux based system.

During the g-2 operation, some parameters of the accelerator (like magnet currents, beam intensities, status of other beam elements) will be stored in the output datastream. This information can be retrieved via a data broker from the accelerator network (ACNet). Retrieval of accelerator related parameters is already implemented at Fermilab in the larger context of a beam database for the intensity frontier experiments (IFbeam) and we will be able to benefit from this existing implementation by adapting it to our needs and software infrastructure. The data is usually stored in PostgreSQL format and can be integrated into our experimental condition database.

A third system that we want to establish communication with are the μTCA crates for the readout of the electron calorimeters and possibly other electronics in the experiment. These crates typically provide internal status parameters (e.g. temperature, fan speeds, error indicators etc.) that are useful to monitor to quickly identify hardware problems or failures. System management and monitoring is achieved by means of software solutions based on the Intelligent Platform Management Interface (IPMI), a standardized computer system interface. A variety of user interfaces can be employed such as web-based GUIs or programmatic interfaces. The latter comprise the Simple Network Management Protocol, an industry standard and the Remote Management Control Protocol (RMCP) which supports the IPMI commands over IP. For now we anticipate establishing an RMCP based client on the slow control side to establish the required monitoring and communication with these central electronics infrastructure in the g-2 experiment.

22.2.4 Alarm system

A stand-alone alarm system will serve the purpose of allowing quick and safe shutdown of certain elements of the g-2 detectors. Similar functionality via the slow control software by changing the demand values of high voltages or a valve status is typically not immediate and for some components of the experiment, the availability of hardware interrupt is preferable. It should be noted that there will be a separate PLC based system handling the more critical components like the cryogenics of the magnet as well as vacuum controls. The system described here will deal with detector components which are not critical in the sense of life threatening unsafe conditions. The interrupts provided by the alarm system are mainly for protection of the detector components and other systems. While this functionality will ideally be unused during operations, it could be beneficial of having such a system readily available in case of unforseen changes in the experimentl conditions.

At this moment, we plan to provide hardware interlocks for the high voltages and the non-flammable gas for the straw detectors which are located inside the vacuum. Scenarios necessitating shutdown of voltages and gas flow could be vacuum leaks in the ring vacuum chambers, overheating or high fluctuations in the straw current that could indicate a developing problem. An interlock for the laser calibration system might be useful to protect the system in case of overheating or other abnormal parameters. Similarly, hardware interlocks

for the SiPM bias voltages could be provided in the same scheme if the request for it arises.

Given the experience with other similar experiments, such an alarm system typically is expanded over time because additional useful interlocks are identified during the design, testing and implementation of detector systems. Therefore, we will adopt a simple basic concept using relays for the various interlock mechanisms. Figure 22.3 shows the schematic design for the system. Components that form a group and are interlocked at the same time will be connected to their own relay (Double Pole Double Throw type). The relay's actuator for such a group is triggered by different sources like the backend computer or a direct hardwired signal. For example, the straw tracker gas flow and high voltage system might be shutdown if the vacuum exceeds a defined threshold. As the vacuum control and readback happens in the PLC, the actuator trigger might come directly from an output channel of the PLC system (see section 14). On the other hand, an interlock of the laser system might only be required if the readback temperature of this system rises above a threshold. As this presumably is a slow process and not time critical, the interlock signal can come from the slow control computer monitoring these temperature readbacks.

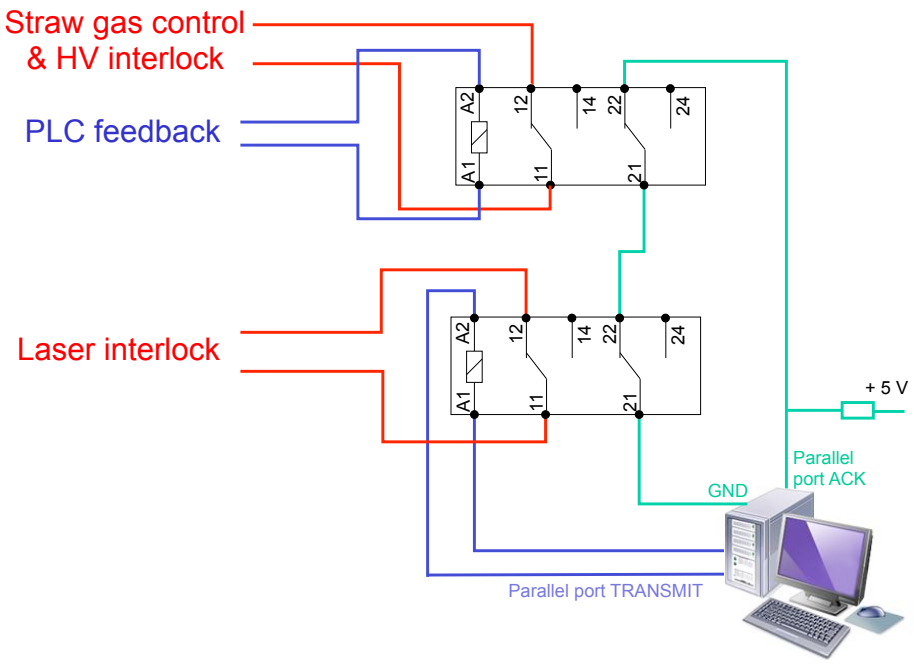

Figure 22.3: Basic conceptual design for the stand-alone slow control alarm system with two examplary interlock groups (straw detector and laser).

The interlocks for each groups are actually activated by the first internal relay switch (contacts 11, 12, 14). The second relay switch (contacts 21, 22, 24) can be used to form a serial loop monitored by the slow control computer's parallel port (acknowledge channel). A triggered actuator of any of the serialized relays would then trigger an alarm on the computers in the g-2 control room. Depending on the criticality of each system, a triggered relay interlock might also include to set off an alarm siren and flashing light. The details of these alarm feedbacks have to be decided for each system. If necessary, one can setup multiple computer feedback loops by adding parallel port interfaces. The concept is very

modular and easily expandable.

It should be noted that the basic concept will be based on the underlying general layout that systems need positive approval (i.e. a running computer, powered PLC system etc.) in order to be functional.

22.2.5 Backend server

The backend server is the central computer in the slow control DAQ to communicate with the various control units and sensors and retrieve all readbacks. Since data rates on the slow control backend server are low (less than 1 MB/s), a standard modern Linux desktop is sufficient. It should provide enough interfaces (RS232, USB, MSCB) for the external devices. As mentioned above, we will work within the MIDAS software framework to coordinate the different tasks. The various sensors and controls can be accessed individually by independent frontend programs which run in parallel within the main MIDAS server. Each frontend has its specific functionality to set experimental parameters (like high voltages for each SiPM), readback parameters, and allow to change readback rates. For MSCB devices, the necessary hardware drivers are provided by MIDAS so that the actual implementation of the frontends is simplified. For other hardware connecting to the backend over RS232 or USB, MIDAS also includes software components that will make integration of these subsystems into the slow control easier. Such frontend code has been developed previously like for the MuLan and MuCap experiments at PSI by some of the current E989 collaborators. Therefore, the implementation of the various frontends for all sensors and controls should not pose a major effort.

22.2.6 Data storage and access tools

For the data storage of slow control parameters, we will use a SQL-based database format (MySQL or PostgreSQL). While MIDAS has already built in options for MySQL handling, Fermilab's preferred choice is PostgreSQL which is the current anticipated choice for E989. Integration of PostgreSQL capabilities into the MIDAS framework should be feasible without too much additional effort. The backend server will have standard ethernet network connection(s) for the communication with external systems (see section 22.2.3) and synchronization of the local database with the remote long term storage at Fermilab. We will employ the automated script-based mechanisms developed at Fermilab for this purpose. Overall, the database handling and storage is expected to nicely integrate into the existing infrastructure.

Any data acquisition requires a well designed interface for the online monitoring and during the offline analysis. For example, a user friendly visualization interface to inspect the large number of different channels (the calorimeter alone has 1300 channels) is very essential during data taking. Based on past developments for muon precision experiments at PSI and current other Intensity Frontier experiments at Fermilab, we will have a variety of options to establish such tools. The IFbeam software tools incorporate the python based Web Server Gateway Interface and subsequent Google Charts to access and display database information in the web browser. The experiments at PSI, MuLan and MuCap, used custom developed web browser based tools to query and display the database information as well as standalone graphics displays within the ROOT framework. At this point, it is not clear

which exact tools we will use for E989. In general, usage of a single tool will increase user friendliness but it could be advantageous to have optimized tools for various different data streams. However, the specific implementation will profit from extensive former experience which will guide the collaboration in making the final decisions in the future.

22.3 Alternative Design Considerations

The information recorded by the slow digitization DAQ is quite independent from any other DAQ system in g-2. Therefore, we have investigated the usage of alternative software packages like the ORCA system. The collaboration has used this system in the ongoing SiPM tests at UW in order to gain practical experience with this system. Another option is the EPICS software which is well supported at the Advanced Photon Source at ANL and at FNAL. However a careful comparison of the three systems has revealed that MIDAS is our best choice for the software framework for the slow control DAQ. Its major advantages are the fact that several of the g-2 collaborators have many years of experience with this system. It has been used successfully by a variety of experiments at PSI and other laboratories. We also have a good relationship with the main developers of MIDAS at PSI. Last but not least, synergies with the fast detector DAQ are obvious as it is based on the same framework. The amount of maintenance and debugging reduces and collaborators on shifts will only need to familiarize themselves with the subtleties of one system.

The default choice of the MSCB for hardware components is tightly connected to the decision for using the MIDAS framework as the latter has easy integration of MSCB components. In addition, the MSCB is optimized for cost efficiency. We have looked into the usage of more commercial products (e.g. National Instruments hardware with possible integration into LabVIEW) but such systems would simply increase the cost. In addition, some of our systems require custom built components (e.g. the extremely stable low voltage power supply for the SiPM) and therefore, we can profit from the simplicity of the MSCB protocol. Finally, the MIDAS and MSCB framework is very open and we have good connections to one of the experts of this system at the Paul Scherrer Institute, Switzerland. We are therefore confident, that development of new modules should be feasible with limited effort. It should also be noted, that we can still rely on non-MSCB off-the-shelf components if it turns out that they are an optimal choice to control or monitor some of our subsystems. Communication with such devices via typical standards of RS232 or USB is available within the MIDAS framework. Our default choice is therefore very modular and expandable but comes at a quite optimal cost.

The alarm system is based on a simple relay concept. There has been good experience with this concept in the muon capture experiment MuCap at PSI where it was used to interlock critical detectors in a similar way as proposed. The stand-alone design (i.e. separate form the main PLC-based control system, see section 14) has the advantage that we can operate detector systems separately which might be very useful during beam tests before the real data taking. However, while the design of the subsystems evolves, it might turn out that this basic concept is inadequate for some of our applications. In that case, we have the alternative to integrate the monitoring and interlock functionality into the PLC based system described in section 14. This will most likely require additional hardware in form of control

and sensor boards, i.e. more channels for the system. Due to the more complex nature of this system, the costs per channel are significantly higher than in the current default design and the implementation of this alternative was dismissed.

22.4 ES&H

The slow control system will involve sensor and control units that mainly need low voltages and currents for operations. If high voltages (like for the SiPM bias voltage or the PMT voltage) are involved, adequate protection (shielded cables, enclosed and fused electronic components) will be employed to comply with Fermilab's safety rules. The components for the slow control do not require any hazardous materials and there are no mechanical hazards since the components are typically small.

The alarm system included in the design of the slow control will mainly interlock non-critical components to prevent direct damage to the hardware. It does not include any life-threating hazards.

22.5 Risks

The default design of slow control relies on the mature MSCB system that has been successfully employed in several experiments. Therefore, there is only a small risk that components will not work appropriately to the specified requirements. Certainly, the exact design and implementation of the stringent bias voltage system for the SiPMs in the calorimeter is crucial in succeeding to meet the gain stability. This specific risk is considered in the calorimeter section (see Sec. 17). Other sensors (like temperature, voltage, currents etc.) are readily available and should be sufficient to meet the requirements in the E989 experiment. If not, a design of an appropriate component would require additional resources. Since the implementation of the MSCB nodes is pretty simple, the associated cost risk is rather small.

A failure in meeting the specified requirements for controlling devices and read back of performance parameters potentially causes an inability of detecting a loss in the data quality during the experiment. This could result in the necessity of dismissing data from the analysis and could result in the need of longer data taking to acquire the full statistics.

During the design phase of various subsystems, it could be found that the current design of the alarm system based on a simple relays layout is inadequate. Examples for such a diagnosis could be that the systems is not reliable enough, that it is not compliant with safety rules that require a more complex system to interlock detectors, that the response is not fast enough. In that case, we might need to integrate its functionality into the more complex PLC based main control system (see section 17). The probability for this risk is very low since we already have good experience with the current scheme from the muon capture experiment at PSI. However, if realized it would certainly increase the costs as we would need additional labor resources to transfer the functionality to the different system and come up with an adequate design. In addition, we would need to purchase necessary hardware channels to control, monitor and interlock the systems appropriately.

Any comnponents installed close to the precision magnetic field (especially electronics

circuits with time-varying currents) can cause a static or dynamic distortion to the homogeneity of the field and possibly decrease the precision in its measurement. Mitigation of this risk is achieved by using non-magnetic materials close to the field region and by testing all components for their magnetic properties in a 1.45 T test magnet and with special designed pickup coils for transient fields.

22.6 Quality Assurance

The implementation of the slow control system relies on well established software in form of the MIDAS framework. In addition, we will employ the very matured MSCB hardware whenever possible or purchase commercially available systems. Quality assurance measures are therefore mainly limited to verifying that custom-built sensors and control units meet the requirements that all systems work properly and comply with all safety regulations. We will extensively test individual components and the full system in dedicated bench tests before the final installation in the experimental hall. As outlined in the risks, these tests will include the verification of the stringent magnetic requirements for components installed in the vicinity of the precision magnetic field of the storage ring.

Since the slow control provides an online monitoring of the status of many systems in the g-2 experiment, care will be taken to properly design the appropriate visualization tools providing easy access to all parameters. This will be an important component in detecting any changes in the quality of the collected data during the experiment.

22.7 Value Management

The usage of freely available open-source MIDAS software and the specifically cost-optimized MSCB hardware is key in keeping the slow control systems overall cost low. Some components that cannot be readily purchased (like the SiPM bias voltage supply with its stringent requirements, see section 17.2.3) and need to be custom-built. Most of these will be designed and implemented by collaborators at universities and outside the US in order to keep the overall cost low. At the same time, the centralized integration of all components at Argonne will allow to verify the full system and detect any interference of different sensors or control units.

22.8 R&D

Necessary R&D for cutom-built components that will be integrated in the slow control system is performed by some of the collaborating institutions and will be described in the appropriate sections in this document. Examples for these are the SiPM bias voltage supply (section 17.2.3) or the laser calibration system (section 17.2.4).

Chapter 23

Simulations

Chapter 24

Search for the muon EDM, d_μ

24.1 Introduction

24.2 Straw Tube Array

24.2.1 The chambers

24.2.2 The readout electronics

24.3 Sensitivity

24.4 ES&H, etc

Chapter 25

Life Cycle Costs